

European Commission

Air pollution research report 83

European Conference on Aviation, Atmosphere and Climate (AAC)

Proceedings of an International Conference

Friedrichshafen, Germany, 30 June to 3 July 2003



Edited by

Robert Sausen, Christine Fichter and Georgios Amanatidis



The photograph for the AAC-Logo was provided by C. König (www.bvbk.de).

Foreword

The "European Conference on Aviation, Atmosphere and Climate (AAC)" in Friedrichshafen (Lake Constance, Germany) 2003 was initiated by the European Commission, Directorate General Research. The conference was organised with the objective of updating our knowledge on the atmospheric impact of aviation, four years after the publication of the 1999 IPCC Special Report "Aviation and the Global Atmosphere" and three years after the European workshop "Aviation, Aerosols, Contrails and Cirrus Clouds (A²C³)" in Seeheim, Germany.

During the recent years many European projects (e.g. AEROCHEM-2, TRADEOFF, PARTEMIS, MOZAIC, AERO2K, SCENIC, INCA) and many national projects have been devoted to increase our knowledge with respect to the topic of the AAC conference. Significant scientific progress has been achieved: the aviation impact on the atmospheric concentrations of ozone and methane and their uncertainties have been better quantified; a consistent quantification of the radiative forcing from linear contrails has been provided; the interaction between aerosols emitted by aircraft and clouds is now better understood; first quantitative estimates of the radiative forcing from contrail cirrus are now available; and we learned about mitigation of aircraft effects on climate.

Despite the progress made, many open questions remain. For instance, how large is the radiative forcing index for aviation, now that first estimates of the effect from contrail cirrus are available? How large is the aviation impact on atmosphere and climate compared with other modes of transport?

115 participants attended the AAC conference and there were 50 oral and 27 poster presentations. Extended abstracts of most of the presentations are included in this book of proceedings. Many of the papers will be revised and after peer review be published in a special issue of the journal *Meteorologische Zeitschrift*.

I am confident that the outcome of this conference will be useful for scientific community and other stakeholders. Sincere thanks are due to my colleagues G. Amanatidis, C. Fichter and R. Sausen for organising this important event.

Anver Ghazi
Head, Global Change Unit
Research DG, European Commission
Brussels

Programme Committee

Prof. Robert Sausen (chair), Deutsches DLR - Oberpfaffenhofen, Germany
Dr. Georgios Amanatidis, European Commission, Brussels, Belgium
Winfried Dewes, DLR-Buro Brussels, Co-ordinator AERONET, Belgium
Dr. Reiner Dunker, European Commission, Brussels, Belgium
Dr. Karlheinz Haag, Lufthansa German Airlines, Frankfurt, Germany
Prof. Ivar Isaksen, University of Oslo, Oslo, Norway
Prof. David S. Lee, University of Manchester, Manchester, United Kingdom
Paul Madden, Rolls-Royce, Derby, United Kingdom
Dr. Corinne Marizy, EADS, Toulouse, France
Dr. Patrick Minnis, NASA, Hampton, USA
Dr. Phillipe Mirabel, University of Strassburg, Strassburg, France
Dr. Helen Rogers, University of Cambridge, Cambridge, United Kingdom
Dr. Claudia Stubenrauch, Laboratoire de Meteorologie Dynamique, France

Table of Contents

Foreword	3
<i>Anver Ghazi</i>	
Programme Committee	4
Table of Contents	5
Conference Agenda	11
Engine Emissions and Plume Processes	
Novel Rates of OH Induced Sulfur Oxidation - Implications to the Plume Chemistry of Jet Aircraft	19
<i>H. Somnitz, G. Gleitsmann, R. Zellner</i>	
Determination of Soot Mass Fraction, Soot Density and Soot Fractal Character in Flame Exhaust Gases (PAZI)	25
<i>C. Wahl, M. Kapernaum, V. Krüger, P. Rainer, M. Aigner</i>	
Overview of Results from the NASA Experiment to Characterize Aircraft Volatile Aerosol and Trace Species Emissions (EXCAVATE)	27
<i>B.E. Anderson, E. Winstead, C. Hudgins, J. Plant, H.-S. Branhan, L. Thornhill, H. Boudries, M. Canagaratna, R. Miake-Lye, J. Wormhoudt, D. Worsnop, T. Miller, J. Ballenthin, D. Hunton, A. Viggiano, D. Pui and H.-S. Han, D. Blake, M. McEchern</i>	
SAE E-31 Committee on Aircraft Exhaust Emission Measurements and an Aerospace Information Report on the Measurement of Non-volatile Particle Emissions	37
<i>R.C. Miake-Lye, V. Zaccardi</i>	
Particle Emissions from Aircraft Engines - An Overview of the European Project PartEmis	41
<i>A. Petzold, M. Fiebig, L. Fritzsche, C. Stein, U. Schumann, C.W. Wilson, C.D. Hurley, F. Arnold, E. Katragkou, U. Baltensperger, M. Gysel, S. Nyeki, R. Hitznerberger, H. Giebl, K. J. Hughes, R. Kurtenbach, P. Wiesen, P. Madden, H. Puxbaum, S. Vrchoticky, C. Wahl</i>	
Emission of Non-Methane Volatile Organic Compounds (NMVOCs) from a Jet Engine Combustor and a Hot End Simulator (HES) During the PartEmis Project	52
<i>R. Kurtenbach, J. C. Lörzer, A. Niedojadlo, M. Petrea, P. Wiesen, M. Kapernaum, C. Wahl</i>	
Modeling of Soot Precursor Formation in Laminar Premixed Flames with C1-, C2- and C6-Fuels	59
<i>E. Goos, M. Braun-Unkhoff, N. Slavinskaya, P. Frank</i>	
Modelling of Volatile Particles during PARTEMIS	67
<i>X. Vancassel, P. Mirabel, A. Sorokin</i>	
Dispersion and Growing of Ice Particles in a Turbulent Exhaust Plume	73
<i>F. Garnier, C. Ferreira Gago, A.-L. Brasseur, R. Paoli, B. Cuenot</i>	
The Effect of Plume Processes on Aircraft Impact	79
<i>I.C. Plumb, L.K. Randeniya, P.F. Vohralik, S.L. Baughcum</i>	

Aerosol and Gas Chemistry of Commercial Aircraft Emissions Measured in the NASA EXCAVATE Experiment <i>H. Boudries, J. Wormhoudt, D. Worsnop, M. Canagaratna, T. Onasch, R. Miake-Lye, B. Anderson</i>	85
Emission of Volatile and Non-Volatile Ultrafine Particles from a Combustion Source During PartEmis <i>M. Fiebig, L. Fritzsche, C. Stein, A. Petzold, S. Nyeki</i>	91
A USA Commercial Flight Track Database for Upper Tropospheric Aircraft Emission Studies <i>D.P. Garber, P. Minnis, K.P. Costulis</i>	96
Validation of the Kinetic Soot Model: An Experimental and Theoretical Study on Soot Formation using LII and SV-CARS <i>K.P. Geigle, Y. Schneider-Kühnle, V. Krüger, M. Tsurikov, R. Lückerrath, M. Braun-Unkhoff, N. Slavinskaya, P. Frank, W. Stricker, M. Aigner</i>	102
AvioMEET Inventory Tool and its Applications <i>M. Bukovnik, M. T. Kalivoda</i>	110
Transport and Impact on chemical composition	
Lightning NO _x Emissions and the Impact on the Effect of Aircraft Emissions - Results from the EU-Project TRADEOFF <i>V. Grewe</i>	116
Impact of Aircraft NO _x Emissions: Effects of Changing the Flight Altitude <i>M. Gauss, I. Isaksen, V. Grewe, M. Köhler, D. Hauglustaine, D. Lee</i>	122
Improved Mass Fluxes in a Global Chemistry-Transport Model: Implications for Upper-Tropospheric Chemistry <i>E.W. Meijer, P.F.J. van Velthoven, A. Segers, B. Bregman, D. Brunner</i>	128
Activities of NASA's Global Modeling Initiative (GMI) in the Assessment of Subsonic Aircraft Impact <i>J.M. Rodriguez, J.A. Logan, D.A. Rotman, D.J. Bergmann, S.L. Baughcum, R.R. Friedl, D. E. Anderson</i>	134
Parametric Study of Potential Effects of Aircraft Emissions on Stratospheric Ozone <i>D.J. Wuebbles, M. Dutta, K.O. Patten, S.L. Baughcum</i>	140
Stratospheric Ozone Sensitivity to Aircraft Cruise Altitudes and NO _x Emissions <i>S.L. Baughcum, I.C. Plumb, P.F. Vohralik</i>	145
Investigating the Global Atmosphere by Using Commercial Aircraft: CARIBIC <i>A. Zahn, C. Brenninkmeijer</i>	151
The Importance of Aviation for Tourism – Status and Trends <i>S. Gössling</i>	156
The SCENIC Project: Impact of Supersonic Aircraft on the Atmosphere <i>O. Dessens, H.L. Rogers, J.A. Pyle</i>	162

A 3D Model Intercomparison of the Effects of Future Supersonic Aircraft on the Chemical Composition of the Stratosphere	166
<i>G. Pitari, E. Mancini, H. Rogers, O. Dessens, I. Isaksen, B. Rognerud</i>	
Modelling the Impact of Subsonic Aircraft Emissions on Ozone: Future Changes and the Impact of Cruise Altitude Perturbations	173
<i>M.O. Köhler, H.L. Rogers, J.A. Pyle</i>	
Nitric Acid Partitioning in Cirrus Clouds and the Role of Interstitial Aerosol	178
<i>M. Krämer, J. Beuermann, C. Schiller, F. Grimm, F. Arnold, T. Peter, S. Meilinger, A. Meier, J. Hendricks, A. Petzold, H. Schlager</i>	
Radiative Forcing on Climate from Stratospheric Aircraft Emissions	184
<i>D.J. Wuebbles, M. Dutta, A.K. Jain, S.L. Baughcum</i>	
Sources of NO _x at Cruise Altitudes: Implications for Predictions of Ozone and Methane Perturbations Due to NO _x from Aircraft	190
<i>T.K. Berntsen, M. Gauss, I.S.A. Isaksen, V. Grewe, R. Sausen, G. Pitari, E. Mancini, E. Meijer, D. Hauglustaine</i>	
Particles and Clouds	
Particles and Cirrus Clouds (PAZI): Overview of results 2000 - 2003	197
<i>B. Kärcher, U. Schumann, S. Brinkop, R. Busen, M. Fiebig, H. Flentje, K. Gierens, J. Graf, W. Haag, J. Hendricks, H. Mannstein, S. Marquart, R. Meyer, A. Minikin, A. Petzold, M. Ponater, R. Sausen, H. Schmid, P. Wendling, M. Aigner, P. Frank, K.-P. Geigle, P. Gerlinger, B. Noll, W. Stricker, C. Wahl, U. Schurath, O. Möhler, S. Schaefers, O. Stetzer, O. Schrems, G. Beyerle, F. Immler, H. Kruse, A. Döpelheuer, M. Plohr, C. Schiller, M. Bläsner, M. Krämer, A. Mangold, A. Wollny, S. Borrmann, J. Curtius, S. Henseler, N. Hock, J. Schneider, S. Weimer, F. Arnold, H. Aufmhoff, K. Gollinger, A. Kiendler, T. Stilp, S. Wilhelm, K.-H. Wohlfrom, C. Timmreck, J. Feichter, U. Lohmann, J. Ström, T. Rother</i>	
Ice-Nucleating Ability of Soot Particles in UT/LS	207
<i>J. Suzanne, D. Ferry F., O.B. Popovicheva, N.K. Shonija</i>	
Experimental Investigation of Homogeneous and Heterogeneous Freezing Processes at Simulated UTLS Conditions	213
<i>O. Möhler, C. Linke, H. Saathoff, M. Schnaiter, R. Wagner, U. Schurath, A. Mangold, M. Krämer</i>	
Detailed Modelling of Cirrus Clouds – an intercomparison of different approaches for nucleation	217
<i>M. Monier, W. Wobrock and A. Flossmann</i>	
Simulation of Contrail Coverage over the USA Missed During the Air Traffic Shutdown	224
<i>P. Minnis, L. Nguyen, D.P. Garber, D.P. Duda, R. Palikonda, D.R. Doelling</i>	
CONUS Contrail Frequency Estimated from RUC and Flight Track Data	232
<i>D. P. Duda, P. Minnis, P. K. Costulis, R. Palikonda</i>	
Contrail Coverage Derived from UARS MLS Measurements	238
<i>M.Y. Danilin, S.L. Baughcum, W.G. Read</i>	

Observations of Contrails and Cirrus Over Europe <i>H. Mannstein, U. Schumann</i>	244
Potential Impact of Aviation-Induced Black Carbon on Cirrus Clouds: Global Model Studies with the ECHAM GCM <i>J. Hendricks, B. Kärcher, A. Döpelheuer, J. Feichter, U. Lohmann</i>	249
Future Development of Contrails: Impacts of Increasing Air Traffic and Climate Change <i>S. Marquart, M. Ponater, F. Mager, R. Sausen</i>	255
A Study of Contrails in a General Circulation Model <i>A. Guldberg</i>	261
Hygroscopicity and Wetting of Aircraft Engine Soot and its Surrogates: CCN/IN Formation in UT <i>O.B. Popovicheva, N.M. Persiantseva, E.E. Likhovitskaya, N.K. Shonija, N.A. Zubareva, J. Suzanne, D. Ferry, B. Demirdjian</i>	266
Microphysics of Cirrus Clouds and its Dependency on Different Types of Aerosols <i>A. Mangold, M. Krämer, O. Möhler, R. Wagner, H. Saathoff, S. Büttner, O. Stetzer, U. Schurath, C. Giesemann, H. Teichert, V. Ebert</i>	272
3-D Simulation of Contrail to Cirrus Transition - the Onset of Sedimentation <i>J.K. Nielsen</i>	278
Heterogeneous Nucleation Effects on Cirrus Cloud Coverage <i>K. Gierens, S. Brinkop</i>	282
Contrail Coverage over the USA Derived from MODIS and AVHRR Data <i>R. Palikonda, D. N. Phan, V. Chakrapani, P. Minnis</i>	288
Contrail Coverage over the North Pacific from AVHRR and MODIS Data <i>P. Minnis, Rabindra Palikonda, J.K. Ayers</i>	294
Survey of Cirrus Properties from Satellite Retrievals Using TOVS and AVHRR Observations <i>C. J. Stubenrauch, R. Meerkötter</i>	300
Comparison of Cirrus Cloud Properties in the Northern and Southern Hemisphere on the Basis of Lidar Measurements. <i>F. Immler, O. Schrems</i>	306
A Fast Stratospheric Aerosol Microphysical Model <i>S. Tripathi, X. Vancassel, R. Grainger, H. Rogers</i>	310
Mitigation	
On the Potential of the Cryoplane Technology to Reduce Aircraft Climate Impact <i>M. Ponater, S. Marquart, L. Ström, K. Gierens, R. Sausen, G. Hüttig</i>	316
Impact of Cruise Altitude on Contrails <i>C. Fichter, S. Marquart, R. Sausen, D.S. Lee, P.D. Norman</i>	322
Policies for Mitigating Contrail Formation from Aircraft <i>R.B Noland, V. Williams, R. Toumi</i>	328

Greener by Design <i>J.E.Green</i>	334
Climate responses to aviation NO _x and CO ₂ emissions scenarios <i>D.S. Lee, R. Sausen</i>	343
Summary	
Aviation, Atmosphere and Climate - What has been learned <i>U. Schumann</i>	349
List of Participants	357
Index of Authors	366

Conference Agenda

Sunday, 29.06.2003

18:00 – 20:00 Registration

Monday, 30.06.2003

09:00 Registration

10:00 Sausen, R: Welcome and Information

Engine emissions and plume processes (1)

Chair: Paul Madden

10:20 Gleitsmann G, Somnitz H, Zellner R: Novel rates of OH induced sulfur oxidation implications to the plume chemistry of jet aircraft

10:40 Wahl C, Kapernaum M, Krüger V, Rainer P, Aigner M: Determination of soot mass fraction soot density and soot fractal character in flame exhaust gases

11:00 *Coffee break*

11:20 Anderson B E, Winstead E L, Hudgins C H, Branham S, Plant J V, Thornhill K L: Overview of results from the NASA experiment to characterize aircraft volatile aerosol and trace species emissions (EXCAVATE)

12:00 Miake-Lye R C, Zaccardi V: SAE E-31 committee on aircraft exhaust emission measurements and an aerospace information report on the measurement of non-volatile Particle Emissions

12:20 Sorokin A, Katragkou E, Arnold F, Busen R, Schumann U: SO₃ and H₂SO₄ in exhaust of an aircraft engine: Measurements and implications for fuel sulfur conversion to S(VI) and SO₃ to H₂SO₄

12:40 *Lunch break*

Engine emissions and plume processes (2)

Chair: Ulrich Schumann

14:00 Schumann U: Welcome, Aeronautic Research at DLR

Ghazi A: Welcome, Perspective EU, Environment and Aviation

14:40 Petzold A, Wilson C W, Arnold F, Baltensperger U, Fiebig M, Fritzsche L, Giebl H, Gysel M, Hitzenberger R, Hurley C D, Katragkou E, Kurtenbach R, Madden P, Nyeki S, Puxbaum H, Schumann U, Stein C, Vrhoticky S, Wahl C, Wiesen P: Particle emissions from aircraft engines - An overview of the european project PARTEMIS

15:20 Kurtenbach R, Kapernaum M, Lörzer J, Niedojadlo A, Petrea M, Wahl C, Wiesen P: Emission of non-methane volatile organic compounds (NMVOCs) from a jet engine combustor and a Hot End Simulator (HES) during the PARTEMIS project

15:40 Goos E, Braun-Unkloff M, Slavinskaya N, Frank P: Modeling of soot precursor formation in laminar premixed flames with C₁- C₂- and C₆-Fuels

16:00 *Coffee break*

Engine emissions and plume processes (3)

Chair: Karlheinz Haag

16:20 Lee D S, Sun C-G, Cooper M, Snape C, Wilson C: Stable carbon isotope signatures of aircraft particles

16:40 Vancassel X, Sorokin A, Mirabel P: Modelling of volatile particles during PARTEMIS

- 17:00 Garnier F, Ferreira-Gago C, Brasseur A L, Uthéza F, Paoli R, Cuenot B: Growing and dispersion of particles in a turbulent exhaust plume
- 17:20 Plumb I, Randeniya L, Vohralik P, Baughcum S L: The effect of plume processes on aircraft impact
- 17:40 Wilson, C W: Aviation fuels - Where are we going and why?
- 18:00 *Break*
- 19:00 *Ice-breaking reception in the Zeppelin museum*

Tuesday, 01.07.2003

Transport and impact on chemical composition (1)

Chair: David S. Lee

- 09:00 Crowther R, Law K, Pyle J, Nedelec P, Smit H, Volz-Thomas, A: NO_y in the UT/LS: A source attribution study utilising MOZAIC measurements
- 09:20 Isaksen I S A: The TRADEOFF project: Goals and achievements
- 09:50 Brunner D, Staehelin J, Hauglustaine D, Jourdain L, Rogers H L, Koehler M O, Pyle J A, Berntsen T K, Gauss M, Meijer E, van Velthoven P, Grewe V, Sausen R, Pitari G, Mancini E, Isaksen I S A: On the quality of chemistry-transport simulations in the upper troposphere/lower stratosphere region
- 10:10 Grewe V: Lightning NO_x emissions and the impact on the effect of aircraft emissions - Results from the EU-project TRADEOFF
- 10:30 *Coffee break*

Transport and impact on chemical composition (2)

Chair: Georgios Amanatidis

- 10:50 Hauglustaine D, Stordal F, Myhre G, Gauss M, Berntsen T, Isaksen I: Impact of present-day and future subsonic aircraft emissions on tropospheric ozone and associated radiative forcing of climate
- 11:10 Gauss M, Köhler M, Grewe V: Impact of aircraft NO_x emissions: Effects of changing the flight altitude
- 11:30 Meijer E, Van Velthoven P, Bregman B, Seger A, Brunner D: Improved mass fluxes in a global chemistry-transport model: implications for upper tropospheric chemistry
- 11:50 Rodriguez J M, Logan J A, Rotman D A, Bergmann D, Baughcum S L, Friedl R R, Anderson D E: Activities of NASA's Global Modeling Initiative (GMI) in the assessment of subsonic aircraft impact
- 12:30 *Lunch break*

Transport and impact on chemical composition (3)

Chair: Ivar Isaksen

- 13:50 Wuebbles D J, Dutta Mayurakshi P, Kenneth O, Baughcum S L: Parametric study of potential effects of aircraft emissions on stratospheric ozone
- 14:10 Baughcum S, Plumb I, Vohralik P: Stratospheric ozone sensitivity to aircraft cruise altitudes and NO_x emissions
- 14:30 Stubenrauch C: Introduction to Poster Session 1
- 14:55 *Poster Session 1 (Engine emissions and plume processes, Transport and impact on chemical composition)*

- 17:20 Brennkmeijer C, Slemr F, Zahn A, Fischer H, Hermann M, Heintzenberg J, Schlager H, Ziereis H: Investigating the global atmosphere by using commercial aircraft: CARIBIC and MOZAIC
- 17:40 Gossling S: The importance of aviation for tourism: Status and trends
- 18:00 *end of sessions*

Wednesday, 02.07.2003

Transport and impact on chemical composition (4)

Chair: Philippe Mirabel

- 09:00 Dessens O, Rogers H, Pyle J, all SCENIC-project members: The SCENIC project: presentation and first results
- 09:20 Pitari G, Mancini E, Rogers H, Dessens O, Isaksen I, Rognerud B: A 3D model intercomparison of the effects of future supersonic aircraft on the chemical composition of the stratosphere

Particles and clouds (1)

Chair: Philippe Mirabel

- 09:40 Kärcher B, Schumann U, Aigner M, Schurath U, Schrems O, Sausen R, Kruse H, Schiller C, Borrmann S, Arnold F, Feichter J, Lohmann U, Ström J, Rother T, Brinkop S, Busen R, Flentje H, Gierens K, Graf J, Haag W, Hendricks J, Mannstein H, Petzold A, Wendling P, Frank P, Gerlinger P, Noll B, Stricker W, Wahl C, Möhler O, Schaefers S, Stetzer S, Immler F, Döpelheuer A, Krämer M, Mangold A, Wollny A, Schneider J, Wilhelm S, Aufmhoff H, Timmreck C: Particles and cirrus clouds (PAZI) - Overview of results 2000-2003
- 10:20 *Coffee break*
- 10:40 Arnold F: Upper tropospheric aerosol formation inside and outside aircraft wakes: new findings from mass spectrometric measurements of gaseous and ionic aerosol precursors and very small aerosols
- 11:10 Baumgardner D, Kok G, Raga G, Diskin G, Sachse G: Single particle black carbon measurements in the UT/LS
- 11:30 Suzanne J, Ferry D, Popovicheva O B, Shonija N K: Ice-nucleating ability of soot particles in UT/LS
- 11:50 Möhler O, Schnaiter M, Wagner R, Schurath U, Mangold A, Krämer M: Experimental investigation of homogeneous and heterogeneous freezing processes at simulated UTLS conditions
- 12:10 Monier M, Wobrock W, Flossmann A: Detailed modelling of cirrus cloud - An intercomparison of different approaches for homogeneous nucleation

12:30 *Lunch break*

Particles and clouds (2)

Chair: Corinne Marizy

- 13:50 Friedl R, WB-57 CRYSTAL-FACE science team: Overview of contrail and cirrus cloud measurements from the WB-57 aircraft in the CRYSTAL-FACE mission
- 14:10 Minnis P, Garber D P, Nguyen L, Duda D P, Palikonda R: Simulation of contrail coverage over the USA missed during the air traffic shutdown
- 14:40 Duda D P, Minnis P, Costulis P K, Palikonda R: CONUS contrail frequency estimated from RUC and flight track data
- 15:00 Danilin M Y, Baughcum S L, Read W G: Contrail properties derived from UARS MLS measurements

- 15:20 *Poster Session 2 (Particles and Clouds, Mitigation)*
- 16:30 Mannstein H: Observations of contrails and cirrus over Europe
- 17:00 Zerefos C, Eleftheratos K, Zanis P, Balis D, Stordal F, Myhre G: Updated perturbations on cirrus and contrail cirrus
- 17:20 Penner J, Liu X: Potential alteration of ice clouds by aircraft soot
- 17:40 *Break*
- 19:30 *boarding: Ship Cruise on Lake Constance with Dinner*

Thursday, 03.07.2003

Particles and clouds (3)

Chair: Winfried Dewes

- 09:00 Hendricks J, Kärcher B, Döpelheuer A, Feichter J, Lohmann U: Potential impact of aviation-induced black carbon on cirrus clouds: Global model studies with the ECHAM GCM
- 09:20 Marquart S, Ponater M, Mager F, Sausen R: Future development of contrail cover optical depth and radiative forcing: Impacts of increasing air traffic and climate change
- 09:40 Guldberg A: A studie of contrails in a general circulation model
- 10:00 *Coffee break*

Mitigation

Chair: Winfried Dewes

- 10:20 Ponater M, Marquart S, Ström L, Sausen R, Gierens K, Hüttig G: On the potential of the cryoplane option to reduce aircraft climate impact
- 10:40 Lee D S, Sausen R, Marquart S, Fichter C, Norman P: Tradeoffs in contrail and CO₂ radiative forcing by altered cruise altitudes
- 11:00 Noland R, Toumi R, Williams V: Policies for mitigating contrail formation from aircraft
- 11:20 Green, J: Greener by Design
- 11:50 *Lunch break*

Summary and Outlook

Chair: Robert Sausen

- 13:30 Schumann, U: What did we learn?
- 14:10 Discussion
- 14:40 Sausen, R.: Homework and Good Bye
- 15:00 *end of conference*

Poster Sessions

1. Engine Emissions and Plume Processes/Transport and Impact on Chemical Composition

Hitzenberger R, Giebl H, Petzold A, Gysel M, Nyeki S, Weingartner E, Baltensperger U, Wilson C W: CCN activation of jet engine combustion particles during PARTEMIS

Worsnop D R, Miake-Lye R, Boudries H, Wormhoudt J, Anderson B: Gas and aerosol chemistry of commercial aircraft emissions measured in the NASA EXCAVATE experiment

Katragkou E, Wilhelm S, Arnold F, Wilson C W: Sulfur (VI) in the simulated internal flow of an aircraft gas turbine engine: first measurements during the PARTEMIS project

Fiebig M, Fritzsche L, Stein C, Nyeki S, Petzold A: Emission of volatile and non-volatile ultrafine particles from a combustion source during PARTEMIS

Sorokin A, Vancassel X, Mirabel P: Kinetics of binary nucleation in aircraft exhaust plume

Garber D P, Minnis P, Costulis P K: A USA commercial flight track database for upper tropospheric aircraft emission studies

Hayashi S, Yamada, H, Takazawa K, Makida M, Kurosawa Y: Interaction of NO and ice crystals produced from combustion generated water vapor in a simulated jet engine exhaust gas plume

Geigle K P, Schneider-Kühnle Y, Krüger V, Tsurikov M, Lücknerath R, Braun-Unkloff M, Slavinskaya N, Frank P, Stricker W, Aigner M: Validation of the kinetic soot model: An experimental and theoretical study on soot formation using LII and shifted vibrational CARS

Gysel M, Nyeki S, Weingartner E, Baltensperger U, Giebl H, Hitzenberger R, Petzold A, Wilson C W: Jet engine combustion particle hygroscopicity under subsaturated conditions during PARTEMIS

Bukovnik M, Kalivoda M: AvioMEET inventory tool and its applications

Leigh P, MacKenzie R, Borrmann S: Air parcel trajectories in the south european UTLS: implications for the impact of air traffic emissions

Gauss M, Isaksen I, Lee D: The impact of aircraft on the chemical composition of the atmosphere and options for reducing the impact A 3D CTM model study

Köhler M O, Rogers H L, Pyle J A: Modelling the impact of subsonic aircraft emissions on ozone

Krämer M, Beuermann J, Schiller C, Grimm F, Arnold F, Peter T, Meilinger S, Meier A, Hendricks J, Petzold A, Schlager H: Uptake of nitric acid in cirrus clouds

Wuebbles D J, Dutta M, Jain A, Baughcum S L: Radiative forcing on climate from aircraft emissions in the stratosphere

Berntsen T, Gauss M, Grewe V, Hauglustaine D, Isaksen I, Mancini E, Meijer E, Pitari G, Sausen R: Sources of NO_x at cruise altitudes, implications for predictions of ozone and methane perturbations due to NO_x emissions from aircraft

2. Particles and Clouds/Mitigation

Minikin A, Petzold A, Fiebig M, Hendricks J, Schröder F: Aerosol properties measured in situ in the free troposphere and tropopause region at midlatitudes

Popovicheva O, Persiantseva N M, Shonia N K: Hygroscopicity and wetting of aircraft engine soot and its surrogates: CCN formation in UT

Mangold A, Büttner S, Ebert V, Gieseemann C, Krämer M, Möhler O, Saathoff H, Schurath U, Stetzer O, Teichert H and Wagner R: Ice water content of cirrus clouds and its dependency on different types of aerosols

Nielsen J K: 3D simulation of cirrus formation from airplane contrails

Gierens K, Brinkop S: Heterogeneous nucleation effects on cirrus cloud coverage

Palikonda R, Phan D, Minnis P: Contrail coverage over the USA derived from MODIS and AVHRR data

Minnis P, Palikonda R, Ayers J K: Contrail coverage over the North Pacific from MODIS and AVHRR Data

Stubenrauch C, Meerkoetter R: Survey of cirrus properties from satellite retrievals using TOVS and AVHRR observations

Immler F, Schrems O: Comparison of cirrus cloud properties in the northern and southern hemisphere on the basis of lidar measurements

Tripathi S, Vancassel X, Grainger R, Rogers H: A Fast Stratospheric Aerosol Microphysical Model (SAMM)

Lee D S, Sausen R: Climate responses of aviation NO_x and CO₂ emissions scenarios

Extended Abstracts

Novel Rates of OH induced Sulfur Oxidation. Implications to the Plume Chemistry of Jet Aircraft

H. Somnitz, G. Gleitsmann, R. Zellner*

Institut für Physikalische Chemie, Universität Duisburg Essen, Campus Essen, Essen, Germany

Keywords: Contrail formation, plume chemistry, OH + SO₂ kinetics

ABSTRACT: Novel rate coefficients for the most important and rate controlling sulfur oxidation reaction, OH + SO₂ → HSO₃, over an extended range of pressure and temperature have been derived from ab initio quantum chemical/RRKM dynamical calculations. From these calculations the rate of oxidation of S(IV) to S(VI) under typical conditions of a jet aircraft plume is predicted to be considerably slower than previously accepted on the basis of interpolations of experimental data (i.e. Tremmel and Schumann, 1999). These kinetic results have been incorporated into a chemical-dynamical code of the jet regime of a B-747 airliner (BOAT code) to predict sulfur conversion efficiencies in this regime of less than 1%. It is concluded therefore that overall conversion efficiencies in the order of several % are caused by corresponding conversions in the combustor and/or turbine of the jet engine and not in the plume.

1 INTRODUCTION

A number of environmental aspects of aircraft emissions such as contrail formation and impact on cirrus formation have been suggested to depend on sulfuric acid formation from the fuel sulfur content (FSC) as a result of the rapid rates of oxidation of S(IV) in the engine and/or the plume. Despite this importance the chemical kinetic data base to assess this oxidation is far from being reliable.

Since many years, the abundance of H₂SO₄ in aircraft plumes has been identified as an important input parameter controlling aerosol dynamics. Up to date the S(VI)/S(IV) conversion of SO₂ has been identified to proceed following the Stockwell and Calvert (1983) mechanism, viz.



The subsequent formation of H₂SO₄ by addition of water molecules to SO₃ proceeds sufficiently fast for SO₃ and H₂SO₄ to be jointly denoted S(VI). Up to now conversion efficiencies in an aircraft plume in the order of $\epsilon = 1\%$ could be reproduced in model calculations in which the emission indices of SO₃ and H₂SO₄ in the engine have been assumed to be zero (cf. for instance: Kärcher et al., 1995; Gleitsmann and Zellner, 1998).

On the other hand, higher conversion efficiencies have been postulated by Fahey et al. (1995) as well as Miake-Lye et al. (1998) which in turn require direct emissions of S(VI) species. Evidence for the latter has emerged from modelling calculations focusing on the gas phase chemistry inside combustor and turbine (Hunter, 1982; Brown et al., 1996; Lukachko et al., 1998; Starik et al., 2002), which yield conversion efficiencies in the order of $\epsilon = 10\%$ even in the engine exit plane.

In order to resolve this discrepancy, both emission indices and rate constants of reaction (R1) need to be critically checked, especially since the available experimental kinetic data only cover limited temperature ranges $T \leq 400$ K (Atkinson et al., 1997; DeMore et al., 1997).

* *Corresponding author:* Reinhard Zellner, Institut für Physikalische Chemie, Universität Duisburg Essen, Campus Essen, D-45117 Essen, Germany. Email: reinhard.zellner@uni-essen.de

2 QUANTUM CHEMICAL CALCULATIONS

In the present study the recombination reaction of the OH radical with SO₂ has been investigated using current theoretical methods. Quantum chemical calculations were performed to locate the stationary points on the Potential Energy Surface (PES) for the recombination/dissociation process, including structures and vibrational frequencies calculated at the B3LYP/aug-cc-pVTZ(+1) and QCISD/6-311G(d,p) level of theory. Furthermore, the energetics are characterised by the application of G3X-theory which provides all sensitive data such as the critical energy barrier and the enthalpy of reaction (see Figure 1 below).

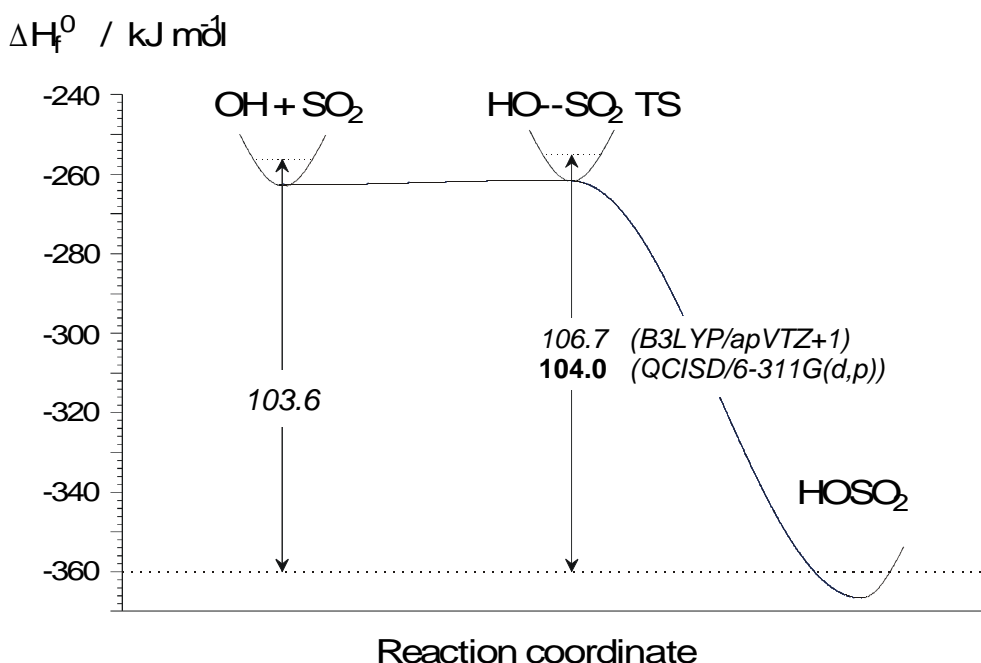


Figure 1. G3X calculated minimum energy path for the dissociation of HOSO₂ to OH+SO₂.

The results obtained give clear evidence for a compact transition state with regards to the dissociation of HOSO₂. Combining the calculated enthalpy of formation for the HOSO₂ radical ($\Delta H_f^0(T=0\text{ K}) = -360.0\text{ kJ/mol}$) and the well known enthalpy of formation for OH and SO₂ this allows the calculation of the temperature dependent equilibrium constant $K_{\text{eq}}(T)$. In addition, a very shallow barrier ($\approx 0.5\text{ kJ/mol}$) is predicted for the recombination process at $T = 0\text{ K}$.

3 STATISTICAL CALCULATIONS ON THE OH + SO₂ KINETICS

These novel data have been used as input to statistical kinetic calculations. Focussing on the reverse process (e.g. the HOSO₂ dissociation), RRKM-theory in conjunction with a subsequent solution of the master equation has been utilised to derive complete fall-off curves for the thermal decomposition of HOSO₂ in a weak collision scenario ($M = N_2$). The final rate coefficients for the recombination reaction of OH + SO₂ are derived by multiplication of the temperature dependent equilibrium constant and the temperature and pressure dependent rate coefficients of the back-dissociation (i.e. $k_{\text{rec}}(T,p) = K_{\text{eq}}(T) k_{\text{diss}}(T,p)$). The final results for $k_{\text{rec}}(T,p)$ are summarised in form of pressure dependent fall-off curves, shown in Figure 2 for selected temperatures in the range of 150 K to 1500 K.

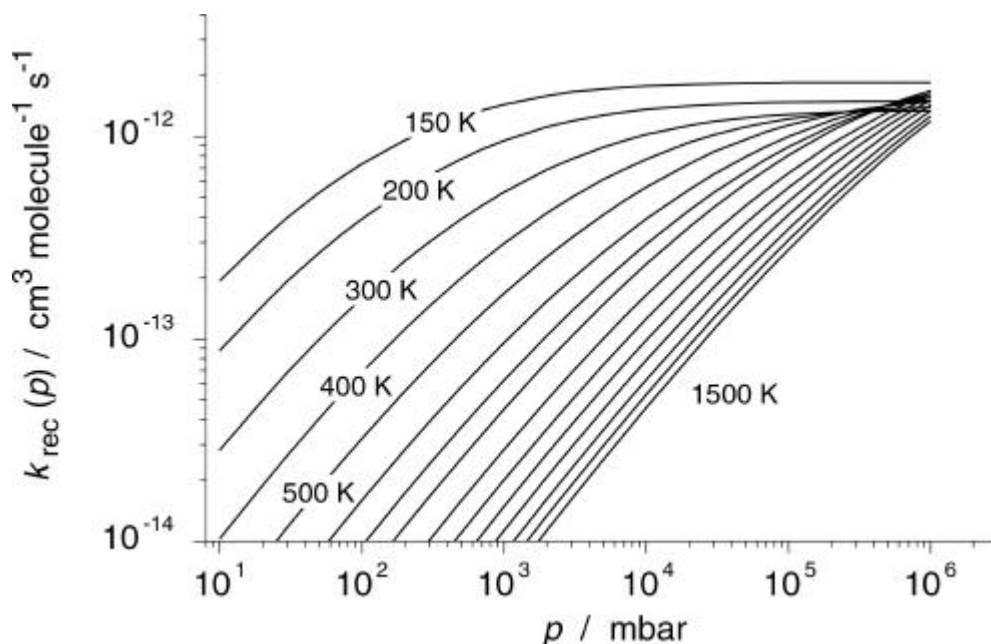


Figure 2. Complete fall-off curves for the recombination reaction of OH + SO₂.

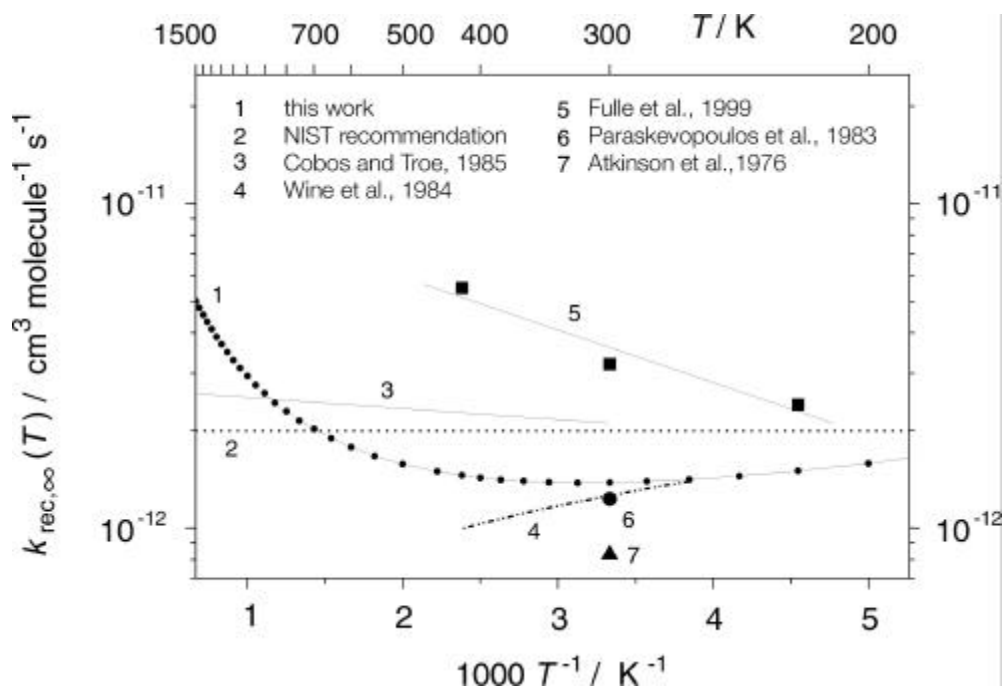


Figure 3. Calculated temperature dependence of the high pressure limiting rate coefficient of the OH + SO₂ recombination compared to extrapolated values known in the literature.

Further topics of this work cover the derivation of Arrhenius expressions for the low and high pressure limits as well as for specific pressures which are of interest in atmospheric chemistry. These have been extracted at each pressure from the "numerically exact" fall-off data, which are shown in the figure above. The resulting kinetic data are compared with rate constants suggested in the literature from experiments up to atmospheric pressures (Atkinson et al., 1997; DeMore et al., 1997) and recently reported measurements performed at temperatures between 220 K – 400 K and pressures up to 96 bar (Fulle et al.; 1999).

Although there is a fair agreement of the absolute magnitude of the rate coefficients at atmospheric pressures and temperatures, our calculation suggest up to a factor of three lower rate coefficients compared to previous extrapolations of the sparse experimental data into the pressure and temperature ranges of interest for combustion modelling. This is mainly due to the more complicated temperature behaviour of the high-pressure limiting rate coefficient of the recombination reaction, which changes from positive to negative Arrhenius-behaviour around $T=300$ K. This is demonstrated in Figure 3, together with a comparison of the available literature data.

The effective rate coefficient for reaction (R1) at 1 bar and as a function of temperature, together with recent values suggested by Tremmel and Schumann (1999) is shown in Figure 4. As can be seen the difference between both sets of data is in the order of a factor of 3 to 5 at temperatures below 700 K but amounts more than an order of magnitude in the combustion temperature regime.

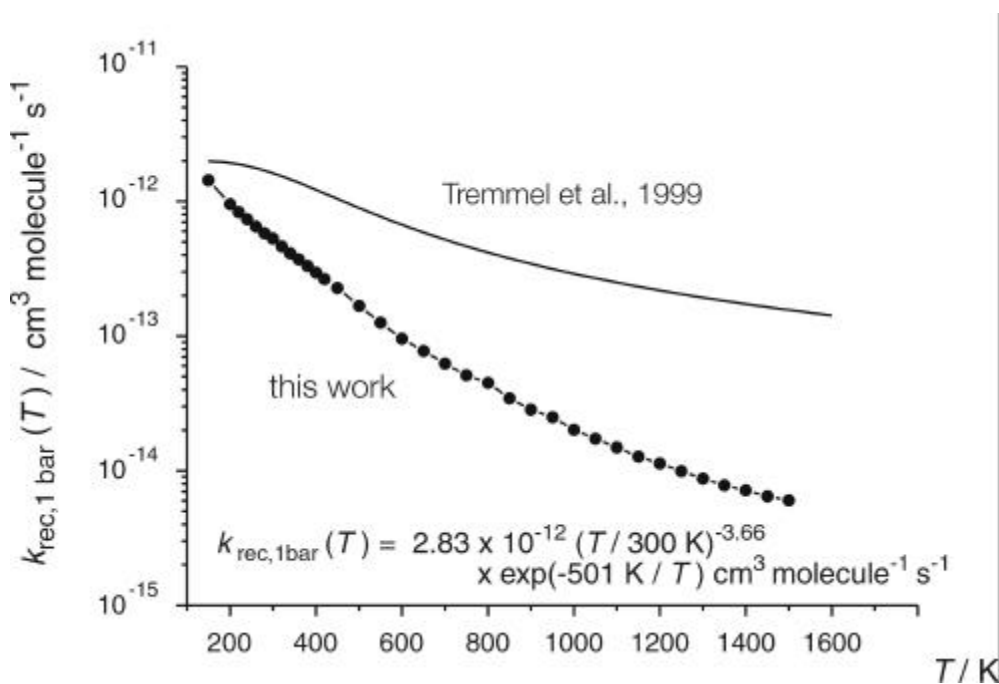


Figure 4. Calculated second order recombination rate coefficients at $p = 1$ bar compared to the values assumed in recent model simulations (Tremmel and Schumann, 1999).

4 CHEMICAL DYNAMICAL BOAT CODE

To describe the chemical/dynamical evolution of the plume the BOAT code has been used (Dash and Pergament, 1978). This model accounts for the detailed dynamical and thermochemical processes in the plume of a modern by-pass jet engine of cylindrical symmetry. In the model the jet plume is subdivided into a number of stream shells for which the Navier-Stokes equations are solved for turbulent flow and transport. Simultaneously, the complex gas phase reaction system is solved using local physical parameters such as temperature and species concentrations. All physical and chemical quantities are calculated as a function of the axial distance from the nozzle exit (cf. Figure 5) as well as of the normalised plume radius. The initial conditions chosen correspond to a CF6-80C2 engine of a B-747 airliner at cruise.

In order to implement our chemical code we have extended the original BOAT model to include, next to O_2 , H_2 , H_2O , CO , and CO_2 , all O_x (O , O_3), HO_x (H , OH , HO_2), NO_x (NO , NO_2 , NO_3 , N_2O_5), NO_y (HONO , HNO_3 , HNO_4), SO_x (SO_2 , SO_3) and SO_y (HSO_3 , H_2SO_4) species.

5 RESULTS

Whereas the water partial pressure in the young plume is given by the corresponding emission index and by subsequent dilution, the H_2SO_4 gas phase concentration is assumed to build up in the plume according to the Stockwell and Calvert (1983) mechanism, i.e. reactions (R1) and (R2) followed by



The rate limiting step in this mechanism for all conditions of the plume (i.e. $T \leq 700$ K) is the recombination of SO_2 with OH radicals (R1). Only at higher temperatures where the decomposition of the HSO_3 adduct becomes reversible the reaction of $\text{HSO}_3 + \text{O}_2$ (Reaction R2) becomes rate determining. Therefore, the impact of reaction (R1) on the overall sulfur oxidation changes from kinetic control at low temperatures to thermodynamic control at higher temperatures. Both quantities ($k_1(p, T)$ and $K_{\text{eq}}(T)$) have been derived in the quantum chemical/statistical mechanical and dynamical calculations described above.

Since both the rate of reaction (R1) and the adduct concentration $[\text{HSO}_3]$ depend on the OH level, sulfur conversion is under all conditions a linear function of the OH concentration. A comparison of the kinetic schemes therefore should be based on comparable assumptions on the OH concentration at the engine exit as well as on the evolution of the OH field in the plume.

In Figure 5 we show the temporal evolution of SO_x and SO_y species as calculated for an OH emission index of 1.35×10^{-5} (Tremmel et al., 1998) for old and new HSO_3 kinetics. As can be seen from this figure the new HSO_3 kinetics produces substantially less S(IV) to S(VI) conversions (less than 1% during the evolution of the plume). It should be noted that using even smaller OH emission indices (i.e. 6×10^{-9}) will of course generate still lower conversions.

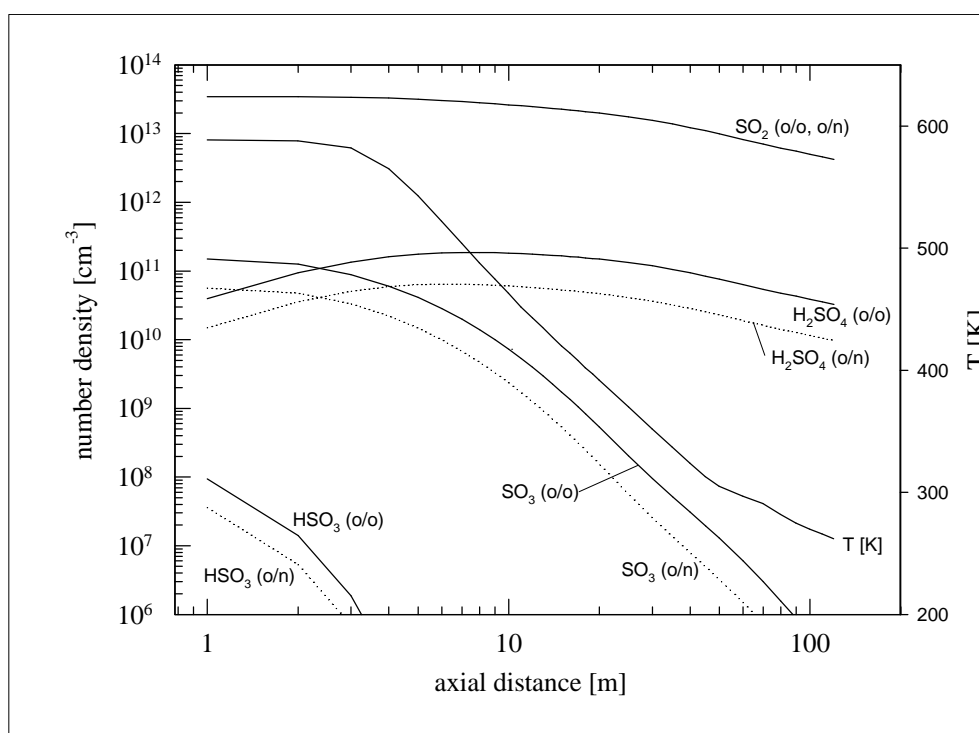


Figure 5. Evolution of SO_x species for old (o) and new (n) HSO_3 kinetics.

6 CONCLUSIONS

In view of improving the understanding of plume chemistry we have revised the conversion of SO_2 into SO_3 (H_2SO_4) in the jet regime of a B-747 airliner. The gas phase reaction scheme (Gleitsmann and Zellner, 1999) has been updated by the novel rate constants and the efficiency of SO_2 to $\text{SO}_3/\text{H}_2\text{SO}_4$ conversion from (R1) has been calculated using a chemical-dynamical code. Since the S(IV) to S(VI) conversion in the early jet regime is predicted to be significantly smaller, it is

concluded from our work, that the well-known conversion ratio of S(IV) to S(VI) of several % as confirmed by a number of airborne experiments, can only be reproduced assuming sufficient formation of SO₃ or H₂SO₄ already inside the engine and/or the turbine. The plume effect on this ratio is less important.

7 ACKNOWLEDGEMENT

Financial support of this work by the EU-project PARTEMIS (GRD-1999-10819) is gratefully acknowledged.

REFERENCES

- Atkinson, R., D.L. Baulch, R.A. Cox, R.F. Hampson, J.A. Kerr, M.J. Rossi, and J. Troe, 1997: Evaluated kinetic and photochemical data for atmospheric chemistry: Supplement VI - IUPAC subcommittee on gas kinetic data evaluation for atmospheric chemistry, *J. Phys. Chem. Ref. Data* 26, 1329-1499
- Brown, R.C., M.R. Anderson, R.C. Miake-Lye, C.E. Kolb, A.A. Sorokin, and Y.Y. Buriko, 1996: Aircraft exhaust sulfur emissions, *Geophys. Res. Lett.* 23, 3603-3606.
- Dash, S.M. and H.S. Pergament, 1978: A computational model for the jet entrainment in the vicinity of the nozzle boattail (The BOAT code), *NASA Contractors report* 3075.
- DeMore, W.B., S.P. Sander, D.M. Golden, R.F. Hampson, M.J. Kurylo, C.J. Howard, A.R. Ravishankara, C.E. Kolb, and M.J. Molina, 1997: Chemical kinetics and photochemical data for use in stratospheric modeling. Evaluation 12., *JPL Publication* 97-4
- Fahey, D.W. E.R. Keim, E.L. Woodbridge, R.S. Gao, K.A. Boering, B.C. Daube, S.C. Wofsy, R.P. Lohmann, E.J. Hints, A.E. Dessler, C.R. Webster, R.D. May, C.A. Brock, J.C. Wilson, R.C. Miake-Lye, R.C. Brown, J.M. Rodriguez, M. Loewenstein, M.H. Proffitt, R.M. Stimpfle, S.W. Bowen, and K.R. Chan, 1995: In situ observations in aircraft exhaust plumes in the lower stratosphere at midlatitudes, *J. Geophys. Res.* 100, 3065-3074.
- Fulle, D., H.F. Hamann, and H. Hippler, 1999: The pressure and temperature dependence of the recombination reaction HO + SO₂ + M → HOSO₂ + M, *Phys. Chem. Chem. Phys.* 1, 2695-2702.
- Gleitsmann, G. and R. Zellner, 1998: A Modelling Study of the Formation of Cloud Condensation Nuclei in the Jet Regime of Aircraft Plumes, *J. Geophys. Res.* 103, 19543-19555.
- Gleitsmann, G. and R. Zellner, 1999: The aerosol dynamics of H₂O-H₂SO₄-HNO₃ mixtures in aircraft wakes. A modeling study, *Phys. Chem. Chem. Phys.* 1, 5503-5509.
- Hunter, S.C., 1982: Formation of SO₃ in gas turbines, *T. ASME J. Eng. Power* 104, 44-51.
- Kärcher, B., Th. Peter, and R. Ottmann, 1995: Contrail Formation: Homogeneous Nucleation of H₂SO₄/H₂O droplets, *Geophys. Res. Lett.* 22, 1501-1504.
- Lukachko, S.P., I.A. Waitz, R.C. Miake-Lye, R.C. Brown, and M.R. Anderson, 1998: Production of sulfate aerosol precursors in the turbine and exhaust nozzle of an aircraft engine, *J. Geophys. Res.* 103, 16159-16174.
- Miake-Lye, R.C., B.E. Anderson, W.R. Cofer, H.A. Wallio, G.D. Nowicki, J.O. Ballenthin, D.E. Hunton, W.B. Knighton, T.M. Miller, J.V. Seeley, and A.A. Viggiano, 1998: SO_x oxidation and volatile aerosol in aircraft exhaust plumes depend on fuel sulfur content, *Geophys. Res. Lett.* 25, 1677-1680.
- Starik, A.M., A.M. Savel'ev, N.S. Titova, and U. Schumann, 2002: Modeling of sulfur gases and chemions in aircraft engines, *Aerosp. Sci. Technol.* 6, 63-81.
- Stockwell, W.R. and J.G. Calvert, 1983: The mechanism of the HO-SO₂ reaction. *Atmos. Environ.* 17, 2231-2235.
- Tremmel, H.G., H. Schlager, P. Konopka, P. Schulte, F. Arnold, M. Klemm, and B. Droste-Franke, 1998: Observation and model calculations of jet aircraft exhaust products at cruise altitude and inferred initial OH emissions, *J. Geophys. Res.* 103, 10803-10816.
- Tremmel, H.G. and U. Schumann, 1999: Model simulations of fuel sulfur conversion efficiencies in an aircraft engine: Dependence on reaction rate constants and initial species mixing ratios. *Aerosp. Sci. Technol.* 3, 417-430.

Determination of Soot Mass Fraction, Soot Density and Soot Fractal Character in Flame Exhaust Gases (PAZI)

C. Wahl*, M. Kapernaum, V. Krüger, P. Rainer, M. Aigner
DLR-Institut für Verbrennungstechnik, Stuttgart Germany

Keywords: Soot mass, soot density, fractal character, SMPS

ABSTRACT: The DLR – Soot Generator was used as a variable and well defined soot source. The particle mean diameter of the log normal size distribution can easily be shifted between 6nm and 250nm. This soot loaded exhaust gas is sucked through a quartz fiber filter via a computer controlled gas sampler. The soot particles are trapped on a quartz fiber filter. This special quartz filter has a sampling efficiency better than 99,9% for particles between 6nm and 250nm. The carbon load on the quartz filter is burned in an oxygen atmosphere. The resulting carbon dioxide concentration is measured with a Fourier Transform IR spectrometer (FTIR). If the gas sampling volume, the gas cell volume and the carbon dioxide concentration is known, a soot mass fraction can easily be calculated. The corresponding size distribution, number concentration and volume concentration are measured by a Scanning Mobility Particle Sizer system (SMPS). Using the soot mass of the filter experiment and the soot volume of the SMPS measurements, a soot density was calculated. This soot density is based on the mobility diameter of the fractal soot particles. The quotient of graphite density and calculated soot density gives the fractal character of the soot.

1 INTRODUCTION

The characterisation of soot nanoparticles by diameter, volume or fractal dimension is ambiguous. Always the corresponding measuring technique must be known, e.g. is it a mobility diameter, an aerodynamic diameter, a geometric diameter and so on (Hinds, 1999).

Modern soot measurement techniques like Laser Induced Incandescence (LII) or Scanning Mobility Particle Sizer (SMPS) give a so called soot volume fraction but no absolute soot mass values. The soot mass fraction given by LII or SMPS are calculated with an assumed soot density. But what is the density of a fractal soot nanoparticle?

2 SOOT SOURCE AND FILTER TEST

For our experiments we used the DLR-Soot Generator (Wahl) as a well defined and stable soot source. The flame soot particles of this generator show a log normal size distribution. The mean diameter of the log normal size distribution can easily be shifted from 6 nm to 250 nm. The number concentration and particle size distribution (PSD) is stable and reproducible.

In a first experiment we checked the trapping efficiency of the quartz fiber filters. The soot generator aerosol was sucked through a fiber filter and the size distribution and number concentration in front and behind the filter was measured with SMPS. The results are shown in the following table:

mean diameter of PSD	trapping efficiency of quartz fiber filter
7.5 nm	99.9 %
36.8 nm	99.99 %
122 nm	99.999 %

*Corresponding author: Claus Wahl, DLR-Institut für Verbrennungstechnik, Pfaffenwaldring 38, 70569 Stuttgart, Germany. Email: claus.wahl@dlr.de

3 FILTER AND SMPS MEASUREMENTS

Due to the excellent trapping efficiency of the fiber filter, it is possible to get the absolute soot mass fraction of the exhaust gas.

Before taking filter soot samples, the quartz fiber filters are heated to 800 °C, in order to burn all organic material on the filter. Then, with a computer controlled gas sampler, a known volume of aerosol was sucked through the filter. In a reaction tube, the volatile organic fraction of the soot loaded filter was burned at 480 K in an oxygen atmosphere. After that procedure the reaction tube was cooled down to room temperature and evacuated again. The remaining black carbon on the filter was burned in a oxygen atmosphere at 800 °C. After cooling down, the resulting CO₂ concentration was measured with a FT-IR spectrometer. The FT-IR system was calibrated with test gases of known CO₂ content. With known exhaust gas sampling volume and known FT-IR gas cell volume, the black carbon mass is calculated via the CO₂ Signal.

The SMPS instrument classifies particles by the so called mobility diameter. Using a sphere model gives the aerosol volume. Our system can work in two measuring ranges, the low flow mode and the high flow mode. If the mean diameter of the measured size distribution is in the mid range of the measuring range, high flow and low flow measurements should give the same volume.

SMPS measurements in low flow mode as well as in high flow mode have been done before and after filter sampling. The mean SMPS soot volume in high flow mode was 3.03E+11 [nm³/ cm³]. The mean SMPS soot volume in low flow mode was 3.78E+11 [nm³/ cm³].

This gives a soot density of 0.74 g/cm³ (high flow) and 0.59 g/cm³ (low flow). The mean soot density of a ethylene flame at 1 bar is $d_{MD} \sim 0.66 \text{ g/cm}^3$. (We name the density d_{MD} , because it is based on the mobility diameter.)

Assuming the primary soot particles consist of graphite similar structures, the density of the primary particles is $\sim 2.2 \text{ g/cm}^3$ like graphite. Therefore a "soot fractal character" can be calculated by dividing the graphite density through the soot density. For our ethylene soot the determined "fractal character" is $2.2 \text{ g/cm}^3 / 0.66 \text{ g/cm}^3 = 3.33 = f_{c_{MD}}$ (again based on mobility diameter).

4 CONCLUSION

A method to determine soot mass, soot density and soot fractal character is shown. Flames under different conditions, or flames of different fuels will have different soot density and soot fractal character. Whenever soot densities are published, it is absolutely necessary to give the method of determine the particle diameter or volume. Because of the fractal character of the soot agglomerates, only soot densities determined with the same method can be compared.

REFERENCES

- Hinds, W. C., Aerosol Technology. John Wiley & Sons, New York 1999
 Wahl, C., M. Aigner, V. Krüger, Russgenerator, Vorrichtung und Verfahren zur kontrollierten Erzeugung von Nano- Russpartikeln. Deutsche Patentanmeldung, Amtl. Aktenzeichen 102 43 307.0

Overview of results from the NASA experiment to characterize aircraft volatile aerosol and trace species emissions (EXCAVATE)

B.E. Anderson^{*}, E. Winstead, C. Hudgins, J. Plant, H.-S. Branhan, and L. Thornhill
NASA Langley Research Center, Hampton VA, USA

H. Boudries, M. Canagaratna, R. Miake-Lye, J. Wormhoudt, and D. Worsnop
Aerodyne Research Incorporated, Billerica, MA, USA

T. Miller, J. Ballenthin, D. Hunton, and A. Viggiano
Air Force Research Laboratory, Hanscom Field, MA, USA

D. Pui and H.-S. Han
University of Minnesota, Minneapolis, MN, USA

D. Blake and M. McEchern
University of California at Irvine, Irvine CA, USA

Keywords: particle formation, particle growth, chemiions, black carbon, aerosol composition

ABSTRACT: EXCAVATE was conducted at NASA Langley Research Center in Hampton Virginia during January, 2002, and obtained detailed measurements of emissions from Langley's T-38 and B-757 aircraft to determine ion densities; the fraction of fuel S converted from S(IV) to S(VI); the concentration and speciation of volatile aerosols and black carbon; and gas-phase concentrations of hydrocarbons in the exhaust of a typical commercial airliner, all as a functions of engine power, fuel composition, and plume age. Our observations indicate that chemiion densities were very high in the exhaust plumes, consistent with values that are presently being used in microphysical models of aerosol formation in exhaust plumes. Both aircraft were found to emit high concentrations of organic aerosols, particularly at low power settings and to produce black carbon concentrations that increased with engine power. Total particle emission indices were typically a factor of 10 higher at 35 meters than at 1 meter behind the engines due to formation of new particles. The concentration of sulfate aerosol was directly dependent upon the fuel sulfur level and increased considerably as sampling took place progressively further downstream from the exhaust plane. For the B757, organic aerosol emissions were very high at engine start and took several minutes to reach much lower, equilibrium values after changes in engine power. This was particularly notable when the engines were reduced from high to low power as might occur during taxi and landing.

1 INTRODUCTION

Aircraft are prolific sources of both primary and secondary aerosol particles [i.e. Anderson et al., 1999]. To assess and predict the impact of these aerosols upon the environment requires a complete understanding of their chemical and microphysical properties and how they are regulated by engine design, temperature and fuel composition, and change as the exhaust plume ages and mixes into the background atmosphere. To gain this information, NASA and European funding agencies have sponsored a number of laboratory and field investigations to characterize and quantify aircraft particulate emissions. Projects such as SUCCESS [Toon et al., 1998], SNIF [Anderson et al., 1998], SONEX [Thompson 1999], POLINAT [Schumann et al., 1998], SULFUR 1-7 [Schumann et al., 2002] have provided a wealth of information regarding aircraft aerosol concentrations and volatility [i.e. Anderson 1998], size distributions [i.e. Brock et al., 2000], and black carbon fraction [Petzold et al., 1999]. These and/or other studies have also examined the impact of fuel sulfur contaminants

^{*} *Corresponding author:* Bruce Anderson, MS483, NASA Langley Research Center, Hampton, VA, USA; bruce.e.anderson@nasa.gov

upon secondary aerosols formation [i.e., Miake-Lye et al., 1998] or, more challengingly, determined the fraction of fuel sulfur that is oxidized to form sulfuric acid in the near field behind the aircraft [i.e., Schumann et al., 2002]. Other studies have characterized and quantified chemiion species in exhaust plumes because these are suspected to play a significant role in new particle formation [Arnold et al., 1999].

Although these investigations have greatly advanced our understanding of particle production by aircraft, a number of significant questions remain unanswered. For example, how does fuel S oxidation vary as a function of engine power and fuel S content? Does unburned fuel and engine oil contribute to formation of aerosols in engine exhaust plumes? In addition, a majority of the information gathered in these studies are pertinent to upper tropospheric/lower stratospheric aircraft operation. How well can these observations be extrapolated to ground-based operations where engines often operate at non-optimum power and fuel/air ratios?

To address these issues, NASA's Atmospheric Effects of Aviation Project (AEAP) and Ultra-Efficient Engine Technology (UEET) Program sponsored the Experiment to Characterize Aircraft Volatile Aerosol and Trace-Species Emissions (EXCAVATE). A ground-based study conducted in an open-air facility, EXCAVATE had as objectives to determine the concentration of chemiions, volatile aerosols, aerosol precursors, black carbon, and selected gas-phase species within the exhaust plume of a modern commercial turbo-fan engine as a function of engine power, fuel composition, and plume age. The experiment took advantage of recent advances in instrumentation and paid particular attention to determining time-dependent aerosol physical properties and composition as well as chemiion speciation. Significant efforts were made to minimize sample line lengths, characterize probe penetration efficiencies and transmission losses, and evaluate the impact of sampling strategies upon measured parameters. Experimental details and summary results in selected focus areas are provided in the paragraphs below.

2 EXPERIMENT

EXCAVATE sampled emissions from the NASA Langley Boeing 757 (B757) and T-38A Talon. The B757 is powered by a pair of Rolls Royce, RB-211-535E4 Turbofan engines as are ~80% of all B757s in service. These three-shaft, high bypass ratio engines produce 40,100 lbs thrust and have a single-stage wide-chord fan, six-stage IP compressor, six-stage HP compressor, single annular combustor, single-stage HP turbine, single-stage IP turbine and a three-stage LP turbine. Langley's T-38 is powered by a pair of J85-GE-5A turbojet engines that produce 3850 lbs thrust. Both aircraft nominally burn commercial Jet A or military JP-5 fuels.

The engine tests were conducted at Langley's aircraft "run-up" facility, a large concrete pad with a blast fence that deflects engine exhaust upward to prevent damage to neighboring vegetation. Anchors are embedded at numerous places in the pad to provide restraining points for aircraft during high power engine runs and were used to secure the sampling probe test stand and sample/electric lines to prevent them from being blown back by the exhaust blast. During tests, the aircraft were parked in front of the blast fence and chocked in place to keep them stationary during the high power engine runs. The probe test stand (Figure 1) was positioned behind engine so that the tips of the sampling probes mounted upon it were 1 m downsteam and on the centreline of the turbine exhaust plane. For the B757, an additional aerosol-sampling inlet was affixed to the blast fence 25 m downstream of the engine exhaust plane. To obtain aerosol samples at 10 and 35 m, the aircraft was rolled forward 9 m and re-chocked. In the case of the T-38, additional aerosol inlets were mounted on weighted stands positioned 10 and 25 m behind the engine exhaust plane. Gas phase measurements were acquired only at 1 m separation distance.

The primary aerosol-sampling probe used in the experiment was carefully designed to introduce a concentric flow of dilution gas as close behind the nozzle tip as possible. Tests conducted at the University of Minnesota using sulfate aerosols indicate the probe is > 80% efficient for extracting particles > 20 nm in diameter from hot gas flows. Boil-off from a liquid N₂ cylinder was used for dilution gas and the dilution ratio was set to approximately 8:1 by monitoring the ratio of CO₂ mixing ratio in the aerosol sample to that in the exhaust plume. Sample air was piped from the probe ~10 m to the aerosol instrument trailer through a combination of 0.5 inch stainless steel and carbon impregnated conductive tubing. The secondary aerosol sampling inlets were constructed

from 0.25 inch Swagelok Tees and stainless tubing, raised to the height of the engine centreline, and connected with 0.5 inch stainless, copper or conductive tubing to 0.5 inch stainless steel ball valves located within the aerosol instrument trailer. The ball valves, in turn, were attached to a common sampling manifold to allow the operator to select sample air from one of the two or three inlets positioned behind the aircraft. The probe used to collect gaseous samples was constructed from standard 2" thick-walled stainless steel pipe and had a tear-drop shaped shield welded to the downstream side to reduce its coefficient of friction and provide protection to wires and tubes connected to sensors mounted near its tip (Figure 2). It was connected with a short length of thin-walled tubing to a sampling manifold located within the test stand that supplied sample air to the Air Force Lab Chemical Ionization (CIMS) and Ion (IMS) Mass Spectrometers and the Aerodyne Tuneable Diode Laser (TDL) Spectrometer and a small CO₂ monitor. The primary aerosol sampling inlet, a Gerdien-tube condenser, a pitot-static tube and a thermocouple mounted were welded on the top and sides of the gas probe, respectively (Figure 2). Along with the TDL, IMS, and CIMS, pressure transducers for the pitot tube, a thermocouple readout, and an electrometer to measure current on the Gerdien Condenser were all placed inside the base of the probe test stand.



Figure 1. Langley B-757 with test stand and probes positioned 1 meter behind engine exhaust plane.



Figure 2. Gas and aerosol inlet probes along with pitot tube and Gerdien Condenser used in 1 and 10 meter sampling behind the B-757.

A list of the measurements that were acquired during EXCAVATE is provided in Table 1. Langley (LaRC) was responsible for measuring the aircraft engine parameters, exhaust CO₂ mixing ratio, total CN concentrations, black carbon, and submicron aerosol size distributions using a Differential Mobility Analyzer (DMA) and Optical Particle Counter (OPC). Aerodyne Research, Inc. made measurements of aerosol composition using their new Aerosol Mass Spectrometer as well as operated the TDL system that determined mixing ratios of CO₂, SO₂, SO₃, and HONO (i.e., Whitefield et al., 2002). The University of Minnesota (UM) provided nucleation mode size distributions for heated and unheated samples using their rapid scanning, nano-Aerosol Size Analyzer (nASA). Air Force Research Lab (AFRL) operated a CIMS and IMS, and a Gerdien tube condenser to measure a variety of species including SO₂, H₂SO₄, HNO₃, total ion densities and ion speciation.

EXCAVATE included a number of sulfur related objectives that required burning fuels of known and varying S concentrations. Although we had originally planned to obtain a low S Jet-A fuel (< 5 ppm) and produce a medium (i.e., 100 ppm) and high S (800 ppm) fuels from it by adding Tetrahydrathiophene (THSP), time and funding constraints forced us to purchase a JP-5 fuel from the local government contractor and to produce a single, higher S content fuel by mixing in THSP sufficient to boost the S level by ~800 ppm. We thus ended with two fuels from a single hydrocarbon matrix containing 1050 and 1820 ppm S for use in the B757 fuel S tests. A third JP-5 fuel obtained from the NASA Langley stock and containing 810 ppm S was used in the T-38 runs

and in B-757 experiments to test the sampling system and to fill the role of low S fuel when the supply of 1050 ppm S fuel was depleted.

Exhaust plumes from both the Langley T-38 and B-757 were sampled during EXCAVATE, with the primary interest in sampling the T-38 being to test and perfect our measurement procedures, determine optimum dilution ratios, to evaluate sampling losses, and to obtain information on particle formation and growth as the exhaust plume cooled and dispersed. Thus, the T-38 test matrix included collecting samples at 3 different distances downstream from the engine exhaust plane (1, 10, and 25 m) as the engine was operated at power settings of 50 (idle), 60, 70, 80, 90, and 100% (takeoff) of maximum turbine rpm. Additionally, the 1 m inlet probe was operated at a number of dilution ratios to evaluate the impact of dilution upon particle losses and measured size distributions. Our objectives in sampling the B-757 aircraft additionally included determining the influence of fuel S on particle formation, thus its test matrix included collecting samples 1, 10, 25 and 35 m downstream of the exhaust plane as the engine was operated at engine pressure ratios (~power) of 1.03 (idle), 1.15, 1.30, 1.40, and 1.50 (1.70 is takeoff) and burned fuels containing 810, 1050, and 1820 ppm S.

Table 1: Exhaust Characterization Measurements

Species/Parameter	Technique	Group
Engine Parameters	Aircraft Systems	LaRC
Fuel Sulfur Content	X-ray Fluorescence	LaRC
Exhaust Parameters (T, P, Velocity)	Pitot tubes, thermocouples	LaRC
Sample and Exhaust CO ₂	IR spectrometer	LaRC
Aerosol Size and Volatility (3 to 100 nm)	nASA	UM
Aerosol Size (10 to 1000 nm)	DMA, OPC	LaRC
Black Carbon	PSAP	LaRC
Nonmethane Hydrocarbons	Grab Samples	UCI
SO ₂ , CO ₂ , SO ₃ , H ₂ O, HONO	TDL	Aerodyne/GRC
Aerosol Composition	Mass Spectrometer	Aerodyne
H ₂ SO ₄ , HONO, HNO ₃ , SO ₂	Chemical Ion Mass Spect	AFRL
Ion Density	Gerdien Condenser	AFRL
Ion Composition	Ion Mass Spec	AFRL

3 SUMMARIES OF RESULTS

3.1 Chemions (AFRL MS Group)

Negative ion mass spectra were obtained for chemions in the T-38 exhaust plume for engine rpm values of 49.5, 60, 70, 80, 90, and 100% of maximum. An example of the IMS mass spectra is shown in Fig. 3. The results show that the total number of ions increases with engine rpm (with one exception discussed below) and that the mass spectrum moves to lower ion mass. Both observations are a result of the increased temperature and higher exhaust velocity (faster sampling) at higher rpm. At 100% rpm the major ion peak is HSO₄⁻, which results from ion-molecule reactions taking place between the combustor and the sampling orifice of the IMS. Some of the ion masses are as yet unassigned to a particular molecular species and may remain unassigned. In earlier work the unidentified masses were declared to be “oxyhydrocarbons,” and this may be the best one can do at the present time.

The “total ion” data, as illustrated in Fig. 3 may be used to estimate the ion concentration (plasma density) at the engine exhaust plane. The ion concentration at the IMS sampling orifice is much lower than at the engine plane because of ion-ion mutual neutralization reactions that take place in the exhaust stream. The ion-ion mutual neutralization reaction rate constant is about 10⁻²⁶ cm⁶ s⁻¹ at atmospheric pressure and is approximately independent of the ion type because the neutralization is mobility-limited at this pressure. A temperature correction must be estimated. To determine the ion concentration at the engine exhaust plane from the total ion data, one needs (a) the

detection efficiency of the IMS, (b) the gas temperature, and (c) the sampling time or velocity of the exhaust gas. Item (a) decreases with temperature because ions are swept into the IMS sampling orifice by the gas in the sampling pipe, and the throughput of gas is temperature dependent. The detection efficiency of the IMS was measured at room temperature in the laboratory at 1 atm pressure and found to be $980 \text{ cm}^{-3} \text{ ion}^{-1} \text{ s}^{-1}$. The result of the calculations, effectively working backwards from the total ion signal to the engine exhaust plane, is shown in Fig. 4. An additional upward correction of the exhaust ion concentration may be made at a later date due to the problem of sampling from a high-velocity stream. The result that the ion concentration at 100% maximum rpm is lower than that at 90% is counterintuitive, but (a) the measurements were quite clear, and (b) both AFRL and NASA-LaRC measured a lower temperature at 100% maximum rpm than at 90%.

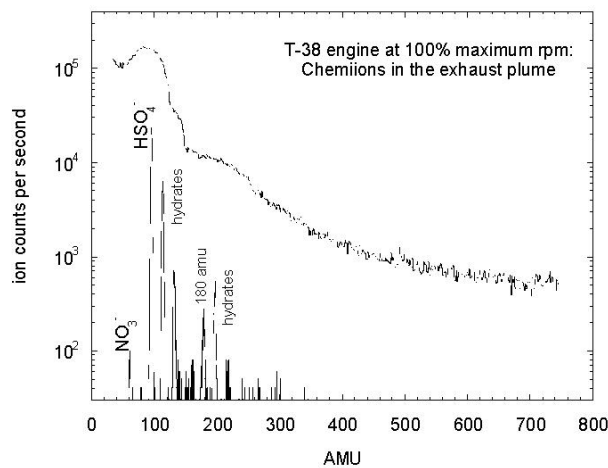


Figure 3. Mass analysis of chemiions in the exhaust of the T-38 jet engine at a point 3.22 m following the engine exhaust plane, at 100% of maximum compressor rpm. The upper line is the total transmitted ion current through the mass spectrometer at zero resolving power.

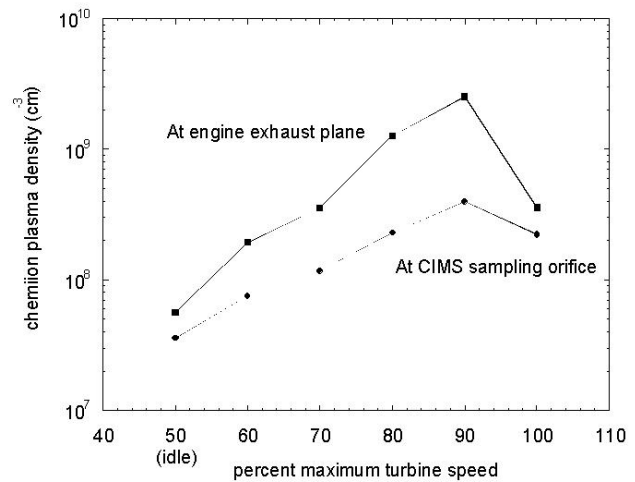


Figure 4. The result of modeling backwards from the total IMS ion signal to obtain the ion concentration at the exhaust plane of the T-38 jet engine. Ion loss in the sampling path is due to ion-ion mutual neutralization.

3.2 HONO (Aerodyne TDL Group)

In the previous NASA/QinetiQ tests (Whitefield et al., 2002), HONO had been measured, both at the combustor exit and, at higher levels, at the engine exit. However, due to substantial etalon fringes, the HONO concentrations measured in those tests had been near the detection limit. Also, because sampling was carried out in a single configuration, it was difficult to rule out the possibility that HONO was being formed from NO and H₂O in the sampling probe.

In the EXCAVATE measurements behind the B757, the detection limit was as low as 100 ppbv in the multipass cell. At high powers, over 2 ppmv of HONO was observed. When converted to emission indices, the B757 HONO results shown in Figure 5 show a clear power dependence, decreasing with decreasing power at the two lower settings but roughly constant at the highest three settings. When the sampling point was moved back to 10m behind the engine, the HONO concentration may have decreased somewhat, though when the total error estimates shown in the figure are taken into account, this decrease is not necessarily significant. In contrast to the B757, which showed much more HONO than observed in the engine exhaust sampled in the 2001 NASA/QinetiQ tests, the T-38 HONO levels were not measurable, meaning they were well below 100 ppbv in the multipass cell. Thus, the EXCAVATE observations contain three points of comparison which suggest HONO formation in the probe is not a serious problem. In the move from sampling at 1m to sampling at 10m, the temperature and composition of the exhaust have changed

substantially, but the HONO fraction of exhaust species has not. In both the case of B757 engine power variation and in the change from B757 to T-38 exhaust, the exhaust properties have changed less than the HONO concentration. This is especially true for the comparison between engines: the change in HONO is more than an order of magnitude, while changes in temperature, NO and H₂O are much less than that. At high power, over 2 ppmv of HONO was detected in the B757 exhaust. These values correspond to EI(HONO) values of up to 0.25 (if nominal values apply to this exhaust, this is somewhat less than 5% of the NO).

3.3 Aerosol Physical Properties (Langley and U. Minnesota Aerosol Groups)

In measurements recorded behind the T-38, aerosol number EIs varied from 0.8 to $23 \times 10^{15} \text{ kg}^{-1}$ and averaged $6 \times 10^{15} \text{ kg}^{-1}$; aerosol mass EIs ranged from ~ 8 to 465 mg kg^{-1} , and averaged 111 mg kg^{-1} ; black carbon varied from 17 to 400 mg kg^{-1} and averaged 111 mg kg^{-1} ; the geometric mean diameter of the number-size distribution varied from 15 to 61 nm, and averaged 23 nm; and the volume mean diameter (VMD) ranged from 31 to 91 nm, and averaged 52 nm. At the 1 m sampling distance where the aerosol should be composed primarily of soot and other nonvolatile species (i.e., metals, PAHs), Number EIs values peaked at $\sim 5 \times 10^{15} \text{ kg}^{-1}$ at idle, then dropped by $>60\%$ and became relatively constant at turbine speeds above 70% of maximum rpm. Conversely, Mass EIs were $\sim 150\text{--}200 \text{ mg kg}^{-1}$ below 70% power, then increased by a factor of two upon reaching 100% power. This inverse relationship between Number and Mass EIs suggests that the particle size increases with engine power which is borne out by the calculated values for GMD and VMD; these parameters increased from 23 to 30 nm and 48 to 66 nm, respectively, in going from idle to full military power. Black Carbon EIS increased from $\sim 85 \text{ mg kg}^{-1}$ at idle to 272 mg kg^{-1} at 100% power and the ratio of BC to Mass EIs changed from 0.44 to 0.67 across this power range, indicating that, perhaps, a higher fraction of the aerosol emissions were composed of nonvolatile organics at the lower combustor temperatures characteristic of low power conditions. Ten meters downstream from the engine exhaust plane, aerosol Number EIs were typically higher and VMD's lower than at 1 m, suggesting that low volatility species had condensed to form new particles as the plume cooled. Because of their small sizes, these aerosols did not significantly add to the mass loading except at idle where the Mass EIs were twice the value observed at 1 m. This might be related to the longer growth period experienced by the aerosols in the low velocity plume, the propensity of the engine to emit more condensable hydrocarbons at low powers, or it might simply be caused by poor sampling statistics. Samples collected from the 25 m inlet exhibited even higher Number EIs but the trend in Mass EIs could not be delineated because, at that sampling distance, concentrations were too variable across the 60 second scan time of the DMA to yield reliable size distributions.

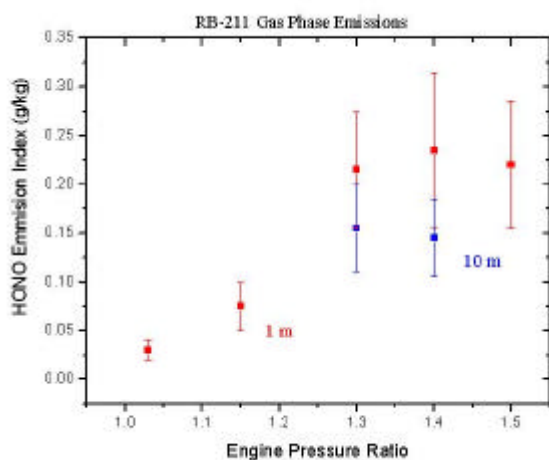


Figure 5. B-757 HONO emissions as measured by a TDL system at 1 and 10 m behind the engine exhaust plane.

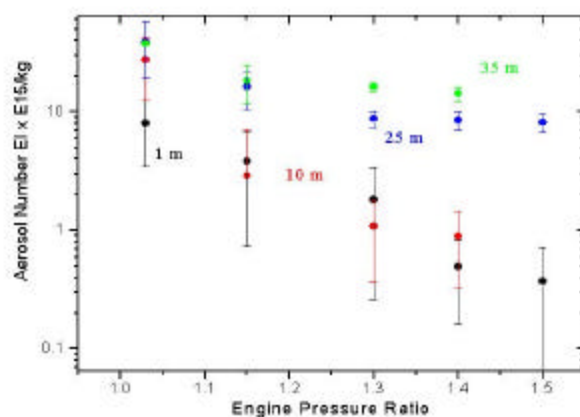


Figure 6. B-757 aerosol number EI for 1820 ppm S fuel as measured at 1, 10, 25 and 35 m behind the engine exhaust plane.

Emissions from the B-757, RB-211 engine were even more variable than those from the T-38. Number EIs ranged from 0.01 to $85 \times 10^{15} \text{ kg}^{-1}$, and averaged $\sim 9 \times 10^{15} \text{ kg}^{-1}$ for the entire data set. Mass EI values ranged from ~ 10 to $>9000 \text{ mg kg}^{-1}$ and averaged $\sim 500 \text{ mg kg}^{-1}$; black carbon varied from 0.6 to 218 mg kg^{-1} and averaged 59 mg kg^{-1} ; the GMD of the number-size distribution varied from 10 to 101 nm, and averaged 27 nm; and VMD values ranged from 31 to 110 nm, and averaged 52 nm. Although fuel S content played an identifiable role, engine power and sampling distance were the primary factors that governed this variability. For 1820 ppm S fuel and 1 m sampling case, Number EIS dropped from $\sim 8 \times 10^{15}$ to $0.37 \times 10^{15} \text{ kg}^{-1}$, or more than a factor of 20, upon increasing power from idle (1.03 EPR) up to 1.5 EPR (Fig. 6). Similarly, for 1820 ppm S and a power setting of 1.4 EPR, Number EIs increased from $\sim 0.4 \times 10^{15}$ to $14.3 \times 10^{15} \text{ kg}^{-1}$, or a factor of 38, between 1 and 35 meters downstream of the engine exit plane. Results from the 1050 ppm S fuel runs exhibited similar trends. A large fraction of the particles present at low engine powers were composed of organic material, thus it is likely that the decrease in particle number emissions with increasing EPR is caused by more efficient combustion of low volatility fuel components as the engine exhaust gas temperature increases from $\sim 355^\circ\text{C}$ at idle to $\sim 630^\circ\text{C}$ at 1.5 EPR. The increasing number concentrations with plume age are caused by formation of a nucleation mode within the aerosol size distribution (Figs 7 and 8) and is also consistent with Aerodyne observations of increasing amounts of relatively small-diameter sulfate aerosols within aged plumes. As for mass emissions, except for the idle condition where the engine emitted variable and sometimes significant amounts of organic aerosols depending on the temperature history of the combustor, EIs tended to increase with power. For 1820 ppm S and 1 m sampling distance, Mass EIs increased from 64 to 98 mg kg^{-1} in going from 1.15 to 1.5 EPR. This positive correlation between Mass EIs and EPR appears to be driven by the tendency of the engine to produce greater amounts of black carbon (BC) aerosols at higher temperatures/engine powers. Comparing DMA mass EIs with BC EIs, for 1 m sampling, we deduce that BC generally accounted for $< 10\%$ of total aerosol mass emissions at idle but almost 100% for the higher power settings. Mass EIs increased with plume age, however, presumably due to condensation of low-volatility material as the emissions cooled. For 1820 ppm S fuel and an EPR of 1.4, Mass EIs increased from 95 to 247 mg kg^{-1} between samples collected at 1 and 35 m. The 1050 ppm S fuel exhibited the same, factor of two-to-three increasing trend. These results were supported by AMS observations of increasing organic and sulfate aerosol mass with plume age.

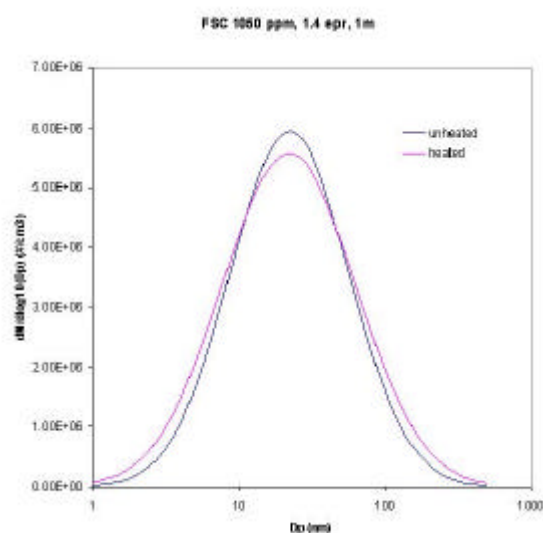


Figure 7. Heated (300°C) and unheated (20°C) B-757 aerosol size distributions recorded at 1 m as the engine burned 1050 ppm S fuel at 1.4 EPR.

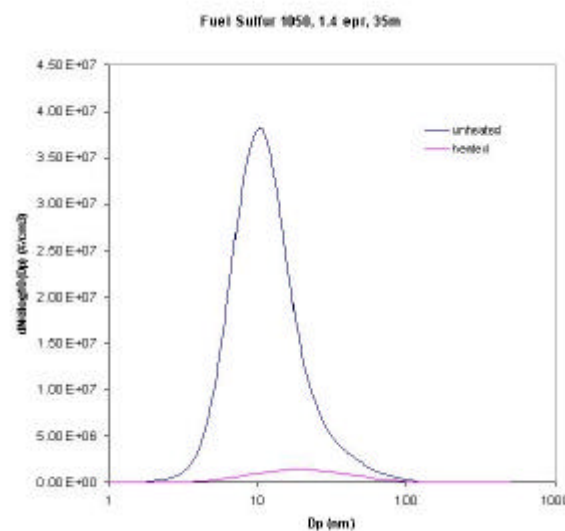


Figure 8. Heated (300°C) and unheated (20°C) B-757 aerosol size distributions recorded at 35 m as the engine burned 1050 ppm S fuel at 1.4 EPR.

3.4 Non refractory PM_{1.0} Composition (Aerodyne Aerosol Mass Spectroscopy Group)

Excluding sampling periods from shortly after engine starts and power changes when sometimes enormous quantities of organic aerosols were emitted, the RB-211 exhaust plume organic and sulfate mass loadings ranged from 1 - 45 $\mu\text{g m}^{-3}$, and 0.1 - 7 $\mu\text{g m}^{-3}$, respectively. Except for measurements made at idle (1.03 EPR), sulfate EIs appeared to be independent of engine power settings, and proportional to the fuel sulfur content. For measurements recorded at 35 m and fuel sulfur contents of 810 ppm, 1050 ppm and 1820 ppm, the average EI of sulfate equaled 0.0025, 0.003 and 0.007 g kg^{-1} of fuel g kg^{-1} of fuel, respectively. The anomalous EIs measured at idle could be due to quantification errors for sulfate due to interference from organics. For organics, the EIs increase with engine power, from 0.018 g kg^{-1} at idle to 0.04 g kg^{-1} of fuel at 1.5 EPR (Boudries et al., this issue, see references). The decrease in EIs as a function of engine power could be explained by better combustion efficiency at high engine power and consequently a reduction in the emissions of unburned fuel and oil. It is also important to note that the EIs of organics as a function of engine power were found to be independent of fuel sulfur content and that the individual organic aerosols exhibited mass signatures more similar to those of turbine engine oil than those of the JP-5 jet fuel.

The relative mass loading of organics and sulfates increased significantly with sampling distance. For instance, at engine power of 1.3 EPR, the organics concentrations increased from 5 to 25 $\mu\text{g m}^{-3}$ and sulfate from 1 to 6 $\mu\text{g m}^{-3}$ between samples collected at 10 and 35 m. This increase could be explained by condensation of gas-phase pollutants on pre-existing aerosols within the aging exhaust plume. Confirming this hypothesis, we found that both the organic and sulfate aerosol size distributions shift to larger sizes when sampled further downstream of the engine exhaust plane, indicating the condensational growth. We also observed distinctly different growth rates for these species, which suggests that they were externally mixed. For example, at 1 m sampling distance, the organics and sulfates exhibited mean aerodynamic diameters of ~ 30 nm whereas at 35 m, the organic modal diameter had increased to 300 nm and the sulfate to 70 nm. These observations are supported by DMA data that indicate the nucleation mode (30 - 70 nm) mass and number concentration was dependent upon fuel sulfur content.

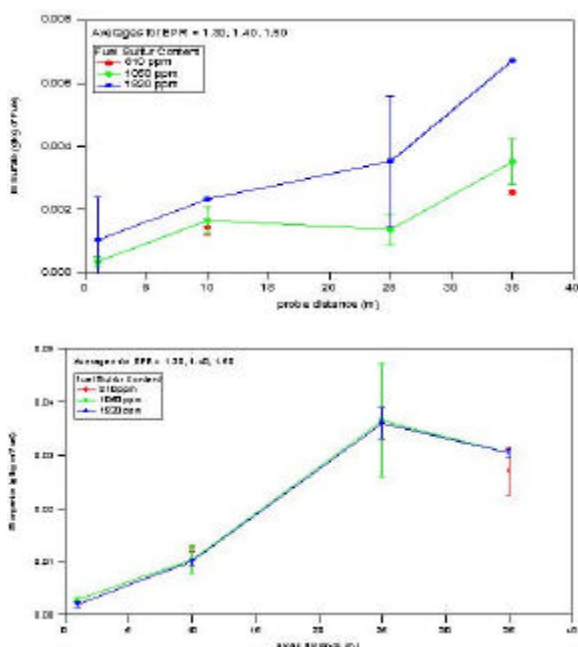


Figure 9. B-757 sulfate and organic aerosol emission indices as functions of sampling distance and fuel S content.

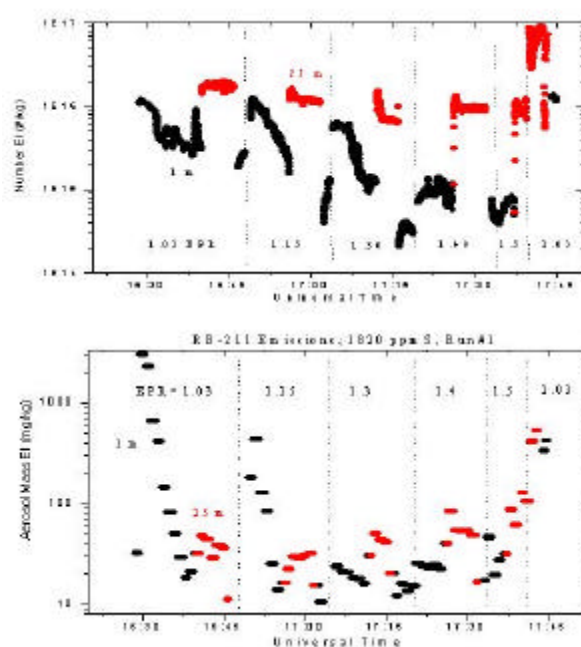


Figure 10. Time series of aerosol number EI (top) and mass EI (bottom) recorded during an engine run that included a cold start followed by a sequence of power changes.

Figure 9 shows the variation of EIs as a function of sampling probe distance measured for all sulfur fuel content. Here the EIs are found to be positively correlated with probe distance. The lowest EIs are measured at 1 m behind the engine and the highest EIs are measured at 35 m behind the engine. For all fuel used, the sulfate emission indices increase with distance suggesting aerosol sulfate growth through gas to particle conversion downstream of the exhaust plumes. This conversion is occurring as the exhaust cools down as a consequence of dilution with ambient air. For sulfate, the EIs are also found to be a function of sulfur fuel content. The lowest EIs are measured for the lowest fuel sulfur content and vice-versa. At 35 m behind the engine, the sulfate EIs increase by a factor of 2.89, while the fuel sulfur content increased by 2.14. Within the uncertainty of our measurement, we can conclude that the EIs are linearly proportional to fuel sulfur content.

3.5 Transient Emissions (Langley and Aerodyne Aerosol Groups)

Emission data acquired at idle and 1.15 EPR were highly variable and depended more on how long the engine had been running and the time since power change than upon the selected test variables of fuel S or plume age. For example, Figure 10 (top) shows a 1-second resolution time-series plot of the RB-211 Number EIS for 1820 ppm S fuel and samples extracted at 1 and 25 m downstream of the engine exhaust plane. The engine had cooled for ~1 hr prior to the beginning of the record. Note that 1 m values are $\sim 10^{16} \text{ kg}^{-1}$ at startup then drift downward by a factor of 5 over the 20 minute run at 1.03 EPR. When power is increased to 1.15 EPR, Number EIs jump back up to 10^{16} kg^{-1} , then begins to drift downward as the engine re-equilibrates to the new fuel flow rates and combustor temperatures, reaching $\sim 10^{15} \text{ kg}^{-1}$ just before the power is increased to 1.3 EPR. Similar jumps in Number EIs occurred after each power change although the subsequent drift was less at the higher EPR settings. Equally dramatic changes were observed in mass emissions (Fig. 10, bottom). For example, at engine start, mass EIs peaked at $\sim 3000 \text{ mg kg}^{-1}$, then decreased to $< 100 \text{ mg kg}^{-1}$ some 10 minutes later. Although a reduction in number concentrations contributed to this change, it was primarily driven by a shift in the modal diameter from $\sim 100 \text{ nm}$ to $< 25 \text{ nm}$ during this time period. The power increase from 1.03 to 1.15 EPR produced similar enhancements in mass emissions (and GMD) that required 3 to 4 minutes to settle back down to a steady state value(s). Order-of-magnitude transients also occurred when power was reduced from 1.5 EPR to idle. In terms of an explanation, simultaneous aerosol mass spectral data indicate the transient aerosols were composed of organic species that possessed mass signatures similar to those of engine oil. After cold starts and power changes in the low EPR range, it takes a few minutes for the compressor stages to reach thermal equilibrium and establish the very tight component tolerances necessary for optimum engine performance. We speculate that during this thermal adjustment period, a minor amount of engine oil leaks around the seals and produces the observed organic aerosol enhancements. It is significant to note that the enhancements were present in samples collected at 1 m where the exhaust gas temperatures were quite high; this supports the idea that they were composed of relatively non-volatile species such as those present in thermally stable turbine engine lubricating fluid. It is also possible that a fraction of these particles was derived from unburned fuel, as whole air samples collected within the plume shortly after engine start contained significant enhancements in relatively low-molecular weight hydrocarbon species. Unburned fuel is certainly present within the exhaust just before combustor ignition and may take a few minutes to volatilize and be cleared from the downstream sections of the engine.

REFERENCES

- Whitefield, P.D., et al., "QinetiQ/NASA Collaborative Programme – Final Report," produced for UK Department of Trade and Industry Under Order/Contract reference F11X1DXX by QinetiQ Ltd, Cody Technology Park, Farnborough, Hampshire GU14 0LX, UK, 2002. Also available as NASA Contractor Report CR-2002-211900.
- Anderson, B.E., et al., Airborne observations of aircraft aerosol emissions, 1, Total and non-volatile particle emission indices, *Geophys. Res. Lett.*, 25, 1689-1692, 1998.
- Anderson, B.E., et al., An assessment of aircraft as a source of particles to the upper troposphere, *Geophys. Res. Lett.*, 26, 3069-3072, 1999.
- Arnold, F., Detection of massive negative chemiions in the exhaust plume of a jet aircraft in flight, *Geophys. Res. Lett.*, 26, 1577-1580, 1999.

- Boudries, H., et al., Aerosol and Gas Chemistry of Commercial Aircraft Emissions Measurements in the NASA EXCAVATE Experiment. This issue.
- Brock, C.A., et al., Ultrafine particle size distributions measured in aircraft exhaust plumes, *J. Geophys. Res.*, *105*, 26,555-26,567, 2000.
- Miake-Lye, R., et al., SO_x oxidation and volatile aerosol in aircraft exhaust plumes depend on fuel sulfur content, *Geophys. Res. Lett.*, *25*, 1677-1680, 1998.
- Petzold, A., et al., In situ observations and model calculations of black carbon emission by aircraft at cruise altitude, *J. Geophys. Res.*, *104*, 22,171-22181, 1999.
- Schumann, U., et al., Pollution from aircraft emissions in the North Atlantic flight corridor: Overview on the POLINAT projects, *J. Geophys. Res.*, *15*, 3605-3631, 2000.
- Schumann, U. et al., Influence of fuel sulfur on the composition of aircraft exhaust plumes: The experiments SULFUR 1-7, *J. Geophys. Res.*, *107*, 10.1029/2001JD000813, 2002.
- Thompson, A., et al., Introduction to special section: Subsonic Assessment Ozone and Nitrogen Oxide Experiment (SONEX) and Pollution from Aircraft Emissions in the North Atlantic Flight corridor (POLINAT 2), *J. Geophys. Res.*, *105*, 3595-3603, 2000.
- Toon, O.B. and R.C. Miake-Lye, Subsonic Aircraft Contrail and Cloud Effects Special Study (SUCCESS), *Geophys. Res. Lett.*, *25*, 1109-112, 1998.

SAE E-31 Committee on Aircraft Exhaust Emission Measurements and an Aerospace Information Report on the Measurement of Non-volatile Particle Emissions

R.C. Miake-Lye*

Aerodyne Research, Inc., Billerica, Massachusetts, USA

V. Zaccardi

Jacobs/Sverdrup, Arnold Air Force Base, Tullahoma, Tennessee, USA

Keywords: particle emissions, SAE, Aerospace Information Report, CAEP

ABSTRACT: The SAE E-31 committee has specified measurement techniques and protocols for aviation emission measurements for many existing regulations and is currently focused on writing an Aerospace Information Report (AIR) on the measurement of non-volatile particle emissions. This AIR is an initial step in developing an Aerospace Recommended Practice (ARP) as have been previously written by E-31 for gaseous emissions (ARP1256) and smoke number (ARP1179). These two ARPs have been incorporated in regulation by the USEPA and ICAO (Annex 16) and are widely used and referenced by the engine measurement community. The motivation for preparing the present AIR on non-volatile particles and its scope and content are described.

1 INTRODUCTION

Agencies responsible for regulating and certifying aviation operations have begun to examine methods for measuring particle emissions from aircraft engines. There is general consensus that the regulations regarding the emission of visible smoke for aircraft engines, which have been in place for decades, do not address and are not relevant to the measurement of particles responsible for health effects and environmental impacts. Working Group 3 of the ICAO Committee on Aviation Environmental Protection (CAEP) has asked the SAE E-31 committee for technical assistance in developing appropriate particulate characterization techniques for routine certification of aircraft turbine engines. The SAE E-31 committee has specified measurement techniques and protocols for aviation emission measurements for many existing regulations and the committee has accepted these requests for the specification of small particle emissions measurement. It is the intent of the E-31 committee to make use of both committee expertise and outside technical advice to develop a set of recommendations that will form the basis for an Aerospace Information Report (AIR). This AIR will be subject to evaluation and review by the regulatory agencies, industry, and the engineering community that performs aviation emissions measurements.

2 E-31 HISTORICAL CONTEXT

SAE (Society of Automotive Engineers) International is an international technical organization serving the transportation industry, including automobiles, heavy duty vehicles, and aerospace. The E-31 Committee was chartered within the aerospace arm of SAE in 1968 "to establish standard methods and instrumentation for all types of exhaust emissions, other than normal atmospheric constituents, from aircraft engines ...". The initial impetus for E-31 was to provide guidance on measuring pollutants from airplanes that were contributing to environmental problems in and around airports. The first activities were to develop Aerospace Recommended Practices (ARPs) for visible smoke (ARP1179, Aircraft Gas Turbine Engine Exhaust Smoke Measurement, 1970) and for

* *Corresponding author:* Miake-Lye, Richard C., Aerodyne Research, Inc., Billerica, Massachusetts, 01821-3976 USA. Email: rick@aerodyne.com

gaseous emissions (ARP1256, Procedure for the Continuous Sampling and Measurement of Gaseous Emissions from Aircraft Turbine Engines, 1971). These ARPs were adopted by regulatory agencies in the USA and internationally via ICAO to prescribe how engine emissions are quantified.

E-31 has updated these two measurement procedure documents over the years as the techniques have improved and been refined. An additional ARP (ARP1533, Procedure for the Calculation of Basic Emission Parameters for Aircraft Turbine Engines) on analyzing the data measured using ARP1256 was developed and released in 1986. In 1990 the E-31 charter was revised to both broaden the scope of measurement and focus the emphasis of its activities specifically to measurement only. The broadening of scope was several fold: to include on-wing engines and auxiliary power units, to explicitly task the committee to continually review and update the ARPs, and to acknowledge the function of the committee in exchanging information and generating discussion on advances in measurement technology. At the same time, it was made clear that E-31 should remain separate from the policy issues of setting emissions level goals or requirements, and that even strategies for minimizing or controlling emissions are outside the purview of the committee, per se. The 1990 charter revision included the following language: "to include aircraft power plants and combustion systems review and maintain standards provide a forum for discussions and the introduction of new ideas..... E-31 will not address engine emissions levels nor control strategies to meet air quality standards".

As part of the broadening of scope, E-31 published ARP4418 in 1995 which addressed the measurement of emissions in cabin bleed air, which is the air obtained from the gas turbine's compressor system and used to pressurize and ventilate the passenger cabin. More recently, the committee has begun to consider complete revision of the measurement procedures due to significant and on-going improvements in measurement technology. The first revisions will be directed at the emissions of particles, partly because the original requirement was to reduce visible smoke and that need has been largely superseded and partly because the environmental and human health issues associated with particles have become much better understood in the intervening years. It is this particle measurement issue that is the topic of the Aerospace Information Report currently being written and reviewed by E-31.

The E-31 committee is primarily composed of technical measurement specialists. A wide range of the aircraft turbine engine community is represented including engine manufacturers, direct users of installed engines (notably commercial airframe and military users), and governmental regulatory agencies and laboratories. The committee membership is international, with strong European involvement representing industry and government labs. The US is well represented both by industry and government, including regulatory agencies (EPA and FAA), NASA, and the Department of Defense. Due to cross memberships, good connections are established and maintained with ICAO Working Group 3 and with ASME Committee on Stationary Gas Turbine Engines. Table 1 summarizes the composition of the committee.

Table 1. E-31 Committee Composition

Composition in Category		US Government	
Engine Manufacturer	4	Air Force	4
Air Frame Manufacturer	1	Navy	1
Industry	3	Army	1
Academia	2	Depart. of Trans.	1
European	5	EPA	2
ICAO WG-3	Chair	FAA	2
ASME Stationary Eng.	Chair	NASA	2

3 AIR ON NON-VOLATILE PARTICLES

The E-31 Committee has had a long interest in particle emissions, starting with its first ARP on smoke. As new measurement technology has become available, E-31 has invited speakers to present work using advanced techniques. Both improved means of measuring visible obscuration and

related techniques for measuring more detailed particle emission parameters have been reviewed by E-31. With this background and driven by requests from ICAO Working Group 3, the US FAA, and US EPA, a Particle Subcommittee was formed to address the need for a standard for measuring particles beyond the existing Smoke Number ARP.

Unlike in the late 1960's when regulations were being formulated and the measurement requirements were perhaps more clearly defined, the subcommittee is faced with suggesting best measurement practice in the absence of specific regulatory requirements. In order to move forward without having a concrete regulatory framework, the subcommittee chose to create a preliminary document to define the problem and outline an approach to addressing it. Thus, in April 2002, the subcommittee released a "Position Paper" which outlined E-31's view of the particle measurement issue and the steps needed to develop, eventually, an Aerospace Recommended Practice on particle measurement.

The Position Paper discusses particle emissions from aircraft engines and the present status of Smoke Number, as has been outlined above. Current controls on all emissions and ARP 1179 for Smoke Number is presented and contrasted with what is needed to understand human health effects and environmental consequences. The need for advanced techniques, such have been developed for a variety of emissions requirements, are discussed and contrasted for their application to aviation emissions in general terms. The point is also made, however, that advanced measurement techniques can be applied to measure specific particle emission parameters, but regulations must specify which parameters are to be measured. And, further, the regulations must be specific enough that the measurement requirements are unambiguous.

The status of particle environmental effects is in a state of rapid flux. The Position Paper acknowledges that both primary particles formed within the engine and condensable gases emitted from the engine can both contribute to the condensed phase particles eventually deposited in the environment. However, the measurement issue that will be addressed at this point will be the measurement of non-volatile particles at the exit plane of the engine. The chemical and surface properties of the emitted particles and the possibility of newly formed volatile particles condensing outside of the engine are specifically excluded from the present measurement technique identification. These latter issues are important and the subcommittee intends to address them in due course if driven by regulation.

Based on the particle emission issue defined in this way, the Position Paper established the intent of the E-31 Particle Subcommittee to write an Aerospace Information Report on the measurement of non-volatile particle emissions. This will allow the most promising techniques for application to aviation engines to be discussed and presented to engine measurement community. Based on the AIR, the measurement community and regulatory agencies can provide feedback on the appropriateness and relevance of the various techniques to the evolving regulatory and technological requirements. Based on this feed back, the AIR can be enhanced and refined to become a recommended practice and a measurement standard as an ARP.

The AIR is currently under review. It begins with a definition of its scope to be non-volatile particles. Then particle measurement techniques are reviewed, first for measuring particle mass, followed by measurement of particle number density and size distributions. For both measurement classes several techniques that have been successfully applied to aviation engine measurement are presented. Other measurement techniques that may be promising for this application are also briefly described. Finally, a discussion of probes is presented, since the probes can significantly affect the particles that are introduced into the measurement instrument. Both sampling losses and perturbations to the particles being sampled are important concerns in the design of sampling systems.

4 DEVELOPMENT OF A RECOMMENDED PRACTICE

The AIR is being written and reviewed as the committee's experts' and advisors' knowledge is assimilated and the report is expected to be completed in the current year. This AIR will be subject to evaluation and review by regulatory agencies, industry, and the engine measurement community. Based on the experience gained and on improvements in measurement practice, the AIR will then be used over the course of several years to develop a set of measurement specifications contained in

an ARP on particle measurements. ARPs are the official statement of the SAE on how emissions measurements should be performed and, as such, have historically provided methodologies acceptable to the regulatory agencies both in the US and internationally. This ARP will then be available for use by regulatory agencies and engine measurement engineers as an authoritative reference point for reliable measurement of aviation particle emissions.

REFERENCES

- SAE E-31, 1990: ARP1256, Procedure for the Continuous Sampling and Measurement of Gaseous Emissions from Aircraft Turbine Engines, Society of Automotive Engineers, Rev. B.
SAE E-31, 1997: ARP 1179, Aircraft gas turbine exhaust measurements, Society of Automotive Engineers, Rev. C.
SAE E-31, 2002: Position Paper on Particle Matter Measurements, Society of Automotive Engineers, 2002.

Particle Emissions from Aircraft Engines - An Overview of the European Project PartEmis

A. Petzold^{*}, M. Fiebig, L. Fritzsche, C. Stein, U. Schumann
DLR, Institute of Atmospheric Physics, Oberpfaffenhofen, Germany

C.W. Wilson, C.D. Hurley
QinetiQ, Farnborough, UK

F. Arnold, E. Katragkou
Max Planck Institute for Nuclear Physics, Heidelberg, Germany

U. Baltensperger, M. Gysel, S. Nyeki
Paul Scherrer Institute, Villigen, Switzerland

R. Hitzemberger, H. Giebl
University of Vienna, Vienna, Austria

K. J. Hughes
University of Leeds, Leeds, UK

R. Kurtenbach, P. Wiesen
University of Wuppertal, Wuppertal, Germany

P. Madden
Rolls Royce plc, UK

H. Puxbaum, S. Vrchoticky
Technical University of Vienna, Vienna, Austria

C. Wahl
DLR, Institute for Combustion Technology, Cologne, Germany

Keywords: particle emissions, combustion aerosol, PartEmis

ABSTRACT: An overview of the goals and achievements of the European PartEmis project (Measurement and prediction of emissions of aerosols and gaseous precursors from gas turbine engines) is presented. PartEmis is focussed on the characterisation and quantification of exhaust emissions from a gas turbine engine. The engine was composed of a combustor and a unit to simulate a 3-shaft turbine section (so-called Hot End Simulator; HES). A comprehensive suite of aerosol, gas and chemi-ion measurements were conducted under different, i) combustor and HES operating conditions, ii) fuel sulphur concentrations. Measured aerosol properties were mass and number concentration, size distribution, mixing state, thermal stability of internally mixed particles, hygroscopicity, cloud condensation nuclei (CCN) activation potential, and chemical composition. Furthermore, chemi-ions, non-methane volatile organic compounds (NMVOCs) and OH were monitored. The combustor operation conditions corresponded to modern and older engine gas path temperatures at cruise altitude, with fuel sulphur contents (FSC) of 50, 410, and 1270 g kg⁻¹. The combustor behaves like a typical aircraft engine combustor with respect to thermodynamic data and main emissions, which suggests that the PartEmis database may be applicable to contemporary aircraft engines.

^{*} *Corresponding author:* Andreas Petzold, DLR Institute of Atmospheric Physics, Oberpfaffenhofen, 82234 Wessling, Germany. Email: andreas.petzold@dlr.de

1 INTRODUCTION

The role of aviation-related particle emissions in the upper troposphere and lowermost stratosphere is a matter of concern, particularly with respect to a possible effect on the composition of upper tropospheric aerosol and the life cycle of cirrus clouds (Boucher, 1999; Schumann and Ström, 2001). Despite recent considerable progress in the characterisation of the aerosol particles emitted from jet engines (e.g., Anderson et al., 1998; Brock et al., 2000; Hagen et al., 2001; Petzold and Schröder, 1998; Petzold et al., 1999; Schumann et al., 2002), microphysical and chemical properties as well as the influence of engine operating conditions still remain poorly characterised with respect to particulate emissions. However, this kind of data set forms a basic pre-requisite for modelling approaches which investigate the role of aviation aerosols and their effect on the environment.

In the framework of the European project PartEmis (“Measurement and prediction of emissions of aerosols and gaseous precursors from gas turbine engines”), the influence of operation conditions and fuel sulphur content (FSC) on the microphysical and chemical properties of particles emitted from a jet engine simulator was investigated. For these purposes, an engine simulator which met the ICAO (International Civil Aviation Organisation) engine emissions smoke standard was operated on a test rig at the QinetiQ test site at Pyestock, UK. This engine simulator consisted of a real jet engine combustor and a so-called Hot End Simulator (HES) which simulates the pressure and temperature profiles found in a jet engine turbine section. In a first experiment, the emission properties of the combustor were studied. These data were then used as boundary conditions for a second experiment which focused on the emission properties of the combustor-HES combination. The aerosol microphysical and chemical properties investigated in this study covered number, size, and mass concentration of primary combustion aerosol particles which form in the combustion process and secondary volatile particles which form outside the combustor in the cooling plume. Furthermore, the volatile fraction of internally mixed combustion particles, particle hygroscopicity, and cloud condensation nuclei (CCN) activation potential were studied. In addition, the emission of chemi-ions, non-methane volatile organic compounds (NMVOCs) and OH was monitored. A detailed description of the PartEmis experiments is given by Wilson et al. (2003).

2 METHODS

A tubo-annular, transpiration cooled combustor was chosen for tests on QinetiQ’s High Pressure Combustion Rig. Air was delivered from a four-stage compressor and heater unit. A back-pressurising valve located downstream of the combustor maintained the correct pressure in the system. The standard test-rig instrumentation covered 41 control parameters, such as temperature, pressure, fuel and air flow rates, as well as CO, CO₂, total hydrocarbons (HC), NO_x, and smoke number. Two engine operating conditions were simulated to represent the thermodynamic conditions found in the turbine stages of legacy referred to here as “old” and modern aircraft cruise conditions at 35,000 feet (~ 11,700 m). This will ensure that the conversion of fuel sulphur to oxidised sulphur species is replicated. These old and modern combustor operating conditions were also chosen to meet the ICAO smoke emission level. Fuel sulphur content (FSC) levels covered the range from low sulphur fuel (50 µg g⁻¹) to the contemporary average (410 µg g⁻¹) and to a maximum of about three times this average (1270 µg g⁻¹) defined here as Low, Mid and High (L, M, H) FSC, respectively. The sulphur content was varied by adding known quantities of benzenethiol (C₆H₅SH) to the low FSC fuel. The operation conditions are summarised in Table 1.

The employed aerosol measurement methods consisted of various size-selective methods, aerosol absorption photometers, thermodenuder methods, a Cloud Condensation Nucleus Counter (Hitzenberger et al., 2003), an extensive set of chemical analytical methods (Petzold et al., 2003), mass spectrometry methods for the detection of sulphur-containing species, and laser-induced fluorescence for OH measurements. A summary of deployed methods is given in Table 2.

The black carbon (BC) mass concentration and the aerosol absorption coefficient in the diluted sample gas were measured using a Particle Soot Absorption Photometer (PSAP; Radiance Research Inc, Seattle, USA). The specific absorption cross section at $\lambda = 0.55 \mu\text{m}$, $\sigma_{\text{abs}} = 6.7 \text{ m}^2 \text{ g}^{-1}$ was used for conversion of light absorption to BC mass. The number concentrations were measured in the size intervals $D = 4 - 7 \text{ nm}$, $7 - 9 \text{ nm}$, $9 - 20 \text{ nm}$, and $20 - 250 \text{ nm}$ with parallel-operated

Condensation Particle Counters (Condensation Particle Size Analyser, CPSA) which were set to different lower instrument cut-off diameters. Particles of size $D > 9$ nm which are detected in CPSA channels 3 and 4, are in the following referred to as N_{10} . Particle size distributions were measured with a commercial Scanning Mobility Particle Sizer (SMPS; TSI Model 3071) and a Volatility-Tandem Differential Mobility Analyser (V-TDMA) in the size range $D > 13$ nm.

Table 1. Combustor operating conditions during the 2001 Combustor and 2002 HES campaigns.

Combustor Parameters	Combustor Campaign		HES Campaign	
	Old	Modern	Old	Modern
T combustor inlet, K	566	766	566	760
T combustor outlet, K	1125	1448	1125	1360
P combustor inlet, 10^5 Pa	7.05	8.2	7.05	8.2
Air mass flow, kg s^{-1}	2.12	2.12	1.90	2.05
Fuel flow, kg s^{-1}	0.032	0.042	0.030	0.035
Air fuel ratio	66	50.3	66	58

The aerosol mixing state and the volatile fraction of the combustion aerosol were determined using thermal denuder methods which differentiate particles according to their thermal stability. Setting the thermal denuder temperatures to 390 K and 573-625 K, respectively, distinguishes volatile (vaporises at 390 K) sulphuric-acid like material from semivolatile (vaporises between 390 and 573 K), and refractory black-carbon like material. The thermal treatment of almost monodisperse particle size fractions which were pre-selected by a DMA provides information whether the aerosol is internally or externally mixed. The ratio of diameters after and before thermal treatment yields the particle shrinkage factor D^3/D_0^3 . This factor describes the particle volume reduction by the thermal treatment, i.e., the volatile volume fraction of internally mixed particles is $1 - D^3/D_0^3$.

The hygroscopic particle growth factor under subsaturated conditions was measured with a Hygroscopicity Tandem DMA. The obtained growth factor describes the particle growth by water uptake from the gas phase at a selected relative humidity. This growth factor indicates the presence of a coating of particles by a hygroscopic substance as, e.g., sulphuric acid. The fraction of particles which become activated as cloud condensation nuclei (CCN) were measured at a super-saturation of 0.7% with respect to liquid water using a Cloud Condensation Nuclei Counter (Giebl et al., 2002). This property becomes important as soon as a possible effect of aircraft engine emissions on atmospheric clouds is studied.

Aerosol samples were collected with filter stack samplers and low pressure Berner impactors for total aerosol and size-resolved chemical mass analysis. The chemical composition of the carbonaceous fraction of the exhaust particles was determined using multi-step combustion methods. Total carbon (TC) was determined by a combustion technique involving combustion in a vertical furnace and detection of CO_2 with a commercial NDIR (non dispersive Infrared spectrometer) unit. Aliquots of a collected filter sample were burnt in the ceramic tube of a combustion furnace with an excess of oxygen at a temperature of 1000 °C. Elemental carbon (EC) was determined by the ‘‘Cachier’’ method, i.e., another aliquot of the filter sample was treated for 2h at 320°C in an oxygen atmosphere to remove organic carbon compounds and then analysed with the same TC analysis method. The remaining carbon was attributed to elemental carbon (EC). Thermograms of the collected carbonaceous material were measured with a thermo-optical evolved gas analysis method (Schmid et al., 2001). To determine anions, e.g., SO_4^{2-} , as well as cations, two Dionex isocratic systems with electrochemical suppression were used.

In addition, the aerosol was sampled on quartz tubes containing glass wool. The aerosol loaded quartz tubes were analysed by 5 min thermodesorption in a Helium atmosphere at 130°C and 350°C, respectively. The desorbed $\text{C}_2 - \text{C}_{12}$ non-methane hydrocarbons (NMHC) were analysed with a gas chromatograph (Hewlett Packard). NMHCs were monitored using a compact GC instrument (Airmovoc 2010) with an enrichment system (cryotrap) and FID detector. $\text{C}_2\text{-C}_{10}$ aliphatic and aromatic NMHCs were measured with a time resolution of 10 min and with detection limits in the pptv range. Selected partially oxidised hydrocarbons (OHCs) such as aldehydes and

organic acids were collected by using special sampling cartridges and measured off-line using HPLC with a photo-array detector. The OHCs were measured with a time resolution of 4 min and with detection limits in the ppbv range.

Gaseous sulphuric acid was measured using a CIMS (Chemical Ionisation Mass Spectrometer) apparatus equipped with an Ion Trap Mass Spectrometer (ITMS). The ITMS allows CID (Collision-Induced-Dissociation) investigations of mass selected ions to be performed which in turn allows much better species identification than can be offered by a conventional mass spectrometer. In order to avoid sampling line losses a relatively short sampling line (150 cm) without dilution and with a temperature exceeding 150°C was used.

OH laser induced fluorescence (LIF) measurements were performed in the exhaust duct of the HES. The experiment comprised a Nd/YAG pumped dye laser set up to generate light at $\lambda = 281.913\text{nm}$ in order to excite the $Q_1(1)$ transition of $\text{OH } A^2\Sigma(v'=1) \leftarrow X^2\Pi(v''=0)$, chosen as it is one of the strongest transitions at the temperature expected at the observation point. Fluorescence was detected perpendicular to the path of the laser from the $v'=0 \rightarrow v''=0$ transition around 309 nm via a lens and a customised interference filter. In order to maximise the signal to noise ratio by discriminating against Raman scatter expected from N_2 and H_2O , an interference filter was centred at 308.75 nm with a band pass of 4.96 nm (FWHM). A gated CCD camera cooled to -30°C was used to collect the signal, allowing signal accumulation over long times in order to enhance sensitivity.

Table 2. Available equipment and parameters.

Parameter	Technique
Volatile condensation particles (number, size)	Condensation Particle Size Analyser (CPSA), Differential Mobility Analyser (DMA) connected to a Thermodenuder
Non-volatile carbonaceous particles (number, size)	Condensation Particle Counter (CPC), Scanning Mobility Particle Sizer (SMPS), DMA connected to a Thermodenuder Volatility Tandem-DMA
Surface density	Diffusion Charger
Aerosol absorption coefficient b_{abs} ,	Aerosol Absorption Photometer
Smoke Number SN	Smoke number method
Water uptake at $\text{RH} \leq 100\%$	Hygroscopicity Tandem-DMA
Cloud condensation nuclei activation	Thermal gradient CCN counter
Chemical composition	Berner low pressure impactor (BLPI) samples; filter stack samples; analysis via gravimetry (total mass), multi-step combustion method (organic/elemental carbon), evolved gas analysis (volatility of carbonaceous compounds) gas chromatography (aliphatic, constituents), ion chromatography (major ions)
CO , CO_2 , HC , NO_x , O_2 , H_2	Standard test rig instrumentation
HONO , HNO_3 ;	Chemical ionisation mass spectrometry
SO_2 , SO_3 , H_2SO_4 ;	Paul Ion Trap Mass Spectrometry (PITMAS)
Chemi-ions	
SO_2	
Gaseous hydrocarbon species	Quasi-on-line gas chromatography (GC); Sampling and off-line analysis
Partially oxidised hydrocarbons	DNPH method
OH	Laser-induced fluorescence (LIF)

Since the full set of applied instruments was connected to separate sampling lines according to specific instrument requirements, the precise determination of the dilution factors was a crucial task. After exit from the traversing probe, the sample was cooled to $\sim 150^\circ\text{C}$ using a water-jacket, and delivered to the undiluted and diluted sample lines. The undiluted line was insulated along its entire length in order to avoid wall losses of combustion products, while sample in the diluted line

naturally attained room temperature ($\sim 25^\circ\text{C}$) after dilution. Dilution with filtered air was necessary for the majority of instruments to reduce concentrations to a measurable level. The sample dilution factor was determined from CO_2 mixing ratios measured in the supplied dilution air, diluted sample, and undiluted sample, as well as from temperature and pressure sensors throughout the sample delivery system. Although stable gaseous species such as CO_2 and water vapour are unaffected by intrusive sampling, aerosols may be lost due to diffusion and sedimentation to the surfaces of the sampling system.

3 RESULTS

3.1 Microphysical Properties

The aerosol emitted from the Combustor is composed of primary particles forming inside the combustor and of volatile condensation particles nucleating in the cooling exhaust gas from gaseous precursors. The aerosol size distribution in the diluted exhaust gas of the combustor is shown in Fig. 1 for conditions with and without condensation particle formation. While the mode of combustion aerosol particles dominates the size range $D > 15$ nm with a maximum at 40 nm, another mode of nanoparticles is present in all cases in the size range $D = 7 - 20$ nm. Condensation particle formation, is occurring only at high FSC conditions and contributes to the size range $D = 4 - 7$ nm.

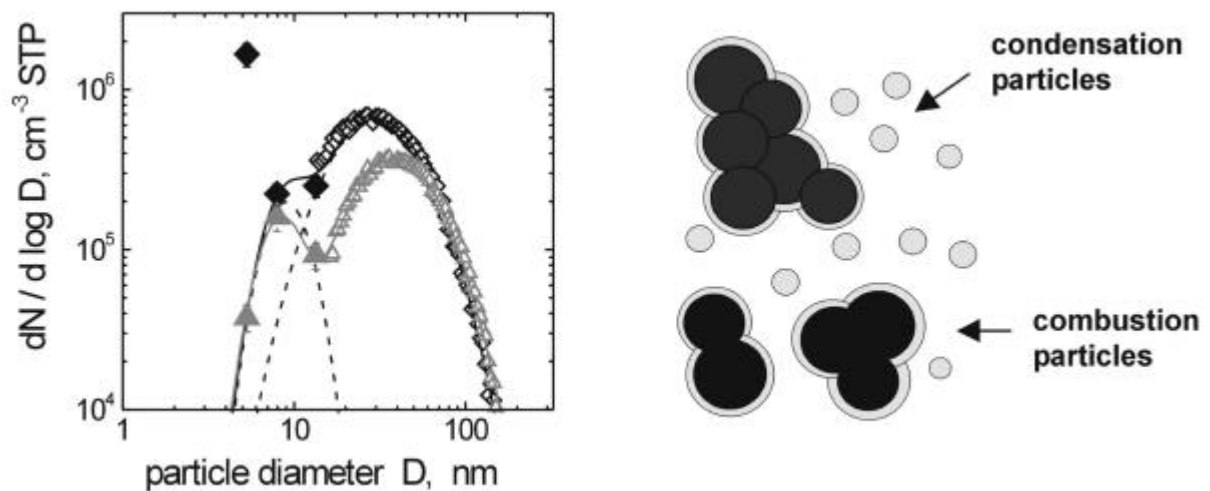


Figure 1. Left: size distribution of combustion aerosol with (◆) and without condensation particle formation (∇). Right: External aerosol mixture composed of volatile condensation particles (○) and coated nonvolatile combustion particles (◐).

The emission properties with respect to the primary aerosol are shown in terms of BC mass (EI_{BC}), TC mass (EI_{TC}), and number (EI_{N10}), emissions per kg of consumed fuel in Fig. 2. The number emission index EI_{N10} refers to particles with diameters $D \geq 10$ nm. In Fig. 2, also the count median diameter (CMD) of the exhaust aerosol size distribution is shown. Plotted are corresponding values for the combustor emissions and emissions from the HES low pressure stage. In the first place, it has to be mentioned that all the results are consistent. At old cruise conditions, an increasing number emission at constant black carbon mass emission is balanced by a decreasing particle size. It should be noted that these results originate from different measurement techniques.

When operated at old engine conditions with low combustor inlet temperature T_{C} , EI_{BC} varies from 0.051 to 0.081 g kg^{-1} . Operated at modern engine conditions with the higher inlet temperature, EI_{BC} ranges from 0.028 to 0.044 g kg^{-1} which is a factor of 2 lower. Similar relations hold for the

other properties. However, the amount of emitted particulate matter is within the range permitted by the ICAO rules in all cases. Mean CMD values are 37 – 41 nm for old engine and 40 – 44 nm for modern engine conditions. The geometric standard deviation of the size distribution is 1.67 (1.6 – 1.8) for both operation conditions (Petzold et al., 2003). The combustor operating conditions were found to have a weak influence on the size, number and mass of emitted particles. The influence of the different HES pressure stages is demonstrated in Fig. 3. Except for a step-like increase from the combustor experiments to the HES experiments which is most likely due to slightly different operating conditions, the HES has no influence on the emission properties of the Combustor-HES combination with respect to combustion aerosol particles. Increasing the FSC slightly increased the total number of emitted particles. Particles smaller than 10 nm contribute less than 10% of the total exhaust aerosol in the low and medium FSC cases. At high FSC levels the formation of volatile condensation particles with diameters $D < 10$ nm was observed. Particles of size $D \geq 30$ nm were almost entirely internally mixed. Smaller particles ($D < 20$ nm) exhibited volume fractions of 10–15% and semivolatile 4–10% for volatile and semi-volatile material, while the volatile fraction decreased to $< 5\%$ for $D \geq 50$ nm particles (Petzold et al., 2003).

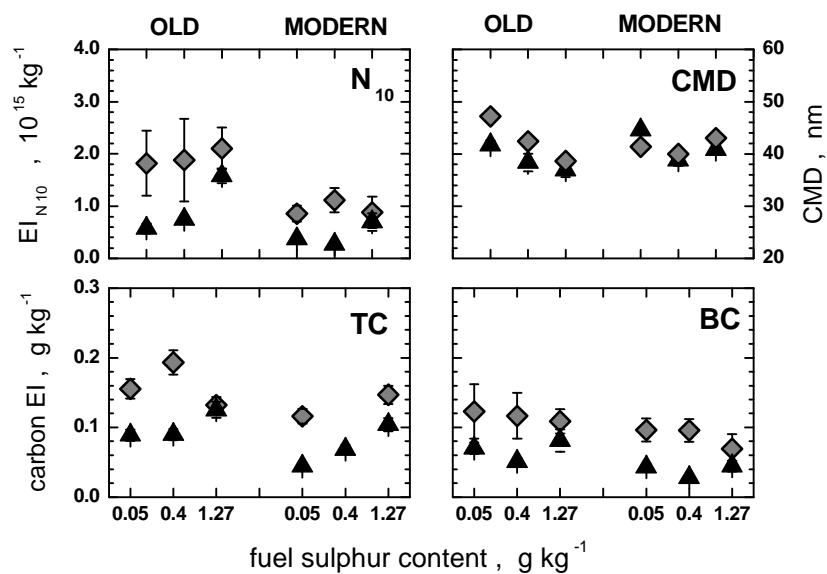


Figure 2. Emission indices in terms of number (N_{10}), total carbon mass (TC), black carbon mass (BC) and count median diameter (CMD) of the combustion aerosol for the Combustor exit (7) and the Hot End Simulator low pressure stage (Δ); values are given for old and modern operation conditions as a function of the fuel sulphur content.

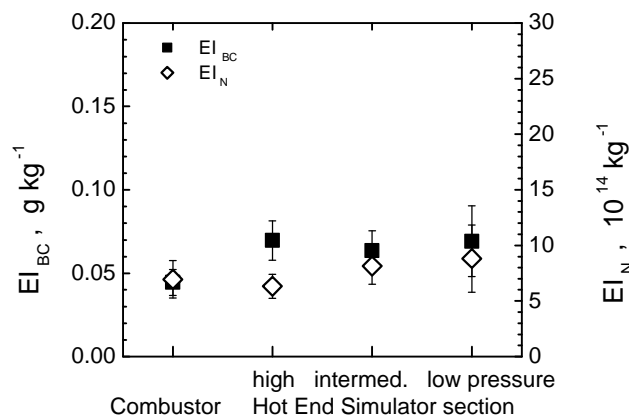


Figure 3. Effect of the Hot End Simulator on the emission properties of the Combustor-HES combination operated at modern conditions.

3.2 Chemical Properties

Primary particles emitted from the combustor are predominantly composed of carbonaceous material (> 95%) and of water-soluble inorganic components. The carbonaceous material is composed of organic compounds and of elemental or black carbon. The organic compounds may be volatile or semi-volatile, i.e., they oxidise at temperatures as low as 400 K. Fig. 4 shows the thermal stability of an exhaust aerosol sampled during operation with low FSC fuel at modern conditions. From an aerosol loaded glass wool sample more than 180 different NMHCs were desorbed under an Helium atmosphere. Only 0.4 wt% of the NMHCs were desorbed at $T \leq 400$ K, whereas 99.6 wt% were desorbed at $T = 400$ -620 K. This is in good agreement with the result of the thermogram in Fig. 4. Elemental (EC) or black carbon (BC), respectively, is chemically almost inert at low and moderate temperatures and thermally stable up to temperatures of about 700 K.

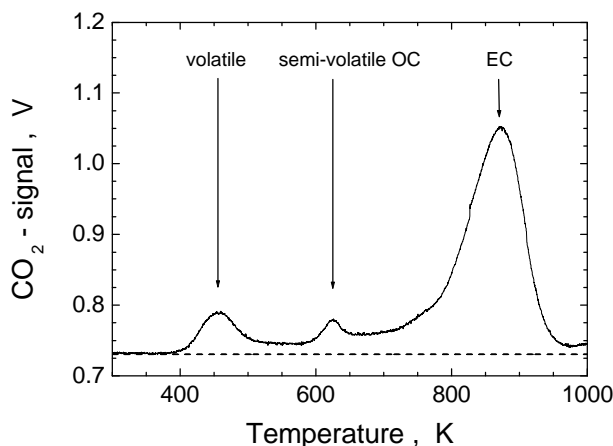


Figure 4: Evolving CO_2 as a function of the sample heating temperature for a Combustor aerosol sample; volatile OC oxidises at 450 K, semi-volatile OC at 600 K, and elemental carbon above 700 K.

During combustion, the sulphur contained in the fuel is oxidised to SO_2 which is then partially converted to S(VI) in the hot exhaust gas. The efficiency of conversion from S(IV) to S(VI) is described by the conversion efficiency ϵ calculated as $\epsilon = \text{S(VI)}/\text{S}_T$ where S_T is the total fuel sulphur. In the combustor campaign the S(VI) increased with increasing FSC. The efficiency of conversion in the combustor campaign ranged between 0.9 ± 0.5 % and 1.3 ± 0.7 %. In the HES campaign S(VI) increased with increasing FSC, fuel flow, and from the high-pressure to the low-pressure HES stage. For FSC=1270 ppm the conversion efficiency was 2.3 ± 1.2 % at the low pressure stage for the modern cruise condition and 1.4 ± 0.7 % for the old cruise. The higher ϵ observed for the modern cruise conditions suggests that modern engines have a larger ϵ compared to old ones.

Chemical composition information was obtained from Berner low pressure impactor samples which were taken at a sample line temperature of 150°C . At these conditions most of the sulphuric acid will remain in the gas phase, while only a small fraction is more strongly bound to or chemisorbed at the particle surface and will be observed in particulate matter samples. The chemical analysis results indicate, that the mass distribution of the carbonaceous matter matches the volume distribution of the aerosol, while the mass distribution of chemisorbed sulphate follows the surface distribution of the aerosol. This observation indicates that the sulphate is chemisorbed at the particle surface. The chemisorbed fraction of sulphuric acid corresponds to a coverage of max. 0.1 monolayer in the high FSC case. This fraction of converted S(VI) corresponds to less than 0.1% of total S(IV), present in the fuel. More than 90% of the S(VI) remains in the gas phase at a gas temperature of about 150°C . The overall partitioning of sulphur-containing species is: 97% SO_2 , ≤ 2.7 % gaseous H_2SO_4 , < 0.3 % chemisorbed.

3.3 Particle hygroscopic properties

Particle hygroscopic properties were measured at ambient conditions using a Hygroscopicity Tandem Differential Mobility Analyser (H-TDMA) system (Gysel et al., 2003). The instrument

measures the hygroscopic growth factor (g) of particles with initial dry sizes $D_o = 30, 50$ and 100 nm over the range $RH \sim 70 - 95\%$ where $g(RH) = D(RH)/D_o$. Growth factors were found to increase with increasing FSC at fixed particle size (e.g. $D_o = 50$ nm; $g(95\%) = 1.01$ and 1.16 for FSC = low and high, respectively), and to decrease with increasing particle size at fixed FSC (e.g. mid FSC; $g(95\%) = 1.14, 1.10$ and 1.03 for $D_o = 30, 50$ and 100 nm, respectively). The results suggest an increasing amount of sulphuric acid adsorbed on combustion particles from the gas phase with increasing FSC.

Cloud condensation nuclei (CCN) were measured in the diluted line using a static thermal diffusion type CCN counter (Giebl et al., 2002). Particles are exposed to controlled supersaturations of water vapour, which enables some of the particles to become activated and grow to large (> 10 μm) droplets. During PartEmis, the supersaturation was set to $\sim 0.7\%$. The fraction of CCN in the aerosol (relative to the concentration of particles $> 10\text{nm}$) increased with increasing FSC, but even for low FSC the fraction of CCN (at 0.755% supersaturation) was higher than the fraction of particles with diameters larger than 0.280 μm , i.e. the size at which wettable insoluble particles are activated according to the Kelvin effect. At high FSC, the fraction of CCN increased by about a factor 5.5 for old and 12 for modern conditions but was still lower by a factor ~ 15 for those particles with $D > 0.03$ μm , i.e. the dry size of sulphuric acid particles which are activated according to Köhler theory. Further details are given by Hitzenberger et al. (2003).

3.4 Gaseous Hydrocarbon Emission

More than 100 different non-methane volatile organic compounds (NMVOCs), such as non-methane hydrocarbons (NMHCs) and selected partially oxidised hydrocarbons (OHCs) emitted from the jet engine combustor and the hot end simulator (HES) were identified and quantified. These species accounted for up to 91 wt % of the total hydrocarbons (THCs). The NMHC emission indices of $5 - 15$ mg kg^{-1} in total are comparable with the AEROTRACE study. Both studies show up to 1000 times lower emission indices in comparison with emissions from vehicular traffic. The influence of the operation conditions on NMHC emissions of the combustor and HES was investigated for the identified NMHCs. From the six conditions which were investigated (2 operation conditions, 3 HES pressure stages), most compounds showed a decrease of NMHC emissions with increasing combustion temperature at the same pressure stage. This is in agreement with results from the combustor exit measurements and with the results of the AEROTRACE study. Emission indices at HES pressure stages high (HP)-, intermediate (IP)- and low pressure (LP) for fixed FSC and combustor operation conditions were also investigated. Most compounds showed a decrease of NMHC emissions with decreasing pressure in the HES at similar combustor operation conditions and fixed FSC. The decrease of the pressure in the HES corresponds to an increase of the residence time in a turbine and indicates a decrease of NMHC emissions along the different turbine sections.

3.5 Emission of ions and charged soot particles

The ions measured during the HES campaign are product ions formed from primary ions via ion molecule reactions involving either few reaction-steps with massive neutral molecules or numerous reaction-steps with relatively small neutral molecules. Their lifetimes with respect to ion-ion recombination are around 9 ms after the high pressure turbine section. The ion emission index E_i is up to 4.5×10^{16} ions per kg fuel burnt. It seems that ion-induced nucleation can explain at least partly the observed volatile aerosols. Electrically charged small positive and negative soot particles (CSP) have also been detected during both PartEmis campaigns. Charged soot particles were found to have diameters around 6 nm and a total concentration of up to 4.5×10^7 cm^{-3} (positive and negative) corresponding to a total emission index of $E_{\text{CSP}} = 2.3 \times 10^{15}$ CSP per kg fuel burnt.

3.6 OH measurements

At high laser energies, observed OH fluorescence was dominated by a photolytic source of OH. At low laser energies, OH in the exhaust duct was successfully detected, although there was still a component present from photolysis. Calibration experiments provide a method to assign the observed OH LIF signals an absolute concentration, and from an estimate or measurement of the errors for each parameter, an overall estimate of the error in the assigned OH concentration was made. From these calibration experiments very low values of less than 1 ppbv were calculated for

the OH concentration in the exhaust gas after exiting the HES. Previous experiments using a combined Raman scattering/LIF technique to look in the exhaust gases 50 cm behind a jet engine exit failed to detect any OH LIF signal, and therefore could only infer an upper limit for OH of 80 ppbv based on the measured detection limit of their apparatus.

4 SUMMARY AND CONCLUSIONS

4.1 Combustion aerosol

- The combustor behaves like a typical aircraft engine combustor with respect to thermodynamic data and main emissions. It may thus be expected that the PartEmis database can be applied as a first order approximation to contemporary aircraft engines.
- The BC concentration is nearly independent of FSC level.
- The number size distribution of primary particles in the diameter range $10 < D < 550$ nm is almost uninfluenced by the FSC level or combustor conditions. But at high FSC levels the formation of volatile condensation particles with diameters $D < 10$ nm was observed.
- The average density of the combustion aerosol is $0.95 - 1.0$ g of total carbon cm^{-3} , referring to a sphere of equivalent diameter; the specific surface area is $80 - 100$ m^2 (g total carbon) $^{-1}$.
- The volatile volume fraction of particles > 50 nm increases from 2 % for low FSC to approx. 5% for high FSC. The volatile volume fraction of particles < 30 nm is $\leq 15\%$.
- Volatility measurements indicate an internally mixed aerosol for particles with $D > 15$ nm; condensation particles are < 15 nm.

4.2 Ultrafine particles

- Formation of condensation particles in the Combustor tests for high FSC at old and modern conditions; “formation strength” ≤ 7 condensation particles / combustion particle;
- Formation of condensation particles in the HES tests for high FSC/modern conditions/low pressure section only; “formation strength” ≤ 14 condensation particles / combustion particle;
- Ultrafine carbonaceous particles of size $7 \text{ nm} < D < 20 \text{ nm}$ are observed independently of the fuel sulphur content; a volatility analysis indicates that these particles are nonvolatile and may be composed of carbonaceous compounds.

4.3 Sulphate-containing species, chemi-ions and OH

- S(VI) was measured in the form of sulphuric acid. Increased FSC resulted in higher S(VI) concentrations. The measured conversion efficiency for fuel sulphur to S(IV) at the combustor exit varied from 0.35 - 1.4% and was independent of the investigated combustor operation conditions and FSC levels.
- 10 - 30% of sulphate is chemisorbed on primary particles; the coverage of primary particles is below 0.1 monolayers of sulphuric acid.
- Sulphur partitioning: 97% SO_2 , $\leq 2.7\%$ gaseous H_2SO_4 , $< 0.3\%$ chemisorbed.
- Positive and negative gaseous ions were detected for the first time in the exhaust of a combustor, with mass numbers up to 1500. The total ion emission index at the HES hp stage was as high as 5.4×10^{17} positive and negative ions per kg fuel burnt. Large ions with mass numbers exceeding 4500 were contributed about 10% to the total ion number concentration.
- OH concentration in the exhaust gas after exiting the HES is < 1 ppbv.

4.4 Hygroscopic growth and CCN activation

- Small differences in particle hygroscopicity are observed between old and modern cruise conditions.
- Strong effect of the fuel sulphur content is observed, particle hygroscopicity increases distinctly with increasing FSC.
- No significant effect of the HES at low and mid FSC level is observed; higher particle hygroscopicity downstream the HES are observed at high FSC compared to the combustor exit.
- CCN activation of combustion particles increases with increasing FSC as a result of larger particle hygroscopicity; additional effects of adsorbed organic matter cannot be excluded.

- CCN activation is about twice as efficient for modern as for old cruise conditions.

4.5 Gaseous organic fraction:

- More than 100 different NMVOCs (aliphatic and aromatic hydrocarbons, carbonyls and acids) were identified and quantified, they accounted for 91 wt % of the total detected compounds.
- A decrease in NMHC emissions from old to modern conditions at fixed HES pressure stage and fuel sulphur content (FSC) was found.
- A decrease of NMHC emissions with decreasing pressure in the HES at fixed combustor operation conditions and FSC was observed.
- No clear influence on the NMHC emissions with changing FSC at the same combustor operation condition was observed.
- High EI's for organic acids are found. Perhaps organic compounds fixed at the sampling line walls are oxidised by the hot exhaust gases. Or the acids are fixed at the surface of the soot particles, which are also trapped in the sampling cartridges.

4.6 Emission properties

- Emission properties regarding combustion aerosol mass, number and size are determined by the combustor; the influence of the Hot End Simulator is weak.
- The processing of exhaust gas and particles during the transfer through the Hot End Simulator increases the particle hygroscopicity and formation strength of condensation particles; both effects are related to gaseous sulphuric acid.

The experimental overview of the EU PartEmis project presents the first comprehensive aerosol and gas measurements to be conducted on a jet engine combustor test-rig. Specific aspects of these measurements are presented elsewhere (Gysel et al.; Hitzenberger et al.; Petzold et al.; 2003). The database will be used for further analyses as well as for plume modelling by other PartEmis groups.

5 ACKNOWLEDGEMENT

The PartEmis project was funded by the European Commission under contract no. G4RD-CT-2000-00207. The authors are very grateful to the test rig operation crew at QinetiQ for their very strong support during the experiments.

REFERENCES

- Anderson, B.E., et al., 1998: Airborne observations of aircraft aerosol emissions, I, Total nonvolatile particle emission indices, *Geophys. Res. Lett.*, 25, 1689-1692.
- Boucher O. , 1999: Influence of air traffic on cirrus occurrence, *Nature*, 397, 30-31.
- Brock, C.A., et al. , 2000: Ultrafine particle size distributions measured in aircraft exhaust plumes, *J. Geophys. Res.*, 105, 26555-26567.
- Giebl, H., A. Berner, G. Reischl, H. Puxbaum, A. Kasper-Giebl, and R. Hitzenberger, 2002: CCN activation of oxalic and malonic acid test aerosols with the University of Vienna cloud condensation nuclei counter. *J. Aerosol Sci.* 33, 1623-1634.
- Gysel, M., S.Nyeki, E. Weingartner, U. Baltensperger, H. Giebl, R. Hitzenberger, A. Petzold, and C.W. Wilson, 2003: Properties of jet engine combustor particles during the PartEmis experiment. Hygroscopicity at subsaturated conditions, *Geophys. Res. Lett.*, 30, 1566, doi:10.1029/2003GL016896.
- Hagen, D.E., P.D. Whitefield, J.D. Paladino, and O. Schmid, 2001: Comparative study of jet engine combustion emissions and engine operating conditions, in Schumann, U. and Amanatidis G. (Eds.), *Aviation, aerosols, contrails and cirrus clouds*, Air pollution research report 74, pp 106-110, European Commission, Brussels.
- Hitzenberger, R., H. Giebl, A. Petzold, M. Gysel, S. Nyeki, E. Weingartner, U. Baltensperger, C.W. Wilson, 2003: Properties of jet engine combustor particles during the PartEmis experiment. Hygroscopic properties at supersaturated conditions, *Geophys. Res. Lett.*, 30, 1779, doi:10.1029/2003GL017294.
- Petzold, A., and F.P. Schröder, 1998: Jet engine exhaust aerosol characterization, *Aerosol Sci. Technol.*, 28, 62-76.

- Petzold, A., A. Döpelheuer, C.A. Brock, and F.P. Schröder, 1999: In situ observations and model calculations of black carbon emission by aircraft at cruise altitude, *J. Geophys. Res.*, *104*, 22171-22181.
- Petzold, A., C. Stein, S. Nyeki, M. Gysel, E. Weingartner, U. Baltensperger, H. Giebl, R. Hitzenberger, A. Döpelheuer, S. Vrchoticky, H. Puxbaum, M. Johnson, C.D. Hurley, R. Marsh, and C.W. Wilson, 2003: Properties of jet engine combustor particles during the PartEmis experiment. Microphysical and chemical properties. *Geophys. Res. Lett.*, *30*, 1719, doi:10.1029/2003GL017283.
- Schmid, H., et al. , 2001: Results of the “carbon conference” international aerosol carbon round robin test stage I, *Atmos. Environ.*, *35*, 2111–2121.
- Schumann, U., et al. , 2002: Influence of fuels sulphur on the composition of aircraft exhaust plumes: The experiments SULFUR 1-7, *J. Geophys. Res.*, *107* (10.1029/2001JD000813), AAC 2-1 – AAC 2-27.
- Schumann, U. and Ström, J. , 2001: Aviation impact on atmospheric composition and climate, in *European research in the stratosphere 1996 – 2000*, European Commission, EUR 19867, Brussels.
- Wilson, C.W., et al. , 2003: Measurement and Prediction of Emissions of Aerosols and Gaseous Precursors from Gas Turbine Engines (PartEmis): An Overview, *Aerosp. Sci. Technol.*, in press.

Emission of Non-Methane Volatile Organic Compounds (NMVOCs) from a Jet Engine Combustor and a Hot End Simulator (HES) During the PartEmis Project

R. Kurtenbach*, J. C. Lörzer, A. Niedojadlo, M. Petrea, P. Wiesen
University of Wuppertal, Wuppertal, Germany

M. Kapernaum, C. Wahl
DLR, Institute for Combustion Technology, Stuttgart, Germany

Keywords: NMVOC emissions, combustion NMVOC, PartEmis

ABSTRACT: During the PartEmis measurement campaigns at QinetiQ, Pyestock in January 2001 and in March 2002 the emissions of non-methane volatile organic compounds (NMVOCs) from a jet engine combustor and a hot end simulator (HES) were measured. In addition, CO₂ measurements were also performed for determining emission indices (EIs). The C₂-C₁₀ aliphatic and aromatic hydrocarbons were monitored using a compact online gas chromatograph (GC) (Airmovoc 2010) with enrichment system and FID detector. The non-methane hydrocarbons (NMHCs) were measured with a time resolution of 10 min and detection limits in the pptV range. Selected partially oxidised hydrocarbons (OHC) such as aldehydes were collected by using special sampling cartridges and measured off-line using HPLC with a photo-array detector. The OHCs were measured with a time resolution of 4 min and detection limits in the ppbV range. A fully automated online GC system (Chromato-sud) with TCD detector was used to monitor CO₂. Measurement cycle and detection limit of this system were 5 min and 10 ppmV, respectively. More than 100 different NMVOCs were identified and quantified and accounted for up to 91 wt % of the total NMVOCs emitted. Sample line effects on the measured data were investigated and were found to be statistically not significant. Generally, the NMVOC emission indices for the combustor and HES measurements from this study and the data from previous studies showed a high variability within two orders of magnitude. In addition, the present studies on aircraft emissions show up to 1000 times lower NMVOC emission indices in comparable with the emissions from vehicular traffic. During the PartEmis campaigns the influence of combustor power, pressure in the different stage of the HES and different fuel sulphur content (FSC) on the emission of the species studied was also investigated. No clear impact of the FSC on the NMHC emissions was observed. A decrease in NMHC emissions with increasing combustor power was found and are comparable with the data from the AEROTRACE (1996) study and the study by Spicer et al. (1994). A decrease of NMHC emissions along the different turbine sections (HES) was observed indicating that chemistry is on-going in the turbine.

1 INTRODUCTION

Although only a few percent of the fossil fuel is currently being burnt by air traffic (Brasseur et al., 1998), most of the combustion emission are being deposited in the very sensible altitude regions of the atmosphere; i.e. the upper troposphere and lower stratosphere, where the compounds may have long life times and where background concentration are usually low. Since only a very limited number of engines have been investigated under realistic flight conditions up to now (Fahey et al., 1995a; 1995b, Schumann, 1997, Slemr et al., 1998, Schumann et al., 2002). Ozone around the tropopause originates partly from the stratosphere and is partly produced photochemically from NMVOC and NO_x as precursors (Ehhalt et al., 1992). The NO_x emission from air traffic is supposed to have caused increased ozone concentrations around the tropopause (Penner et al., 1999). The

* Corresponding author: Ralf Kurtenbach, University of Wuppertal, Wuppertal, 42110 Wuppertal, Germany. Email: kurtenba@uni-wuppertal.de

impact of the NMVOC emission from air traffic is generally considered to be small (Haymann and Markiewicz, 1996). However, these studies are based on a few measurements of individual NMVOCs (Spicer et al., 1994, Slemr et al., 1998). In addition, in-flight studies and modelling (Kärcher et al., 1998, Schumann et al., 2002) have shown the potential importance of unburnt, NMVOCs on the formation of condensation particles in the exhaust of an aircraft engine. One objective of the extensive measurement programme within the PartEmis was to perform measurements for individual NMVOCs from a series of combustor and hot end simulator (HES) tests. Detailed information on the PartEmis experiments is given by Petzold et al. (2003).

2 METHODS

The C₂-C₁₀ aliphatic and aromatic non-methane hydrocarbons (NMHCs) were monitored using a compact online gas chromatograph (GC) (Airmovoc 2010) with enrichment system (cryotrap) and FID detector. The system has been described in more detail elsewhere (Gomes and Benter, 2003).

The smallest combustor operation interval for some test point during the campaigns was about 10 min. However, the measurement procedure for the C₂-C₁₀ aliphatic and aromatic NMHCs only allowed a time resolution of at least 20 min. Therefore, two similar GCs were operated with a time shift of about 10 min, which enabled the measurement at each test point. The GC instruments including the sampling system were calibrated with a certified standard mixture from the UK National Physical Laboratory (NPL-UK) containing 30 different C₂-C₉ NMHCs in nitrogen. The GC system reached an accuracy of 10-20% for aliphatic and 15% for aromatic NMHCs and a precision of 15%-20% for aliphatic and 10% for aromatic NMHCs. The detection limits for all NMHCs were in the pptV range.

Selected partially oxidised hydrocarbons (OHCs) such as aldehydes and ketones were collected by using special sampling cartridges coated with 2,4-dinitrophenylhydrazine. The 2,4-dinitrophenylhydrazine forms with the reactive carbonyls a stable hydrazone compound. The hydrazones were eluted out of the cartridge with acetonitrile and separated in a high performance liquid chromatograph (HPLC) with diode array detector (DAD). The compounds were identified via retention time and absorption spectra. The OHCs were measured with a time resolution of 4 min and detection limits in the ppbV range.

A fully automated online GC system with TCD detector (Chromato-sud) was used to monitor CO₂. Measurement cycle and detection limit of this system were 5 min and 10 ppmV, respectively. The sample time and sample volume were 0.1 min and 1 ml, respectively. The system has been described in more detail elsewhere (Becker et al., 1999). In order to increase the sampling time, offline measurements were also performed. The exhaust gas was sampled into 4 litre stainless steel canisters. Sample flow and sample time were 600 ml/min and 9–14 min, respectively. After sampling, the stainless steel canisters were analysed with the online GC-TCD system. Calibration of the GC-TCD system including the sampling system was performed using certified CO₂ gas mixtures (Messer-Griesheim). The GC-TCD system had an accuracy of 5% and a precision of 2%.

The undiluted exhaust gases were transferred from the combustor and HES to the GC sampling system through a heated sampling line system set up by QinetiQ. The sampling system used during the PartEmis campaigns is schematically shown in Fig. 1.

Sampling line losses in the undiluted line without and with exhaust were investigated for the NMHCs. The certified NMHC gas mixture from the NPL-UK was added to the sampling line system at the inlet air valve with a flow rate of 2 l/min (see Fig. 1) and the difference between calculated (exhaust gas value + gas mixture value = calculated value) and measured concentration values at the end of the sampling line was determined. For OHC's no sampling line effects were investigated, because no stable gaseous mixtures of the OHCs were available.

addition, the present studies on aircraft emissions show up to 1000 times lower emission indices in comparison with emissions from vehicular traffic (Gomes and Benter, 2003).

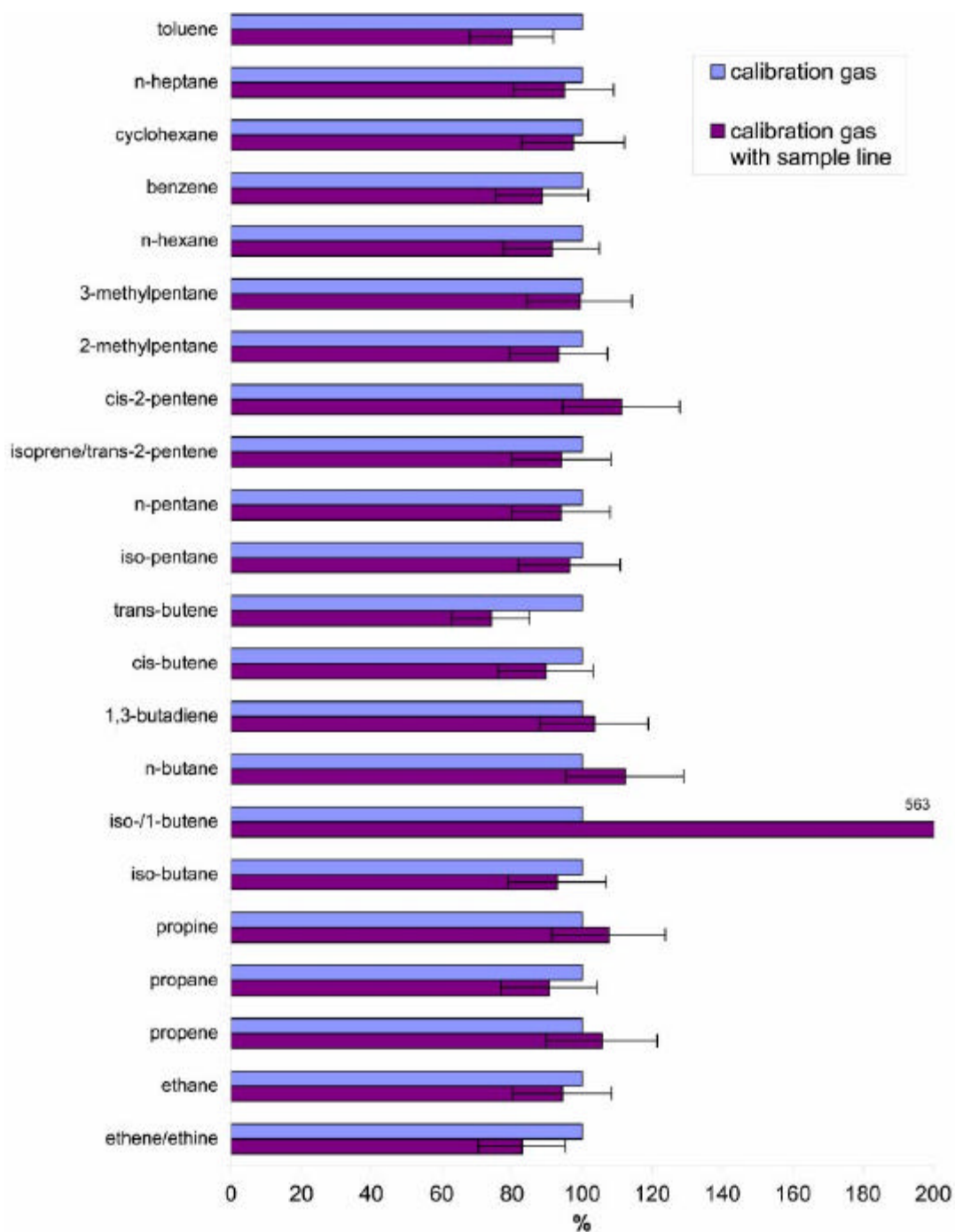


Figure 2. Comparison of the NMHC measurements with and without using the sampling line system of QinetiQ. The results without using the sampling line system are normalised to 100%.

From the median emission values, listed in table 1 the percent distribution of the NMVOCs classes, aromatic NMHCs, aliphatic NMHCs and OHCs were calculated and are shown in Fig. 3. A median contribution of 12% aromatic NMHCs, 47% aliphatic NMHCs and 41% OHCs was found. Among the class of aromatic NMHCs, benzene (0.38 mg/kg), among aliphatic NMHCs, ethane (2.22 mg/kg) and among OHCs, hexanal (1.89 mg/kg) showed the largest emission index. In addition, a total NMVOC EI of 10.4 mg/ kg fuel burnt was calculated.

Table 1. Calculated NMVOC emission indices (mg/ kg fuel burnt) of the PartEmis study for cruise power condition in comparison with other studies.

Compound	PARTEMIS Study	AEROTRACE 1996	Slemr et al. 1998	Spicer et al. 1994
	Range (Median)	Range (Median)	Range (Median)	Range (Median)
ethyne, ethene	0.02 – 8.79 (0.63)	-	38.3 – 130.9 (93.8)	173.5
ethane	0.70 – 4.13 (2.22)	-	-	1.46 – 2.23 (1.85)
propene	0.01 – 0.62 (0.19)	0.03 – 0.96 (0.34)	4.22 – 21.3 (11.1)	0.34 – 17.5 (8.91)
propane	0.01 – 0.34 (0.09)	0.81 – 3.90 (2.33)	-	0.36 – 0.44 (0.40)
propyne	0.00 – 0.44 (0.32)	-	0.37 – 1.99 (1.27)	-
iso-butane	0.00 – 0.24 (0.02)	0.18 – 3.00 (1.67)	-	-
1-butene, iso-butene	0.22 – 0.47 (0.28)	9.10 – 17.2 (11.8)	1.66 – 10.6 (3.91)	-
1,3-butadiene, n-butane	0.10 – 0.55 (0.35)	6.20 – 6.80 (6.60)	0.66 – 3.51 (2.30)	11.63
trans-2-butene	0.00 – 0.18 (0.06)	-	-	-
cis-2-butene	0.02 – 0.46 (0.09)	-	-	0.34 – 2.08 (1.21)
iso-pentane	0.00 – 0.63 (0.08)	-	-	-
acetone	0.00 – 0.27 (0.07)	-	-	7.51 – 11.5 (9.50)
n-pentane	0.01 – 0.04 (0.02)	-	-	-
isoprene, trans-2-pentene	0.00 – 0.05 (0.02)	-	0.34 – 1.78 (0.90)	-
cis-2-pentene	0.00 – 0.08 (0.02)	-	0.15 – 0.55 (0.16)	-
2,3-dimethylbutane	0.00 – 0.12 (0.04)	-	-	-
cyclopentane,2-methylpentane	0.04 – 0.43 (0.18)	-	-	-
3-methylpentane	0.00 – 0.56 (0.08)	-	-	-
n-hexane	0.00 – 0.03 (0.01)	-	-	-
benzene	0.29 – 1.70 (0.38)	0.27 – 5.10 (1.78)	3.39 – 12.0 (9.60)	0.63 – 18.9 (9.78)
cyclohexane	0.00 – 0.06 (0.04)	-	-	-
iso-octane	0.00 – 0.04 (0.00)	-	-	-
n-heptane	0.01 – 0.92 (0.04)	-	-	-
2,3,4-trimethylpentane	0.01 – 0.10 (0.06)	-	-	-
2-, 3-methylheptane	0.01 – 0.23 (0.06)	-	-	-
toluene	0.02 – 0.21 (0.12)	0.34 – 1.20 (0.58)	0.70 – 2.98 (2.20)	0.32 – 4.27 (2.30)
ethylbenzene	0.09 – 0.21 (0.16)	-	-	0.79
m-, p-xylene	0.01 – 1.68 (0.17)	0.02 – 1.60 (0.31)	-	3.15
o-xylene	0.03 – 0.56 (0.26)	0.02 – 0.43 (0.07)	-	1.18
mesitylene	0.06 – 0.67 (0.18)	-	-	-
formaldehyde	0.16 – 0.61 (0.42)	0.88 – 1.45 (0.97)	-	56.1 – 106.9 (81.5)
acetaldehyde	0.10 – 0.56 (0.17)	0.54 – 1.35 (0.93)	-	1.60 – 33.3 (17.5)
propanal	0.00 – 0.35 (0.04)	-	-	0.46 – 6.77 (3.62)
butanal	0.00 (0.00)	-	-	1.06 – 6.76 (3.91)
acrolein	0.01 – 0.76 (0.60)	1.11 – 5.14 (2.28)	-	19.41
methacrolein	0.00 – 0.85 (0.40)	-	-	-
glyoxal	0.20 – 0.80 (0.34)	-	-	2.89
methylglyoxal	0.07 – 2.12 (0.24)	0.50 - 1.18 (0.98)	-	-
benzaldehyde	0.00 – 0.60 (0.13)	-	-	3.15
hexanal	1.19 – 2.85 (1.89)	-	-	-

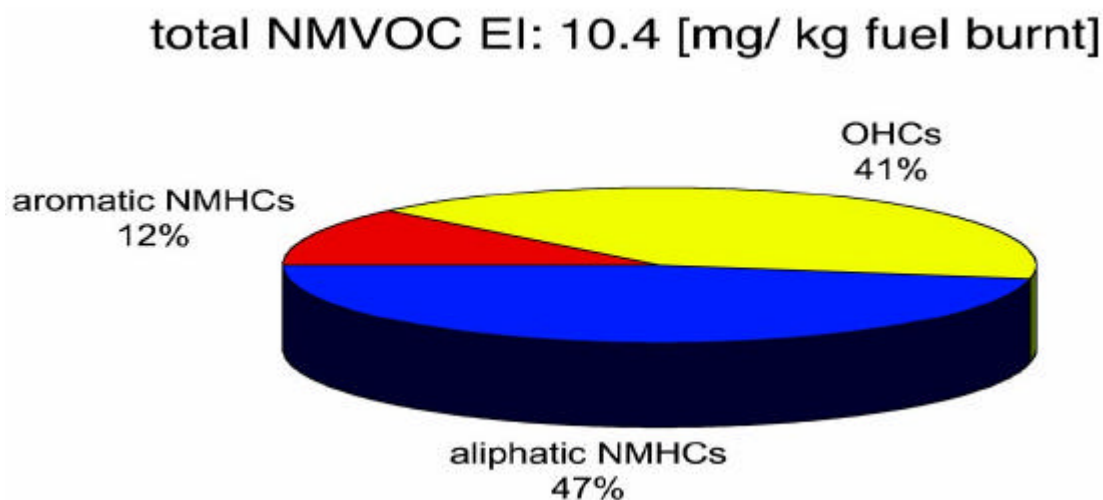


Figure 3. Median distribution of the NMVOC classes (mg/kg fuel burnt).

3.3 Influence of the fuel sulphur content (FSC), on the NMHC emission of the combustor.

From the measured emission indices emission ratios X ; $X = EI_{\text{low FSC}} / EI_{\text{high FSC}}$ for each NMHC at different combustor power settings (old and modern cruise) were calculated. $54 \pm 20\%$ of the NMHCs showed an emission ratio $X > 1$ on average. No clear impact of the FSC variation on the NMHC emission was observed.

3.4 Influence of power setting, old – and modern cruise on NMHC emission of the combustor and HES.

From the emission indices at different engine power settings, old cruise and modern cruise at fixed FSC and pressure stage an emission ratio X ; $X = EI_{\text{old cruise}} / EI_{\text{modern cruise}}$ for each NMHC was calculated. Most NMHCs showed an emission ratio of $X > 1$ on average. This indicates a decrease of NMHC emissions with increasing combustor power. This is in agreement with results of the previous European AEROTRACE study (1996) and the study by Spicer et al. (1994).

3.5 Influence of the pressure stage, high (HP)-, intermedium (IP)- and low pressure (LP) on the NMHC emission in the HES.

In addition, from the emission indices at different pressure stage; high (HP)-, intermedium (IP)- and low pressure (LP) at fixed FSC and combustor power an emission ratio X ; $X = EI_{\text{HP}} / EI_{\text{IP}}$ and $X = EI_{\text{IP}} / EI_{\text{LP}}$ for each NMHC were calculated. Most NMHCs showed an emission ratio of $X > 1$. This indicates a decrease of NMHC emissions with decreasing pressure in the HES. The decrease of the pressure in the HES is comparable with the increase of the resident time in a turbine and indicates a decrease of NMHC emission along the different turbine sections, which shows that chemistry is on-going in the turbine.

4 SUMMARY AND CONCLUSIONS

- More than 100 different NMVOCs (aliphatic and aromatic hydrocarbons and carbonyls) were identified and quantified: these species accounted for up to 91 wt % of the total NMVOC emission.
- Sampling line effects on the measured data were investigated for the NMHCs and were found to be statistically not significant.
- Generally, the NMVOC emission indices for the combustor and HES measurements from this study and the data from previous studies showed a high variability within the range of 0–82 mg/kg fuel burnt.

- The PartEmis and the previous studies on aircraft emissions show up to 1000 times lower NMVOC emission indices in comparable with the emissions from vehicular traffic.
- No clear impact of the FSC on the NMHC emissions was observed.
- A decrease in NMHC emissions with increasing combustor power was found and this result is comparable with the data from AEROTRACE study (1996) and the study by Spicer et al. (1994).
- A decrease of NMHC emissions along the different turbine sections (HES) was observed indicating that chemistry is on-going in the turbine.

REFERENCES

- Becker, K. H., J. C. Lörzer, R. Kurtenbach, P. Wiesen, T. Jensen and T. J. Wallington, 1999: Nitrous oxide (N₂O) emissions from vehicles. *Environ. Sci. and Technol.*, 33, 4134-4139.
- Brasseur, G. P., R. A. Cox, D. Hauglustaine, I. Isaksen, J. Lelieveld, D. H. Lister, R. Sausen, U. Schumann, A. Wahner and P. Wiesen, 1998: European scientific assessment on the atmospheric effects of aircraft emissions. *Atmos. Environ.*, 32, No. 13, 2329-2418.
- Ehhalt, D. H., F. Rohrer and A. Wahner, 1992: Sources and distribution of NO_x in the upper troposphere at northern mid-latitudes. *J. Geophys. Res.*, 97, 3725-3738.
- Fahey, D. W., E. R. Keim, K. A. Boering, C. A. Brock, J. C. Wilson, H. H. Jonsson, S. Anthony, T. F. Hanisco, P. O. Wennberg, R. C. Miake-Lye, R. J. Salawitch, N. Louisnard, E. L. Woodbridge, R. S. Gao, S. G. Donnelly, R. C. Wamsley, L. A. Del Negro, S. Solomon, B. C. Daube, S. C. Wofsy, C. R. Webster, R. D. May, K. K. Kelly, M. Loewenstein, J. R. Podolske and K. R. Chan, 1995a: Emission measurements of the Concorde supersonic aircraft in the lower stratosphere, *Science*, 270, 70-74.
- Fahey, D. W., E. R. Keim, E. L. Woodbridge, R. S. Gao, K. A. Boering, B. C. Daube, S. C. Wofsy, R. P. Lohmann, E. J. Hintsa, A. E. Dessler, C. R. Webster, R. D. May, C. A. Brock, J. C. Wilson, R. C. Miake-Lye, C. A. Brown, J. M. Rodriguez, M. Loewenstein, M. H. Proffitt, R. M., Stimpfle, S. W. Bowen and K. R. Chan, 1995b: In situ observations in aircraft exhaust plumes in the lower stratosphere at mid-latitudes. *J. Geophys. Res.*, 100, 3065-3074.
- Gomes, A. and Th. Benter, 2003: Impact of road traffic emissions on the ozone formation in Germany. *Report no. 61, University of Wuppertal, Germany, ISSN 1436-2198.*
- Hayman, G.D. and M. Markiewicz, 1996: Chemical modeling of the aircraft exhaust plume, in "Pollutions from Aircraft Emissions in the North Atlantic Flight Corridor (POLINAT)", U. Schumann ed, *Air Pollution Research Report 58 (EUR 16978 EN), European Commission.*
- Kärcher, B., F. Yu, F. P. Schröder and R. P. Turco, 1998: Ultrafine aerosol particles in aircraft plumes: Analysis of growth mechanisms. *Geophys. Res. Lett.*, 25, 2793-2796.
- Penner, J., D. H. Lister, D. J. Griggs, D. J. Dokken and M. McFarland (eds.), 1999: Aviation and the global atmosphere: a special report of IPCC working groups I and III, Cambridge University Press, *ISBN 0-521-66404-79.*
- Petzold, A., M. Fiebig, L. Fritzsche., C. Stein, U. Schumann, C. W. Wilson, C. D. Hurley, F. Arnold, E. Katragkou, U. Baltensperger, M. Gysel, S. Nyeki, R. Hitzenberger, H. Giehl, K. J. Hughes, R. Kurtenbach, P. Wiesen, P. Madden, H. Puxbaum, S. Vrchoticky and C. Wahl, 2003: Particle emissions from aircraft engines – An overview of the European project PartEmis, this issue.
- Slemr, F., H. Giehl, J. Slemr, R. Busen, P. Schulte and P. Haschberger, 1998: In-flight measurement of aircraft non-methane hydrocarbon emission indices. *Geophys. Res. Lett.*, 25, no 3, 321-324.
- Spicer, C. W., M. W. Holdren, R. M. Riggan and T. F. Lyon, 1994: Chemical composition and photochemical reactivity of exhaust from aircraft turbine engines. *Annales Geophysicae*, 12, 944-955.
- Schumann, U., 1997: The impact of nitrogen oxides emissions from aircraft upon the atmosphere at flight altitudes – Results from AERONOX project., *Atmos. Environ.*, 31, No. 12, 1723-1733.
- Schumann, U., F. Arnold, R. Busen, J. Curtius, B. Kärcher, A. Kiendler, A. Petzold, H. Schlager, F. P. Schröder and K. H. Wohlfrom, 2002: Influence of fuel sulphur on the composition of aircraft exhaust plumes: The experiments SULFUR 1-7, *J. Geophys. Res.*, 107 (10.1029/2001JD000813), AAC 2-1 – AAC 2-27.

Modeling of Soot Precursor Formation in Laminar Premixed Flames with C1-, C2- and C6-Fuels

E. Goos*, M. Braun-Unkhoff, N. Slavinskaya, P. Frank

Institut für Verbrennungstechnik, Deutsches Zentrum für Luft- und Raumfahrt (DLR), Stuttgart, Germany

Keywords: Fuel break-up kinetics, Polyaromatic hydrocarbons, Soot precursor, Soot volume fraction

ABSTRACT: In the present study models for formation and growth of polycyclic aromatic hydrocarbons (PAH) which are the base of particle formation by coagulation of the PAHs leading to soot, are compared with experimental species profiles in laminar premixed flames running with different fuels. The detailed modeling of the concentration profiles of these soot precursors was carried out by comparing two comprehensive gas phase reaction models. The experimental flame data stem from literature values for the fuels methane, ethene and benzene. Additionally, for recent experimental results from the investigation of sooting laminar ethene and propene flames, soot volume fraction profiles have been simulated by using a soot model, which combines a gas phase mechanism and a model for particle inception, coagulation, surface growth and oxidation. The aim of the present investigations is to establish a comprehensive PAH model for soot precursor kinetics which can be reduced in a sufficient manner to allow implementation into a CFD-code for modeling soot formation and oxidation in turbulent combustion processes.

1 INTRODUCTION

Aromatics and polycyclic aromatic hydrocarbons (PAH) are of particular concern in combustion processes because of their potentially adverse health effects. They are formed in the combustion of hydrocarbon fuels (e.g. kerosene) and have been identified as key precursors of soot. A soot model which is able to consider the fuel specificity for the prediction of the dynamics of particle formation and oxidation during the combustion process has to rely on a comprehensive gas phase fuel break-up and PAH formation reaction mechanism. Former investigations of flame and shock tube experiments, especially at high pressures, have shown the importance of PAH growth submodels on soot particle inception and on calculated soot volume fractions (Frenklach and Wang (1994), Böhm et al. (2003)). As in nearly all current soot models particle inception is described exclusively by coagulation of different large mass PAH, the influence of different PAH on the onset and the amount of soot has to be investigated systematically. Modeling studies (Hu et al. (2000)) reveal that only a few PAH species have to be considered for the simulation of the inception regime. A still open question is whether for different fuels the same major pathways of PAH formation and growth are found during combustion or whether the route to particle inception is not predictable with the same comprehensive gas phase reaction model. Therefore the investigation of PAH routes in laboratory flames is regarded as a tool for getting more insight into this problem.

However, for high pressure conditions, due to the very thin reaction zone, it is not possible to measure PAH profiles within and close to the very thin reaction zone. Therefore, PAH profiles measured in recent experiments with laminar premixed flames at atmospheric pressure have been used as data base for simulation. In these slightly sooting flames of aliphatic (methane, ethane, (Melton et al. (1998), Harris et al. (1998)) and aromatic hydrocarbons (benzene (Tregrossi et al. (1999))), a large variety of PAH (besides aliphatic compounds) has been measured by gas chromatography in combination with mass spectrometry ranging from two- to five-fused aromatic rings.

* Corresponding author: Elke Goos, Deutsches Zentrum für Luft- und Raumfahrt (DLR), Pfaffenwaldring 38-40, 70569 Stuttgart, Germany. Email: Elke.Goos@dlr.de

For comparing calculations, a recent comprehensive gas phase mechanism from literature (Appel et al. (2000)) and a gas phase mechanism established by the authors were used. The DLR mechanism which has been used with two modifications contains detailed chemistry for PAH growth including combinative growth steps of aromatic species and reactions to form species with up to 30 carbon atoms. Measured and predicted PAH profiles were compared to identify main routes for PAH growth. The different reaction pathways for the formation of PAH, the dominant species for soot precursor formation, were examined numerically to obtain a deeper understanding of the soot inception process.

2 GAS PHASE AND SOOT MODEL

At present, detailed modeling of soot formation and destruction is executed by using different, relatively large gas phase reaction mechanisms coupled with a mechanistic soot model that will be described later.

2.1 Gas phase reaction mechanisms

To describe the growth of polyaromatic species, the reaction mechanism given by Wang and Frenklach (1997) which comprises the reactions of aromatic species up to pyrene was updated with reactions of combinative growth steps of aromatic species as proposed by Böhm and Jander (1999) as well as reactions to form species with up to 30 carbon atoms (Richter et al. (1999)). Also, results of shock tube experiments for reactions of cyclopentadiene (Roy et al. (1998)) and the propargyl radical (Scherer et al. (2000)) and investigations focusing on the mono-aromatic species were taken into account: like decomposition of toluene and phenyl (Braun-Unkloff et al. (1988)), benzyl (Braun-Unkloff et al. (1990)) and phenylacetylene (Herzler et al. (1992)), and oxidation of phenyl (Frank et al. (1994)). In particular, the branching ratio of reactions with aromatic species turned out to be of importance with respect to formation of soot precursors. For example, the recombination of propargyl radicals leads essentially to the formation of benzene and not to phenyl and H-atoms; furthermore, propargyl radicals can react with benzyl, which is produced by pyrolysis of benzene, leading to indene.

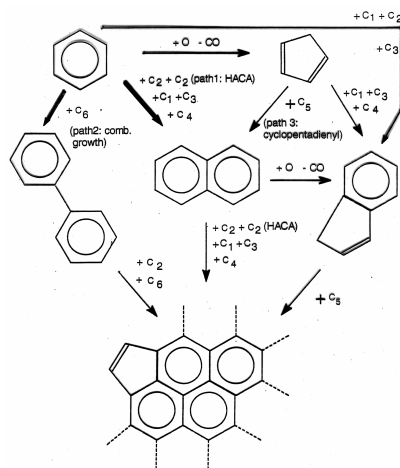


Figure 1: Principal reaction scheme for initial PAH formation

Figure 1 depicts the principal starting routes of the PAH growth submodel which contains about 45 species and 350 elementary reaction steps. Dominant routes are for example the hydrogen-abstraction-carbon-addition (HACA) path 1, the combinative growth path 2 which leads to the formation of biphenyl by the reaction of benzene and phenyl, and the cyclopentadienyl recombination (path 3) both producing naphthalene, and additional routes to form indene which then can grow by further reactions with cyclopentadienyl. The experimental data base for the rate constants in the PAH mechanism is extremely poor, and most of the data have to be estimated from

the comparison with similar reactions of smaller aromatics. Additionally, the thermodynamic data of the polyaromatic species is important for calculating the reverse rate constant, but often the needed thermodynamic data is not available or calculated with big errors.

The complete updated mechanism with a total of more than 600 reactions and 170 species was used to describe in detail the evolution of the gaseous species up to the entry of the particle inception model. Most of the gas phase reactions are treated as reversible with rate coefficients for the reverse reactions evaluated from the respective equilibrium constant. Only a few reaction steps, representing preferentially isomerization reactions, are considered with separate rate coefficient expressions for forward and reverse direction. The DLR new# mechanism contains the same PAH growth submodel as the DLR old# mechanism. In the new# version, the detailed C1- C3 chemistry is replaced through the fitted rate coefficients from the GRI-mechanism (GRI 3.0 (1998)).

For comparison, a recently published reaction mechanism from Appel et al. (2000) was used which has been applied and validated under a variety of experimental conditions. This model comprises a relatively small PAH growth mechanism with 45 species, up to pyrene ($C_{16}H_{10}$), and about 190 elementary reactions.

2.2 Soot model

After calculating the concentration profiles with different reaction mechanisms, the same soot model is used for calculating PAH growth, particle inception, coagulation of particles, condensation, surface growth and soot particle oxidation. It is based on a model from Frenklach and Wang (1994) using the method of moments for solving the differential equation system. The particle inception is described by PAH coagulation. All large PAHs species (starting with $C_{16}H_{10}$) which are formed in the PAH growth model were assumed to collide giving rise to nucleus. Consequently, the sum of all calculated concentration profiles of species with 16 carbon atoms or more were used as inputs to the actual soot model. In addition to the original program, the pressure dependence of the coagulation of soot particles has been implemented into Smoluchowsky's equation (Hu et al. (2000)). Further growth of the particles results from surface mass growth with PAHs and other aliphatic gas phase species e.g. C_2H_2 and H_2 . An essential quantity for the surface mass growth is the steric parameter α , which accounts for the fraction of surface sites available for corresponding reactions and which is a function of temperature and particle age, respectively. In the soot model used for this study, gas phase chemistry and soot dynamics are decoupled. Thus the conservation equations of soot on the gas phase are not taken into account. Neglecting these effects can lead to a slight overprediction of soot under the given conditions.

3 RESULTS

For comparison with the calculated data, experimental literature values from premixed flames with fuels like methane (Melton et al. (1998)), ethene (Harris et al. (1988)) and benzene (Tregrossi et al. (1999)) were used. The calculation of the concentration versus height profiles has been executed with the 1-dimensional PREMIX-code of the CHEMKIN-package (Kee et al. (1985)). As an example for the prediction of the combined gas phase and soot model, recent soot volume fraction profiles measured by Geigle et al. (2002) in ethene and propene flames were used.

3.1 Aliphatic hydrocarbons

The comparison between model calculation and experimental data in Figure 2 shows that acetylene, the most important gaseous component for PAH and surface growth, is reproduced well by the reaction model for the benzene / air flame under slightly sooting conditions (Fig. 2a) and for the strongly sooting ethylene / oxygen / argon flame (Fig. 2b). It is also to be seen from Fig. 2a that the prediction with DLR#new where the C_1 - and C_2 -kinetics is based on the GRI-mechanism gives definitely too low concentration values. Figure 2 also shows that the profiles of other aliphatic hydrocarbons such as ethene (Fig. 2a) and diacetylene (Fig. 2b) are predicted sufficiently well.

3.2 Aromatics

Measured concentration profiles of different aromatics ranging from one- to four-membered rings, some of them with a side chain, are compared with model predictions in Figures 3-5 which

correspond to the three flame investigations. The names of the PAHs were assigned in the graphs to the usual symbols (Table 1).

Table 1: Chemical notation of the used aromatics

Name	Structure	Mass (a.m.u.)	Graph	Name	Structure	Mass (a.m.u.)	Graph
Benzene	C_6H_6	78	A1	Naphthalene	$C_{10}H_8$	128	A2
Phenylacetylene	$C_6H_5C_2H$	102	A1C ₂ H	Acenaphthalene	$C_{12}H_8$	152	A2R5
Styrene	$C_6H_5C_2H_3$	104	A1C ₂ H ₃	Phenanthrene	$C_{14}H_{10}$	178	A3
Biphenyl	$C_6H_5-C_6H_5$	154	P2	Pyrene	$C_{16}H_{10}$	202	A4

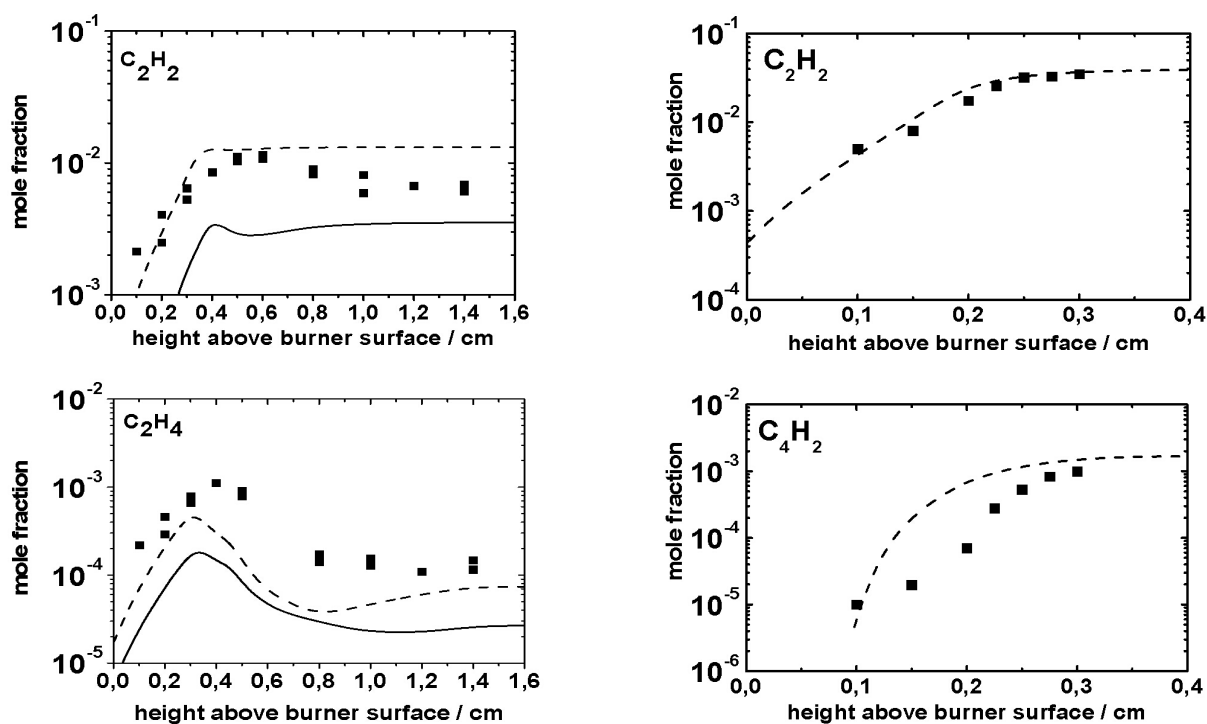


Figure 2: Comparison between model prediction and experiment for smaller aliphatic hydrocarbons in premixed laminar atmospheric flames. Experiment: \blacksquare , model: dashed line (DLR#old), full line (DLR#new). Fig. 2a (left side): benzene / air with $C/O = 0.72$ (Tregrossi et al.(1999)). Fig. 2b (right side): ethene / oxygen / argon with $C/O = 0.92$ (Harris et al. (1988)).

3.2.1 Al-aromatics

Benzene profiles are well reproduced by the DLR model for the benzene / air (Fig. 5) and ethene / oxygen / argon flames (Fig. 4). The mechanism from Appel et al. is too slow for the benzene decomposition and therefore higher values at larger flame heights are predicted. In the methane / oxygen-flame (Fig. 3), benzene concentration is overpredicted by about one order of magnitude by the DLR mechanism and something less by the Appel mechanism. Biphenyl which is formed via path 2 of the reaction scheme displaced in Fig. 1 has been measured only in the benzene flame. The prediction by all models reproduces the shape of the profile well, but the Appel mechanism overpredicts the concentration values by up to one order of magnitude.

For the predictions of concentration profiles for the premixed laminar ethene flame (Fig. 4), the calculations were done only with the DLR base model (DLR#old). The model predictions match the profiles for C_2H_2 (see Fig. 2a) and benzene (Fig. 4) properly and therefore the profile of $A1C_2H$ as well, because $A1C_2H$ is formed by the reaction of C_6H_5 with C_2H_2 . In the methane flame (Fig. 3), the initial rise of $A1C_2H$ concentration fits well, but the concentration level at larger flame heights is overpredicted by both models by factors of 2-4. Styrene is expected to play only a minor role for

soot precursor formation because it is formed only via a side route reaction sequence. The model fails to simulate the measured profile of $A1C_2H_3$ (Fig. 4) sufficiently, but it has to be pointed out that the mechanism is optimized with respect to acetylene addition reactions.

3.2.2 A2–aromatics

Naphthalene, which is generally considered to play a central role for the growth of the PAHs (see Fig. 1), is best reproduced by the Appel model in the methane flame (Fig. 3) and by DLR#old in the benzene flame (Fig. 5). Also, the values for acenaphthalene which has been measured only in the benzene flame at similar concentrations like naphthalene, are reproduced by the DLR#old model.

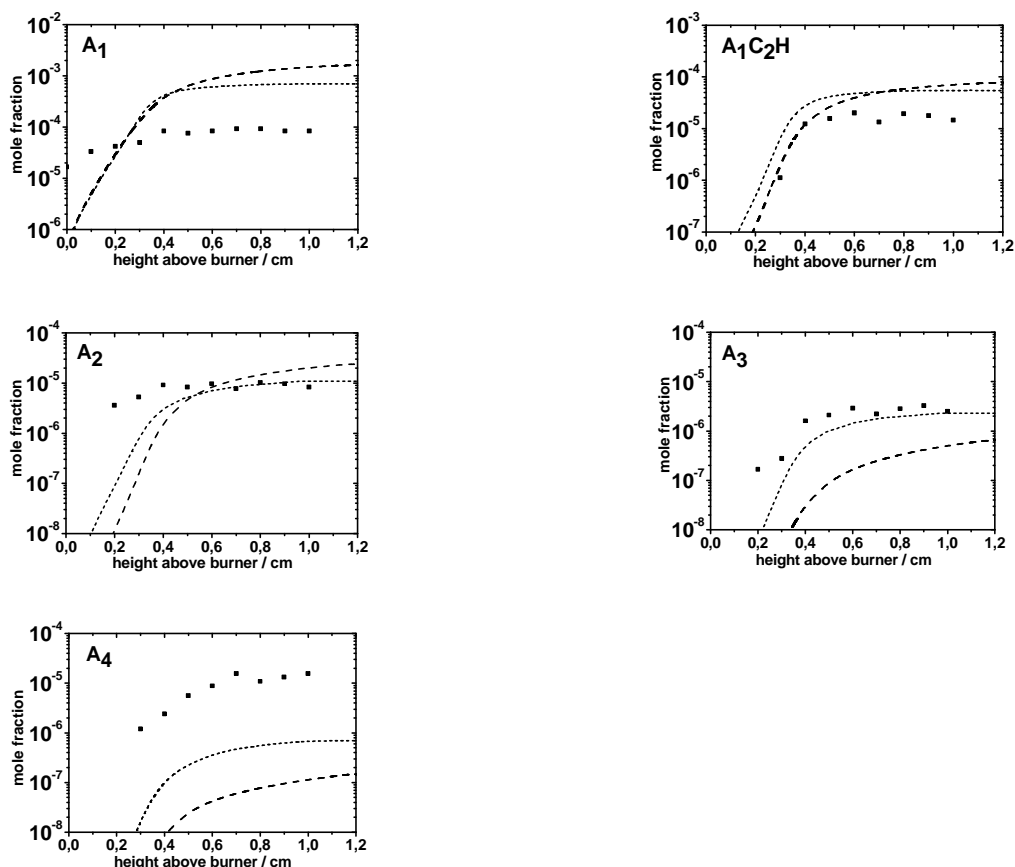


Figure 3: Comparison between model prediction and experimental data for aromatic species in a premixed laminar atmospheric flame with methane / oxygen / argon at $C / O = 0.60$ (Melton et al. (1998)). Experiment: \cdot , model: dashed line (DLR#old), short dashed line (Appel et al. (2000)).

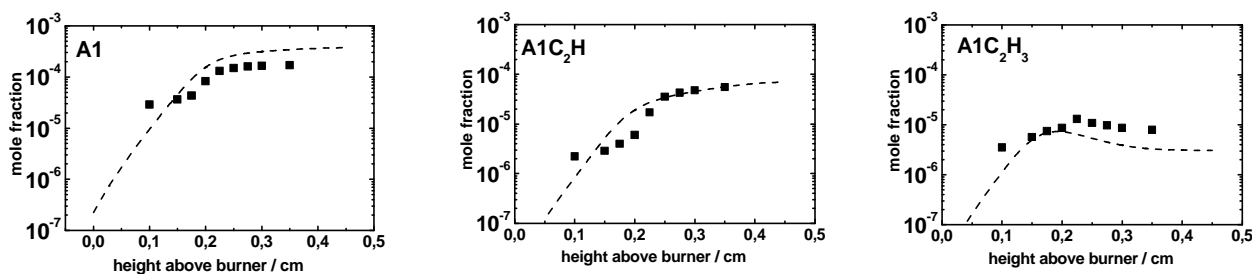


Figure 4: Comparison between model prediction and experimental data for aromatic species in a premixed laminar atmospheric flame with ethene / oxygen / argon at $C / O = 0.92$ (Harris et al. (1988)). Experiment: \cdot , model: dashed line (DLR#old).

3.2.3 A3-A4-aromatics

In the methane flame, phenanthrene is reproduced sufficiently well by the Appel model (Fig. 3) whereas both versions of the DLR model are far above or below the measured data points. In the benzene flame (Fig. 5), all models fail to reproduce the shape of the measured phenanthrene profile, but the quasi constant concentration level at larger heights is at least fit by the DLR#old model. It is not possible to fit the pyrene profiles in both flames. In the methane flame, (Fig. 3) pyrene is underpredicted by Appel and DLR#old by more than one order of magnitude, whereas in the benzene flame (Fig. 5), in the post reaction zone regime, Appel and DLR#new overpredict the experimental data by about two orders of magnitude. DLR#old overpredicts to a lesser extent the post flame data points. As mentioned before, the experimental data base for the rate constants in the PAH mechanism is extremely poor and most of the data have to be estimated from the comparison with similar reactions of smaller cyclic hydrocarbons. Additionally, the thermodynamic data of the polyaromatic species is important for calculating the reverse rate constant, but in the most cases the required thermodynamic data are not available or were deduced from calculations exhibiting enormous error bars. Therefore it is not surprising that the prediction of the concentration profiles for larger aromatic species is not satisfactory.

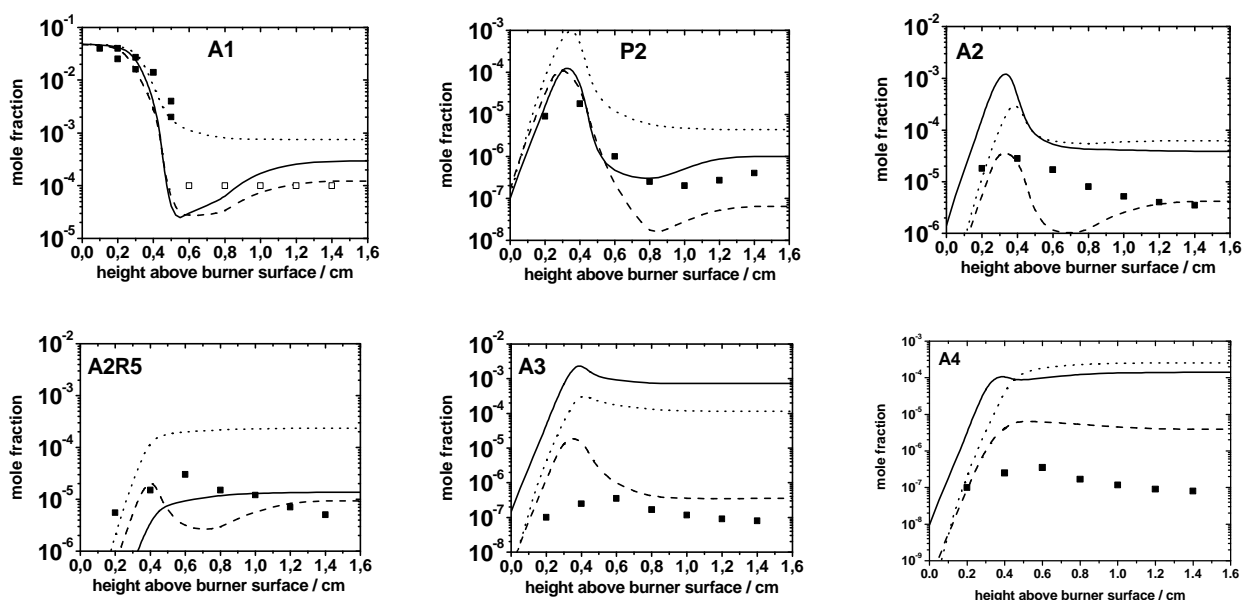


Figure 5: Comparison between model prediction and experimental data for aromatic species in a premixed laminar atmospheric flame with benzene / air at $C / O = 0.72$ (Tregrossi et al. (1999)). Experiment: \blacksquare , model: dashed line (DLR#old), full line (DLR#new), dotted line (Appel et al. (2000)).

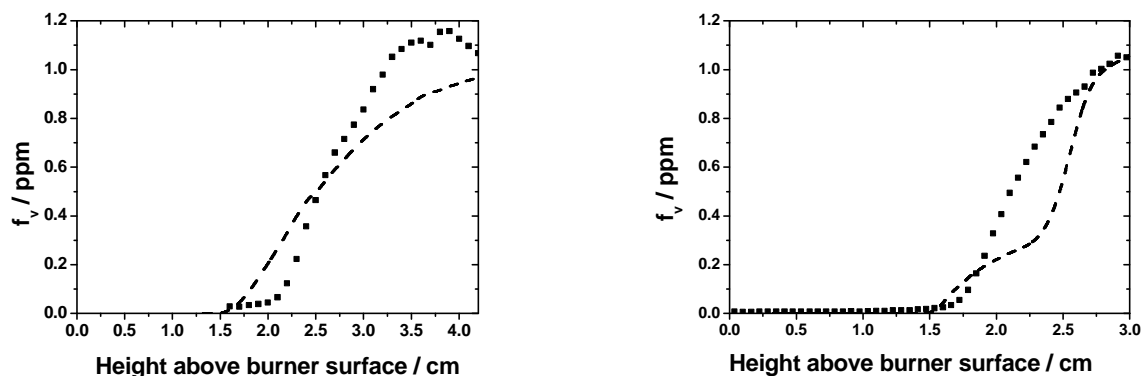


Figure 6: Comparison between model prediction and experimental data of soot volume fraction, f_V (ppm), in a premixed laminar atmospheric flame (Geigle et al. (2002)) with ethene / air at $C / O = 0.83$ (left side) and propene / air at $C / O = 0.74$ (right side). Experiment: \blacksquare , model: dashed line (DLR#old + soot module).

3.3 Soot volume fraction

Figure 6 shows measured soot volume fractions f_v for rich premixed ethene / air- and propene / air- flames at atmospheric pressure. The temperature profile has been determined by using shifted CARS (Schneider-Kühnle (2003)) with a high spatial resolution, especially close to the burner surface. This provides for a much higher reliability in the simulation of the reaction zone kinetics and therefore for the applied soot model, too. For comparison, Figure 6 presents also model prediction for f_v using the same reaction mechanism for simulation of soot production in the C_2H_4 and C_3H_6 flame. Reasonable agreement with the experimental data is found.

4 CONCLUSIONS

Different gas phase reaction mechanisms were used as base for the prediction of concentration profiles of soot precursors. One mechanism has been published recently by Appel et al. (2000). The others, DLR#old and DLR#new, which contains a modified version for C1-C2-chemistry, have been developed by the authors and were updated by incorporating recent chemical kinetic data for C5 and C6 species. The model predictions were compared with experimental data from laminar premixed flames using different fuels.

The modeling study showed that for different fuels both reaction mechanisms reproduce the measured profiles for C2- to C4-species well, thus indicating that the fuel break-up kinetics is simulated satisfactory. For aromatic A1-to A4-species, which are most important for the formation and growth of soot precursors, the PAH reaction mechanisms show particularly significant differences in the prediction of individual PAHs. The Appel mechanism exhibits smaller deviations from the measured data in the post reaction zone of the methane flame for different PAH levels than the DLR model. This is not surprising because the C1-C3-chemistry in the Appel mechanism is based on the methane GRI 3.0 mechanism. Evidently, the growth of the smaller hydrocarbons to the first ring aromatics reflects the fuel specificity better. On the other hand, the DLR#old model gives values definitely closer to the measured data for the fuels ethene and benzene which is caused by the more detailed kinetic model for the formation of the first ring aromatics. Furthermore, it was shown that the PAH prediction (DLR#new) with benzene as fuel becomes definitely worse for modifying the initial C1-C2- submodel by using a standard methane model (GRI 3.0).

It has been also demonstrated that the model, combined with the particle formation module, is able to simulate the main features of soot production in laminar premixed flames for different fuels, namely ethene and propene.

The results of the present work suggest investigating in more detail the formation routes to higher mass aromatics like pyrene. Such experiments could be done by using tools like single pulse shock tubes or high temperature flow reactors with high temporal resolution. These devices have the advantage of well defined initial conditions, and they allow conducting experiments at much higher pressures. Thus, the experimental data base could be enlarged considerably and may lead to a better understanding of the formation and growth of polycyclic aromatic hydrocarbons as main soot precursors.

REFERENCES

- Appel, J., H. Bockhorn, and M. Frenklach, 2000: *Combust. Flame* 121, 122-136.
- Böhm, H. and H. Jander, 1999: *Phys. Chem. Chem. Phys.* 1, 3775.
- Böhm, H., M. Braun-Unkhoff, and P. Frank, 2003: *Progress in Computational Fluid Dynamics* 3, 145-150.
- Braun-Unkhoff, M., P. Frank, and Th. Just, 1988: *Proc. Combust. Inst.* 22, 1059-1061.
- Braun-Unkhoff, M., P. Frank, and Th. Just, 1990: *Ber. Bunsenges. Phys. Chem.* 94, 1417-1425.
- Frenklach, M. and H. Wang, 1994: *Detailed Mechanism and Modeling of Soot Particle Formation*. In: *Soot Formation in Combustion, Mechanisms and Models*, [Ed. H. Bockhorn], Springer-Verlag Berlin, Springer Series in Chemical Physics 59 (1994), pp. 165-190.
- Geigle, K.P., V. Krüger, and Y. Schneider-Kühnle, 2002: DLR Stuttgart, private communication.
- GRI 3.0, American Gas Research Institute, see http://www.me.berkeley.edu/gri_mech/ (1998).
- Harris, S.J., A.M. Weiner, and R.J. Blint, 1988: *Combust. Flame* 72, 91-109.
- Herzler, J. and P. Frank, *Ber. Bunsenges.* 1992: *Phys. Chem.* 96, 1333-1338.

- Hu, D., M. Braun-Unkhoff, and P. Frank, 2000: *Z. Phys. Chem.* 214 (4), 473-491.
- Kee, R.J., J.F. Grcar, M.D. Smooke, and J.A. Miller, 1985: "PREMIX", Sandia National Laboratories, Livermore, CA, Report: SAND85 8240.
- Melton, T.R., A.M. Vincitore, and S.M. Senkan, 1998: *Proc. Combust. Inst.* 121, 1631– 1637.
- Richter, H, W.J. Grieco, and J.B. Howard, 1999: *Combust. Flame* 119, 1-20.
- Roy, K., C. Horn, P. Frank, V. Slutsky, and Th. Just, 1998: *Proc. Combust. Inst.* 27, 329-336.
- Scherer, S., Th. Just, and P. Frank, 2000: *Proc. Combust. Inst.* 28, 1511-1518.
- Schneider-Kühnle, Y., 2003: Experimentelle Untersuchungen russender Hochdruckflammen mit laserdiagnostischen Messmethoden. PhD Thesis, DLR Stuttgart, in preparation.
- Tregrossi, A., A. Ciajolo, and R. Barbella, 1999: *Combust. Flame* 117, 553-561.
- Wang, H. and M. Frenklach, 1997: *Combust. Flame* 110, 173-221.

Modelling of Volatile Particles during PARTEMIS

X. Vancassel, P. Mirabel*

Centre de Géochimie de la Surface, Université Louis Pasteur, Strasbourg, France

A. Sorokin

Central Institute for Aviation Motors, Moscow, Russia

Keywords: nucleation, aerosol, aircraft emissions, modelling

ABSTRACT: A microphysical model has been used in order to study volatile particles formation in the sampling system of the PartEmis European experiment. The fraction ϵ of the fuel sulphur S(IV) converted into S(VI) has been indirectly deduced from comparisons between model results and measurements. ϵ has been found to be in the range 2.5 % to 6 %, depending on the combustor settings and on the microphysical approach used. Different processes have been investigated, comprising soot particles activation and possible growth. Growth factors of monodisperse particles transported in the line and then exposed to high relative humidity (95 %) have been calculated and compared with experimental results. Results show interesting trends of increasing growth factors with decreasing size.

1 INTRODUCTION

Volatile particles formed in aircraft exhaust plumes may play an important role on the atmosphere chemical composition, radiation processes and cloud coverage (IPCC, 1999). The understanding of the potential impacts of aircraft generated aerosol still requires a better knowledge of the mechanisms of particle precursors formation and of ultrafine volatile particles generation. Numerous papers, involving in-situ measurements (e.g. Schröder et al., 1998) and also modelling studies have emphasized the role of sulphur, chemi-ion and organic compounds on aircrafts plume microphysical processes (e.g. Kärcher et al., 1998; Yu et al., 1999). However, the effect of engine operating conditions on the formation of these particles is not yet well understood. There is evidence that the number of volatile particles increases with increasing levels of sulphur in the fuel, but the conversion rate ϵ at which the original sulphur IV is transformed to S(VI) i.e. SO₃ and H₂SO₄ remains highly discussed as a wide range of values has already been suggested (Schumann et al., 2002).

An extensive set of gaseous species and aerosol measurements have been conducted on a jet engine combustor test rig, in the frame of the EU project PartEmis. One of the goals of PartEmis was to gain more information about the rate of sulphur conversion. For this, gaseous S(VI) (SO₃+H₂SO₄) has been measured by chemical ionization mass spectrometry (Katrakou et al., *subm.*). Liquid aerosol particles measurements were achieved by operating a multi-channel Condensation Particle Size Analyzer (CPSA). Only the concentrations of particles in the size range 4-7 nm, have shown a dependency on the Fuel Sulfur Content (FSC) used during the test campaign (Petzold et al., 2003). Furthermore, the hygroscopic properties of particles with dry diameters > 30 nm were measured with a Hygroscopicity Tandem Differential Mobility Analyzer (H-TDMA). To support these experiments, several modelling studies have been undertaken and in this article, we present modelling studies of the formation of volatile particles and of the hygroscopic properties of soot particles. The calculations have been performed with a microphysical comprehensive model.

* *Corresponding author:* Philippe Mirabel, Centre de Géochimie de la Surface, Université Louis Pasteur, 1 rue Blessig, 67084, Strasbourg, France. Email: mirabel@illite.u-strasbg.fr

2 EXPERIMENTAL SETUP AND SAMPLING SYSTEM

A brief description of the combustor and test-rig used during PartEmis, is given below, and further details can be found in Wilson et al. (2003). The exhaust was sampled close to a combustor exit by a probe (4 mm inner diameter), laterally moved to eleven traverse positions (position 6 was central). This allowed the lateral distribution of gaseous precursors and particles to be measured. After exiting the probe, the sample temperature was rapidly quenched to minimise post sampling reactions, by a water cooling system, bringing its temperature to about 420 K avoiding any condensation of water and unburnt hydrocarbons in particular. The exhaust was then split and delivered to a diluted and to an undiluted sampling line which supplied each participant with the desired fraction of the sample. The diluted line, which concerns this study, was not insulated (contrarily to the undiluted line sample) and the sample naturally attained room temperature ($\sim 20^\circ\text{C}$) after dilution by a factor of about 60-65. Dilution was achieved by means of a capillary tube with particulate free air at ambient conditions (293 K, 1052 hPa). The last part of the sampling line had an inner diameter of 21.12 mm and the total transit time was approximately 0.9 s from the tip of the probe to the measurement devices. Two settings were used, in order to reproduce "old" and "modern" cruise conditions and three different fuel sulphur contents FSC = 50, 410 and 1270 ppm have been tested. As the extraction probe was very close to the exit smile, the temperature of the exhaust gases in the first part of the sampling line remained high (above 430 K) until the dilution point was reached. Therefore, no condensation was expected in this part of the sampling line. On the contrary, the dilution of the sample with air at ambient temperature cooled it down very rapidly (more than 100°C in less than 10 ms), leading to a local supersaturation of the condensing vapors. Therefore, particle formation was expected to take place only in the sampling line, just after the mixing of the sample with the cold diluting air. Indeed, volatile particles were detected at the end of the sampling line, in the 4-7 nm size range but only for the high fuel sulphur case (FSC = 1270 ppm). The model calculations made confirm that only for these high FSC volatile particles are expected to be analysed with this experimental set up.

3 MODEL DESCRIPTION

Classical homogeneous heteromolecular nucleation theory, generally invoked to explain the formation of volatile particles seems unable to properly describe their formation in aircraft plumes because of the use of a steady state approach leading to time lag effects in a fast changing system (e.g. Taleb et al. 1997). Indeed, in a plume, the temperature cools down very rapidly due to the entrainment of very cold ambient air in the wake. As a consequence, we have used a "kinetic" microphysical approach, similar to the one used by Yu and Turco (1997) (see also Yu and Turco, 2001). The model, based on coagulation processes in the sulphuric acid-water binary mixture (Sorokin et al., 2001) takes into account both charged (ions or charged clusters) and neutral species (molecules or clusters), the presence of charges having a stabilizing effect on clusters and enhances growth and coagulation. Contrarily to the classical nucleation theory which assumes that particles result from collisions between clusters and single molecules (or hydrates), the kinetic approach includes in addition cluster-cluster collisions. Given the very strong binding energy between sulphuric acid and water molecules, the formation of hydrates is expected in the vapor phase (e.g. Heist and Reiss, 1974). The initial distribution of sulphuric acid hydrates has been calculated following Wilemski and Wyslouzil self consistent assumptions (Wilemski and Wyslouzil, 1995). The subsequent growth due to coagulation of these clusters and condensation (condensation has been treated as a special case of coagulation) has led to the formation of stable particles, classified into "size-bins" according to their acid content. In addition to volatile particles, the presence of soot particles in the exhaust has been considered. A log normal distribution has been proposed from measurements results, depending on the probe position. The emission index was typical for common aircraft engines ($\text{PEI}=10^{14}$ to 10^{15} /kg fuel) and the mean size was around 37-40 nm, for old and modern cruise respectively. The interactions between soot particles and gaseous species (water and sulphuric acid) as well as their interaction with volatile particles have been included in the model. Another key parameter for volatile particles modelling is the Chemi-Ion emission index at the combustor exit. A value of the CI emission index of $5.3 \cdot 10^{17}$ /kg has been proposed by the

Max Planck Institut (MPI) of Heidelberg. We mainly used this value as a reference one although we have performed a sensitivity analysis of the CI effects on volatile particles growth. The system of intrusive sampling used to carry out measurements during the Partemis campaign has required the integration of peculiar processes to describe the evolution of species in the exhaust plume. The possible interaction between aerosols (volatile particles and soot) or gaseous species with the flow pipe walls has been taken into consideration. Concerning soot adsorption on the surfaces of the sampling line, we have followed the work by Hurley (1996) who provided the ratio $N_{\text{soot}}/N_{\text{soot}}^0$ of leaving to entering soot number densities in a tube. It is interesting to note that the losses were found independent of the particle number density and size. For stainless steel, the losses have been calculated according to the following semi-empirical equation:

$$\frac{N_{\text{soot}}}{N_{\text{soot}}^0} = \exp\left(-\left(1.05 \times 10^{-4} V + 2.27 \times 10^{-4}\right) \frac{L}{dV}\right) \quad (1)$$

where V is the sample mean velocity, L the pipe length and d its diameter. Equation 1 has been used for the series of pipes of different sections with varying flow rate, which constitute the PartEmis sampling line geometry. Concerning volatile particles, wall losses have been neglected from the tip of the probe to the diluter, as the sample was heated at 423 K to prevent condensation. But after dilution, the estimated material losses due to wall effects, enhanced by the turbulent behaviour of the flow (Reynolds number $Re > 30000$), was estimated following for instance the work of Brockmann et al. (1982). The volatile particles number density evolution in the tube can be calculated using the first order equation :

$$\frac{\partial N(r,t)}{\partial t} = -\frac{4k_T(r,T)}{d} N(r,t) \quad (2)$$

where $N(r,t)$ is the number density of volatile particles of radius r at time t after the diluter, k_T is the mass transfer coefficient determined according to Friedlander (1977) (see for example Brockmann et al., 1982)

$$k_T = 0.042 V f^{1/2} Sc^{-2/3} \quad (3)$$

where f is the friction factor, Sc the Schmidt number which estimates the ratio between the viscosity of air and the particle diffusivity.

4 RESULTS AND DISCUSSION

4.1 Volatile particles

One of the main uncertainties to calculate the losses is the value to be affected to the sticking coefficient, i.e to determine a collision efficiency (CE) between particles or clusters colliding on the tube walls. Several values of CE have been used, from 50 % to 100 % (maximum possible value) as this parameter remains poorly known. Actually, even for condensation and particles collisions, theoretical studies as well as experiments have led to quite different values of accommodation coefficient (Van Dingenen and Raes, 1991; Clement et al., 1996). Figure 1 which gives the results of the simulations for high FSC, shows the sulphur conversion factor required for the model to provide a good agreement with measured volatile particles concentration in the size range from 4 to 7 nm. The different curves correspond to different values for the assumed CE and sulphur conversion factor ϵ . For the maximum possible value $CE = 100\%$, the sulphur conversion factor reaches a mean value of about 5.2 % for old and 5.7 % for modern cruise conditions. However, if the CE is reduced to 50 % (still a rather high value), ϵ mean values translate to 2.5 % and 2.8 % respectively. These last values provide very reasonable agreement both with the measured concentration of volatile particles and ϵ values deduced by the MPI group, although most of these results have been determined in the wake, and not at the combustor exit (e.g Curtius et al., 2002). Note that results for the first and last positions of the probe, close to the combustor wall have not been presented here, as the air fuel ratio (AFR) in these cases was much higher than the average value (approximately twice the average AFR). It should also be noted that even for a sulphur

conversion > 5 % no volatile particles are expected to be seen at the end of the sampling line from our results, for the low and medium sulphur case which has been confirmed by observations. The sulphur conversion ε and the collision efficiency on walls are not the only parameters which have an influence on particles growth. Chemi-ion concentrations, which were measured during PartEmis, may play also a major role. As already noted, we have used an emission index of $5.3 \cdot 10^{17}$ /kg at the combustor exit but a variation of a factor ten in this concentration has only a limited influence on the results presented in Figure 1.

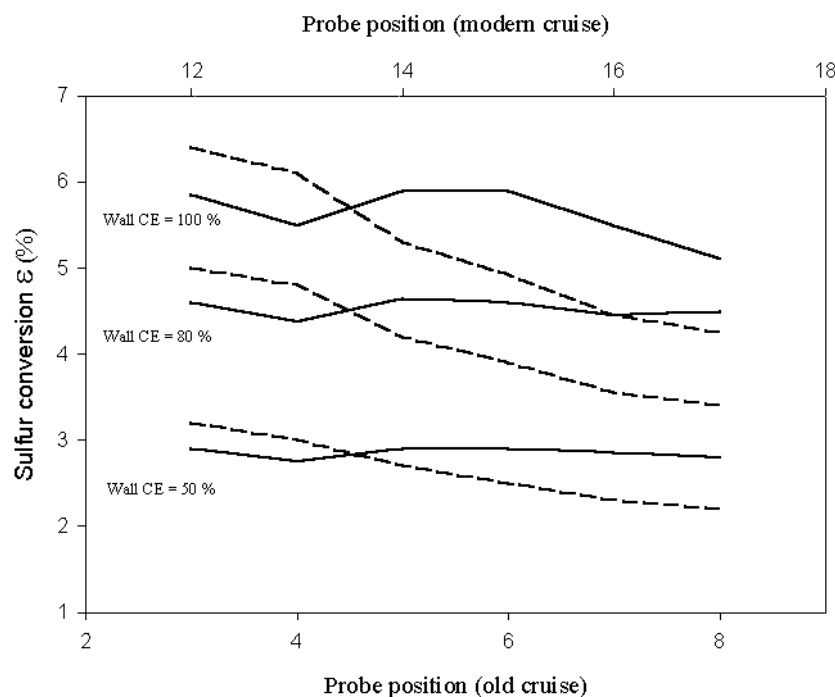


Figure 1. Required SC to fit DLR volatile particles measurements as a function of the probe position. Case of high FSC (1270 ppm). Old cruise conditions: position 3 to 8. Modern cruise conditions: position 12 to 17. dashed lines: old cruise (bottom axis). Full lines: modern cruise (top axis)

4.2 Hygroscopic properties of soot particles

Soot particles have been taken into account in our calculations and we have studied the ability of the model to reproduce soot particles growth measurements, as they have been carried out by Gysel et al. (2003). Actually, studies of soot hygroscopicity are of main importance as soot activation is a key process for their subsequent growth and transformation into contrails. To summarize briefly these experiments, a monodisperse fraction of particles has been sampled, at the end of the sampling line, and then exposed to a rather high relative humidity (up to 95 %). Although soot activation has recently been observed to occur even with sulphur free kerosene (O. Popovicheva, pers. comm.), Gysel et al. (2003) have shown a clear dependence between the fuel sulphur content and the growth factor defined as the ratio between the wet and the dry (initial) diameter of soot particles, calculated once they have been exposed to high humidity conditions. As volatile and soot particles undergo scavenging processes, soot particles have gained a sulphuric acid-water coating as they have been transported in the sampling line. We have then checked if the model results could match experimental results, concerning both the measured growth factor and the estimated sulphuric acid weight fraction of the layer. The growth factor is characterized by a slight increase close to the diluter when the sample is mixed with the diluting air whose humidity is higher. Then the liquid coating evaporates slightly as both water and sulphuric acid molecules are lost on the walls or are depleted due to nucleation and condensation processes. At the end of the sampling line, when the sample enters the H-TDMA the sudden increase of relative humidity, up to 95 % brings about a sudden growth of soot particles. As noted by Gysel et al. (2003), the smaller the particles, the larger

the growth factors are and no significant difference was detected between old and modern conditions (especially if error bars are included). These observations were confirmed by our modelling study since the calculated growth factors are 1.14, 1.11 and 1.07 respectively for particles having initial diameters of 30, 40 and 50 nm before extraction. These values are close to those calculated for other probe positions and have been obtained using a wall CE of 50 % and a sulphur conversion corresponding to the one required to fit volatile particles concentration to the measurements carried out by the DLR ($\epsilon = 2.5\% - 2.8\%$).

Table 1 gives a comparison between calculated and measured growth factors and acid volume fractions of the surface layer, for the high FSC case (FSC=1270 ppm). One notes a good agreement for the general trends, i.e. increase of both growth factors and acid volume fractions with decreasing size. However, the values may be quite different, especially for the acid volume fraction.

Table 1. Experimental (Gysel et al., 2003) and model results (this work). Comparison of soot particles growth factor and sulphuric acid volume fraction for modern cruise operating conditions at high FSC (1270 ppm). The growth factor is calculated as the ratio between the particles diameters considered just before they enter the condensation chamber and after they reach equilibrium in it.

Dry diameter	Calculated growth factor	Measured growth factor	Calculated acid volume fraction	Estimated acid volume fraction
nm			%	%
30	1.14	1.23	14.0	21.0
50	1.11	1.16	9.6	9.5
100	1.07	1.07	8.4	3.0

5 CONCLUSIONS

A modelling study of volatile particle formation has been presented in the frame of the PartEmis project, in order to study the role of sulphuric acid on particles formation and growth. A sulphur conversion factor ϵ has been indirectly deduced from the comparison between experimental results and model calculations. Taking into account the absence of accurate monitoring of water vapour along the line, and the lack of line transmission information, average values in the ranges 2.5 % - 5.7 % have been calculated, depending on the collision efficiency of particles and clusters on the walls. The last value of ϵ cited (5.7 %) represents an upper limit since it has been deduced for the maximum collision efficiency between particles and sampling line walls. The soot growth factor study has pointed out similar trends between measured and calculated values. In particular, the growth factor increased as the soot particle size decreased (Gysel et al., 2003). The role of sulphuric acid remains very important, although the binary system may not be completely able to predict accurately particles concentration, especially in a complex system such as a sampling line. Our modelling study did not include the possible contribution of organics on the growth process. However, previous studies have shown that this role appears to be important only for low FSC (of the order of 100 ppm or less). Another source of uncertainty is the possible presence of ammonia (which was not monitored) in the diluting air, as ammonia is known to lead to ternary nucleation with the sulphuric acid-water mixture. If ammonia was indeed present, nucleation would have been enhanced and the value of ϵ needed in the model would have been reduced. Again, this confirms that the ϵ values given in this work should be considered as upper limits.

6 ACKNOWLEDGEMENTS

Support of this work by the European Community through contract G4RD-CT-2000-00207 (PartEmis) and by the INTAS project OPEN 2000-460, as well as fruitful discussions with the PartEmis participants are gratefully acknowledged.

REFERENCES

- Brockmann, J.E., P.H. McMurry, and B.Y.H. Liu, 1982: On simultaneous coagulation and diffusional loss of free molecule aerosols in turbulent pipe flow. *Aeros. Sci. Tech.* 1, 163-178.
- Clement, C.F., M. Kulmala, and T. Vesala, 1996: Theoretical considerations on sticking probabilities. *J. Aeros. Sci.* 27, 869-882.
- Curtius J., F. Arnold and P. Schulte, 2002: Sulfuric acid measurements in the exhaust plume of a jet aircraft in flight: Implications for the sulphuric acid formation efficiency. *Geophys. Res. Let.* 29, doi: 10.1029/2001GL013813.
- Friedlander, S. K.: 1977, Smoke, Dust and Haze, Eds Wiley, New York.
- Gysel, M., S. Nyeki, E. Weingartner, U. Baltensperger, H. Giebl, R. Hintzenberger, A. Petzold, and C.W. Wilson, 2003: Properties of jet engine combustor particles during the PartEmiss experiment. Hygroscopicity at subsaturated conditions. *Geophys. Res. Let.* 30, 1566, doi: 10.1029/2003GL016896.
- Heist, R.H., and H. Reiss, 1974: Hydrates in supersaturated binary sulfuric acid-water vapor. *J. Chem. Phys.* 61, 573-581.
- Hurley, C.D., 1996: Measurements of particulates from an engine combustor. AEROTRACE proceedings, Impact of Aircraft Emissions upon the Atmosphere, Paris. Vol. 1, 113.
- Intergovernmental Panel on Climate Change (IPCC), 1999: Aviation and the Global Atmosphere. Cambridge Univ. Press, New-York.
- Kärcher, B., F. Yu, F.P. Schröder and R.P. Turco, 1998: Ultrafine aerosol particles in aircraft plumes: Analysis of growth mechanisms. *Geophys. Res. Let.* 25, 2793-2796.
- Katragkou, E., S. Wilhelm, F. Arnold, and C. Wilson, 2003: Sulfur (VI) in the simulated internal flow of an aircraft turbine engine: first measurements. Submitted to *Geophys. Res. Let.*
- Petzold, A., C. Stein, S. Nyeki, M. Gysel, E. Weingartner, U. Baltensperger, H. Giebl, R. Hintzenberger, A. Dopelheuer, S. Vrchoticky, H. Puxbaum, M. Johnson, C.D. Hurley, R. Marsh, C.W. Wilson, 2003: Properties of jet engine combustion particles during the PartEmiss experiment: Microphysics and Chemistry. *Geophys. Res. Let.* 30, doi: 10.1029/2003GL017283.
- Schröder, F., B. Kärcher, A. Petzold, R. Baumann, R. Busen, C. Hoell, and U. Schumann, 1998: Ultrafine aerosol particles in aircraft plumes: in situ observations. *Geophys. Res. Let.* 25, 2789-2792.
- Schumann, U., F. Arnold, R. Busen, J. Curtius, B. Kärcher, A. Kiendler, A. Petzold, H. Schlager, F. Schröder, and K.-H. Wohlfrom, 2002: Influence of fuel sulfur on the composition of aircraft exhaust plumes: The experiments SULFUR 1-7. *J. Geophys. Res.* 107, doi: 10.1029/2001JD000813.
- Sorokin, A., X. Vancassel and P. Mirabel, 2001: On volatile particle formation in aircraft exhaust plumes. *Phys. Chem. Earth (C)*. 26, 557-561.
- Taleb, D. E., R. McGraw, and P. Mirabel, 1997: Time lag effects on the binary homogeneous nucleation of aerosols in the wake of an aircraft. *J. Geophys. Res.* 102, 12885-12890.
- Van Dingenen, R., and F. Raes, 1991: Determination of the condensation accommodation coefficient of sulphuric acid on water-sulphuric acid aerosol. *Aero. Sci. Tech.* 15, 93-106.
- Wilemski, G., and B.E. Wyslouzil, 1995: Binary nucleation kinetics. I. Self consistent size distribution. *J. Chem. Phys.* 103, 1127-1136.
- Wilson, C.W., A. Petzold, F. Arnold et al., 2003: Measurement and prediction of emissions of aerosols and gaseous precursors from gas turbine engines (PartEmiss): An experimental overview. Submitted to *Aerosp. Sci. Technol.*
- Yu, F., and R.P. Turco, 1997: The role of ions in the formation and evolution of particles in aircraft plumes. *Geophys. Res. Let.* 24, 1927-1930.
- Yu, F., R.P. Turco, and B. Kärcher, 1999: The possible role of organics in the formation and evolution of ultrafine aircraft particles. *J. Geophys. Res.* 104, 4079-4087.
- Yu, F., and R.P. Turco, 2001: From molecular clusters to nanoparticles: Role of ambient ionization in tropospheric aerosol formation. *J. Geophys. Res.* 106, 4797-481.

Dispersion and Growing of Ice Particles in a Turbulent Exhaust Plume

F. Garnier^{*1,2}, C. Ferreira Gago¹, A.-L. Brasseur¹

¹Office National d'Etudes et de Recherches Aéronautiques – O.N.E.R.A - France

²Université de Marne-la-Vallée, – L.E.T.E.M - France

R. Paoli, B. Cuenot
CERFACS/CFD - France

Keywords: Wake vortices, Numerical simulation, Exhaust jet, Turbulence, Contrails, Two-phase flows

ABSTRACT: Contrails may have an impact on cloudiness and may affect the Earth's radiative budget balance. In order to better understand their formation, preliminary study on the dispersion of gas and particles (soot and ice) in the exhaust jet and on their modification by wake processing has been performed. This work is focused on the 3D numerical simulation of dynamics and microphysics in a near-field of an aircraft wake. Large Eddy Simulations have been carried out at realistic flight Reynolds number to evaluate the effects of turbulent mixing and wake vortex dynamics on gas and particle mixing.

1 INTRODUCTION

Aircraft exhaust contains products resulting from combustion in gas or solid phase. Ice particles that mainly nucleate on exhaust soot and volatile aerosols can lead to the formation of contrails which may have an impact on cloudiness and may affect the Earth's radiative budget balance. In order to better understand the formation of contrails, fundamental studies on the dispersion of gaseous and particles (soot and ice particles) in the near field of an aircraft wake and their modification by plume processing are necessary.

In this article a condensed survey is given on unsteady numerical simulations of the plume processes that were in part already described in previous publications. A detailed description of the different numerical approaches is given in the works of Ferreira Gago *et al.* (2002), Paoli *et al.* (2002) and Paoli *et al.* (2003).

The numerical simulations of the flow are based on the use of 3D temporal DNS/LES of the compressible Navier-Stokes equations. In the LES approach, these equations are filtered in order to reduce the number of scales to be solved. Among the various subgrid scale viscosity and heat flux models used in the LES works, the compressible version of the hybrid Smagorinsky model (linear combination of the Smagorinsky and the similarity model) and the Structure Function model displayed the best performances, especially when dealing with the turbulent stresses and the turbulent heat flux (Ferreira Gago *et al.*, 2003; Métais and Lesieur, 1992). The LES equations are solved by using a sixth-order compact scheme in space and the time marching scheme is a three-order Runge-Kutta algorithm.

In the present work we have focused on the simulation of contrail formation and early-stage evolution in the near field of an aircraft wake (i.e. up to a few seconds from the emission time).

Eulerian two-fluid models of particle-laden flow are based on a volume averaging approach, describing macroscopic properties (phase volume fractions, average solute mass fractions and velocities...) of a two-phase mixture. This work uses the alternative Lagrangian particle tracking approach. It seems more suited to the future modeling needs of microscopic phenomena occurring in the exhaust jet and vortex wake of an aircraft (activation of soot, ice crystal condensation and

* Corresponding author: Garnier, ONERA - DMPH/EAG - 29 avenue de la Division Leclerc - BP 72 - 92320 Chatillon - FRANCE. Email: f.garnier@onera.fr

coagulation of volatile aerosols). Due to the small size of the soot-ice particles (from tens of nanometers to a few microns), their relaxation time is negligible compared to the characteristic times to the filtered variables. This allows them to be treated as a tracer. In addition due to the high number density (about $2.5 \cdot 10^{11} \text{ m}^{-3}$, Karcher *et al.*, 1996), we can carry only packets of particles where each one containing a large number (10^{+6}) physical particles. In the coupling terms which are involved in the LES equations, we only consider the mass exchange, i.e. vapor condensation on the soot particles (so the thermal coupling will be neglected).

2 AIRCRAFT PLUME DYNAMICS

2.1 Jet/vortex interaction

In the near field of the aircraft wake, the exhaust jets of the engine are entrained into the counter-rotating wingtip vortices. The entrainment process and the associated turbulent mixing are complex and it is convenient to identify two overlapping regimes (Garnier *et al.*, 1997): the jet and interaction regimes. The first one is that of usual co-flowing jets and it scales with the jet diameter. Later, the interaction of exhaust jet and the wake vortex characterizes the second regime. The convection and shearing processes associated with the tangential velocity field of the trailing vortex strongly affect the exhaust jet dispersion. In the present numerical study, these two regimes are modeled sequentially. The axial length of the domain of 6 nozzle radii corresponds to twice the wave length of the maximum growth rate of the first azimuthal instability of a spatially evolving jet (Michalke and Herman, 1982). An unstable nozzle outlet velocity profile is prescribed. When the jet simulation has reached an age that corresponds to a downstream distance of 0.5 wingspans, the cross section of the domain is enlarged and a Lamb-Oseen vortex is superimposed on the flow field at a distance of 14 vortex core radii from the jet center.

An experiment detailed in Brunet *et al* (1999), delivers a database that can be used for improving the numerical simulations. The wake of a generic model corresponding to a rectangular plan form NACA0012 equipped with two heated jets is investigated. The experimental results comprise mean and fluctuating velocity fields (measured with a LDV system) and mean temperature field (measured with thermocouples). Unsteady aspects of the flow are also described by means of hot wire measurements. The experimental results show that the flow does not affect the engine jet behaviour until a downstream distance of 0.5 wing spans. For modern large transport aircraft, the characteristic size of the jet regime is of the order of 1-50 diameters of the nozzle exit, while the deflection regime, scaled to the wingspan, extends downstream of the aircraft to a distance of about 0.5-10 wingspans.

Thereafter numerical results are compared with the experimental database, and an example of the results is shown in Figure 1 where the downstream variations of temperature T peak values are represented. The temperature evolution throughout the near field of the wake as obtained from numerical predictions is in agreement with the experimental results.

2.2 Gaseous exhaust mixing

In order to illustrate the entrainment and mixing processes of the gas exhaust, we examine the contours of axial vorticity and species concentration (defined as a passive scalar concentration) as shown in Figure 2. The turbulence induced by the exhaust jet is wrapped around the wing-tip vortex. This interaction results in the generation of small scale motions close to the vortex core and rearranges to coherent secondary vorticity structures (but now ring shaped) of opposite signs. The region very close to the core retains its positive axial vorticity contours, but they are no concentric anymore. At this stage, one can see that the gaseous exhaust dispersion is mainly controlled by these new organized structures.

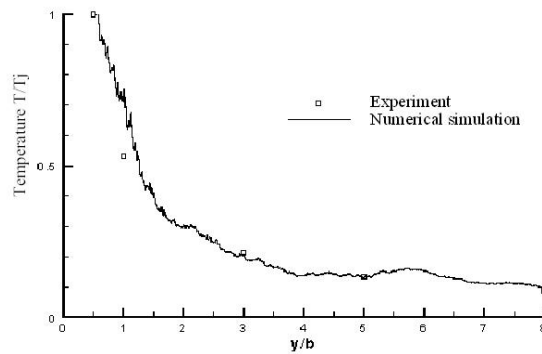


Figure 1. Downstream evolution of the dimensionless temperature T/T_j , where T_j is the nozzle exit temperature. Comparison with experimental data.

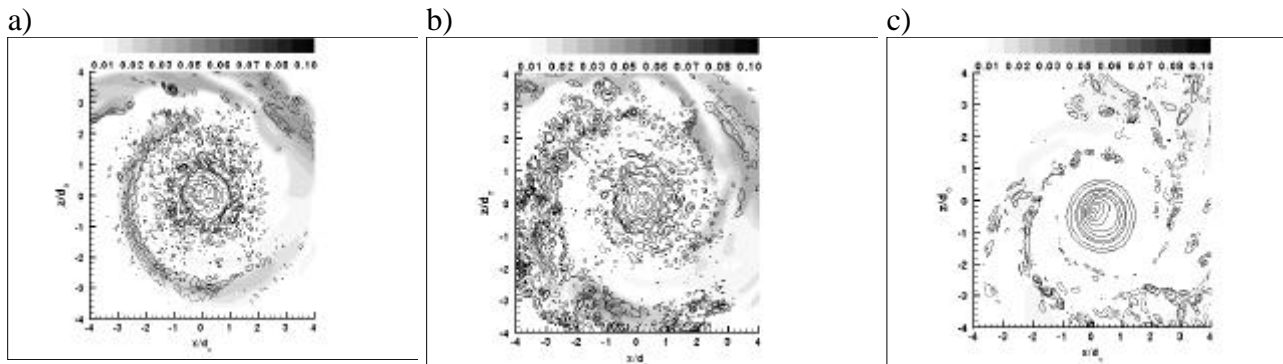


Figure 2. Numerical axial component of vorticity Ω_y in a meridional cross plane. Contour range from -1 to 4 in steps of 0.2 for levels between -1 and 1 , and in steps of 0.5 for levels between 1 and 4 . Exhaust gas concentration is represented by gray flood contours. (a) $y/b=6.5$, (b) $y/b=9.2$, (c) $y/b=13.1$.

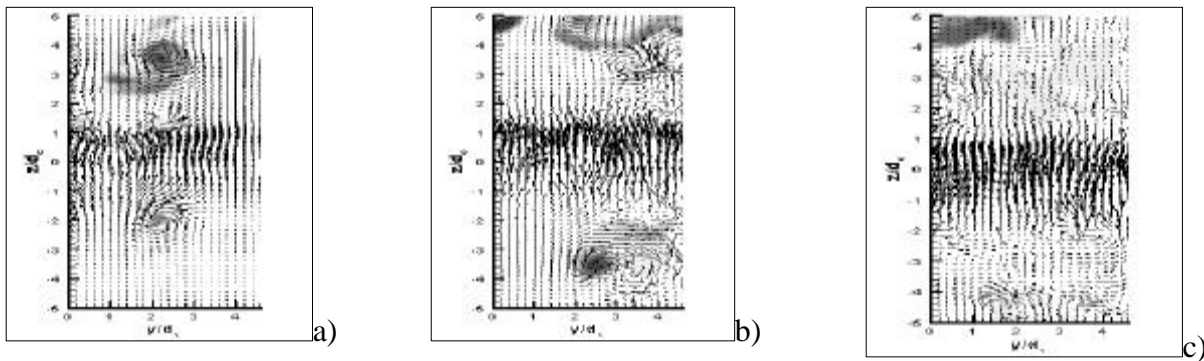


Figure 3. Velocity vector fields in (y,z) plane, at $x = 0$. Exhaust gas concentration is represented by gray flood contours. (a) $y/b=6.5$, (b) $y/b=9.2$, (c) $y/b=13.1$.

It is also noticed in Figure 3 where velocity vectors are superimposed on the species distribution. Entrainment process results in the trapping of the gas exhaust into the large scale secondary vortices (see Figures 3a and 3b). The species concentration provides a reliable signature of where the helical instability occurs outside the vortex core. Finally, the resulting species field distribution shows no aircraft exhaust products inside the primary vortex core as observed in Figures 2c and 3c.

3 CONTRAIL FORMATION

This paragraph describes the results of the simulation of ice formation in the near field of an aircraft.

A simple micro-physics model for ice growth has been used to couple ice and vapor phases. LES have been carried out at a realistic flight Reynolds number to evaluate the effects of turbulent mixing and wake vortex dynamics on ice growth characteristics and vapor thermodynamic properties.

In the first simulation, the micro-physics ice growth model is switched off. The aim is to obtain a reference mixing case at high Reynolds numbers typical of aircraft wake configurations. It was also useful to analyse the spatial distribution of supersaturated particles and identify the regions where ice formation is most likely to occur.

All particles are initially (at $t = 0.16$ s) placed below the saturation curve $p_s(T)$ because they are still concentrated inside the hot jet region. Due to the mixing with cold air, particles cool, until some of them become supersaturated (crossing of p_s curve at $t = 0.56$ s). The spatial distribution of supersaturated particles is given in Figure 4, together with a plane cut of water vapor content at two times during the jet phase. The figure shows that air first saturates around the particles, placed at the edges of the jet where the temperature is fallen and there is sufficient vapor to condense.

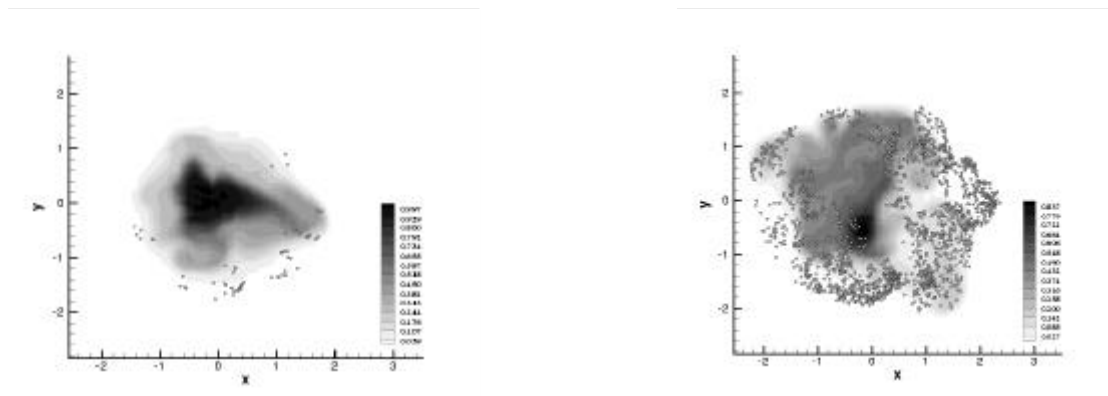


Figure 4. Passive particle case (jet phase). Plane cut of vapor content and distribution of supersaturated particles ; left, $t = 0.56$ s ; right, $t = 0.7$ s.

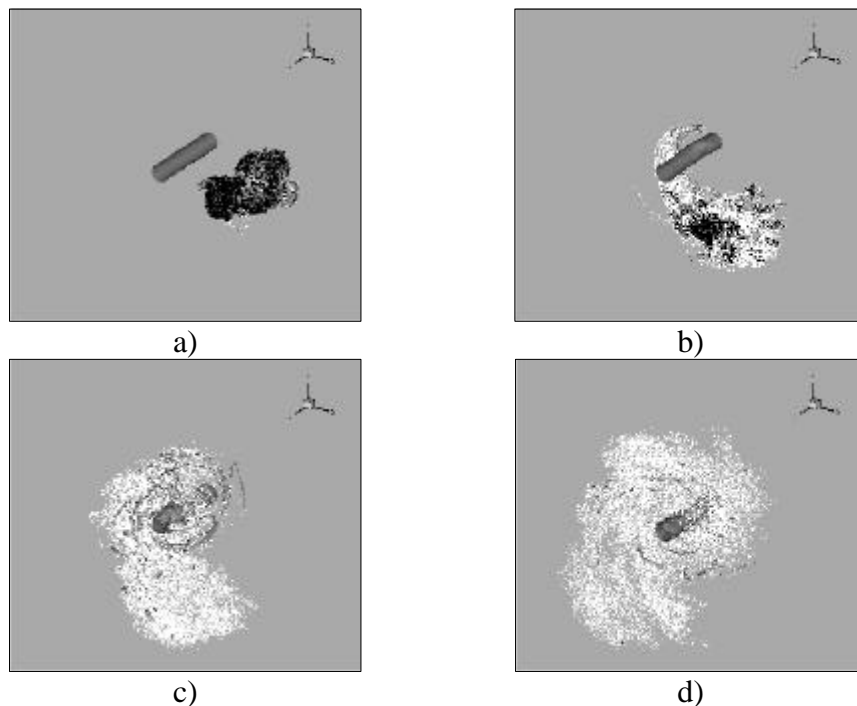


Figure 5. Passive particle distribution during the jet/vortex interaction phase. Dry soot particles are represented in black, iced supersaturated particles in white. Total vorticity iso-surface identifies the vortex core and the secondary vortical structures due to the interaction with the jet ; a) $t = 0.7$ s ; b) $t = 1$ s ; c) $t = 1.5$ s ; d) $t = 2$ s.

The dynamics of the interaction phase are dominated by formation of three-dimensional structures of azimuthal vorticity associated to the entrainment of the jet inside the vortex field. These structures progressively decay ($t = 2$ s, see Figure 5(d)), corresponding to complete entrainment of the exhaust jet. This mechanism of entrainment enhances mixing with external air : therefore, exhaust cooling and vapor condensation are favored by the presence of vortex. Figure 5 shows that at $t = 2$ s all particles are supersaturated and contrail can form everywhere in the wake.

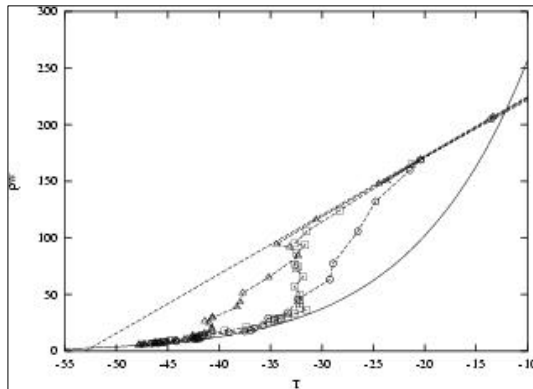


Figure 6. Trajectories of three sample particles in a $T - p_w$ plane.

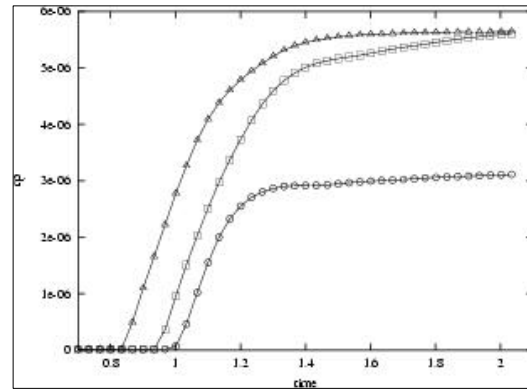


Figure 7. Time evolution of three sample particles radius.

In the second simulations set, the ice growth model is activated. The aim of this calculation is to analyse the early-stage evolution of the contrail and how it influences mixing and the thermodynamic properties of the vapor. Figure 6 displays the trajectories of three sample ice interaction phase when ice/vapor-pressure plane (results are reported only during the interaction phase when ice/vapor coupling is significative). The figure shows that condensation causes large deviations from the mixing line because of vapor removal and the consequent decrease in water partial pressure p_w . In addition, all the particles finally collapse on the saturation curve, $p_s(T)$, which indicates the thermodynamic equilibrium between vapor and ice phases. This is confirmed in Figure 7 by the evolution of ice-particle radii which attain plateau values between 3 and 6 μm .

4 CONCLUSION

This work is focused on the simulation of contrails and early stage evolution in the near-field of an aircraft wake. A numerical simulation of the interaction between an engine jet and a wake vortex has been performed.

To illustrate the entrainment and mixing processes of the exhaust gas, the examination of axial vorticity contours showed that the turbulence induced by the exhaust jet is wrapped around the wing-tip vortex. Results show that the dynamics of the interaction phase are dominated by formation of three-dimensional coherent structures associated to the entrainment of the jet inside the vortex field. The evolution of this interaction (i.e. generation of small scale motions close to the vortex core and rearrangement to coherent secondary structures) mainly controls the gaseous exhaust dispersion.

To study the formation of contrail, a simple micro-physics model for ice growth has been used to couple ice and vapor phases. LES have been carried out at a realistic flight Reynolds number to evaluate the effects of turbulent mixing and wake vortex dynamics on ice growth characteristics and vapor thermodynamic properties.

Two simulation sets are made:

- The first simulation is carried out when the micro-physics model is switched off in order to obtain a reference mixing case at high Reynolds numbers, typical of aircraft wake configurations. This analysis provided the spatial distribution of supersaturated particles and it

identified the regions where ice formation is most likely to occur. Furthermore, results show that the exhaust cooling and vapor condensation are favored by the presence of vortex.

- The second numerical simulation is performed accounting for ice growth process in order to analyse the early-stage evolution of the contrail and its influence on the mixing and the thermodynamic properties of the vapor. Results show that condensation causes large deviations from the mixing line because of vapor removal and the consequent decrease in water partial pressure. In addition, all the particles finally collapse on the saturation curve and their radii reach plateau values between 3 and 6 μm .

REFERENCES

- S. Brunet, L. Jacquin, P. Geoffroy, 1999 : Experiment on heated jet/wake vortex interaction, *ONERA RTY 15/2496 DAFE/Y*.
- C. Ferreira Gago, F. Garnier and F. Uthéza, 2003 : Direct testing of subgrid scale models in large eddy simulation of a non-isothermal turbulent jet, *International Journal for Numerical Methods in Fluids (in press)*.
- C. Ferreira Gago, F. Garnier and F. Uthéza, 2002 : Numerical investigation of turbulent mixing in a jet/vortex interaction, *AIAA Journal*, 40, 276-284.
- F. Garnier, C. Baudouin, N. Louinard, 1997 : Engine Emission alteration in the nearfield of an aircraft, *Atmospheric Environment*, 31, 1767-1781.
- B. Karcher, T. Peter, U. Biermann and U. Schumann, 1996 : The initial composition of jet condensation trails, *Journal of Atmospheric Science*, 53, 3066-3083.
- O. Metais and M. Lesieur, 1992 : Spectral large-eddy simulation of isotropic and stably stratified turbulence, *Journal of Fluid Mechanics*, 239, 157-194.
- A. Michalke and G. Hermann, 1982 : On the inviscid instability of a circular jet with external flow, *Journal of Fluid Mechanics*, 114, 343-359.
- R. Paoli, F. Laporte, B. Cuenot, T.J. Poinsot, 2003 : Dynamics and mixing in a simple configuration of jet/vortex interaction. *Physics of Fluids*, 15, 1843-1860
- R. Paoli, J. Hélie, T.J. Poinsot, S. Ghosal, 2002 : Contrail formation in aircraft wakes using large-eddy simulations, *Center for Turbulence Research, proceedings of summer Program*.

The Effect of Plume Processes on Aircraft Impact

I.C. Plumb^{*}, L.K. Randeniya, P.F. Vohralik
CSIRO Telecommunications and Industrial Physics, Lindfield, NSW, Australia

S.L. Baughcum
Boeing Company, Seattle, WA 98124, USA

Keywords: Aircraft emissions, Plume chemistry, NO_x, NO_y, HO_x

ABSTRACT: In the present study, we investigate the chemistry of expanding aircraft exhaust plumes for a range of conditions (latitude, altitude, season, plume expansion rate, time of day of emissions, aircraft type, composition of emissions and background air mass). The effect of plume chemistry on 2-D global model calculations of the impact of subsonic aircraft emissions on ozone is discussed.

1 INTRODUCTION

Plume processes are inherently sub-grid scale in multi-dimensional global models, so they need to be studied using off-line models with dimensions of the order of plume dimensions and the effects of plume processes parameterized for inclusion in multi-dimensional models. Several studies have been made of plume processes (Danilin et al., 1994; Meijer et al., 1997; Petry et al., 1998; Moulik and Milford, 1999; Karol et al., 2000; Kraabol and Stordal, 2000; Kraabol et al., 2000b) and different parameterizations have been developed. Kraabol et al. (2002) obtained reductions of 15-18% in calculated ozone changes at cruise altitude due to subsonic aircraft emissions in a 3-D model study when plume processes were included. Meijer et al. (1997) reported similar percent reductions in ozone changes due to aircraft when they included plume processes in their 3-D model study. That study, however, did not include O₃ effective emissions. When these were included, ozone change reductions due to inclusion of plume processes decreased to 0-5% in January and -5% to 10% in July (Meijer, 2001). There is thus considerable uncertainty in the importance of plume processes for aircraft assessment studies.

In the present study, a Gaussian plume model was developed and used to study the chemistry of expanding aircraft plumes for a wide range of conditions. The plume model is described briefly in Section 2. Plume processes were described in terms of two different parameterizations: emission conversion factors and relative emission changes. These parameterizations are defined in Section 3. Section 4 describes some of the results obtained using this model, with particular emphasis on the effect of composition of the background atmosphere on plume composition. These studies allow insight to be gained on the processes which are important for determining the conversion of NO_x to NO_y in the plume and on the production of ozone. Section 5 describes results obtained when results of these plume studies were incorporated into the CSIRO 2-D chemical transport model, using both of the parameterizations described in Section 3.

2 PLUME MODEL

The plume model used in the present studies is based on the Gaussian plume model of Melo et al. (1978). The plume is represented as a set of expanding concentric elliptical annuli, with dimensions based on analytical solutions of the diffusion equation for a Gaussian profile (Konopka, 1995). Diffusion coefficients are from Durbeck and Gerz (1995). The vortex and dispersion phases of the aircraft plume are modelled for times up to approximately 24 hours after emission. The tropospheric

^{*} *Corresponding author:* Ian Plumb, CSIRO Telecommunications and Industrial Physics, Lindfield, NSW 2070, Australia. Email: Ian.Plumb@csiro.au

chemistry reaction scheme contains 110 species and approximately 400 reactions with rate coefficients from Sander et al. (2000) and Atkinson et al. (1999).

2.1 Composition of background atmosphere

Conversion of aircraft exhaust products is dependent on the composition of the background atmosphere. Sensitivity of the results to the background atmosphere was studied using atmospheric compositions from the SONEX campaign. A base case reference atmosphere consisting of the background case in Table 2 of Jaegle et al. (2000) was used, in addition to other air masses identified during the SONEX campaign. In addition, a global climatology was derived, based on a number of measurement campaigns, together with ozone, temperature and water vapour climatologies from the literature.

3 PARAMETERIZATIONS OF PLUME PROCESSING

In an assessment model, the emissions from all aircraft trajectories within each model grid cell over a given period of time are averaged and represented as a time-varying emission rate for each emitted species. What is required from a plume parameterization is a modification to the emissions (or a set of effective emissions), which takes into account the chemistry in the expanding plume. There have been two proposals on how this should be done.

The first (Kraabol et al., 2000a; Meijer, 2001) uses the plume model to calculate the chemical composition of the plume when the plume has expanded to dimensions corresponding roughly to a model grid cell. Emission conversion factors ECF are defined for each species X which is emitted or produced in the plume

$$ECF_x(t) = \frac{X(t) - X_a(t)}{NOy(t) - NOy_a(t)} \quad (1)$$

where subscript a denotes ambient concentration into which the emission occurs.

The second approach (Petry et al., 1998) compares the composition of the plume after it has expanded to the dimensions of a model grid cell with a calculation in which aircraft emissions are diluted at time of emission into the same volume as occupied by the plume at the end of the integration. This “instantaneous dispersion” calculation is taken to represent the multi-dimensional model without plume corrections. The difference between these two calculations is used to calculate a set of effective emission indices to use in the multi-dimensional model. For each species X emitted or produced in the plume, a correction $\mathbf{d}(X)$ is calculated which must be added to the concentration change $\Delta(X)$ produced by instantaneous dispersion. The relative emission change for X is then given by

$$\mathbf{d}_{rel}(X) = \frac{\mathbf{d}(X)}{\Delta(NOx)} \quad (2)$$

These relative emission changes can be used to define effective emission indices for each species X

$$EI_{eff}(X) = \frac{m_x}{m_{NOx}} \mathbf{d}_{rel}(X) EI(NOx) \quad (3)$$

These two approaches for including the effects of plume processes in multi-dimensional models are fundamentally quite different and there has been little discussion in the literature as to their relative merits. Both $ECFs$ and \mathbf{d}_{rel} values have been calculated in the present study and used in the 2-D model studies in Section 5.

4 RESULTS OF PLUME MODEL STUDIES

4.1 Dependence on dynamical variables

Dynamical variables affect the plume chemistry primarily through determining the cross-sectional area of the plume as a function of time. The evolution of the plume area can be changed either by changing the diffusion coefficients or by changing the wind shear. Wind shear results in stretching of the plume along its major axis, but little change in the dimension along the minor axis. Changing the wind shear from 0 to 0.01 s^{-1} results in a change in the cross-sectional area of the plume after 24 hours from $5.6 \times 10^6 \text{ m}^2$ to $1.7 \times 10^8 \text{ m}^2$, or approximately a factor of 30. Figure 1 shows relative emission changes for NO_y species and for ozone as functions of wind shear for the background atmosphere. All relative emission changes tend to zero as the wind shear is increased (although not monotonically in all cases). This is to be expected, as the simulation approaches the instantaneous dispersion case. On the other hand, emission conversion factors (not shown) approach limiting values which are non-zero.

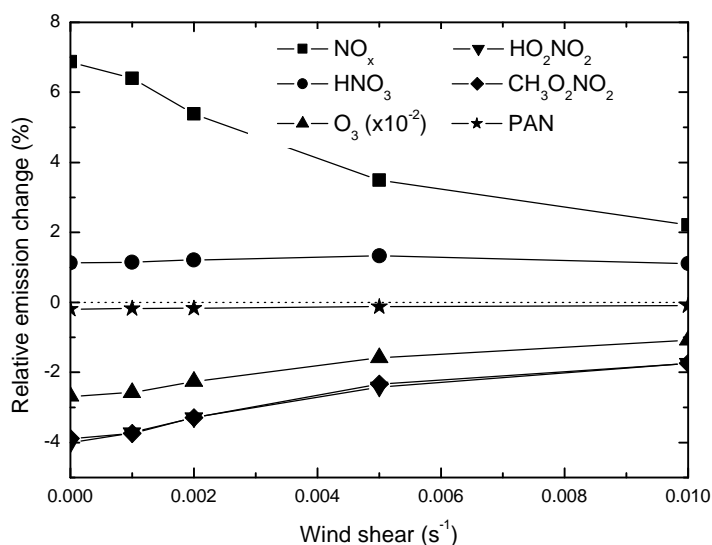


Figure 1. Relative emission changes (as percentages) as functions of wind shear for the base case.

Table 1. Important characteristics of different air masses used to study the influence of background atmosphere on plume processes.

Parameter	Background Influence	Stratospheric marine	Tropical marine	Midlatitude	Continental	Cirrus
Temperature (K)	227	223	225	231	223	231
H_2O ($\mu\text{mol mol}^{-1}$)	120	42	195	208	128	338
O_3 (nmol mol^{-1})	55	149	33	47	55	50
NO_x (pmol mol^{-1})	93	135	60	68	593	83
HO_x (pmol mol^{-1})	3.8	1.8	4.8	4.8	0.98	5.2
Aerosol SA ($\mu\text{m}^2 \text{cm}^{-3}$)	7.8	8.1	4.4	10	11.4	27.8

4.2 Dependence on composition of background atmosphere

Calculations were performed to determine the effect of composition of the background atmosphere on plume processing. The air masses considered are those identified in the SONEX campaign (Jaegle et al., 2000) and the important differences between the different air masses are summarized in Table 1.

Figure 2 shows emission conversion factors for NO_x in the plume after 24 hours for the different air masses. There are clearly significant differences in the fractions of NO_x remaining for the

different background air masses. The continental air mass has the smallest conversion of NO_x to products, while the stratospheric influence air mass has the largest.

Another notable feature of Figure 2 is the comparatively small variation in the amount of NO_x remaining with time of day of the emissions. Other authors have reported larger variations (Karol et al., 2000; Kraabol et al., 2000a; Meijer, 2001). The reason for this can be understood by reference to Figure 3. This diagram shows the fraction of the initial NO_y remaining as NO_x as a function of time after emission for different emission times for the background atmosphere. For all times other than 24 hours after emission, there are much larger differences between the NO_x for different emission times. This is because there are two main conversion routes for NO_x: the daytime, which is dominated by reactions of NO₂ with OH and HO₂, and the night time, which is dominated by conversion to N₂O₅ and ultimately to HNO₃ via heterogeneous chemistry. As can be seen in Figure 3, conversion is more rapid during the day. As long as a 24-hour integration is used, the same total lengths of daytime are seen for all emission times, and similarly for night time.

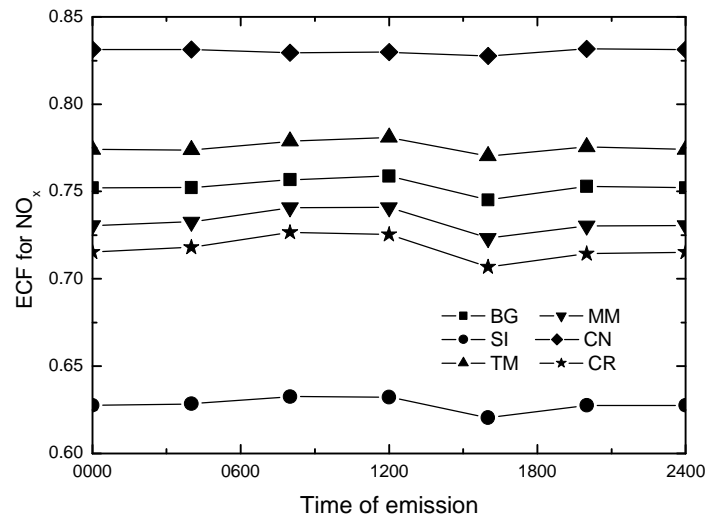


Figure 2. Emission conversion factors for NO_x 24 hours after emission as functions of emission time for different air masses (BG = background, SI = stratospheric influence, TM = tropical marine convection, MM = mid-latitude marine convection, CN = continental convection and CR = cirrus cloud), for 1 November.

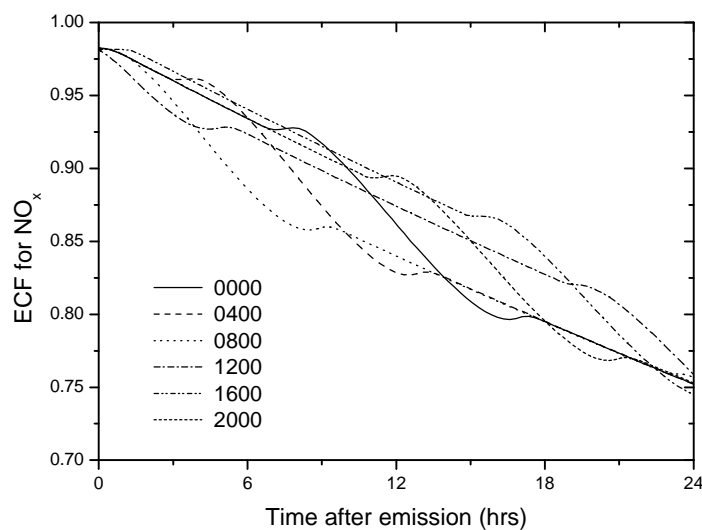


Figure 3. Emission conversion factors for NO_x as functions of time after emission and emission time for background atmosphere, for 1 November.

The differences in conversion of NO_x shown in Figure 2 can be explained in terms of differences in NO_x, HO_x and O₃ in the background atmospheres. For the air of stratospheric origin, the higher O₃ content means greater conversion to N₂O₅ at night, which more than compensates for the comparatively low HO_x in this air mass. For the continental convection air mass, the high background NO_x results in suppression of HO_x and other peroxy radicals, so that formation of HO₂NO₂, CH₃O₂NO₂ and PAN are all reduced.

4.3 Dependence on location and time of year of emissions

Studies were made of the dependence of conversion of aircraft exhaust products on latitude, altitude and time of year. As an example, Figure 4 shows ECFs for NO_y components as functions of altitude at 40°N, 1 October. As can be seen in Figure 4, there is a marked decrease in conversion of NO_x to NO_y with increasing altitude. At high altitudes, N₂O₅ and HNO₃ become the major products, due to increasing O₃ with altitude. At lower altitudes, HO₂NO₂, CH₃O₂NO₂ and PAN become significant, with PAN the largest product at 8 km.

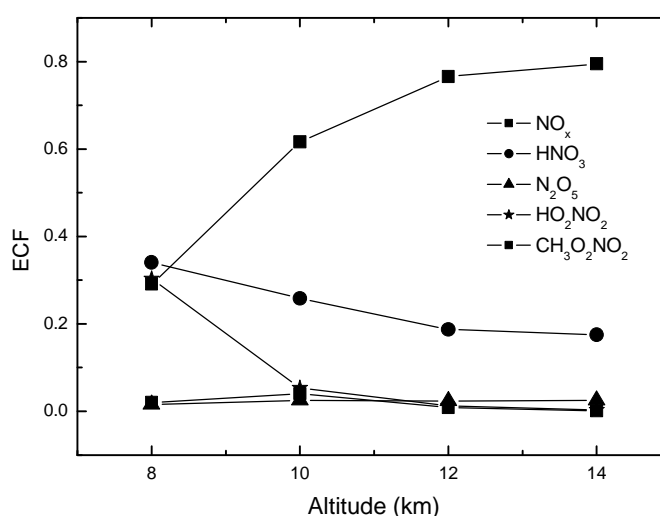


Figure 4. Emission conversion factors for NO_y species 24 hours after emission as functions of altitude for 8 am emission time, for 1 October.

5 2-D MODEL CALCULATIONS

A first-order estimate of the importance of plume processes on aircraft assessment studies for the current subsonic aircraft fleet was made using the CSIRO 2-D CTM. This was done by comparing aircraft impact calculations without inclusion of plume processes with calculations made using either emission conversion factors or relative emission changes derived using the plume model. Several simplifying assumptions were made in the plume parameterizations. The plume parameters were derived for a single aircraft type (B747-400), using fixed dynamical variables, and using 24-hour-average mid-latitude plume corrections at all latitudes in the northern hemisphere.

For both plume parameterizations, the calculated annual-average NH mid-latitude subsonic aircraft perturbation changed by less than 3% when plume effects were included. This is much smaller than changes of 15-18% reported in a recent 3-D study of Kraabøl et al. (Kraabøl et al., 2002) but more comparable to changes reported by Meijer (Meijer, 2001).

6 CONCLUSIONS

Conversion of aircraft exhaust products in the expanding plume is a strong function of composition of the background atmosphere, altitude, latitude and season. Most results can be explained in terms of daytime conversion of NO_x to NO_y via HO_x chemistry and night-time conversion via heterogeneous chemistry. Inclusion of either of the two plume parameterizations used in the present study in a global model results in changes to calculated subsonic impact at northern mid latitudes of less than 3%.

REFERENCES

- Atkinson, R. et al., 1999: Evaluated kinetic and photochemical data for atmospheric chemistry, organic species: Supplement VII, *J. Phys. Chem. Ref. Data*, 28, 191-393.
- Danilin, M. Y. et al., 1994: Evolution of the concentrations of trace species in an aircraft plume: Trajectory study, *J. Geophys. Res.*, 99, 18951-18972.
- Durbeck, T. and T. Gerz, 1995: Large-eddy simulation of aircraft exhaust plumes in the free atmosphere: effective diffusivities and cross-sections, *Geophys. Res. Lett.*, 22, 3203-3206.
- Jaegle, L. et al., 2000: Photochemistry of HO_x in the upper troposphere at northern midlatitudes, *J. Geophys. Res.*, 105, 3877-3892.
- Karol, I. L. et al., 2000: Plume transformation index (PTI) of the subsonic aircraft exhausts and their dependence on the external conditions, *Geophys. Res. Lett.*, 27, 373-376.
- Konopka, P., 1995: Analytical Gaussian solutions for anisotropic diffusion in a linear shear flow, *J. Non-Equilib. Thermodyn.*, 20, 78-91.
- Kraabøl, A. G. et al., 2002: Impacts of NO_x emissions from subsonic aircraft in a global three-dimensional chemistry transport model including plume processes, *J. Geophys. Res.*, 107, doi:10.1029/2001JD001019.
- Kraabøl, A. G., F. Flatoy, and F. Stordal, 2000a: Impact of NO_x emissions from subsonic aircraft: Inclusion of plume processes in a three-dimensional model covering Europe, North America, and the North Atlantic, *J. Geophys. Res.*, 105, 3573-3581.
- Kraabøl, A. G. et al., 2000b: Modelling chemistry in aircraft plumes 1: comparison with observations and evaluation of a layered approach, *Atmos. Environ.*, 34, 3939-3950.
- Kraabøl, A. G. and F. Stordal, 2000: Modelling chemistry in aircraft plumes 2: the chemical conversion of NO_x to reservoir species under different conditions, *Atmos. Environ.*, 34, 3951-3962.
- Meijer, E. W., 2001: Modelling the Impact of Subsonic Aviation on the Composition of the Atmosphere, thesis, Technische Universiteit Eindhoven, Eindhoven.
- Meijer, E. W. et al., 1997: The effects of the conversion of nitrogen oxides in aircraft exhaust plumes in global models, *Geophys. Res. Lett.*, 24, 3013-3016.
- Melo, O. T., M. A. Lysis, and R. D. S. Stevens, 1978: Mathematical modelling of dispersion and chemical reactions in a plume - oxidation of NO to NO₂ in the plume of a power plant, *Atmos. Environ.*, 12, 1231-1234.
- Moulik, J. B. and J. B. Milford, 1999: Factors influencing ozone chemistry in subsonic aircraft plumes, *Atmos. Environ.*, 33, 869-880.
- Petry, H. et al., 1998: Chemical conversion of subsonic aircraft emissions in the dispersing plume: Calculation of effective emission indices, *J. Geophys. Res.*, 103, 5759-5772.
- Sander, S. P. et al., 2000: Chemical Kinetics and Photochemical Data for Use in Stratospheric Modeling Supplement to Evaluation 12: Update of Key Reactions, *JPL Publication*, 00-003.

Aerosol and Gas Chemistry of Commercial Aircraft Emissions Measured in the NASA EXCAVATE Experiment

H. Boudries*, J. Wormhoudt, D. Worsnop, M. Canagaratna, T. Onasch, R. Miake-Lye
Aerodyne Research, Inc., Billerica, Massachusetts, USA

B. Anderson
NASA Langley Research Center, Hampton VA, USA

Keywords: PM1.0, Aircraft aerosol composition, Size distribution, HONO, organics, sulfates.

ABSTRACT: Results from ground-based measurements carried out in January of 2002 as part of the EXCAVATE (EXperiment to Characterize Aircraft Volatile Aerosol and Trace species Emissions) field campaign at NASA Langley Research Center (Hampton, Virginia, USA) of exhaust components emitted by a Boeing 757 aircraft with a Rolls-Royce turbo engine RB-211 are presented. During the EXCAVATE experiment, all measurements were made in-situ and in real time. The non-refractory PM1.0 chemical composition and size distribution were measured by an Aerodyne Aerosol Mass Spectrometer (AMS) and the gaseous constituents such as HONO (nitrous acid) and SO₂ (sulfur dioxide) by a Tunable Infrared Laser Differential Adsorption Spectrometer (TILDAS). During these measurements, the aerosol chemical compositions and size distributions for different engine thrust levels (varying from idle to 1.5 EPR (Engine Pressure Ratio)), fuels with three sulfur contents (810, 1050 and 1820 ppmv), and four different sampling distances behind the engine (1, 10, 25 and 35 meters) were characterized. The HONO concentration was found to increase with engine power by over an order of magnitude. Total particulate organics and sulfates were found in a range 1-45 $\mu\text{g m}^{-3}$, and 0.1-7 $\mu\text{g m}^{-3}$, respectively. During the start up of the engine (increase of engine power from 1.03 (idle) to 1.15EPR, and during the shift-down of the power from 1.5 to 1.03EPR, significant increases in particulate organics were observed and were found to be 3 to 5 orders of magnitude larger than those measured for engine powers between 1.15 and 1.5 EPR. The size distribution analysis shows the presence of externally mixed aerosols composed of organics and sulfates and a clear increase in the average size distribution between 30 nm and 300 nm when sampled further downstream from the engine.

1 INTRODUCTION

During the EXCAVATE (EXperiment to Characterize Aircraft Volatile Aerosol and Trace species Emissions) experiment, a series of experimental measurements were conducted in-situ and in real-time to characterize the gas and particle chemical composition and size distribution of major and trace chemical components present in the exhaust of a Boeing 757 equipped with a Rolls-Royce RB-211 engine. A Tunable Infrared Laser Differential Adsorption Spectrometer (TILDAS) was used to measure SO₂, SO₃, HONO and CO₂, while an Aerodyne Aerosol Mass Spectrometer (AMS) was used to measure the particle chemical composition and size distribution of non-refractory PM1.0. In this paper, the mass and size distributions of total particulate organics, particulate sulfates and the concentration of gas phase HONO will be reported and discussed for engine in steady condition.

2 SAMPLING AND ANALYSES

The exhaust gas and particles from the Rolls-Royce RB-211-535E4 engine were sampled through a sampling probe especially built for the EXCAVATE experiment by NASA Langley Research

* Corresponding author: Boudries, Hacene, Aerodyne Research, Inc., Billerica, Massachusetts, 01821-3976 USA.
Email: hboudries@aerodyne.com

Center. Detailed information about the probe used during this experiment is documented in Anderson et al. (this issue). Table 1 summarizes the conditions of engine thrust, fuel sulfur content and sampling distance behind the jet engine used during EXCAVATE. As shown in Table 1, exhausts from three different fuel sulfur contents (FSC) were tested (low sulfate fuel 810 ppmv, intermediate 1050 ppmv and high sulfate fuel 1820 ppmv), five-engine thrust levels measured in Engine Pressure Ratio (EPR), (1.03 (Idle), 1.15, 1.3, 1.4, 1.5 EPR), and four sampling distances (1, 10, 25 and 35 meters) behind the Rolls-Royce RB-211 jet engine were used during this experiment. The exhaust aerosols PM_{1.0} emitted by the engine were sampled and immediately diluted using pure nitrogen and then sent to the AMS through a 20 m long and 1.27 cm internal diameter stainless steel tube at a flow rate of about 10 L min⁻¹.

Table 1: Aerosol and gas sampling conducted during EXCAVATE experiment. The fuel sulfur content used are 810, 1050 and 1820 ppmv and symbolized by +, x and o, respectively.

Probe Engine power	1 m	10 m	25 m	35 m
1.03	+ x o	+ x o	x o	+ x o
1.15	x o	+ x o	x o	+ x o
1.3	+ x o	+ x o	x o	+ x o
1.4	x o	+ x o	x o	+ x o
1.5	x o		x o	

2.1 Aerodyne Aerosol Mass Spectrometer

Ambient aerosols are sampled into a vacuum and focused in an aerodynamic lens. The focused particle beam exiting the lens is directed into the particle-sizing chamber maintained at a pressure of 10⁻⁵ Torr. By modulating the particle beam with a chopper and using the time-of-flight of particles between the chopper and the detector, the particle velocity and the aerodynamic diameter can be obtained. The particle detection scheme consists of an oven that is coupled to a quadrupole mass spectrometer. When the particles hit the oven surface, the volatile and semi-volatile components of particles are flash vaporized. The vaporization plume is ionized by an electron impact ionizer mounted at the entrance of a quadrupole mass spectrometer, operated at 70eV electron energy and scanned in a range of 1-300 atomic mass units. Detailed information about the Aerosol Mass Spectrometer is well documented in Jayne et al. (2000).

2.2 Tunable Infrared Differential Adsorption Spectrometer (TILDAS)

Ambient gaseous species were sampled and analyzed in real time by the TILDAS instrument. The laser diodes and infrared detectors used in the TILDAS measurement are all contained in a single liquid nitrogen dewar. Data acquisition and analysis software on the TILDAS computer collects and averages absorption scans and can least-squares fit them to model spectra to derive real-time outputs of multiple species concentrations. However, most data were saved as averaged spectra for post-test analysis. Detailed information about the TILDAS and sampling configuration is documented in Boudries et al., (2004).

3 RESULTS AND DISCUSSION

3.1 Aerosol chemical composition and size distributions

Figure 1 illustrates a typical temporal trend of organics' and sulfates' mass loadings measured for five different engine power settings (1.03, 1.15, 1.3, 1.4 EPR) and two sampling probe distances (1 and 25 meters) and FSC of 1050 ppmv of sulfure. Significant increases in organic mass loadings were observed during start-up, when the engine thrust was increased from 1.03 to 1.15 EPR, and also during the power downshift from 1.5 to 1.03 EPR. These transient periods are associated with high emissions of particulates, 3 to 5 orders of magnitude higher than the concentrations measured during engine powers from 1.15 to 1.5 EPR. These transients are shown off-scale at 11:35, 11:50 and 12:45 in Figure 1. Detailed analysis of these transient periods will be presented in detail in Boudries et al. (2004) and will not be discussed further here.

During steady engine conditions, the particulate organic and sulfate mass loadings were found to be in a range $1\text{--}45\ \mu\text{g m}^{-3}$, and $0.1\text{--}7\ \mu\text{g m}^{-3}$ respectively. As presented in Figure 1, a significant increase in organics and sulfate mass loadings was observed when sampling was switched between 1 and 25 meters. For instance, at an engine power of 1.3 EPR, the organics concentrations increased from 4 to $40\ \mu\text{g m}^{-3}$. During the same period, sulfate particles also exhibited similar behavior, increasing from 0.5 to $3\ \mu\text{g m}^{-3}$. The increase in concentration between 1 and 25 meters may be explained by the condensation of gas-phase pollutants on pre-existing aerosols occurring downstream of the exhaust plume. If this hypothesis is true, we would expect to see an increase in the mean particle size further downstream in the engine exhaust. Figure 2 shows the average size distribution of organics and sulfate for engine powers 1.3, 1.4, and 1.5 EPR measured at 1 and 25 m. This figure shows that the size distribution shifts to larger sizes when sampled further downstream in the engine exhaust. This shift in size distribution confirms the presence of particle growth. Organics and sulfate have similar aerodynamic diameters of about 40 nm when measured at 1 m behind the engine and increase when measured further downstream. The increase in the aerodynamic diameter of organic aerosols is found to be more pronounced than that of sulfate particles. For organics, the aerodynamic diameters increase from 40 to 300 nm, and for sulfate from 40 to 65 nm. The different growth behavior of the sulfate and organic containing particles suggests that they are externally mixed.

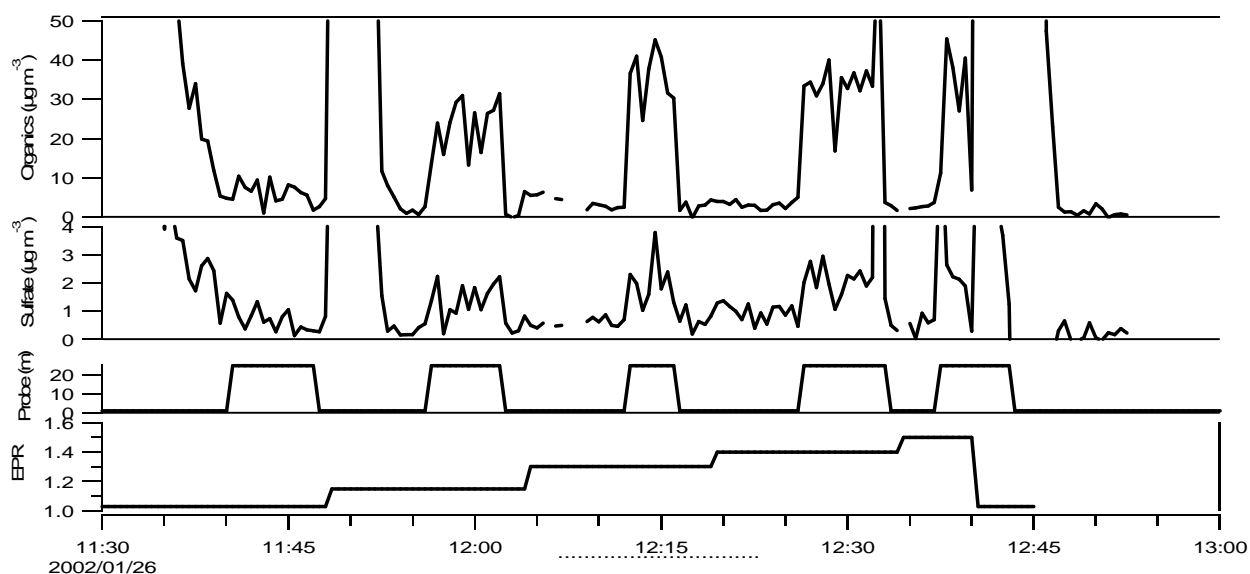


Figure 1: Time-series of total particulate organics and sulfates measures during EXCAVATE experiment.

3.2. Particle emission indices

The emission indices (EI) of sulfate and organics have been calculated for all engine power settings, fuel sulfur content and sampling distances behind the engine exhaust plume. All EI are normalized to CO₂ to account for dilution effect. Figure 3 shows the variation of EI for sulfate and organics as a function of engine power. Only EI measured at 25 m are represented here. The results show that the EI of organics increases with engine power. At high engine power (1.5 EPR), the organic EI is 0.04 g kg⁻¹ of fuel, while at idle (1.03 EPR) the average EI is about 0.018 g kg⁻¹ of fuel. It is also important to note that the EI of organics as a function of engine power is found to be independent of fuel sulfur content. The emission indices of sulfate appear to be independent of engine power settings, and proportional to the fuel sulfur content. The highest EI correspond to the highest sulfur fuel content. For fuel sulfur content of 1050 ppm and 1820 ppm, the average EI values of sulfate are found to be 0.0013 and 0.0023 g kg⁻¹ of fuel, respectively.

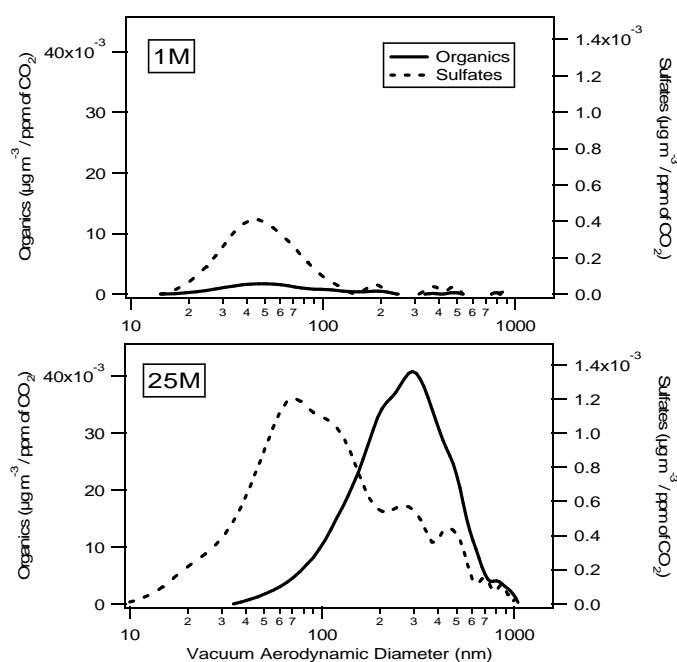


Figure 2: Variation of average aerodynamic diameter of sulfate and organics at 1 and 10 M for engine power of 1.3, 1.4, and 1.5 EPR.

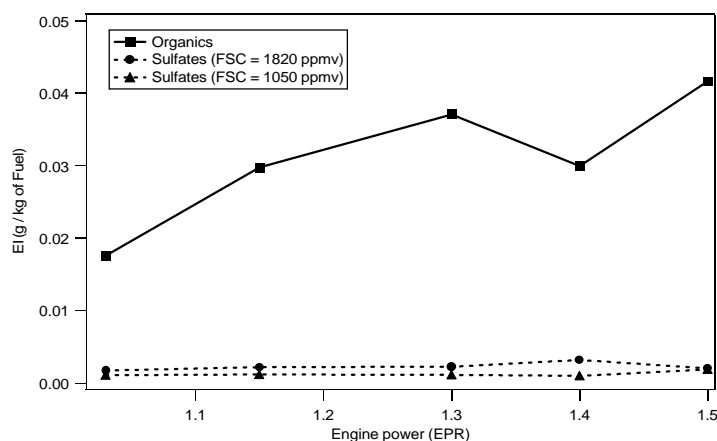


Figure 3: Average emission indices versus engine power measured 25 M behind the Engine.

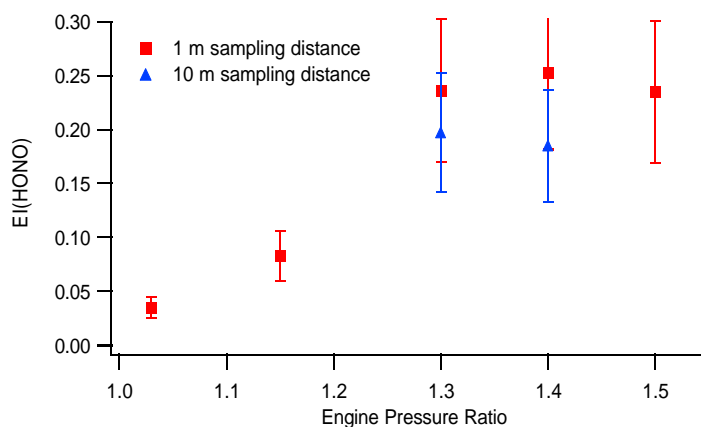


Figure 4: HONO emission indices in g/kg of Fuel measured at 1 m and 10 m behind the engine.

3.3 HONO measurement

During EXCAVATE experiment the detection limit for HONO was as low as 100 ppbv in the multipass cell of the TILDAS instrument. At high power (1.3 to 1.5 EPR), over 2 ppmv of HONO was observed. When converted to emission indices, the B757 HONO results shown in Figure 4 shows a clear power dependence, decreasing with decreasing power at the two lower settings but roughly constant at the highest three settings. These results are also consistent with the particulate organics emission already reported above. When the sampling point was moved back to 10 m behind the engine, the HONO concentration may have decreased somewhat, though when the total error estimates shown in Figure 4 are taken into account, this decrease is not necessarily significant. Results of SO₂ measured by the TDL instrument at 1m and 10m behind the engine showed good agreement with the total fuel sulfur. At 1m, the ratios of sulfur in SO₂ to total fuel sulfur lie in the range 0.75 to 1.0, while at 10 m they are distributed evenly above and below at ratio of 1.

4 CONCLUSION

During the EXCAVATE experiment, particulate and gaseous emissions from a Boeing 757 equipped with a RB-211 Rolls Royce engine were studied. Chemical composition and size distribution of PM_{1.0} were measured in real time with a resolution of 30 seconds. Time series profiles of total particulate organics were found in a range 1 to 45 $\mu\text{g m}^{-3}$ and 0.1 to 7 $\mu\text{g m}^{-3}$, respectively when measured between 1 and 35 m behind the engine exit plume. Both particulate organics and sulfate show a clear increase of total mass loading when measured further downstream in the engine exhaust. Sulfate emission indices were found to be dependent on fuel sulfur content, and to be positively correlated to the sampling probe distance. Organics emissions are also found positively correlated with sampling distance but independent of sulfur fuel content. Gas phase HONO was found in the exhaust at concentrations above 2 ppmv. Similar to particulate organics and sulfate, the HONO emission index increases with increasing power. The average size distribution showed that sulfates and organics exhibit the same average vacuum aerodynamic diameter of 40 nm and increase to larger sizes when measured further downstream from the engine. The presence of two distinct average aerodynamic diameters for sulfate and organics measured further downstream in the exhaust suggests that they are externally mixed.

ACKNOWLEDGMENTS

This work was supported by the engine emissions characterization element of the UEET program through NASA Glenn Research Center.

REFERENCES

- Boudries H., et al., Real time characterization of aircraft particulate and gas emissions during Excavate 2002. *In preparation*.
- Anderson B.E., et al., Overview of results from the NASA experiment to characterize aircraft volatile aerosol and trace species emissions (EXCAVATE). *This issue*.
- Jayne J., et al., Development of an Aerosol Mass spectrometer for size and composition analysis of submicron particles. *Aerosol Science and Technology* 33, 49-70, 2000.

Emission of Volatile and Non-Volatile Ultrafine Particles from a Combustion Source During PartEmis

M. Fiebig*, L. Fritzsche, C. Stein, A. Petzold

Institut für Physik der Atmosphäre, Deutsches Zentrum für Luft- und Raumfahrt Oberpfaffenhofen, Germany

S. Nyeki

Paul-Scherrer Institut, Villigen, Switzerland

Keywords: PartEmis, particulate jet-engine emissions, aerosol data inversion, ultrafine particles

ABSTRACT: During the PartEmis experiment, aerosol properties and precursor gas concentrations were measured in the exhaust of a jet engine combustion chamber. The particle size distribution in the ultra-fine range was investigated using a cascade of condensation particle counters together with a differential mobility analyser. To extract the full information from the data, a novel data inversion algorithm was developed and applied to the PartEmis data. The measured particle size distribution exhibited two modi centred at ~10 and ~30 nm consisting of carbonaceous combustion particles. An additional mode of secondary volatile particles with diameters < 10 nm was present at high fuel sulphur content.

1 INTRODUCTION

The PartEmis experiment was designed to improve the knowledge about the properties and formation processes of carbonaceous and volatile aerosol particles formed in jet engine combustion chambers as a function of the operating conditions and the fuel sulphur content (FSC). To this end, aerosol properties and precursor gas concentrations were measured simultaneously at the exit of a jet engine combustion chamber on a test rig. This work focuses on the ultra-fine fraction of the aerosol with particle diameters between 3 and 20 nm.

2 GENERAL PROPERTIES OF COMBUSTION AEROSOL PRODUCED BY JET ENGINES

The aerosol emitted by a jet engine combustion chamber consists on the one hand of carbonaceous, non-volatile combustion particles (CCP). These are formed by incomplete combustion and typically larger than 10 nm in particle diameter. Their size distribution exhibits two distinct maxima which are centred at approximately 10 nm and 30 nm particle diameter.

The other dominating particle species in jet engine combustion aerosol are volatile condensation particles. They are formed by nucleation from gaseous precursors, primarily sulphuric acid, and have particle diameters smaller than 10 nm. Also, combustion particles may be coated with volatile material. Figure 1 shows the described particle size distribution of CCP and volatile particles.

Figure 2 illustrates the state of mixture of CCP and volatile particles. When precursor species condense, they first form a coating on the surface of the CCP. If condensable precursor material is present in excess, additionally volatile particles are formed from the gas phase. This leads to an external mixture of coated CCP and volatile condensation particles.

* *Corresponding author:* Markus Fiebig, Institut für Physik der Atmosphäre, Deutsches Zentrum für Luft- und Raumfahrt Oberpfaffenhofen, D-82234 Wessling, Germany. Email: Markus.Fiebig@dlr.de

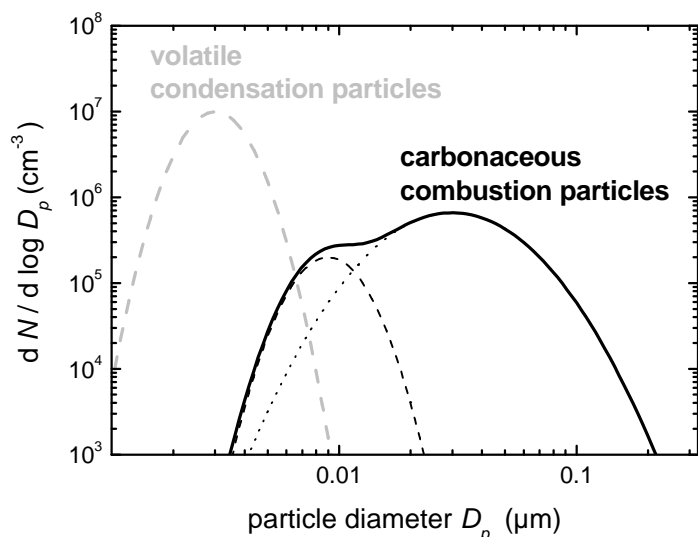


Figure 1. Exemplary size distribution of carbonaceous combustion and volatile condensation particles in jet engine combustion aerosol.

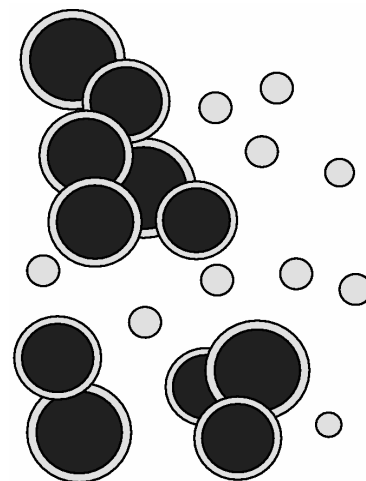


Figure 2. Sketch illustrating the state of mixture of coated carbonaceous combustion and volatile secondary particles.

FORMATION OF VOLATILE PARTICLES

The particle size distribution in the ultra-fine range was measured during PartEmis with the Condensation Particle Size Analyser (CPSA) (Stein et al., 2001). The CPSA is a cascade of 4 condensation particle counters (CPCs). A CPC measures the integral concentration of particles larger than an approximate threshold diameter. To this end, the aerosol sample is saturated with alcohol vapour and subsequently cooled to reach super-saturation with respect to the alcohol vapour. Particles larger than the threshold diameter are activated as condensation nuclei, grow by condensation of alcohol vapour onto the nuclei and are counted optically. The threshold diameter depends on the super-saturation reached in the CPC. In the CPSA, the approximate threshold diameters of the four channels are set to nominally 4, 7, 9, and 20 nm, respectively.

Figure 3 shows the data obtained with the CPSA in combustion aerosol sampled at the exit plane of a jet engine combustion chamber. By taking the differences of the particle concentrations measured by the CPSA channels, the concentrations of particles in the size ranges 4 – 7 nm, 7 – 9 nm, and 9 – 20 nm are obtained and normalised by the concentration of particles larger than 20 nm. The result is plotted in Figure 3 as function of fuel sulphur content (FSC) and operating state of the combustion chamber.

It is obvious that the contribution of particles between 7 – 9 nm and 9 – 20 nm are almost independent of the FSC. These are therefore thought to consist of CCP. Particles between 4 – 7 nm occur 20 times less frequently than CCP for low FSC, but 7 times more frequently at high FSC. These are volatile, secondary particles formed from excess gaseous sulphuric acid that was not deposited on the surface of the CCP.

3 INVERSION OF SIZE DISTRIBUTION DATA

3.1 Inversion Method

The threshold particle diameter at which a CPC begins to count particles is not a sharp boundary. The transfer function describes the counting efficiency of a CPC as a function of particle diameter. Figure 4 shows the measured transfer functions of the 4 CPSA channels.

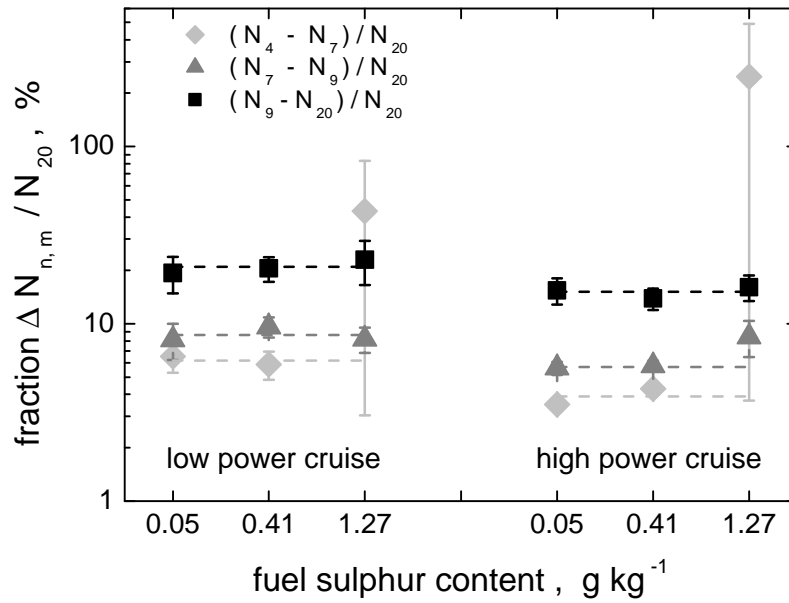


Figure 3. Concentrations of nano-particles in the size intervals measured by the CPSA, normalised to the concentration of particles larger than 20 nm, as a function of fuel sulphur content and operating state of the combustion chamber

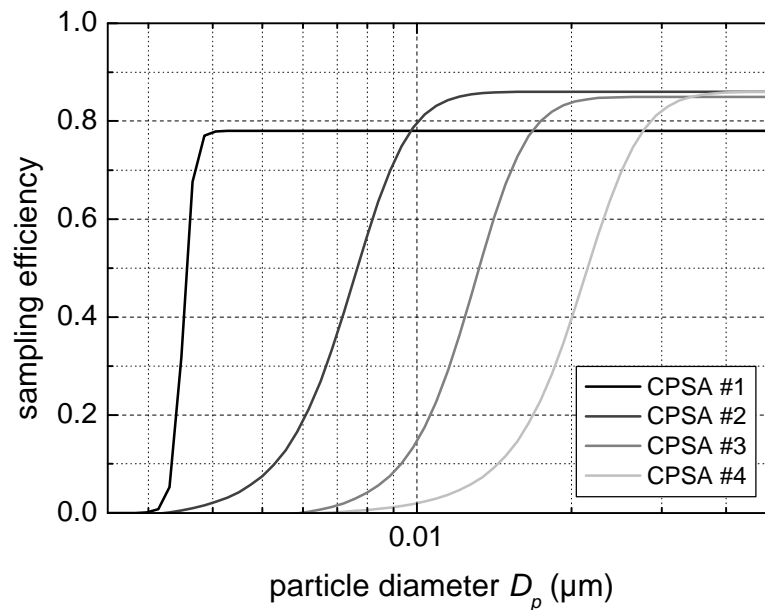


Figure 4. Measured transfer functions of the four CPSA channels for laboratory conditions.

To extract the full size distribution information from the CPSA data, a data inversion is required which is described by the equation

$$\|\mathbf{A}\mathbf{x} - \mathbf{b}\| \rightarrow 0. \quad (1)$$

Here, the vector \mathbf{x} contains the discretised size distribution, the vector \mathbf{b} the particle concentration measured by each CPSA module, and the rows of matrix \mathbf{A} the counting efficiency as function of particle diameter (transfer function) for each CPSA module.

Since the matrix equation is usually underdetermined, i.e. there are less measurements than points on the size distribution or less rows than columns in matrix \mathbf{A} , it is postulated that the resulting size distribution is smooth. The corresponding smoothing matrix is added to matrix \mathbf{A} .

The resulting equation is solved by the Non-Negative Linear Least-Squares Solver (NNLS) algorithm (Lawson and Hanson, 1974) requiring the solution also to be non-negative.

The transfer function of the CPSA modules depends sensitively on the temperatures of the saturation and condensation paths within the individual modules. Since the transfer functions of the CPSA were measured for a whole range of internal temperatures, it is possible to calculate the transfer functions contained in **A** based on the measured internal temperatures for each respective data-set before inverting equation (1).

3.2 Resulting Particle Size Distributions

To complement the CPSA measurements during PartEmis, the size distribution for particle diameters $D > 20$ nm was measured in high resolution by a differential mobility analyser (DMA). Figure 5 shows the obtained composite particle size distributions from CPSA and DMA data for low (50 $\mu\text{mol} / \text{mol}$) and high (1270 $\mu\text{mol} / \text{mol}$) FSC. Here, the CPSA data was evaluated in a first step by approximating the transfer functions of the CPSA modules by step functions. Already in this analysis, the CPSA detects a second mode of particles centred at ~ 10 nm in addition to the CCP mode measured by the DMA. Both modi are present independently of the FSC and must therefore consist of CCP. At high FSC, a third particle mode of volatile particles with $D < 7$ nm is present.

Figure 6 compares the result of the approximate CPSA evaluation with the respective size distribution obtained with the inversion method, both for medium (410 $\mu\text{mol} / \text{mol}$) FSC. Both methods use the high resolution DMA data to determine the position of the larger CCP mode. As obvious from Figure 6, the approximate evaluation method leads to numerical broadening of the small CCP mode and to a shift of the mode median diameter to smaller particle diameters. The inversion method extracts the whole size distribution information from the CPSA data and yields the true position, width and height of the small CCP mode at 12 nm.

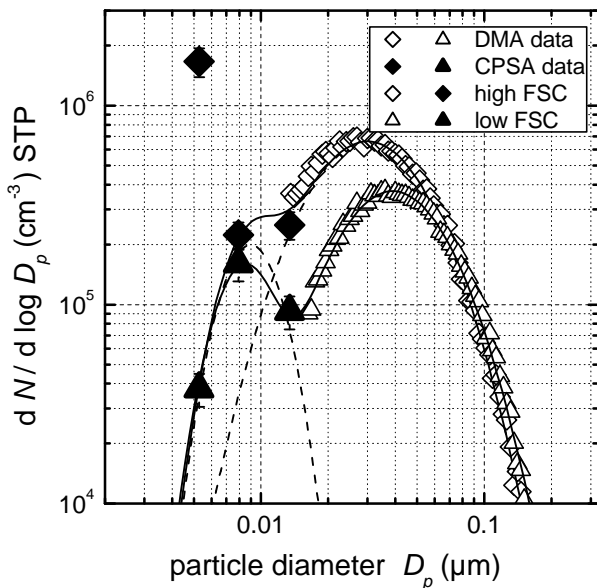


Figure 5. Ultra-fine range particle size distribution of jet engine combustor exhaust aerosol for high and low FSC. The size distributions are based on CPSA and DMA data..

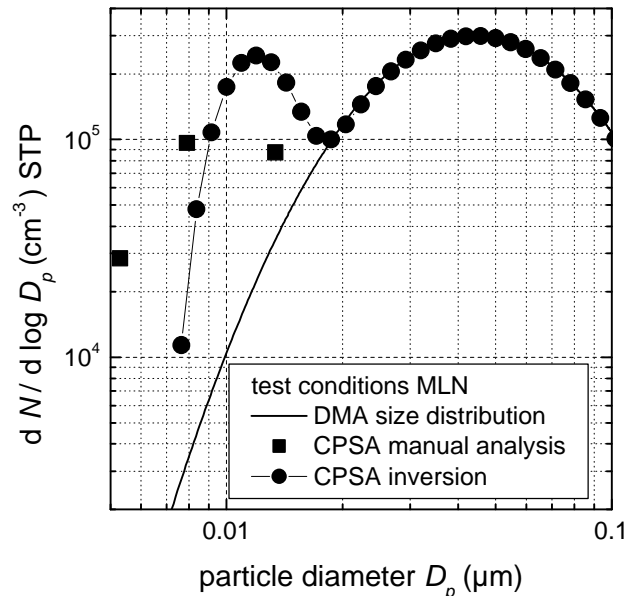


Figure 6. First results of inversion method applied to CPSA plus DMA data obtained in jet engine combustor aerosol. The size distribution obtained by data inversion is compared with the conventional analysis of the same data.

4 CONCLUSIONS

During PartEmis, the size distribution of ultra-fine particles in the range of 3 to 20 nm particle diameter was measured in the exhaust aerosol of a jet engine combustor using the CPSA. This data

was augmented by measurements with a DMA for particle diameters larger than 20 nm. The size distributions measured consisted of two modi centred at ~10 and ~30 nm. Since the presence of these modi was independent of FSC, they had to consist of CCP. For high FSC, a third mode of secondary volatile particles with diameters < 10 nm was present.

To extract the full size distribution information from the CPSA data and transfer functions, an inversion algorithm was developed. The algorithm is robust and solves the inversion equation with the boundary conditions of non-negativity and smoothness of the size distribution. It takes the dependence of the CPSA transfer functions on the internal instrument temperatures into account.

REFERENCES

- Lawson, C.L., and R.J. Hanson, 1974: *Solving Least Squares Problems*, Prentice-Hall, Englewood Cliffs.
- Stein, C., F. Schröder, and A. Petzold, 2001: The condensation particle size analyzer: A new instrument for the measurement of ultrafine aerosol size distributions. *J. Aerosol Sci.* 32, S1, S381 – S382.

A USA commercial flight track database for upper tropospheric aircraft emission studies

Donald P. Garber, Patrick Minnis¹, and Kay P. Costulis

Atmospheric Sciences, NASA Langley Research Center, Hampton, Virginia, USA

Keywords: air traffic, flight tracks, aircraft emission, contrail simulation

ABSTRACT: A new air traffic database over the contiguous United States of America (USA) has been developed from a commercially available real-time product for 2001-2003 for all non-military flights above 25,000 ft. Both individual flight tracks and gridded spatially integrated flight legs are available. On average, approximately 24,000 high-altitude flights were recorded each day. The diurnal cycle of air traffic over the USA is characterized by a broad daytime maximum with a 0130-LT minimum and a mean day-night air traffic ratio of 2.4. Each week, the air traffic typically peaks on Thursday and drops to a low Saturday with a range of 18%. Flight density is greatest during late summer and least during winter. The database records the disruption of air traffic after the air traffic shutdown during September 2001. The dataset should be valuable for realistically simulating the atmospheric effects of aircraft in the upper troposphere.

1 INTRODUCTION

Air traffic is expected to increase globally by a factor of 5 or 6 between 1990 and 2050 with a commensurate rise in emissions and contrails that may significantly affect air quality and climate (IPCC, 1999). Some of the aircraft exhaust effects, especially those impacting contrail and cirrus clouds, are still highly uncertain requiring exhaustive research to more accurately prognosticate the climatic impact of enhanced commercial fleets. Contrail formation, growth, and dissipation and their optical properties are highly dependent on aircraft engine type, and the temperature, humidity, and wind speed and direction at flight altitude. The contrail-cirrus radiative effects, which ultimately affect the average state of the atmosphere, depend on the underlying conditions (surface temperature and albedo), the contrail optical properties, air traffic density and altitude, and the time of day when the contrails are formed. Thus, to accurately assess current air traffic effects and future flight scenarios, it is necessary to simultaneously know the meteorological state and the distribution of flights at a given location. This report addresses the latter need for the contiguous United States (CONUS) with a focus on the upper tropospheric portions of commercial flights.

The release of United States of America (USA) near-real time air traffic control information to the commercial sector during the late 1990's made the collection of more refined flight path data much easier than before. This report documents the collection, reduction, analysis, and availability of commercial flight information taken above 25,000 ft over the CONUS since late 2000. The result of the analysis is a flight track database that can be easily accessed and used by modelers.

2 DATA AND ANALYSIS

Commercial flight information taken in real time over the USA from the FlyteTrax system (FlyteComm, Inc.) has been purchased and archived at NASA Langley Research Center since September 2000. The raw data consist of 2, 5, or 10-minute reports of flight number, aircraft type, download time, latitude, longitude, altitude, heading, destination and origination locations, speed, and departure and arrival times. All portions of flights above 25,000 ft (7.6 km) within the domain (20°N - 50°N and 60°W - 135°W) were quality controlled and sorted by flight number and time.

¹ *Corresponding author:* Patrick Minnis, MS 420, NASA Langley Research Center, Hampton, VA, USA 23681. Email: p.minnis@nasa.gov

Table 1: Monthly sampling statistics for flight track database.

Month	2001 (number of days)				2002 (number of days)			
	Full	Partial	Empty	% Full	Full	Partial	Empty	% Full
Jan	12	1	18	39	18	2	11	58
Feb	0	0	28	0	22	1	5	79
Mar	17	2	12	55	29	1	1	94
Apr	21	8	1	70	30	0	0	100
May	11	18	2	35	26	4	1	84
Jun	20	10	0	67	29	1	0	97
Jul	19	11	1	61	31	0	0	100
Aug	25	3	3	81	31	0	0	100
Sep	30	0	0	100	26	3	1	87
Oct	24	3	4	77	29	1	1	94
Nov	21	1	8	70	21	7	2	70
Dec	26	4	1	84	24	2	5	77

The summary statistics for each month in Table 1, which shows the number days in each month that have complete (full), partial, or no (empty) sampling, indicate that the best sampling occurred during late 2001 and 2002. No military flights are available in this database. Not all flights over Mexico and Canada are represented either. All commercial and private flights over the USA should be included for those days noted as complete.

Flights remaining after passing the quality control checks were then used to develop the database, which is divided into two parts: linear and gridded. The former computes the node points for each flight track on a 1° latitude-longitude grid using interpolation along great circle arcs between each report. These standardized flight track positions comprise the linear database in the form of one file for each day consisting of a series of flights, each with its own header describing the general flight characteristics and followed by a series of flight segments. The gridded database, provided in cell files, uses the segmented flight tracks to determine for each hour the number and total length of flights within a 1-km vertical range in a given 1° grid box. The linear dataset should be useful for detailed simulation studies, while the gridded data should be more valuable for use in climate simulations.

3 RESULTS

The main parameters of interest for this database are the number of flights and the cumulative flight length (CFL). CFL can be computed as the sum of all flight segment lengths within a given box or domain for a selected time period, usually 1 hour.

3.1 Spatial Variability

The 1° CFL distribution for 10 September 2001 is sliced by altitude ranges in Figure 1. The maximum CFL in a single 1° box in the lowest altitude range is only $\sim 22,000$ km over southern Michigan and northern Virginia. Most CFLs within that layer are less than 4000 km with many flights occurring in southern California, northern Florida, and the Midwestern USA. Flights at these lower levels consist of portions of longer legs near the terminals or of the apex segments of short-distance commuter flights. The maximum CFL between 9 and 11 km exceeds 40,000 km over parts of eastern Ohio and western West Virginia. In addition to the large area of heavy traffic over the northeastern USA, a relatively dense traffic lane is evident over the Atlantic coast south of New York City. These flights are generally mid-range or longer flights. The maxima over the western USA are found over Nevada and the border between New Mexico and Arizona away from the large hubs at San Francisco and Los Angeles. The CFLs at the highest altitudes (Figure 1c), generally consisting of long distance flights, are greatest over Lake Erie, the central Great Plains, southern Utah, and coastal north Florida. The combined levels in Figure 1d yield a large number of regions with total CFL $> 40,000$ km. These include much of the northeastern USA exclusive of New England, the Atlantic coast, central Great Plains, the Southwest, and lower Mississippi Valley. The

few CONUS areas with total CFL < 4,000 km are found along the western Canadian and central Mexican borders.

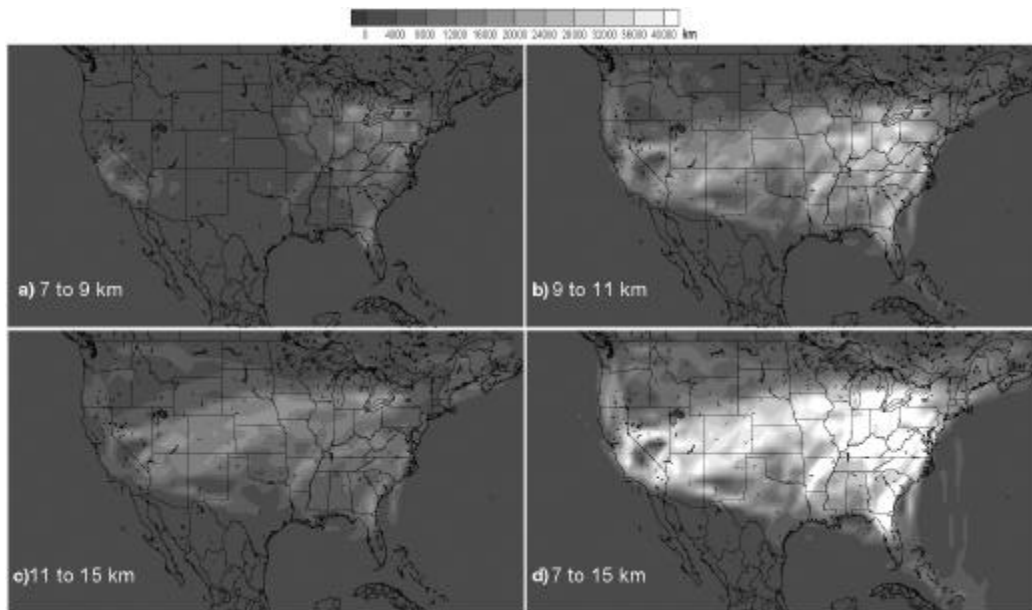


Figure 1. Cumulative flight lengths for 1° regions, 10 September 2001.

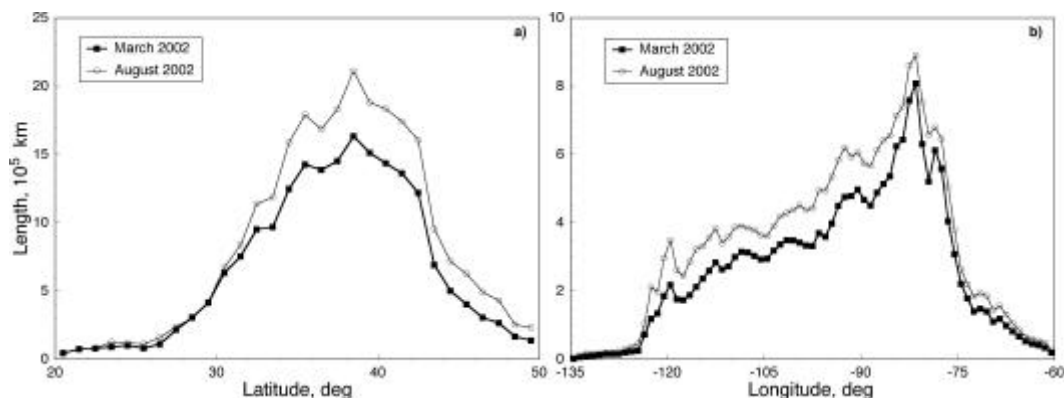


Figure 2. Mean daily cumulative flights lengths as a function of (a) latitude and (b) longitude over USA.

The latitudinal and longitudinal variations of the mean daily CFLs are summarized in Figure 2. Peak traffic occurs between 38°N and 39°N with a secondary maximum around 35.5°N (Figure 2a). A relative maximum (Figure 2b) at 120°W corresponds to the southern California traffic followed in the eastward direction by a dip and a relatively steady increase to the overall maximum at 81.5°W . The traffic then tails off to 30,000 km at 60°W . More flights are evident over the Atlantic than over the Pacific. The shapes of the longitudinal and zonal mean CFL curves are very similar for both March and August suggesting more of a general increase in traffic during summer than a changing of the air traffic patterns. The maximum CFL for the entire domain occurs between 10 and 11 km followed by the layer between 11 and 12 km (Figure 3). The March-August increase in air traffic is greatest between 10 and 11 km. The total daily CFLs for the domain are 19.6 and 25.1 million km during March and August, respectively.

3.2 Temporal Variability

The diurnal cycle over the entire domain is summarized in Figure 4 using monthly means from March and August 2002. The variation with in Figure 4a shows a rapid increase in flights after 1100 UTC to a peak around 1830 UTC during March with a secondary maximum around 2330 UTC. The minimum occurs near 0730 UTC. During August, the air traffic begins in earnest an hour earlier than during March because of a shift to daylight savings time. The maximum during August occurs

at 2230 UTC. Overall, the air traffic during August is ~28% greater than during March. The diurnal variation of air traffic shows no seasonal shift in local time (LT) with the daily cycle beginning in earnest after 0500 LT, reaching two maxima at 0930 and 1230 LT with a minimum at 0130 LT (Figure 4b). Considering the hours 0600 – 1800 LT as daytime and the remaining hours as night, a rough estimate of the day-night ratio in cumulative flight length is 2.5 and 2.3, respectively, during March and August 2002. The true day-night ratio, valuable for calculating the relative shortwave and longwave radiative forcing by contrails, is more accurately determined for each month by considering the actual hours of daylight for each location and month. Such information can be easily computed from the gridded database. The plots begin at 0400 UTC because it corresponds to local midnight in the easternmost portion of the domain.

The number of CONUS flights has a distinct weekly cycle. The mean air traffic minimum occurs on Saturday following a peak of 25,500 takeoffs and landings on Thursday. The range in the number of flights per day of week is typically around 5,000 except for the extreme minima occurring during certain holidays or as a result of the air traffic shutdown period after September 11, 2001. The weekly range in the average daily number of flights is 18%.

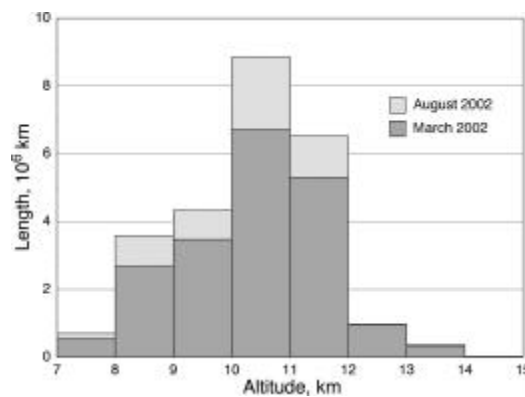


Figure 3. Mean daily layer CFL over USA domain.

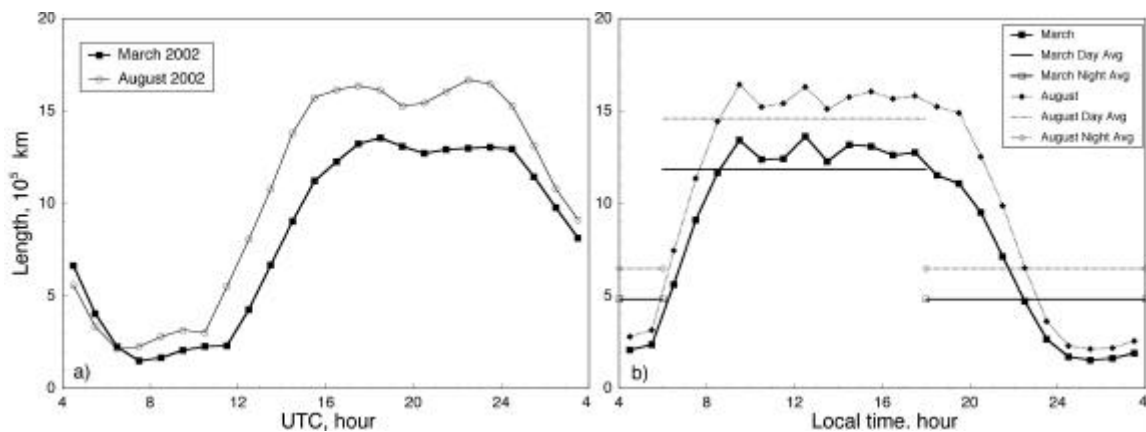


Figure 4. Mean hourly and day-night average CFL, (a) local time and (b) UTC.

4 DISCUSSION

While providing unprecedented air traffic detail, it should be noted that this dataset does not include flights below 25,000 ft, military air traffic, and some air traffic over oceans, Canada, Mexico, and Cuba. Development of a total inventory for this domain would require additional input. Data acquisition, while nominally continuous, was not complete except for a few months. Actions taken to account for the missing data when computing monthly means should minimize the impact of the poor data. Data were initially acquired from FlyteComm, Inc. every 2 minutes and the only time associated with each flight number was the local time on the acquisition computer. Thus, the actual

flight time could be overestimated by up to 2, 5, or 10 minutes depending on the time interval of reporting for a given flight. Despite these uncertainties in actual time, the data should provide a realistic representation of air traffic over the CONUS.

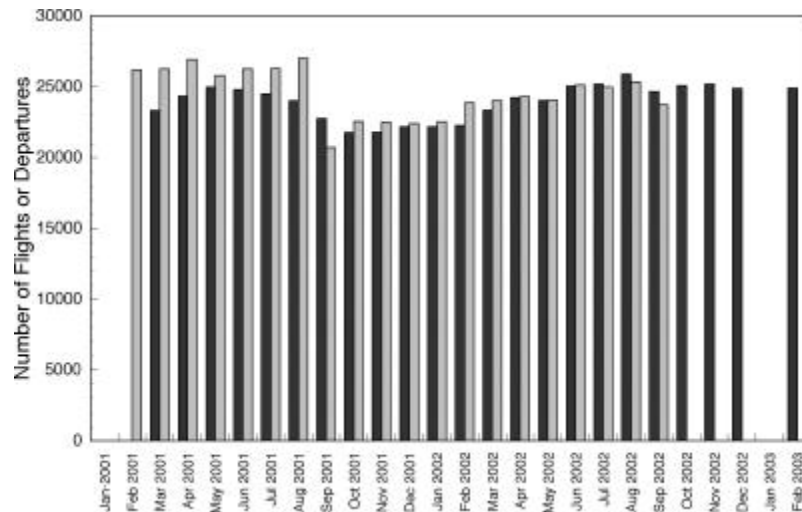


Figure 5. Mean number of daily flights above 7.6 km from FlyteTrax data (black) and departures of commercial carriers from OAI database (shaded).

Previous air traffic fuel usage data from USA sources were developed for 1992 (Baughcum, 1996, Gardner 1998) and include military sources (Metwally, 1995). A comparison of the fuel usage above 7 km from that earlier dataset (Figure 17 in Minnis et al. 1997) and the CFL distribution in Figure 1d reveal some differences that may be due to the lack of military and foreign flights and changes in air traffic patterns since 1992. For example, flights between California and Mexico evident in the 1992 dataset are absent in Figure 1d, while flights from Texas and the eastern USA to Acapulco and Mexico City (Figure 1d) are not as defined in the 1992 dataset. Air traffic over the Pacific is confined to a few narrow air lanes in the earlier dataset compared to the more diffuse air lanes in Figure 6d. Despite many similarities between the two datasets, this air-lane versus diffuse distribution difference is apparent over much of the domain. For example, the maximum fuel expenditure in the 1992 dataset is confined to a latitude strip between 40°N and 42°N between Philadelphia, PA and Iowa with a few secondary maxima over Las Vegas, NV and southern California. In Figure 1d, the maximum CFL covers a much larger area including the relatively narrow strip in the 1992 data. New secondary maxima are evident over northeastern Florida, eastern Arkansas, and eastern Kansas in Figure 1d. Perhaps, additional tourist traffic and the expansion of overnight delivery services with major hubs at Memphis, TN, Wilmington, OH, and Louisville, KY could have increased the traffic over the Midwest and Florida.

The seasonal variation in air traffic in the current dataset appears to be somewhat different than can be inferred from the seasonal variation in North American high-altitude aircraft emissions from the 1992 inventory (Figure 2-7, Friedl, 1997). The earlier data have a peak in NO_x emissions during August followed by a 4% drop into September, nearly constant values through December, a 9% decrease to the January minimum, a gradual increase to May, and a rapid rise to the summer maximum. Figure 5 shows an initial May maximum with flight frequency decreasing into October. The number of flights remains depressed until March 2002 when they begin increasing until August 2002. A 6% decrease in flights during September is slightly offset by a 2% rise into October. The flight frequency remained steady through February 2003. This irregular variability is influenced by a number of factors, including the September 11, 2001 terrorist attacks, which can account for part of the October 2001 – February 2002 lull. The first maximum in May 2001 is probably due to sampling deficiencies that were not properly considered. The USA freight traffic, as expressed in overall ton-miles for scheduled and non-scheduled aircraft, increased almost monotonically by a factor of 2.7 between 1981 and 2000 with minor lulls during 1991 and 1999 (OAI, 2003). Similarly, the number of passenger originations increased by a factor of 2.4 during the same period. Both

parameters decreased during 2001, especially the air passenger originations. The overall number of scheduled and non-scheduled airport departures for large certified air carriers, which account for most of the high-altitude air traffic are in good agreement with the current database (Figure 5) except for the period prior to September 2001 when sampling was the worst. When these sampling effects are taken into account, the monthly averages for the earlier period will probably be in better agreement.

The diurnal variation of flights is generally consistent with the available information on contrails over the CONUS. The unnormalized frequency of persistent contrails more than doubles between 0600 LT and 0800 LT when it reaches a maximum around 0900 LT (Minnis et al. 2003). The average CFL also increases by more than a factor of 2 between 0600 and 0800 LT and reaches a peak at 0930 LT (Figure 4). Mean CFL decreases very slowly during the daylight hours without a significant drop until after 1800 LT, while the contrail frequency also gradually decreases after 0800 LT before dropping at 1800 LT. The lack of contrail frequency data during the night precludes further comparison. However, the correspondence between contrails and flight lengths during the daytime suggests that the CFL data could be used to estimate the relative hourly frequency of contrail occurrence at night.

5 CONCLUDING REMARKS

This new database constitutes a different characterization of air traffic than previously available. It provides explicit flight paths and flight density in terms of cumulative flight length rather than fuel usage. Actual flight paths were used instead of estimated flight paths between terminals. Because of data dropouts, caution must be used when simulating the air traffic for a particular day. The statistics provided here represent an initial summary of the dataset but have not accounted for all of the effects of missing data. After final quality control has been completed (tentatively late 2003), the database will be made available via the World Wide Web.

Air traffic over the USA is marked by distinct daily, weekly, and annual cycles that can affect evaluations of aircraft effects on the atmosphere. When properly used, the dataset described herein should prove valuable for realistically simulating air traffic at a variety of scales.

REFERENCES

- Baughcum, S. L., 1996: Subsonic aircraft emission inventories, In: *Atmospheric Effects of Aviation: First Report of the Subsonic Assessment Project*, NASA RP-1385, pp. 15-29.
- Friedl, R. R. (ed.), 1997: *Atmospheric Effects of Subsonic Aircraft: Interim Assessment Report of the Advanced Subsonic Technology Program*, NASA RP 1400, 168 pp.
- Gardner, R.M. (ed.), 1998: *ANCAT/EC Aircraft Emissions Inventory for 1991/92 and 2015*. Final Report EUR-18179, ANCAT/EC Working Group. Defence Evaluation and Research Agency, Farnborough, United Kingdom, 108 pp.
- IPCC, 1996: *Climate Change 1995: The Science of Climate Change. Contribution of Working Group I to the Second Assessment Report of the Intergovernmental Panel on Climate Change* [Houghton, J.T., L.G. Meira Filho, B.A. Callander, N. Harris, A. Kattenberg, and K. Maskell (eds.)] and WMO/UNEP. Cambridge University Press, Cambridge, United Kingdom and New York, NY, USA, 572 pp.
- Metwally, M. 1995: *Jet Aircraft Engine Emissions Database Development--1992 Military, Charter, and Non-scheduled Traffic*, NASA CR-4684.
- Minnis, P. J. K. Ayers, and S. P. Weaver, 1994: *Surface-Based Observations of Contrail Occurrence Frequency Over the U.S., April 1993 - April 1994*, NASA RP 1404.
- Minnis, P. J. K. Ayers, M. L. Nordeen, and S. P. Weaver, 2003: Contrail frequency over the USA from surface observations," *J. Climate*, in press.
- OAI, 2003: *Air Traffic Statistics and Airline Financial Statistics, Historical Air Traffic Data for 1981-2001*, U.S. Department of Transportation, Bureau of Transportation Statistics, <http://www.bts.gov/oai/indicators/top.html>.

Validation of the Kinetic Soot Model: An Experimental and Theoretical Study on Soot Formation using LII and SV-CARS

K.P. Geigle*, Y. Schneider-Kühnle, V. Krüger, M. Tsurikov, R. Lückerrath, M. Braun-Unkloff, N. Slavinskaya, P. Frank, W. Stricker, M. Aigner
DLR - Institut für Verbrennungstechnik, Stuttgart, Germany

Keywords: laser-induced incandescence, CARS, soot formation, kinetics

ABSTRACT: Temperature and soot concentration measurements from laminar, premixed flames at different conditions (pressures P , equivalence ratios ϕ and fuels), provide an excellent data base for the modelling of soot formation. For the verification of numerical simulations of sooting flames, the use of accurate, spatially and temporally resolved data measured with non-intrusive *in situ* measurement tools is necessary. We present the application of a recently developed technique for temperature measurements in sooting flames. Soot concentrations measured by laser-induced incandescence (LII) are compared to calculated profiles of soot formation, based on the measured temperatures. The overall agreement is quite satisfactory for the experimental conditions presented.

1 INTRODUCTION

Environmental concerns and decreasing pollutant emission limits are driving the need for a reduction of emissions such as soot. Therefore, fundamental understanding of soot formation and destruction is a current issue for industry and research. The first step to a better understanding is based on a separation of effects interacting in a complex way in realistic combustion systems. Thus, as one part of the problem, pure chemistry (no turbulence) needs to be investigated. Since chemistry is strongly dependent on temperature, the development and validation of a soot model needs accurate temperature information and soot concentrations measured under several flame conditions. Most practical combustion devices are operated at elevated pressure, but little data are available for flame experiments focusing on soot model validation at these conditions (Hanisch et al., 1994; Braun-Unkloff et al., 1998). To provide the required information, we used laser-based, non-intrusive diagnostics which yield spatially-resolved data, necessary for resolving steep gradients. The main advantage of this approach over commonly-used line-of-sight techniques is that the assumption of a homogeneous distribution of the quantity of interest over large dimensions is not required (and in many flames not justified). The experiments are used to support kinetic computations in two respects. First, the measured temperature information is used for the calculation, thus including energy loss by radiation. Second, the predicted soot formation can be compared to the experimental soot volume fraction profiles. This comparison permits further refinement of the kinetic soot formation model.

2 EXPERIMENTAL SET-UP

2.1 Burner configuration

Validation experiments in high pressure flames for the support of a kinetic soot model without any influence of turbulence are a highly demanding challenge for burner design. First, a completely laminar flow resulting in a stable flame without flickering is required. In this case, a direct correlation of height above burner (HAB) with the time scale of the combustion process under study is possible.

* Corresponding author: Klaus Peter Geigle, DLR – Institut für Verbrennungstechnik, Stuttgart, D-70569 Stuttgart, Germany. Email: klauspeter.geigle@dlr.de

Furthermore, the flame needs to be sufficiently homogeneous over the measurement volume. For a comparison with 1D kinetical computations, any influence from the flame edges has to be excluded. Our design, based on the requirements stated above, is similar to the ones described in Hanisch et al. (1994) and Jander et al. (1995). Its main feature is the use of a non-sooting shielding flame ($d = 61.3$ mm), surrounding the axisymmetric inner flame to be studied ($d = 41.3$ mm). The additional flame reduces oxidising influences from the flame edges and provides a hot shielding film against the surrounding cold coflowing air ($d = 150$ mm). Moreover, two separately operated flames are useful while changing flame conditions (P , ϕ , flow rates), since they behave as mutually pilot flames. Both flames were stabilised on water cooled sintered bronze matrices (cell size $12 \mu\text{m}$). Additional flow conditioning and mixing of fuel and air was achieved by using glass beads below the matrices. For finding the required stable flames, the stoichiometries of both flames and the exit velocities of three cold gases (methane/air, fuel/air of studied flame, coflowing air) must be carefully adjusted. The flow rates, supplied by five in-house calibrated massflow controllers, are chosen to avoid horizontal flickering and vertical fluctuations, and to ensure a sufficiently homogeneous radial temperature and soot distribution within the detection volume of the used laser techniques. Premixing of the fuel and the corresponding air took place approximately one meter before the burner.

The entire burner inlet system was mounted into a high pressure housing with large windows for optical access. For further flame stabilisation, particularly at high pressures, a stabilising grid was positioned at a height of 40 or 45 mm above the burner plate, depending on the position of soot formation (Pape, 1993). For the experiments with toluene, the required combustion air was passed through a toluene bubbler consisting of several sealed bottles immersed in a water bath whose temperature was precisely controlled. A part of the air-toluene mixture was sampled and the toluene volume fraction determined *ex situ*. Each of the flame settings (Table 1) has been checked for reproducibility, the different measurements were usually performed the same day.

Table 1. Flame settings for the presented flames. All flow rates are in standard liters per minute. Pressure is in bars.

Fuel	Inner flame			Ring flame		Coflow	P	Fuel	Inner flame			Ring flame		Coflow	P
	ϕ	Q_{fuel}	Q_{air}	Q_{CH_4}	Q_{air}				ϕ	Q_{fuel}	Q_{air}	Q_{CH_4}	Q_{air}		
C ₂ H ₄	2.30	0.7	4.4	1.0	4.6	110	1	C ₃ H ₆	1.95	1.17	13	9.9	58	490	5
C ₂ H ₄	2.30	1.7	11	5.7	38	390	3	C ₃ H ₆	2.00	1.20	13	9.9	58	490	5
C ₃ H ₆	2.23	0.3	3.1	1.5	11	200	1	C ₃ H ₆	2.10	1.26	13	9.9	58	490	5
C ₇ H ₈	1.88	0.064	1.5	1.9	11	98	1	C ₃ H ₆	2.15	1.29	13	9.9	58	490	5

2.2 Temperature measurements in sooting flames with SV-CARS

While the use of thermocouples provides the easiest way of extracting temperature information from the flame, the accuracy in sooting flames is too low for model validation and, furthermore, any object introduced into the flame clearly disturbs the flame (Stricker, 2002). An ideal tool for *in situ*, non-intrusive temperature measurements in flames is Coherent Anti-Stokes Raman Scattering (CARS), which is based on measuring the population of rotational and vibrational energy levels of the nitrogen molecule (Eckbreth, 1996) and comparing these to simulated spectra. Conventional CARS uses the frequency-doubled output of a Nd:YAG laser (532 nm) for the pump beam. However, in a sooting flame, the exciting beams produce C₂ molecules from laser heated soot particles, which in turn cause fluorescence (Swan bands) at the same wavelength as the CARS signal (473 nm). Our approach is to use a narrowband dye laser (591 nm) for the pump beam, thus shifting the CARS signal out of the Swan band region. So the CARS signal is spectrally shifted from 473 nm to 520 nm resulting in completely undisturbed spectra (Fig. 1a). For non-sooting parts of a flame this shifted vibrational CARS signal was validated with conventional CARS, resulting in good agreement. The accuracy for SV-CARS measurements is $\pm 3\%$ (Schneider-Kühnle, 2003).

In our experiment, a frequency-doubled Nd:YAG laser was used to pump a narrowband dye laser and a custom-built broadband dye laser, whose beams were overlapped in BOX-CARS geometry and focused to a 4 mm long, 0.2 mm wide probe volume. All beams were equipped with polarisers and half wave plates for intensity control; an additional analyser could be implemented for background

suppression in the case of pressurised flames. Two translation stages allowed a fast shift of the CARS measurement probe volume above the burner surface. The CARS signal was resolved in a spectrometer and detected with an intensified CCD camera.

2.3 Soot distributions with laser-induced incandescence

An excellent tool for *in situ* non-intrusive measurements of soot distributions is provided by laser-induced incandescence (LII), based on the emission of blackbody radiation resulting from strong laser induced heating of soot particles. In recent years, LII has matured into a reliable tool for the measurement of qualitative soot distributions and, with calibration, even for quantitative measurements in flames (Santoro and Shaddix, 2002). For calibration, an extinction measurement is typically performed. Uncertainties in the exact knowledge of the refractive index of soot, particularly at the position of the calibration measurement (Choi et al., 1994), determine the accuracy of calibration via extinction. To ensure a proper excitation especially in strongly sooting absorbing flames we used a power meter to monitor the energy in the laser sheet after it passed through the flame.

For excitation of the LII signal we used the 1064 nm output of a Nd:YAG laser. A set of sheet forming optics and a rectangular aperture produced a homogeneous excitation sheet of approximately 30 mm in height and 170 μm in width. The laser power was tuned by a half wave plate followed by a polariser to keep an energy of close to 35 mJ/pulse behind the flame. The LII signal was filtered at 450 nm and detected with an intensified CCD camera with two-frame capability. During the first gate immediately before the laser pulse, the flame luminosity was detected. The second gate of 40 ns duration over the laser pulse was used for detection of the signal.

For the extinction measurement the same optical pathway was used by the 532 nm output of the laser at low power (0.2 mJ/pulse in the sheet) to avoid processes other than extinction in the flame. Before entering the burner chamber a part of the laser sheet was reflected into a reference dye cell. The rest of the sheet was partially absorbed by the flame and afterwards refocused to a second dye cell. The use of an additional mirror in front of the CCD camera and changing to a 700 nm interference filter allows the detection of an extinction profile immediately after the LII measurement with the same camera. This approach is applicable since the measurement object is temporally stable. In contrast to other published data, where the integral extinction over the whole flame is measured (Axelsson et al., 2001) our set-up allows us to choose the best height for the calibration. While in the lowest regions of the flame extinction by soot is low, absorption by other species might influence the extinction measurement in a non-negligible way (Choi et al., 1994). Furthermore, in the region of initial soot production the soot properties are the least representative for the whole flame and not well known. High in the flame soot particles start aging, which again changes the optical properties. For data analysis we used the region between these extremes where the determined calibration constant remains stable (as indicated in Figure 1b).

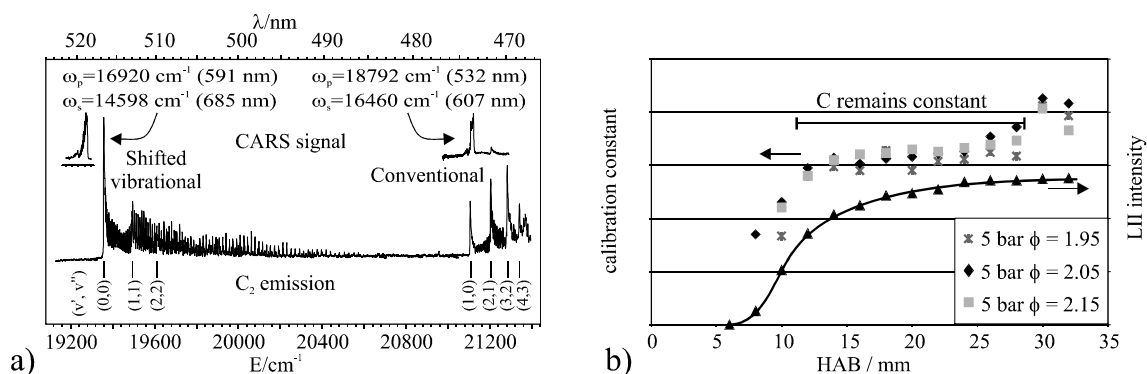
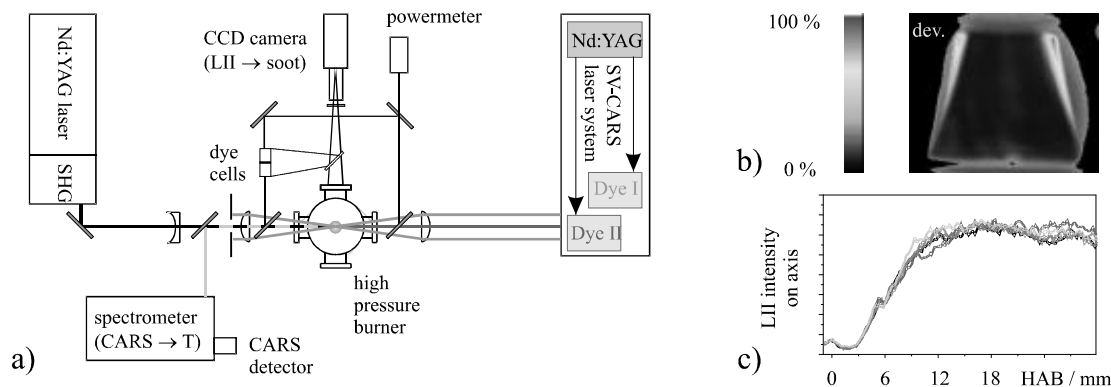


Figure 1. a) Spectral position of the conventional and the SV-CARS signal in the C₂ Swan-Band system. b) Variation of the calibration constant with height in different propene/air flames at 5 bar. Also shown for comparison is a LII signal intensity profile for the $\phi = 2.15$ flame.

Since in strongly sooting flames the effect of signal trapping is not negligible, we followed the approach described in Bryce et al. (2000) to correct for signal losses by absorption in the flame. The

refractive index used in the data analysis was $1.60 - 0.59i$ (Charalampopoulos and Felske, 1987). A change of optical pathways necessary for the mentioned techniques (CARS, LII, extinction) took only a few seconds by using the aforementioned translation stage system (Fig. 2a).

Figure 2a. Experimental set-up; translation stages enable a quick change between SV-CARS, LII and extinction measurements. b and c: Stability of the studied flames demonstrated for a 3 bar ethene/air flame;



the upper image shows the standard deviation over a sequence of 100 LII images, the lower image displays some subsequently detected LII profiles along the burner axis.

3 KINETIC SOOT MODEL

At present, detailed modelling of soot formation and destruction is executed by using a relatively large gas phase reaction mechanism - including an improved model which contains detailed chemistry for PAH growth - coupled with a mechanistic soot model for particle inception, coagulation of particles, condensation, surface growth by gaseous species and soot particle oxidation (based on Frenklach and Wang, 1994).

A recently published reaction mechanism (Wang and Frenklach, 1997), which comprises the reactions of aromatic species up to pyrene, was updated by taking into account results obtained by shock tube experiments, especially on reactions of toluene, phenol, phenylacetylene, cyclopentadiene, propargyl and phenyl and benzyl radicals (Hu et al., 1999). This updated mechanism was validated by modelling the concentration profiles measured in a laminar, sooting ethene/O₂/Ar flame operated at atmospheric pressure (Harris et al., 1988). Measured species profiles of C₁-, C₂- and first aromatic ring compounds were reproduced very well.

As the base model for calculating the measured soot volume fraction f_v , the original soot model (Frenklach and Wang, 1994) was applied without any changes. This soot model describes PAH growth by linear lumping in which reactions of hydrocarbons with different numbers of condensed 6C rings (ranging from 3 to 7) are described by a replicating HACA (Hydrogen Abstraction Carbon Addition) reaction sequence. Particle inception occurs via PAH coagulation, starting with A4 (pyrene, C₁₆H₁₀). Further growth of the particles proceeds by coagulation of the particles and by surface growth controlled by reactions of the soot surface with OH and O₂.

One aim of the present study was to replace the PAH growth described by the HACA sequence by a comprehensive reaction mechanism which contains detailed kinetics for PAH species including the elementary reaction steps used in the HACA sequence. A reaction mechanism from MIT (Richter et al., 1999) comprising detailed kinetics for form species up to C₃₀ was chosen. All the large PAHs formed in the PAH growth model were assumed to collide giving rise to nuclei: different combinations of PAH monomers are assumed to collide and form dimers; in a second step, these dimers collide with other monomers or dimers producing trimers etc. If the growing PAH has an amu > 760, a nucleus is born (Hu et al., 2000).

4 RESULTS AND DISCUSSION

Several flames using different fuels at different equivalence ratio and pressure were studied. LII intensity fluctuations in the central part of the flames typically remain below 15 % indicating sufficiently stable objects of measurement (Fig. 2b, c). Figure 3a shows the results for a 1 bar ethene/air flame at $\phi=2.3$. The figure shows measured soot volume fraction and temperature as a function of HAB, along with soot volume fraction results from the kinetic soot model. The soot plateau level of 0.8 ppm fits into the set of measurements of Jander et al. (1995) and Axelsson et al. (2001). The used soot model which was improved in the present work especially with respect to the growth of PAH, gives better agreement with measured soot concentration profiles than the initial soot model by Frenklach and Wang (1994) that used only the lumped HACA mechanism (alternating H-abstraction and C_2H_2 addition) for PAH growth. This is caused by an increased particle inception predicted by the detailed model for PAH growth as a consequence of the increased rate of soot precursor formation and thus that of particles. A comparison of our measured temperatures with published temperatures for similar flames is not useful. Temperatures depend strongly on flow speed (losses to the burner plate) and radiative losses to the specific surroundings. Additionally, the published results are based on thermocouple data or line of sight measurements thus not providing the accuracy and spatial resolution to be used as input for simulations. Our CARS measurements resulted in peak temperatures of 1715 K. Evidence for radiative energy loss is given by the downstream temperature decrease. When performing statistical analysis of 600 single CARS spectra, even in the very steep temperature rise, the single pulse temperature distribution at one location is shown to be relatively narrow (± 100 K), proof of the excellent temporal and spatial stability of this flame and excluding height fluctuations of the reaction zone larger than 0.5 mm.

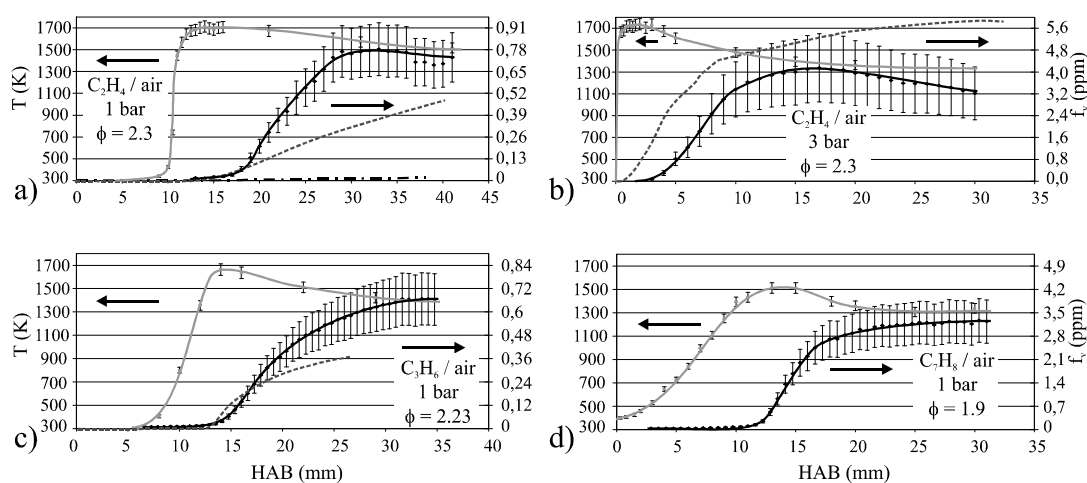


Figure 3. Measured temperature profiles (left scale) and soot volume fractions (right scale) for laminar premixed flames under the indicated profiles. Apart from the toluene flame (d) the actual kinetic computation results containing detailed gas phase chemistry are shown (dashed line). For the upper left flame (a) additionally a comparison with the pure HACA mechanism (dash dotted) is visible.

A clear benefit of the experimental set-up for simulations is to be emphasised: Even a lifted flame can be stabilised above the matrix surface by using the second (ring) flame. Thus, temperature measurements below the reaction zone can be performed resulting in well known starting conditions for the modelling.

It should be mentioned that the existence of a spatially resolved temperature profile measured with high accuracy is of great advantage with respect to the soot modelling especially as pressure increases and the reaction zone becomes very thin as in Figure 3a. Because temperature dominates the onset of soot formation, it is clear that modelling dynamic soot formation requires a realistic temperature profile between burner surface and post flame zone (Hu et al., 2000).

Increasing the pressure changes the profiles dramatically (Fig. 3b). At the lowest accessible height of 0.3 mm the temperature is already higher than 1600 K, indicating that the reaction takes place immediately above the burner surface. Absence of C_2 interferences at these high soot levels indicates the full functionality and reliability of the modified technique. At 3 bar the detected peak temperature was 1730 K, similar to the 1 bar case. At 2 mm above the reaction zone the soot concentration begins to rise, achieving a maximum of 4 ppm at 14 mm HAB.

These plateau soot volume fractions result in more than 30 % absorption of emitted LII signal, giving evidence to the need of correction for signal trapping.

For this flame, the starting conditions, i.e. the temperature at HAB = 0 for kinetic calculations, are not as well defined as in the 1 bar case. For the simulation a linear interpolation was performed between the first measured temperature and estimated room temperature at the burner surface. While the position of the soot rise is predicted too low, the slope of the calculated profile is in good agreement with the experiments and the final soot level is overestimating the measured values. Nevertheless, the overall agreement is satisfying.

Changing the fuel to propene does not dramatically influence the shape of the measured profiles (Fig. 3c). As for ethene, a lifted propene flame could be stabilised at atmospheric pressure and even the measured plateau soot level of 0.7 ppm is similar. The measured peak temperature is close to 1660 K. As in the former examples, there is good agreement of the calculated soot volume fraction with the measured one, clearly showing the correct trends.

Increasing the pressure to 5 bar resulted in significant problems in flame stabilisation. Even though the outer flame shape remained stable, the best achieved flames exhibited fluctuations of 1 – 2 mm at the lower edge and pronounced soot streaks at randomly changing positions. This caused unacceptable fluctuations in the CARS spectra, preventing accurate temperature measurements (i.e. narrow distribution at one position). Averaging 100 LII images removed the streaky structures completely, providing satisfactory qualitative information. Figure 4 shows LII images at 5 bar with inner flame $\phi=1.95$ to 2.15. Since only the inner fuel flow rate was varied slightly (by less than 1 % of the total inner flow rate), the overall flow conditions are about the same for all flames. The richer the flame is the higher the plateau soot level.

The main components of aeroengine fuel are aliphatic hydrocarbons based on the above described ones. Even for longer chained hydrocarbons, the reaction mechanisms are not expected to be completely different. At lower concentrations available in the fuel but exhibiting higher soot forming potential, aromatic hydrocarbons are an essential object of interest for chemical kinetics. In particular, conventional models are based on soot formation over aromatic hydrocarbons after an initial fuel fragmentation. Thus, a direct study of an aromatic compound as fuel gives additional insight into the process of soot formation and the role of these species in the network of chemical reactions. As representative of aromatic molecules, toluene was chosen. Using the aforementioned liquid bubbler system, a laminar premixed toluene/air flame was stabilised at atmospheric conditions (Fig. 3d). Two main differences to the above described profiles are obvious: First, the temperature rise is much slower, proceeding over 8 mm and reaching a maximum of 1500 K, approximately 300 K below the adiabatic temperature for $\phi = 1.9$, caused by the very low flow speed accompanied by radiative losses. Second, the plateau soot level is much higher indicating the large soot formation potential of aromatic compounds.

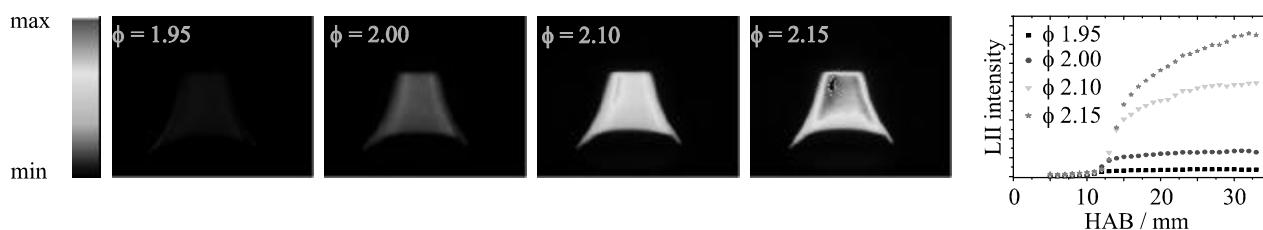


Figure 4. Soot distributions and vertical profiles upon change of the equivalence ratio for propene/air flames at 5 bar, not corrected for LII signal scattered at the burner surface.

5 CONCLUSIONS

For the measurement of accurate model validation data the need for spatially resolved, *in situ*, nonintrusive measurement methods has been addressed. The presented work describes the application of a modified CARS excitation scheme for temperature determination in sooting flames (SV-CARS) in combination with soot volume fraction measurements by LII. To obtain a comprehensive data set for the soot model development and validation, accurate measurements of temperature and soot concentration have been performed in quasi 1D flames for ethene, propene, and toluene with various equivalence ratios and at pressures up to 5 bar. These experimental data could successfully be used for comparison with soot formation calculated by kinetic computations. The model predictions showed satisfactory agreement with the measurements; the main features of the measured soot profiles are correctly predicted. Further research is necessary with respect to the transition from PAH species to the first coagulating particles (e.g. incorporation of combinative reactions, Böhm et al., 2003) and to soot oxidation.

6 ACKNOWLEDGEMENTS

The authors want to thank Dr. R. Hadeff for support during measurements and data analysis, funded by the Alexander von Humboldt-Foundation, the Helmholtz-Gemeinschaft Deutscher Forschungszentren (HGF) for funding during the research program "Particles and cirrus clouds" (PAZI), and M. Kapernaum for performing the volumetric analysis of the toluene mixture.

REFERENCES

- Axelsson, B., R. Collin, P.E. Bengtsson, 2001: Laser-induced incandescence for soot particle size and volume fraction measurements using on-line extinction calibration. *Appl. Phys. B* 72, 367.
- Böhm, H., M. Braun-Unkloff, P. Frank, 2003: Investigations on initial soot formation at high pressures. *Progress in Computational Fluid Dynamics 3 (2-4)*, in press.
- Braun-Unkloff, M., A. Chrysostomou, P. Frank, E. Gutheil, R. Lücknerath, W. Stricker, 1998: Experimental and numerical study on soot formation in laminar high-pressure flames. 27th Symp. (Int.) on Combustion, The Combustion Institute, Pittsburgh, p. 1565.
- Bryce, D.J., N. Ladommatos, H. Zhao, 2000: Quantitative investigation of soot distribution by laser-induced incandescence. *Appl. Opt.* 39, 5012.
- Choi, M.Y., A. Hamins, G.W. Mulholland, T.Kashiwagi, 1994: Simultaneous optical measurement of soot volume fraction and temperature in premixed flames. *Combustion and Flame* 99, 174.
- Charalampopoulos, T.T., J.D. Felske, 1987: Refractive indices of soot particles deduced from in-situ laser light scattering measurements. *Comb. Flame* 68, 283.
- Eckbreth, A.C., 1996: Laser diagnostics for combustion temperature and species. Overseas Publishers Association, Amsterdam B.V.
- Frenklach, M., H. Wang, 1994: Detailed mechanism and modelling of soot particle formation. Springer-Verlag Berlin, Springer Series in Chemical Physics 59, 165.
- Hanisch, S., H. Jander, T. Pape, H.G. Wagner, 1994: Soot mass growth and coagulation of soot particles in C₂H₄/air-flames at 15 bar. 25th Symp. (Int.) on Combustion, The Combustion Institute, Pittsburgh, p. 577.
- Harris, S.J., A.M. Weiner, R.J. Blint, 1988: Formation of small aromatic molecules in a sooting ethylene flame. *Combust. Flame* 72, 91.
- Hu, D., M. Braun-Unkloff, P. Frank, 1999: Modelling study on soot formation at high pressures. *Combust. Sci. & Technol.* 49, 79.
- Hu, D., M. Braun-Unkloff, P. Frank, 2000: Modelling study on initial soot formation at high pressures. *Z. Phys. Chem.* 214 (4), 473.
- Jander, H., N. Peterleit, D.M. Razuš, 1995: The influence of carbon density on soot growth in atmospheric C₂H₄ (air, O₂)-flames. *Z. Phys. Chem.* 188, 159.
- Pape, T., 1993: Optische Untersuchungen zum Rußwachstum in vorgemischten Ethen-Luft Flammen bei 15 bar. Diplom-Thesis, Göttingen, 17 pp.
- Richter, H., W.J. Grieco, J.B. Howard, 1999: Formation mechanism of polycyclic aromatic hydrocarbons and fullerenes in premixed benzene flames. *Combust. Flame* 119, 1.
- Santoro, R.J., C.R. Shaddix, 2002: Laser-induced incandescence. In: Applied Combustion Diagnostics [K. Kohse-Höinghaus, J.B. Jeffries (eds.)]. Taylor & Francis, New York, 252, and references therein.

- Schneider-Kühnle, Y., 2003: Experimentelle Untersuchung rußender Hochdruckflammen mit Laserdiagnostischen Messmethoden. PhD Thesis, DLR Stuttgart, in progress.
- Stricker, W., 2002: Measurement of temperature in laboratory flames and practical devices. In: Applied Combustion Diagnostics [K. Kohse-Höinghaus, J.B. Jeffries (eds.)]. Taylor & Francis, New York, 155.
- Wang, H., M. Frenklach, 1997: A detailed kinetic modelling study of aromatics formation in laminar premixed acetylene and ethylene flames. *Combust. and Flame* 110, 173.

AvioMEET Inventory Tool and its Applications

M. Bukovnik*, M. T. Kalivoda
psiA-Consult GmbH, Vienna, Austria

Keywords: air traffic, emission factors, calculation software, application

ABSTRACT: Increasing numbers of flights and still unknown effects of exhaust gasses on the high atmosphere have drawn most attention on air traffic and its emissions. In Europe, many institutions are working in this area, collect traffic and emission data, create emission inventories and assess effects. That lead to some work done in parallel while using different databases and methodologies which often lead to results that cannot be compared or matched. COST 319 action and MEET project were a starting point for a dialogue and discussions between the different communities involved and thus gave an incentive for harmonisation. MEET project came up with a methodology for estimating air pollutant emissions from present and future air traffic. Methodology and emission indices are now used for strategic environmental assessment and transport policy making. The COST 319 working group D2 – air traffic – has proposed minimum requirements for an harmonised approach to generate emission indices. This seems to be the only way make results from different inventories comparable and exchangeable. Harmonisation work is going on under the umbrella of the Thematic Network Aeronet. Methodology used in MEET project and presented here is based on a flexible design that allows to adjust it to the user requirements as well as on air traffic data and emission factors (easily) available. Based on the MEET methodology an MS-Access computer tool was created, called AvioMEET, which uses most of the Emission Indices published in the Emission Index Sheets of MEET/Deliverable 18. TRENDS finally uses all this more or less theoretical knowledge to apply it on existing traffic activity data to come up with a database of environmental indication for air transport.

1 INTRODUCTION

However with the number of aircraft movements ever increasing coupled with the fact that the impact that these gases have on the atmosphere varies in a non-linear manner with altitude has drawn considerable attention on this transport sector. For this reason many institutions have been working on collecting traffic and emissions data, generating emission inventories and assessing the effect that air transport has on the atmosphere. As well as work on the current situation, research into future scenarios and trends has also been undertaken.

Owing to much interest in the area a lot of research was conducted in parallel resulting in much duplication of work. As is to be expected with such a scenario many different results were reached. Also methodologies, tools and emission factors of various quality were used.

As this field of research has gained such attention it became apparent that a standard system would be needed in order for future work to be acceptable. COST 319 marked the start of a dialogue between the main players in this area in Europe. This dialogue has lead to steps being made towards harmonising methodologies and concentrating the activities with DG VII's support.

The COST 319 working group D2 – air traffic – has worked out a proposal for a harmonised approach to generate emission indices (EIs). From the working group's point of view this harmonisation is necessary to make results from different inventories and actions like Corine, IPCC etc. comparable and exchangeable.

2 THE MEET AIR TRAFFIC METHODOLOGY

MEET stands for Methodologies for Estimating Air Pollutant Emissions from Transport. The MEET project - funded by the European Commission under the transport RTD programme of the 4th framework programme - has been undertaken in order to provide a basic, Europe-wide procedure for evaluating the impact of transport on air pollutant emissions and energy consumption.

A methodology for estimating air pollutant emissions from air traffic was created. Although military operational flights and VFR (Visual Flight Rules) flights are included IFR (Instrument Flight Rules) flights were focused on. EIs for components NO_x, CO, HC, CO₂, H₂O, SO₂ and fuel consumption are published for 30 aircraft/engine combinations.

2.1 Outline methodology for baseyear

In common with the other MEET methodologies for emission calculations, estimation of air traffic emissions combines an estimate of the amount of transport activity with emission factors per unit of activity to derive total emissions (Kalivoda/Kudrna 1997). As with the other modes of transport, there needs to be a classification of the transport activity to take into account the differences between types of aircraft/engine combination, their different operating modes, the different pollutants and so on. The method used follows those for the other non-road modes: an initial estimate is made of the fuel consumed during an air transport operation and pollutant emissions are calculated using fuel-specific emission factors.

Three main classes of air transport can be distinguished:

- flights performed under Instrument Flight Rules (IFR)
- flights performed under Visual Flight Rules (VFR)
- military operational air traffic (MOT)

For each category a typical data set is available for traffic characteristics and engine emissions, although the accuracy of the data within the three categories is different.

2.2 ATEMIS simulation program: Methodology for IFR flights

Methodology for IFR flights is based on standard flight profiles for about 35 aircraft/engine combinations which represent about ¾ of European air traffic. Dividing each flight profile into several sectors of constant performance (= standard operating conditions SOC) and emission characteristics allows to adapt the algorithm to different user requirements (i.e. airport/in flight emissions) and gives the chance to improve results by increasing resolution:

$$TE_p = \sum_r \sum_j SE_{j,p,r} \cdot N_{j,r} \tag{1}$$

$$SE_{j,p,r} = \sum_s FC_{j,s}(CR_{ALT}(D_r)) \cdot EI_{j,p,s}(CR_{ALT}(D_r)) \tag{2}$$

- TE_p Total emission of pollutant p [kg per period]
- $SE_{j,p,r}$ Specific emission of pollutant p , of aircraft/engine combination j on a route r [kg per aircraft]
- $N_{j,r}$ Number of aircraft of category j on route r per period [aircraft per period]
- $FC_{j,s}(CR_{ALT})$ Total fuel consumption of aircraft category j for standard operating condition s [kg_{FUEL}/SOC]
- $EI_{j,p,s}(CR_{ALT})$ Emission index of aircraft category j for pollutant p and SOC s [kg_{EMISSIONS}/kg_{FUEL}]
- D_r Distance between city pair (=route r) [km]
- j Aircraft/engine category
- p Pollutant
- r Route from airport to airport
- s standard operating condition s

That leads to a set of emission indices (EI, the mass of pollutant produced per mass of fuel used) for eight typical operational conditions, which may be combined to cover most of an aircraft's operation during a flight profile. The standard operating conditions are:

- starting up engines,
- taxi out, take off,
- climb, cruise, descent,
- landing, taxi in.

Emission factors are based on engine certification data in the ICAO (International Civil Aviation Organisation) Engine Exhaust Emission Databank [ICAO 1995]. This databank contains data sets of thrust (engine performance), fuel flow and emissions of components CO, NO_x and VOC which apply to four different power settings, Mach number 0 and altitude 0 m.

Table 1. Example for an aircraft emission index sheet

B 737 generic		Boeing B 737 with engine mix								
		duration	distance	Fuel burned		specific Emission parameters				
		of OS	of OS	total	specific	EI.NO _x	EI.CO	EI.HC		
		[s]	[km]	[kg]	[kg/s]	[g/kg]	[g/kg]	[g/kg]		
operational state (OS) Index		<i>DUR</i>	<i>D</i>	<i>FC</i>	<i>SFC</i>	<i>SENO_x</i>	<i>SECO</i>	<i>SEHC</i>		
1	engine start	es	global figures for duration and HC emissions,			see chapter 3.5				
2	taxi out	txo	default		const	const	const	const	const	const
3	take off	tff	default		const	const	const	const	const	const
4	climb	cl		f(cralt)	f(cralt)		f(cralt)	f(cralt)	f(cralt)	f(cralt)
5	cruise	cr				f(cralt)	f(cralt)	const	const	const
6	descent	dsc		f(cralt)	f(cralt)		f(cralt)	f(cralt)	f(cralt)	f(cralt)
7	landing	ld	default		const	const	const	const	const	const
8	taxi in	txi	default		const	const	const	const	const	const
9	ground operations	go	global figures for duration and HC emissions,			see chapter 3.5				
	EI.CO ₂		[g/kg]	default						
	EI.SO ₂		[g/kg]	default						
	EI.H ₂ O		[g/kg]	default						

Using additional information on the aircraft performance during the flight from the emission simulation model ATEMIS (Kalivoda/Feller 1995) leads to average emission indices. Simulations were carried out for thirty of the most common aircraft used in Europe, representing about 70% of flights. Components of the burnt fuel include H₂O, CO₂, CO, NO_x, VOC and SO₂. There is a great uncertainty about other pollutants such as soot, PAH, CH₄, NO₂ or NH₃ so these cannot be included at the moment.

For each of the 30-aircraft/engine combination, all essential parameters and all necessary information for calculating an emission profile are given in a so-called Emission Index Sheet (EIS). Table 2 gives an example of such a data sheet. Default values (*default*) are provided for duration of taxi out, take off, landing, taxi in as well as for the ground operations. Fields marked with '*const.*' contain a single number for fuel burned or EI. The rest of the EIs are strongly depending on the (*average*) cruise altitude (*cralt*). A grey box in the sheet means no data available or provided at the moment.

Distance flown (*D*) and cruise altitude (*CRALT*) are the two basic input parameters to determine the geometric shape of a flight profile on a mission. The total distance of a city-pair is the sum of the distances flown during the three operational states climb, cruise and descent. The average climb and descent rate has been defined so climb and descent distance are just a function of cruise altitude (*CRALT*). Finally the aircraft type is needed to determine the profile. Additional information which is useful:

- average duration of taxi out [s]
- average duration of taxi in [s].

2.3 Methodology for VFR and military flights

EI for military and VFR flights are based on hours of operation and average fuel consumption per hour because of limitations in the nature of the data available. Components included are H₂O, CO₂, CO, NO_x, VOC and SO₂. Data availability for VFR flights is very similar to that of military air traffic. That means no detail information on flight path and specific emissions is available so an algorithm is used which is the same as for military.

$$TVE_p = \sum_v EI_{v,p} \cdot FC_v \cdot H_v \quad (3)$$

- TVE_p* Total VFR flight emission of pollutant *p* [kg per period]
- H_v* Hours of operation of aircraft class *v* per period [hours per period]
- FC_v* Fuel consumption of aircraft class *v* per hour [kg_{FUEL}/hour]
- EI_{v,p}* Emission index for pollutant *p* [g_{EMISSIONS}/kg_{FUEL}]
- v* VFR aircraft class
- p* Pollutant

The ICAO engine exhaust emission databank does not provide any information since there is no ICAO certification of such engines.

3 AVIOMEET SOFTWARE TOOL

The software tool AvioMEET is based on the data published in the Emission Index Sheets of MEET/Deliverable 18. This methodology includes the emission profiles for a single flight on a city pair, or mission, emission functions for fuel flow, NOX, CO and HC which allows an estimate of the total fuel consumption and emissions for each part of the mission. However there are slight changes to the MEET Methodology

- Additional aircraft types e.g. Boeing B737-400, B737/500/600/700/800, B747-400, ATR42, ATR72, BAe 146,
- Emission Indices were harmonised with ANCAT/EC2 data within UNECE Emission Inventory Guide Book,
- Additional fuel consumption and emission functions, for climb to 3000 ft and final approach down from 3000 ft, which are necessary to calculate ground related emissions
- Additional fuel consumption and emission functions, for climb to 3000 ft and final approach down from 3000 ft, which are necessary to calculate ground related emissions are added for ICAO category.
- For long distance step cruise was included in this computer tool as it is known from the ANCAT/EC2 global NOX emission inventory.

3.1 Cluster screen

When generating an emission inventory it is important to have a tool that helps to group air traffic movement data. Some users might wish to make an inventory for a whole country but airport-wise. In this case it is recommended to define each airport as an emission cluster and put movement data of this specific airport of a certain year into this cluster. What you will get at the end is emissions per airport (=cluster).

So the emission cluster concept is a most effective and useful way to input and maintain movement data. The emission cluster can be defined individually depending on the specific question to be answered.

3.2 Single Aircraft screen

Based on Eurocontrol data, average flight altitudes for each aircraft and distance of mission were added to the AvioMEET software tool. The user has the ability to use own data with this program. Figure 8 shows the software’s input screen. For an aircraft/engine combination selected an emission profile is generated for the components:

- Fuel Consumption and its related species CO₂, H₂O and SO₂, NO_x, UHC, CO.
- The minimum input data to generate such an emission profile is
- Aircraft type, number of aircraft (of this type) on this mission, distance of mission in km
- From the AvioMEET database defaults are proposed for:
- Cruise altitude in ft, time for taxi out and taxi in for the COST 319 category LTO-cycle , percentage of total cruise distance at a certain cruise altitude, seat capacity and load factor.

The main outputs from the tool are:

- Fuel consumption and emissions for the COST 319 category,

- Specific fuel consumption and Emission Indices for climb, cruise and descent,
- Fuel consumption, emissions and time for COST 319 category LTO-cycle or for the ICAO LTO cycle,
- Fuel consumption, emissions and distance for cruise and cruise related climb and descent,
- Total fuel consumption and total emissions for 1 aircraft on 1 mission,
- Specific fuel consumption and specific emissions per seat kilometre and passenger kilometre,
- Total fuel consumption and total emissions for n missions of n aircraft.

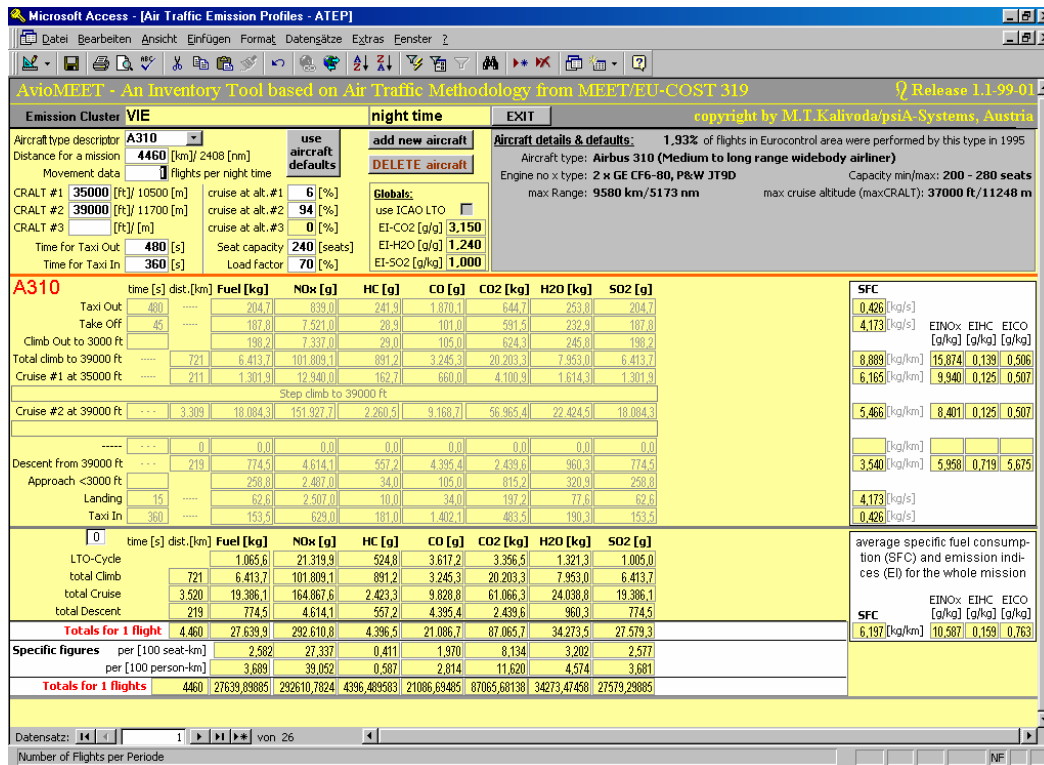


Figure 8. MS-Access form ATEPT for emission profiling

4 APPLICATION OF THE MEET/AVIOMEET METHODOLOGY

4.1 ANCAT/ECAC

ANCAT (Abatement of Nuisance Caused by Air Transport) represents a group of experts within the European Civil Aviation Conference (ECAC). The ANCAT/EC2 inventories prepared a global air traffic fuel and NOx inventory for base 1991/92 and forecast 2005. A subgroup developed an ANCAT/ECAC methodology for emission calculation were the UNECE methodology. Turboprop data from the ARTEMIS project (5th FP/DG TREN) have been verified and included in the methodology.

4.2 EMEP/CORINAIR ATMOSPHERIC Emission Inventory Guidebook

The EMEP/CORINAIR ATMOSPHERIC Emission Inventory Guidebook presents common guidelines for the estimation of emissions from traffic. The methodology presented for air transport (European Environmental Agency EEA 1997) includes three approaches (the very-simple methodology, the simple methodology and the detailed methodology) all based on fuel sold statistics.

Emissions associated with domestic aviation are to be reported to UNFCCC using the IPCC source sector split. International aviation emissions should be presented for information purposes only, but are not included in the national totals. Emissions associated with the LTO-cycle are to be reported to the ECE/CLRTAP. Activities include air traffic movements of scheduled and charter passenger and freight air traffic as well as taxiing, helicopter traffic and general aviation. Military

air traffic is included if possible only. The detailed methodology is adopted in accordance with the COST 319 proposal (table above) and emission indices are used from ANCAT/EC2 (fuel consumption, NO_x) and MEET (CO, HC).

4.3 TRENDS

Trends (TRansport and ENvironment Database System) is a joint DG VII/Eurostat project. The purpose of the study is to develop a system for calculating a range of environmental pressures due to transport. These environmental indicators include air emissions and energy consumption from the four main transport modes, i.e. road, rail, ships and air. These data give a general picture of the absolute environmental loads, in different time and spatial resolutions.

A user software with emission database was developed, where the calculation for air traffic was based on the MEET/AvioMEET methodology. The output of these software are emissions and fuel consumption per person and ton kilometre or per aircraft and engine type for the years 1975 up to 2015.

5 CONCLUSION

From the above discussion it is apparent that COST 319 and MEET were incentives that greatly advanced and harmonised joint activities in Europe in the field of air traffic emission calculation. This can be seen in the manner by which the air traffic community and the environmental community have adopted these Methodologies.

Although the research into calculating emissions and the efforts to harmonise the approach of calculations does not change the impact that emissions have on the environment nor does it make air traffic more environmentally friendly it does create an essential tool for policy making and in deciding which measures have the best effect on the environment.

However, due to the fact that the basic input data for the MEET methodology as well as for AvioMEET software tool are ICAO data from 1995, it should be addressed for decision makers that it is urgent necessary to invest in an update Databank combined with new data available from several influences like real life data, instead of certification data, engine age, weather conditions, as well as inflight emissions.

REFERENCES

- Brasseur, G.P. et al.: 1997, European Scientific Assessment of the Atmospheric Effects of Aircraft Emissions, Environment and Climate Programme of the European Commission, October
- Bundesamt für Zivilluftfahrt (ed): 1993, Die Auswirkungen der Luftfahrt auf die Umwelt - Synthese. Bern
- Bundesamt für Zivilluftfahrt (ed): 1993, Die Auswirkungen der Luftfahrt auf die Umwelt - Kurzfassung. Bern.
- EEA (ed.): 1997, EMEP/CORINAIR ATMOSPHERIC Emission Inventory Guidebook – Sub-sector Air traffic, Copenhagen (<http://www.eea.eu.int>).
- Gardner R. M.: 1996, A Global Inventory of Aircraft NO_x Emissions (ANCAT/EC 2) - A revised inventory (1996) by the ECAC/ANCAT&EC working group. Int. Colloquium Impact of Aircraft Emissions upon the Atmosphere, ONERA, Paris.
- Gardner R. M.(ed.): 1998, ANCAT/EC2 Global Aircraft Emissions Inventories for 1991/92 and 2015, ECAC-EC Publication, Eur.No 18179, ISBN 92-828-2914-6,.
- International Civil Aviation Organization (ICAO): 1995, ICAO Engine Exhaust Emissions Data Bank, First Edition 1995, Doc 9646-AN/943, Montreal.
- Kalivoda M. T., Feller R: 1995, ATEMIS - A tool for calculating air traffic emissions and its application. The Science of the Total Environment 169, 241-247.
- Kalivoda M. T., Kudrna M.: 1997, Methodologies for Estimating Emissions from Air Transport, MEET deliverable no.18, CEC DG VII contract ST-96-SC.204, Perchtoldsdorf
- Samaras Z. (ed.): 1999, Development of a Database System for the Calculation of Indicators of Environmental Pressure Caused by Transport, Transport and Environment Database System (TRENDS). LAT, University of Thessaloniki, Thessaloniki.
- ANCAT/ECAC: 2002, Sub Group on Emissions Calculation, Guidance Material

Lightning NO_x emissions and the impact on the effect of aircraft emissions - Results from the EU-Project TRADEOFF

V. Grewe*

DLR-Institut für Physik der Atmosphäre Oberpfaffenhofen, Germany

Keywords: Aircraft NO_x, Lightning, global modelling, ozone

ABSTRACT: The intercomparison of upper troposphere and lower stratosphere NO_x measured on board of commercial aircraft with results of the chemistry-climate model E39/C revealed an underestimation of summertime simulated NO_x concentrations. A further investigation of the causes within the EU-project TRADEOFF, using new satellite data, indicated a deficiency in the lightning parameterisation. A new parameterisation has been developed, which is based on the convective massflux. The effect of individual emissions on the NO_x and ozone concentration is shown. Tropical lightning emissions have the potential to enhance the mid-latitude NO_x concentration via transport through the lowermost stratosphere. This transport process enhances ozone at mid-latitudes to the same magnitude as mid-latitude lightning. Compared to the previous formulation of lightning the impact of air traffic is reduced when applying the new lightning parameterisation, although the absolute amount of emitted NO_x by lightning was not affected, but the horizontal and vertical location of the emitted NO_x. The contribution of air traffic to the NO_x budget in the northern upper troposphere is reduced from 30%-40% to 20%-30% and the contribution to ozone is reduced from 3%-4% to 2.5%.

1 INTRODUCTION

The impact of aircraft NO_x emissions on the chemical composition of the atmosphere was investigated on the basis of 6 chemistry transport and chemistry climate models for 1999 IPCC assessment report (IPCC, 1999). Besides that all models showed an ozone increase caused by air traffic, the pattern of the ozone change was quite different from one model to another. One aim of the EU project TRADEOFF was to better understand those differences and in case of an identification of deficiencies, to enhance the model's quality based on intercomparison with observational data. A comprehensive model-observation intercomparison had been performed by Brunner et al. (2003). Prior to that an intercomparison was performed between NO_x and ozone measurements on board a commercial aircraft (NOXAR-data) with the climate chemistry model E39/C (Grewe et al., 2000), which clearly indicated too low NO_x values in the mid-latitude summer tropopause region and a weak seasonal cycle. In principle, there are two processes leading to this deficiency: (1) Underestimated vertical transport of NO_x emitted at the surface or (2) underestimated lightning NO_x emissions. Although satellite data of the occurrence of convective systems are available, almost no data are available, which are suitable to validate vertical convective mass fluxes. On the other hand, new observational data are available to get more insights into the occurrence of lightning. One result was that mid-latitude lightning is underestimated in summer and that the seasonal cycle is too weak in that region, which gives reasons for the discrepancy of the mid-latitude upper troposphere NO_x budget. Based on those data an intercomparison was performed and a new lightning parameterisation was derived yielding much better agreements with observations (Grewe et al, 2001; Kurz and Grewe, 2002) than in the previous version. After a short description of the climate chemistry model E39/C, the lightning parameterisation and the NO_x emissions from lightning are introduced. Section 4 describes how tropical lightning contributes to the mid-latitude NO_x budget, which then alters the effect of aircraft NO_x emissions. How the new

* *Corresponding author:* Volker Grewe, DLR-Institut für Physik der Atmosphäre, Oberpfaffenhofen, D-82205 Wessling, Germany. Email: volker.grewe@dlr.de

lightning parameterisation, which does not change the total amount of emitted NO_x, alters the ozone increase caused by air traffic is given in section 6.

2 THE CLIMATE-CHEMISTRY MODEL E39/C

The coupled climate-chemistry model E39/C (ECHAM4, 39 levels up to 10 hPa, chemistry module CHEM, Hein et al., 2001) is based on the spectral general circulation model (GCM) ECHAM4 (Roeckner et al., 1996) with increased vertical resolution from 19 to 39 levels (Land, 1999), i.e., from around 2 km to 700 m at tropopause altitudes. The chemical module CHEM (Steil et al., 1998) has already been coupled to ECHAM3 and used in a variety of studies regarding tropospheric and stratospheric chemistry (Dameris et al., 1998; Grewe et al., 1999, 2001). It includes stratospheric heterogeneous and homogeneous ozone chemistry and tropospheric NO_x-CH₄-CO-HO_x-O₃-chemistry with 107 photochemical reactions and 37 species. An upper boundary condition for NO_y and ClO_y is applied to account for CFC and N₂O photolysis above 10 hPa.

Surface NO_x emissions (industry, traffic, soils, biomass burning) of 33.1 TgN per year, and aircraft NO_x emissions of 0.56 TgN per year are included in the E39/C model, respectively. The lightning parameterisations generate NO_x interactively with the convection scheme according to Grewe et al. (2001). Details are given below. Wash-out is calculated interactively with the cloud schemes.

The model has been validated with respect to a variety of species and processes (Hein et al., 2001, Grewe et al., 2001, Stenke and Grewe, 2003; Lauer et al., 2002, Shine et al., 2003).

3 LIGHTNING NO_x EMISSION

The lightning parameterisation (Grewe et al., 2001) is based on a correlation between model's convective mass flux (Tiedke, 1989) and flash frequency. This correlation has been derived from an observed correlation between flash frequencies and convective cloud top heights (Price and Rind, 1992, PR92) and a correlation between the simulated cloud top heights and simulated convective mass fluxes, which then directly relate the simulated mass fluxes with flash frequencies. The correlation between flash frequencies and convective cloud top heights, derived by PR92 was only valid for continental thunderstorms. Ocean storms have similar cloud top heights but only less lightning and lower mass fluxes (DelGenio and Kovari, 2002). Since E39/C is able to simulate different mass fluxes for ocean and land conditions also the lightning intensity of ocean thunderstorms is significantly lower than over land, which makes an artificial differentiation between land and ocean lightning obsolete. Summertime continental mid-latitude lightning is much better represented in absolute amounts and patterns compared to the PR92 parameterisation based on OTD satellite data (Kurz and Grewe, 2002). Therefore a better representation of mid-latitude upper troposphere NO_x can be expected.

This parameterisation provides a horizontal distribution of lightning. Additionally a parameterisation for intra-cloud and cloud-to-ground separation depending on the „cold cloud area“, which is the thickness of the cloud with temperatures below 0°C, is applied (Price and Rind, 1993). Intra-cloud flashes are assumed to be 10 times less energy efficient than cloud-to-ground flashes and therefore produce 10 times less NO_x. The NO_x emissions are then vertically distributed from the ground to the cloud top using C-shape profiles (Pickering et al., 1998). The resulting NO_x emission is shown in Figure 1. The centres of the lightning emissions are clearly separated from air traffic corridors. However, transport mixes those airmasses.

4 THE IMPACT OF TROPICAL LIGHTNING NO_x EMISSIONS ON OZONE

The mixing of airmasses owning lightning characteristics with airmasses owning air traffic characteristics is manifold. At mid-latitudes upper troposphere airmasses will definitely be mixed with airmasses, which experienced lightning in the mid-latitudes. In contrast, lower stratosphere airmasses (where also aircraft fly) are much less effected by mid-latitude lightning, since vertical

mixing is less effective (Holton et al., 1995; Grewe and Dameris, 1996; Schoeberl and Morris, 2002; Grewe et al., 2002a). However, tropical lightning has the potential to emit NO_x at much higher altitudes. Those airmasses can be transported to mid-latitudes, which has been shown by aircraft measurements (Hoor et al., 2002), and contribute to the NO_y and NO_x budgets. E39/C model simulations suggest that this transport significantly contributes to the NO_x budget in the mid-latitude tropopause region. It also affects the ozone budget because ozone is produced in the tropical mid and upper troposphere and also on the way through the lowermost stratosphere. There, the simulated ozone production is small compared to the tropics, but the residence times of air masses are much larger than in the upper troposphere, which leads to a significant contribution of ozone produced in the lowermost stratosphere by lightning NO_x from tropical origin. E39/C simulations show that the lightning induced ozone increase at mid-latitudes in the tropopause region is caused by 50% by tropical lightning (Figure 2; Grewe et al., 2002a).

In July (Figure 3), this leads to a contribution of lightning to the ozone budget of 30% in the tropics and southern hemisphere and around 15% to 20% in the northern troposphere, where also other sources are of importance. Aircraft effects are mainly restricted to the northern hemisphere troposphere. Although, air traffic in the southern hemisphere also leads ozone changes there, and tropical air traffic can lead to ozone increase in the lowermost stratosphere similar to the transport-chemistry interaction discussed above. On the other hand air parcels emitted in the tropopause region of the northern hemisphere rarely have the chance to be transported to higher altitudes. Trajectory analysis of E39/C model data showed that air parcels from the tropopause region of the northern mid-latitudes only have the chance to be transported to the southern lowermost stratosphere by upward lifting in the tropical troposphere (Figure 4).

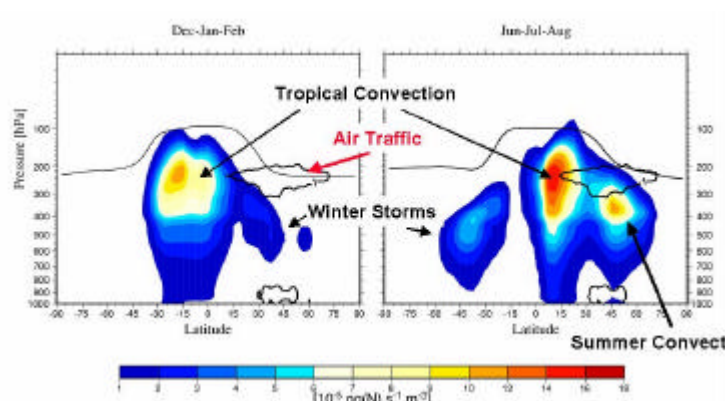


Figure 1. Zonal mean lightning NO_x emissions simulated with the chemistry-climate model E39/C [10^{-5} ng(N) s⁻¹ m⁻³]. The thin black line indicates the simulated tropopause and the heavy line the air traffic NO_x emissions [10^{-5} ng(N) s⁻¹ m⁻³]. Main centres of lightning emissions are marked.

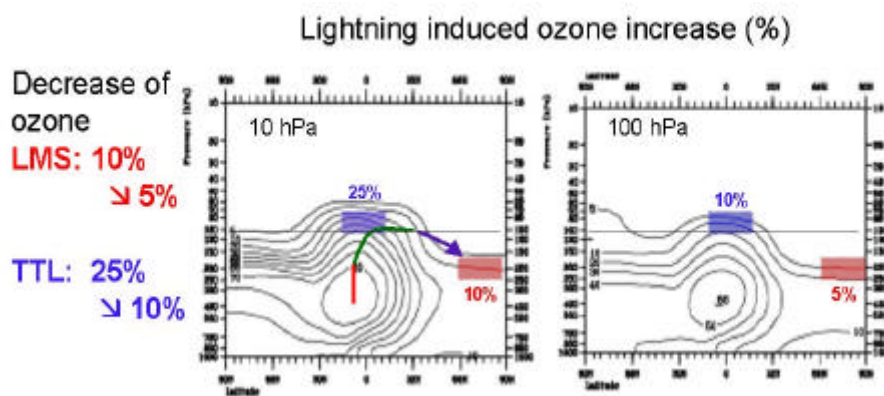


Figure 2. Annual mean ozone increase [%] caused by lightning NO_x emissions calculated with the E39/C climate-chemistry model using the standard version (left) and applying a NO_y upper boundary at 100 hPa (right). The horizontal line indicates the location of the lowered upper boundary. The isolines are 5%, 10%, 20%, 50%, 60%, 70%, and 80%. Areas are shaded for better intercomparison.

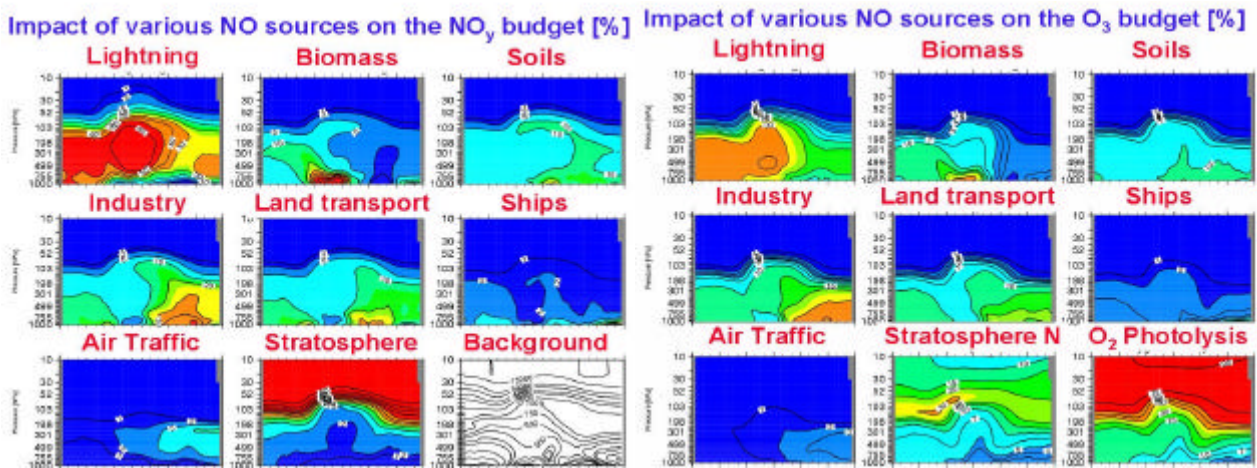


Figure 3. Impact of various NO_x sources to the NO_y (left) and ozone (right) budget [%] for an individual simulated July. Isolines are 1%, 2%, 5%, 10%, 20%, 30%, 40%, 50%, and 60% for Noy and 1%, 2%, 3%, 4%, 5%, 7%, 10%, 15%, 20%, 30%, 50%, 70%, 90% for ozone. Note: Here contributions are presented, whereas Figure 2 shows enhancements.

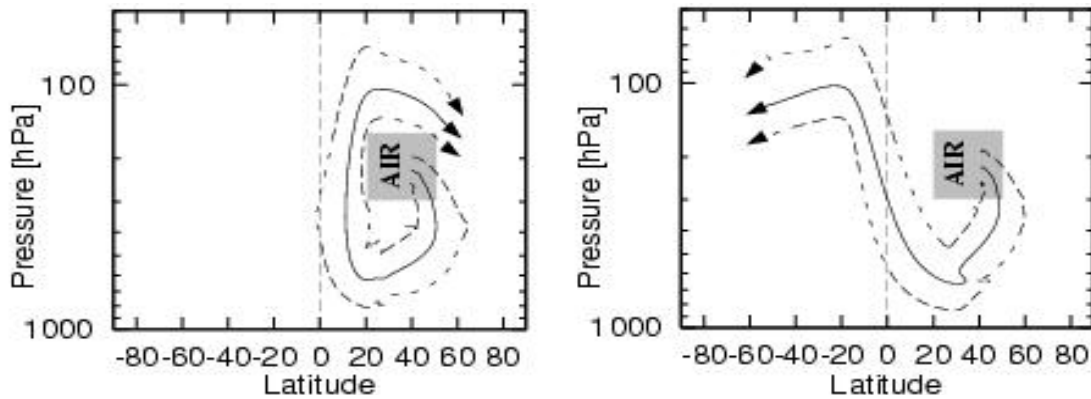


Figure 4. Pathways of air parcels from the upper troposphere (air traffic corridor) to the lower-most stratosphere.

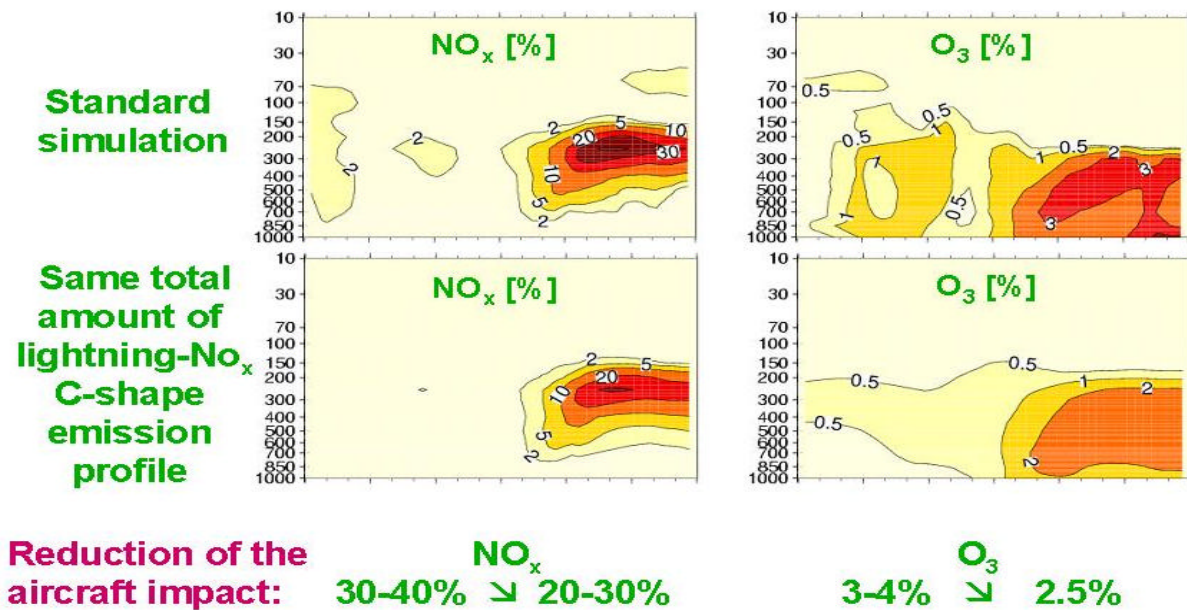


Figure 5. Annual mean contributions [%] of air traffic emissions to the atmospheric burden of NO_x (left) and ozone (right) in the standard E39/C simulation (top) and a simulation with a new lightning parameterisation (bottom).

5 THE IMPACT OF LIGHTNING NO_x EMISSIONS ON THE EFFECT OF AIR TRAFFIC

The new lightning parameterisation leads to higher background NO_x concentrations in the upper troposphere especially in July (see discussion above). This affects the ozone production efficiency of a NO_x molecule emitted by an aeroplane, which is reduced from 3.5 to 2.6 10⁸ kg per year in the main perturbation region (20°N to 70°N; 500 to 200 hPa) (Grewe et al., 2002b). It therefore reduces the impact of air traffic on ozone. Figure 5 shows these effects for NO_x and ozone in the case of the ,old‘ lightning parameterisation and the ,new‘ parameterisation. The NO_x enhancement cause by air traffic is reduced from 30% to 40% down to 20% to 30%. The ozone increase is reduced from 3%-4% to 2.5%.

6 CONCLUSIONS

The EU-project TRADEOFF aimed at a better understanding of the effect of aircraft NO_x emissions on the atmospheric composition. Based on the outcome of a comparison of upper troposphere and lower stratosphere measurements with the climate-chemistry model E39/C, the model's quality has been enhanced by developing a new lightning parameterisation (Grewe et al., 2001). The effect of lightning has been investigated. Tropical lightning has the potential to contribute significantly to the mid-latitude NO_x and ozone concentration at tropopause altitudes, by transport through the lowermost stratosphere (Grewe et al., 2002a), which has been also observed by aircraft measurements (Hoor et al., 2002).

Since the new lightning parameterisation enhances the UTLS NO_x concentration the effect of air traffic on the ozone production is reduced and also the contribution to the NO_x and ozone budget. Simulations with the coupled climate-chemistry model E39/C showed a reduction of the air traffic NO_x contribution from 30%-40% to 20%-30% and a reduction of the ozone contribution from 3%-4% to 2.5% (Grewe et al., 2002b).

The study clearly showed that upper troposphere and lower stratosphere data of chemical species are of outstanding importance for the evaluation of climate-chemistry models, if they provide seasonal climatologies and frequency distributions (see also Grewe et al., 2001), like data from the NOXAR and MOSAIC projects. Further, the study implied that lightning effects the ozone concentration globally, so that the knowledge of tropical storm systems and lightning is of importance also for the understanding of mid-latitude effects, like air traffic. EU-projects like TROCCINOX and HIBISCUS will help to reduce uncertainties linked to tropical lightning.

REFERENCES

- Brunner, D., J. Staehelin, H.L. Rogers, M.O. Köhler, J.A. Pyle, D. Hauglustaine, L. Jourdain, T.K. Berntsen, M. Gauss, I.S.A. Isaksen, E. Meijer, P. van Velthoven, G. Pitari, E. Mancini, V. Grewe, and R. Sausen, 2003: An evaluation of the performance of chemistry transport models by comparison with research aircraft observations. Part 1: Concepts and overall model performance. *Atmos. Chem. Phys. Discuss.* 3, 2499-2545.
- Dameris, M., Grewe, V., Köhler, I., Sausen, R., Brühl, C., et al., 1998: Impact of Aircraft NO_x-Emissions on Tropospheric and Stratospheric Ozone. Part II: 3-D Model Results.. *Atmos. Environ.* 32, 3185-3200,
- Del Genio, A, and W Kovari, 2002: Climatic properties of tropical precipitating convection under varying environmental conditions, *J. Climate* 15, 2597-2615.
- Grewe, V., Dameris, M., 1996: Calculating the Global Mass Exchange between Stratosphere and Troposphere.. *Ann. Geophys.* 14, 431-442.
- Grewe, V., M. Dameris, R. Hein, I. Köhler, and R. Sausen, 1999: Impact of future subsonic aircraft NO_x emissions on the atmospheric composition. *Geophys. Res. Lett.* 26, 47-50.
- Grewe, V., Grenfell, J.L., Shindell, D.T., Dameris, M., Hein, R., et al. 2000: Origin and Variability of Upper Tropospheric Nitrogen Oxides and Ozone at Northern Mid-Latitudes. Quadrennial Ozone Symposium 2000, Hokkaido University, Sapporo, Japan, 3-8 July 2000, 781-782.
- Grewe, V., Brunner, D., Dameris, M., Grenfell, J.L., Hein, R., et al. 2001: Origin and Variability of Upper Tropospheric Nitrogen Oxides and Ozone at Northern Mid-Latitudes. *Atmos. Environ.* 35, 3421-3433.

- Grewe, V., Dameris, M., Fichter, C., Sausen, R. 2002a: Impact of Aircraft NO_x Emissions. Part 1: Interactively Coupled Climate-Chemistry Simulations and Sensitivities to Climate-Chemistry Feedback, Lightning and Model Resolution. *Meteorol. Z.* 11, 177-186.
- Grewe, V., Reithmeier, C., Shindell, D.T., 2002b: Dynamic-Chemical Coupling of the Upper Troposphere and Lower Stratosphere Region. *Chemosphere* 47, 851-861.
- Hein, R., Dameris, M., Schnadt, C., Land, C., Grewe, V., et al. 2001: Results of an Interactively Coupled Atmospheric Chemistry-General Circulation Model: Comparison with Observations. *Ann. Geophys.* 19, 435-457.
- Holton J.R., Haynes, P.H., McIntyre, M.E., Douglass, A.R., Rood, R.B., and Pfister, L., 1995. Stratosphere-troposphere exchange, *Reviews of Geophysics* 33, 403-439.
- Hoor, P., Fischer, F., Lange, L., Lelieveld, J., Brunner, D., 2002. Seasonal variations of a mixing layer in the lowermost stratosphere as identified by the CO-O_3 correlation from in-situ measurements, *J. Geophys. Res.*, 107, DOI 10.1029/2000JD000289.
- IPCC - Intergovernmental Panel on Climate Change, 1999. Aviation and the global atmosphere, eds. J.E. Penner, D.H. Lister, D.J. Griggs, D.J. Dokken, M. McFarland, Cambridge University Press, Cambridge, U.K.
- Kurz, C., Grewe, V., 2002: Lightning and Thunderstorms, Part 1: Observational Data and Model Results. *Meteorol. Z.* 11, 379-393.
- Land, C. (1999) Untersuchungen zum globalen Spurenstofftransport mit dem Atmosphärenmodell ECHAM4.L39(DLR), *Ph.D. Thesis*, Fakultät für Physik, Ludwig-Maximilians-Universität München, Germany.
- Lauer, A., Dameris, M., Richter, A., Burrows, J.P. 2002: Tropospheric NO_2 Columns: A Comparison between Model and Retrieved Data from GOME Measurements. *Atmos. Chem. Phys.* 2, 67-78,
- Pickering, K.E., Yansen, W., Wei-Kuo, T., Price, C. Muller, J.-F. 1998: Vertical distributions of lightning NO_x for use in regional and global chemical transport models, *J. Geophys. Res.* 103, 31,203-31,216.
- Price, C., Rind, D. 1992: A simple lightning parameterization for calculating global lightning distributions, *J. Geophys. Res.* 97, 9919-9933.
- Price, C., Rind, D. 1993: What determines the cloud-to-ground lightning fraction in thunderstorms?, *Geophys. Res. Lett.* 20, 463-466.
- Roeckner, E., Arpe, K., Bengtsson, L., Christoph, M., Claussen, M., Dümenil, L., Esch, M., Giorgetta, M., Schlese, U., Schulzweida, U. 1996: The atmospheric general circulation model ECHAM4: Model description and simulation of present-day climate, *MPI-Report* 218, ISSN 0937-1060, Max-Planck-Institut für Meteorologie, Hamburg, Germany.
- Schoeberl, M.R., Morris, G.A., 2000. A Lagrangian simulation of supersonic and subsonic aircraft exhaust emissions, *J. Geophys. Res.* 105, 11,833-11,839.
- Shine, K.P., Bourqui, M.S., Forster, P.M. de, Hare, S.H.E., Langematz, U., et al.:2003 A Comparison of Model Simulated Trends in Stratospheric Temperatures. *Q. J. R. Met. Soc.* 129, 1565-1588.
- Stenke, A., Grewe, V., 2003: Impact of Ozone Mini-Holes on the Heterogeneous Destruction of Stratospheric Ozone. *Chemosphere* 50, 177-190.
- Steil, B., Dameris, M., Brühl, C., Crutzen, P.J., Grewe, V., et al. 1998: Development of a Chemistry Module for GCMs: First Results of a Multiannual Integration. *Annales Geophysicae* 16, 205-228.
- Tiedke, M. 1989: A comprehensive mass flux scheme for cumulus parameterization in large-scale models. *Mon. Wea. Rev.* 117, 1779-1800.

Impact of Aircraft NO_x Emissions: Effects of Changing the Flight Altitude

M. Gauss^{*}, I. Isaksen

Department of Geophysics, University of Oslo, Norway

V. Grewe

Institute for Atmospheric Physics, DLR Oberpfaffenhofen, Weßling, Germany

M. Köhler

Centre for Atmospheric Science, University of Cambridge, United Kingdom

D. Hauglustaine

LSCE, CNRS-CEA, Gif-sur-Yvette, France

D. Lee

Manchester Metropolitan University, Manchester, United Kingdom

Keywords: model study, aircraft NO_x emissions, impact on ozone, cruising altitude

ABSTRACT: Within the framework of the European TRADEOFF project, model studies have been performed to investigate the altitude dependence of the impact of NO_x emissions from aircraft on the chemical composition of the atmosphere. Here we present results for present (year 2000) conditions from two chemical transport models and two coupled climate-chemistry models. We consider five different aircraft emissions scenarios, which were developed for TRADEOFF. Effects of changes in flight altitude and concomitant changes in fuel consumption are investigated separately.

1 INTRODUCTION

Aircraft are operated at or near the boundary between the troposphere and the stratosphere, i.e. two atmospheric regions with highly different physical and chemical characteristics. E.g. wash-out processes of water-soluble species such as HNO₃ are common in the upper troposphere while they are negligible in the lower stratosphere. In the lower stratosphere, the high vertical stability allows pollutants to accumulate much more efficiently than in the troposphere. For these reasons lower emission heights of NO_x will result in shorter residence times of aircraft NO_x in the atmosphere. In addition, chemical processes controlling ozone depend on altitude. E.g. the importance of the ozone production cycle through oxidation of methane and other hydrocarbons decreases with height while ozone loss cycles involving NO_x become more efficient.

Therefore, it has been suggested that a change in flight altitude can reduce the impact of aircraft emissions. In this study, which was performed for the EU FP5 project TRADEOFF, we have used four models to calculate the aircraft impact for three different cases: 1) a standard case assuming normal cruise altitudes, 2) aircraft cruising 2000 ft higher, and 3) aircraft cruising 6000 ft lower. Due to the altitude dependence of combustions and fuel and efficiency both an increase and a decrease in flight altitude will result in higher NO_x emissions. By considering additional scenarios where the total NO_x emission is normalized to the base case, we have separated the effect of changing cruise altitudes and concomitant increases in fuel consumption.

In sections 2 and 3 the models and emission scenarios used in this study are briefly described, while the results are presented in section 4.

^{*} *Corresponding author:* Michael Gauss, University of Oslo, Department of Geosciences, PO 1022 Blindern, 0315 Oslo, Norway. Email: michael.gauss@geo.uio.no

2 THE MODELS AND EMISSION SCENARIOS USED IN THIS STUDY

Brief descriptions of the four models applied in this study (two chemistry transport models and two coupled climate chemistry models) are given in the following sections.

2.1 The TOMCAT model (CTM)

TOMCAT is a global chemistry transport model that integrates a tropospheric chemistry scheme on 31 hybrid pressure levels from the surface to 10 hPa. The chemistry scheme includes methane oxidation with additional reactions for ethane and propane degradation. The species are transported on a T21 horizontal grid (i.e. 5.6° by 5.6°) using an advection scheme that conserves second-order moments (Prather, 1986). A description of the model has been given by Law et al. (2000).

2.2 The UiO model (CTM)

The Oslo CTM-2 (**UiO**) is a comprehensive chemistry transport model that includes non-methane hydrocarbon chemistry and stratospheric O₃ production/destruction chemistry. The model is operated on a T21 resolution over 40 vertical levels between the surface and 10 hPa. The meteorology is taken from ECMWF forecast data for 1997. Advection is based on the Prather (1986) Second Order Moments scheme, and photodissociation coefficients are calculated on-line once every hour. Chemistry in aircraft plumes is included following Kraabøl et al. (2002). A recent description has been given by Gauss et al. (2003).

2.3 The DLR model (GCM)

ECHAM.L39(**DLR**)/CHEM (Hein et al., 2001) is based upon the German community climate model, ECHAM 4 (Roeckner et al., 1996; Land et al., 1999). It is operated on a T30 resolution over 39 vertical levels. The stratospheric/tropospheric chemistry scheme includes 37 species, grouped into families, which are transported using a semi-Lagrangian advection scheme. The chemistry computations have been configured to feedback on the dynamics of the coupled atmosphere/ocean model. In addition, the ECHAM.L39 model has been used to calculate contrail coverage and radiative forcing/temperature responses as described by Ponater et al. (2002).

2.4 The IPSL model (GCM)

LMDz-INCA (**IPSL**) couples the LMDz GCM on-line to the chemistry and aerosol model INCA. The version of the GCM used for this study is based on prescribed SSTs and relaxed winds towards ECMWF (re)analysis. The model includes 45 tracers and is operated for chemical computations on a regular grid (3.75° longitude × 2.5° latitude) over 19 vertical levels. It incorporates tropospheric O₃ chemistry from CH₄, NO_x and CO represented by 100 chemical reactions. At present, the chemical scheme does not feed back onto the dynamical part (Hauglustaine et al., in preparation, 2003).

3 AIRCRAFT EMISSION SCENARIOS

Aircraft emission scenarios were provided on a basic 1° × 1° latitude/longitude grid with a vertical resolution of 2,000 feet (610 m), evenly spaced. Emission calculations were made with the FAST model based upon the ANCAT/EC2 movements database (i.e. for 1991/1992). Thus, as in ANCAT, the data were for months 1, 4, 7 and 10 (January, April, July, October). Scenario 1 is the standard scenario for the year 2000 with 'normal' cruise altitudes. Scenarios 3 and 5 are for reduced (-6 kft) and enhanced (+2 kft) cruising altitude, respectively. A summary of the aircraft emission scenarios used in this study is given in Table 1. In the 'b' scenarios, changes in fuel consumption were taken into account, while the 'a' scenarios are normalized, i.e. the total fuel consumption is the same as in scenario 1.

The meteorology for the year 1995 was used for TOMCAT, while UiO used the year 2000. For the GCM simulations, an appropriate 1990's meteorology was used.

Table 1. Year 2000 aircraft emission scenarios used in this study.

Abbr.	Description	Fuel consumption	NO _x emission
0	no aircraft	-	-
1	Tradeoff standard case (standard flight altitudes)	151.9 Tg/year	0.59 Tg(N)/year
3a	Lower cruise altitude (-6000ft), normalized	151.9 Tg/year	0.59 Tg(N)/year
3b	Lower cruise altitude (-6000ft), enhanced	160.8 Tg/year	0.62 Tg(N)/year
5a	Higher cruise altitude (+2000ft), normalized	151.9 Tg/year	0.59 Tg(N)/year
5b	Higher cruise altitude (+2000ft), enhanced	151.2 Tg/year	0.60 Tg(N)/year

4 RESULTS

Figure 1 shows zonal-mean perturbations in the TRADEOFF base case scenario 1 with respect to the ‘no aircraft’ scenario. Both the TOMCAT and the UiO models calculate clear ozone enhancements due to aircraft in the upper troposphere and lower stratosphere in Northern mid- to high latitudes. The TOMCAT model has a higher peak perturbation at the North Pole. Also at other locations, especially in the tropical tropopause, perturbations are larger compared to the UiO simulation. Some of the difference can be explained by chemical processes in aircraft plumes in the UiO model, which have the effect of reducing the NO_x impact (see Kraabøl et al. 2002).

Figures 2 to 5 show zonal-mean perturbations in July 2000 due to changes in flight altitude, i.e. with respect to the standard scenario 1. The models agree in regard to the spatial pattern of changes. However, the magnitudes differ. In the lower stratosphere, the UiO decrease in ozone change due to a reduction in flight altitude is largest while the corresponding DLR decrease is smallest. The tropospheric ozone increase is largest in the UiO and TOMCAT models, while it is smallest in the IPSL model. For an increase in flight altitude (case 5) the three participating models calculate an increase, with UiO yielding the largest increase, but spatially more confined than in the other models.

The maximum zonal-mean ozone perturbation with respect to the ‘no aircraft’ case is plotted for the UiO model in Figure 6 as a function of season. The perturbations as well as the differences in perturbations are largest in the summer season, mainly as a result of solar radiation.

The separate effect of changes in total NO_x emissions resulting from a change in flight altitude is shown for the TOMCAT model in Figure 7. For the case of reduced flight altitude the increased total NO_x output results in an upward shift of the level of zero-change (see Figure 3). In the case of enhanced flight altitude, about one third of the increase in the ozone perturbation at the high Northern latitude tropopause is due to the enhanced NO_x output. In the UiO model (not shown) the importance of changes in total NO_x output is less important.

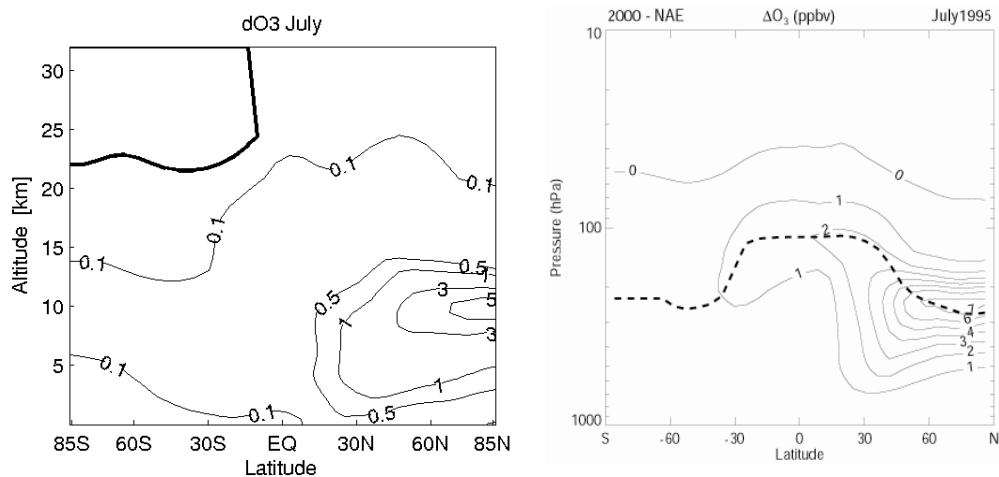


Figure 1: Zonal-mean ozone change due to aircraft in July 2000 (scenario 1 minus scenario 0) calculated by the UiO (left) and the TOMCAT (right) models. Unit: ppbv.

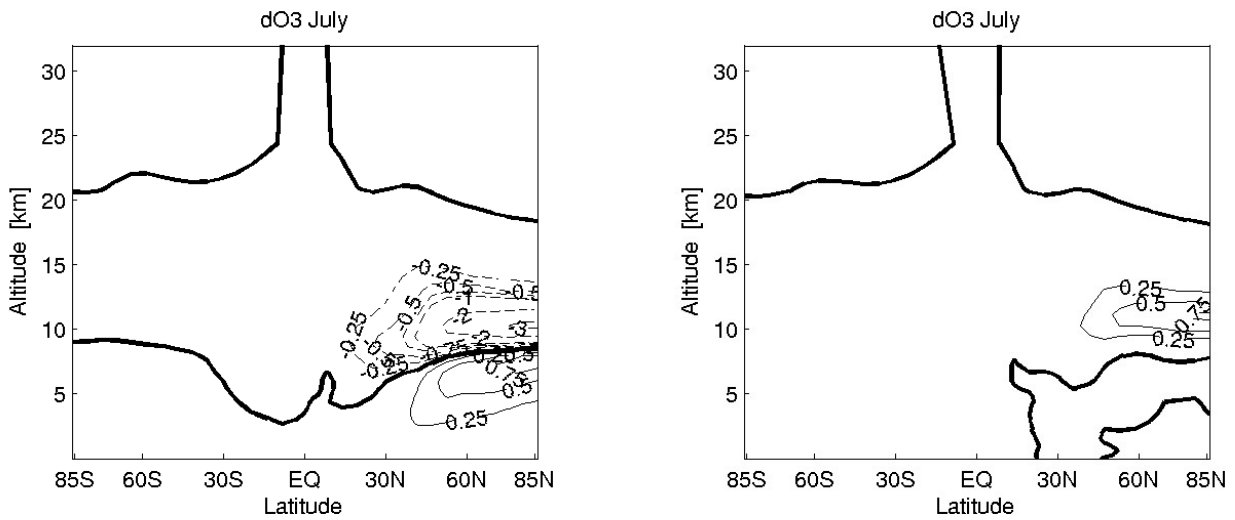


Figure 2: Effect of a change in cruise altitude on the aircraft-induced zonal-mean ozone perturbation in July 2000 calculated by the UiO model. Left panel: ‘3b minus 1’, i.e. the effect of reducing the flight altitude. Right panel: ‘5b minus 1’, i.e. the effect of increasing the flight altitude. Unit: ppbv.

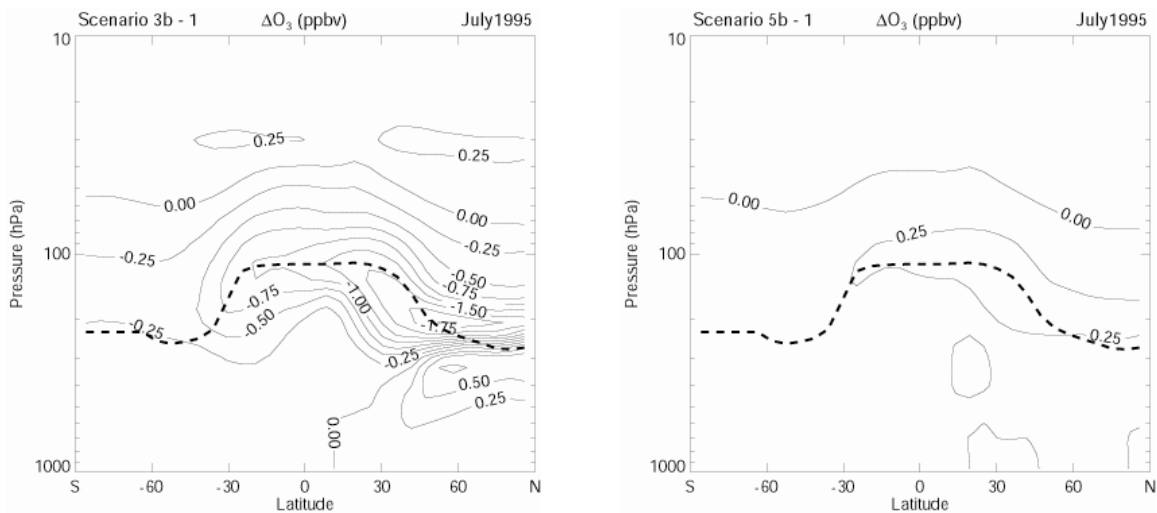


Figure 3: As Figure 2, but with results from the TOMCAT model. Left: ‘3b minus 1’, right: ‘5b minus 1’.

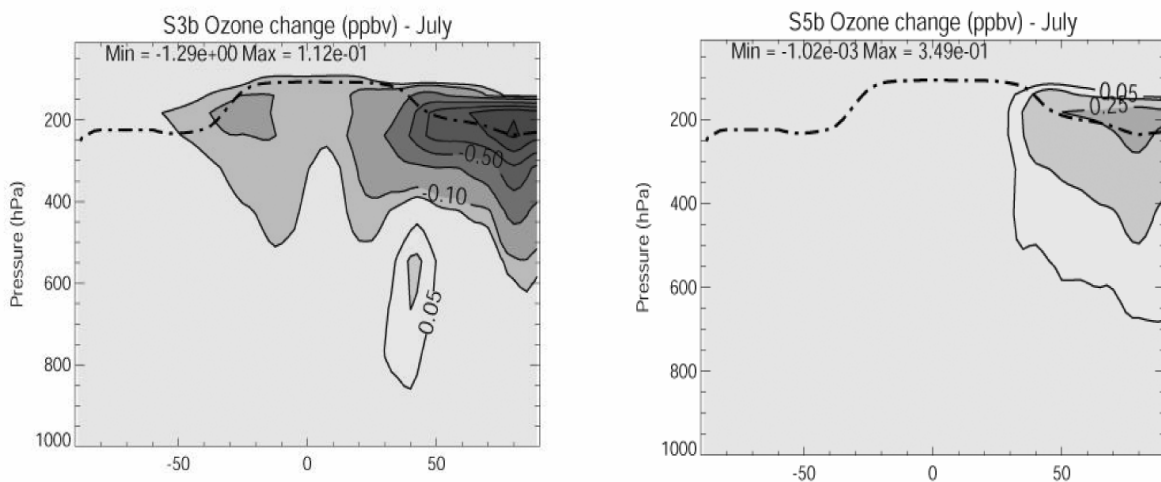


Figure 4: As Figure 2, but with results from the IPSL model. Left: ‘3b minus 1’, right: ‘5b minus 1’.

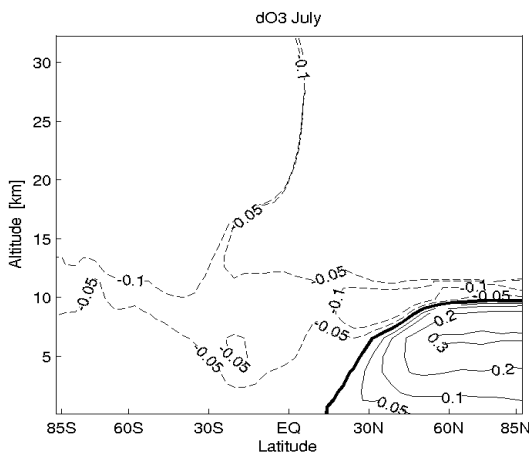


Figure 5 (left panel): ‘3b minus 1’, i.e. the effect of lowering the flight altitude, calculated by the DLR model. Unit: ppbv. The Figure has to be compared with the left panels of Figures 2, 3, and 4. (The DLR model did not participate in the case 5 study.)

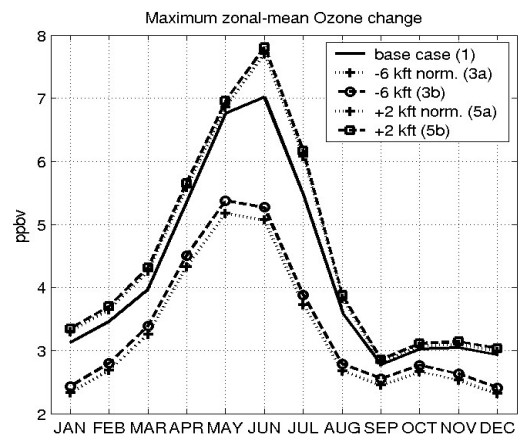


Figure 6 (right panel): Maximum zonal-mean ozone perturbation as a function of season, calculated by the UiO model for the different TRADEOFF scenarios considered in this study.

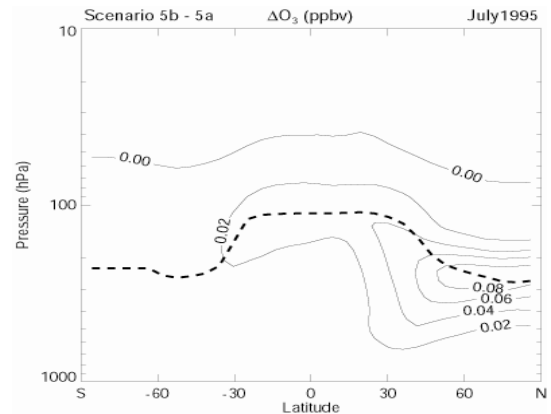
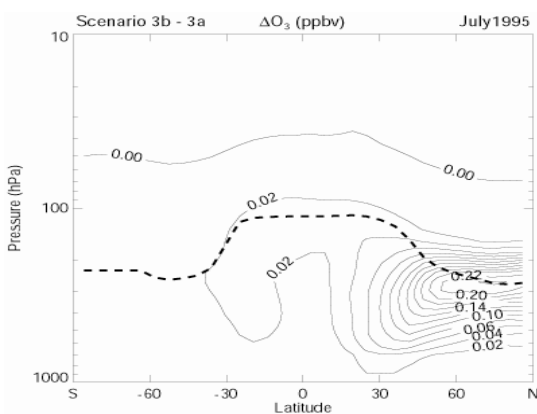


Figure 7: Effect of fuel consumption and increased NO_x output due to a change in flight altitude, calculated by the TOMCAT model. Left: ‘3b minus 3a’, right: ‘5b minus 5a’. Unit: ppbv.

Finally, Figure 8 shows the impact on the tropospheric and stratospheric ozone columns. The impact is strongly dependent on season. In case 3b there is a high degree of cancellation between the positive tropospheric change and the negative stratospheric change. However, the negative change dominates in most times of the year, especially at low latitudes, due to the weakening of the positive tropospheric change by wash-out processes. The contrary is true for case 5 where a positive change in the total ozone column is modelled at nearly all locations throughout the year, except for winter at high Northern latitudes.

5 CONCLUSIONS

This model study has investigated the impact of changes in flight altitude on aircraft-induced changes in ozone and has found the modifications in the ozone impact to be strongly dependent on height and season. A reduction in flight altitude is likely to result in a reduction of the aircraft-induced total ozone column increase in most times of the year.

It has to be stressed, however, that only changes in ozone were investigated. Other issues such as the impact on cirrus cloud formation are beyond the scope of this paper but will be addressed in

other publications of the TRADEOFF project. Also, radiative forcing calculations are being made based on the calculated perturbations in ozone and will be published in the near future.

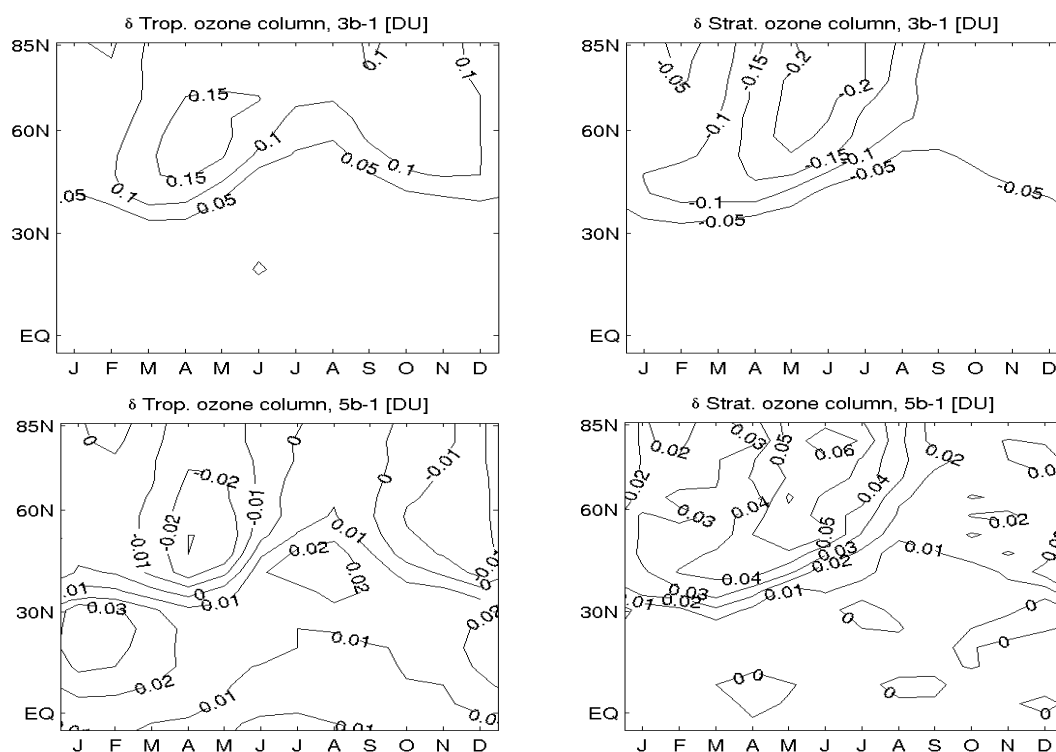


Figure 8: Ozone column change due to changes in flight altitude, calculated by the UiO model.

REFERENCES

- Gauss, M., I. S. A. Isaksen, S. Wong, and W.-C. Wang, 2003: Impact of H₂O emissions from cryoplanes and kerosene aircraft on the atmosphere, *J. Geophys. Res.*, 108(0), XXXX, doi:10.1029/2002JD002623.
- Hauglustaine, D., F. Hourdin, L. Jourdain, M.-A. Filiberti, S. Walters, J.-F. Lamarque, 2003: Interactive chemistry in the Laboratoire de Météorologie Dynamique General Circulation Model : description and background tropospheric chemistry evaluation, in preparation.
- Hein R., M. Dameris, C. Schnadt, C. Land, V. Grewe, I. Köhler, M. Ponater, R. Sausen, B. Steil, J. Landgraf, C. Brühl, 2001: Results of an interactively coupled atmospheric chemistry – general circulation model: Comparison with observations, *Annales Geophysicae* 19, 435-457.
- Kraabøl A.G., F. Stordal, T. Berntsen, and J. Sundet. 2002: Impacts of NO_x emissions from subsonic aircraft in a global 3-D CTM including plume processes. *J. Geophys. Res.*, 10.1029/2001JD001019.
- Land, C., M. Ponater, R. Sausen, E. Roeckner, 1999: The ECHAM4.L39(DLR) atmosphere GCM, Technical description and climatology, DLR-Forschungsbericht 1991-31, 45 pp., ISSN 1434-8454, Deutsches Zentrum für Luft- und Raumfahrt, Köln, Germany.
- Law et al. 2000: Comparison between global chemistry transport model results and measurements of ozone and water vapor by airbus in-service aircraft (MOZAIC) data. *J. Geophys. Res.* 105(D1), 1503-1525.
- Ponater, M., S. Marquart, and R. Sausen, 2002: Contrails in a comprehensive global climate model: parameterisation and radiative forcing results, *J. Geophys. Res.*, 107 (D13), 4164, doi:10.1029/2001JD000429.
- Prather M. J., 1986: Numerical advection by conservation of second-order moments. *J. Geophys. Res.* 91, 6671–6681.
- Roeckner, E., K. Arpe, L. Bengtsson, M. Christoph, M. Claussen, L. Dümenil, M. Esch, M. Giorgetta, U. Schlese, U. Schulzweida, 1996: The atmospheric general circulation model ECHAM4: Model description and simulation of present-day climate, MPI-Report 218, ISSN 0937-1060, Max-Planck-Institut für Meteorologie, Hamburg, Germany.

Improved Mass Fluxes in a Global Chemistry-Transport Model: Implications for Upper-Tropospheric Chemistry

E.W. Meijer*, P.F.J. van Velthoven, A. Segers, B. Bregman
Royal Netherlands Meteorological Institute, De Bilt, Netherlands

D. Brunner
Institute for Atmospheric and Climate Science, ETH Zurich, Switzerland

Keywords: atmospheric chemistry, modelling, hydroxyl, ozone, ozone production, aviation

ABSTRACT: A new method that solves the imbalance between the mass transport and the surface pressure tendency, a problem existing in most global chemistry-transport models, has been evaluated by comparing model results with observations of the age-of-air and trace gases, such as CO and ozone. Furthermore we have investigated the implications for upper-tropospheric chemistry by comparing the modelled and observed hydroxyl reaction rates. The model reproduced these rates reasonably well. On average the modelled ozone production was 20% larger than the observed one, if samples exposed to recent convection and lightning were excluded from the analysis.

1 INTRODUCTION

Calculating the impact of aircraft emissions is a particularly difficult task, since the largest fraction of these emissions occurs in the upper troposphere and lowermost stratosphere (UTLS). Global chemistry-transport models have great difficulties to simulate trace gas concentrations in this region that is characterised by strong cross-tropopause concentration gradients and mixing between the stratosphere and the troposphere. Thus model results for this region are very sensitive to errors in the mass fluxes. Yet it is near the tropopause where radiative forcing is most sensitive to the greenhouse gas perturbations.

One source of error in the mass fluxes arises from an imbalance between the surface pressure tendency and the vertically integrated mass change. This imbalance exists in most global chemistry-transport models (CTMs) and models have to be corrected for this. Previous corrections, proposed amongst others by Heimann and Keeling (1989), proved to be unsatisfactory in recent studies on ozone in the lowermost stratosphere (Bregman et al., 2001). However, recently one of us (Segers et al., 2002) has developed a new solution by calculating the mass fluxes from wind fields in a spherical harmonical form (divergence and vorticity) rather than in grid coordinates, thus mimicking the physics of the weather forecast model (ECMWF) as closely as possible.

In this study we evaluated how this solution for the mass-imbalance problem improved the ability of our CTM to simulate the composition and chemistry of the tropopause region, and consequently its ability to quantify the impact of aviation. First the new method was evaluated in more general terms by comparing model results with observed age-of-air and ozone concentrations. This will show that this new method gives significantly better simulated age-of-air and ozone fields than previous approaches (Bregman et al., 2003). Secondly we investigated modelled trace gas concentrations with observations from the TRADEOFF database (Brunner et al., 2003; website <http://www.lapeth.ethz.ch/~dominik/tradeoff/>). This database was especially compiled in order to evaluate the performance of global CTMs with respect to the effects of aviation on the atmospheric composition. In this work we restrict our results to comparison with the 5-minute averaged observations of the SONEX campaign that were included in this database. The completeness of the SONEX data set allows analysis of the implications of our new method for upper-tropospheric chemistry by comparing modelled chemical rates for hydroxyl (OH) with observed rates from the

* *Corresponding author:* Ernst Meijer, Royal Netherlands Meteorological Institute, P.O. Box 201, 3730 AE De Bilt, Netherlands. Email: meijere@knmi.nl

SONEX. We will show that there is a small but significant improvement in the modelling of the OH chemistry.

The next section gives a brief description of our CTM along with the old and new method of processing the mass fluxes, followed by a section stating the results for the age-of-air experiments and the comparison with observed ozone fields. These two sections (2 and 3) form basically a summary of the work of Bregman et al. (2003), except for the application of ECMWF 40-years reanalysis (ERA40) data in one of the age-of-air calculations. Section 4 describes the comparison with the SONEX observations, followed with a discussions section about the CTM's ability to quantify the effects of aviation on ozone. Section 6 summarises the conclusions.

2 MODEL DESCRIPTION

The global Tracer Model Version 3 (TM3) used in this study is a 3D-CTM, originally developed by Heimann (1995). TM3 is driven by 6-hourly meteorological fields from the forecast model of the European Centre for Medium-range Weather Forecasts (ECMWF). Detailed model descriptions can be found elsewhere (i.e. Houweling et al., 1998; Meijer et al., 2001; Bregman et al., 2001; and references therein).

In the old method the mass-imbalance was adjusted by adding small horizontal correction fluxes to the vertically integrated mass fluxes (details in Segers et al., 2002). This method introduced errors in the mass fluxes, since these corrections lack physical grounds. Furthermore, the mass fluxes were derived from the ECMWF spectral data, gridded on $1^{\circ}\times 1^{\circ}$ resolution, followed by interpolation to the desired grid, adding multiple interpolation errors.

The new processing method solves these problems. The mass balance is much better maintained by taking the divergence, vorticity, and the surface pressure into account. The new processing method is performed in the ECMWF spherical harmonics representation, thereby avoiding interpolation errors. Again, details can be found in Segers et al. (2002).

3 EVALUATION OF THE NEW MASS FLUX PROCESSING METHOD

We have performed two tracer studies to evaluate the new processing method for the mass fluxes: one age-of-air experiment to assess the large-scale effects and one ozone tracer experiment to assess the effects on shorter time-scales.

3.1 Age-of-air experiments

The age spectrum, formally developed by Hall and Plumb (1994), is the probability distribution function of transit times from a source region to the sample region. With a tracer model the age spectrum is directly obtained from a passive tracer simulation with a small source region where the mass mixing ratio is a delta-function in time. The response is then simply the age spectrum. In order to include all transit time-scales into the age-spectrum, the simulation was continued for 20 years, using ECMWF 1996 meteorology repeatedly. The results of the age-of-air simulations were compared with the age-of-air at 20 km altitude, derived from in situ observations of CO₂ (Andrews et al., 2001). Figure 1 shows the observed mean age-of-air at 20 km together with the zonally averaged simulated age-of-air. The results for the new method constitute a significant improvement with respect to the old method, but the mean age of air remains too young in the extra-tropics. An additional run based on ECMWF ERA40 meteorology with the aim to improve results further, revealed anomalously large vertical transport. The simulation was performed at a lower resolution and compared with ECMWF operational data (OD) at a similar resolution. In both cases the mass fluxes were processed with the new method.

3.2 Ozone tracer experiment

Next we performed simulations with TM3 containing an ozone tracer with prescribed loss rates from a 2-D stratospheric model (Pitari et al., 1993) constrained by an ozone climatology down to 50 hPa, scaled with total ozone column data from the Global Ozone Monitoring Experiment (GOME) for 1996. Figure 2 shows the seasonally averaged ozone mean mixing ratios $\pm 1\sigma$ from simulations

with the old and new mass fluxes, compared with data from MOZAIC flights routes Frankfurt–New York (FRA-NEW) and Vienna–Tokyo (VIE-TOK) (Marenco et al., 1998). The new mass flux processing method shows an excellent overall agreement. The large overestimate in all seasons, except for summer, has disappeared. Even in summer the observed variability is well represented by TM3.

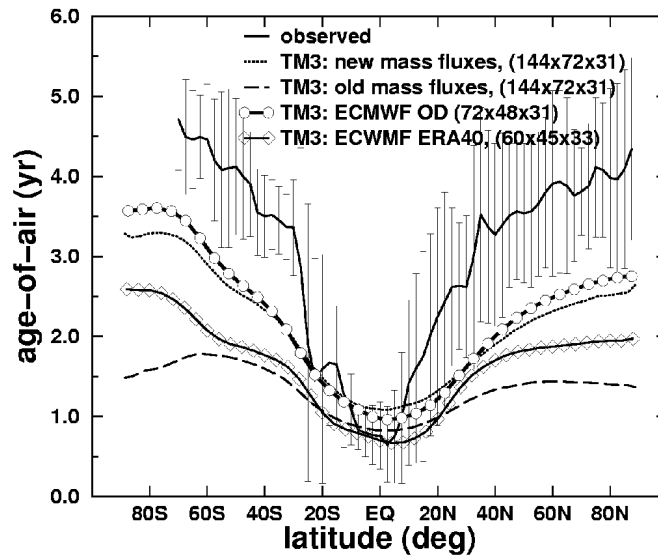


Figure 1. Simulated and observed mean age of air at 20 km altitude as a function of latitude.

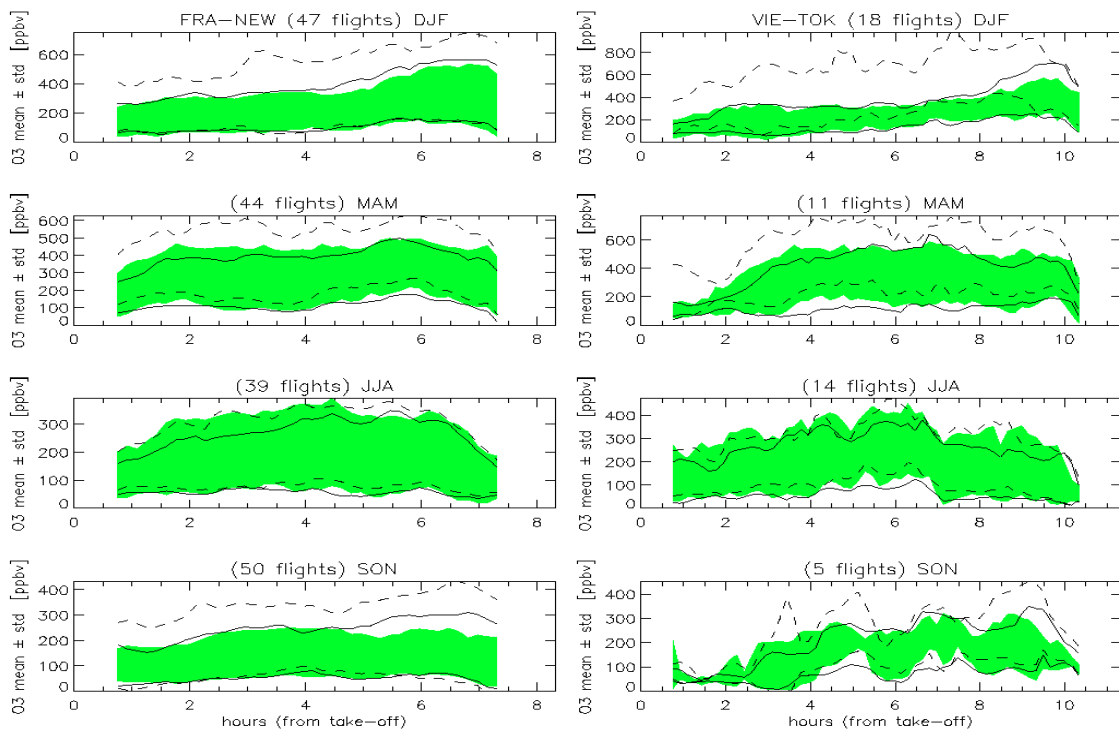


Figure 2. Seasonal mean ozone mixing ratios (ppbv) ($\pm 1\sigma$) as observed during the MOZAIC project (filled grey) and simulated with TM3 using the old (dashed) and new (solid) mass flux processing method.

4 IMPLICATIONS FOR UPPER-TROPOSPHERIC CHEMISTRY

Next we applied the full tropospheric chemistry version of TM3 and compared the results with the observations made during the SONEX campaign (Singh et al, 1999). These observations are very complete, allowing a detailed analysis of the chemistry and are representative for cruise flight conditions. The model output was interpolated to the positions of the 5-minute averaged observations. Table 1 summarises the results for the species CO, ozone, OH, and HO₂ by stating the correlations and overall biases (the relative mean difference) between observed and modelled (with the old and new method) concentrations. Differences in the mass fluxes affect primarily the concentrations of the long-lived tracers, such as CO and ozone, which ultimately cause changes in concentrations of OH and HO₂. The correlations for all tracers, except for CO, are reasonably good (>0.6) regardless of the mass flux processing method. The biases on the other hand are quite large. Nevertheless the overall bias improves for CO and ozone, and OH with the new method. The bias for HO₂ is not affected significantly. Considering the central role of OH in driving tropospheric chemistry, the new method has a positive effect on chemistry.

Table 1. Correlations and overall biases (%) between observed and modelled (using the old and new mass flux processing methods) trace gas concentrations of the SONEX campaign.

	O ₃		CO		OH		HO ₂	
Method	Old	New	Old	New	Old	New	Old	New
Correlation	0.72	0.68	0.53	0.56	0.57	0.69	0.76	0.78
Bias	33%	29%	35%	15%	-32%	-25%	27%	29%

Next we investigated the upper-tropospheric chemistry in more detail by comparing the modelled with the observed reaction rates that produce or destroy OH. Again the comparison occurred by interpolation to the locations of the observations. Figure 3 shows the modelled and observed rates, averaged over all samples between 150 and 300 hPa. The most important production and loss reactions are NO+HO₂? NO₂+OH and CO+OH? CO₂+H, respectively, which were underestimated by TM3. Other large differences between model and observations exist, but do not contribute significantly to the OH concentration (i.e. the photolysis of H₂O₂). Furthermore the differences between the results with the old and new method are small.

However, removal of the samples that were influenced by continental convection and/or lightning improved the comparison considerably for the simulation based on the new mass method (see Fig. 4). Elevated NO_x/NO_y concentration (>0.5) ratios and NO_y concentrations (>500 pptv) over large spatial scales (>20 km) were interpreted as resulting from the continental boundary layer or recent lightning activity (Jaeglé et al., 2000 and references therein). In our analysis about 30% of the samples fitted this criterion. Without these samples the model results for the new method are in much better agreement with the observations. Furthermore, application of the new mass flux processing method improved the model results for all considered chemical rates.

5 DISCUSSION

Previously, we investigated the contributions of different NO_x sources to the composition of the North-Atlantic flight corridor (Meijer et al., 2000). This study demonstrated that the aircraft contributions to the total NO_x concentration could be quantified for moderate cases without recent influence from convection or lightning. Ozone perturbations could not be attributed to specific sources due to the large natural variability of this tracer in the tropopause region.

Taking into account that the ozone production is approximately equal to the rate of reaction NO+HO₂? NO₂+OH, there is evidence that TM3 with the new mass flux processing method is now capable to calculate the ozone perturbation due to aviation with a moderate accuracy for cases without recent influence from convection and lightning. The modelled rate of this reaction was

about 20% higher than the observed rate for all SONEX observations without convective/lightning influence (and about 30% lower for all points).

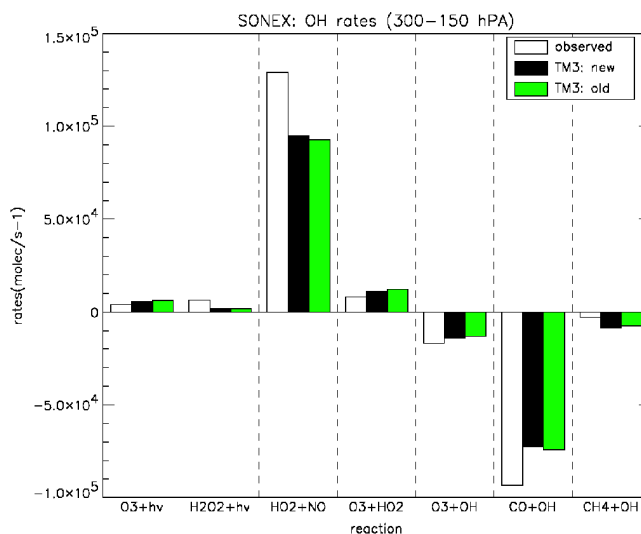


Figure 3. The most important production and loss rates of OH, averaged for all observation points between 150 and 300 hPa compared with modelled rates, using the new and old method. The model results are also averages of model output that interpolated to the observation points.

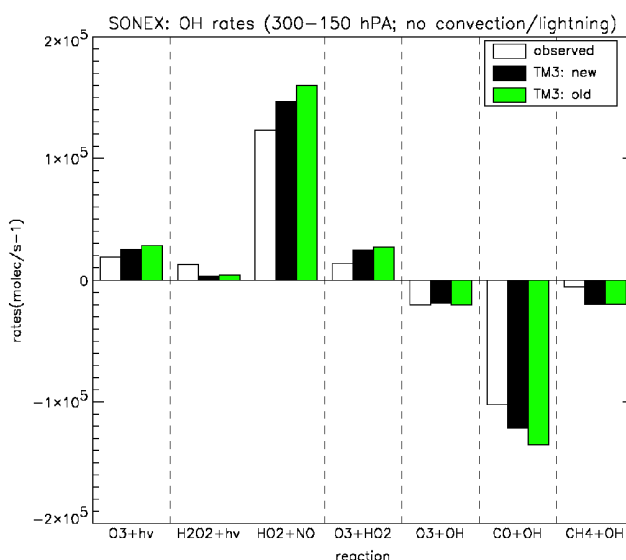


Figure 4. As in Figure 3, but averaged over samples not influenced recently by convection and lightning (samples with $\text{NO}_x/\text{NO}_y > 0.5$ and $\text{NO}_y > 500$ pptv).

6 CONCLUSIONS

We have investigated a new method for processing the mass fluxes for the TM3 model that solves earlier reported mass-imbalance problems. The model improvement was demonstrated by the comparison of age-of-air calculations and ozone tracer simulations with observations. Application of ERA40 data of ECMWF revealed anomalously large vertical circulation in this data set.

The new method improves the model results for long-lived tracers, such as ozone and CO, in the upper troposphere and lowermost stratosphere. This ultimately has a positive effect on the OH concentration, as indicated by point-by-point comparison with SONEX observations. Analysis of the important chemical rates that produce or destroy OH showed that TM3 is capable of simulating the upper-tropospheric chemistry well, if samples exposed to recent convection or lightning were

excluded from the analysis. The approximate ozone production from the simulations was 20% higher than the observed. This is an indication that the model is also capable to calculate the aircraft-induced ozone perturbations for these cases, given the fact that the model simulates aircraft-induced NO_x perturbations reasonably well.

With all samples included, the approximate ozone production from the simulations was 30% lower than observed, and there was a small improvement with the new mass flux processing method. Application of the on-line convective mass fluxes from ECMWF ERA40 might improve the model results further (Olivié, submitted). This is now under investigation.

REFERENCES

- Andrews, A., Boering, K., Daube, B., Wofsy, S., Loewenstein, M., Jost, H., Podolske, J., Webster, C., Herman, R., Scott, D., Flesh, G., Moyer, E., Elkins, J., Dutton, G., Hurst, D., Moore, F., Ray, E., Romanschkin, P., and Strahan, S.: Mean ages of stratospheric air derived from in situ observations of CO_2 , CH_4 , and N_2O , *J. Geophys. Res.*, 106, 32295-32314, 2001.
- Bregman A., Krol, M., Teyssède, H., Norton, W., Chipperfield, M., Pitari, G., Sundet, J., and Lelieveld, J.: Chemistry-transport model comparison with ozone observations in the midlatitude lowermost stratosphere, *J. Geophys. Res.*, 106, 17479-17496, 2001.
- Bregman A., Segers, A., Krol M., Meijer E., and van Velthoven, P.: On the use of mass-conserving wind fields in chemistry-transport models, *Atmos. Chem. Phys.*, 3, 447-457, 2003.
- Brunner D., Staehelin J., Rogers, H.L., Köhler, M.O., Pyle, J.A., Hauglustaine, D., Jourdain, L., Berntsen, T.K., Gauss, M., Isaksen, I.S.A., Meijer, E., van Velthoven, P., Pitari, G., Mancini, E., Grewe, V., and Sausen, R.: An evaluation of the performance of chemistry transport models by comparison with research aircraft observations. Part 1: Concepts and overall model performance, *Atmos. Chem. Phys. Discuss.*, 3, 2499-2545, 2003.
- Hall, T. and Plumb, R.: Age as a diagnostic of stratospheric transport, *J. Geophys. Res.*, 99, 1059-1070, 1994.
- Heimann, M.: The global atmospheric tracer model TM2: DKRZ TM2 model documentation, Techn. Rep., 10, Max-Planck-Inst. für Meteorol., Hamburg, Germany, 1995.
- Heimann, M. and Keeling, C.: A three-dimensional model of atmospheric CO_2 transport based on observed winds, 2: Model description and simulated tracer experiments, *Geophys. Mon.*, 55, 237-257, 1989.
- Houweling, S. M., Dentener, F., and Lelieveld, J.: The impact of nonmethane hydrocarbon compounds on tropospheric chemistry, *J. Geophys. Res.*, 103, 10,673-10,696, 1998.
- Jaeglé, L., Jacob, D.L., Brune, W.H., Faloon, J., Tan, D., Heikes, G., Kondo, Y., Sachse, G.W., Anderson B., Gregory, G.L., Singh, H.B., Poeschel, R., Ferry, G., Blake, D.R., and Shetter E.R., Photochemistry of HO_x in the upper troposphere at northern midlatitudes, *J. Geophys. Res.* 105, 3833-3850, 2000.
- Marengo, A., Thouret, V., Nedelc, P., Smit, H. Helten, M., Kley D., Karcher, F., Simon, P., Law, K., Pyle, J., Poschmann, G., von Wrede, R., Hume, C., and Cook, T.: Measurements of ozone and water vapor by Airbus in-service aircraft: the MOZAIC airborne program, an overview: *J. Geophys. Res.*, 103, 25631-25642, 1998.
- Meijer E.W., van Velthoven, P.F.J., Thompson, A.M., Pfister, L., Schlager, H., Schulte, P., and Kelder H.: Model calculations of the impact of NO_x from air traffic, lightning, and surface emissions, compared with measurements, *J. Geophys. Res.* 105, 3877-3892, 2000.
- Meijer, E.W., van Velthoven, P.F.J., Brunner, D.W., Huntrieser H., and Kelder, H.: Improvement and evaluation of the parameterisation of nitrogen oxide production by lightning, *Phys. Chem. of the Earth* 26, 557-583, 2001.
- Olivié, D., van Velthoven, P.F.J., Beljaars, A.C.M., and Kelder, H.M.: Comparison between archived and off-line diagnosed convective mass fluxes in the chemistry transport model TM3, submitted to *J. Geophys. Res.*, 2003.
- Pitari, G., Rizi, V., Ricciardulli, L., and Visconti, G.: High-speed civil transport impact: Role of sulfate, nitric acid trihydrate, and ice aerosols studied with a two-dimensional model including aerosol physics, *J. Geophys. Res.* 98, 23141-23164, 1993.
- Segers, A., van Velthoven P., Bregman, B. and Krol, M.: On the computation of mass fluxes for Eulerian transport models from spectral meteorological fields, in: Proc. of the 2002 Intern. Conf. on Computational Science, Lecture Notes in Computer Science (LNCS), Springer Verlag, 1769-1770, 2002.
- Singh, H.B., Thompson, A.M., and Schlager, H.: SONEX airborne mission and coordinated POLINAT-2 activity: overview and accomplishments, *Geophys. Res. Lett.*, 26, 3053-3056, 1999.

Activities of NASA's Global Modeling Initiative (GMI) in the Assessment of Subsonic Aircraft Impact

J. M. Rodriguez*

Rosenstiel School of Marine and Atmospheric Science, University of Miami, Miami, FL., USA

J. A. Logan

Harvard University, Cambridge, MA, USA

D. A. Rotman, D. J. Bergmann

Lawrence Livermore National Laboratory, Livermore, CA

S. L. Baughcum

Boeing Company, Seattle, WA, USA

R. R. Friedl

Jet Propulsion Laboratory, Pasadena, CA, USA

D. E. Anderson

NASA Headquarters, Washington, DC USA

Keywords: Aircraft, impact, ozone, troposphere

ABSTRACT: The Intergovernmental Panel on Climate Change (Penner et al., 1999) estimated a peak increase in ozone ranging from 7-12 ppbv (zonal and annual average, and relative to a baseline with no aircraft), due to the subsonic aircraft in the year 2015, corresponding to aircraft emissions of 1.3 TgN/year. This range of values presumably reflects differences in model input (e.g., chemical mechanism, ground emission fluxes, and meteorological fields), and algorithms. The model implemented by the Global Modeling Initiative allows testing the impact of individual model components on the assessment calculations. We present results of the impact of doubling the 1995 aircraft emissions of NO_x, corresponding to an extra 0.56 TgN/year, utilizing meteorological data from NASA's Data Assimilation Office (DAO), the Goddard Institute for Space Studies (GISS), and the Middle Atmosphere Community Climate Model, version 3 (MACCM3). Comparison of results to observations can be used to assess the model performance. Peak ozone perturbations ranging from 1.7 to 2.2 ppbv of ozone are calculated using the different fields. These correspond to increases in total tropospheric ozone ranging from 3.3 to 4.1 Tg/O₃. These perturbations are consistent with the IPCC results, due to the difference in aircraft emissions. However, the range of values calculated is much smaller than in IPCC.

1 INTRODUCTION

The emission of trace gases and particles by subsonic aircraft can lead to changes in the chemical composition of the atmosphere which in turn could affect Earth's radiative balance. Concern has been raised about the impact of emission of greenhouse gases (CO₂), ozone precursors (NO_x, non-methane hydrocarbons), soot, and sulfate particles, as well as the direct and indirect effects of contrail formation, modification of cirrus cloud coverage and properties, and changes in the lifetime of greenhouse gases such as CH₄ (Penner et al., 1999). In particular, the potential increase in upper tropospheric NO_x from aircraft emissions can lead to increases in O₃ production and abundances in the corridor region. At the same time, increases in NO_x can also lead to decreased OH abundances and longer lifetimes for methane.

The latest assessment of these effects by IPCC (Penner et al., 1999) indicated ozone increases of 7-12 ppbv in the upper troposphere, and a decrease in the methane lifetime of 1.6-2.9%, due to NO_x

* Corresponding author: Jose M. Rodriguez, RSMAS/MAC, University of Miami, 4600 Rickenbacker Causeway, Miami, FL 33149 USA. Email: jrodriguez@rsmas.miami.edu

aircraft emissions of 1.3 TgN/year for 2015 conditions. The almost factor of 2 range in the estimated impacts reflect the different algorithms, chemical mechanisms, ground emission fluxes, lightning contribution, meteorological fields, and assumptions in the models utilized. Because each of these models includes a large number of processes, it is difficult to ascertain the reason for the above variability.

We present here preliminary results from calculations carried out by NASA's Global Modeling Initiative (GMI) of the impact of doubling the 1996 aircraft NO_x emissions, while keeping all model inputs and components constant except for the meteorological fields. Our results indicate a smaller variability in the ozone calculated ozone perturbations, with magnitudes consistent with previous assessments.

2 DESCRIPTION OF CALCULATIONS

We utilize the GMI chemistry-transport model (Rotman et al., 2001), modified for tropospheric calculations. The modular architecture of this model allows for simulations that keep all model components the same except for a chosen one, thus permitting a more accurate assessment of the impact of a particular process. For the simulations presented here, we have chosen to change the input meteorological data. For this, we have utilized three set of meteorological fields: a) assimilated data for 1996 conditions, provided by the NASA/Goddard Data Assimilation Office (DAO), but utilized as a "perpetual" year; b) meteorological data from the Goddard Institute for Space Studies (GISS) general circulation model, version II' (D. Rind, private communication; c) meteorological data from the Middle Atmosphere Community Climate Model, version (MACCM3).

Although these fields extend from the boundary later to the mesosphere, only tropospheric chemistry is included in these calculations. The tropospheric chemical mechanism is the same as that utilized in Harvard's GEOS-CHEM model (Bey et al., 2001), and the numerical solver for the chemistry is the SMVGEAR-II (Jacobson, 1995). Stratospheric ozone fluxes are simulated by incorporating an ozone synthetic tracer (SYNOZ; MacLinden et al., 2000), with a source in the tropical stratosphere corresponding to 475 TgO₃/year. This approach guarantees the same total flux of ozone through the tropopause for all simulations, although the spatial distribution will depend on the meteorological field. A similar approach was utilized for NO_x fluxes from the stratosphere. The tropopause was diagnosed to occur at SYNOZ concentrations of approximately 150 ppbv.

Aircraft emissions were interpolated to the year 1995 based on previously published inventories of aircraft emissions for scheduled flights for 1992 (Baughcum, et al., 1996), 1999 (Sutkus, et al., 2001), and projected to 2015 (Baughcum, et al., 1998), as well as unscheduled traffic (Mortlock, et al., 1998). Annual emissions of NO_x by aircraft were 0.56 TgN/year. Other natural and anthropogenic surface emissions were updated and scaled from those used in the GEOS-CHEM model (Bey et al., 2000). Emission of NO_x by lightning was fixed at 5 TgN/year for all three simulations. The spatial distribution was also fixed for all simulations, using the parameterization of Price and Rind (1992), with corrections to the vertical distribution (Pickering, private communication).

Simulations were carried out for a "base" scenario approximating 1995-1996 conditions, and one for which the aircraft simulations described above were doubled. Both baseline and perturbation calculations were carried for 18 model years, of which the last 12 months were analyzed. Since there were no other changes in other boundary conditions or meteorology in the double aircraft scenario, the results presented here are not to be interpreted as a "future" prediction, but rather as a study of the sensitivity of the results to increases in aircraft emissions using different meteorological inputs.

3 RESULTS AND CONCLUSIONS

3.1 Validation of baseline calculations

The baseline results have been compared to ozone-sonde climatologies (Logan, 1999), CO and O₃ observations at surface sites, radionuclide observations, and data from different tropospheric

aircraft campaigns. These and other validation efforts are being summarized in a series of manuscripts in preparation. The ultimate purpose of these comparisons is to develop a methodology to document and assess model performance when utilizing different meteorological (and other) inputs. Ideally, such evaluation of model performance would lead to the selection of a series of inputs that best fit data. However, the current evaluation does not clearly point to a preferred set of meteorological input in the context of agreement with observations. Thus, the results presented below can be seen as reflecting the existing uncertainty due to the different meteorological assumptions represented by the fields adopted.

An example of how the model results compare with observations is presented in Figure 1, where calculated ozone mixing ratios at three tropospheric levels are shown along with the ozone sonde climatology, for stations situated in the Northern Hemisphere at high to mid-latitudes. In this particular instance, only the DAO fields seem to compare reasonably to the observations at 300 and 500 hPa, while all three fields perform reasonably well at lower altitudes. Part of the disagreement at high altitudes may reflect the limitations of the SYNOZ approach in reproducing the spatial distribution of the stratospheric ozone flux. It would be tempting to prefer the DAO results to those of other fields when predicting aircraft perturbations. However, such decision cannot be based on a limited comparison. For example, the calculated lifetimes of CH_3CCl_3 against removal by tropospheric OH are 4.9 years for DAO and MACCM3 fields, and 5.5 years for GISS fields, which points to the GISS fields as performing better under this criterion. Further work is needed by the modeling community to identify measurements that best constrain model results in the context of a particular assessment.

3.2 Aircraft perturbation results

Our calculated perturbations to NO_x and O_3 are shown in Figures 2. Peak changes in NO_x mixing ratios for the month of July range from about 20 pptv using DAO meteorological fields, to about 45 pptv in calculations using MACCM3 fields. As seen in Figure 2 the NO_x accumulation between the three meteorological fields is strikingly different, although the changes in ozone (right column) are more similar. These should be compared to changes ranging from 60–150 pptv calculated by the models participating in the IPCC assessment, for 2015 conditions (Penner et al., 1999). Although the relative spread in NO_x perturbations is similar for both IPCC and our calculations, our results are smaller than those of IPCC. This can be easily understood if we compare the increase in aircraft emissions in both instances, 1.3 Tg/year for IPCC vs. 0.56 TgN/year in our calculations.

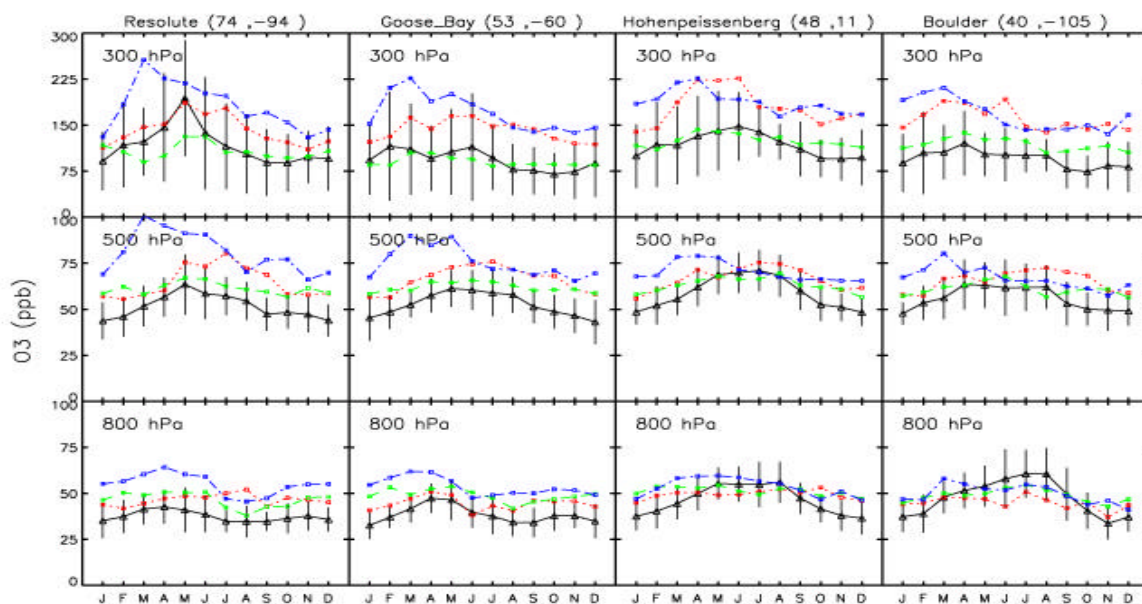


Figure 1. Calculated ozone mixing ratios utilizing DAO (green line), GISS (blue line), and MACCM3 (red line) meteorological fields. Climatological data from ozonesondes (Logan, 1999) with their standard deviation are also shown for comparison.

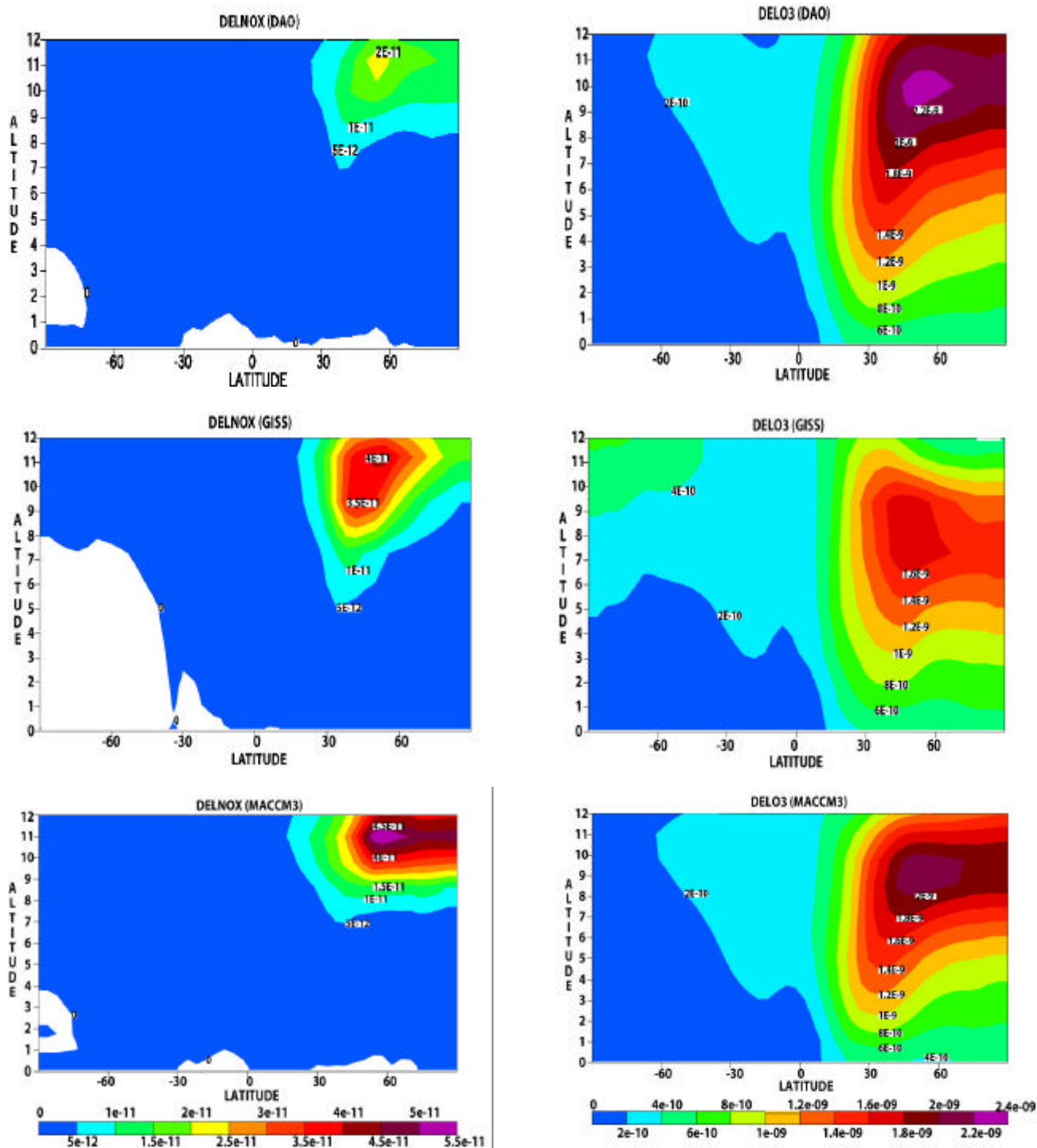


Figure 2 Calculated change in NO_x (left column) and O₃ mixing ratios using meteorological fields from the DAO, GISS, and MACCM3 models. The NO_x calculations are for the month of July, while the O₃ results denote annual averages. The altitude scale has been calculated from a standard atmosphere

In contrast to the NO_x results, the ozone perturbations shown in Figure 2 exhibit a much smaller variability in the magnitude of the perturbation. Peak ozone perturbations range from 1.8 ppbv using GISS fields to 2.2 ppbv with DAO fields. These peak perturbations are consistent with the lower limit of the perturbations calculated by IPCC, i.e., 7–12 ppbv, were we to assume simple scaling of the perturbation with NO_x emissions by aircraft. A better comparison to IPCC results is obtained if we examine the total increases in tropospheric ozone, which are: 4.1, 3.3 and 3.7 Tg/O₃ for calculations utilizing DAO, GISS, and MACCM3 fields, respectively. The IPCC report showed increases in tropospheric O₃ ranging from about 4–8 Tg/O₃ for the 1992 scenario, whose aircraft emission (0.5 TgN/year) is similar to our adopted increase. Thus, our calculated ozone

perturbations are consistent with the lower range of the IPCC results. We note, however, that the range in ozone perturbations using three meteorological fields is smaller than that obtained by the IPCC models.

Our simulations also obtained increases in tropospheric OH. This led to reductions in the atmospheric lifetime of methane by 0.95% for DAO fields, 0.76% for GISS fields, and 1 % for MACCM3. These reductions are somewhat smaller than those calculated by IPCC for the 1992 scenario, which ranged from 1.2 to 1.4%.

For convenience, we summarize our results in Table 1, and compare them to those shown in the IPCC report, whenever possible.

Table 1: Comparison of GMI Simulations with those of IPCC*

	IPCC	GMI-DAO	GMI-GISS	GMI-MACCM3
ΔNO_x Peak July zonal average [pptv]	60-150	20	40	45
ΔNO_x Tropospheric total, July [Tg N]		0.0021	0.0033	0.0027
ΔO_3 Peak annual, zonal average [ppbv]	7-12	2.2	1.6	2.0
ΔO_3 Tropospheric total, annual average [Tg O_3]	4-8 ^a			
	9-18	4.1	3.3	3.7
ΔCH_4 lifetime [percent]	-1.2 to -1.4 ^a	-0.95	-0.76	-1.0
	-1.6 to -2.6			

*IPCC results are shown for the 2015 simulations, as in Figure 1 and 2, corresponding to a 1.27 TgN/year aircraft source of NO_x . For comparison, we also include IPCC results (denoted by ^a) corresponding to 1992 simulations with 0.5 TgN/year. The results of the 1992 IPCC simulations are more comparable to ours, since the aircraft NO_x sources are similar. However, the spatial distribution of the perturbations were not reported in IPCC for 1992.

3.3 Conclusions

We have presented simulations of the “chemical” impact of subsonic aircraft NO_x on the chemical composition of the troposphere, with particular emphasis on the increases in ozone concentrations and decreases in methane lifetimes. Our model simulations differ only in the adopted meteorological fields. Other model components are kept constant. The results are consistent (although slightly on the low side) of the results presented in the IPCC assessment (Penner et al., 1999), but the range of results is much smaller than that obtained from the different models participating in IPCC.

The differences in model results in assessment of aircraft perturbations have justly been ascribed to the difference in model inputs and approaches. Although not explicitly proven or stated, differences in the calculated or adopted meteorological fields are sometimes suspected to be one of the main causes of these variabilities. The results presented here indicate that this is not necessarily the case, particularly for the extremely buffered chemical processes responsible for producing ozone in the upper troposphere. In a manner similar to the above exercise, GMI can be used as a testbed for different model components to discern which model inputs/components induce the largest uncertainty in the results, thus focusing efforts in narrowing assessment uncertainties.

REFERENCES

- Baughcum, S. L., et al., 1996: *Scheduled Civil Aircraft Emission Inventories for 1992: Database Development and Analysis*, NASA Contractor Report 4700, Washington, DC.
- Baughcum, S. L., et al., 1998: *Scheduled Civil Aircraft mission Inventories Projected for 2015: Database Development and A nalysis*, NASA/CR-1998- 207638
- Bey, I. et al., 2001: Global modeling of tropospheric chemistry with assimilated meteorology: Model description and evaluation, *J. Geophys. Res.*, *106*, 23,073-23,096.
- Logan, J. A., 1999: An analysis of ozonesonde data for the troposphere: Recommendations for testing models, *J. Geophys. Res.*, *104*, 16151-16170.
- McLinden, C. A., et al. 2000: Stratospheric ozone in 3-D models: A simple chemistry and the cross-tropopause flux, *J. Geophys. Res.*, *105*, 14653-14665.

- Mortlock, A. M., and R. Van Alstyne, 1998: *Military, Charter, Unreported Domestic Traffic and General Aviation: 1976, 1984, 1992, and 2015 Emission Scenarios*, NASA CR- 1998-207639.
- Penner, J. E., et al. (ed) 1999: *Aviation and the Global Atmosphere: A Special Report of IPCC Working Groups I and II*. Cambridge University Press, 1999.
- Price, C., and D. Rind, 1992: A simple lightning parameterization for calculating global lightning distribution, *J. Geophys. Res.*, *97*, 9919-9933.
- Rotman, D. A., et al, 2001: Global Modeling Initiative Assessment model: Model description, integration, and testing of the transport shell. *J. Geophys. Res.*, *106*, 1669-1691.
- Sutkus, D. J., S. L. Baughcum, and D. P. DuBois, 2001: Scheduled Civil Aircraft Emission Inventories for 1999: Database Development and Analysis, NASA/CR-2001-211216.

Parametric Study of Potential Effects of Aircraft Emissions on Stratospheric Ozone

D.J. Wuebbles*, M. Dutta, K.O. Patten

Department of Atmospheric Sciences, University of Illinois at Urbana Champaign, Urbana, Illinois, USA

S.L. Baughcum

The Boeing Company, Seattle, Washington, USA

Keywords: stratospheric ozone, aircraft emissions, nitrogen oxides, atmospheric processes

ABSTRACT: There has been much consideration over the last decade of the potential impacts on the environment of projected fleets of passenger jets with cruise altitudes in the lower stratosphere. Existing ozone-impact studies have not fully analyzed the potential extent of possible flight and emissions criteria for such aircraft. In addition, recent improvements to our understanding of atmospheric chemical and physical processes would also affect earlier conclusions. In this study, a series of parametric studies are done with our recently updated state-of-the-art numerical zonally-averaged model of atmospheric chemistry and physics to examine potential effects of emissions from hypothetical fleets of stratospheric-flying aircraft on stratospheric ozone. The new studies examine how the modeling of aircraft effects has changed since the 1999 IPCC assessment (Aviation and the Global Atmosphere).

1 INTRODUCTION

The IPCC has assessed the potential effects that aviation, both subsonic and supersonic, have had in the past and may have in the future on stratospheric ozone depletion and climate change (Penner, et al., 1999). For NASA, Kawa, et al. (1999) assessed the stratospheric impacts of high flying aircraft. In addition to the fleets of the supersonic High Speed Civil Transport (HSCT) aircraft studied in the 1990s, lately other aircraft have been under consideration that might fly faster and higher than current commercial aircraft. So, evaluation of the potential effects of such aircraft on the global environment remains valuable. In particular, it should be noted that existing ozone-impact studies have not fully analyzed the potential extent of possible flight and emissions criteria for such aircraft. In this study, we calculate the ozone impact of a range of parametric scenarios in which cruise altitudes and nitrogen oxides (NO_x) emission levels are varied systematically. This study has focussed on aircraft that would cruise at altitudes primarily in the upper troposphere/lower stratosphere region; this includes the faster commercial aircraft that would primarily be used for intercontinental flights longer than 2500 nautical miles and a small fleet of Supersonic Business Jets (SSBJs).

2 METHODOLOGY

2.1 Model Description

The UIUC two-dimensional (2D) chemical-radiative-transport model is a zonally-averaged model of the chemistry and physics of the global atmosphere. The model is often used to study human related and natural forcings on the troposphere and stratosphere, but, because it is zonally-averaged, the analysis of tropospheric processes is limited. The model determines the atmospheric distributions of 78 chemically active atmospheric trace constituents. In addition to 56 photolytic reactions, the model incorporates 161 thermal reactions in the chemical mechanism, including heterogeneous

* *Corresponding author:* Donald J. Wuebbles, Department of Atmospheric Sciences, University of Illinois at Urbana Champaign, 105 S. Gregory St., Urbana IL-61801, USA. Email: wuebbles@atmos.uiuc.edu

reactions (e.g., see Wuebbles et al., 2001, or Wei et al., 2001). Reaction rates and photolysis cross-sections in the model are based on recommendations from NASA's Chemical Kinetics Review Panel (e.g., DeMore et al., 1997; Sander et al., 2000).

In the last year, there have been substantial improvements made to the model. Enhancements to treatments of atmospheric chemical processes include updating the nitrogen pentoxide (N_2O_5) and chlorine nitrate (ClONO_2) hydrolysis and several hypochlorous acid (HOCl) and hydrochloric acid (HCl) reactions that affect the NO_x chemistry. The temperature distribution in the model, the atmospheric radiative transfer code and PSC treatment are improved as well. The treatment of tropospheric and stratospheric dynamical processes have been updated with better data-based boundary topography and boundary winds. All of these changes in the model have resulted in significant changes in lower stratospheric ozone response to NO_x and water vapor (H_2O) emissions.

2.2 Comparison of Model results with IPCC (1999)

The current version of the UIUC-2D model generally shows much higher sensitivity to NO_x emissions from HSCT aircraft than the IPCC (1999) assessment models. Table 1 documents the percentage change in northern hemisphere total column ozone as calculated by the 1999 version and the most recent version of the UIUC-2D model. The scenarios are those evaluated in Chapter 4 of IPCC (1999). The overall difference with the 1999 analyses is largely due to several changes in the recommended chemistry for nitrogen oxides in the lower stratosphere, resulting in an increased sensitivity of NO_x emissions on stratospheric ozone.

Table 1. Percentage Change in Northern Hemisphere Total Column Ozone for IPCC(1999) HSCT scenarios

Scenario	Fleet Size	EI (NO_x) (g / kg of fuel)	IPCC models	UIUC-2D 1999	UIUC-2D 2003
S1b	500	0	-0.3 to -0.6	-0.37	-0.29
S1c	500	5	-0.2 to -0.4	-0.34	-0.49
S1d	500	10	-0.3 to -0.6	-0.49	-0.70
S1e	500	15	-0.4 to -0.9	-0.76	-1.39
S1i	1000	5	-0.4 to -0.9	-0.66	-0.95
S1k	500	5, SA5	-0.2 to -0.8	-0.48	-0.51
S9h	1000	5, SA6	-0.6 to -1.1	-0.72	-0.80

2.3 Description of Scenarios of the Parametric Studies

The set of emission scenarios used for this study were developed by Baughcum (2002b) for NASA's Ultra-Efficient Engine Technology (UEET) Program. For these parametric scenarios, the scheduled data were filtered to only consider flights with great circle distances greater than 2500 nautical miles. These scenarios span a range of flight altitudes and emission characteristics for possible future aircraft which would fly faster than today's commercial aircraft. The particular variables chosen for the parametric studies to evaluate the atmospheric effects of this type of aircraft are fuel burn (73 Mlbs / day and 146 Mlbs / day), cruise altitude (13–21 km) and E.I.(NO_x) (5–20 g / kg of fuel). From fuel burn, one can readily determine the emissions of water vapor (and carbon dioxide and several other types of emissions).

In the model, the background atmosphere was set to a 2020 atmosphere with the source gas concentrations of the long-lived species changed according to the A2 scenario recommended in IPCC (Houghton et al., 2001). All results are obtained from steady state model simulations and then analyzed relative to the corresponding 2020 base that included projected subsonic emissions developed by Baughcum (2002b).

3 RESULTS AND DISCUSSION

A total of 32 scenarios have been evaluated for the conventional routing greater than 2500 nautical miles fleet scenarios from Baughcum (2002b). All the results are obtained from steady state model simulations where the model is run for 10 years with the same species input, heating rates input and

climatological input files and differing aircraft emission input files according to the scenarios studied. Figure 1 shows the relationship between the percentage change of total column ozone in the northern hemisphere relative to E.I.(NO_x) for the four different altitude bands and a total fuel burn of 73 Mlbs / day (dashed line) and 146 Mlbs / day (solid line) respectively. From this plot it is evident that the percentage change in total column ozone holds a linear relationship with E.I.(NO_x) for all the four altitude bands studied. The 13-15 km altitude band series has a slight positive slope owing to the net formation of ozone in that region of the atmosphere.

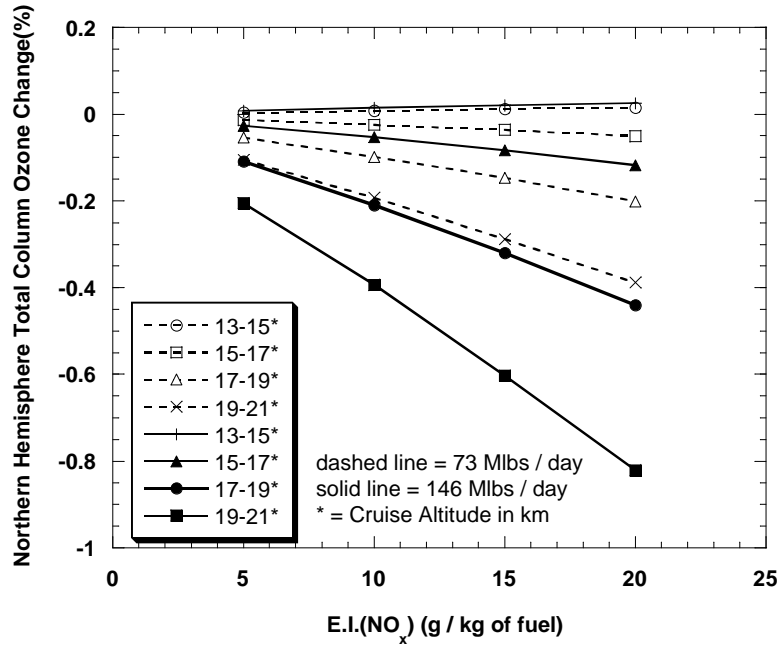


Figure 1. Percentage change in Northern Hemisphere total column zone as a function of E.I.(NO_x) at different altitude bands for a total fuel burn of 73 and 146 Mlbs / day.

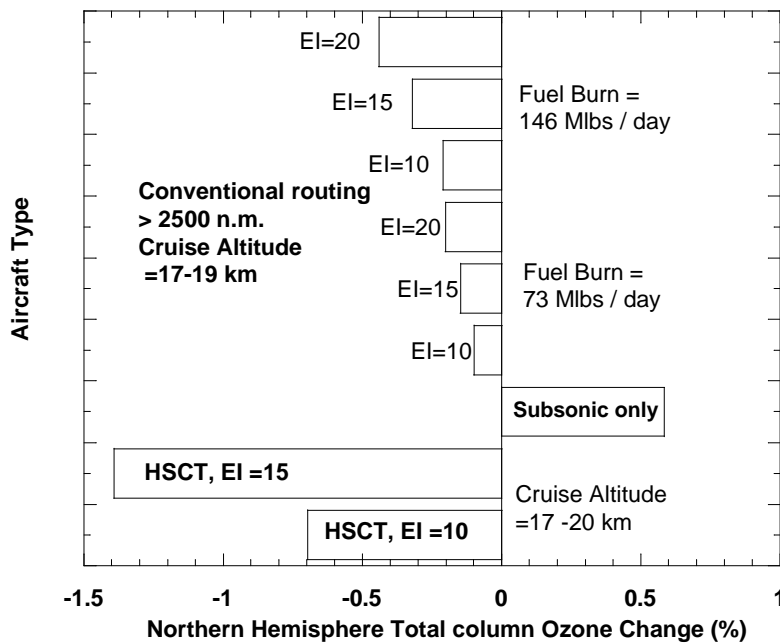


Figure 2. Comparison of effects on Northern Hemisphere change in total column ozone from UIUC-2D model studies of IPCC (1999) HSCT scenarios, the conventional routing greater than 2500 nautical miles scenarios evaluated here, and a 2020 subsonic aircraft fleet emissions case.

3.1 Scenarios in Perspective with IPCC(1999) scenario:

Figure 2 shows the effect on column ozone for the 17-19 km cruise altitude parametric case. For comparison, results using the HSCT scenarios (Baughcum and Henderson, 1998) are also shown. All the results in Figure 2 are calculated using the current version of the UIUC-2D model. The parametric case has a smaller fuel use at cruise altitudes, a different geographical distribution since no constraints are assumed for flights overland (unlike the HSCT scenarios), and a different cruise altitude band. The parametric scenarios are developed under the premise that any economically viable faster aircraft would have to be more fuel efficient than the HSCT concept. The calculated column ozone impact of the subsonic fleet is positive but such tropospheric perturbations are better posed for 3-dimensional CTM calculations.

3.2 Supersonic Business Jets

A number of aerospace companies have shown some interest in the concept of a supersonic business jet, commonly termed as SSBJ, over the last decade (Baughcum, 2002a). These aircraft would be designed to accommodate up to roughly 12 passengers and might fly at a speed of Mach 1.6 to 2. A set of parametric scenarios, which might be representative of future SSBJ fleets has been developed by Baughcum (2002a). A total of 24 SSBJ scenarios have been evaluated for determining their potential impact on stratospheric ozone. For this class of aircraft also it is found that ozone concentrations show a strong linear correlation with fuel burn and E.I.(NO_x).

Figure 3 below presents the calculated column ozone impact for the Northern Hemisphere as a function of cruise altitude for the two E.I.(NO_x) of 10 and 20 g / kg of fuel and the two fuel burn cases of 12 and 18 Mlbs/day. In this figure the altitude sensitivity of the studies show the point in the lower atmosphere where the effect on ozone transitions from a positive effect on ozone to a negative impact. The inflection point is near 14.5 km. When these SSBJ scenarios are compared with the effect on Northern Hemisphere total column ozone due to the fleets of HSCT (IPCC, 1999), they show much smaller effects. The effect of the SSBJ aircraft is seen to be at least a factor of 10 less than the HSCTs studied in IPCC (1999).

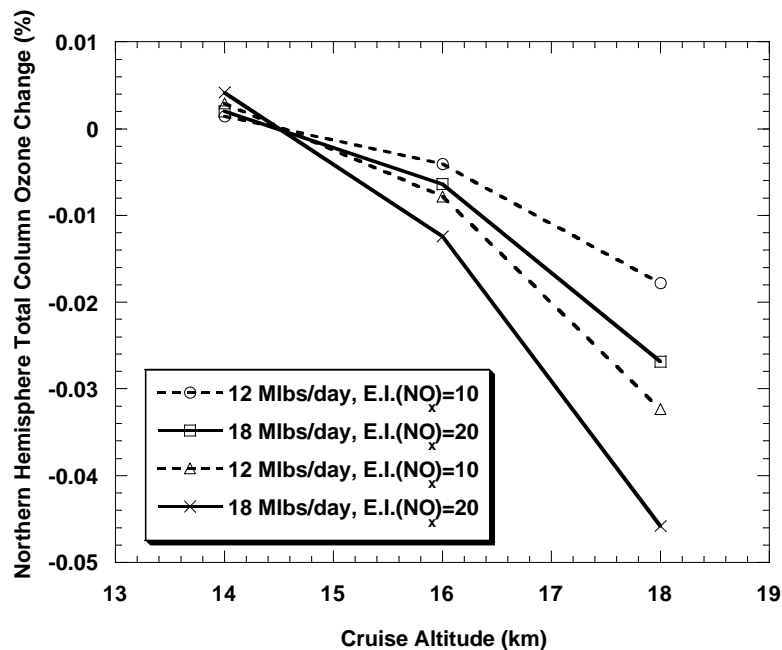


Figure 3. Calculated total column ozone impact for the Northern hemisphere as a function of cruise altitude for E.I.(NO_x) = 10 and 20 g/kg of fuel for two fuel burns of 12 and 18 Mlbs/day respectively.

4 CONCLUSIONS

Some of the key conclusions from this study start with the effects of the new NASA chemistry recommendations, where emissions of NO_x from stratospheric aircraft emissions are now more effective at destroying ozone than in IPCC (1999) whereas water emissions are less effective at ozone depletion. The series of parametric analyses show that ozone concentrations have strong sensitivity to cruise fuel use, cruise altitude and E.I.(NO_x). The ozone change is linear with cruise fuel use and EI(NO_x) for the cases studied.

Emissions near the tropopause at midlatitudes result in slight ozone increases (13-15 km scenarios; 43,000-49,500 kft) due to chemistry related to the smog cycle.

Effects on total ozone get more and more negative for higher cruise altitudes, higher E.I.(NO_x) and higher fuel use. The altitude in the atmosphere above which net ozone depletion begins due to these projected flights is around 14.5 km. As in past studies, the largest local ozone effects have been determined at northern hemisphere high latitudes.

REFERENCES

- Baughcum, S. L., and S. C. Henderson, 1998: *Aircraft Emission Scenarios Projected in Year 2015 for the NASA Technology Concept Aircraft (TCA) High Speed Civil Transport*, NASA/CR-1998-207635.
- Baughcum, S. L., 2002a: First Order Ozone Impact of a Fleet of Supersonic Business Jets (SSBJS). Report prepared for NASA Glenn Research Center, , NASA/CR-2002-211898, pp 35.
- Baughcum, S. L., 2002b: Informal Report Describing the Development of Parametric Emission Scenarios, NAS3-01140 Revolutionary Aero-Space Engine Research Task Order #5 prepared for NASA Glenn Research Center, Cleveland, pp 13.
- DeMore, W. B., S. P. Sander, D. M. Golden, R. F. Hampson, M. J. Kurylo, C. J. Howard, A. R. Ravishankara, C. E. Kolb, and M. J. Molina, 1997: *Chemical Kinetics and Photochemical Data for Use in Stratospheric Modeling*, Evaluation Number 12, Jet Propulsion Laboratory (JPL) Publication 97-4, Pasadena, California.
- IPCC, 2001: *Climate Change 2001 The Scientific Basis. Contribution of Working Group I to the Third Assessment Report of the Intergovernmental Panel of Climate Change* [Houghton, J. T., Y. Ding, D. J. Griggs, M. Noguer, P. J. van der Linden, X. Dai, K. Maskell, and C. A. Johnson (eds)], Appendix II, Cambridge University Press, Cambridge, UK, pp 807-816.
- Isaksen, I., C. Jackman, S.L. Baughcum, F. Dentener, W. Grose, P. Kashibatla, D. Kinnison, M. Ko, J. McConnell, G Pitari, and D. Wuebbles., 1999: Modeling the Chemical Composition of the Future Atmosphere, Chapter 4 in the Intergovernmental Panel of Climate Change (IPCC) Special Report on *Aviation and the Global Atmosphere*, [J.E. Penner, D.H. Lister, D.J. Griggs, D.J. Dokken, and M. McFarland (eds.)], Cambridge University Press, Cambridge, UK, pp121-163.
- Kawa, S. R., J. G. Anderson, S. L. Baughcum, C.A. Brock, W.H. Brune, R.C. Cohen, D.E. Kinnison, P.A. Newman, J.M. Rodriguez, R.S. Stolarski, D. Waugh, and S.C. Wofsy, 1999: *Assessment of the Effects of High-Speed Aircraft in the Stratosphere: 1998*, NASA/TM-209237, chap 4, Greenbelt, Maryland, pp 71-101.
- Sander, S. P., R. R. Friedl, W. B. DeMore, D. M. Golden, M. J. Kurylo, R. F. Hampson, R. E. Huie, G. K. Moortgat, A. R. Ravishankara, C. E. Kolb, and M. J. Molina, 2000: *Chemical Kinetics and Photochemical Data for Use in Stratospheric Modeling*, Supplement to Evaluation 12: Update of Key Reactions, Jet Propulsion Laboratory (JPL) Publication 00-3, Pasadena, California.
- Wei, C. -F., S. M. Larson, K. O. Patten and D. J. Wuebbles, 2001: Modeling of ozone reactions on aircraft-related soot in the upper troposphere and lower stratosphere, *Atmospheric Environment*, 35, 6167-6180.
- Wuebbles, D. J., K. Patten, M. T. Johnson and R. Kotamarthi, 2001: New Methodology for Ozone Depletion Potentials of short-lived compounds:n-Propyl bromide as an example, *J. Geophys. Res.*, 106, 14,551-14,571.

Stratospheric Ozone Sensitivity to Aircraft Cruise Altitudes and NO_x Emissions

S. L. Baughcum*

The Boeing Company, Seattle, Washington, USA

I. C. Plumb, P. F. Vohralik

Commonwealth Scientific and Industrial Research Organization (CSIRO), Telecommunications and Industrial Physics, Lindfield, New South Wales, Australia

Keywords: ozone, NO_x, aircraft emissions

ABSTRACT: The stratospheric ozone impact of higher flying aircraft is sensitive to the cruise altitude, NO_x emission levels, and fleet fuel use at cruise altitude. In this paper, we explore the sensitivity of stratospheric ozone impact for a fleet of supersonic aircraft to the choice of the recommended rate constant compilations (e.g., JPL97, JPL00 or JPL02) using the CSIRO 2-D chemical transport model (CTM). We also present the results obtained for a range of parametric aircraft emission scenarios using the JPL00 recommendations. The parametric scenarios were based on aircraft emissions for long range (greater than 2500 nautical mile) missions projected to the year 2020. Cruise altitudes were varied in 2 km increments over the 13 to 21 km altitude range and NO_x emission indices [EI(NO_x)] of 5, 10, 15, and 20 grams(NO₂)/kilogram fuel use are considered. The column ozone impact was found to depend strongly on cruise altitudes for flights above 15 km. Very little impact on annual average column ozone was calculated for emissions at 13-15 km, but this would be an altitude band better suited for studies with a coupled stratosphere/troposphere 3-D CTM. Ozone response was found to depend linearly on NO_x emissions.

1 INTRODUCTION

The impact on stratospheric ozone by emissions from fleets of supersonic aircraft has been of interest for a number of years. Most recently, the impact of possible fleets of Mach 2.4 supersonic aircraft (referred to as high speed civil transport, HSCT) cruising at altitudes of 18-20 km was evaluated by the IPCC (Isaksen et al., 1999, hereafter referred to as IPCC99) and by NASA (Kawa et al., 1999). These studies concluded that both NO_x and water vapor emissions could contribute to ozone loss in the stratosphere. In addition, production of sulfate aerosols in the exhaust plume was shown to have an effect if conversion of SO₂ to SO₃ in the engine was high (i.e., tens of percent). More recent studies (Curtius et al., 2002) have shown that the conversion of SO₂ to sulfate in the plume is 2-3%, which is smaller than the values used in the IPCC report. The ozone perturbation is sensitive to the competition between NO_x, HO_x, and ClO_x chemistry in the lower stratosphere. As a consequence, recent changes in recommended reaction rate constants from those used in the IPCC99 studies may change the calculated perturbations.

In this study, we use the CSIRO two-dimensional chemical transport model to evaluate the stratospheric ozone impact of a parametric scenario for aircraft emissions as a function of cruise altitude and NO_x emission index (EI), focusing on cruise altitudes higher than the current subsonic fleet of commercial aircraft. Results are evaluated using the same rate constant set (DeMore et al., 1997, hereafter referred to as JPL97) used in the IPCC report and more recent recommendations (Sander et al., 2000, referred to as JPL00; Sander et al., 2003, referred to as JPL02).

* Corresponding author: Steven L. Baughcum, Boeing Company, P. O. Box 3707, MC 02-XL, Seattle, WA 98124, USA. Email: Steven.L.Baughcum@boeing.com

2 SENSITIVITY OF HSCT OZONE IMPACT TO MODEL CHANGES

The CSIRO 2-dimensional chemical transport model (Randeniya et al, 2002 and references cited therein) has been upgraded since its use in the IPCC report. Major changes include the following: 1) The addition of low temperature aerosol chemistry; 2) Radiative heating rates are now calculated using the NCAR CCM column radiation model using NCEP temperatures, the MMII ozone climatology (Park et al., 1999), and mean ISCCP cloud parameters (Rossow and Schiffer, 1991); 3) Zonal temperature variations based on the NCEP reanalysis (Kalnay et al., 1996) are used for both gas phase and heterogeneous chemistry calculations; 4) A complete implementation of the JPL00 chemical and photolysis recommendations is used as the baseline although other reaction rate sets can be used; 5) The vertical resolution of the model has been upgraded to 1 km, while the latitudinal resolution remains 5 degrees.

To evaluate the sensitivity of the calculated ozone impact to changes in the model and sensitivities to the choice of reaction rate constants, the HSCT emission scenarios (Baughcum and Henderson, 1998) used in IPCC99 were run for the case of a fleet of 500 HSCTs with NO_x emission indices of 5, 10, and 15 grams of NO₂ per kilogram of fuel. The SA0 case (no additional sulfate aerosol) from the IPCC99 study was chosen with a 2015 background atmosphere.

Figure 1 shows the results comparing four cases: the IPCC99 results using the 1997 version of the CSIRO model, the current version of the model using the JPL97 rate recommendations, the current version of the model using the JPL00 rate recommendations, and the current version of the model using a partial update to the JPL02 recommendations in which the bimolecular and termolecular reactions have been updated but not the photolysis rates.

As seen in Figure 1, the current version of the model using JPL97 chemistry (curve labelled JPL97) predicts a larger ozone impact than the IPCC99 version. The new version has greater accumulation of exhaust emissions and lofts more NO_x to the higher altitudes where NO_x chemistry dominates the ozone removal process. As a consequence, the current version of the model predicts a stronger dependence on EI(NO_x). Updating the reaction rate constants and photolysis cross sections to the JPL00 recommendations increases the calculated ozone perturbation. The partial update to the JPL02 recommendations results in a further increase in the impact, but not as large as that from JPL97 to JPL00 chemistry. More discussion of the latter awaits a complete implementation of the JPL02 recommendations.

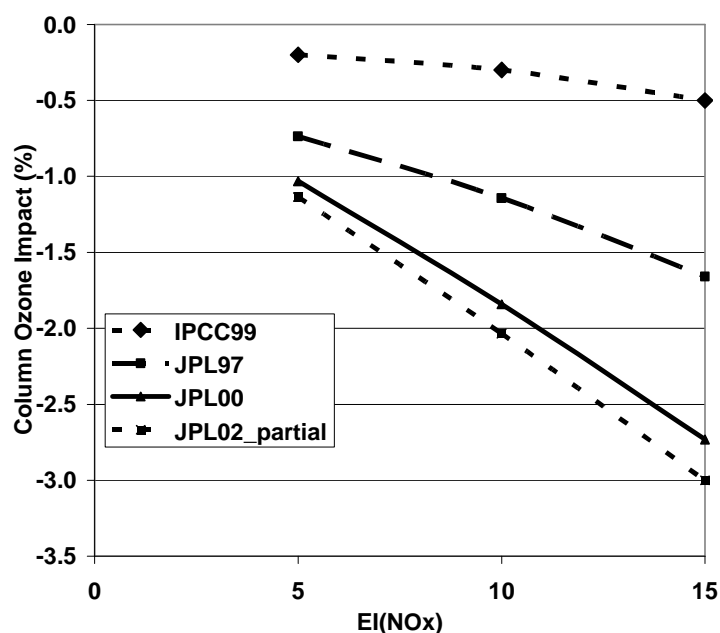


Figure 1. Annual average column ozone change (%) in the Northern Hemisphere as a function of EI(NO_x) for different model versions and choice of reaction rate recommendations for an assumed fleet of 500 HSCTs flying at 18-20 km cruise altitudes.

3 PARAMETRIC SENSITIVITY

As aircraft speed increases, the cruise altitude increases. Emission scenarios for possible future aircraft types need to consider the accessible market, airplane/engine performance, emissions characteristics, and possible route structure. These will vary depending on the size, range, detailed design, year of entry into service, and cost of the aircraft with different markets for different airplane concepts. Rather than trying to forecast different scenarios for different airplane types, in this study we consider a parametric approach in which the geographical distribution of the emissions is fixed and the emissions are moved up/down systematically in altitude. The fleet fuel use at cruise altitudes depends on the number of aircraft, the single airplane fuel use rate, and the number of hours spent at cruise altitude. For the results presented here, we treat fleet fuel use as a constant and systematically vary cruise altitude and EI(NO_x).

The parametric aircraft scenarios are based on a projection of scheduled air traffic for 2020 (Sutkus et al., 2003). For this study, we focus on aircraft which are faster than today's commercial aircraft and which would presumably be used primarily on long range routes where speed is important. We therefore include only flights longer than 2500 nautical miles. The 2020 scenario was rerun using only such flights. The geographical distribution of the projected fuel use of this 2020 long range scenario on a 1 degree latitude x 1 degree longitude grid in the 9-13 km altitude band was used as the geographical distribution for the parametric scenarios. Such flights account for approximately 50% of the total projected cruise fuel use in 2020 which was projected to be 242 Tg/year.

The geographical distribution of the fuel consumption in the parametric scenarios is shown in Figure 2. For the parametric studies, we assume that a viable new airplane type could account for approximately 20% of the cruise fuel use of the flights longer than 2500 nautical miles (24 Tg/year). The cruise emissions are then assumed to be uniformly distributed vertically over a 2 km band. These parametric emissions are then added to the base case 2020 scenario. Model runs are done using these combined parametric scenarios and then the perturbations are calculated relative to a model run with the base case emissions only. For comparison, the earlier HSCT studies assumed a cruise fuel use of 47 Tg/year but the HSCT was a very fuel-inefficient concept compared to modern subsonic aircraft.

For the parametric calculations of altitude and NO_x level, a 2020 background atmosphere based on the IPCC SRES A2 scenario (IPCC, 2001) is used. The stratospheric aerosol background was assumed to be that of the SA0 case from IPCC99. These model runs were done using the JPL00 recommendations for rate constants and photolysis cross sections. Four altitude bands were considered: 13-15 km, 15-17 km, 17-19 km, and 19-21 km. These altitudes are higher than those of current subsonic aircraft and correspond to higher speeds than today's commercial aircraft. As a sensitivity study, EI(NO_x) values of 5, 10, 15, and 20 grams (NO₂)/kg(fuel) were considered to cover a range of possible emission technology levels from the very aggressive (EI=5) to a value four times higher. The model calculations consider both NO_x and water vapor emissions but do not consider the effects of sulfate aerosol emissions.

The change in absolute ozone profile as a function of height for the four different aircraft cruise altitudes is shown in Figure 3. For each parametric scenario considered, the major impact on ozone column occurs at altitudes above the cruise altitudes with the ozone impact increasing with higher cruise altitudes.

Since most of the emissions are predicted to occur in the Northern Hemisphere, the largest ozone impact occurs there with increasing impact at higher latitudes (not shown). As shown in Figure 4, the model predicts a strong dependence of ozone impact on cruise altitude, increasing with higher cruise altitudes and with higher NO_x levels. The ozone impact for aircraft flying in the 13-15 km altitude band is calculated to be very small. However, a 3-dimensional model calculation is required to support this conclusion because of the limitations of using a 2-D CTM near the tropopause. The sensitivity to NO_x increases with flight altitudes, as shown by the slopes of the lines in Figure 4.

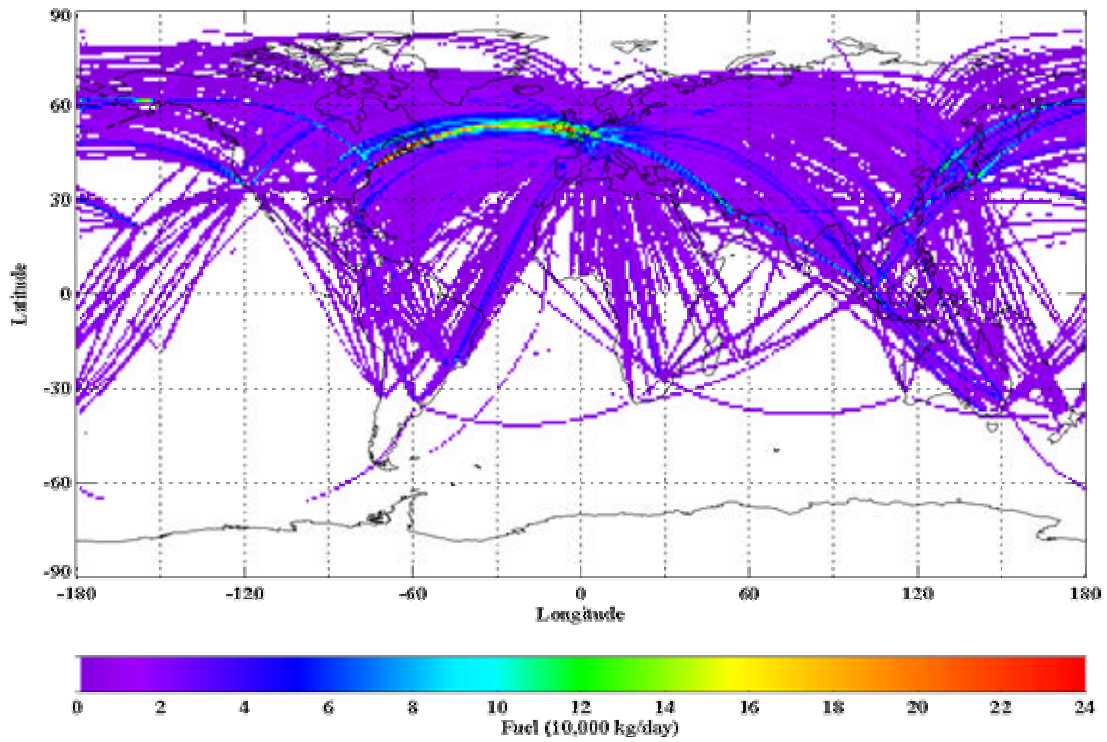


Figure 2. Geographical distribution of cruise fuel use in parametric scenarios.

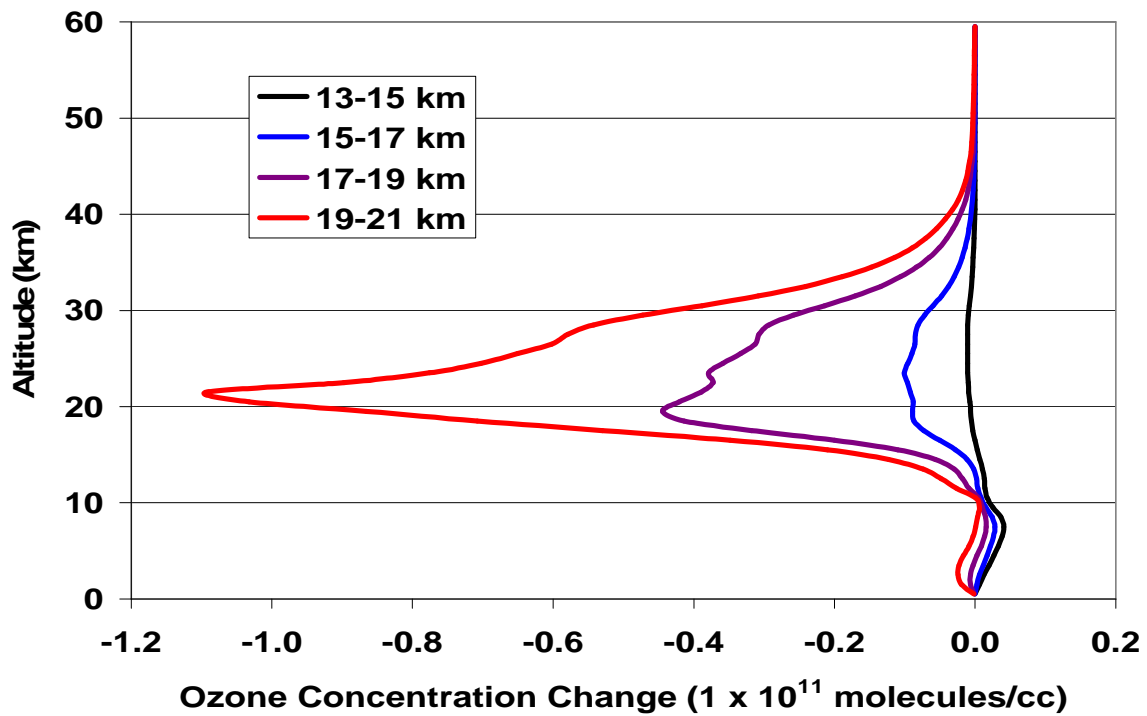


Figure 3. Absolute ozone concentration change as a function of altitude for four different cruise altitudes. The results shown are for the EI(NO_x)=10 case at 40-45 degree North latitude in July.

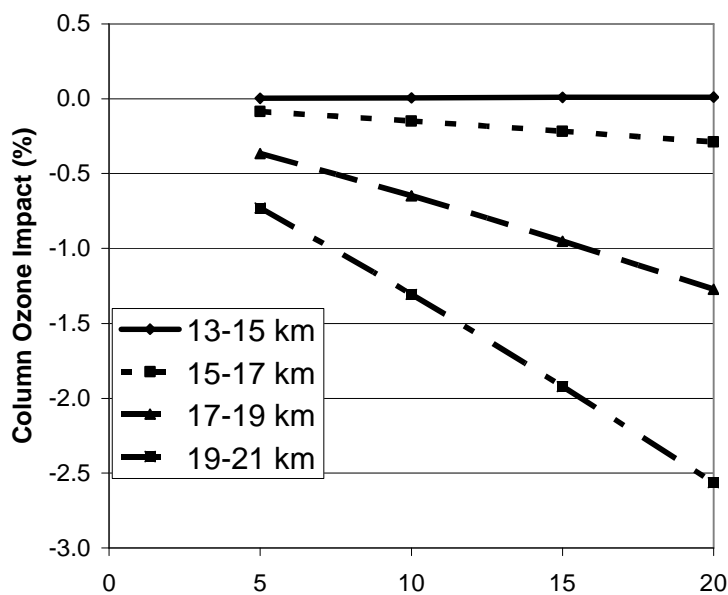


Figure 4. Annual average northern hemisphere column ozone change for the parametric emission scenarios as a function of EI(NO_x) for four different cruise altitude bands.

4 CONCLUSIONS

The updated version of the CSIRO 2-D model calculates larger ozone perturbations for aircraft flying at 18–20 km than were obtained using the older version of the model in the IPCC99 assessment. These differences are due to both changes in the model transport and to the use of the updated JPL reaction rate coefficients (e.g., the reduced rate of the $\text{OH} + \text{NO}_2 + \text{M} \rightarrow \text{HNO}_3 + \text{M}$ reaction) and photolysis cross sections. This results in a greater sensitivity of ozone depletion to NO_x emission levels than in the previous assessments. We expect that other models (both 2-D and 3-D) will calculate larger ozone impacts when using the latest JPL recommendations.

The parametric results showed the calculated ozone impact was small for cruise altitudes in the 13–15 km altitude band. The ozone depletion increased sharply as the flight altitudes exceeded 15 km. The sensitivity of ozone to NO_x emissions was found to increase with higher cruise altitudes. This suggests that low NO_x combustors will be important if large fleets of supersonic aircraft ever become viable.

Uncertainties in the transport and accumulation of aircraft emissions remain significant, particularly for cruise altitudes near the tropopause. This will require continued development of models (e.g., 3-D models) to better quantify the aircraft impact.

REFERENCES

- Baughcum, S. L., and S. C. Henderson, 1998: *Aircraft Emission Scenarios Projected in Year 2015 for the NASA Technology Concept Aircraft (TCA) High Speed Civil Transport*, NASA/CR-1998-207635.
- Curtius, J., F. Arnold, and P. Schulte, 2002: Sulfuric acid measurements in the exhaust plume of a jet aircraft in flight: Implications for the sulfuric acid formation efficiency, *Geophys. Res. Lett.*, 29, No. 7, 10.1029/2001GL013813.
- DeMore, W. B., S. P. Sander, D. M. Golden, R. F. Hampson, M. J. Kurylo, C. J. Howard, A. R. Ravishankara, C. E. Kolb, and M. J. Molina, 1997: *Chemical Kinetics and Photochemical Data for Use in Stratospheric Modeling, Evaluation Number 12*, JPL Publication 97-4. (<http://jpldataeval.jpl.nasa.gov/>)

- IPCC, 2001: *Climate Change 2001: The Scientific Basis. Contributions of Working Group I to the Third Assessment Report of the Intergovernmental Panel on Climate Change* [Houghton, J. T., Y. Ding, D. J. Griggs, M. Noguer, P. J. van der Linden, X. Dai, K. Maskell, and C. A. Johnson (eds.)]. Cambridge University Press, Cambridge, United Kingdom, 881 pp.
- Isaksen, I., C. Jackman, S. L. Baughcum, F. Dentener, W. Grose, P. Kasibhatla, D. Kinnison, M. Ko, J. McConnell, G. Pitari, and D. Wuebbles, 1999: "Modeling the Chemical Composition of the Future Atmosphere," Chapter 4 in the *Intergovernmental Panel on Climate Change (IPCC) Special Report on Aviation and the Global Atmosphere*, [J. E. Penner, D. H. Lister, D. J. Griggs, D. J. Dokken, and M. McFarland (eds.)] Cambridge University Press.
- Kalnay, E., et al., 1996: The NCEP/NCAR 40-year reanalysis project, *Bull. Am. Meteorol. Soc.*, 77, 437-471.
- Kawa, S. R., J. G. Anderson, S. L. Baughcum, C. A. Brock, W. H. Brune, R. C. Cohen, D. E. Kinnison, P. A. Newman, J. M. Rodriguez, R. S. Stolarski, D. Waugh, and S. C. Wofsy, 1999: *Assessment of the Effects of High-Speed Aircraft in the Stratosphere: 1998*, NASA Technical Report TP-1999-20923.
- Park, J. H., M. K.W. Ko, C. H. Jackman, R. A. Plumb, J. A. Kaye, and K. H. Sage, 1999: *Models and Measurements Intercomparison II*, NASA/TM-1999-209554.
- Randeniya, L. K., P. F. Vohralik, and I. C. Plumb, 2002: Stratospheric ozone depletion at northern mid latitudes in the 21st century: The importance of future concentrations of greenhouse gases nitrous oxide and methane, *Geophys. Res. Lett.*, 29, No. 4, 10.1029/2001GL014295.
- Rossov, W.B. and R.A. Schiffer, 1991: ISCCP cloud data products, *Bull. Am. Meteorol. Soc.*, 72, 2-20.
- Sander, S. P., R. R. Friedl, W. B. DeMore, A. R. Ravishankara, D. M. Golden, C. E. Kolb, M. J. Kurylo, R. F. Hampson, R. E. Huie, M. J. Molina, G. K. Moortgat, 2000: *Chemical Kinetics and Photochemical Data for Use in Stratospheric Modeling, Supplement to Evaluation 12: Update of Key Reactions, Evaluation Number 13*, JPL Publication 00-3. (<http://jpldataeval.jpl.nasa.gov/>)
- Sander, S. P., R. R. Friedl, D. M. Golden, M. J. Kurylo, R. E. Huie, V. L. Orkin, G. K. Moortgat, A. R. Ravishankara, C. E. Kolb, M. J. Molina, and B. J. Finlayson-Pitts, 2003: *Chemical Kinetics and Photochemical Data for Use in Atmospheric Studies, Evaluation Number 14*, JPL Publication 02-25. (<http://jpldataeval.jpl.nasa.gov/>)
- Sutkus, D. J., S. L. Baughcum, and D. P. DuBois, 2003: *Commercial Aircraft Emission Scenario for 2020: Database Development and Analysis*, NASA contractor report NASA/CR-2003-212331. (<http://gltrs.grc.nasa.gov/reports/2003/CR-2003-212331.pdf>)

Investigating the Global Atmosphere by Using Commercial Aircraft: CARIBIC

Andreas Zahn*

Forschungszentrum Karlsruhe, Institute of Meteorology and Climate Research, Karlsruhe, Germany

Carl Brenninkmeijer

Max-Planck-Institute for Chemistry, Atmospheric Chemistry Division, Mainz, Germany

Keywords: passenger aircraft, stratosphere-troposphere exchange, chemical composition troposphere and stratosphere

ABSTRACT: CARIBIC (Civil Aircraft for the Regular Investigation of the atmosphere Based on an Instrument Container, www.caribic-atmospheric.com) is based on the deployment of an automated laboratory inside an airfreight container that is loaded once or twice per month for conducting measurements during intercontinental flights. The advantages of this approach are obvious: for moderate effort and costs it allows detailed (>60 trace gases and aerosol parameters) and long-term (>10 years) monitoring of the upper troposphere / lower stratosphere (UTLS) along certain flight routes. The data are especially suitable for comparisons with model results and satellite observations and allows for instance the determination of seasonal variations of the species measured (which is hardly possible using data from dedicated short-term aircraft campaigns). Here, we give an overview about results gained in CARIBIC phase I (1997-2002) using a Boeing 767 by LTU Airlines and about the technical design planned for a new container deployed onboard a new Airbus A340-600 by Lufthansa AG as of 2004 (CARIBIC phase II).

1 THE USE OF PASSENGER AIRCRAFT FOR ATMOSPHERIC RESEARCH

There are some intrinsic originalities of the deployment of passenger aircraft for atmospheric research, in the following listed for CARIBIC phase II: (a) the endurance of the Airbus A340-600 is 14.800 km which enables an almost global data coverage, (b) Lufthansa promised the use of the CARIBIC container for at least 10 years which leads to a total measurement duration of more than 15 years, (c) 16 instruments are integrated which enables the measurement of more than 60 trace gases and 20 aerosol parameters, and (d) the flight costs (only airfreight costs) are (for doing research) quite moderate (~300 Euro per hour). For Lufthansa on the other hand it is financially attractive to transport the container which will guarantee the long-term deployment.

2 OBJECTIVES OF CARIBIC

The major objectives of CARIBIC are: (a) to systematically monitor the chemical composition of the UTLS (in support of the Montreal and Kyoto protocol) over a long period of time, (b) to collect representative data for the validation of results from detailed atmospheric models and satellite observations, (c) to better quantify the budgets of various trace gases and aerosol particles in UTLS, in particular to distinguish between natural and anthropogenic processes, but also to better assess the impact of aircraft emissions, (d) to better specify the emissions of the continents (possible by comparing the data measured upwind and downwind of the continents), (e) to better quantify tracer transport from the Earth surface to the UTLS and in the UTLS (convection, long-range transport, stratospheric-tropospheric exchange), and (f) to study various specific atmospheric processes such as aerosol particle formation and life cycle, the oxidation capacity of the atmosphere, cirrus clouds formation in the UT/LS etc.

* Corresponding author: Andreas Zahn, Forschungszentrum Karlsruhe, Institute of Meteorology and Climate Research, P.O. Box 3640, D-76021 Karlsruhe, andreas.zahn@imk.fzk.de

3 STATUS OF CARIBIC

In 1993 LTU Airlines agreed to help to realize CARIBIC and to carry a measurement container (type: LD 4) for atmospheric research. After a planning and construction phase, the first measurement phase (80 flights along three flight routes) took place between November 1997 and April 2002 using a Boeing 767-ER. The CARIBIC consortium steadily increased from 3 German institutes to nowadays 11 European institutions (www.caribic-atmospheric.com).

As of spring 2004 a new, larger container (LD 11) having a gross weight of ~1.4 tons will be flown onboard an Airbus A340-600 of Lufthansa AG. The new inlet system installed just in front of the belly fairing is shown in Figure 1.

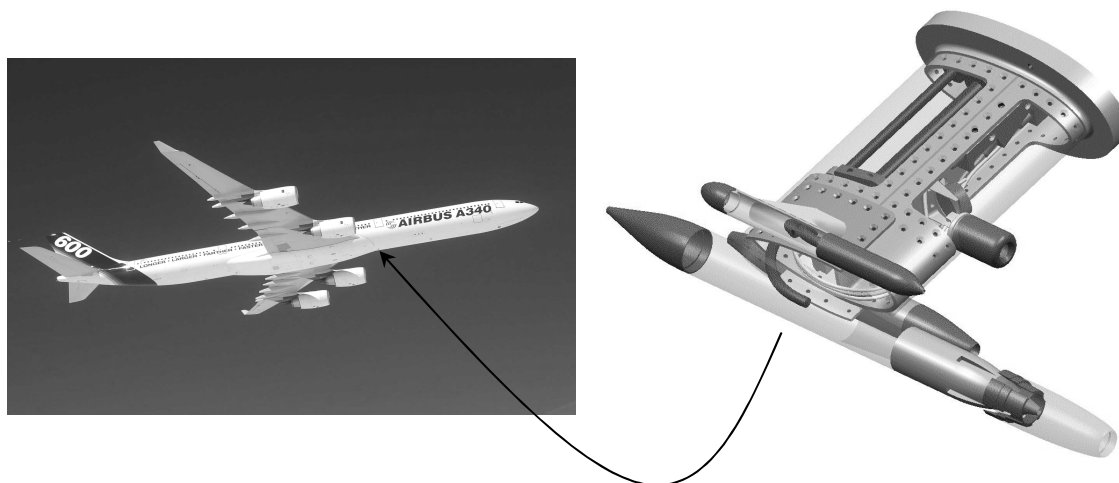


Figure 1: The new CARIBIC Airbus A340-600 with the air inlet system. It has 4 inlet tubes, a camera, and 3 telescopes for a DOAS spectrometer. Various heating foils prevent icing on the surface and minimize the absorption of sticky species such as H_2O or HNO_3 within the lines to the container.

4 MEASUREMENTS (1997-2002)

4.1 Tropospheric distributions of ozone and carbon monoxide

Figure 2 displays the seasonal variations of O_3 and CO in tropospheric air along the flight route Germany – Indian Ocean.

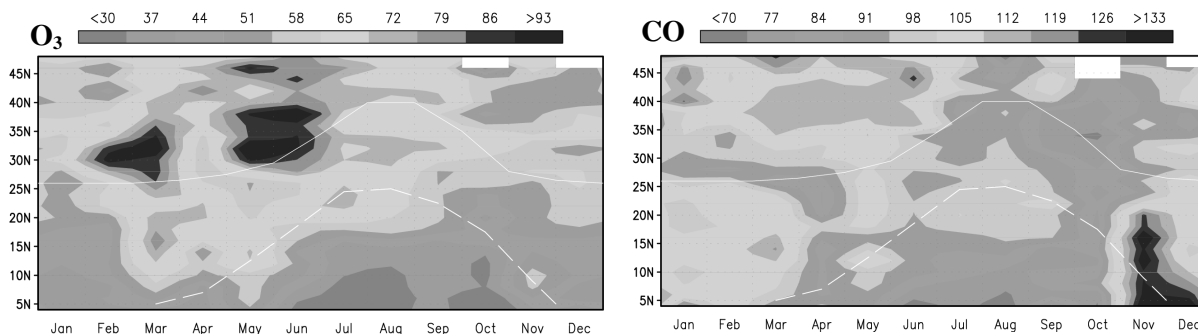


Figure 2: Seasonal variation of the mean mixing ratio (in ppbv) of O_3 (left) and CO (right) along the flight track Germany - Indian Ocean at 9-11 km altitude. The dashed line marks the mean location of the ITCZ and the straight line indicates the mean location of the subtropical jet stream.

In the extra-tropics, O_3 minimizes early winter, in spite of its just then maximum chemical lifetime. This demonstrates that the sum of the two O_3 sources, import from the stratosphere and photochemical generation in the troposphere, minimizes during early winter north of $\sim 20^\circ N$. In the tropics, O_3 minimizes (at ~ 30 ppbv) from July to October which is caused by the northern location of the ITCZ that leads to supply of O_3 -poor southern hemispheric air. The maximum in ozone is found from March to June, just north of the subtropical jet stream; this alludes to some stratospheric influence. The springtime O_3 maximum extends even into the tropics (from March to May) suggesting that injection of stratospheric O_3 near the sub-tropical jet significantly impacts the O_3 budget of the tropical troposphere, in agreement with findings by Zachariasse *et al.* [2000].

CO undergoes significant, but compared to the ground weak seasonal and latitudinal variations, on which occasional high CO events are superimposed. North of $30^\circ N$, CO maximizes from February until as late as June and minimizes in September-October. Along the sub-tropical jet stream low CO mixing ratios are found. This is due to the fact that this region is primarily affected by clean, chemically aged air subsiding in the downward branch of the Hadley cell. Around $20^\circ N$ no clear seasonality in CO appears. This is mainly because of the unusually high concentrations from July to September, just when the actual short chemical CO lifetime (~ 8 weeks) suggests the lowest CO levels. This CO excess of ~ 30 ppbv over an estimated background of ~ 65 ppbv is due to outflow of the ITCZ that is located just below the CO plume (Figure 2). The ITCZ outflow area covers an extensive region at 9-11 km altitude from 10° to $30^\circ N$ and 40° to $75^\circ E$, that are at least 7×10^6 km². Our CO data (supported by other CARIBIC data) thus provide strong evidence that large amounts of pollutants emitted in southern Asia (Indian, Bangladesh, China, Indonesia) are lofted into the upper troposphere during the Indian summer monsoon.

South of $20^\circ N$, CO minimizes from June to October (with ~ 75 ppbv) when the ITCZ is situated far north (reaching $\sim 25^\circ N$ in August), and hence, mainly cleaner southern hemispheric air was probed. The pronounced tropical CO plume in November/December is due to forest fires in Indonesia, a region ~ 4000 km south-east of the CARIBIC flight corridor, confirming that these fires can also constitute a considerable source of pollutants to the tropical free troposphere.

4.2 Correlation between O_3 and CO in tropospheric air

At the ground the enhancement ratio $\Delta O_3/\Delta CO$ (with ΔO_3 and ΔCO denoting the excess in the examined air mass over background air) is frequently used as a measure of the net O_3 formation that has occurred. In the upper troposphere where the excess values ΔO_3 and ΔCO are mostly small and where the air masses are mostly chemically aged, the slope of the O_3 -CO correlation dO_3/dCO will give the more meaningful information on the origin of ozone [Zahn *et al.*, 2002a]. In Figure 3 the seasonal variation of the mean slope dO_3/dCO observed in tropospheric air is shown.

In the tropics, clearly positive O_3 -CO slopes are measured at all seasons, i.e. 0.20-0.25 in autumn/winter and ~ 0.50 in spring/summer. Furthermore, the O_3 -CO slopes are almost identical. Both findings demonstrate that the O_3 budget of the tropical 10 km altitude range is controlled by in situ photochemical O_3 formation year-around and that the fraction of stratospheric O_3 is small. Model calculations likewise estimate that in the tropics only 10-15 % [Roelofs and Lelieveld, 1997] and 5-10 % [Lamarque *et al.*, 1999], respectively, of the O_3 abundance at 10 km altitude originates from the stratosphere.

The annual mean O_3 -CO slope observed in the tropics allows us to roughly estimate the net ozone production in the NH tropical troposphere arising from surface emission of O_3 precursors. Using the formula given by Parrish *et al.* [1993] and Mauzerall *et al.* [1998, 2000], this net ozone production is calculated as product of the “tropical ground-based CO emission plus atmospheric CO generation by the oxidation of hydrocarbons below 11 km” and the annual mean O_3 -CO slope measured during CARIBIC in the tropics of 0.37. An annual net ozone production of 564 Tg O_3 or 17.6×10^{10} O_3 molecules $cm^{-2} s^{-1}$ is inferred [Zahn *et al.*, 2002a]. This is somewhat higher than the O_3 export from East Asia in the mid-1980s estimated by Mauzerall *et al.* [2000] to 13.2×10^{10} O_3 molecules $cm^{-2} s^{-1}$ and a factor of 2.5-5.9 larger than the annual mean flux of stratospheric O_3 into the troposphere estimated to be $3-7 \times 10^{10}$ O_3 molecules $cm^{-2} s^{-1}$ [Lelieveld and Dentener, 2000; McLinden *et al.*, 2000; and references therein].

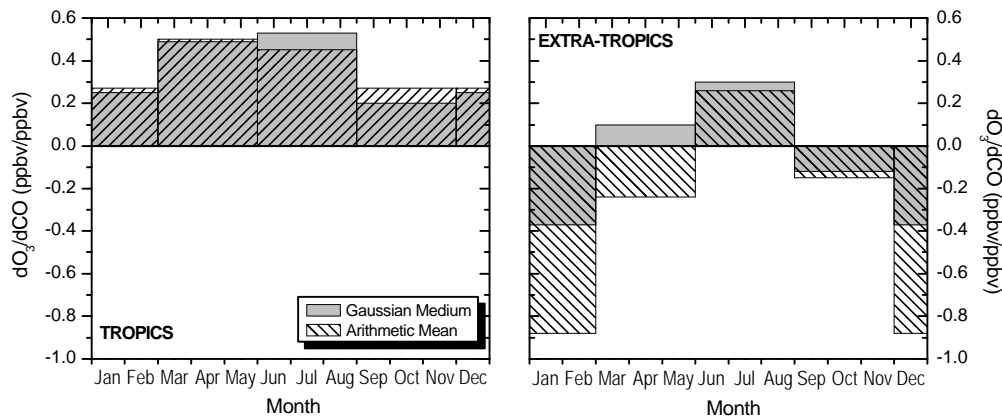


Figure 3: Seasonal variation of mean O₃/CO slopes averaged along flight distances of 200–500 km. Grey bars: Mean values of the line centers of the Gaussian curves fitted to the distribution of O₃-CO slopes. Shaded bars: Arithmetic mean O₃/CO slopes. Left: 4–28° N (tropics), right: 28–51° N (extra-tropics).

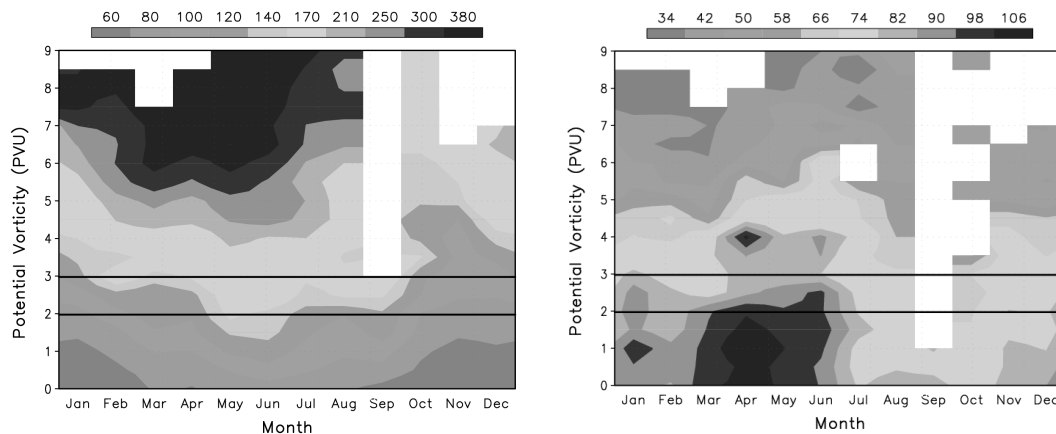


Figure 4: Mean seasonal variation of ozone (left, in ppbv) and carbon monoxide (right, in ppbv) observed during CARIBIC in the UTLS from 1997 to 2002, as function of the potential vorticity taken from ECMWF analysis.

In the extra-tropics, per contra, the two O₃-CO slopes agree well only in summer and autumn, whereas both O₃-CO slopes are negative in autumn and winter. This indicates that in winter/spring and maybe even in autumn the stratosphere is a major O₃ source for the extra-tropical 10 km altitude range, but of minor importance in summer. In summer, photochemical O₃ production clearly dominates. A more detailed analysis of the partitioning of stratospheric influx and photochemical formation is given in [Zahn *et al.*, 2002a].

4.3 Bi-directional tracer exchange across the extra-tropical tropopause

In Figure 4a mean CARIBIC ozone data are plotted relative to PV iso-surfaces of up to 9 PVU, which cover the upper troposphere and the lowest ~2.5 km of the lowermost stratosphere. It illustrates the downward propagation of stratospheric ozone into the troposphere. In the LS, ozone clearly maximizes in late winter/spring and strongly decreases towards the tropopause, as seen in other studies, e.g. [Logan, 1999].

The time lag of the O₃ maximum between the 7–9 PVU PV iso-surface (~2 km above the tropopause), and the dynamical tropopause (2–3 PVU) is ~4 weeks. Figure 4 does not take into account the 3-dimensional nature of downward transport, so that the inferred transport time of 4 weeks has to be interpreted with care. Moreover, as ozone is quite long-lived in the lowermost stratosphere, the strong O₃ decrease towards the tropopause has largely to do with dilution of inflow of (O₃-poor) tropospheric air. This in-flow of tropospheric air into the LS is traced by the CO data (see Figure 4b). CO decreases from 70–100 ppbv at the tropopause to 35–40 ppbv at PV = 8–9

PVU, strongly exceeding the chemical equilibrium level in the LS of 10-20 ppbv. Moreover, CO undergoes a clear seasonal variation in the LS, with a gradual phase shift with altitude above the tropopause. CO maximizes in April in the UT and at the tropopause, but in mid-summer at PV = 8-9 PVU, i.e. ~2 km above the tropopause. This phase shift must also be associated with the seasonal variation of the in-flow of tropospheric air. Chemistry would result in an opposite seasonal variation in the LS, because the lifetime of CO reaches its minimum of ~2 months in summer. The gradual phase shift with altitudes can only be explained by the increasing impact of in-flowing CO-rich tropospheric air at higher potential temperatures (lower latitudes), which is expected to maximize in summer.

5 CONCLUSIONS

The first measurement phase of CARIBIC from fall 1997 to spring 2002 (with ~80 measurement flights) demonstrated the strength of using a measurement container onboard passenger aircraft. This approach guarantees a long-term and multi-tracer monitoring of the UTLS on an almost global scale. One major strength is the collection of distributions of trace gases and aerosol in the UTLS which allows to identify seasonal and (for certain species) inter-annual variations (such as CO) and trends (such as SF₆). Substantial seasonal and latitudinal variations of the distributions of O₃ and CO and of the partitioning between influx of stratospheric O₃ and photochemical O₃ production are found. The distinction of the two major O₃ sources is accomplished by applying CO as a tracer of O₃ precursors. Positive O₃-CO co-variations are assigned to O₃ formed photochemically and negative ones to O₃ imported from the stratosphere. In the tropics, photochemical O₃ production clearly dominates year around, which is demonstrated by the ever positive O₃-CO slopes of 0.20-0.27 in autumn/winter and of 0.45-0.53 in spring/summer. In the extra-tropics, the well-documented O₃ maximum was confirmed. Stratospheric O influx and photochemical O₃ production contribute equally to this maximum. In winter, the O₃-CO slopes are with -(0.4-0.8) strongly negative, indicating dominance of import of stratospheric O₃. In summer, on the contrary, the O₃-CO slopes are with 0.3 positive and photochemical O₃ formation clearly dominates. In autumn, both O₃ sources are weak. Strong seasonal variations of O₃ and CO are observed above the extra-tropical tropopause. These seasonal variations can only be explained by active bi-directional tracer exchange across the extra-tropical tropopause. Further details can be found in Zahn *et al.* [2002a, 2002b] and Zahn and Brenninkmeijer [2003].

REFERENCES

- Lelieveld, J., and F.J. Dentener, What controls tropospheric ozone?, *J. Geophys. Res.*, *105*, 3531-3551, 2000.
- Logan, J.A., An analysis of ozonesonde data for the troposphere: Recommendations for testing 3-D models and development of a gridded climatology for tropospheric ozone, *J. Geophys. Res.*, *104*, 16,115-16,149, 1999.
- Mauzerall, D.L., et al., Photochemistry in biomass burning plumes and implications for tropospheric ozone over the tropical south Atlantic, *J. Geophys. Res.*, *103*, 8401-8423, 1998.
- Mauzerall, D.L., D. Narita, H. Akimoto, L. Horowitz, S. Walters, D.A. Hauglustaine, and G. Brasseur, Seasonal characteristics of tropospheric ozone production and mixing ratios over East Asia: A global three-dimensional chemical transport and model analysis, *J. Geophys. Res.*, *105*, 17,895-17,910, 2000.
- McLinden, C.A., S.C. Olsen, B. Hannegan, O. Wild, M.J. Prather, and J. Sundet, Stratospheric ozone in 3-D models: A simple chemistry and the cross-tropopause flux, *J. Geophys. Res.*, *105*, 14,653-14,665, 2000.
- Zahn, A., C.A.M. Brenninkmeijer, P.J. Crutzen, G. Heinrich, H. Fischer, J.W.M. Cuijpers, and P.F.J. van Velthoven, Distributions and relationships of O₃ and CO in the upper troposphere: The CARIBIC aircraft results 1997-2001, *J. Geophys. Res.*, *105(D17)*, 4337, doi: 10.1029/2001JD001529, 2002a.
- Zahn, A., et al., The origin of tropospheric "ozone clouds", *J. Geophys. Res.*, *105(D22)*, 4638, doi: 10.1029/2001JD002345, 2002b.
- Zahn, A., C.A.M. Brenninkmeijer, New Directions: A chemical tropopause defined, *Atmos. Environment*, *37(3)*, 439-440, 2003.

The Importance of Aviation for Tourism – Status and Trends

S. Gössling*

Dept. of Service Management, Lund University, Sweden

Keywords: Air travel, disease, energy use, risk perception, tax, tourism, terror, war

ABSTRACT: In industrialized countries, leisure-related travel has continuously increased and accounts now for about 50% of all distances traveled. On average, leisure-related mobility in industrialized countries is in the order of 20 pkm per capita per day, with air travel accounting for 15-20% of the distances covered (3.5 pkm per capita per day). In the future, air travel is likely to increase substantially, both as a result of changing leisure conceptions in industrialized countries, the emergence of low fare airlines, and the increasing participation of people from developing countries in air travel. There is, however, some uncertainty about i) the role of energy taxes, soon to be introduced in industrialized countries, and ii) the changing risk perception of tourists and its consequences for travel behavior; this is, the importance of terror attacks, war, and globally spreading diseases such as SARS. The paper seeks to discuss the development of leisure-related air travel with respect to these aspects and makes suggestions for mitigation strategies.

1 INTRODUCTION

Purposes of travel can be divided into leisure, work, service/shopping, and other (Carlsson-Kanyama and Lindén, 1999). Evidence from travel surveys suggests that leisure-related travel accounts for about 50% of all travel in the industrialized countries. This proportion has, for example, been found in travel surveys in Norway (for travel distance, Høyer, 2001), Sweden (for travel time, travel distance, and travel frequency; Carlsson-Kanyama and Lindén, 1999), Germany (for travel distance, excluding travel abroad; Heinze, 2000) and Austria (for travel distance; Knoflacher, 2000). In more detail, the average per capita mobility in Norway was about 33 pkm per day in 1992, half of this (17 pkm) for leisure-related purposes (Høyer, 2001). In Australia, average mobility was about 44 pkm per day (Lenzen, 1999), and in Sweden, daily travel was 45 pkm in 2000 (car: 33 pkm, other: 12 pkm), about 45% of this for leisure (SCB/SIKA, 2001). In Germany, per capita mobility was 33 pkm in 1995 (car: 24 pkm, air travel: 4 pkm, train: 2 pkm, other: 3 pkm), about half of this for leisure-related purposes (BMV, 1996, excluding distances traveled abroad). An analysis by Schafer (2000) indicates daily per capita travel distances of 29 pkm in Great Britain (1995/97, leisure-related: 41%), 41 pkm in The Netherlands (1995, leisure-related: 36%), 33 pkm in Switzerland (1994, leisure-related: 50%), and 62 pkm in the United States (1995, leisure-related: 31%).

Available data seem to indicate that daily mobility in industrialized countries is in the order of 40 pkm per day, about half of this for leisure-related purposes. Out of the roughly 20 pkm traveled for leisure, car travel may account for 70-75%, air travel for 15-20%, and other means of transport for 5-10%. The distribution of the means of transport is different in reforming and developing countries (cf. Schafer and Victor, 1999; Schafer, 2000), with a lower share of leisure-related travel and a greater proportion of public transport. Table 1 shows the distribution of leisure distances traveled in industrialized, reforming and developing countries.

According to this estimate, world travel was 23,970 billion pkm in 2001, which compares to 23,231 billion pkm calculated by Schafer and Victor (1999) for the mid 1990s. Leisure-related travel may, according to this estimate, only constitute one third of the total global (roughly 8 billion pkm), which is mainly a result of the low proportion of leisure-related travel in reforming and developing countries. Overall, leisure-related transport is unequally distributed: the industrialized countries, which constitute only 15% of the world's population, account for 82% of the global leisure-related transport. This figure is even more skewed with respect to air travel. The

* *Corresponding author:* Stefan Gössling, Department of Service Management, Lund University, Box 882, SE-251 08 Helsingborg, Sweden. Email: stefan.gossling@msm.hbg.lu.se

industrialized countries account for 97.5% of the distances covered globally by air for leisure-related purposes (Table 2).

Table 1. Leisure mobility in industrialized, reforming and developing countries², 2001

	Industrialized countries		Reforming countries		Developing countries	
	% distances	pkm/day	% distances	pkm/day	% distances	pkm/day
Car	70-75	14.5	40	1.5	20	0.1
Air travel	15-20	3.5	5	0.2	0	< 0.1
Other	5-10	2.0	55	3.8	80	0.5

Source: Gössling 2002a

Table 2. Distances Travelled Globally by Air in 2001, Leisure-related Purposes

	billion pkm	% total
Industrialized countries	1,150	97.5
Reforming countries	29	2.5
Developing countries	<0.1	<0.1
Total	1,179	100

Source: Gössling 2002a

Furthermore, the calculation suggests that global air travel for leisure-related purposes may have accounted for roughly 50% (1,179 billion pkm) of the total passenger kilometers flown (2,410 billion pkm in 1996; Schumann, 1997). However, this is a comparison of data for 1996 and 2001, and the actual figure may thus be somewhat lower than 50%, even though it also needs to be considered that some national statistics exclude distances traveled by air abroad (cf. Heinze, 2000 for Germany). The leisure-related proportion of air travel in the industrialized countries may thus be underestimated: for example, in the UK, international leisure trips represented 79% of all air trips (in 1996; Graham 2000), and in Germany, leisure trips accounted for 69% of the total distances flown (in 1993; Knisch and Reichmuth, 1996).

In order to calculate the energy use associated with leisure-related air travel, the passenger kilometers flown were multiplied by factor of 2.0 MJ per pkm. Leisure related air travel may thus have contributed with 2,360 PJ to global energy use, which represents about 18% of the leisure mobility-related energy use of 13,200 PJ, or 0.6% of the global energy use in 2001. It should be noted, though, that these figures are conservative because they do not consider the energy used during the life-cycle of an aircraft for production, maintenance, etc. Lenzen (1999), for example, assumes that such energy requirements are the order of 25% to 65% of the direct energy use for passenger transport.

2 CONTINUED GROWTH?

In 2001, about 715 million international tourist arrivals were counted, the large majority of these originating from the industrialized countries (WTO, 2003a). The World Tourism Organization (WTO) predicts growth rates of 4.1% per annum to 2020 (WTO, 2001). Air travel seems to gain importance: while the observed growth rate in international tourist arrivals was on average 5.2% per year in the period 1991-1996, arrivals by air increased by 7.8% per year during the same period. In the following, the driving and limiting factors of air-travel related tourism development will be discussed.

² 1) Industrialized countries: Australia, Canada, *Europe*, New Zealand, Japan, USA; Reforming countries: Bulgaria, Chile, Croatia, Czech Republic, Estonia, Hungary, South Korea, Lithuania, Latvia, Macedonia, Malaysia, Poland, Romania, Russia, Slovak Republic, Ukraine; Developing countries: all other

2.1 *Factors that may lead to further growth*

Travel surveys indicate a strong correlation between income, education and distances travelled. For example, in Sweden, men with postgraduate education and men in the highest income group, travelled 70% and 54% more (travel distances) than men on average (SCB/SIKA, 2001). With globally rising incomes and better education, it can thus be assumed that leisure-related travel will see further growth, particularly if the so far largely underrepresented reforming and developing countries will start to travel more frequently. Furthermore, within the industrialized countries, growth in air travel has been accelerated through the emergence of low fare carriers. For example, Ryanair announced to have carried more than 2 million passengers in July 2003. In order to "celebrate" this, the airline offers 2 million seats from £15 one way on routes within Europe, including all taxes, fees and charges (Ryanair, 2003). Prices for air travel in many European countries are now far lower than those for trains and busses. With respect to international journeys, there is a strong trend towards last-minute tourism, reflecting the fact that destinations become increasingly replaceable. The price for a vacation and the time it takes to get there are now dominating many travel decisions. This, in turn, has led to more competition within the travel markets, often with the result of further decreasing prices.

From a psychological point of view, the growth in leisure-related travel can be explained with changes in the perception and understanding of the environment, a process of cosmopolitization (Gössling 2002b). Social identities emerge out of particular social structures that incorporate the elements space, time, and memory. These elements are continuously negotiated, a process in which travel plays an important role. While limited or virtual travelling (e.g. by watching TV) might enforce local embedment in juxtaposition to an imagined or perceived other (such as a neighbouring country), massive mobility might instead transform social identities towards a cosmopolitan configuration of the self as localities and their characteristics lose importance (Urry, 1995). In other words: the world may "shrink" in the eyes of frequent travellers, and travel, both for work and tourism, may disrupt the very sense of what is a person's home. Without this sense, citizens do not perceive themselves as part of places any longer, and develop cosmopolitan identities. Tourism could thus be seen as an agent of modernization, which decontextualizes and dissolves the relationships individuals have with certain places. In the context of global environmental change, this is problematic because cosmopolitan people may increasingly lose their understanding of the ecological limits of places, for which local knowledge is required, and, ultimately, they may also lose the very responsibility to care for places. As a result of this process, the environment becomes "global" and global mechanisms need to be found for safeguarding it. This is problematic, because it is individual behavior that sums up to global problems, and thus individual behavior that can reduce environmental problems - however, cosmopolitan people tend to travel more frequently, and thus cause more environmental problems. In this context, another aspect deserves to be mentioned. One of the major factors leading to the global increase in tourism is an environmental consciousness, which results in an interest to experience unknown places or other environments (Urry, 1995). Environmental consciousness comes basically into existence through education, film, or written media and the comparison of the character of the physical and built environment of different places. It has thus been argued that tourism will lead to a growing environmental consciousness and interest. However, as tourism is also a result of this very environmental consciousness, the entire process could be seen as self-reinforcing, leading to more travel.

2.2 *Factors that may inhibit growth*

Given a stable economic situation, two major aspects could counter the current trend of growing tourist numbers. First, as mentioned above, the price of a vacation has a strong influence on travel decisions. There are some signs that a tax on aviation fuels will be introduced in the industrialized countries (WTO, 2003b), which could inhibit growth in air travel, even though Brons et al. (2002) have shown that price elasticities in air travel are indeed very complex. Second, the tourists' risk perception plays an important role, as it guides travel behaviour. Three important events have influenced tourism in the last years: terror attacks, war, and the global spread of diseases such as SARS. The single most important event in 2001 was the 11th September. Immediately after the event, 40–50 per cent of tourist reservations were canceled, and after three months international tourism had dropped by about 30 per cent on average (di Castri, 2002b). However, seen over the

entire year, international tourist arrivals declined by only 0.6%. In 2002, a range of attacks on tourists occurred. 19 tourists were killed in Djerba, 202 in Bali and 16 in Kenya. Despite of these events, which were also reported on the global news, international tourist arrivals grew by 3.1%. Finally, in 2003, the Severe Acute Respiratory Syndrome (SARS) spread worldwide. On June 2003, 8,459 cases had been reported in more than 30 countries, leading to 60% less long-distance arrivals in the region of origin of the disease, Hongkong. Furthermore, the United States and Great Britain waged a war in Iraq, which received broad media-coverage. Nevertheless, the WTO (2003a) reports that tourist arrivals are on the increase and it seems likely that international visitor numbers will outpace those of 2002. In conclusion, tourism seems surprisingly resilient to terror, war, and epidemics, which is reflected in constantly growing tourist numbers. However, countries with travel warnings or countries that are immediately affected by such events may see plummeting tourist numbers, as tourists tend to travel to regions perceived as safe instead.

3 SUSTAINABILITY

The tourism industry argues that air travel accounts only for a minor share of the global energy use, and – given its economic importance – that it thus be neglected when planning for sustainability. This view ignores the fact that a minor proportion of the world's population is responsible for this energy use. With respect to leisure, one estimate is that 5% of the world's population is responsible for about 40% of the global leisure-related energy use, in particular including air-based transport (cf. Gössling, 2002a). Per capita calculations of energy use, CO₂-equivalent emissions, or ecological footprints associated with air travel all suggest that air travel is not sustainable (cf. Carlsson-Kanyama and Lindén, 1999; Gössling, 2000; Gössling et al., 2002; Høyer, 2001). The environmental impacts of air travel should thus be calculated on a per capita level, which can be illustrated with an example: extrapolating the current level of air travel in industrialized countries to reforming and developing countries would result in a six-fold increase of passenger kilometres flown (to 7,730 billion pkm), with a corresponding energy use of 15,460 PJ.

In view of aviation's current impact on the environment, mitigation strategies have been suggested. These are so far primarily technological in character (see, for instance, Ponater et al.; Noland et al. this volume), and the potential of socio-economic mitigation strategies should thus also be analyzed. Some suggestions will be made here, even though it is beyond the scope of this paper to provide an in-depth analysis of this topic. First of all, the knowledge that flying is harmful to the environment seems not as widespread as one might think. There has certainly been some media-coverage in the late 1990s, but judging from current developments in air travel, the broader public seems not concerned. A first step towards mitigation might thus be to launch information campaigns about the environmental consequences of aviation in order to ensure that everybody is aware of these. However, this might not necessarily lead to changing travel behavior. For example, the Germans with the highest environmental consciousness were also identified as those traveling most for leisure-related purposes (Preisendörfer, 1998). Environmental knowledge needs thus to go along with the right attitude to result in altered travel behavior. Information should thus be provided in combination with attempts to change basic attitudes (Nilsson and Küller, 2000), while prices for air travel should be substantially increased (cf. Crouch, 1994; Brons et al., 2001). In this context it is worth mentioning that future aircraft powered by hydrogen and/or fuel cells might have a substantial effect on travel behavior – less because of the additional costs involved (30-50 billion of dollars for the development of this aircraft seem likely, and operating costs will also be higher), but rather because such aircraft would be 20-40% slower in cruise flight (Paul Peeters, 2003; personal communication).

Another aspect to be considered is that a minor proportion of tourists accounts for the majority of the distances covered – this has been termed the 20 : 80 rule of thumb (Paul Peeters, 2003; personal communication), which implies that 20% of the journeys cause 80% of the environmental impact. In Germany, for example, the 14% of the longer vacation journeys to destinations outside Europe were responsible for almost 55% of the energy use (in 1993; Knisch and Reichmuth, 1996). An identification of these most harmful journeys and their substitution for other forms of vacations could thus be of great help in reducing the overall impact of air travel. Obviously, the tourist

industry and their advertisement campaigns play an important role in this process, particularly in the supply-driven tourist markets.

Finally it should be acknowledged that the tourist industry itself has now recognized that leisure tourism is a problem for the environment (WTO, 2003b). However, there is still a tendency to play down the importance of aviation, and claims for action seem purely rhetoric. Furthermore, there is a trend to present the benefits of tourism to the public in order to create a positive discourse. For example, the new buzzword of the World Tourism Organization is "sustainable tourism - poverty alleviation", and the TUI, Germany's largest tour operator, claims that the world needs more tourism in order to shut down environmentally harmful industries.

4 CONCLUSIONS

Some basic conclusions can be drawn from this analysis. First, the spatial globalization of travel seems to have reached its limits: virtually any place in the world is accessible within 24 hours, provided the financial means. However, not all regions of the world are equally connected to each other, and it can thus be expected that the network of airports will become denser, particularly in reforming and developing countries. In line with these developments, the societal globalization of travel, this is the participation of all human beings in air travel on an equal footing, will lead to further growth in international tourist arrivals.

The article has also shown that leisure tourism is responsible for half of the distances travelled by air, and its share is continuously increasing. Given the current trends in low fare air travel, the wish to experience other places, and tourism's resilience to terror, war, and globally spreading diseases, growth in leisure-related mobility seems likely even from this perspective.

Finally, mitigation strategies should consider socio-economic aspects and not purely focus on technical solutions in order to make aviation more sustainable.

REFERENCES

- Brons, M., E. Pels, P. Nijkamp, P. Rietveld, 2002: Price elasticities of demand for passenger air travel: a meta-analysis, *Journal of Air Transport Management* 8 (3): 165-175
- Bundesverkehrsministerium (BMV), 1996: Verkehr in Zahlen. Deutsches Institut für Wirtschaftsforschung, Berlin.
- Carlsson-Kanyama, A. and A.-L. Lindén, 1999: Travel patterns and environmental effects now and in the future: implications of differences in energy consumption among socio-economic groups. *Ecological Economics* 30, 405-417.
- Crouch, G. I., 1994: Demand Elasticities for Short-Haul versus Long-Haul Tourism. *Journal of Travel Research*, Fall 1994: 2-7.
- di Castri, F., 2002b: 'Tourism revisited after 11 September 2001', in F. di Castri and V. Balaji (eds), *Tourism, Biodiversity and Information*, Leiden, The Netherlands: Backhuys Publishers, pp. 483-8.
- Gössling, S., 2000: Sustainable tourism development in developing countries: some aspects of energy-use. *Journal of Sustainable Tourism* 8(5), 410-425.
- Gössling, S., C. Borgström-Hansson, O. Hörstmeier and S. Saggel, 2002: Ecological Footprint Analysis as a Tool to Assess Tourism Sustainability. *Ecological Economics* 43(2-3): 199-211.
- Gössling, S., 2002a: Global environmental consequences of tourism. *Global Environmental Change* 12(4): 283-302.
- Gössling, S., 2002b: Human-environmental relations with tourism. *Annals of Tourism Research* 29(4): 539-556.
- Graham, A., 2000: United Kingdom. In European Conference of Ministers of Transport (ECMT) (ed.) *Transport and Leisure. Report of the hundred and eleventh round table on transport economics*. Paris, 15-16th October 1998. ECMT, Paris: 147-173.
- Heinze, G.W., 2000: Germany. In European Conference of Ministers of Transport (ECMT) (ed.) *Transport and Leisure. Report of the hundred and eleventh round table on transport economics*. Paris, 15-16th October 1998. ECMT, Paris: 5-51.
- Høyer, K.G., 2001: Sustainable Tourism or Sustainable Mobility? The Norwegian Case. *Journal of Sustainable Tourism* 8(2), 147-160.

- Knisch, H. and M. Reichmuth, 1996: Verkehrsleistung und Luftschadstoffemissionen des Personenflugverkehrs in Deutschland von 1980 bis 2010. Texte des Umweltbundesamtes, 16/96. Umweltbundesamt, Berlin.
- Knoflacher, H., 2000: Austria. In European Conference of Ministers of Transport (ECMT) (ed.), Transport and Leisure. Report of the hundred and eleventh round table on transport economics. Paris, 15-16th October 1998. ECMT, Paris: 53-88.
- Lenzen, M., 1999: Total requirements of energy and greenhouse gases for Australian transport. *Transportation Research Part D* 4, 265-290.
- Nilsson, M. and R. Küller, 2000: Travel behaviour and environmental concern. *Transportation Research Part D* 5: 211-234.
- Preisendörfer, P., 1998: Umwelteinstellungen und Freizeitmobilität. *Tourismus Journal* 2(4): 441-456.
- Ryanair, 2003: Available at: www.ryanair.com. Accessed 6 August 2003.
- Schafer, A., 2000: Regularities in Travel Demand: An International Perspective. *Journal of Transportation and Statistics*, December 2000: 1-31.
- Schafer, A. and D.G. Victor, 1999: Global passenger travel: implications for carbon dioxide emissions. *Energy* 24, 657-679.
- Schumann, U., 1997: The impact of aviation on the atmosphere - An overview on atmospheric research within the programme 'Pollutants from Air Traffic'. In Schumann, U., A. Chlond, A. Ebel, B. Kärcher, H. Pak, H. Schlager, A. Schmitt and P. Wendling, (eds.), Pollutants from Air Traffic - Results of Atmospheric Research 1992-1997. Deutsches Zentrum für Luft- und Raumfahrt, Mitteilung 97-04 (pp. 1-21), Oberpfaffenhofen.
- Statistiska centralbyrån/Statens institut för kommunikationsanalys (SCB/SIKA) 2001: RES 2000. Den nationella reseundersökningen. Birger Gustafsson AB, Stockholm.
- Urry, J., 1995: *Consuming Places*. Routledge, London.
- World Tourism Organization (WTO), 2003a: News Release. World Tourism in 2002: Better than expected. Available at: [http://www.world-tourism.org/newsroom/Releases/2003/jan/numbers 2002.htm](http://www.world-tourism.org/newsroom/Releases/2003/jan/numbers%202002.htm). Accessed 6 August 2003
- World Tourism Organization (WTO), 2003b: Climate Change and Tourism. Available at: <http://www.world-tourism.org/sustainable/climate/final-report.pdf>. Accessed 6 August 2003.
- World Tourism Organization (WTO), 2001: *Tourism 2020 Vision*. World Tourism Organization, Madrid.

The SCENIC Project: Impact of Supersonic Aircraft on the Atmosphere

O. Dessens, H.L. Rogers, J.A. Pyle.

Centre for Atmospheric Science, University of Cambridge, Lensfield Road, Cambridge, CB2 1EW, United Kingdom

ABSTRACT: New model calculations suggest that the potential impact on the atmosphere of a future fleet of supersonic aircraft, for the year 2015, is highly dependent upon the amount of nitrogen oxides (NO_x) emitted from the fleet. This result contrasts with the most recent assessment which suggested that the impact of supersonic aircraft on the atmosphere was primarily through the role of water vapour emissions both on atmospheric ozone and climate change.

1 INTRODUCTION

In the 1970s, plans to build a large fleet of high-flying supersonic aircraft led to concerns that their exhaust emissions (principally NO_x , but also H_2O , SO_2 , hydrocarbons, etc.) could cause a reduction in stratospheric ozone (Johnston 1971, Crutzen 1972). In the event, only a small number of supersonic passenger aircraft were built, and attention switched to other possible causes of ozone depletion. However, in recent years, the growth in the number of long-haul subsonic passenger aircraft, and the projection for further expansion in the future, has reawakened a general concern for the effects of aircraft on the atmosphere. The *IPCC Special Report* went some way to quantifying the impact of aircraft on the atmosphere. However, our recent modelling calculations have produced conclusions significantly different from those reached in that report. This difference has resulted from an update of atmospheric reaction rates which now act to reduce modelled column ozone in the presence of supersonic aircraft emissions.

2 MODEL CALCULATIONS

In this study, an established 3D chemical transport model, SLIMCAT (Chipperfield 1999, Rogers *et al.* 2000) has been used to assess the impact of aircraft emissions. The model has been used with a resolution of 7.5° in latitude and longitude and with 12 vertical levels from 12 to 60 km. The model is driven by daily meteorological data. Each simulation begins with a 6-year spin-up of repeated annual meteorological data, and is followed by a one year integration.

All the calculations for the reference atmosphere and the perturbations due to the supersonic fleet emissions are as describe in chapter 4 of the *IPCC Special Report* and are listed in table 1.

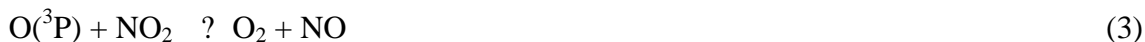
Table 1 SLIMCAT Model Simulations Performed

Scenario	EI(NO_x)-supersonic*
D	2015 Reference
S1b	0
S1c	5
S1d	10
S1e	15

*EI(NO_x) (in $\text{g}(\text{NO}_2)/\text{kg}(\text{fuel})$) is the nitrogen oxides emission index for the supersonic fleet.

The 2015 reference atmosphere, scenario D, includes only subsonic aircraft emissions, whilst scenarios S1 include additional supersonic aircraft emissions under various EI(NO_x) conditions. Both subsonic and supersonic aircraft emissions of NO_x and H_2O are prescribed using the NASA-2015 database (Baughcum *et al.* 1998).

Crucially for this study the SLIMCAT model has been updated to include new kinetic data. The main reactions affected include the formation of HNO_3 from NO_2 and OH, the reduction of NO_2 to NO and the oxidation of HNO_3 by OH:



With the new data the first reaction rate affected (R1) shows a strong decrease in the conversion rate of NO_2 to HNO_3 in the lower stratosphere (Brown *et al.* 1999a). The rate coefficient of the second reaction (R2) has been modified to increase its temperature and pressure dependence (Brown *et al.* 1999b) resulting in a doubling of the rate in the lower stratosphere. Reaction R3 leads to ozone destruction, and its rate is increased by 20 to 30% in the lower stratosphere (Gierzack *et al.* 1999). The combination of these reaction rates lead to higher concentrations of NO_x in the lower stratosphere and therefore to lower ozone concentrations.

3 DISCUSSION

Fig. 1 shows the percentage change in ozone column over the northern hemisphere, due to various supersonic aircraft NO_x emission indices (S1b to S1e), each referenced to scenario D. Comparing these results with those given in the *IPCC Special Report* highlights the effect of the new kinetic data in the SLIMCAT model. Formerly an increase in the $\text{EI}(\text{NO}_x)$ had only a small effect on the ozone column, with H_2O emissions having the most significant impact. For all models shown in the report, there are only modest changes in ozone with $\text{EI}(\text{NO}_x)$. In contrast, with the inclusion of the updated rates, an increase in the $\text{EI}(\text{NO}_x)$ has a significant effect on the ozone column, with a reduction in the Northern Hemisphere ozone column of -3.2% for $\text{EI}(\text{NO}_x)=15$.

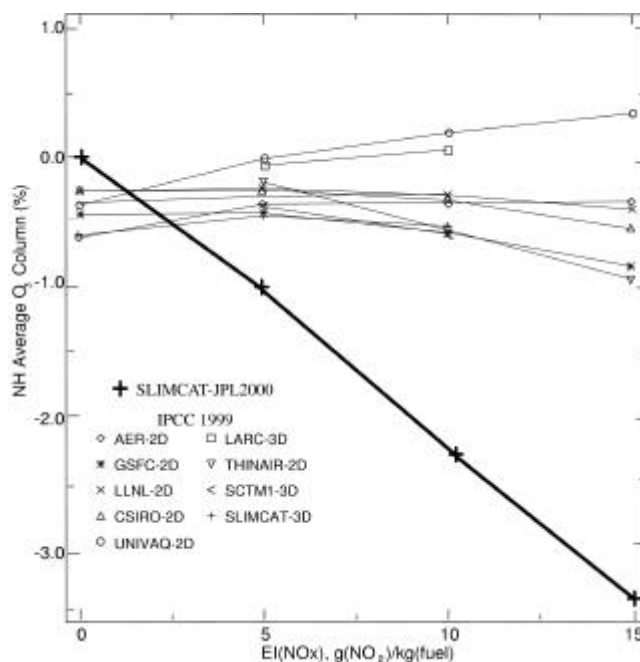


Figure 1: Northern Hemisphere total ozone column change as a function of $\text{EI}(\text{NO}_x)$ in 2015 for a supersonic fleet with SA0 sulfate distribution. The black line with symbol '+' represents the SLIMCAT model calculation with updated reaction rates. The grey lines are taken from the *IPCC Special Report*.

The reason for the large dependence of column ozone on $EI(NO_x)$ can be seen by considering the zonal mean ozone perturbation due to supersonic aircraft emissions. Fig. 2 shows the modelled effect of supersonic aircraft emissions with $EI(NO_x)=5$ (scenario S1c) on the zonal mean ozone distribution for June 2015. The top panel presents the SLIMCAT calculation previously included in the *IPCC Special Report*. The bottom panel uses the SLIMCAT calculation performed with the new kinetic data. In the *IPCC Special Report* a cross-over point in the ozone chemical production and destruction terms, due to NO_x chemistry, could be seen at an altitude of ~ 20 km. With the new kinetic data the cross-over point is at a much lower altitude in the model calculations. With the injection of supersonic aircraft emissions at ~ 18 km almost all NO_x and H_2O emissions now take place in the region of ozone chemical destruction. This has resulted in an ozone decrease throughout the stratosphere and therefore in the ozone column.

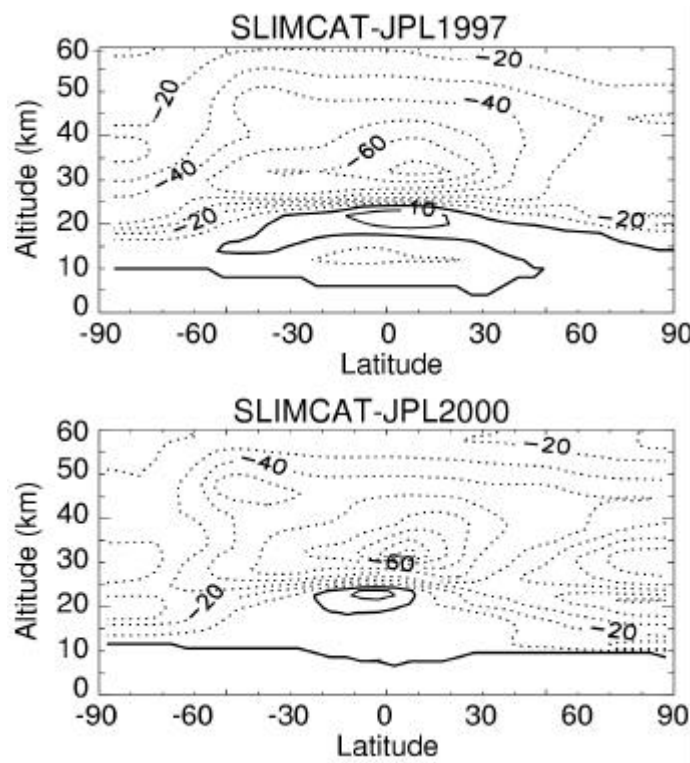


Figure 2: Ozone profile change (in ppbv) for S1c [$EI(NO_x)=5$, SA0] relative to D [reference, SA0] in June 2015 (top : SLIMCAT-IPCC1999, bottom: SLIMCAT-updated).

4 CONCLUSION

The results of this study, highlight the impact of supersonic aircraft emissions with varying $EI(NO_x)$. This is in contrast to the results from previous assessments such as the *IPCC Special Report*. This significant difference results from the inclusion of new kinetic data in our atmospheric chemical-transport model. This conclusion underlines the potential impact of a fleet of supersonic aircraft on the atmosphere and emphasises the necessity to continue to develop low NO_x combustion engines for the future as well as the importance of maintaining state of the art kinetic data.

REFERENCES

Baughcum, S.L., Sutku Jr., D.J. & Henderson, S.C. Year 2015 aircraft emissions scenario for scheduled air traffic (*Contractor Rep. No. 207638*, NASA Langley Research Center, 1998).

- Brown, S., Talukdar, R. & Ravishankara, A., Rate constants for the reaction $\text{OH} + \text{NO}_2 + \text{M} \rightarrow \text{HNO}_3 + \text{M}$ under atmospheric conditions, *Chem. Phys. Lett.*, **299**, 277-284 (1999a).
- Brown, S., Talukdar, R. & Ravishankara, A., Reconsideration of the rate constants for the reaction of hydroxyl radical with nitric acid, *J. Phys. Chem. A*, **103**, 3031-3037 (1999b).
- Chipperfield, M.P. Multiannual simulations with a three-dimensional chemical transport model. *J. Geophys. Res.* **104**, 17811805 (1999).
- Crutzen, P.J. SSTs: a threat to the earth's ozone shield. *Ambio* **1**, 41-51 (1972).
- IPCC Special Report : Aviation and the Global Atmosphere*. Intergovernmental Panel on Climate Change (Rep. No. 8, World Meteorological Organisation and United Nations Environment Programme, Cambridge University Press, UK, 1999).
- Johnston, H.S. Reduction of stratospheric ozone by nitrogen dioxide catalysts from supersonic transport exhaust. *Science* **173**, 517-522 (1971).
- Rogers, H.L., Chipperfield, M.P., Bekki, S. & Pyle, J.A. The effects of future supersonic aircraft on stratospheric chemistry modeled with varying meteorology, *J. Geophys. Res.* **105**, 29359-29367 (2000).
- Gierczak, T., Burkholder, J.B. & Ravishankara, A., Temperature dependent rate coefficient for the reaction $\text{O}(^3\text{P}) + \text{NO}_2 \rightarrow \text{NO} + \text{O}_2$, *J. Phys. Chem. A*, **103**, 877-883 (1999)
- The SCENIC project webpage: <http://www-scenic.ch.cam.ac.uk/>

A 3D Model Intercomparison of the Effects of Future Supersonic Aircraft on the Chemical Composition of the Stratosphere

Giovanni Pitari^{*}, Eva Mancini
Dipartimento di Fisica - Università L'Aquila -Italy

Helen Rogers, Olivier Dessens
Department of Chemistry - University of Cambridge – UK

Ivar Isaksen, Bjorg Rognerud
Department of Geophysics – University of Oslo- Norway

Keywords: Supersonic Aircraft, Stratospheric Chemistry, Aerosol, Ozone, Global Models

ABSTRACT: Gas and aerosol emissions from future supersonic aircraft may affect the chemical composition of the stratosphere in a significant way. The large scale accumulation of H₂O and NO_y is one key point to be assessed with models. The relative importance of the different catalytic cycles for ozone depletion is another key point, and for this it is important to determine the ability of models to predict the actual background abundance of radical species affecting the ozone photochemistry (i.e. OH, HO₂, NO₂, ClO, BrO). Here we focus on pure photochemical effects and compare the results of three completely independent three-dimensional chemical-transport models (CTM) (University of L'Aquila, University of Cambridge, University of Oslo), as part of the EC-funded TRADEOFF project. It should be noted that the 1999 IPCC assessment was largely based on the results of zonally averaged two-dimensional models. The University of L'Aquila CTM is run in interactive mode with a microphysics code for aerosol formation and growth, in order to calculate the aircraft forced changes of surface area density (SAD) of sulphuric acid aerosols. This SAD perturbation is then provided off-line to the other two models, in order to assess the sensitivity of the three CTMs to both NO_x and SO_x emissions. We first validate the aerosol results in the stratosphere (surface area density) and then discuss similarities and differences between the three CTMs in terms of the effect of aircraft forced changes of ozone and radical species on atmospheric chemistry.

1 INTRODUCTION

In the last decade several modelling studies have been made on the issue of supersonic aircraft impact on the chemical composition of the stratosphere (NASA, 1992; IPCC, 1999). The net effect on the global ozone distribution is not easy to assess with photochemical models, due to the complex interactions of different catalytic cycles for ozone destruction in the stratosphere, with partially opposing effects at different altitudes (Weissenstein et al., 1991). A realistic transport parameterization is essential to obtain a proper spatial and seasonal behaviour of the radical species involved in the ozone photochemistry (i.e. OH, HO₂, NO₂, ClO, BrO) and also to simulate in a realistic way the large-scale accumulation of gases emitted by the aircraft (H₂O, NO_y, SO₂, particles). To a first approximation, these emissions can be considered as localized tracers (Rogers et al., 2002). In addition, ozone and water vapour absorb planetary radiation in the middle atmosphere, so that changes in their distribution may feedback on stratospheric dynamics (Pitari and Mancini, 2001).

Here we focus on the pure photochemical effects and compare the results of three independent 3D global chemical-transport models (CTM) of the stratosphere for the purpose of assessing, in a

^{*} *Corresponding author:* G.Pitari, Dipartimento di Fisica, Università dell'Aquila, Via Vetoio, 67100, L'Aquila, Italy. Email: gianni.pitari@aquila.infn.it

more accurate way, the tracer distribution in the lower stratosphere compared with the previously considered zonally averaged 2D models. Another important update with respect to the IPCC (1999) assessment is that here the models include the new rate constants for the NO_x reactions (Brown et al., 1999a; Brown et al., 1999b; Gierczak et al., 1999) that significantly increase the relative importance of the NO_x catalytic cycle with respect to the previous numerical simulations including the rates listed in JPL (1997).

2 DESIGN OF MODEL EXPERIMENTS

The overall strategy of this study was to run three independent CTMs under similar conditions: the same chemistry boundary conditions appropriate for the year 2015 (IPCC, 2001; WMO, 2002); the same chemistry kinetics and photochemical data (JPL, 1997); NASA emission scenarios (IPCC, 1999) for future supersonic aircraft (HSCT); and meteorology appropriate for present time conditions (i.e. year 2000). An important exception to the chemical rates reported in JPL (1997) are the three reactions relevant for stratospheric NO_x (i.e. $\text{NO}_2 + \text{O}(^3\text{P})$; $\text{NO}_2 + \text{OH} + \text{m}$; $\text{HNO}_3 + \text{OH}$): for these we use the values listed in Brown et al. (1999a, 1999b) and in Gierczak et al. (1999).

The participating models are: the SLIMCAT model from the University of Cambridge (UCAM), SCTM-1 model from the University of OSLO (UiO) and the CTM model from the University of L'Aquila (ULAQ). All three models have chemical schemes containing the main stratospheric families for ozone depletion and include heterogeneous reactions on PSCs and sulphuric acid aerosols. The UCAM model is an off-line CTM for the stratosphere formulated on isentropic surfaces, with forcing winds from the UKMO analyses. The UiO and ULAQ models use pre-calculated transport fields from the output of climate-chemistry models, GISS and ULAQ respectively. The ULAQ model is a low-resolution global CTM coupled to a microphysics code for aerosol formation and growth. For more details see Pitari et al. (2001).

Ten numerical experiments have been made by each model, with 10-year spin-up to allow a meaningful steady-state: one without aircraft emissions, another one with subsonic aircraft only, and the remaining eight including also supersonic aircraft emissions with $0 \leq \text{EI-NO}_x \leq 15$, with and without the perturbation of the aerosol surface area density calculated off-line in the ULAQ model. The latter assumption allows the same distribution of aerosols in all three models. The major assumptions made for sulphur emissions by supersonic aircraft are: $\text{EI-SO}_2 = 0.4 \text{ g/kg-fuel}$, with 10% fraction of sulphuric acid plume particles and a radius of aircraft emitted aerosols of 5 nm.

We will first discuss the calculated impact of sulphur emissions by HSCT on the stratospheric surface area density of sulphuric acid aerosols (SSA-SAD), and then the combined effects of sulphur and NO_x emissions on stratospheric tracers, ozone and radical species affecting the ozone photochemistry.

3 RESULTS

3.1 Aerosol surface area density

Fig. 1 shows how the ULAQ model calculation of aerosol surface area density compared with observations in the stratosphere (SAGE-II data for 1996-2000), and the magnitude of the predicted change forced by sulphur emissions from HSCTs. The aircraft perturbation of SAD has a maximum in the source region (close to 45N at 20 km altitude) and our calculation predicts a change as large as $0.27 \mu\text{m}^2/\text{cm}^3$, that is close to 40% of the background value, with a much smaller penetration in the Southern Hemisphere. Ultrafine plume particles are the major cause of this SAD increase. A significant enhancement of N_2O_5 and BrONO_2 hydrolysis is to be expected as a consequence of this large increase of the sulphuric acid aerosol surface area (IPCC, 1999; Weisenstein et al., 1998).

3.2 HSCT perturbation on chemical species

Water vapour and NO_y are the chemical species directly affected by HSCT emissions in the lower stratosphere. Transport rates in the CTMs affect the accumulation of these tracers, so that we may expect a significant spread in the magnitude of the perturbation close to the source region and also

in the model ability to export tracers on the planetary scale outside the flight corridors (see Rogers et al. (2002) for a comprehensive study of the evolution of localized tracers in numerical models). Fig. 2 summarizes the model results for the accumulated H_2O and NO_y . Typical features are: ULAQ has a tendency to keep the tracers more efficiently confined into the emission region (this is consistent with the results of the Rogers et al. (2002) paper); $\Delta \text{H}_2\text{O}$ from UiO is about half that calculated by the other two models (0.15-0.3 ppmv compared with 0.3-0.5 ppmv in the 20-30 km altitude layer); ΔNO_y in the UCAM model penetrates more efficiently above the source region, compared with UiO and ULAQ (0.8 ppbv compared with 0.4 ppbv at 30 km, with $\text{EI-NO}_x=10$ g/kg).

An enhancement of water vapour produces more OH and thus increases the mid-stratospheric ozone loss; it also affects lower stratospheric ozone via the HO_x catalytic cycle and indirectly by converting more NO_2 into nitric acid. Emissions of NO_x make the odd nitrogen catalytic cycle more efficient and thus increase the ozone loss above 20 km, where the NO_x cycle dominates. The net effect on ozone above the tropopause up to about 20 km depends on the balance between the nearly compensating effects of the increasing efficiency of the NO_x cycle, with the decreasing efficiencies of Cl, Br and HO_x cycles. Fig. 3 summarizes the vertical profile changes of those radical species which strongly affects mid-latitude lower stratospheric ozone (OH, NO_2 , ClO). As expected from Fig. 2, the mid-stratospheric OH increase in the UiO model is smaller than in the other two models. The NO_2 percent increase in the UiO model is 30 to 50% larger than in UCAM and ULAQ even though the absolute perturbation of NO_y is similar or smaller (Fig. 2). The reason is that the Oslo model predicts a rather low amount of $\text{NO}+\text{NO}_2$ below 25 km altitude (see above). UCAM and ULAQ models are generally very consistent in the prediction of these relative changes of the radicals, although the ClO response to the NO_2 increase is larger in the ULAQ model: this may have a significant impact on ozone below 20 km altitude.

Fig. 4 shows the ozone profile changes for a set of EI-NO_x and EI-S cases. $\text{EI-NO}_x=0$ corresponds to a pure water vapour emission by the aircraft: here OH increases and NO_2 decreases, more efficiently when the aerosol SAD is enhanced by HSCT emissions. The fact that in this last case ozone increases in the UCAM model (opposite to ULAQ and UiO) is a clear indication that the ozone response in the lower stratosphere is dominated by the NO_x cycle in the Cambridge model. This becomes even more clear when direct injection of NO_x is considered ($\text{EI-NO}_x > 0$): ULAQ and UiO show a clear cross-over point in the ozone profile change at about 20 km altitude (O_3 increase below and decrease above) while in UCAM the ozone depletion is extended to all heights. In addition the enhancement of aerosol SAD produces an increase of ozone loss in ULAQ and UiO models contrary to UCAM. These are clear indications that any perturbation of the NO_x in the lower stratosphere is more effectively compensated in ULAQ and UiO models by changes of OH, ClO and BrO than in UCAM (see Fig. 3).

The behaviour of the model calculated ozone profile changes discussed above is again visible in Fig. 5, where we present the globally integrated ozone changes with respect to the pure subsonic case for different EI-NO_x and EI-S values. An interesting comparison can be made with the values reported in the IPCC (1999) volume with fixed SSA-SAD: in that case the ULAQ-2D model ranges between -0.35% (with $\text{EI-NO}_x = 0$) and 0.35% (with $\text{EI-NO}_x = 15$ g/kg), while here ULAQ-3D ranges between -0.35% and -0.25% . The corresponding ΔO_3 spread for SLIMCAT was about -0.6% (with $\text{EI-NO}_x = 0$) to -0.5% (with $\text{EI-NO}_x = 10$ g/kg) in IPCC (1999), versus -0.03% (with $\text{EI-NO}_x = 0$) to -2.85% (with $\text{EI-NO}_x = 15$ g/kg) in the present study. The update of the NO_x cycle reaction rates to the Brown et al. (1999a, 1999b) and in Gierczak et al. (1999) values seems to affect the UCAM results much more than those from the ULAQ model, at least with high EI-NO_x values.

A validation of background model results (i.e. pure subsonic case) for mid-latitude conditions is presented in Fig. 6. The models are rather consistent with satellite observations. Notable exceptions are however water vapour, where UCAM underestimates the observations, and NO_x and NO_y where in the mid-stratosphere UiO underestimates the observations and in the mid-stratosphere ULAQ and UCAM overestimate the observations. Some caution has to be used for the NO_x data in the lowermost stratosphere, due to the residual abundance of Pinatubo aerosols in March 1993, which make heterogeneous conversion of NO_x into NO_y faster than during volcanically clean conditions. It should be noted that UCAM has tested the O_3 sensitivity to HSCT emissions with a doubled lower stratospheric H_2O content, and the results discussed above are only marginally affected.

Figure 1. (Left) ULAQ-CTM calculations (solid lines) and SAGE-II measurements (symbols) of springtime mid-latitude SSA-SAD; units are 10^{-8}cm^{-1} . (Right) Annually averaged SAD changes due to HSCTs at 20 km.

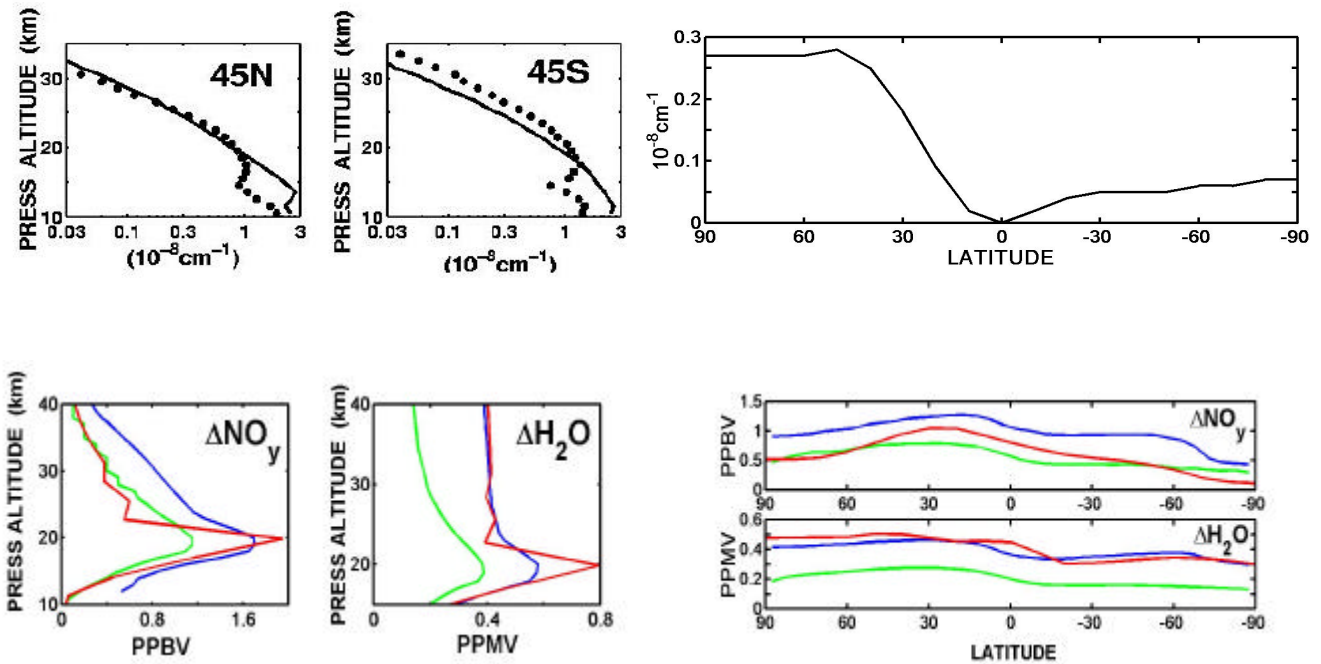


Figure 2. (Left) Vertical profiles of annually averaged changes of NO_y (ppbv) and H_2O (ppmv) at 45N, due to HSCT emissions ($\text{EI-NO}_x=10 \text{ g/kg}$). (Right) Calculated NO_y and H_2O changes in the 20 - 30 km layer. Blue, green and red lines are for UCAM, UiO and ULAQ models, respectively.

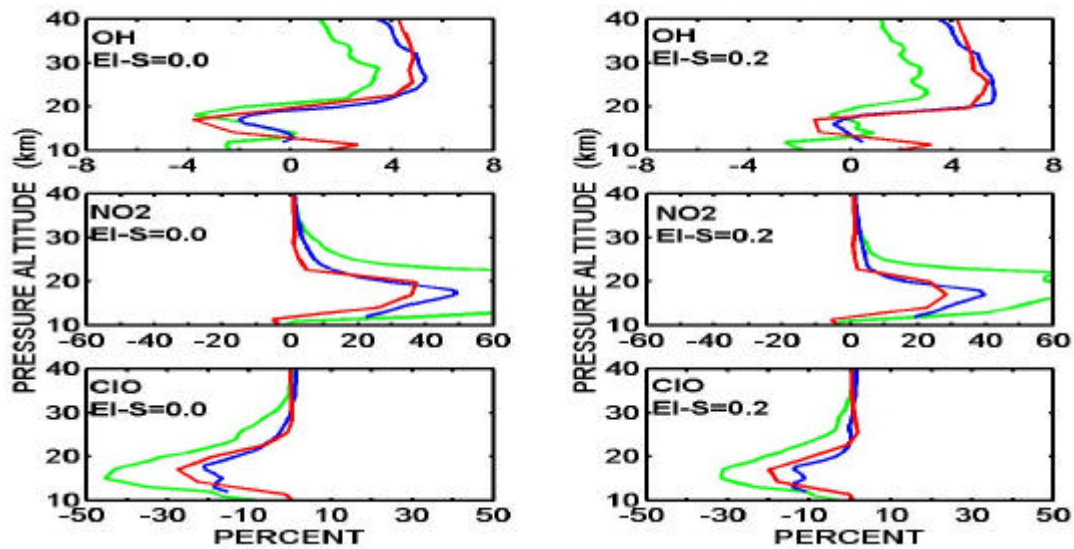


Figure 3. As in Fig. 2, but for percent changes of OH, NO_2 and ClO in the 30N-60N band for the $\text{EI-NO}_x=10 \text{ g/kg}$ experiment. Left panels are with unchanged SSA-SAD; right panels include the SAD change of Fig. 1.

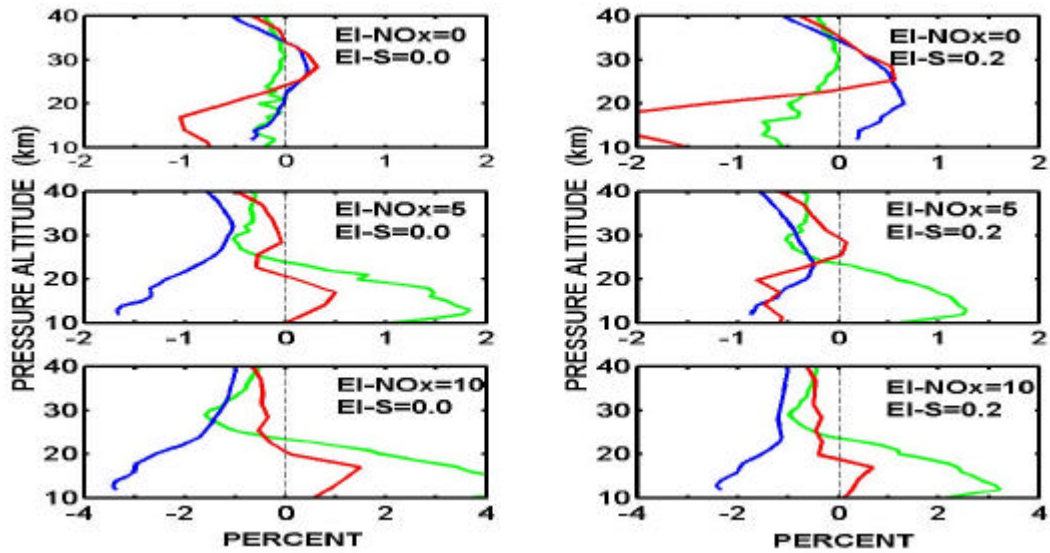


Figure 4. As in Fig. 3, but for ozone percent changes with $EI-NO_x=0, 5, 10$ g/kg.

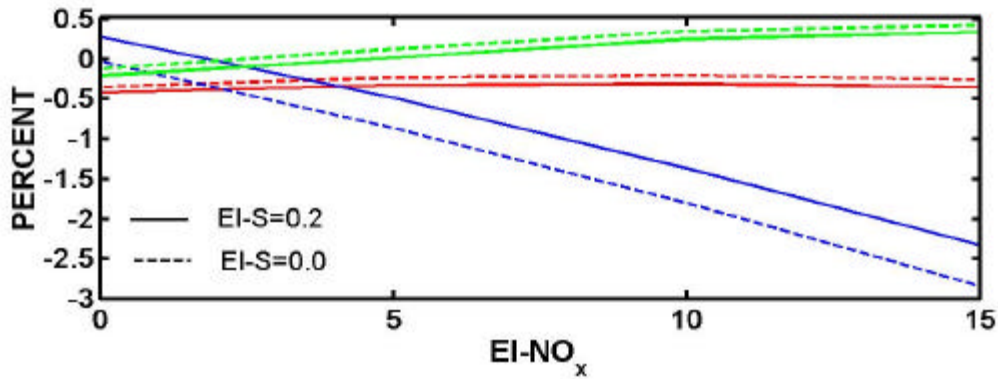


Figure 5. Global ozone percent changes as a function of $EI-NO_x$ and $EI-S$. Colours are as in Fig. 2.

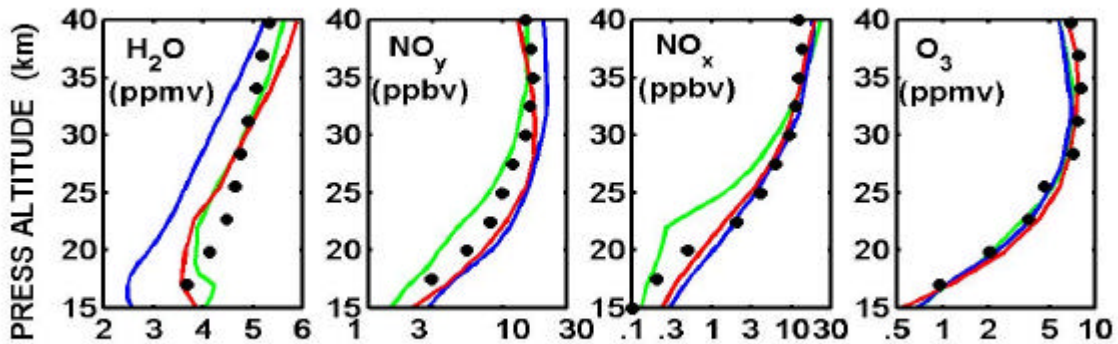


Figure 6. Calculated annually averaged vertical profiles in the 30N-60N latitude band. Colours are as in Fig. 2; symbols are for observations: H_2O (HALOE, April 1992); NO_x (HALOE, March 1993); NO_y (HALOE NO_x + CLAES HNO_3 , March 1993); O_3 (climatology) (NASA, 1999).

4 CONCLUSIONS

The main conclusion of this study is that, while relative profile changes of the most important radical species affecting the ozone photochemistry (i.e. NO_x , HO_x , ClO , BrO), are similar between the three models (with respect to the pure subsonic case), the perturbation to ozone is increasingly variable with increasing EI-NO_x . In particular, the UCAM model no longer predicts a crossover point between ozone production and destruction in the lower stratosphere with updated kinetic rates. For $\text{EI-NO}_x > 5 \text{ g/kg}$: here the mid-stratospheric ozone depletion penetrates below 20 km, having an impact on the ozone column much larger and negative compared with the ULAQ and UiO models. Analysis of the results shows that a possible cause for this difference is that any perturbation of the NO_x amount in the lower stratosphere is more effectively compensated for in the ULAQ and UiO models by changes of OH , ClO and BrO than in UCAM.

Even assuming a rather low sulphur emission index ($\text{EI-S} = 0.2 \text{ g/kg}$) and a lower limit estimate for plume particle formation (4% of total emitted sulphur), a future fleet of 500 HSCTs may produce a substantial perturbation of SSA-SAD (up to 40% at 20 km). In the ULAQ and UiO models, for a given NO_x injection, SO_x emissions increase the O_3 loss by removing part of NO_x and increasing reactive Cl/Br . In UCAM the prevailing effect of the additional SSA-SAD is to decrease reactive nitrogen (i.e. prevailing NO_x effect), so that the ozone loss decreases. A more systematic comparison of the models performance in the lower stratosphere, as well as a comparison of the calculated O_3 loss rates for the different catalytic cycles, will be made in the current EC-project SCENIC.

5 ACKNOWLEDGEMENTS

This work is supported by the EC, contract ENK2-CT-1999-00030.

REFERENCES

- Brown, S., R. Talukdar and A. Ravishankara, 1999a: Rate constants for reaction $\text{OH} + \text{NO}_2 + \text{M} \rightarrow \text{HNO}_3 + \text{M}$ under atmospheric conditions, *Chem. Phys. Lett.*, 299, 277-284.
- Brown, S., R. Talukdar and A. Ravishankara, 1999b: Reconsideration of the rate constants for reaction of hydroxyl radical with nitric acid, *J. Phys. Chem.*, 103, 3031-3037.
- Gierczak, T., J.B. Burkholder and A. Ravishankara, 1999: Temperature dependent rate coefficient for the reaction $\text{O}(^3\text{P}) + \text{NO}_2 \rightarrow \text{NO} + \text{O}_2$ An ozone climatology based on ozonesonde and satellite measurements, *J. Phys. Chem.*, 103, 877-883.
- IPCC, 1999: *Special report on aviation and the global atmosphere*, J. E. Penner et al. Eds. Cambridge University Press, Cambridge, 373 pp.
- IPCC, 2001: *Climate change 2001- The Scientific Basis*, J.T. Houghton et al. Eds. Cambridge University Press, Cambridge, 881 pp.
- JPL, 1997: *Chemical kinetics and photochemical data for use in stratospheric modeling*, JPL publ. 97-4, Pasadena, California.
- NASA, 1992: *The atmospheric effects of stratospheric aircraft: A first program report*, M.J. Prater et al. Eds., *NASA Ref. Publ.* 1272.
- NASA, 1999: *Model and Measurements Intercomparison II*, J.H. Park et al. Eds., NASA/TM-1999-209554.
- Pitari, G., and E. Mancini, 2001: Climatic impact of future supersonic aircraft: role of water vapour and ozone feedback on circulation, *Phys. Chem. of Earth C*, 26/8, 571-576.
- Pitari, G., E. Mancini, A. Bregman, H.L. Rogers, J.K. Sundet, V. Grewe, and O. Dessens, 2001: Sulphate particles from subsonic aviation: Impact on upper tropospheric and lower stratospheric ozone, *Phys. Chem. of Earth C*, 26/8, 563-569.
- Rogers, H.L., H. Teyssedre, G. Pitari, V. Grewe, P. van Velthoven, and J. Sundet, 2002: Model intercomparison of the transport of aircraft-like emissions from sub- and supersonic aircraft, *Meteorol. Z.*, 11, 151-159.

- Weisenstein, D.K., M.K.W. Ko, J.M. Rodriguez, and N.-D. Sze, 1991: Impact of heterogeneous chemistry on model-calculated ozone change due to high speed civil transport aircraft, *Geophys. Res. Lett.*, *18*, 1991-1994.
- Weisenstein, D.K., M.K.W. Ko, I. Dyominov, G. Pitari, L. Ricciardulli, G. Visconti and S. Bekki, 1998: A model intercomparison of the effects of sulfur emissions from HSCT aircraft, *J. Geophys. Res.*, *103*,1527-1547.
- WMO, 2002: *Scientific Assessment of Ozone Depletion: 2002*, WMO/UNEP rep. # 47, Geneva, Switzerland.

Modelling the Impact of Subsonic Aircraft Emissions on Ozone: Future Changes and the Impact of Cruise Altitude Perturbations

M.O. Köhler*, H.L. Rogers, J.A. Pyle

Centre for Atmospheric Science, Chemistry Department, University of Cambridge, Cambridge, U.K.

Keywords: Atmospheric Chemistry and Composition, Aircraft NO_x Emissions, UTLS Ozone, Cruise Altitude Perturbations

ABSTRACT: The impact of aircraft NO_x emissions on ozone in the UTLS region has been studied within the framework of the TRADEOFF project. Model integrations have been performed using TOMCAT, a 3-dimensional tropospheric chemistry transport model. Perturbations to aircraft emissions have been incorporated by changing the cruise altitude and flight routing of the present day subsonic fleet. The effects of tropospheric gas-phase chemistry on ozone mixing ratios and tropospheric ozone column have been investigated. A selection of results from the TRADEOFF project will be presented here.

1 MODEL DESCRIPTION

TOMCAT is a global 3D Eulerian chemistry transport model, and integrates a tropospheric methane-oxidation scheme with included ethane/propane degradation (Carver et al., 1998) on 31 hybrid pressure levels. The model uses an advection scheme that conserves 2nd order moments (Prather, 1986). A more detailed description of the TOMCAT model can be found in Law et al. (2000). The model has undergone recently a complete overhaul with numerous improvements, which include the treatments of photolysis, deposition, mid-level convection and cumulus downdraft, and makes use of updated emission data sets. Standard emissions appropriate for the year 2000 are chosen according to recommendations from IPCC (2001). Surface emissions appropriate for the year 2050 are chosen according to the IPCC SRES Scenario A2 (IPCC, 2000). Emissions for NO_x, CO, CH₄ and NMHCs are implemented with a seasonal cycle, aircraft emissions appropriate for the year 2050 are chosen according to Scenario Fa1 from IPCC (1999).

2 SCENARIO OVERVIEW

All TOMCAT model integrations have been performed using identical boundary conditions in order to achieve optimal comparability. All integrations have been forced by meteorological analyses from the European Centre for Medium-Range Weather Forecast (ECMWF) of the year 1995. Both the initialisation of the chemical model fields as well as a 7-month "spin-up" integration have been performed identically for each of the experiments listed in Table 1. Scenarios 3a, 3b, 5a, and 5b have been performed using equal surface emissions for the year 2000 and specifically developed aircraft emissions, appropriate for the year 2000, reflecting the corresponding cruise altitude perturbations for each of the four scenarios have been used. The treatment of chemistry and dynamics in the model remains consistent between model integrations. The TOMCAT model output is provided every 6 hours, at a horizontal resolution of $5.6^\circ \times 5.6^\circ$ for a 13-month period from 1 January, 1995, to 31 January, 1996.

* *Corresponding author:* Marcus Köhler, Centre for Atmospheric Science, Department of Chemistry, Lensfield Road, Cambridge, CB2 1EW, United Kingdom. Email: marcus.koehler@atm.ch.cam.ac.uk

Table 1. Scenario Overview

Scenario	Surface Emissions	Aircraft Emissions
NAE	2000 IPCC TAR	no aircraft
2000	2000 IPCC TAR	2000 TRADEOFF
2050[A]	2000 IPCC TAR	2050 IPCC Fa1
2050	2050 IPCC SRES A2	2050 IPCC Fa1

Scenario	Perturbation to Cruise Altitudes	
3a	cruise altitude 6000 feet lower	(normalized to 2000)
3b	cruise altitude 6000 feet lower	(non-normalized)
5a	cruise altitude 2000 feet higher	(normalized to 2000)
5b	cruise altitude 2000 feet higher	(non-normalized)

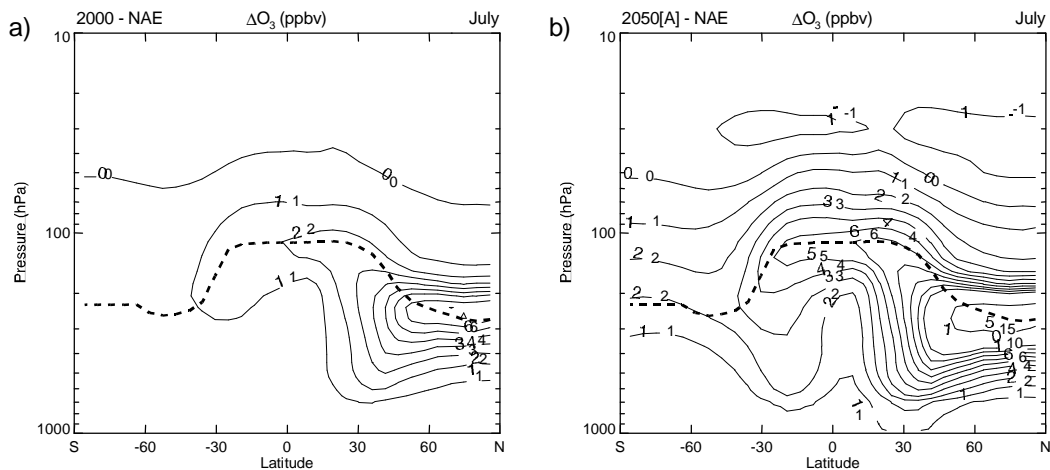


Figure 1. Zonally averaged ozone perturbation produced by aircraft emissions in 2000 (left figure) and 2050 (right figure).

3 AIRCRAFT IMPACT IN 2000 AND 2050

Present-day aircraft emissions lead to the production of ozone in the UTLS region and in the northern upper and middle troposphere. Aircraft NO_x emissions released inside the stratosphere have the capability to catalytically destroy ozone and lead to small reductions in ozone mixing ratios in the stratosphere. The maximum ozone increase due to present-day aircraft in the troposphere ranges between 4–9 ppbv, depending on season, which corresponds to approximately 4–6%. The largest perturbations occur around the northern hemispheric tropopause where the bulk of the aircraft emissions is released (Fig. 1a).

Increasing aircraft and surface emissions, projected for the year 2050, lead to increases in the tropospheric ozone column. These increases are strongest in the northern hemisphere, where the emissions are predominantly higher. In the northern hemisphere the tropospheric ozone column is increased by 30%. The increase in aircraft emissions projected for the year 2050 leads to enhanced ozone formation in the UTLS region and throughout the troposphere and moreover to a stronger reduction in stratospheric ozone. The strongest ozone increases are between 9–18 ppbv in the UTLS region, also depending on season (Fig. 1b).

Increasing methane surface emissions in the year 2050 lead to a larger abundance of hydroxyl radicals in the tropical lower stratosphere and subsequently to enhanced formation of nitric acid, which represents a sink for stratospheric nitrogen oxides. The correlation between NO_x and O_3 burdens in the northern hemisphere exhibits near-linearity for small perturbations to present-day aircraft emissions (NAE, 2000 and 2050[A] scenarios). Larger perturbations to surface emissions (2050 scenario) however lead to a non-linear increase in the ozone burden (Fig. 2).

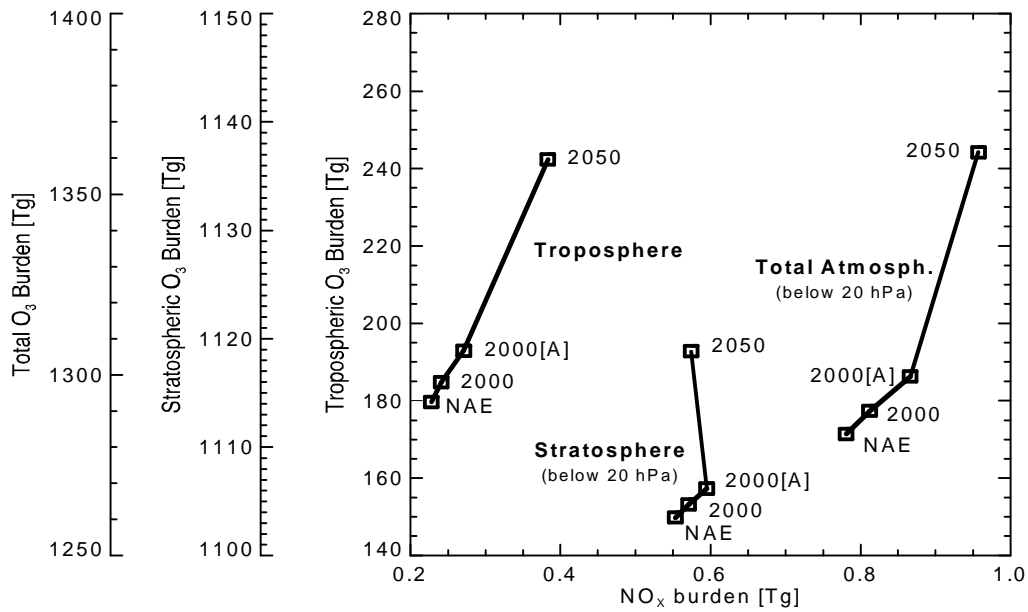


Figure 2. NO_x and O₃ burden correlations in the troposphere, stratosphere and total atmosphere (stratosphere and total atmosphere below 20 hPa only).

4 CRUISE ALTITUDE PERTURBATIONS

A change in cruise altitude will lead to perturbations in the geographical distribution of aircraft emissions. Due to the large variability in atmospheric dynamics and chemistry the shift in the location of aircraft emissions has potentially large implications for atmospheric chemistry. Experiments with both higher and lower cruise altitudes have been performed with respect to a “present-day” scenario. For each perturbation a normalized scenario, where the location of cruise altitude has been changed without globally altering the total amount of emissions, and a non-normalized experiment, which additionally accounts for a change in the EI(NO_x) due to the changes in operational procedure, have been performed.

The experiments have shown that changes in cruise altitudes can lead to significant differences in ozone mixing ratios. The transport of aircraft emissions by atmospheric motion is highly dependent upon the geographical location and the altitude at which the emissions are released. The amount of emissions released, in combination with the NO_x mixing ratio of the ambient air, determine the amount of ozone produced from aircraft emissions.

In order to evaluate the total impact of the ozone changes in the northern hemisphere, both the tropospheric ozone column (from the surface to the tropopause) and the stratospheric ozone column (between the tropopause and 20 hPa, approximately 27 km altitude) have been calculated. The altitude range of the stratospheric ozone column was chosen as a suitable domain to represent the region of perturbation due to subsonic aircraft. Figure 3 displays the average value for the northern hemispheric ozone column under “present-day” conditions (s1) and for both higher (s5a, s5b) and lower (s3a, s3b) cruise altitudes.

In the stratosphere the ozone column below 20 hPa exhibits an almost linear relationship with the change of cruise altitude (Fig. 3a). The magnitude of ozone column change due to a 2000 ft rise in cruise altitudes is approximately a third of that resulting from a 6000 ft fall in cruise altitudes. The difference in ozone column change between the normalized scenarios (s3a, s5a) and the non-normalized scenarios (s3b, s5b) is negligible and as such indicates that the ozone column change in the stratosphere is independent of the total amount of aircraft emissions.

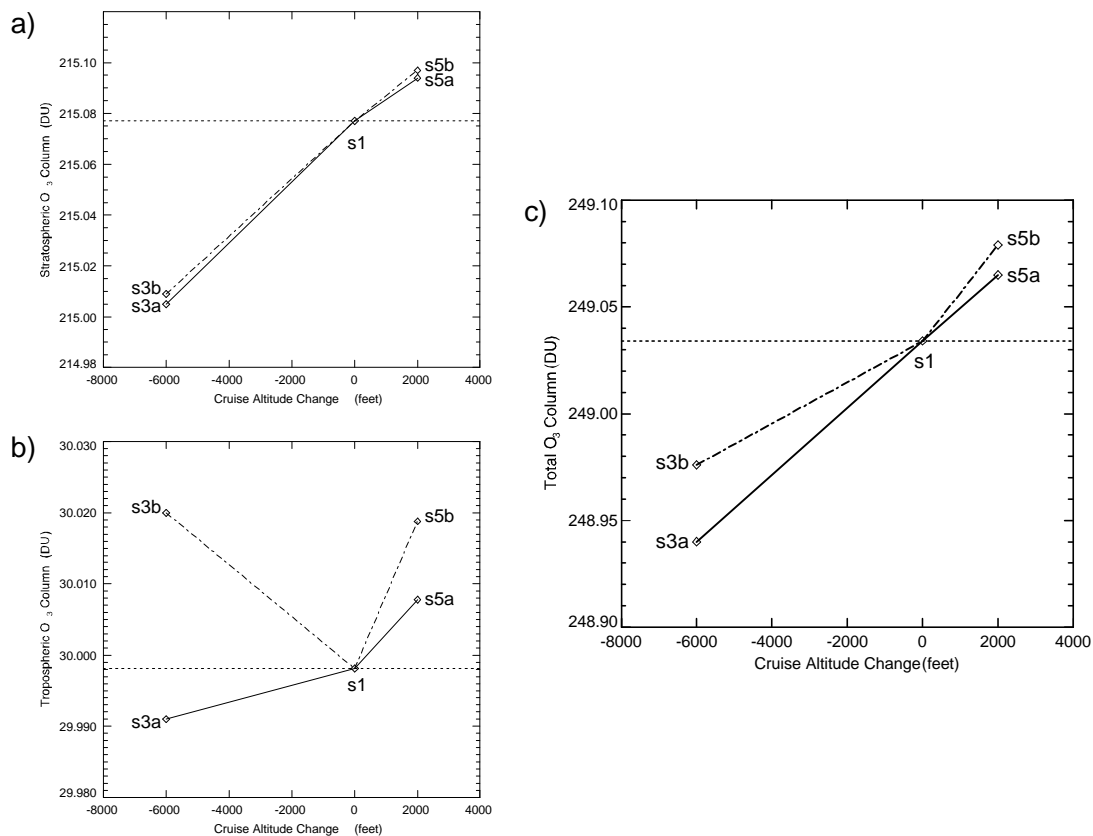


Figure 3. Average northern hemispheric ozone column and perturbations due to changes in cruise altitudes (stratosphere and total atmosphere below 20 hPa only).

The tropospheric ozone column shows a substantial difference between the normalized and non-normalized scenarios (Fig. 3b). In the experiments with normalized aircraft emissions the magnitude of the ozone column change for a reduction in cruise altitude by 6000 ft is ~30% smaller than the change in ozone column due to an increase in cruise altitude by 2000 ft. The relationship between the perturbed ozone column and the change in cruise altitude is therefore non-linear. In the non-normalized experiments, where the total emitted NO_x varies, both cruise altitude perturbations lead to an increase in tropospheric ozone column. This shows that the tropospheric ozone column is sensitive to the total amount of aircraft emissions. This difference between normalized and non-normalized scenarios in the troposphere and stratosphere could be explained by the low background NO_x mixing ratios in the troposphere in comparison with the lower stratosphere. An increase in NO_x due to aircraft emissions in the troposphere (where background values are low) could result in a higher chemical ozone production rate compared to the stratosphere.

The total ozone column up to 20 hPa shows that an increase in cruise altitudes leads to an increase of ozone column and lower cruise altitude lead to a reduction in total ozone for both scenarios (Fig. 3c). In each case the main effect occurs around the tropopause region where increased NO_x will increase ozone in the model. For scenarios with normalized emissions the relationship between ozone column and cruise altitude appears again to be almost linear. For non-normalized emissions the reduction of ozone column due to lower cruise altitudes is decreased by approximately 30% relative to the normalized emission scenario. Similarly, the increase in ozone column at higher cruise altitudes is further enhanced by nearly 30% relative to normalized emissions.

5 CONCLUSIONS

On a global scale NO_x emissions from the 2000 aircraft fleet have only a small effect on atmospheric ozone (4–9 ppbv), which can be observed predominantly in the northern UTLS region

and mid-troposphere. The 2050 aircraft fleet however has a more substantial effect (9–18 ppbv), exhibiting a similar zonal distribution in the perturbations. In the case of the 2000 atmosphere it has been shown that for small perturbations (e.g. the addition of the global aircraft fleet) the ozone perturbation is linearly dependent upon the NO_x enhancement.

Results have also shown that changes in cruise altitude affect the total ozone column (below 20 hPa) in the northern hemisphere. Lower cruise altitudes lead generally to a decrease in the total ozone column, such that for scenarios with normalized emissions the relationship between ozone column and cruise altitude appears to be almost linear. For non-normalized emissions the reduction of ozone column due to lower cruise altitude is decreased by approximately 30% relative to the normalized scenario. Similarly, the increase in ozone column at higher cruise altitude with non-normalized emissions is further enhanced by nearly 30% relative to higher cruise altitudes with normalized emissions.

REFERENCES

- Carver, G.D., P.D. Brown, and O. Wild, 1998: The ASAD atmospheric chemistry integration package and chemical reaction database. *Comput. Phys. Commun.*, 105, 197–215.
- IPCC, 1999: *Aviation and the Global Atmosphere. A Special Report of Working Groups I and III of the Intergovernmental Panel on Climate Change*. Edited by J.E. Penner et al., Cambridge Univ. Press, Cambridge, UK and New York, NY, USA, 373 pp.
- IPCC, 2000: *Emissions Scenarios. A Special Report of Working Group III of the Intergovernmental Panel on Climate Change*. Edited by N. Nakicenovic and R. Swart. Cambridge Univ. Press, Cambridge, UK, 570 pp.
- IPCC, 2001: *Climate Change 2001: The Scientific Basis. Contribution of Working Group I to the Third Assessment Report of the Intergovernmental Panel on Climate Change*. Cambridge Univ. Press, Cambridge, UK, and New York, NY, USA, 881 pp.
- Law, K.S., P.-H. Plantevin, V. Thouret, A. Marenco, W.A.H. Asman, M. Lawrence, P.J. Crutzen, J.-F. Muller, D.A. Hauglustaine, and M. Kanakidou, 2000: Comparison between global chemistry transport model results and Measurement of Ozone and Water Vapor by Airbus In-Service Aircraft (MOZAIC) data. *J. Geophys. Res.*, 105 (D1), 1503–1525.
- Prather, M.J., 1986: Numerical advection by conservation of second order moments. *J. Geophys. Res.*, 91 (D6), 6671–6681.

Nitric Acid Partitioning in Cirrus Clouds and the Role of Interstitial Aerosol

M. Krämer*, J. Beuermann, C. Schiller

FZ Jülich, Institut für Chemie der Geosphäre I: Stratosphäre, Germany

F. Grimm, F. Arnold

MPI für Kernphysik, Heidelberg, Atmosphärenphysik, Germany

T. Peter

ETH Zürich, Institut für Atmosphärenphysik, Switzerland

S. Meilinger

MPI für Chemie Mainz, Abt. für Het. Chemie und Mikrophysik, Germany

A. Meier

Universität Köln, Inst. für Geophysik & Meteorologie, Germany

J. Hendricks, A. Petzold, H. Schlager

DLR Oberpfaffenhofen, Inst. für Physik der Atmosphäre, Germany

Keywords: cirrus clouds, HNO₃ partitioning, interstitial particles

ABSTRACT: The parameters controlling the partitioning of HNO₃ in cirrus clouds between ice particles, interstitial aerosol and the gas phase are identified from field, laboratory and model studies in the temperature range 190 K – 240 K. Temperature, ice surface area and chemical composition of the interstitial particles are found to govern the HNO₃ partitioning. Moreover, the partitioning is very sensitive on the in-cloud relative humidity with respect to ice (RH_{ice}), which recently is found to range from 1.0 – 1.6.

1 INTRODUCTION

Cirrus clouds have attracted increasing attention in recent years, in particular because of their role in the forcing of climate, both through direct radiative and through indirect aerosol forcing. Further, cirrus clouds are important for the chemistry of upper tropospheric ozone. One possible mechanism relevant for atmospheric chemistry and trace gas distribution is the denitrification of the tropopause region by sedimenting cirrus ice particles (Lawrence and Crutzen, 1998).

However, up to now the question on the partitioning of nitric acid (HNO₃) under cirrus cloud conditions is not satisfactorily answered. It is unclear which parameters determine the HNO₃ partitioning between the gas phase, ice particles and interstitial aerosol particles. The interstitial aerosol particles grow to liquid solutions inside a cirrus cloud in dependence on the in-cloud relative humidity, thereby taking up HNO₃ according to their chemical composition. In spite of the potential importance of interstitial aerosol particles, however, their impact on HNO₃ partitioning is largely unexplored.

Here, we present a preliminary overview of the HNO₃ partitioning in cirrus clouds derived from field, laboratory and model studies for the temperature range 200 K < T < 230 K. To investigate the impact of interstitial aerosol in HNO₃ partitioning, we performed sensitivity model studies on the uptake of HNO₃ in interstitial particles at different in-cloud relative humidities, different initial amounts of HNO₃, and assuming two different particle compositions, namely ternary HNO₃-H₂SO₄-H₂O or ammoniated, quarternary (HNO₃-H₂SO₄-H₂O-NH₃) solutions.

* *Corresponding author:* Martina Krämer, Forschungszentrum Jülich GmbH, D-52425 Jülich, ICG-I, Germany.
Email: m.kraemer@fz-juelich.de

2 METHODS

The partitioning of HNO_3 is determined – assuming ternary and quaternary solution interstitial particles – with the help of the interactive gas-particle equilibrium model AIM (Aerosol Inorganics Model, <http://www.hpc1.uea.ac.uk/~e770/aim.html>) for the field experiments POLSTAR 1997 (199 K), POLSTAR 1998 (202 K), SUCCESS 1996 (209 K), a model study (225 K) and a laboratory study on ice particles (230 K) (Meilinger et al., 1999; Krämer et al., 2003; Weinheimer et al., 1998; Meier and Hendricks, 2002 and Arora et al., 1999). For a detailed description of the procedure see Krämer et al. (2003).

The equilibrium model is also used to perform sensitivity studies for different particle compositions, initial amounts of HNO_3 and in-cloud RH_{ice} . It is not yet known to which degree the gaseous HNO_3 equilibrates with the interstitial and ice particles inside a cirrus at RH_{ice} larger than the saturation value. Since the aim of this study is to identify the parameters controlling the partitioning of HNO_3 in cirrus, the sensitivity studies are performed at equilibrium conditions.

3 RESULTS

3.1 Nitric acid partitioning: results from field, model and laboratory studies

The HNO_3 partitioning in cirrus clouds is shown in Table 1. The upper three rows show the relative partitioning of HNO_3 between the interstitial particles, the gas phase and the ice particles. The straight numbers show the partitioning in case the interstitial particles are ternary solutions, the slanted numbers represent the partitioning in the presence of quaternary solution interstitial particles. The middle rows show the basic measured (black) and calculated (grey) parameters and the lower three rows the temperature, H_2O and the ice surface.

Interstitial particle HNO_3 ($\text{HNO}_3^{\text{ptcl}}$): in the presence of ternary solution interstitial aerosol, a substantial amount of HNO_3 was found in the interstitial particles. This amount decreases with increasing ambient temperature (see also Figure 1, upper left panel). If the interstitial particles are quaternary solutions, this temperature dependence is also seen, but more HNO_3 resides in the interstitial particles, because the additional large amount of ammonia causes, by neutralizing the sulphuric acid, a stronger uptake of HNO_3 (see also Figure 1, lower left panel).

Gas phase HNO_3 ($\text{HNO}_3^{\text{gas}}$): in the presence of ternary solution interstitial particles, a large amount of the initial HNO_3 remains in the gas phase. A smaller amount is found in the presence of quaternary solutions, but the gas phase is still not completely depleted.

Ice particle HNO_3 ($\text{HNO}_3^{\text{ice}}$): For both particles types, only very little HNO_3 was taken up by the ice particles under cold cirrus conditions (see also Meilinger et al., 1999), while in warm cirrus the main fraction of HNO_3 is scavenged by ice particles. This increase is related to the ice surface area ($A = f(\text{H}_2\text{O})$), which in turn increases with the temperature.

In summary we find that both $\text{HNO}_3^{\text{ptcl}}$ and $\text{HNO}_3^{\text{ice}}$ are controlled by the temperature of the cirrus: $\text{HNO}_3^{\text{ptcl}} = f(1/T)$ and $\text{HNO}_3^{\text{ice}} = f(A(\text{H}_2\text{O}(T)))$ for both types of interstitial particles, ternary and quaternary solutions. In cold cirrus clouds with low water content and a small ice surface area, the partitioning is in favour of the interstitial particles, while in warmer cirrus clouds with a greater water content and a large ice surface area the uptake on ice preponderates. Denitrification via sedimenting ice particles may happen merely in the – most frequently appearing – warm cirrus clouds with large ice surface areas.

3.2 Nitric acid partitioning: sensitivity studies

The calculations and measurements of $\text{HNO}_3^{\text{ptcl}}$ and $\text{HNO}_3^{\text{ice}}$ shown in section 3.1 are made at different initial HNO_3 concentrations ($\text{HNO}_3^{\text{init}} = \text{HNO}_3^{\text{total}}$ in Table 1), which has an influence on the uptake in particles and on ice. For a higher/lower initial HNO_3 vapour pressure $\text{HNO}_3^{\text{ptcl}}$ and $\text{HNO}_3^{\text{ice}}$ would be larger/smaller.

A further aspect influencing $\text{HNO}_3^{\text{ptcl}}$ is the in-cloud amount of water. $\text{HNO}_3^{\text{ptcl}}$ could be larger, if the H_2O vapour pressure inside cirrus exceeds its saturation value $\text{RH}_{\text{ice}} = 1.0$. In this case the interstitial particles can take up more water and subsequently more $\text{HNO}_3^{\text{ptcl}}$. Ovarlez et al. (2002)

re-cently reported from field measurementst that RH_{ice} inside a cirrus can reach values up to 1.6, the threshold for homogeneous ice nucleation.

In this section we present some simple equilibrium sensitivity studies to get an insight in the dependence of HNO_3^{ptcl} on HNO_3^{init} and RH_{ice} and to identify the main parameters controlling the partitioning of HNO_3 in cirrus clouds. The sensitivity studies are performed on the basis of the data of POLSTAR 1998, event II.

Table 1: HNO_3 partitioning between gas phase, interstitial aerosol and ice particles in cirrus clouds from field, labora-tory and model studies. a: ternary solutions: HNO_3 - H_2SO_4 - H_2O , b: quaternary solutions HNO_3 - H_2SO_4 - H_2O - NH_3 ; the gas-particle equilibrium calculations are performed using the interactive aerosol models AIM (<http://www.hpc1.uea.ac.uk/~e770/aim.html>); ★: based on data of Meilinger et al. (1999) with ★¹: data taken from Schiller et al. (1999); §: based on data of Weinheimer et al. (1998) with §¹: data taken from Baumgardner et al. (1998) and §²: data taken from Jensen et al. (1998); ‡: based on data of Meier and Hendricks (2002); †: data taken from Schlager (2002); note that in-cloud $RH_{ice} = 1.0$ is assumed here; for more details see text.

Nitric acid partitioning in cirrus clouds:

	Field experiments						Model study		Lab. experiment		
	POLSTAR 1997*		POLSTAR 1998				SUCCESS 1996		<i>M & H</i>		<i>Arora et al.</i>
			I	II		<i>Weinh. (1998)</i> §		<i>(2002)</i> ‡		<i>(1999)</i>	
HNO_3 partitioning											
	Interst. particles:		ternary ^a quaternary ^b				solutions				
Interst. particles (%)	33.2	88.6	33.2	69.3	21.2	68.1	3.8	72.2	0.0	7.8	–
Gas phase (%)	66.5	11.3	66.2	30.4	71.6	29.1	0.0 ?	0.0 ?	34.0	31.4	65 – 0.0
Ice particles (%)	0.3	0.1	0.6	0.3	7.2	2.8	96.2	27.8	66.0	60.8	35 – 100
	(0.1 – 0.9)		(0.2 – 2.0)		(2.2 – 25.2)						
Basic measured and calculated parameters											
$H_2SO_4^{total}$ (ppb)	0.600	0.60	0.55	0.55	0.70	0.70	0.50	0.50	0.60	0.60	–
NH_3^{total} (ppb)	–	0.70	–	0.70	–	0.70	–	0.70	–	0.70	–
HNO_3^{total} (ppb)	0.075	0.44	0.75	1.64	0.26	0.653	0.052	0.18	0.47	0.51	≈ 6.7
HNO_3^{ptcl} (ppb)	0.025	0.39	0.25	1.14	0.06	0.445	0.002	0.13	0.0	0.04	0.0
HNO_3^{gas} (ppb)	0.05		0.5		0.19		0.0 ?		0.16		≈ 4.4 – 0.0
HNO_3^{ice} (ppt)	0.2		4.6 [†]		18 [†]		50		310		≈ 2300 – 6700
Altitude (km)	11.8		12.5		11.0		–		–		–
Ozone (ppb)	60 ^{★1}		200		50		–		–		–
Pot. Temp. (K)	313		325		311		–		–		–
Pressure (hPa)	200		178		219		193 ^{§1}		270		–
Temp. (K)	196		199		202		209 ^{§2}		225		230
H₂O (ppm)	20		21		41		–		215		–
Ice surface ($\frac{\mu m^2}{cm^3}$)	≈ 120		≈ 125 [†]		≈ 330 [†]		≈ 2000		≈ 5.100		(59 – 1300) · 10 ³

3.2.1 Dependence of HNO_3^{ptcl} on HNO_3^{init}

The HNO_3 uptake in interstitial particles is calculated for low, middle and high initial HNO_3 (0.05 ppbv, 0.26 ppbv and 1.7 ppbv; the values are taken from Table 1) in the temperature range 190 K – 230 K for ternary and quaternary solution interstitial aerosol and at $RH_{ice} = 1.0$.

The results of the sensitivity studies are shown in Figure 1, upper and lower left panels. At first, the results of the field and model studies shown in section 3.1 are confirmed: if the interstitial

particles are quaternary solutions (Figure 1, lower left panel), more HNO_3 resides in the particles over the whole temperature range than in the case of ternary solution particles (Figure 1, upper left panel). Secondly, it becomes obvious that the temperature dependence of HNO_3 uptake in interstitial aerosol dominates the influence on the initial HNO_3 amount for both types of interstitial particles.

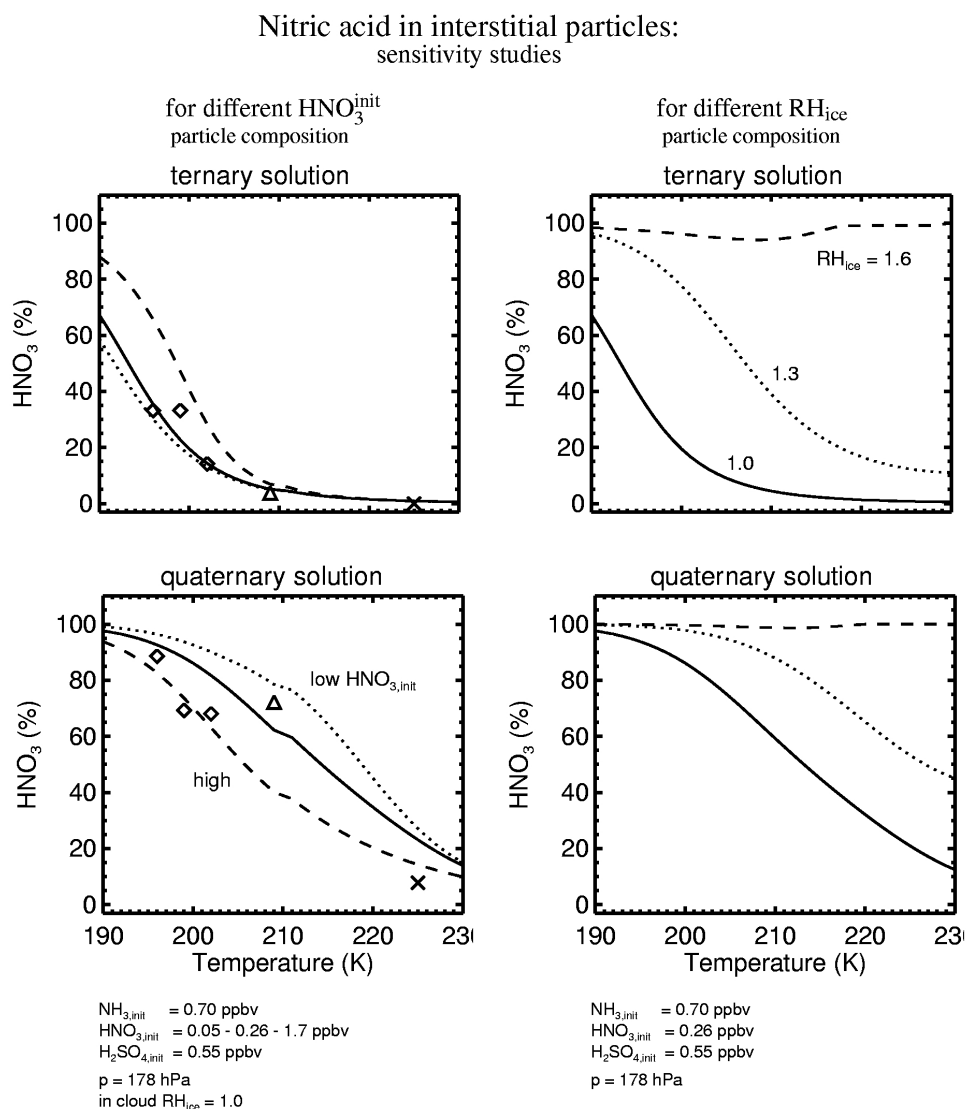


Figure 1: Nitric acid in interstitial particles versus temperature for two types of particles. Ternary solutions: $\text{H}_2\text{O}-\text{H}_2\text{SO}_4-\text{HNO}_3$; quaternary solutions: $\text{H}_2\text{O}-\text{H}_2\text{SO}_4-\text{HNO}_3-\text{NH}_3$; sensitivity studies are presented as solid, dotted and dashed lines; in addition, the field measurements POLSTAR (\diamond) and SUCCESS (Δ), and the model study (X) from Table 1 are plotted. For more details see text.

3.2.2 Dependence of $\text{HNO}_3^{\text{ptcl}}$ on in-cloud RH_{ice}

The HNO_3 uptake in interstitial particles is determined for $\text{RH}_{\text{ice}} = 1.0, 1.3$ and 1.6 (see Figure 1, upper and lower right panels). For both ternary and quaternary solution interstitial aerosol, a strong dependence of the HNO_3 uptake on RH_{ice} is found: the more water is available, the more HNO_3 is taken up by the interstitial particles, even at higher temperatures. At $\text{RH}_{\text{ice}} = 1.6$, almost all HNO_3 would be taken up in the interstitial aerosol independently on the temperature. In this case, competition between the uptake of HNO_3 in interstitial and ice particles could take place (see section 3.2.3) and therefore denitrification via sedimenting cirrus ice particles may not occur.

3.2.3 Implications for cirrus clouds

Considering the findings of the sensitivity studies, the history of cirrus formation and development may be regarded under new aspects:

During the cooling process of the air, RH_{ice} increases to values up to 1.6. Depending on the supersaturation and the particle chemistry, HNO_3 is scavenged by those particles grown by water uptake due to rising RH_{ice} . When ice particles are forming, a part of the HNO_3 freezes together with the water. The amount of HNO_3 in ice originating from this freezing path depends on the fraction of frozen on the total particle number. If only few particles are frozen, as in most cases, then only a small part of the HNO_3 in ice will originate from this process. But in a case where a large part of the particles would be frozen, a major part of the HNO_3^{ice} could be captured via this path by the ice particles. Friedl (2003) observed very high HNO_3 coverages in contrail ice particles, coupled with a high number of small ice crystals. The above described pathway could explain these observations.

After this first freezing step, RH_{ice} reduces to a certain value between 1.0 and 1.6. The interstitial particles equilibrate to that lower value by evaporating H_2O and HNO_3 (the evaporation of HNO_3 from the interstitial particles for $RH_{ice} = 1.0$ is demonstrated for POLSTAR 1997 by Meilinger et al., 1999 in a detailed model study). The amount of HNO_3 available for adsorption on the ice surface is now determined by the current RH_{ice} , temperature and particle composition. At low RH_{ice} , the interstitial particles will evaporate HNO_3 to the favour of the ice particles, similar to the Bergeron-Findeisen process known for water. At high RH_{ice} , the inverse effect will take place: HNO_3 resides in the interstitial particles to the disadvantage of the ice particles.

The in-cloud RH_{ice} can rise again after the first freezing cycle (Haag et al., 2003). Then, the repeated growth of interstitial particles by water vapour and uptake of HNO_3 can transform them to ice nuclei that induce a second freezing step. After that, equilibrium of H_2O and HNO_3 between ice and interstitial particles has to be established again. For a complete understanding of these complex interactions in cirrus clouds, more and detailed kinetic studies considering the total system of H_2O , HNO_3 and coexisting ice and interstitial particles are needed.

4 SUMMARY AND CONCLUSIONS

From field, laboratory and model studies it is found that the parameters controlling the HNO_3 partitioning in cirrus clouds between ice particles, interstitial aerosol and the gas phase are temperature, ice surface area and chemical composition of the interstitial particles. Moreover, from a sensitivity model study there is a hint that HNO_3 is very sensitive to the in-cloud RH_{ice} .

A part of nitric acid always remains in the gas phase as long as the in-cloud RH_{ice} remains smaller than the maximum value of 1.6. In this case, the amount of HNO_3 residing in the interstitial particles is dependent on temperature: in cold cirrus clouds ($T < 205$ K) with small ice surface areas the partitioning is in favour of the interstitial particles, while in warmer cirrus clouds with large ice surface areas the uptake on ice preponderates. This dependence is observed for both, ternary and quaternary solution interstitial particles, whereby the quaternary solutions contain a larger amount of HNO_3 . When RH_{ice} comes close to 1.6, almost all nitric acid resides in the interstitial particles independent on temperature and particle composition. Here, denitrification via sedimenting cirrus ice particles may not occur even at higher temperatures. Consequently, extensive uptake of nitric acid on ice with subsequent denitrification likely occurs in the most frequently appearing warm cirrus clouds at low RH_{ice} .

An additional hypothesis concerning the HNO_3 distribution in cirrus clouds arises from the sensitivity studies: adsorption on the ice surface seems not to be the only pathway for HNO_3 to ice particles. When the ice particles form at high RH_{ice} from grown interstitial particles, HNO_3 was already incorporated in those particles and freezes together with the water. In a case where a large part of the particles would be frozen, a major part of the HNO_3 could be captured via this pathway by the ice particles. For a better understanding of the complex interactions in cirrus clouds, we encourage more and detailed kinetic model studies considering the total system of H_2O , HNO_3 and coexisting ice and interstitial particles.

REFERENCES

- Arora, O., D. Cziczo, A. Morgan, J. Abbatt, and R. Niedziela, 1999: Uptake of nitric acid by sub-micron-sized ice particles. *Geophys. Res. Lett.*, 26, 3621-3621.
- Baumgardner, D. and B. E. Gandrud, 1998: A comparison of the microphysical and optical properties of particles in an aircraft contrail and mountain wave cloud. *Geophys. Res. Lett.*, 25, 1129-1132.
- Friedl, R., WB-57 CRYSTAL-FACE science team, 2003: Overview of contrail and cirrus cloud measurements from the WB-57 aircraft in the CRYSTAL-FACE mission. Conference on Aviation, Atmosphere and Climate (AAC), Friedrichshafen, Germany.
- Haag, W., B. Kärcher, J. Ström, A. Minikin, U. Lohmann, J. Ovarlez, and A. Stohl, 2003: Freezing thresholds and cirrus cloud formation mechanisms inferred from in situ measurements of relative humidity. *Atmos. Chem. Phys. Discuss.*, 3, 3267-3299.
- Jensen, E. J., O. B. Toon, A. Tabazadeh, G. W. Sachse, B. E. Anderson, K. R. Chan, C. W. Twohy, B. Gandrud, S. M. Aulenbach, A. Heymsfield, J. Hallett and B. Gary, 1998: Ice nucleation processes in upper tropospheric wave-clouds observed during SUCCESS. *Geophys. Res. Lett.*, 25, 1363-1366.
- Krämer, M., J. Beuermann, C. Schiller, F. Grimm, F. Arnold, Th. Peter, S. Meilinger, A. Meier, J. Hendricks, A. Petzold and H. Schlager, 2003: Nitric acid partitioning in cirrus clouds: a synopsis based on field, laboratory and model studies. *Atmos. Chem. Phys. Discuss.*, 3, 413-443.
- Lawrence, M., and P. Crutzen, 1998: The impact of cloud particle gravitational settling on soluble trace gas distributions. *Tellus*, 50B, 263-289.
- Meier, A., and J. Hendricks, 2002: Model studies on the sensitivity of upper tropospheric chemistry to heterogeneous uptake of HNO_3 on cirrus ice particles. *J. Geophys. Res.*, 107, 4696, doi:10.1029/2001JD000735.
- Meilinger, S., A. Tsias, V. Dreiling, M. Kuhn, C. Feigl, H. Ziereis, H. Schlager, J. Curtis, B. Sierau, F. Arnold, M. Zöger, C. Schiller and T. Peter, 1999: HNO_3 partitioning in cirrus clouds. *Geophys. Res. Lett.*, 26, 2207-2210.
- Ovarlez, J., J.-F. Gayet, K. Gierens, J. Ström, H. Ovarlez, F. Auriol, R. Busen, and U. Schumann, 2002: Water vapour measurements inside cirrus clouds in Northern and Southern hemispheres during INCA. *Geophys. Res. Lett.*, 29, 1813, doi:10.1029/2001GL014440.
- Schiller, C., A. Afchine, N. Eicke, C. Feigl, H. Fischer, A. Giez, P. Konopka, H. Schlager, F. Tuitjer, F.G. Wienhold and M. Zöger, 1999: Ice particle formation and sedimentation in the tropopause region: A case study based on in situ measurement of total water during Polstar 1997. *Geophys. Res. Lett.*, 26, 2219-2222.
- Schlager, H., A. Petzold, H. Ziereis, A. Dörnbrack, F. Grimm, F. Arnold and C. Schiller, 2000: In situ observations of particulate NO_y in cirrus clouds for different atmospheric conditions. Proceedings of the workshop 'Aviation, aerosols, contrails and cirrus clouds (A2C3)', Seeheim (Frankfurt), Germany, 68-73.
- Weinheimer, A. J., T. L. Campos, J. G. Walega, F. E. Grahek, B. A. Rodley, B. D. C. H. Twohy, and B. Gandrud, 1998: Uptake of NO_y on wave-cloud ice particles. *Geophys. Res. Lett.*, 25, 1725-1728.

Radiative Forcing on Climate from Stratospheric Aircraft Emissions

D.J. Wuebbles*, M. Dutta, A.K. Jain

Department of Atmospheric Sciences, University of Illinois at Urbana Champaign, Urbana, Illinois, USA

S.L. Baughcum

The Boeing Company, Seattle, Washington, USA

Keywords: radiative forcing, aircraft emissions, stratospheric ozone, water vapor

ABSTRACT: The 1999 Intergovernmental Panel on Climate Change report on Aviation and The Global Atmosphere estimated that emissions from a fleet of one thousand High Speed Civil Transport aircraft (flying at Mach 2.4) could produce a non-negligible impact on the radiative forcing driving changes in climate. The radiative forcing for this fleet was $+0.1 \text{ Wm}^{-2}$, with $+0.10 \text{ Wm}^{-2}$ coming from the increase in stratospheric water vapor, along with smaller contribution from increased CO_2 ($+0.01 \text{ Wm}^{-2}$) and from effects on stratospheric ozone (-0.01 Wm^{-2}). In this study, we reexamine the radiative forcing from fleets of aircraft flying at stratospheric altitudes. We use our narrowband radiative transfer model in these studies, along with model calculations of calculated changes in ozone and water vapor from our zonally-averaged model of atmospheric chemical and physical processes. The radiative transfer model used here has higher resolution in the tropopause and lower stratosphere region than the models used in the IPCC assessment. Preliminary results suggest that the radiative forcing for the water vapor emissions from aircraft was overestimated in the IPCC assessment. Along with reconsideration of the radiative forcing for the HSCT scenarios used in IPCC, we also consider the radiative forcing from a set of parametric scenarios for which the cruise altitudes are systematically varied.

1 INTRODUCTION

Aircraft emissions can affect climate both directly and indirectly. Direct effects on climate from aircraft emissions can occur due to resulting changes in the atmospheric distributions of radiatively important gases, especially carbon dioxide (CO_2) and water vapor (H_2O). Changes in ozone, resulting from emissions of nitrogen oxides and water vapor, can produce an indirect effect on climate from aircraft emissions. In the troposphere, under the right conditions, water vapor emissions can produce contrails that can radiatively affect climate directly, but also can affect climate indirectly through possible resulting changes in natural cloudiness (Ponater et al., 1996; Rind et al., 1996; Seinfeld, 1998; IPCC, 1999).

Even though several studies indicate aircraft emissions of water vapor in the troposphere are unlikely to be important contributors to climate change, emissions of water vapor in the lower stratosphere, where natural levels of water vapor are much smaller, could produce a potentially significant radiative effect on climate.

The IPCC (1999) assessment on Aviation and The Global Atmosphere used several radiative transfer models to examine the potential effects of fleets of High Speed Civil Transport (HSCT) aircraft. These studies concluded that a fleet of 1000 HSCTs, with assumed very low emission of nitrogen oxides (NO_x), could result in radiative forcing of $+0.006 \text{ Wm}^{-2}$ from the additional CO_2 , -0.010 from ozone concentration changes, and $+0.10 \text{ Wm}^{-2}$ from increased stratospheric H_2O . At this point, these findings have not been verified in the literature, and there remain questions about the validity of the relatively large radiative forcing from the increase in stratospheric water vapor.

* *Corresponding author:* Donald J. Wuebbles, Department of Atmospheric Sciences, University of Illinois at Urbana Champaign, 105 S. Gregory St., Urbana IL-61801, USA. Email: wuebbles@atmos.uiuc.edu

An important goal in this study is to reexamine the effects on climate associated with changes in radiative forcing resulting from the perturbations to stratospheric ozone and water vapor as a result of aircraft emissions in the stratosphere. In addition to reexamining the radiative effects on climate from fleets of HSCTs, we will also consider more recent scenarios that parametrically consider the effects of cruise altitudes while holding the geographical distribution and fuel use constant.

2 MODEL DESCRIPTIONS

2.1 Two-Dimensional Chemistry Transport Model

The UIUC two-dimensional (2D) chemical-radiative-transport model is a zonally-averaged model of the chemistry and physics of the global atmosphere. The model is often used to study human related and natural forcings on the troposphere and stratosphere, but, because it is zonally-averaged, the analysis of tropospheric processes is limited. The model determines the atmospheric distributions of 78 chemically active atmospheric trace constituents. In addition to 56 photolytic reactions, the model incorporates 161 thermal reactions in the chemical mechanism, including heterogeneous reactions (e.g., see Wuebbles et al., 2001, Wei et al., 2001). Reaction rates and photolysis cross-sections in the model are based on recommendations from NASA's Chemical Kinetics Review Panel (e.g., DeMore et al., 1997; Sander et al., 2000).

In the last year, there have been substantial improvements made to the model, which have resulted in significant changes in lower stratospheric ozone response to NO_x and H_2O emissions.

2.2 Radiative Transfer Model

The narrowband radiative transfer model (RTM) is used in these studies is a component of the Integrated Science Assessment Model (ISAM) (Jain et al., 2000). In addition to water vapor and ozone changes considered in this study, the model calculates radiative forcing due to other gases such as carbon dioxide (CO_2), methane (CH_4), nitrous oxide (N_2O), chlorofluorocarbons (CFCs), and other halocarbons. This model was formulated for efficiency (allowing infrequent calculation of atmospheric absorptivity and emissivity), as well as generality ($5\text{-}10\text{cm}^{-1}$ spectral resolution allows easy incorporation of many trace gases). The radiative transfer analyses are evaluated on a 5° latitude grid from 82.5°S to 82.5°N . The thickness of vertical layers is 100 mbar in the troposphere, decreasing to 5-10 mbar near the tropopause and lower stratosphere.

The long wave component of the radiative transfer model is a Malkmus random band model. The model calculates absorptivities and emissivities in the $0\text{-}3000\text{cm}^{-1}$ range band with of 10 cm^{-1} for H_2O and 5 cm^{-1} for CO_2 , O_3 , CH_4 , and N_2O . The short-wave radiative fluxes are based on the Delta-Eddington model developed by Briegleb (1992). Line parameters for H_2O , CO_2 , O_3 , CH_4 , and N_2O , were based on the HITRAN-1992 database (Rothman et al., 1992). Absorption cross-section data for CFC-11, and CFC-12 were taken from McDaniel et al. (1991). The vertical profiles of temperature, H_2O , and O_3 are important parameters in the calculations of radiative forcing. The latitudinal and seasonal variations of temperature, H_2O , O_3 , and clouds are based on in situ and satellite data. A detailed description of the data used in this study can be found in Jain et al. (2000).

The adjusted calculations are performed by allowing stratospheric temperatures to adjust such that stratospheric heating/cooling rates are identical to values calculated for the pre-perturbation stratosphere. This approach essentially assumes a fixed dynamical heating/cooling approximation. Temperature are adjusted iteratively until the net heating rate changed by less than 0.5×10^{-3} per day at all levels above the tropopause.

3 RESULTS AND DISCUSSION

3.1 Radiative forcing from HSCT Scenarios

Of the many scenarios considered for analyses of effects on stratospheric ozone from fleets of HSCT aircraft in Chapter 4 (Isaksen et al., 1999) of the IPCC assessment, only two were considered for analyses of radiative forcing in Chapter 6 (Prather et al., 1999) (see Table 1).

Table 1. Percentage change in Northern Hemisphere total column ozone for HSCT scenarios used for calculation of radiative forcing in Chapter 6 (IPCC 1999)

IPCC Scenario	Fleet Size	E.I.(NO _x) [g/kg of fuel]	Sulphate Conversion (%)	Cl _y (ppbv)	IPCC Models	AER model	UIUC -2D model
S1k	500	5	10 (SA5)	3.0	-0.2 to -0.8	-0.8	-0.51
S9h	1000	5	10 (SA6)	2.0	-0.3 to -1.1	-0.8	-0.8

Table 2. Comparison of radiative forcing, after stratospheric adjustment, due to water vapor and ozone perturbations from the two HSCT scenarios discussed in Table 1. The radiative forcing values are calculated using the UIUC RTM, for AER and UIUC-2D model results and compared with the results shown in Chapter 6 (Prather et.al., IPCC 1999).

IPCC scenario	IPCC (1999)		AER model		UIUC model	
	H ₂ O	O ₃	H ₂ O	O ₃	H ₂ O	O ₃
S1k	+0.050	-0.010	+0.019	-0.013	+0.039	-0.006
S9h	+0.100	-0.010	+0.034	-0.014	+0.048	-0.007

For the changes in ozone, Chapter 6 reports radiative forcing values of -0.010 Wm^{-2} for both scenarios, with a range amongst the models of -0.040 to $+0.010$. The adjusted radiative forcings for the two scenarios, -0.006 for S1k and -0.007 for S9h, are shown in Table 2. For perturbations of water vapor our radiative transfer model calculates a radiative forcing of $+0.039$ and $+0.048$ as compared to $+0.050$ and $+0.100$ for the two scenarios respectively.

We also considered results used in the IPCC assessment from the AER chemical-transport model. The derived radiative forcing due to ozone are in good agreement with the IPCC(1999) values. But water vapor perturbations derived from AER model give radiative forcings of $+0.019 \text{ Wm}^{-2}$ for S1k and $+0.034 \text{ Wm}^{-2}$ for S9h scenarios (see Table 2), much lower than the IPCC assessment findings. We are currently trying to investigate this underestimation of water vapor impact on radiative forcing as calculated in our RTM compared to the IPCC(1999). The differences in the radiative transfer models, like the higher altitude and wavelength resolutions used in our model could make a significant difference. We are also analysing the role of the difference in treatments of transport of water vapor emissions in the different CTMs used in the IPCC (1999) and our UIUC 2D model.

3.2 Radiative forcing from Parametric Scenarios

Current considerations for new aircraft concepts are quite different than the original HSCT concept. Such aircraft would likely have different cruise speeds, and hence cruise altitudes, different sizes, different design ranges, and different markets, than the original HSCT concept. A set of parametric emissions scenarios has been developed to evaluate the sensitivity of the atmospheric perturbations to cruise altitudes by Baughcum (2002). One set of parametric scenarios in Baughcum (2002) is based on conventional routing for scheduled flights greater than 2500 nautical miles. The changes in ozone calculated with the two-dimensional model for these scenarios are presented in Table 3.

Table 3. Percentage change in Northern Hemisphere total column ozone calculated with the UIUC-2D model for eight conventional routing greater than 2500 nautical miles scenarios relative to 2020 background atmosphere for E.I.(NO_x) = 10 g/kg of fuel. These results were then used in radiative forcing studies.

Fuel Burn [Mlbs/day]	E.I.(NO _x) [g/kg of fuel]	Cruise Altitudes (km)			
		13-15	15-17	17-19	19-21
73	10	0.0081	-0.0239	-0.0989	-0.1930
146	10	0.0148	-0.0525	-0.2090	-0.3930

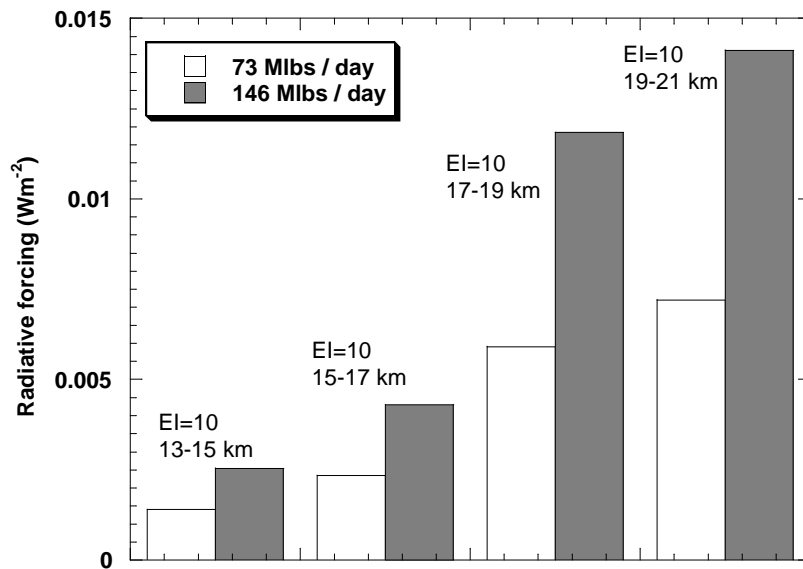


Figure 1. Annually and globally averaged radiative forcing due to water vapor perturbation, after stratospheric adjustment foreign aircraft parametric study scenarios

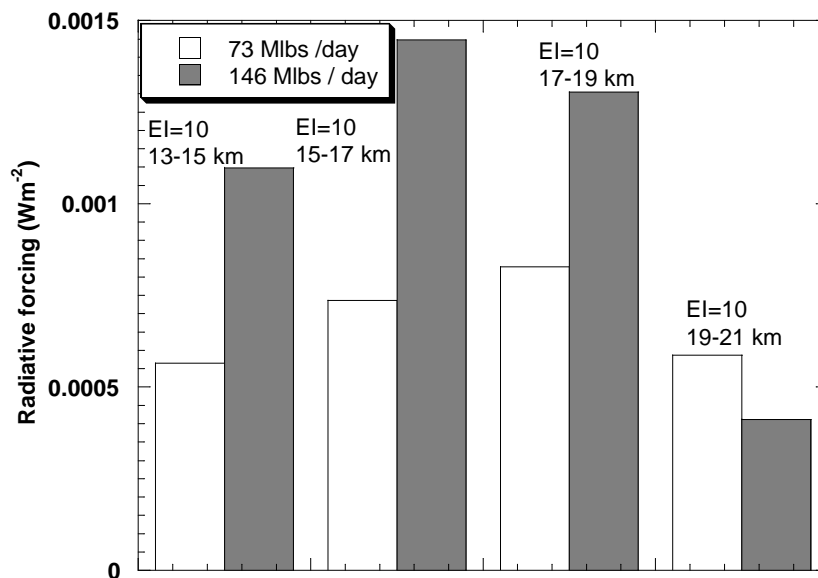


Figure 2. Annually and globally averaged radiative forcing due to ozone perturbation, after stratospheric adjustment, for eight aircraft parametric scenarios

The annually and globally averaged radiative forcing, after stratospheric adjustment, from the water vapor perturbations are shown in Figure 1, while Figure 2 shows the same for ozone perturbations from the parametric scenarios chosen. From Figure 1 we can conclude that radiative forcing of water vapor shows a linear scaling with fleet size. In Figure 2 we see that the radiative forcing increases in the lower two cruise altitude bands of 13-15 and 15-17 km, whereas it has a decreasing trend for the higher altitude bands of 17-19 and 19-21 km. In the troposphere and lower stratosphere region, ozone increases with increase in fuel burn and above the cross over point, the derived decrease in ozone gets larger with increase in fuel burn. The balance in the ozone concentration below and above the cross over point determines the net radiative forcing. Although these effects likely explain the results in the figures, we are still investigating this further. The figures also indicate that the radiative forcing impact of water vapor is much more significant than that due to ozone, which is consistent with the IPCC(1999) conclusions.

The derived radiative forcing in each of the cases is much smaller for both the ozone and the water vapor perturbations than those for the HSCT scenarios analyzed in Isaksen et al. (1999) and the first part of this study. The parametric scenarios are based on assumptions of lower fleet use than the HSCT case and most consider cruise altitudes lower than the 18–20 km altitudes projected for the HSCT. For the scenario of 13–15 km cruise altitude, E.I. (NO_x) = 10 g/kg of fuel and fuel burn of 146 Mlbs/day, the radiative forcing from water vapor perturbation is less than $+0.0025 \text{ Wm}^{-2}$ and for ozone perturbation it is less than $+0.0011 \text{ Wm}^{-2}$.

3.3 Sensitivity Experiment

There have been increases in stratospheric water vapor observed in recent decades, which may have contributed significantly to both stratospheric cooling and tropospheric warming (Forster and Shine, 2002). Although our results are smaller than those from IPCC, future fleets of aircraft flying extensively in the lower stratosphere could raise radiative forcing concerns related to stratospheric water vapor increases. The recent paper by Zhong and Haigh (2003) has studied the effect of increased stratospheric water vapor on radiative forcing and compared it with five broad and multiple band radiation schemes. For testing the model sensitivity to stratospheric water vapor, we follow the experiment done by Zhong and Haigh (2003). The effective cloud cover was set to zero and the concentration of all other absorbing gases except water vapor was set to negligible amounts. Above the tropopause of the particular latitude belt, an increase of 0.7 ppmv has been imposed in the background water vapor profile. Table 4 compares the results obtained with line-by-line (LBL) reference calculations, showed in Zhong and Haigh (2003) and we see that the derived instantaneous radiative forcing from our model agrees well with their results, much better than some of the models they analysed in their study.

Table 4. Comparison of instantaneous shortwave radiative forcing (Wm^{-2}) in our narrowband radiative transfer model due to a 0.7 ppm increase in stratospheric water vapor relative to the LBL calculation described in Zhong and Haigh (2003).

Type of Radiation Model	Solar Zenith Angle (degrees)	Radiative forcing (Wm^{-2})
LBL	30	-0.102
	70	-0.060
ISAM narrowband	30	-0.121
	70	-0.066

4 CONCLUSIONS

For the HSCT scenarios analyzed in IPCC (1999), our derived stratospheric adjusted radiative forcing for perturbations to ozone are within the range of the results presented in Chapter 6 (Prather et al., 1999) of that assessment. However, our evaluation of the radiative forcing for the water vapor perturbations from these scenarios suggests that the overall evaluation in Prather et al. (1999) may have overestimated the stratospheric adjusted radiative forcing for the water vapor changes derived from these scenarios. Additional studies are currently underway to better evaluate these differences. Results also indicate that the radiative forcing impact of the water vapor perturbation is much more significant than that due to ozone, which is consistent with the IPCC(1999) conclusions.

One of the advantages in the radiative transfer model we used in this study compared to those used in the IPCC assessment is that our radiative transfer model has higher altitude resolution near the tropopause and in the lower stratosphere. We also fully calculate the effects of seasonal variations on the derived radiative forcing, whereas one of the two models calculating the radiative forcing with stratospheric adjustment presented in IPCC (1999) used a similar approach to ours and the other used annual mean concentrations in determining the radiative forcing.

Zhong and Haigh (2003) have discussed how the typical broad-band radiation schemes underestimate the instantaneous shortwave radiative forcing due to increased stratospheric water vapor. The sensitivity analysis performed in this study indicates that the shortwave derivation for

water vapor in our radiative transfer model is not subject to this error discussed in Zhong and Haigh (2003).

REFERENCES

- Baughcum, S. L., 2002: Informal Report Describing the Development of Parametric Emission Scenarios, NAS3-01140 Revolutionary Aero-Space Engine Research Task Order #5 prepared for NASA Glenn Research Center, Cleveland, pp 13.
- Briegleb, B., 1992: Delta-Eddington approximation for solar radiation in the NCAR Community Climate Model. *J. Geophys. Res.*, *97*, 7603-7612.
- Forster, P. M. deF., and K. P. Shine, 2002: Assessing the climate impact of trends in stratospheric water vapour, *Geophys. Res. Lett.*, *29*, doi: 10.1029/2001GL013909.
- Isaksen, I., C. Jackman, S. L. Baughcum, F. Dentener, W. Grose, P. Kasibhatla, D. Kinnison, M. K. W. Ko, J. C. McConnell, G. Pitari, D. J. Wuebbles, T. Berntsen, M. Danilin, R. Eckman, E. Fleming, M. Gauss, V. Grewe, R. Harwood, D. Jacob, H. Kelder, J.-F. Muller, M. Prather, H. Rogers, R. Sausen, D. Stevenson, P. von Velthoven, M. van Weele, P. Vohralik, Y. Wang, and D. Weisenstein, 1999: Modeling the Chemical Composition of the Future Atmosphere. Chapter 4 in Intergovernmental Panel on Climate Change, *Aviation and the Global Atmosphere*. J. E. Penner, D. H. Lister, D. J. Griggs, D. J. Dokken, and M. McFarland (eds.), Cambridge University Press. Cambridge, UK.
- Jain, A.K., B. P. Briegleb, K. Minschwaner, D. J. Wuebbles, 2000: Radiative forcings and global warming potentials of thirty-nine greenhouse gases. *J. Geophys. Res.*, *105*, 20,773-20,790.
- McDaniel, A. H., C. A. Cantrell, J. A. Davidson, R. E. Shetter, and J. G. Calvert, 1991: The temperature dependent infrared absorption cross-sections for chlorofluorocarbons: CFC-11, CFC-12, CFC-13, CFC-14, CFC-22, CFC-113, CFC-114, CFC-115. *J. Atmos. Chem.*, *12*, 211-227.
- Ponater, M., S. Brinkop, R. Sausen, and U. Schumann, 1996: Simulating the global atmospheric response to aircraft water vapour emissions and contrails – a first approach using a GCM. *Annales Geophysicae*, *14*, 941-960.
- Prather, M., R. Sausen, A. S. Grossman, J. M. Haywood, D. Rind, B. H. Subbaraya, P. Forster, A. Jain, M. Ponater, U. Schumann, W.-C. Wang, T. M. L. Wigley, and D. J. Wuebbles, 1999: Potential Climate Change from Aviation. Chapter 6 in Intergovernmental Panel on Climate Change, *Aviation and the Global Atmosphere*. J. E. Penner, D. H. Lister, D. J. Griggs, D. J. Dokken, and M. McFarland (eds.), Cambridge University Press. Cambridge, UK.
- Rind, D., P. Lonergan, and K. Shah, climatic effects of water vapor release in the upper troposphere. *J. Geophys. Res.*, *101*, 29395-29406, 1996.
- Rothman, L. S., et al., 1992: The HITRAN molecular database: Editions of 1991 and 1992. *J. Quant. Spectrosc. Radiat. Transfer*, *48*, 469-507.
- Seinfeld, J. H., Clouds, contrails, and climate. *Nature*, *391*, 837-838, 1998.
- Wei, C. -F., S.M.Larson, K.O. Patten and D.J. Wuebbles, 2001: Modeling of ozone reactions on aircraft-related soot in the upper troposphere and lower stratosphere. *Atmospheric Environment*, *35*, 6167-6180.
- Wuebbles, D.J., K. Patten, M.T. Johnson and R. Kotamarthi, 2001: New methodology for Ozone Depletion Potentials of short-lived compounds: n-Propyl bromide as an example. *J. Geophys. Res.*, *106*, 14,551-14,571.
- Zhong, W., and J. D. Haigh, 2003: Shortwave radiative forcing by stratospheric water vapor. *Geophys. Res. Lett.*, *30*, doi:10.1029/2002GL016042.

Sources of NO_x at cruise altitudes: Implications for predictions of ozone and methane perturbations due to NO_x from aircraft

T.K. Berntsen^{*}, M. Gauss, I.S.A. Isaksen
Department of Geophysics, University of Oslo, Norway

V. Grewe, R. Sausen
Deutsches Zentrum für Luft- und Raumfahrt e.V. (DLR), Germany

G. Pitari, E. Mancini
University of L'Aquila (ULAQ), Italy

E. Meijer
Royal Dutch Meteorological Institute (KNMI), The Netherlands

D.Hauglustaine
Centre Nationale de la Recherche Scientifique (IPSL), France

Keywords: Aircraft emissions, Ozone, Methane, NO_x emissions

ABSTRACT: The impact of NO_x background levels in the upper troposphere on the predicted ozone and methane perturbations caused by NO_x emissions from aircraft has been studied with five global chemical transport models (CTMs) within the EU-project TRADEOFF. The relative contribution from the different NO_x sources to concentration levels at cruise altitudes varies significantly between the CTMs. The calculated ozone perturbations caused by NO_x emitted by aircraft vary between 1 and 4 ppbv at northern mid-latitudes for July, due to differences in the vertical mixing in the CTMs, as well as the NO_x background levels. The average reduction of the methane lifetime due to NO_x from aircraft is 1.2 %/Tg(N)/yr with a range from 0.7 to 1.9. There is a tendency that the CTMs that give the largest ozone perturbations by aircraft (positive RF) give the smallest decrease in the lifetime of methane (negative RF).

1 INTRODUCTION

NO_x emissions from aviation in the upper troposphere and lower stratosphere (UTLS) cause radiative forcing of climate through enhanced concentrations of ozone and reduced lifetime of methane. Assessments using global chemical tracer models (CTMs) have shown significant differences between the estimated impacts (e.g. IPCC, 1999). Due to the non-linear nature of the photochemistry of the atmosphere, the impact of additional NO_x from aircraft is very dependent on the background concentrations of NO_x. In this region of the atmosphere NO_x can originate from a many sources, mainly from lightning, convective transport of NO_x from surface sources, downward transport from the stratosphere (from N₂O oxidation), and from in-situ aircraft emissions. To improve our understanding of the possible environmental impacts of NO_x emissions from aircraft, it is of key importance to be able to simulate the background NO_x chemistry, which requires the calculation of the contributions of all other NO_x sources.

Within the EU-project TRADEOFF we have intercompared calculations with 5 global CTMs of the contributions from the different sources to the NO_x levels at cruise altitude. The total global NO_x emissions were differentiated into the following 6 source categories: Fossil fuel combustion at the surface, biomass burning, biogenic emissions from soils, lightning, aircraft, oxidation of N₂O in the stratosphere and transport to the UTLS region. Based on a reference simulation using the emissions according to the OXCOMP intercomparison (IPCC, 2001; Prather et al., 2003; Gauss et

^{*} *Corresponding author:* Terje Berntsen, Dept. of Geophysics, University of Oslo, P.O.Box 1022, Blindern, 0315 Oslo, Norway. Email: t.k.berntsen@cicero.uio.no

al., 2003), each CTM calculated the effects of a 10% perturbation (enhancement) of each source category (one at the time) on the chemical composition. From the results of the reference and each perturbation simulation we calculated the contributions of the total NO_x emission of the considered source category, assuming that a 10% perturbation has a linear effect on the atmospheric composition. The 5 CTMs that participated in this exercise were: The TM3 model operated by KNMI (Dentener et al., 1999; Bregman et al., 2000), the OsloCTM2 model from University of Oslo (Kraabøl et al., 2002), the ULAQ model of the University of l'Aquila (Pitari et al., 1997), the LMDzINCA model from IPSL, and the ECHAM4/CHEM model run at DLR (Hein et al., 2001).

2 THE NO_x BUDGET

A rigorous evaluation of the models, by comparing the results with trace gas observations from all major research aircraft campaigns, commercial airlines, and ozone soundings in the period 1995-1998, has been reported elsewhere (Brunner et al., 2003). Here we focus on the relative contribution from the different NO_x sources to the background NO_x concentrations in the UTLS region. Figures 1 and 2 show the percentage contribution from lightning and fossil fuel combustion to zonally averaged NO_x concentrations for July.

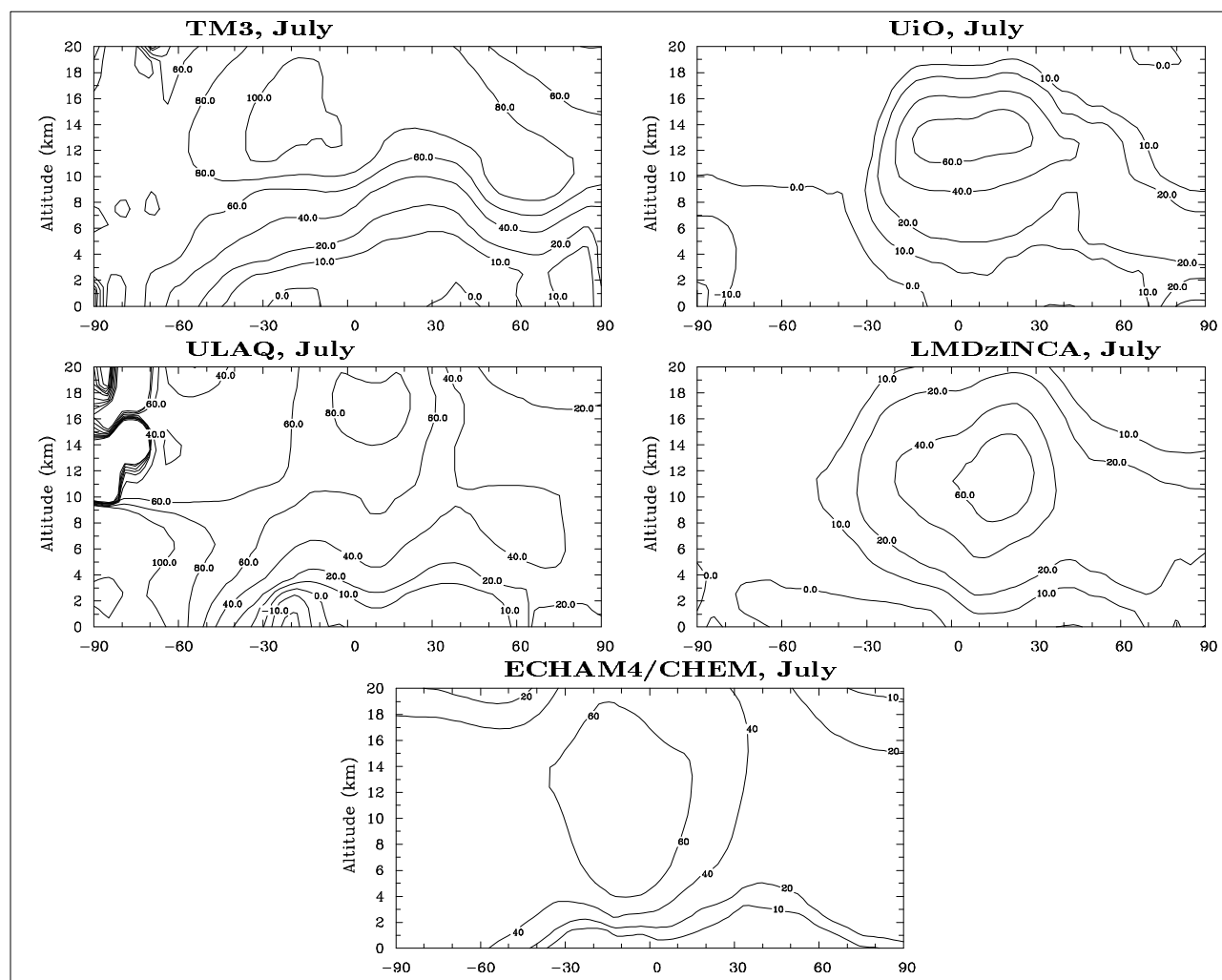


Figure 1. Contribution (%) to the zonally averaged background NO_x levels by NO_x from lightning (5 Tg(N)/yr in all models).

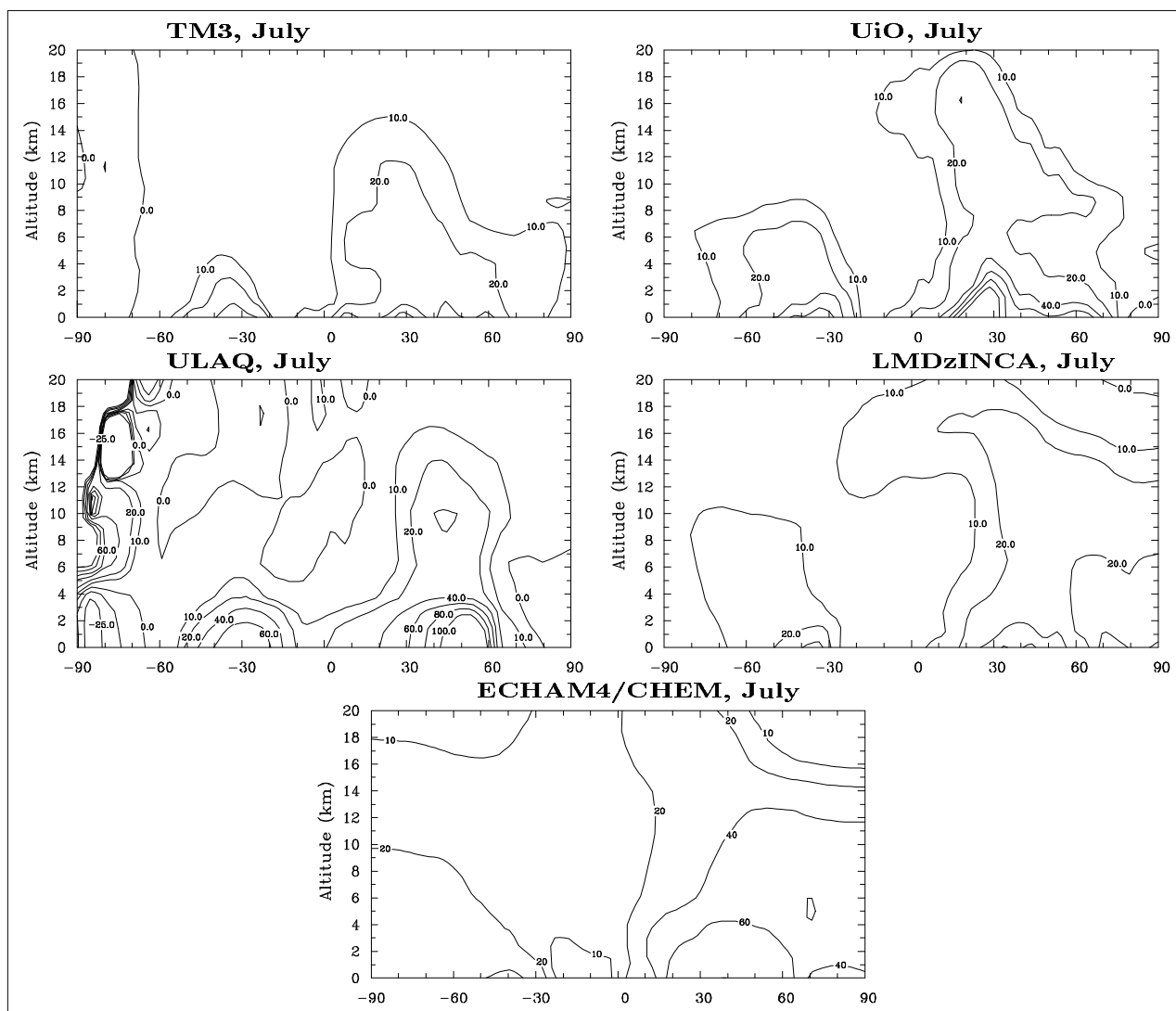


Figure 2. Contribution (%) to the zonally averaged background NO_x levels by NO_x from fossil fuel combustion from surface sources.

In the region with largest impact of aircraft NO_x (10–12 km altitude, 45–65°N) all CTM results for July show significant contributions from the other sources. The positioning and magnitude of the lightning emissions are linked to key parameters in the description of the convective processes (including generation of convective precipitation) in the models. The vertical lifting of NO_x from ground sources depends mainly on the convective transport as the lifetime of NO_x is too short for the advection to play a major role. In the TM3 model the impact of lightning extends northwards to 70°N contributing to about 80% of the NO_x levels, while in the other models the effect is mostly south of 40°N, contribution about 30% in the aircraft region. The very high contributions in the tropical tropopause region in TM3 were recently corrected, but that correction does not affect the findings presented here. The contribution from ground based fossil fuel combustion is 20 and 45% in OsloCTM2, LMDzINCA and ECHAM4/CHEM, while in TM3 and the ULAQ models it is lower (10–20%) due to large impact of lightning in TM3 and less efficient convection in the ULAQ model. The impact of aircraft emissions itself are smallest during summer and constitutes a contribution of 10–15% in all models except in the ULAQ model where it is 50% due to less efficient vertical mixing by convection (cf. Rogers et al., 2002)

3 CHANGES IN OZONE AND METHANE LIFETIMES DUE TO NO_x FROM AIRCRAFT

Figure 3 shows the ozone perturbations for July due to current subsonic aircraft emissions in the 5 CTMs. The estimate for current (2000) aircraft emissions of 0.59 Tg(N)/yr of NO_x were used in all CTMs. Enhancements of the zonally averaged ozone concentrations in the free troposphere range from 1.3 to 5 ppbv between the 5 CTMs. All models, except the LMDzINCA model, show a maximum in the ozone perturbation in the polar regions of the northern hemisphere during July. The ULAQ model is the only one which shows a summer (July) maximum, while the other models give a maximum in late winter or spring. The summer maximum in the ULAQ model is probably related to the less efficient vertical mixing in this model by convection. This is illustrated in Figure 4 which is taken from a previous study (EU project AEROCHEM-II, Isaksen et al., (2000)) involving three of the CTMs used in TRADEOFF. The OsloCTM2 and ECHAM4/CHEM models give maximum increase in the tropospheric column of ozone at 35-45°N in May, while the maximum in the ULAQ model is founding July over the North Pole. During summer increased convection at mid-latitudes tends to mix ozone produced at cruise altitude down to lower altitudes or even to the ground where it is lost more rapidly. Efficient vertical mixing, as indicated in the weak vertical gradient in the fossil fuel contribution to NO_x (Figure 2), is probably the reason for the small ozone perturbation in LMDzINCA.

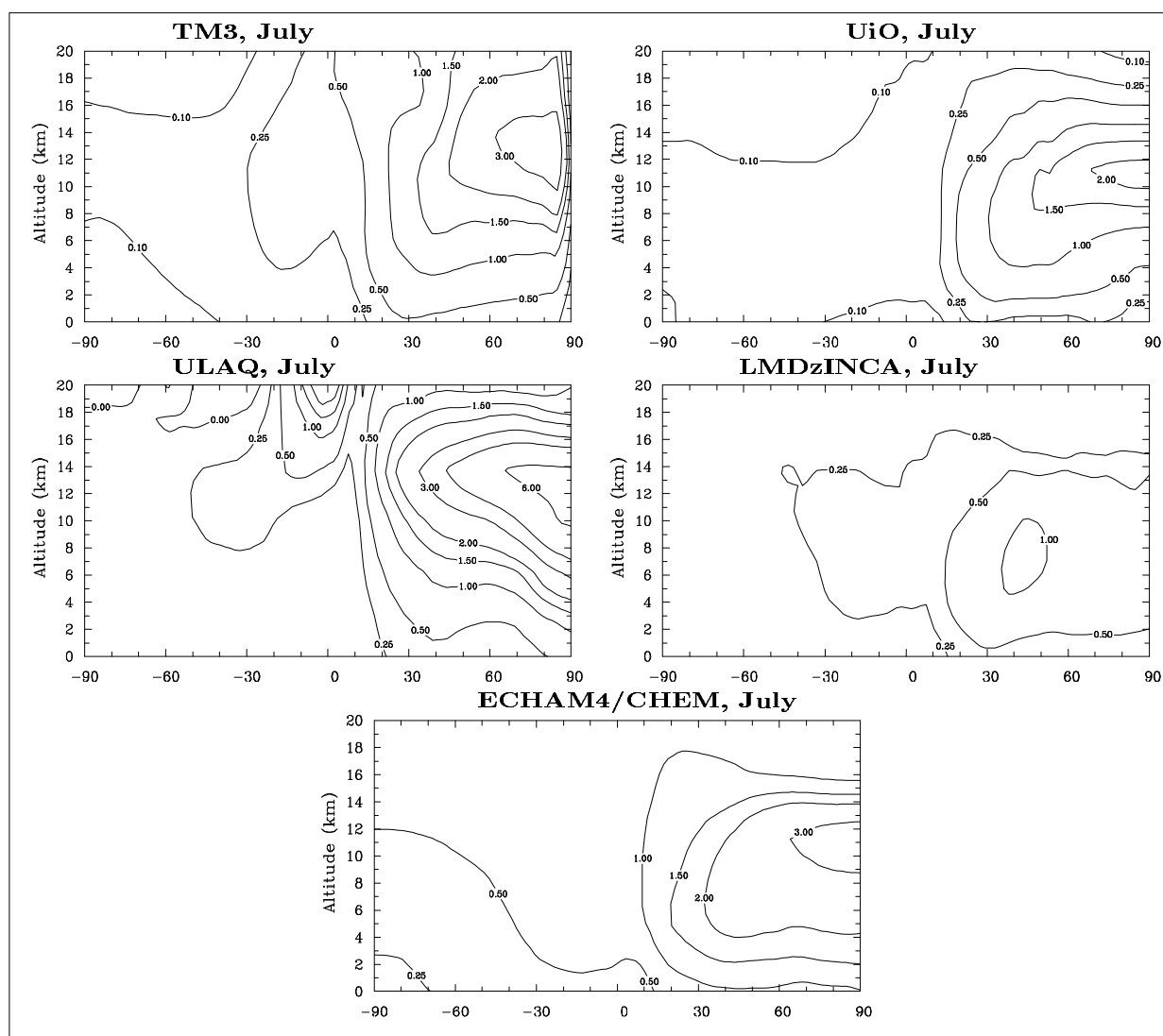


Figure 3. Zonally averaged ozone change (ppbv, July) due to aircraft emissions of NO_x.

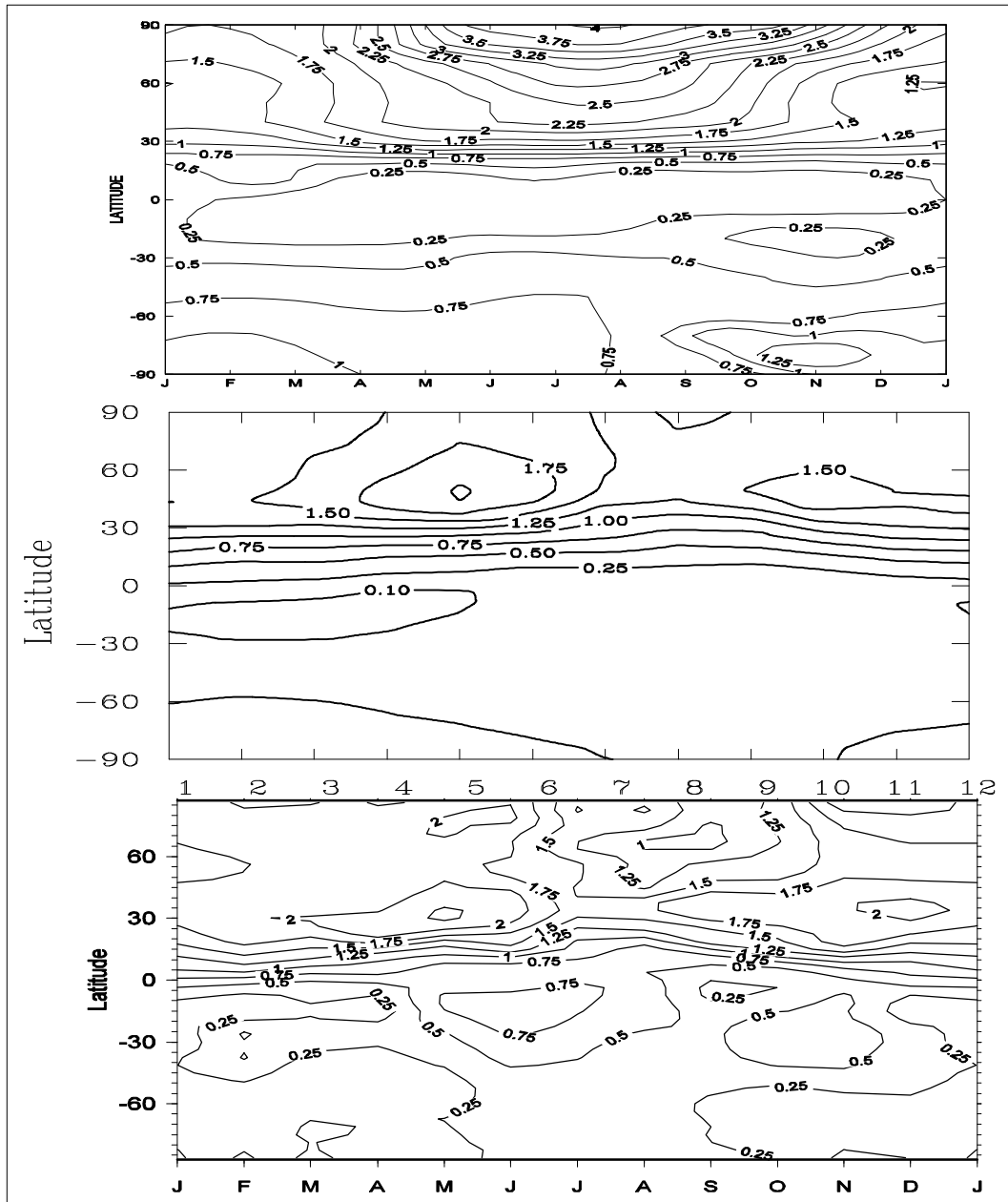


Figure 4. Zonally averaged tropospheric ozone column increase (in Dobson Units) due to 2015 aircraft emissions of NO_x (1.08 Tg(N)/yr) from ULAQ (top), OsloCTM2 (middle) and ECHAM4/CHEM models (From AEROCHEM-II final report).

To study how differences in the calculated background NO_x budget affect the calculated ozone perturbations, two additional model experiments with enhanced emissions from lightning and fossil fuel combustion by 30% were performed with the TM3 and UiO models. Simulations with and without aircraft emissions were performed with these enhanced NO_x emissions from lightning and fossil fuels. Increasing the NO_x emissions from fossil fuels by 30% reduced the maximum ozone perturbations due to aircraft by 150 pptv in both models. Increasing the NO_x emissions from lightning by 30% reduced the maximum ozone perturbations due to aircraft by 600 pptv in TM3 and only 100 pptv in the UiO model. The latter experiment shows how the northerly shift in the NO_x production by lightning in the TM3 model towards the main flight routes enhances the background NO_x concentrations and thereby lowers ozone production efficiency of the additional NO_x from aircraft.

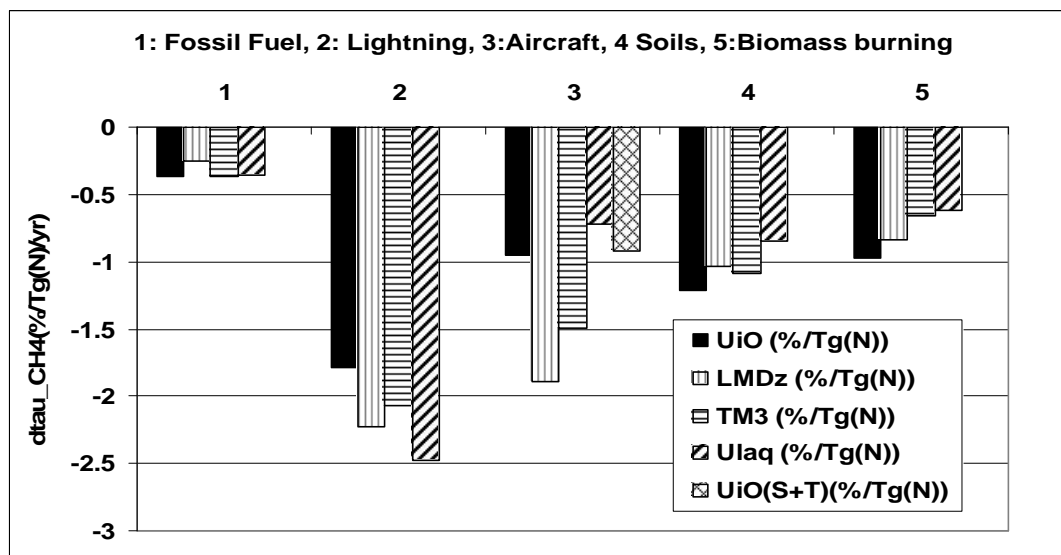


Figure 5. Sensitivity of the methane lifetime due to perturbations of various NO_x sources. The figure shows the relative change in the lifetime of methane normalized to the perturbations (+10%) of each of the NO_x sources. The OsloCTM2 model is denoted UiO in the figure. UiO (S+T) denotes the extended version of the UiO model including both the troposphere and stratosphere.

Emissions of NO_x from aircraft also lead to changes in the lifetime of methane. Concentrations of the hydroxyl radical (OH) increase and thus the lifetime of methane in the atmosphere is reduced through:

- Increased ozone giving OH through $O_3 + hv \rightarrow O(^1D) + O_2$ and $O(^1D) + H_2O \rightarrow 2OH$
- $NO + HO_2 \rightarrow NO_2 + OH$
- Interaction with CO perturbations at cruise levels and transport of the signal to low altitudes and latitudes (IPCC, 1999)

The CTM results show consistently that per mass unit emission of NO_x, lightning has the largest impact on the methane lifetime, and fossil fuel (FF) emissions have the least. Lightning occurs in regions with low background NO_x levels and consequently the impact on OH is much larger than for fossil fuel emissions that occur mainly in high background NO_x regions at mid-latitudes. The aircraft source has the second largest impact in the LMDzINCA and TM3 models, while in the OsloCTM2 and ULAQ models the impact of aircraft is about equal to the impact of NO_x from soils and biomass burning. However, the difference between the models is significantly larger for aircraft, indicating that perturbations in the UTLS region are particularly difficult to model since there is such a close interaction between chemistry and transport in this region of the atmosphere. There is a tendency that the CTMs that give the largest ozone perturbations by aircraft (positive RF) give the smallest decrease in the lifetime of methane (negative RF). This is an important observation since the radiative impact is a net effect of a positive contribution from ozone and a negative contribution from methane. This can be explained by the fact that little vertical mixing keeps the pollutants (NO_x and ozone) aloft, while the reduction of the lifetime of methane is believed to be caused by transport of a CO signal to lower altitudes.

4 CONCLUSIONS

The contribution to the tropospheric NO_x contributions from 6 different NO_x source categories has been studied with 5 global chemistry transport models. Although all models give a reasonable representation of the observed NO_x concentrations in the UTLS region (Brunner et al., 2003) there are significant differences in the relative contribution from the different NO_x sources in this region of the atmosphere. This is particularly pronounced at northern mid-latitudes, which is most important with respect to the impacts of aircraft, due to the importance of convective lifting of the

large surface emissions from fossil fuel combustion. The calculated ozone perturbations caused by NO_x emitted by aircraft vary between 1 and 4 ppbv at northern mid-latitudes for July, due to differences in the vertical mixing in the CTMs, as well as the NO_x background levels. The average reduction of the methane lifetime due to NO_x from aircraft is 1.2 %/Tg(N)/yr with a range from 0.7 to 1.9. An important finding is that there is a tendency that the CTMs that give the largest ozone perturbations by aircraft (causing positive RF) give the smallest decrease in the lifetime of methane (negative RF), probably due to less efficient vertical mixing in these models. Since the net RF caused by aircraft through ozone and methane perturbations is the difference between two numbers of similar magnitude, this impact of vertical mixing will give a much larger inter model variability in the net effect than in the ozone or methane effects separately.

ACKNOWLEDGEMENT

This work has been supported by the European Community grant (TRADEOFF, contract no. EVK2-1999-00030)

REFERENCES

- Bregman B. et al., 2000: The N₂O and ozone relationship in the lowermost stratosphere: diagnostic for mixing processes as represented by a three dimensional model, *J. Geophys. Res.*, **105**, 17,279, 17,290.
- Brunner, D., J. Staehelin, H.L. Rogers, M.O. Köhler, J.A. Pyle, D. Hauglustaine, L. Jourdain, T.K. Berntsen, M. Gauss, I.S.A. Isaksen, E. Meijer, P. van Velthoven, G. Pitari, E. Mancini, V. Grewe, and R. Sausen, 2003: An evaluation of the performance of chemistry transport models by comparison with research aircraft observations. Part 1: Concepts and overall model performance. *Atmos. Chem. Phys. Discuss.* **3**, 2499-2545.
- Dentener F., H. Feichter, and A. Jueken, 1999: Simulations of the transport of Rn222 using on-line and off-line global models at different horizontal resolutions: a detailed comparison with measurements, *Tellus*, **51**, 573-602.
- Gauss, M., G. Myhre, G. Pitari, M. J. Prather, I. S. A. Isaksen, T. K. Berntsen, G. P. Brasseur, F. J. Dentener, R. G. Derwent, D. A. Hauglustaine, L. W. Horowitz, D. J. Jacob, M. Johnson, K. S. Law, L. J. Mickley, J.-F. Müller, P.-H. Plantévin, J. A. Pyle, H. L. Rogers, D. S. Stevenson, J. K. Sundet, M. van Weele, O. Wild, 2003: Radiative forcing in the 21st century due to ozone changes in the troposphere and the lower stratosphere, *J. Geophys. Res.*, **108**, 4292, doi:10.1029/2002JD002624.
- Hein R., Dameris, M., Grewe, V., Schnadt, C., Steil, B., and Landgraf, J., 2001: Results of an interactively coupled atmospheric chemistry - general circulation model: Comparison with observations, *Ann. Geophysicae*, **19**, 435-457.
- IPCC, 1999: Aviation and the global atmosphere, Ed. by J.E. Penner, D.H. Lister, D.J. Griggs, D.J. Dokken, and M. McFarland. Cambridge University Press, New York. pp. 373.
- Isaksen I.S.A. (Ed.) 2000. AERO-CHEM-II, Modelling of the impact on ozone and other chemical compounds in the atmosphere from airplane emissions, May 1998-April 1999, Final Report, Contract No. ENV4-CT97-0621.
- Kraabøl A.G., F. Stordal, T. Berntsen, and J. Sundet. 2002: Impacts of NO_x emissions from subsonic aircraft in a global 3-D CTM including plume processes. *J. Geophys. Res.*, 10.1029/2001JD001019.
- Pitari G., B. Grassi, and G. Visconti, 1997: Results of a chemical transport model with interactive aerosol microphysics, *R.D. Bojkov and G. Visconti. Eds., XVIII Ozone symp. proc.*, 759-763.
- Prather, M., M. Gauss, T. Berntsen, I. Isaksen, J. Sundet, I. Bey, G. Brasseur, F. Dentener, R. Derwent, D. Stevenson; P.I. Grenfell, D. Lee; D. Hauglustaine, L. Horowitz, D. Jacob, L. Mickley, M. Lawrence, R. von Kuhlmann, J.-F. Müller, G. Pitari, H. Rogers, M. Johnson, J. Pyle, K. Law, M. van Weele, O. Wild, 2003: Fresh air in the 21st century?, *Geophys. Res. Lett.* **30(2)**, 1100, 10.1029/2002GL016285.
- Rogers, H., H. Teysseire, G. Pitari, V. Grewe, P. van Velthoven, and J. Sundet, 2002: Model intercomparison of the transport of aircraft-like emissions from sub- and supersonic aircraft, *Met. Z.*, **11**, 151-161.

Particles and Cirrus Clouds (PAZI): Overview of results 2000 - 2003

B. Kärcher*, U. Schumann, S. Brinkop, R. Busen, M. Fiebig, H. Flentje, K. Gierens, J. Graf, W. Haag, J. Hendricks, H. Mannstein, S. Marquart, R. Meyer, A. Minikin, A. Petzold, M. Ponater, R. Sausen, H. Schmid, P. Wendling
DLR-Institut für Physik der Atmosphäre, Oberpfaffenhofen, Germany

M. Aigner, P. Frank, K.-P. Geigle, P. Gerlinger, B. Noll, W. Stricker, C. Wahl
DLR-Institut für Verbrennungstechnik, Stuttgart, Germany

U. Schurath, O. Möhler, S. Schaefers, O. Stetzer
Forschungszentrum Karlsruhe, Institut für Meteorologie und Klimaforschung, Karlsruhe, Germany

O. Schrems, G. Beyerle, F. Immler
Alfred-Wegener-Institut für Polarforschung, Sektion Physik und Chemie der Atmosphäre, Bremerhaven, Germany

H. Kruse, A. Döpelheuer, M. Plohr
DLR-Institut für Antriebstechnik, Köln, Germany

C. Schiller, M. Bläsner, M. Krämer, A. Mangold, A. Wollny
Forschungszentrum Jülich, Institut für Stratosphärenchemie, Jülich, Germany

S. Borrmann, J. Curtius, S. Henseler, N. Hock, J. Schneider, S. Weimer
Universität Mainz, Institut für Physik der Atmosphäre, and Max-Planck-Institut für Chemie, Abteilung Wolkenphysik und Chemie, Mainz, Germany

F. Arnold, H. Aufmhoff, K. Gollinger, A. Kiendler, Th. Stilp, S. Wilhelm, K.-H. Wohlfrom
Max-Planck-Institut für Kernphysik, Bereich Atmosphärenphysik, Heidelberg, Germany

C. Timmreck, J. Feichter
Max-Planck-Institut für Meteorologie, Hamburg, Germany

U. Lohmann
Dalhousie University, Department of Physics and Atmospheric Science, Halifax, Nova Scotia, Canada

J. Ström
Stockholm University, Institute of Applied Environmental Research, Stockholm, Sweden

T. Rother
DLR-Deutsches Fernerkundungsdatenzentrum, Oberpfaffenhofen, Germany

Keywords: aerosols, cirrus clouds, contrails, combustion, chemi-ions, soot, freezing, humidity, climate.

ABSTRACT: PAZI is a national research project supported by the German Secretary of Education and Research (BMBF) through the Helmholtz-Gesellschaft Deutscher Forschungszentren (HGF). Research in PAZI is performed in concert with the projects SiA, INCA, PartEmis, and PARTS funded by the European Commission. PAZI investigates the interaction of aerosols with cirrus clouds, with an emphasis on aviation-produced aerosols and contrails, and their impact on atmospheric composition, radiation, clouds, and climate. This overview summarizes important results obtained during the first phase and highlights the following issues. Measurements and models addressing the formation and evolution of black carbon (BC) particles in burners and jet engines; physico-chemical characterization of aircraft-produced BC particles; measured freezing properties of liquid and BC particles; calculated global atmospheric distribution of BC from various sources; observed differences in cirrus properties between clean and polluted air masses; correlations between air traffic and cirrus cloud cover deduced from satellite observations; process

* *Corresponding author:* Bernd Kärcher, DLR-Institut für Physik der Atmosphäre, Oberpfaffenhofen, D-82234 Weßling, Germany. Email: bernd.kaercher@dlr.de

studies of aerosol-cirrus interactions; parameterization of cirrus cloud formation; representation of ice supersaturation and cirrus clouds in a climate model and possible aviation impact on global cirrus properties.

1 THE PAZI PROJECT

The project studied the formation of soot particles and other aerosols in jet engines and in the atmosphere, their influence on the formation of the ice phase in contrails and cirrus clouds, and their impact on air composition, cirrus, and climate. It provided a first estimate of the contribution of aviation to changes of the upper tropospheric aerosol and ice particle budget.

To achieve these goals, the participating teams employed highly innovative and complementary methods: combustion test facility, aerosol/cloud chamber, ground-based lidar, research aircraft, satellite sensors, process and climate models. One cornerstone of the project was the close collaboration with projects funded externally by the European Commission and other agencies. Partners from industry such as Lufthansa, MTU, and Rolls-Royce Germany also contributed to PAZI.

Work in PAZI was organized in four main workpackages, the results of which are presented in Section 2 and summarized in Section 3. The workpackages contained several subprojects, each of which was represented by a responsible scientist. Collaboration within and between the subprojects and workpackages proved to be very fruitful, resulting in a large number of joint publications summarized in Section 4 (as of fall 2003).

2 WORKPACKAGE RESULTS

It is not possible to cover every single result of a large-scale project in the limited space available in workshop proceedings. What follows is a brief overview of some of the highlights of PAZI and its associated EU projects.

2.1 *Soot emissions and aerosol precursors*

This workpackage consists of three subprojects dealing with soot particle formation and prediction of global, fleet-averaged aerosol emission indices (Plohr et al., 2000; Döpelheuer, 2000, 2002; Kärcher et al., 2000; Kunz et al., 2001; Braun-Unkhoff et al., 2001; Noll et al., 2002; Schumann et al., 2002; Böhm et al., 2003; Krüger et al., 2003; Wahl and Aigner, 2003). Measurement campaigns were carried out in laboratory flames, behind real jet engines and segments of combustors (hot end simulator), and in DLRs novel high pressure combustor test facility Stuttgart (HBK-S). The various techniques employed allowed the teams to characterize exhaust gas and aerosol chemical speciation as well as size distribution and state of mixing of exhaust aerosols.

The laminar coflame burner fueled with various non-methane hydrocarbons was used to measure temperature and soot volume mixing ratios. With this device, basic soot formation and oxidation processes were systematically studied as a function of operating pressure and fuel stoichiometry. With the data base set up over three years, a kinetic soot model describing soot formation was considerably improved. The HBK-S contains a subscale combustion chamber that operates with high mass fluxes, fully turbulent under high pressures, and with kerosene. It was shown that this device produces soot particles with size distributions similar to those measured in flight.

The combustor measurements carried out within PartEmis confirmed the weak dependence of soot emissions on the fuel sulfur content known from airborne campaigns, but more clearly revealed that exhaust soot contains significant amounts of organic material, besides fully oxidized sulfur. This enhances the hygroscopicity of soot particles and may probably influence their ice-nucleating behavior. Surprisingly, a new electrically charged soot mode at very small sizes (<10 nm in diameter) has been detected in mass spectrometric data of chemi-ions and carbon-containing particles and, independently, in measurements of the size distribution. The role of these ultrafine soot particles in ice formation is unclear and will remain under scrutiny.

An empirical model to estimate mass and number emission indices, size distributions, and total surface area concentrations of soot particles emitted by aircraft engines in flight conditions has been

developed. This model requires only a few basic parameters as input, namely pressure and temperature at the combustor inlet and soot mass concentration at the combustor exit, which are correlated with the above soot properties. Using this correlation model in conjunction with the DLR fuel usage inventory from 1992, fleet-averaged global spatial and temporal profiles of soot emission quantities have been generated for use in the ECHAM general circulation model (see Section 2.4).

2.2 *Ice formation in the atmosphere*

This workpackage integrates four subprojects dealing with the measurement of freezing processes in atmospheric aerosols in cirrus conditions (Szakáll et al., 2001; Gierens et al., 2002; Ovarlez et al., 2002; Möhler et al., 2003; Kärcher and Haag, 2003; Haag et al., 2003a/b; Ström et al., 2003; Kärcher, 2003). A key tool to study ice nucleation in PAZI - with many instruments simultaneously determining thermodynamic conditions, gas concentrations, and the state of aerosol and ice particles - is the aerosol-cloud chamber AIDA in Karlsruhe. Data from the Microwave Limb Sounder (MLS) were analyzed to provide a global view of ice supersaturated regions. Ice supersaturation was measured on the cloud scale with aircraft in relatively clean and relatively polluted air masses during the INCA project.

Measurements in the AIDA very closely mimic real atmospheric conditions prevailing in cirrus or polar stratospheric ice clouds in terms of temperature, relative humidity, and cooling rate conditions. The ability of the numerical simulations carried out with DLR's microphysical cirrus model APSC (Advanced Particle Simulation Code) to provide detailed explanations of the observed formation of ice in supercooled aqueous sulfuric acid particles greatly increased confidence in attempts to model this process under real atmospheric conditions, provided that accurate temperature and humidity measurements are available. It was found that the threshold values of relative humidity for homogeneous freezing from recent laboratory studies, however, may not exactly hold when applied to atmospheric conditions, as enhanced supersaturations and non-equilibrium compositions of the largest liquid particles caused by rapid cooling and low temperatures can lead to somewhat higher values than determined assuming equilibrium conditions.

Besides supercooled liquid particles, heterogeneous ice formation triggered by pure and coated soot and mineral dust particles was also observed in the AIDA. The measurements indicate that these ice nuclei may initiate the formation of the ice phase at relative humidities over ice some 25% below the homogeneous thresholds (>145%). Interpretation of these data sets is ongoing, and more coordinated measurements and detailed comparisons are needed to understand existing differences between available laboratory data sets for soot and dust aerosols.

The fact that supersaturation of ice in the upper troposphere and tropopause region is a global phenomenon was corroborated by analyses of MLS data. For example, at 215 hPa, ice supersaturation is seen not only in the tropical and polar regions, but is also common at midlatitudes, in particular along the storm tracks. Naturally, these satellite data do not capture local variability. High supersaturations up to the homogeneous freezing thresholds have been measured in situ near but outside of and inside cirrus clouds during INCA. It was found that the onset of freezing over Prestwick occurred at relative humidities over ice significantly lower (at ~130%) than required for homogeneous freezing, suggesting that the northern hemisphere background aerosol over Prestwick exhibited signatures of pollution in terms of cirrus nucleation, in contrast to the data taken over Punta Arenas in the southern hemisphere. The ice formation mechanisms at work there likely involved a limited number of efficient heterogeneous ice nuclei. The most likely cause for the observed difference in the data sets are differences in chemical and morphological particle properties.

2.3 *Measurements of aerosols and cirrus clouds*

This workpackage encompasses three subprojects (Rother et al., 2001; Baehr et al., 2002; Gayet et al., 2002; Kärcher, 2002; González et al., 2002; Marquart and Mayer, 2002; Immler and Schrems, 2002a/b, 2003; Immler, 2003; Kärcher and Ström, 2003; Mannstein and Schumann, 2003; Minikin et al., 2003; Meyer et al., 2002, 2003; Seifert et al., 2003a/b/c). The main objective was to characterize aerosols and cirrus clouds in the atmosphere using a wide range of instruments: the large set of meteorological, chemical, optical, and microphysical probes employed in the INCA campaigns, Aerodyne's aerosol mass spectrometer operated by the University of Mainz, AWIs

Mobile Aerosol Raman Lidar (MARL), DLRs aerosol and water vapor lidars, and remote sensing data from METEOSAT and ATSR-2 (Along Track Scanning Radiometer).

Vertical profiles of aerosol properties were taken at northern and southern hemisphere midlatitudes and in the tropics. The midlatitude data sets show surprisingly high concentrations of non-volatile particles at the respective tropopause, probably indicating that soot or dust particles reach these altitudes via complex transport processes in the lower(most) stratosphere. Ambient concentrations of nonvolatile condensation nuclei at 10-12 km altitude are $\sim 35 \text{ cm}^{-3}$ (Prestwick) and $\sim 12 \text{ cm}^{-3}$ (Punta Arenas). This demonstrates the potential for insoluble particles from natural and anthropogenic sources to influence the formation of cirrus clouds.

The counterflow virtual impactor (CVI) allowed the INCA team to accurately determine the total number density of ice crystals, down to the aerodynamic size range of a few μm . The derived distributions of number density show a predominant peak at values $0.1\text{-}10 \text{ cm}^{-3}$ and a broad feature extending to the detection limit of $\sim 0.3 \text{ l}^{-1}$. The primary maximum at high concentrations is very likely caused by homogeneous freezing in vertical wind fields at times generated by rapid mesoscale temperature fluctuations and occasionally by convection. The broad feature at lower concentrations is determined by the variability in cooling rates, dynamically-induced dilution of cloudy air parcels, sedimenting ice crystals, and, in the case of the Prestwick data, heterogeneous freezing processes. It was inferred that buoyancy waves with mean wave periods of 10-20 min (horizontal length scales of several 10 km) induce mean updraft speeds of 25-35 cm/s were responsible for the generation of the high number densities of small ($<20 \mu\text{m}$) ice particles in young cirrus. Such high cooling rates tend to minimize the impact of heterogeneous freezing on the total crystal number density (Section 2.2).

These results have important implications for climate studies. Climate change may bring about changes in the global distribution of updraft speeds, air mass temperatures, and aerosol properties. These changes could significantly modify the probability distribution of cirrus ice crystal concentrations. In any effort to ascribe cause to trends of cirrus properties, a careful evaluation of dynamical changes in cloud formation should be done before conclusions regarding the role of other anthropogenic factors, such as changes in aerosol composition, are made.

Mass spectrometric measurements were performed in one of the PAZI field campaigns carried out over Central Europe. The data confirm that sulfate is a prominent chemical constituent of accumulation mode aerosol there, and that aerosol nitrate was very low during these observations. The OLEX lidar detected an extremely tenuous cirrus cloud at $52^\circ\text{N}/10^\circ\text{E}$ at an altitude of 13 km. The cloud was geometrically thin and optically invisible: it barely showed up in the backscatter signal at 523 nm wavelength, but clearly showed backscatter signal and volume depolarisation at 1064 nm. The H_2O lidar was operated simultaneously and recorded mixing ratios near 15-20 ppm. A rough analysis suggests that cirrus particles of 2-4 μm mean radius caused the aerosol lidar signals. Taken together, the observed midlatitude subvisible cirrus cloud appears to be comparable to the ultrathin tropical tropopause clouds detected during APE/THESEO in 1999 – an interesting finding that requires further studies but demonstrates how little is actually known about this type of clouds.

The MARL recorded a large data set of cirrus cloud optical depths during INCA. Like OLEX, this lidar is sensitive to even very thin cirrus and can detect cloud with optical depths as low as several 0.0001 in the visible. The probability distributions of cirrus optical depth over Punta Arenas and Prestwick are similar, peaking around 0.2, the largest value being ~ 7 . However, the distribution is skewed towards small optical depths, and about 1/3 of the measurements revealed the presence of subvisible cirrus with values < 0.02 . These lidar studies thus confirm the surprisingly high frequencies of occurrence of subvisible cirrus clouds at midlatitudes reported earlier from measurements taken at the Observatoire Haute Provence, France.

The cirrus cloud cover over Europe was determined with the help of METEOSAT data in conjunction with actual air traffic movement data provided by EUROCONTROL. Typical background cirrus coverages amount to 20-25% in this area. Both data sets were correlated, revealing a linear relationship between coverage and mean air traffic density, which saturates at the highest traffic densities near 30-35% coverage. This result could be explained by persistent contrails being spread out through the action of wind shear, i.e., the generation of contrail cirrus, although indirect effects caused by freezing of soot particles without contrail formation or natural cirrus formation in the flight corridors cannot be fully ruled out. By implication, this study confirms the frequent presence and large extent of ice-supersaturated regions in the upper troposphere.

One subproject spent efforts on improving retrievals of cirrus parameters in the presence of lower level water clouds. A convincing case study was analyzed with ATSR-2 data during INCA. Yet another improvement concerned the use of ATSR-2 reflectances from the 0.87 μm and 1.6 μm channels to retrieve optical depth and effective particle radius in frontal cirrus over the North Sea. The APOLLO cloud classification tool was used to detect cirrus over sea and the cirrus properties were then retrieved by comparing the radiances calculated by the comprehensive radiative transfer package libRadtran with the radiances measured by the ATSR-2.

2.4 *Modeling of aerosols and cirrus clouds*

This workpackage integrates three subprojects dealing with process studies and global modeling (Ponater et al., 2002; Lin et al., 2002; Lohmann and Kärcher, 2002; Kärcher and Lohmann, 2002a/b, 2003; Lohmann et al., 2003; Gierens, 2003; Marquart et al., 2003; Hendricks et al., 2003a/b; Lauer et al., 2003). Two subprojects devoted their work to interpreting observations from INCA and MOZAIC, improving microphysical cloud models, and developing innovative parameterization schemes used in the climate model ECHAM. The global modeling subproject synthesized results from all workpackages and provided a first preliminary global assessment of soot-cirrus interaction.

Physically-based parameterizations of homogeneous freezing, heterogeneous immersion freezing, and initial growth of the pristine ice crystals were developed and validated with parcel model simulations. The DLR aerosol/cirrus model APSC and the cloud-resolving model MESOSCOPI participated in model intercomparison exercises in the frame of the GEWEX (Global Energy and Water Cycle Experiment) Cloud System Study (GCSS) activity. Both, parameterizations and numerical solutions reveal a strong dependence of the number of ice crystals formed on the vertical velocity and the temperature. Aerosol size effects are comparatively less important, except for very efficient ice nuclei. Using the homogeneous scheme, the first interactive simulations of ice-supersaturation and cirrus were carried out in ECHAM, addressed further below.

Liquid particles may compete with heterogeneous ice nuclei during cirrus formation, as it was probably the case over Prestwick during INCA. Which particle type dominates depends on the relative concentrations, sizes, and freezing properties of the aerosol particles, the temperature and spectrum of vertical winds. The critical number densities of ice nuclei above which homogeneous freezing is suppressed were calculated analytically. Evaluating this solution at typical conditions prevailing during INCA (freezing temperature 222 K, mean updraft speed 20-30 cm/s, heterogeneous ice nucleation at 130%) reveals that less than 0.03-0.08 ice nuclei per cm^3 of air must have been present during the measurements, because homogeneous freezing did take place. It was concluded from the Prestwick observations that heterogeneous ice nuclei triggered the first ice particles but was not the dominant freezing mode (see Sections 2.2 and 2.3), consistent with this estimate. Efforts to corroborate this hypothesis with detailed microphysical simulations are underway.

The implementation of the new cirrus parameterization and the simultaneous abandonment of the frequently used saturation adjustment scheme resulted in the first calculations of global relative humidity in ice-supersaturated regions. Comparisons with MOZAIC data showed that the typical, quasi-exponential shape of the distribution function could be reproduced by the model. Previously, excess humidity created during one time step was removed instantaneously and defined as cloud ice. Basic cirrus parameters such as the total number of crystals and the effective radius used in subsequent radiative calculations were prescribed. With the new parameterizations, the simulated ice water contents are lower and the total crystal concentrations are significantly higher than those computed with the standard saturation adjustment schemes, in better agreement with observations.

The improved cloud scheme enables a self-consistent treatment of cirrus, rendering new studies of cirrus cloud-triggered feedbacks in the climate system possible. It was shown that even very strong enhancements of the background sulfate aerosol mass caused by the Mount Pinatubo eruption likely caused only weak changes in cirrus properties, consistent with a recent reevaluation of ISCCP (International Satellite Cloud Climatology Project) data. However, alterations of the properties of very thin and subvisible cirrus by volcanic eruptions could not be excluded. This implies that the initially very small (5-10 nm) aviation-produced volatile aerosols, albeit present in relatively high number concentrations, do not exert any significant impact on cirrus cloud formation.

The global distribution of black carbon soot was reevaluated with the global model ECHAM. The simulations were based on updated emission inventories, including the aircraft soot emission

model described in Section 2.1. It was found that several 0.1 cm^{-3} soot particles in the upper troposphere and tropopause region originate from aircraft emissions (annual mean figure); compared to the $<0.03\text{-}0.08 \text{ cm}^{-3}$ heterogeneous ice nuclei that influenced cirrus formation over Prestwick (see above), these emissions seem to be sufficiently high to impact cirrus formation in principle, provided that a corresponding fraction of the soot particles act as efficient ice nuclei. The exact magnitude of the calculated aircraft-induced perturbations of the soot budget depends on the relative contributions of the other black carbon sources and on details of soot ageing processes in the atmosphere on time scales of several weeks, both of which are not well known.

A first attempt to calculate the global impact of aircraft soot emissions on cirrus was also undertaken at the very end of the project. For this purpose, two scenarios were defined. The default scenario calculates cirrus formation caused by homogeneous freezing only. This is contrasted with a scenario where heterogeneous freezing of aircraft-emitted soot particles is prescribed, but only in regions where the aircraft soot concentrations exceed 0.5 cm^{-3} (to compensate for errors in the simulated vertical winds that are too low compared with observations); otherwise cirrus form homogeneously as in the first case. The soot increase by aircraft emissions was maximized by assuming minimal particle losses during ageing. In treating this indirect effect of soot-cirrus interactions, the direct effect of spreading contrails (as noted in Section 2.3) has been neglected in these studies.

By comparing annually averaged results from ten years of ECHAM simulations, total ice crystal concentrations are found to be reduced by several tens of percent at northern hemisphere midlatitudes. This is explained by the fact that the assumed soot threshold concentration above which homogeneous freezing is suppressed at the prevailing model updraft speeds is frequently surpassed by aircraft emissions. In another conceivable scenario, where soot particles (irrespective of their origin) as well as mineral dust particles can serve as heterogeneous ice nuclei, aviation leads to enhancements of ice crystal concentrations. Feedbacks of the cirrus changes on cloud cover have not been considered in the two scenarios. However, the ECHAM results obtained here reveal the potential of aircraft-induced soot particles to cause significant changes in cirrus microphysical properties.

3 SUMMARY AND CONCLUSIONS

- Among all exhaust particles, soot is key in further studies of potential aerosol-cirrus interactions
- Kinetic algorithms improve the prediction of soot physical properties in combustion models
- Accurate measurements better define the chemical composition and the size distributions of soot particles emitted by aircraft jet engines
- Innovative measurements in an aerosol/cloud chamber suggest early freezing of soot particles in cirrus conditions
- Interpretation of freezing experiments in the chamber increases confidence in the current ability to model homogeneous freezing and growth of small ice crystals in cirrus
- In-situ studies unambiguously confirm the presence of high number densities of small ice crystals in cirrus, tied to homogeneous freezing
- Aircraft-based, size-resolved chemical analysis of aerosol particles in the accumulation mode become available, providing important information on freezing aerosols in future campaigns
- Field measurements reveal mesoscale variability in vertical velocities as the key factor controlling cirrus formation
- Lidar studies confirm surprisingly high frequencies of occurrence of midlatitude subvisual cirrus
- Retrieval algorithm allows remote sensing of cirrus cloud optical properties in the presence of low level stratus
- Satellite analysis reveals close correlation between cirrus cloud cover changes and air traffic density
- Global model studies better constrain the apportionment of black carbon soot to a large number of sources, including aircraft
- Freezing parameterization enables more realistic predictions of ice supersaturation and cirrus clouds in global models

- First preliminary global assessment of soot-cirrus interaction shows potentially significant indirect impact of aircraft soot on cirrus crystal concentrations, if the effect is maximized

Future progress in the area of aerosol-cirrus-radiation interaction depends crucially on a better understanding of

- small-scale dynamical variability;
- indirect aerosol effects on cirrus;
- cirrus radiative properties and cover;

and the representation of these effects in global atmospheric models.

The viewgraphs of the invited talk presented at the workshop are available under <http://www.pa.op.dlr.de/aac/>. Most of the material presented here has been published in the open literature and we refer to the list of references for more details. In addition, the following contributions in this volume provide further information: Wahl et al., Petzold et al. (Section 2.1); Möhler et al., Mangold et al. (Section 2.2); Immler et al., Mannstein et al. (Section 2.3); Marquart et al., Hendricks et al. (Section 2.4).

REFERENCES

- Arnold, F., Th. Stilp, R. Busen, and U. Schumann. Jet engine exhaust chemiion measurements: Implications for gaseous SO₃ and H₂SO₄. *Atmos. Environ.*, 32, 3073-3077, 1998.
- Arnold, F., K.-H. Wohlfrom, M.W. Klemm, J. Schneider, K. Gollinger, and U. Schumann. First gaseous ion composition measurements in the exhaust plume of a jet aircraft in flight: Implications for gaseous sulfuric acid, aerosols, and chemiions. *Geophys. Res. Lett.*, 25, 2137-2140, 1998.
- Arnold, F., J. Curtius, B. Sierau, V. Bürger, and R. Busen. Detection of massive negative chemiions in the exhaust plume of a jet aircraft in flight. *Geophys. Res. Lett.*, 26, 1577-1580, 1999.
- Arnold, F., A. Kiendler, V. Wiedemer, S. Aberle, Th. Stilp, and R. Busen. Chemiion concentration measurements in jet engine exhaust at the ground: Implications for ion chemistry and aerosol formation in the wake of a jet aircraft. *Geophys. Res. Lett.*, 27, 1723-1726, 2000.
- Baehr, J., H. Schlager, H. Ziereis, P. Stock, P. van Velthoven, R. Busen, J. Ström, and U. Schumann. Aircraft observations of NO, NO_y, CO, and O₃ in the upper troposphere from 60°N to 60°S – Interhemispheric differences at midlatitudes. *Geophys. Res. Lett.*, 30, 1598, doi:10.1029/2003GL016935, 2003.
- Braun-Unkhoff, M., und P. Frank. *Untersuchungen zum Start der Rußbildung bei hohen Drücken*, VDI Berichte 1629, 467, VDI Verlag Düsseldorf, 2001.
- Böhm, H., M. Braun-Unkhoff, and P. Frank. *Investigations on Initial Soot Formation at High Pressure*, Progress in Computational Fluid Dynamics, Vol.3, No.2-4, in press, 2003.
- Döpelheuer, A. *Aircraft Emission Parameter Modelling*, Dossier "Aviation and the Environment" in: Air & Space Europe, Editions Elsevier, ISSN 1290-0958, May-June 2000.
- Döpelheuer, A., *Anwendungsorientierte Verfahren zur Bestimmung von CO, HC und Ruß aus Luftfahrttriebwerken*. Dissertation, DLR-FB 2002-10, DLR Institut für Antriebstechnik, Köln, 2002.
- Eichkorn, S., K.-H. Wohlfrom, F. Arnold, and R. Busen. Massive positive and negative chemiions in the exhaust of an aircraft jet engine at ground level: Mass distribution measurements and implications for aerosol formation. *Atmos. Environ.*, 36, 1821-1825, 2002.
- Gayet, J.-F., F. Auriol, A. Minikin, J. Ström, M. Seifert, R. Krejci, and A. Petzold, G. Febvre, and U. Schumann. Quantitative measurement of the microphysical and optical properties of cirrus clouds with four different in situ probes: Evidence of small ice crystals. *Geophys. Res. Lett.*, 29, 2230, doi:10.1029/2001GL014342, 2002.
- Gierens, K.M., M. Monier, and J.-F. Gayet. The deposition coefficient and its role for cirrus clouds. *J. Geophys. Res.*, 108, 4069, doi:10.1029/2001JD001558, 2003.
- Gierens, K. On the transition between heterogeneous and homogeneous freezing. *Atmos. Chem. Phys.*, 3, 437-446, 2003.
- González, A., P. Wendling, B. Mayer, J.-F. Gayet, and T. Rother. Remote sensing of cirrus cloud properties in the presence of lower clouds: An ATSR-2 case study during the Interhemispheric Differences in Cirrus Properties From Anthropogenic Emissions (INCA) experiment. *J. Geophys. Res.*, 107, doi:10.1029/2002JD002535, 2002.

- Gysel, M., S. Nyeki, E. Weingartner, U. Baltensperger, H. Giebl, R. Hitzenberger, A. Petzold, and C.W. Wilson. Properties of jet engine combustion particles during the PartEmis experiment: Hygroscopicity at subsaturated conditions. *Geophys. Res. Lett.*, 30, doi:10.1029/2003GL016896, 2003.
- Haag, W., B. Kärcher, S. Schaefers, O. Stetzer, O. Möhler, U. Schurath, M. Krämer, and C. Schiller. Numerical simulations of homogeneous freezing processes in the aerosol chamber AIDA. *Atmos. Chem. Phys.*, 3, 195-210, 2003a.
- Haag, W., B. Kärcher, J. Ström, A. Minikin, U. Lohmann, J. Ovarlez, and A. Stohl. Freezing thresholds and cirrus cloud formation mechanisms inferred from in situ measurements of relative humidity, *Atmos. Chem. Phys.*, 3, in press, 2003b.
- Hendricks, J., B. Kärcher, A. Döpelheuer, J. Feichter, and U. Lohmann. Simulating the global atmospheric black carbon cycle: A revisit to the contribution of aircraft emissions, in preparation, 2003a.
- Hendricks, J., B. Kärcher, and U. Lohmann. Potential impact of aviation-induced soot particles on cirrus clouds: Global model studies with the ECHAM GCM, in preparation, 2003b.
- Hitzenberger, R., H. Giebl, A. Petzold, M. Gysel, S. Nyeki, E. Weingartner, U. Baltensperger, and C.W. Wilson. Properties of jet engine combustor particles during the PartEmis experiment. Hygroscopic properties at supersaturated conditions. *Geophys. Res. Lett.*, 30, doi:10.1029/2003GL017294, 2003.
- Immmler, F., and O. Schrems. LIDAR measurements of cirrus clouds in the northern and southern hemisphere during INCA (55°N, 53°S): A comparative study. *Geophys. Res. Lett.*, 29, 1809, doi:10.1029/2002GL015077, 2002a.
- Immmler, F., and O. Schrems. Determination of tropical cirrus properties by simultaneous LIDAR and radiosonde measurements. *Geophys. Res. Lett.*, 29, doi:10.1029/2002GL015076, 2002b.
- Immmler, F., and O. Schrems. Vertical profiles, optical and microphysical properties of Saharan dust layers determined by a ship-borne lidar. *Atmos. Chem. Phys. Discuss.*, 3, 2707-2737, 2003.
- Immmler, F. A new algorithm for simultaneous ozone and aerosol retrieval from tropospheric DIAL measurements, *Appl. Phys.*, B76, doi:10.1007/s00340-003-1157-z, 593-596, 2003.
- Jensen, E. J., O.B. Toon, S.A. Vay, J. Ovarlez, R. May, P. Bui, C.H. Twohy, B. Gandrud, R.F. Pueschel, and U. Schumann. Prevalence of ice-supersaturated regions in the upper troposphere: Implications for optically thin ice cloud formation. *J. Geophys. Res.*, 106, 17253-17266, 2001.
- Kärcher, B., R.P. Turco, F. Yu, M.Y. Danilin, D.K. Weisenstein, R.C. Miake-Lye, and R. Busen. A unified model for ultrafine aircraft particle emissions. *J. Geophys. Res.*, 105, 29379-29386, 2000.
- Kärcher, B. Properties of subvisible cirrus clouds formed by homogeneous freezing. *Atmos. Chem. Phys.*, 2, 161-170, 2002.
- Kärcher, B., and U. Lohmann. A parameterization of cirrus cloud formation: Homogeneous freezing of supercooled aerosols. *J. Geophys. Res.*, 107, 4010, doi:10.1029/2001JD000470, 2002a.
- Kärcher, B., and U. Lohmann. A parameterization of cirrus cloud formation: Homogeneous freezing including effects of aerosol size. *J. Geophys. Res.*, 107, 4698, doi:10.1029/2001JD001429, 2002b.
- Kärcher, B. Simulating gas-aerosol-cirrus interactions: Process-oriented microphysical model and applications, *Atmos. Chem. Phys. Discuss.*, 3, 4129-4181, 2003.
- Kärcher, B., and U. Lohmann. A parameterization of cirrus cloud formation: Heterogeneous freezing. *J. Geophys. Res.*, 108, 4402, doi:10.1029/2002JD003220, 2003.
- Kärcher, B., and J. Ström. The roles of dynamical variability and aerosols in cirrus cloud formation, *Atmos. Chem. Phys.*, 3, 823-838, 2003.
- Kärcher, B., and W. Haag. Factors controlling upper tropospheric relative humidity, *Ann. Geophys.*, 21, in press, 2003.
- Krüger, V., K.P. Geigle, W. Stricker, and M. Aigner. Soot particle size measurements with laser-induced incandescence: Validation of the signal interpretation model in flames, in preparation, 2003.
- Kunz, O., B. Noll, R. Lückerrath, M. Aigner, and S. Hohmann. Computational combustion simulation for an aircraft model combustor. *AIAA paper* 2001-3706, 2001.
- Lauer, A., J. Hendricks, B. Schell, H. Hass, J. Feichter, and S. Metzger. Global modelling of tropospheric aerosols with ECHAM4/MADE, in preparation, 2003.
- Lin, R.-F., D.O'C. Starr, P.J. DeMott, R. Cotton, K. Sassen, E. Jensen, B. Kärcher, and X. Liu. Cirrus parcel model comparison project. Phase 1: The critical components to simulate cirrus initiation explicitly. *J. Atmos. Sci.*, 59, 2305-2329, 2002.
- Lohmann, U., and B. Kärcher. First interactive simulations of cirrus clouds formed by homogeneous freezing in the ECHAM GCM. *J. Geophys. Res.*, 107, 4105, doi:10.1029/2001JD000767, 2002.
- Lohmann, U., B. Kärcher, and C. Timmreck. Impact of the Mt. Pinatubo eruption on cirrus clouds formed by homogeneous freezing in the ECHAM GCM. *J. Geophys. Res.*, 108, 4568, doi:10.1029/2002JD003185, 2003.
- Mannstein, H., and U. Schumann. Contrail cirrus over Europe, submitted manuscript, 2003.

- Marquart, S., and B. Mayer. Towards a reliable GCM estimation of contrail radiative forcing. *Geophys. Res. Lett.*, 29, 1179, doi:10.1029/2001GL014075, 2002.
- Marquart, S., M. Ponater, F. Mager, and R. Sausen. Future development of contrail cover, optical depth and radiative forcing: impacts of increasing air traffic and climate change. *J. Climate*, 16, 2890-2904, 2003.
- Meyer, R., H. Mannstein, R. Meerkötter, U. Schumann, and P. Wendling. Regional radiative forcing by line-shaped contrails derived from satellite data. *J. Geophys. Res.*, 107, 4104, doi:10.1029/2001JD000547, 2002.
- Meyer, R., R. Büll, C. Leiter, H. Mannstein, S. Marquart, T. Oki, and P. Wendling. Contrail observations over Southern and Eastern Asia in NOAA/AVHRR data and intercomparison to contrail simulations in a GCM. *Int. J. Remote Sensing*, submitted, 2003.
- Minikin, A., A. Petzold, J. Ström, R. Krejci, M. Seifert, H. Schlager, P. van Velthoven, and U. Schumann. Aircraft observations of the upper tropospheric fine particle aerosol in the northern and southern hemispheres at midlatitudes. *Geophys. Res. Lett.*, 30, 1503, doi:10.1029/2002GL016458, 2003.
- Möhler, O., O. Stetzer, S. Schaefers, C. Linke, M. Schnaiter, R. Tiede, H. Saathoff, M. Krämer, A. Mangold, P. Budz, P. Zink, J. Schreiner, K. Mauersberger, W. Haag, B. Kärcher, and U. Schurath. Experimental investigations of homogeneous freezing of sulphuric acid particles in the aerosol chamber AIDA. *Atmos. Chem. Phys.*, 3, 211-223, 2003.
- Noll, B., R. Kessler, P. Theisen, H. Schütz, M. Aigner, and S. Hohmann. Flow Field Mixing Characteristics of an Aero-Engine Combustor - Part II: Numerical Simulations. *AIAA paper 2002-3708*, 2002.
- Ovarlez, J. J.-F. Gayet, K. Gierens, J. Ström, H. Ovarlez, F. Auriol, R. Busen, and U. Schumann. Water vapour measurements inside cirrus clouds in Northern and Southern hemispheres during INCA, *Geophys. Res. Lett.*, 29, 1813, doi:10.1029/2001GL014440, 2002.
- Petzold, A., C. Stein, S. Nyeki, M. Gysel, E. Weingartner, U. Baltensperger, H. Giebl, R. Hitzinger, A. Döpelheuer, S. Vrchoticky, H. Puxbaum, M. Johnson, C.D. Hurley, R. Marsh, and C.W. Wilson. Properties of jet engine combustion particles during the PartEmis experiment: Microphysics and chemistry. *Geophys. Res. Lett.*, 30, doi:10.1029/2003GL017283, 2003.
- Plohr, M., A. Döpelheuer, and M. Lecht. The gas turbine heat cycle and its influence on fuel efficiency and emissions, Paper 34 in "Gas Turbine Operation and Technology for Land, Sea and Air Propulsion and Power Systems". RTO MP-34, AC/323(AVT)TP/14, 2000.
- Ponater, M., S. Marquart, and R. Sausen. Contrails in a comprehensive global climate model: parameterisation and radiative forcing results, *J. Geophys. Res.*, 107, 10.1029/2001JD000429, 2002.
- Rother, T., K. Schmidt, and S. Havemann. Light scattering on hexagonal ice columns. *J. Opt. Soc. Am. A*, 18, 2512-2517, 2001.
- Schumann, U., R. Busen, and M. Plohr. Experimental test of the influence of propulsion efficiency on contrail formation. *J. Aircraft*, 37, 1083-1087, 2000.
- Schumann, U. Influence of propulsion efficiency on contrail formation. *Aerosp. Sci. Technol.*, 4, 391-401, 2000.
- Schumann, U., J. Ström, F. Arnold, T.K. Berntsen, P.M. de F. Forster, J.-F. Gayet, and D. Hauglustaine. Aviation impact on atmospheric composition and climate, in: *European Research in the Stratosphere 1996-2000*. Chapter 7, EUR 19867, pp. 257-307, European Commission, Brussels, 2001.
- Schumann, U. Contrail Cirrus, in: D. K. Lynch, K. Sassen, D. O'C. Starr, and G. Stephens (Eds.), *Cirrus*, Oxford Univ. Press, p. 231-255, 2002a.
- Schumann, U. Aircraft Emissions. *Encyclopedia of Global Environmental Change*, Wiley, Vol. 3, 178-186, 2002b.
- Schumann, U., F. Arnold, R. Busen, J. Curtius, B. Kärcher, A. Kiendler, A. Petzold, H. Schlager, F. Schröder, and K.-H. Wohlfrom. Influence of fuel sulfur on the composition of aircraft exhaust plumes: The experiments SULFUR 1-7. *J. Geophys. Res.*, 107, 4247, doi:10.1029/2001JD000813, 2002.
- Seifert, M., J. Ström, R. Krejci, A. Minikin, A. Petzold, J.-F. Gayet, U. Schumann, and J. Ovarlez. In situ observations of aerosol particles remaining from evaporated cirrus crystals: Comparing clean and polluted air masses. *Atmos. Chem. Phys.*, 3, 1037-1049, 2003a.
- Seifert, M., J. Ström, R. Krejci, A. Minikin, A. Petzold, J.-F. Gayet, H. Schlager, H. Ziereis, U. Schumann, and J. Ovarlez. Aerosol-cirrus interactions: A number based phenomenon at all? *Atmos. Chem. Phys. Discuss.*, 3, 3625-3657, 2003b.
- Seifert, M., J. Ström, R. Krejci, A. Minikin, A. Petzold, J.-F. Gayet, H. Schlager, H. Ziereis, U. Schumann, and J. Ovarlez. Thermal stability analysis of particles incorporated in cirrus crystals and of non-activated particles in between the cirrus crystals: Comparing clean and polluted air masses. *Atmos. Chem. Phys. Discuss.*, 3, 3659-3679, 2003c.
- Starik, A.M., A.M. Savel'ev, N.S. Titova, and U. Schumann. Modeling of sulfur gases and chemiions in aircraft engines. *Aerosp. Sci. Technol.*, 6, 63-81, 2002.

- Ström, J., M. Seifert, B. Kärcher, J. Ovarlez, A. Minikin, J.-F. Gayet, R. Krejci, A. Petzold, F. Auriol, R. Busen, U. Schumann, W. Haag, and H.-C. Hansson. Cirrus cloud occurrence as a function of ambient relative humidity: A comparison of observations obtained during the INCA experiment, *Atmos. Chem. Phys.*, 3, in press, 2003.
- Szakáll, M., Z. Bozóki, M. Krämer, N. Spelten, O. Möhler, and U. Schurath. Evaluation of a photoacoustic detector for water vapor measurements under simulated tropospheric/lower stratospheric conditions, *Environ. Sci. Technol.*, 35, 4881-4885, 2001.
- Wahl, C., and M. Aigner. Aircraft gas turbine soot emission tests under technically relevant conditions in an altitude test facility and validation of soot measurement techniques. Paper No. GT 2003-38797, *ASME*, 2003.

Ice-nucleating ability of soot particles in UT/LS

J. Suzanne*, D. Ferry F.

CRMC2-CNRS, Campus de Luminy, Case 913, F-13288 Marseille cedex 9, France

O.B. Popovicheva, N.K. Shonija

Department of Microelectronics, Institute of Nuclear Physics, Moscow State University, Moscow, Russia

Keywords: soot, ice nucleation, atmosphere, cirrus formation, neutron scattering

ABSTRACT: Morphology, microstructure and water adsorbability of laboratory made kerosene soot taken as an aircraft soot surrogate were studied to establish the correlation between the morphology porosity and the ice nucleation ability of the soot surface. Quasi-Elastic Neutron Scattering (QENS) and neutron diffraction (ND) have been used to highlight the dynamics and structure of water/ice confined in the porous soot network. The routine of these experiments roughly followed the evolution of temperature (T) and relative humidity (RH) in the plume and down to UT/LS conditions. There is a depression of the homogeneous nucleation point and ~ 15% of the water is in a highly supercooled state down to 204K. The frozen water is a mixture of amorphous ice probably located in the soot pores coexisting with ice Ih at the soot surface. At 220 K, 75% of ice component inside the soot pores increase the ability of soot to act as secondary ice nuclei for cirrus clouds.

1 INTRODUCTION

In-situ studies have shown that carbonaceous particles are primary components in evaporated contrail residues at cirrus altitudes (Petzhold et al. 1999). Observational and numerical investigations have shown that soot particles may play a role as potential ice nuclei in contrail formation (Kärcher et al. 1996). Enhancement in the occurrence frequency of cirrus clouds up to 10% per decade over North America has attracted the attention of the scientific community on the effect of emitted soot aerosols on contrails and cirrus formation. An unambiguous evidence that soot particles are directly involved in ice formation is difficult to obtain from *in situ* measurements. Hence the nucleating ability of exhaust soot is still poorly understood.

To improve this situation, kerosene flame soot produced by burning aviation kerosene in an oil lamp has been used to mimic the behavior of aircraft engine soot in a laboratory scale procedure (Diehl and Mitra, 1998). Investigations of their ice nucleating ability showed that the kerosene-burner exhaust particles act as immersion freezing nuclei in supercooled exhaust polluted drops at temperatures colder than about 250K. This result support the assumption that contrails observed near threshold formation conditions are formed by frozen water on soot particles (Kärcher et al. 1996). X-ray and neutron scattering studies of the structure of water wetting activated charcoal powder confirmed the formation of the hexagonal Ih and amorphous ices depending on water content (Bellissent-Funel et al., 1996). But a comprehensive study of the kerosene soot microstructure and its role in ice nucleation is still lacking.

This paper is devoted to a study of the structure and dynamics of adsorbed water on kerosene flame soot surface in a wide range of temperatures and relative humidities related to the conditions in expanding plume and in upper troposphere. Quasi-Elastic Neutron Scattering (QENS) and Neutron Diffraction (ND) together with adsorption/structural analysis yield information about water freezing and the ice structure in the kerosene soot pore network.

* Corresponding author: Jean Suzanne, CRMC2-CNRS, Campus de Luminy Case 913, F-13288 Marseille cedex 9, France. Email: suzanne@crmc2.univ-mrs.fr

2 EXPERIMENTS

The soot has been obtained by burning aviation kerosene in a laboratory oil lamp and was collected at a distance of 15-20 cm above the flame. A gravimetric setup equipped with McBain scales as well as a conventional volumetric apparatus were used for C₆H₆ and Kr isotherm adsorption measurements to obtain the surface area and texture characteristics. The internal microstructure of the soot particles has been analyzed by transmission electron microscopy TEM (JEM 2000 FX) with a resolution of 2.8 Å at 200 kV using the phase-contrast imaging method. Holey amorphous carbon films on microgrids were used to support the soot particles. TEM was coupled with X-ray energy dispersive spectroscopy (XREDS) for chemical composition analysis (Popovitcheva et al., 2000).

The neutron experiments were performed at the Laboratoire Leon Brillouin (Saclay, France). Two kinds of experiments have been done : i) Incoherent quasi-elastic neutron scattering (QENS) on the MIBEMOL (G6.2) high-resolution time-of-flight spectrometer ($\lambda = 8 \text{ \AA}$, energy resolution $\Delta E = 39 \text{ \mu eV}$), ii) Neutron diffraction (ND) on the two-axes diffractometer 7C.2 ($\lambda = 1,10 \text{ \AA}$, $\Delta Q/Q = 10^{-2}$ where Q stands for the scattering wave vector modulus).

QENS allows to measure the rotational and translational mobility of the water molecules through the broadening of the elastic peak. ND gives access to the structure of the soot on the one hand and of the adsorbed water (ice) on the other hand.

A cell with 0.9g of soot was introduced in the sample part of the spectrometers. Normal water H₂O was used for QENS measurements since hydrogen atoms have a large incoherent cross section. Heavy water D₂O has to be used for ND experiments since deuterium atoms have large coherent and weak incoherent cross sections. Experiments were carried out for three different amounts of water corresponding to 40, 60 and 100% relative humidity (RH). In the ND experiments we also have condensed a thick ice film on soot at 180K in order to obtain a reference ice Ih spectrum.

The neutron spectra were recorded during about 13 hours when thermodynamical equilibrium was reached. Prior to any spectrum analysis, the background due to the [cell + bare soot sample] was subtracted from the [cell + soot + water] neutron spectrum.

3 RESULTS

3.1 Soot texture

The kerosene soot morphology and structure has been described elsewhere (Popovitcheva et al., 2000). Briefly, soot particles have a spherical-like nature with diameters in the 30 to 50 nm range has shown by TEM. They feature disordered graphitic microcrystallites about 2nm wide and thickness of about 1 nm arranged in concentric layers leading to an onion-like structure. It is similar to that of jet engine combustor soot (Popovitcheva et al., 2000). A specific surface area S near 43 m²/g was determined from the linear BET plot of a Kr isotherm up to $p/p_s \cong 0.3$ (p_s is the saturation vapor pressure) assuming a Kr molecular surface area σ_{Kr} of 0.19 nm² (Gregg and Sing, 1982). $S \cong 33 \text{ m}^2/\text{g}$ was determined from a C₆H₆ isotherm for the same p/p_s range ($\sigma_{C_6H_6} \cong 0.43 \text{ nm}^2$). The Kr adsorption isotherm was classified as Type I and the mechanism of adsorption was discussed in terms of the pore filling Dubinin's theory (Gregg and Sing, 1982). The micropore volume and characteristic energy of adsorption has been determined by means of the fundamental Dubinin-Astakhov equation (Dubinin and Stoeckli, 1980). In the case of kerosene soot, the adsorption isotherms of both Kr and C₆H₆ can be approximated by a complex structure with two types of micropores (Ferry et al. 2002). The volumes of the two micropore sets have been estimated to $W_{01} \cong 4 \cdot 10^{-3} \text{ cm}^3 \text{ g}^{-1}$ and $W_{02} \cong 10^{-2} \text{ cm}^3 \text{ g}^{-1}$. The specific behavior of C₆H₆ hysteresis extending down to complete desorption indicates a slit-like nature of the micropores with half widths $x_1 \cong 0.5 \text{ nm}$ and $x_2 \cong 2 \text{ nm}$ that enables one to differentiate the smallest micropores from supermicropores in kerosene soot. Mesopores with size larger than 2 nm exist as cavities between particles. The mesopore volume V_{me} may be roughly estimated as the difference between the total volume of adsorbed amount at $p/p_s \cong 0.95$ and both W_{01} and W_{02} that gives us $V_{me} \approx 4 \cdot 10^{-3} \text{ cm}^3/\text{g}$.

3.2 Dynamics of water on soot

The analysis of the QENS spectra is based on the measurement of the elastic peak broadening due to neutrons scattering from the water molecules adsorbed on the soot surface and in the pores. As usual, the single particle dynamical structure factor of water is obtained as a convolution of dynamical structure factors for the translational and rotational motions under the assumption of their decoupling. The theoretical background can be found in the literature (Teixeira et al., 1984; Chen and Teixeira, 1986; Toubin et al., 2001). From this analysis we can determine both the rotational D_r and translational D_t diffusion coefficients of the water molecules and the water liquid-like fraction L_f of the water/ice mixture. The rotational diffusion is characterized by a relaxation time $\tau_r = (6D_r)^{-1}$. We interpret our spectra as resulting from two components: one solid-like, represented by a narrow elastic peak, and one liquid-like, responsible for the wings and represented by a Lorentzian function (Toubin et al., 2001). This allows us to estimate the respective integrated parts of solid and fluid components and thus to obtain the liquid/solid-like fraction L_f . For each experimental condition (T, RH) a set of 10 spectra corresponding to 10 sets of Q_s ($0.4 \text{ \AA}^{-1} \leq Q \leq 1.48 \text{ \AA}^{-1}$) are measured. The spectra were obtained at five different temperatures, 283K, 260K, 245K, 220K and 204K and were normalized to the spectrometer monitor (that is to the number of incident neutrons).

Figure 1 shows typical QENS spectra taken at three temperatures and RH = 100% for $Q = 1.25 \text{ \AA}^{-1}$. The peak broadening is reduced with decreasing temperature due to the reduction of the water molecules mobility. It indicates that there is a decrease of the translational and rotational diffusion coefficients due to the nucleation of supercooled water in the highly constrained regions of the micropores and supermicropores. This effect causes a depression of the homogeneous nucleation point and therefore maintains some water in a highly supercooled state at 204K.

Table 1 gives the parameters extracted from QENS spectra fits for all examined temperatures at RH=60% and 100%. For comparison, the values τ_r obtained for supercooled bulk water (Teixeira et al., 1984) are shown; one sees that they are 2,5 - 4 times smaller than our values. Hence, the rotational motion of water molecules is more hindered in our soot sample than in bulk water or in the above mentioned hydrophilic adsorbates likely due to the confinement of water in the soot micropores and supermicropores. Strong active sites of oxidized soot particles may also participate to the hindrance of the molecule motion. It should be noted that at 283K 35% of the adsorbed water is in a solid-like state as deduced from the low translational diffusion coefficient ($D = 10^{-6} \text{ cm}^2 \text{ s}^{-1}$).

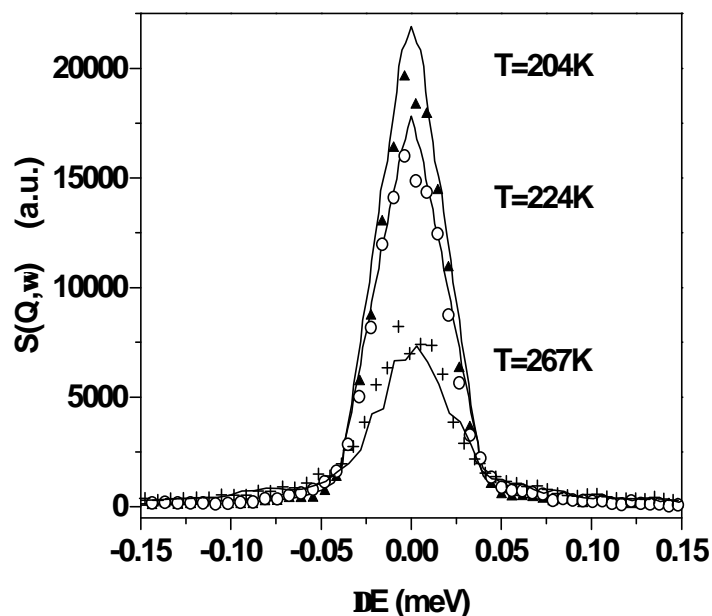


Figure 1. QENS spectra at $Q = 1.25 \text{ \AA}^{-1}$ and RH = 100% at 267, 224 and 204 K. The scattered intensity $S(Q, \omega)$ of the quasi-elastic peak is plotted versus the energy transfer ΔE .

Table 1 - Translational D_t and rotational D_r diffusion coefficients and rotational relaxation time τ_r for water adsorbed on kerosene soot at RH 60% and 100%.

T, K(°C)	D_t (10^{-5} cm ² /s) 2D isotropic model (Unfrozen water %)	D_t^* (10^{-5} cm ² /s) bulk water	D_r (10^{10} s ⁻¹)	τ_r (ps)	τ_r^* (ps) bulk water
283(+10)	2±1 (65)	1.25	5±3	0.33	
267(-6)	1±0.5 (60)	0.66	2±1	0.82	1.57
257 (-15)	1±0.5 (50)	0.5	2±1	0.82	1.92
242 (-31)	0.75±0.35 (35)		2±1	0.82	
224 (-49)	0.5±0.25 (30)		1±0.5	1.66	
204 (-69)	0.5±0.25 (15)		0.5±0.25	3.3	

Values marked by * are taken from (Teixeira et al., 1984) for bulk water

3.3 Ice nucleation and structure

The ND spectra at $T = 283$ K, 260 K and 180 K are shown in Fig. 2 and 3. The spectrum at 283 K features a broad intense peak centered at $Q = 1.9 \text{ \AA}^{-1}$ and two smaller broad peaks at 4 \AA^{-1} and 7.8 \AA^{-1} . These peaks correspond to the well known structure of liquid water (Chen and Teixeira, 1986). Two spectra are measured at 260 K : i) the 260 K (1) spectrum (fig. 3a) which has been measured during 13 hours after adsorption of the water at 260K followed by 3 hours of equilibrium time and ii) the 260 K (2) spectrum (fig. 3b) which has been measured after the cycle of cooling the soot down to 204 K, measuring spectra at 245 K, 220 K and 204K and warming it up again to 260K. Besides the cycle of cooling down and warming up, about 2 days have elapsed between the two measurements. The 260 K(1) spectrum presents a broad peak centered at $Q = 1.73 \text{ \AA}^{-1}$ and a narrower peak at $Q = 2.28 \text{ \AA}^{-1}$ assigned to the (102) reflection of ice Ih. To explained the broad peak we propose two hypotheses. (i) It may be assigned to low density amorphous ice (Chen and Teixeira, 1986) or (ii) it comes from diffraction broadening of the three ice reflections (102), (002) and (101). In the latter hypothesis, application of the Scherrer formula leads to crystallite sizes of the order of 4.0 nm. However, one sees that the (102) peak is narrow indicating a crystal growth anisotropy. Such crystallites could form inside the mesopores and (or) on the external surfaces of the soot particles. It should be noted that the (102) reflection is slightly shifted toward low Q 's since the expected value for bulk ice Ih is 2.35 \AA^{-1} (fig. 3c), which corresponds to an increase of the d_{102} spacing of about 3%.

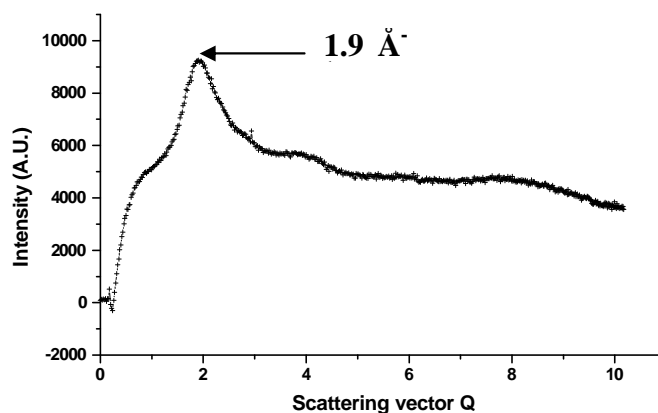


Figure 2. Neutron diffraction spectrum of water adsorbed on soot at $T = 283$ K

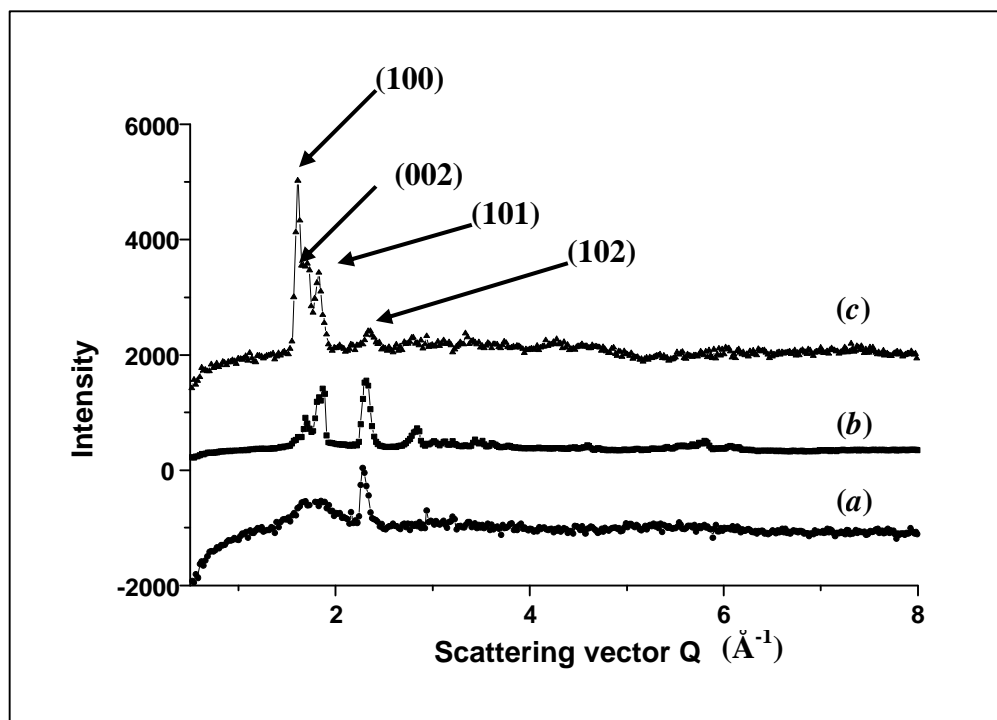


Figure 3. Neutron diffraction spectra of water adsorbed on soot at (a) $T = 260$ K (1); (b) $T = 260$ K (2); (c) $T = 180$ K. The 180 K spectrum is characteristic of the ice Ih structure

The 260 K(2) spectrum is quite different from 260 K(1). The broad peak at 1.73 \AA^{-1} has been replaced by narrower peaks, signature of crystalline ice Ih. It is interesting to remark that even after the annealing cycle, broad wings still persist below the (100), (002) and (101) peaks. That is a remainder of the broad peak observed in the 260 K(1) spectra and centered at $Q = 1.73 \text{ \AA}^{-1}$. This broad peak does not exist in the bulk ice spectra as shown in Fig. 3c and can be considered as a remainder of either amorphous ice or small crystallites as explained above.

We would like to point out that in the neutron spectrum at 283K there is also a weak broad peak around 2.7 \AA^{-1} . Such a peak has been observed for low-density amorphous ice (Bellissent-Funel et al., 1996). Since we have found in our QENS experiments that about 35% of adsorbed water is in a solid-like state at 283K, we may wonder whether this solid-like water fraction presents a short range ordered structure close to that of low-density amorphous ice. More experiments are needed to confirm this hypothesis.

4 CONCLUSION AND ATMOSPHERIC IMPLICATIONS

By using two techniques namely quasi-elastic neutron scattering and neutron diffraction, combined with adsorption/texture analysis, we have shown that kerosene soot features a high freezing potential for ice nucleation and existence of a liquid water fraction down to $\cong 200$ K.

If aircraft-emitted soot particles have properties similar to kerosene soot studied here, we may conclude that at the saturation plume conditions, $T=240\text{K}$, $\approx 30\%$ of the water adsorbed is transformed into ice probably in the soot mesopores > 2 nm and on the external surface. But the ice nucleation/growth process is completely suppressed in the soot supermicropores because near 35 % of the water remains liquid under these conditions. At the upper troposphere conditions, at subsaturation level and $T \cong 220\text{K}$, there are stable water/ice components inside the soot pores since 25% of the water content is unfrozen. Moreover, $\approx 15\%$ of the water confined in the soot supermicropores may remain liquid down to 200K, temperature of the low stratosphere.

Upon reaching the water supersaturation conditions, ice germs may increase the freezing probability of water nuclei on soot particles and facilitate the growth of large ice crystals in

contrails. Upon evaporation of the aircraft contrail, new ice forming nuclei containing the soot particles may appear in the atmosphere. Retention of ice in the cavities of the residual soot cores after evaporation will serve as germ for secondary nucleation of ice crystals (Hobbs, 1974) which potentially grow into cirrus clouds in the supersaturated air (preactivation effect of cirrus clouds).

We would like to emphasize that recent results obtained with soot collected from a jet engine working under normal take-off and cruise conditions show that this soot is much more hydrophilic than our laboratory kerosene soot (O.B. Popovicheva, unpubl.). This behavior can be related to the high sulfur content of these soot particle. Hence we may infer an even higher ice nucleating ability for real aircraft engine soot.

REFERENCES

- Bellissent-Funel, M.-C., Chen, S.H., and J.-M. Zanotti, 1995: Single particle dynamics of water molecules in confined space. *Phys. Rev. E* 51, 4558.
- Bellissent-Funel, M.-C., Sridi-Dorbez, R., and L. Bosio, 1996: X-ray and neutron scattering studies of the structure of water at a hydrophobic surface. *J. Chem. Phys.* 104, 10023.
- Chen, S.-H., and J. Teixeira, 1986: Structure and dynamics of low temperature water as studied by scattering techniques in *Advances in Chem. Phys.* Vol. 64, I. Prigogine and S.A. Rice (eds), J. Wiley & Sons, New-York.
- Diehl, K., and S.K. Mitra, 1998: A laboratory study of the effects of kerosene burner exhaust on ice nucleation and the evaporation rate of ice crystals. *Atm. Environ.* 32, 3145.
- Dubinin, M.M., and H.F. Stoeckli, 1980: Homogeneous and heterogeneous micropore structures in carbonaceous adsorbents.. *J. Colloid Interf. Sci.* 75, 34.
- Ferry, D., Suzanne, J., Nitsche, S., Popovicheva, O.B., and N.K. Shonija, 2002: Water adsorption and dynamics on kerosene soot under atmospheric conditions. *J. Geophys. Res.* 107, 4734.
- Gregg, S.J., and K.S.W. Sing: 1982: Adsorption, surface area and porosity (2nd ed.), Acad. Press, San Diego
- Hobbs P.V., 1974: Ice Physics. Clarendon. Press, Oxford.
- Kärcher, B., Peter, Th., Biermann, U.M., and U. Schumann, 1996: The initial composition of jet condensation trails. *J. Atm. Sci.* 53, 3066.
- Petzhold, A., Doppelheuer, A., Brock, C.A., and F.P. Schroder, 1999: In-situ observations and model calculations of black carbon emission by aircraft at cruise altitude. *J. Geophys. Res.* 104, 22171-22181.
- Popovicheva, O.B., Persiantseva, N.M., Trukhin, M.E., Rulev, G.B., Shonija, N.K., Buriko, Y.Y., Starik, A.M., Demirdjian, B., Ferry, D., and J. Suzanne, 2000: Experimental characterization of aircraft combustor soot: microstructure, surface area, porosity and water adsorption. *Phys. Chem. Chem. Phys.* 2, 4421.
- Teixeira, J., Bellissent-Funel, M.C., Chen, S.-H., and A.J. Dianoux, 1984: Dynamics of supercooled water studied by neutron scattering. *J. Phys. (France)* 45, C7, 65.
- Toubin, C., Picaud, S., Hoang, P.N.M., Girardet, C., Demirdjian, B., Ferry, D., and J. Suzanne, 2001: Dynamics of ice layers deposited on MgO(001): Quasi-elastic neutron scattering experiments and molecular dynamics simulations. *J. Chem. Phys.* 114, 6371.

Experimental investigation of homogeneous and heterogeneous freezing processes at simulated UTLS conditions

O. Möhler*, C. Linke, H. Saathoff, M. Schnaiter, R. Wagner, U. Schurath
Institute of Meteorology and Climate Research, Forschungszentrum Karlsruhe, Germany.

A. Mangold, M. Krämer
ICG-1, Forschungszentrum Jülich, Germany.

Keywords: Ice nucleation, soot, coating, sulphuric acid, ammonium sulphate.

1 INTRODUCTION

Ice nucleation (IN) in the UTLS region can occur either by homogeneous freezing of solution droplets below about 235 K, or be heterogeneously induced by so-called ice nuclei. At temperatures below 200 K, homogeneous IN requires high ice supersaturations of up to 60%, which are frequently observed in the upper troposphere (Gierens et al., 2000; Jensen et al., 2001). High updraft velocities favour cirrus formation at the homogeneous freezing threshold. At lower updrafts, however, heterogeneous ice nuclei, e.g. soot particles emitted from aircraft engines, may selectively be activated at lower supersaturation. The pristine ice crystals grow by water uptake, thus eventually limiting the maximum supersaturation to values below the homogeneous freezing threshold. This mechanism could explain optically thin cirrus layers with ice particles of low number concentration and large size. The large coolable and evacuable aerosol chamber AIDA (Aerosol Interaction and Dynamics in the Atmosphere) at Forschungszentrum Karlsruhe can be used as a moderate expansion cloud chamber to study processes of ice formation at simulated cirrus conditions like temperature, cooling rate, and ice supersaturation (Möhler et al., 2003; Haag et al., 2003). In this paper we briefly discuss recent ice nucleation experiments in relevant aerosol systems, e.g. soot particles coated with sulphuric acid and ammonium sulphate layers.

2 EXPERIMENTAL

Experimental methods and the instrumentation of the AIDA cloud chamber facility are described by Möhler et al. (2003) and will only briefly be reviewed here. Figure 1 shows the aluminium aerosol vessel (volume 84 m³) located in a thermally insulated box that can homogeneously be cooled to any temperature down to 183 K. At constant wall and gas temperature, ice saturation is maintained by a thin ice layer on the chamber walls. Controlled pumping, typically from 1000 to 800 hPa, causes gas expansion and therefore ice supersaturation by adiabatic cooling. Change of ice supersaturation (up to 50 %/min) results from adiabatic cooling as well as heat and water flux from the ice-coated aluminium walls into the chamber volume. Heat and mass flux are mainly driven by the increasing difference between the almost constant wall temperature and the decreasing gas temperature T_g inside the aerosol chamber which is homogeneously mixed with a ventilator, and the difference of the water vapour saturation pressure above the wall ice coating and the water vapour pressure decreasing during pumping and after formation of cold ice particles. The relative humidity with respect to ice (RH_i) is calculated from the saturation water vapour pressure at T_g and total water concentration measured with the FISH instrument (Zöger et al., 1999). In the most recent experiments, the interstitial water vapour pressure is also measured in situ by folded-path tunable diode laser absorption. After pumping is stopped at 800 hPa, the gas temperature starts to increase

* *Corresponding author:* Ottmar Möhler, Forschungszentrum Karlsruhe, Institute for Meteorology and Climate Research, Postfach 3640, 76021 Karlsruhe, Germany. Email: Ottmar.Moehler@imk.fzk.de

by heat flux from the aluminium walls approaching the wall temperature with a time scale of about 15 min. Ice particles evaporate within about the same time period and the chamber can be refilled with synthetic air to atmospheric pressure to start another expansion and ice nucleation cycle with the same aerosol.

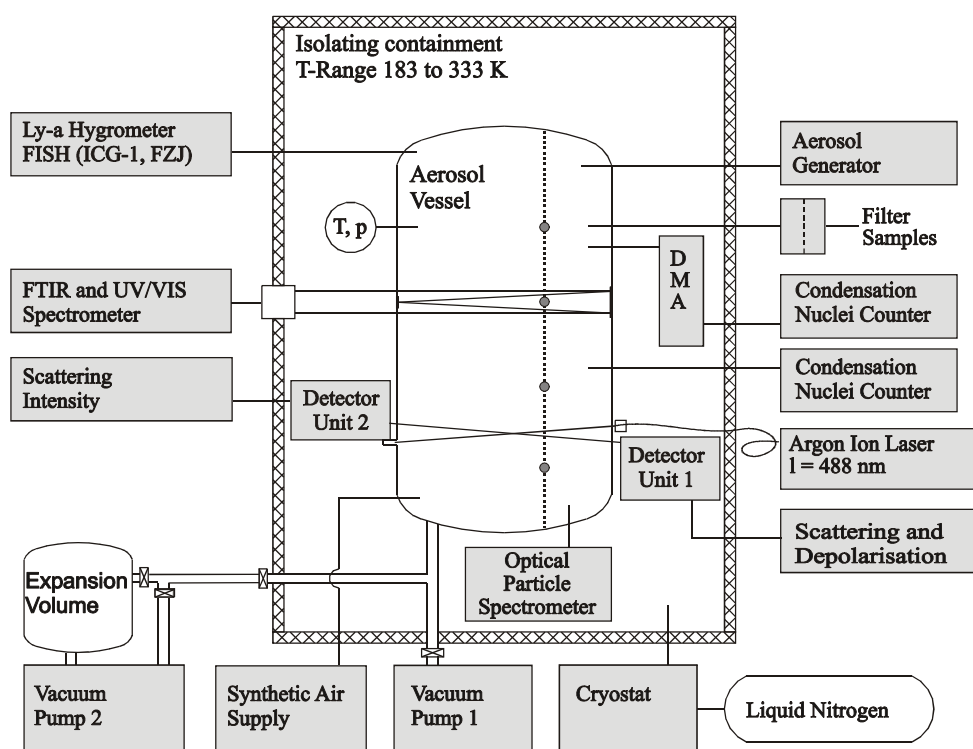


Figure 1. Schematic of the AIDA cloud chamber facility with instrumentation used for ice nucleation experiments.

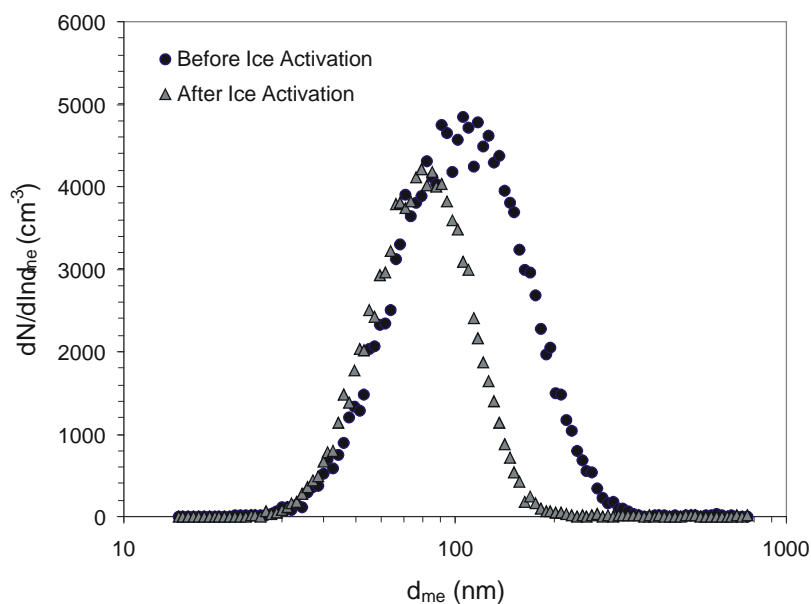


Figure 2. Size distribution of graphite sparc generator soot used for AIDA ice activation experiments. After ice activation the mobility equivalent particle diameters are smaller due to restructuring processes.

Before each set of up to 5 subsequent expansion cycles at the same temperature but different pumping speeds and cooling rates, the aerosol vessel was pumped off to below 1 hPa and refilled with particle free synthetic air to atmospheric pressure. Soot aerosol from a graphite sparc generator was added to the aerosol chamber with number concentrations between about 1000 and 3000 cm^{-3} . The soot agglomerates with mobility equivalent diameters between 30 and 300 nm (Fig. 2) are composed of primary particles with diameters between 4 and 8 nm. Ice activation caused the formation of more compact soot agglomerates which is indicated in Figure 2 by the smaller mobility equivalent diameters after ice activation. In this paper we show only ice activation results of first activations after soot aerosol formation.

Coating of soot particles with sulphuric acid was achieved in a temperature controlled flow tube system. Soot aerosol was mixed with synthetic air saturated with sulphuric acid vapour at a temperature between about 150°C and 200°C. Flow rates and cooling profile in the flow tube were adjusted in order to condense sulphuric acid vapour on the soot particles and to avoid nucleation of pure sulphuric acid droplets. The coated particles were then added to the aerosol chamber. In some experiments, the sulphuric acid coating was, after first ice activations, transferred into an ammonium sulphate coating by adding ammonia to the aerosol chamber. Therefore, the influence of both sulphuric acid and ammonium sulphate coating on the ice forming potential was investigated for the same soot aerosol.

Pristine ice crystals nucleated inside the aerosol chamber immediately after exceeding the critical ice supersaturation S_{IN} are sensitively detected by the depolarisation increase of back-scattered laser radiation at 488 nm. The growth of nucleated ice crystals was also detected with an optical particle counter located below the chamber and by FTIR extinction spectra measured in situ using a multi-path optical cell (see Fig. 1).

3 RESULTS

The heterogeneous IN on graphite sparc generator soot aerosol was investigated at temperatures between 184 and 240 K (Fig. 3). The critical ice saturation ratio S_{IN} at freezing onset was measured as described above. At temperatures above 235 K, ice nucleation on pure soot particles only occurred close to or slightly above water saturation (dashed line in Figure 3). Liquid water seems to condense on the soot particles before ice forms (condensation freezing).

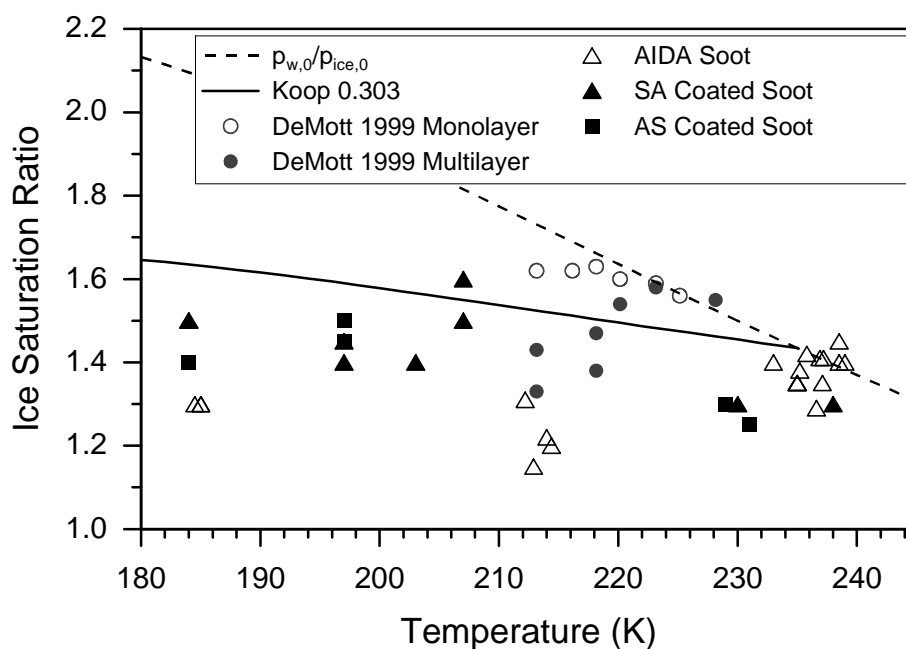


Figure 3. Ice saturation ratios measured for ice nucleation on pure soot and soot coated with sulphuric acid (SA) and ammonium sulphate (AS). The AIDA data is compared to results of DeMott et al. (1999).

At lower temperatures, ice is formed significantly below the liquid water saturation threshold and also below the threshold for homogeneous freezing nucleation of supercooled liquid solution droplets indicated by the solid line (Koop et al., 2000). Decreasing S_{IN} with decreasing temperatures was also found by DeMott et al. (1999) who measured IN on redispersed Degussa soot at temperatures between 213 and 233 K. In that study, significant decrease of S_{IN} below the values of homogeneous IN was only measured for soot with ‘multilayer’ sulphuric acid coating. At 213 K, S_{IN} measured for multi-layer sulphuric acid coated Degussa soot by DeMott et al. (1999) agrees with the AIDA data measured for untreated sparc generator soot. The first AIDA measurements below 213 K indicate a slight increase of S_{IN} . This trend has to be confirmed by further data currently analysed.

Coating of soot particles with significant amount of sulphuric acid (up to some ten percent by particle mass) increases the freezing relative humidity by about 10 to 20 % at temperatures below 220 K. This is in contrast to the results by DeMott et al. (1999) who found decreasing freezing relative humidity with increasing amount of sulphuric acid coating. Neutralisation of the sulphuric acid coating to ammonium sulphate in some AIDA experiments did not significantly change the onset of ice nucleation.

4 SUMMARY AND CONCLUSION

In the AIDA experimental facility, the freezing relative humidity was measured for pure graphite sparc generator soot and soot coated with sulphuric acid and ammonium sulphate. At temperatures above 235 K, IN on untreated soot seems to occur only after liquid activation of the soot particles, whereas at lower temperatures deposition freezing was measured at ice saturation ratios between 1.2 and 1.3 which is significantly below water saturation and below the critical ice saturation for homogeneous IN of solution droplets. Coating of soot particles with sulphuric acid and ammonium sulphate increases the freezing relative humidity by about 10 to 20 % at temperatures below 220 K. In further experiments the effect of organic carbon content on the IN of soot particles will also be investigated.

REFERENCES

- DeMott, P. J., Y. Chen, S. M. Kreidenweis, D. C. Rogers, and D. E. Sherman, 1999: Ice formation by black carbon particles. *Geophys. Res. Lett.* 26, 2429-2432.
- Gierens, K., U. Schumann, M. Helten, H. Smit, and P. H. Wang, 2000: Ice supersaturated regions and subvisible cirrus in the northern midlatitude upper troposphere. *J. Geophys. Res.* 105, 22743-22753.
- Haag, W., B. Kärcher, S. Schaefers, O. Stetzer, O. Möhler, U. Schurath, M. Krämer, and C. Schiller, 2003: Numerical simulations of homogeneous freezing processes in the aerosol chamber AIDA. *Atmos. Chem. Phys.*, 3, 195-210.
- Jensen, E. J., O. B. Toon, S. A. Vay, J. Ovarlez, R. May, T. P. Bui, C. H. Twohy, B. W. Gandrud, R. F. Pueschel, and U. Schumann, 2001: Prevalence of ice supersaturated regions in the upper troposphere: Implications for optically thin ice cloud formation. *J. Geophys. Res.* 106, 17253-17266.
- Koop, T., B. P. Luo, A. Tsias, and T. Peter, 2000: Water activity as the determinant for homogeneous ice nucleation in aqueous solutions. *Nature* 406, 611-614.
- Möhler, O., O. Stetzer, S. Schaefers, C. Linke, M. Schnaiter, R. Tiede, H. Saathoff, M. Krämer, A. Mangold, P. Budz, P. Zink, J. Schreiner, K. Mauersberger, W. Haag, B. Kärcher, and U. Schurath, 2003: Experimental investigation of homogeneous freezing of sulphuric acid particles in the aerosol chamber AIDA. *Atmos. Chem. Phys.*, 3, 211-223.
- Zöger, M., A. Afchine, N. Eicke, M.-T. Gerhards, E. Klein, D. S. McKenna, U. Mörschel, U. Schmidt, V. Tan, F. Tuitjer, T. Woyke, and C. Schiller, 1999: Fast in situ stratospheric hygrometers: A new family of balloon-borne and airborne Lyman γ photofragment fluorescence hygrometers. *J. Geophys. Res.* 104, 1807-1816.

Detailed Modelling of Cirrus Clouds – an intercomparison of different approaches for nucleation

M. Monier*, W. Wobrock and A. Flossmann

Laboratoire de Météorologie - Physique, CNRS / OPGC, Université Blaise Pascal, Clermont-Ferrand, France

Keywords: cirrus microphysics, homogeneous and heterogeneous nucleation, residual aerosol particles

ABSTRACT: An explicit treatment of ice microphysics is presented to describe the formation and evolution of cirrus clouds and their interaction with interstitial aerosol particles and droplets. Three different mechanisms for homogeneous and heterogeneous nucleation, respectively, will be used to study the influence of the nucleation rate on ice crystal formation. The results will be compared with those of other detailed models given in literature. In addition the modelled residual particle distributions of the ice crystals were calculated and compared to the CVI measurements performed during INCA. This comparison shows that most of the actually used nucleation schemes cannot reproduce reasonably well the observed residual particle spectra found in cirrus clouds during INCA.

1 INTRODUCTION

In order to improve the treatment of the ice forming processes in cirrus models numerous schemes for nucleation of ice crystals were developed, mainly based on the results of laboratory and field experiments. Most parameterisations assume a homogeneous nucleation process of solution droplets of nitric or sulphuric acid which give reasonable crystal concentrations for temperatures below -40°C . Measurements in cirrus clouds during the flight campaign INCA (Ström et al., 2002) however document that significant numbers of ice crystals also occurs for temperatures strongly above -40°C . Thus an important question to answer is: which mechanism - homogeneous or heterogeneous nucleation – dominates the ice crystal formation. Three parameterisations for homogeneous and heterogeneous nucleation resp. are used in the dynamical frame of an air parcel model. The model results are compared with those of Lin et al. (2002) and with the residual particle spectra observed during INCA.

2 MODELLING OF MICROPHYSICAL PROCESSES

Aerosol particles grow by water vapour diffusion to solution droplets or further to cloud drops and thus serve as cloud condensation nuclei. At low temperatures and under ice supersaturated conditions aerosol particles can also be ice nuclei and thus form ice crystals. In order to consider all these components in a cloudy atmosphere we make use of two number distributions: one for solution droplets or liquid cloud droplets and another for the ice crystals.

The number distribution of droplets $f_{wat}(m, m_{AP,N}, x_i)$ is treated as a function of the total particle mass m , the dry aerosol mass $m_{AP,N}$, and the chemical composition x_i of the aerosol particle. In this study we follow only one type of aerosol particles and do not consider an external mixture. If $m \gg m_{AP,N}$ drops are present while for solution droplets m and $m_{AP,N}$ differ only by a factor of 3 or less. For $m = m_{AP,N}$, f_{wat} represents the dry aerosol particle distribution (as provided by measurements with optical particle counters or differential mobility analysers).

The number distribution of ice crystals $f_{ice}(m, m_{AP,N}, x_i)$ is given by the same variables. However,

* Corresponding author: Marie Monier, Laboratoire de Météorologie-Physique, 24 ave. des Landais, F-63177 Aubière Cedex, France. Email: monier@opgc.univ-bpclermont.fr

m represents the mass of the “solid” water. As above, only one species x_i of aerosol particles is treated for this study.

Both number distributions f_{wat} and f_{ice} are calculated by numerical integration of equations (1) and (2). The first term on the right hand side of eq.(1) describes the time evolution of f_{wat} by condensational or evaporational growth. As the growth of dry aerosol particles to wet particles or droplets is continuously described by the Köhler theory, no additional term for the nucleation of solution droplets occurs. The growth velocity $(dm/dt)_{wat}$ is used as given in Pruppacher and Klett (1997). For the description of cirrus clouds we have to consider the loss in wet aerosol particles due to their *nucleation* as crystals as well as their collision or riming on existing ice crystals.

Consequently, these two processes appear in equation (2) as source terms. The depositional growth of the ice crystals with the growth velocity dm/dt is calculated as given in Pruppacher and Klett (1997). We notice that the key parameter controlling $(dm/dt)_{ice}$ is the ice supersaturation.

$$\begin{aligned} \frac{\partial f_{wat}(m, m_{AP,N}, x_i)}{\partial t} = & - \frac{\partial}{\partial m} \left[f_{wat}(m, m_{AP,N}, x_i) \frac{dm}{dt} \Big|_{wat} \right] && \text{condensation / evaporation} \\ & - f_{wat}(m, m_{AP,N}, x_i) J_{\text{hom/het}} && \text{loss by ice nucleation} \\ & - \int_{m_{0crys}}^{\infty} f_{wat} K(m_{crys}, m_{drop}) f_{ice} dm_{crys} && \text{loss due to riming} \end{aligned} \quad (1)$$

$$\begin{aligned} \frac{\partial f_{ice}(m, m_{AP,N}, x_i)}{\partial t} = & - \frac{\partial}{\partial m} \left[f_{ice}(m, m_{AP,N}, x_i) \frac{dm}{dt} \Big|_{ice} \right] && \text{diffusional growth} \\ & + f_{wat}(m, m_{AP,N}, x_i) J_{\text{hom/het}} && \text{hom. and het. nucleation} \\ & - \int_{m_{0drop}}^{\infty} f_{wat} K(m, m_{drop}) f_{ice} dm && \text{riming} \\ & + \int_{m_{0drop}}^{\infty} \left(\int_{m_{0crys}}^m f_{wat} K(m_{crys}^*, m_{drop}) f_{ice} dm_{crys}^* \right) dm_{drop} \end{aligned} \quad (2)$$

For the riming of wet aerosol particles with ice crystals we use the collection kernel K given by Martin et al. (1980) et Wang and Wusheng (2000). The different nucleation rates J used in this study for homogeneous nucleation J_{hom} and for heterogeneous nucleation J_{het} will be presented in the following chapter.

3 HOMOGENEOUS AND HETEROGENEOUS NUCLEATION

3.1 Homogeneous nucleation

Three different methods for the calculation of the nucleation rate J_{hom} will be compared: These are given by Tabazadeh et al. (2000), DeMott et al. (1997) and Koop et al. (2000).

The classical approach of Tabazadeh et al. is based on the results of laboratory studies for surface tension, density, and activation energy for a solution of sulphuric acid. These values are fitted as a function of temperature and weight percentage w . As our model concept with $f_{wat}(m, m_{AP}, x_i)$ directly provides $w (= m_{AP}/m)$ a further fit for w as used in the work Tabazadeh et al. (2000) is not needed.

The method of DeMott et al. follows the classical approach for homogeneous nucleation of pure water (Pruppacher and Klett, 1997). Herein the effect of the solution is considered by the use of a so called effective temperature, which corrects the droplet temperature by the freezing point depression.

Koop et al. (2000) found by laboratory studies that the homogeneous nucleation rate is independent of the solute nature of the aerosol and only depends on water activity. Thus, the key parameters for this approach of the nucleation rate are temperature and humidity.

3.2 Heterogeneous nucleation

For the heterogeneous nucleation we use the empirical approaches of Meyers et al. (1992) and DeMott et al. (1997) and DeMott et al. (1998) which are based on field or laboratory experiments.

$$N_{IN} = F \times 10^{-3} \times \exp(-0.639 + 12.96 \times S_{v,ice}) \quad (3)$$

The parameterisation of Meyers et al. (eq. 3) only needs the knowledge of the ice supersaturation $S_{v,ice}$. F represents a positive value ≤ 1 , which allows to reduce the number of ice crystal nucleated due to the environmental conditions.

$$N_{IN} = 1.04 \times 10^{-4} \times 4\pi r_{soot}^2 \times (T_0 - T_{eff})^{7.767} \quad (4)$$

The approach of DeMott et al. (1997), similar to their approach for homogeneous nucleation, works with the effective temperature. In addition, this parameterisation (eq. 4) takes the surface of the insoluble soot particles into account, implying that the nucleation rate of insoluble particles increases with size (T_0 = triple point of water).

$$N_{IN} = N_{CN} \times 1.3 \times 10^{-23} \times (T_0 - T_{eff})^{11.75} \quad (5)$$

The third approach for heterogeneous nucleation of DeMott et al. (1998) is mainly based on aircraft observations in cirrus clouds. In this experiment DeMott et al. found a strong correlation between the number of cloud nuclei (N_{CN}) and ice nuclei (N_{IN}). This parameterisation for ice nuclei (eq. 5) also takes the effective temperature into account.

4 RESULTS FROM AIR PARCEL MODELLING

Analogously to the recent comparative study of Lin et al. (2002) on detailed cirrus models we performed the following calculation in the dynamical frame of an air parcel model moving wet adiabatically upwards in an ice supersaturated atmosphere. Two scenarios are investigated: a cold air case, where the air parcel starts at 170 hPa, $T = -60^\circ\text{C}$ and $R_{hi} = 100\%$, and a warm case starting at 340 hPa, $T = -40^\circ\text{C}$ and $R_{hi} = 100\%$. The aerosol particles distribution was supposed to consist in a single mode log normal distribution with a total number of $N = 200 \text{ cm}^{-3}$, a mean radius $r_{\text{MEAN}} = 20 \text{ nm}$, and a standard deviation $\sigma = 2.3$. More details on the dynamical and microphysical model setup are given in Lin et al. (2002).

4.1 Air parcel results for homogeneous nucleation

Figure 1 presents the results for the modelled ice number concentration after a vertical ascent of 800 m. The results for the cold case are displayed on the left hand side, the warm case is displayed on the right. Each case was run for a vertical wind speed of 4, 20, and 100 cm/s. For each case and each updraft speed three different rates for homogeneous nucleation (see section 3.1) were compared. The letter T on the abscissa of Figure 1 stands for the approach of Tabazadeh et al. (2000), K for the parameterisation of Koop et al. (2000), and D for DeMott et al. (1998).

The elevated bar for each case and each updraft velocity gives the range of the results found in Lin et al. (2002) for the same parcel studies. These authors compared 7 different detailed numerical cirrus models, which essentially used the same three parameterisations for homogeneous nucleation which we abbreviated by T, K, and D.

Figure 1 displays that the number of ice crystals formed increases significantly with the intensity of the vertical wind. The reason for this behaviour results from the increase of the ice supersaturation with increasing vertical wind speed (see Tab. 1). However the influence of the air temperature on ice crystal production is less pronounced. In our study a number increase for the cold case only becomes visible for the highest updraft speed of 1 m/s. In Lin et al. on the other side an increase in ice crystal number at colder temperatures becomes obvious for the lower updraft velocities of 4 and 20 cm/s.

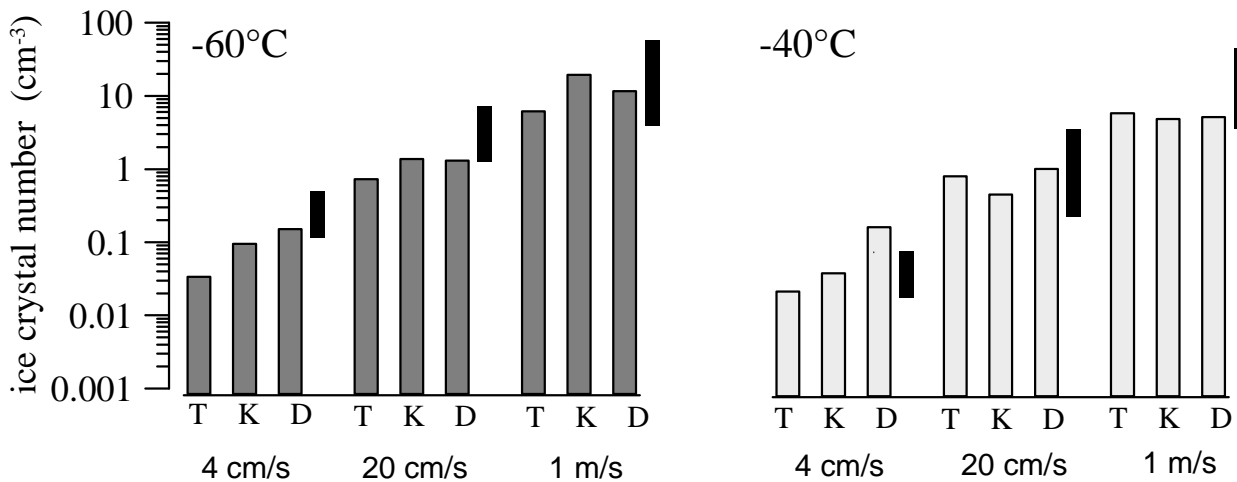


Figure 1. Total number of ice crystals formed by homogeneous nucleation using different vertical updraft velocities w and different nucleation rates T, K, or D. The elevated bars represent the range of results found in Lin et al. (2002) for the same scenarios.

Table 1. Maximum ice supersaturation (%) calculated for different schemes of homogeneous nucleation.

nucleation scheme	cold case			warm case		
	4 cm/s	20 cm/s	100 cm/s	4 cm/s	20 cm/s	100 cm/s
T	43.4	52.8	67.2	41.6	44.5	46.2
K	45.9	47.4	49.0	41.5	42.6	43.9
D	48.7	49.6	51.9	42.1	42.9	44.9

The difference in number concentration between the three nucleation rates T, K, and D for cases with $w \geq 20$ cm/s in Figure 1 is significantly weaker than in the study of Lin et al. This is not surprising as we used one numerical cloud model wherein only the rate of nucleation varied, while Lin et al. (2002) compared the results of seven different numerical cloud models in which each of them treated one (of the three) nucleation rates individually.

For the two cases with low vertical winds of 4 cm/s our range of variability in ice number concentration modelled is the same as in Lin et al. We can see from these cases with low updrafts that it is the parameterization T which always gives the lowest ice crystal numbers. The same statement holds for all updraft conditions in the cold case below -60°C .

In order to understand the behaviour of the different nucleation rates we displayed in Figure 2 the homogeneous nucleation rate J as a function of the ice supersaturation for a small (radius = 40 nm) and a medium size aerosol particle (200 nm). We can detect from Figure 2 that larger solution droplets start to nucleate at lower supersaturations than the smaller ones. This behaviour is most pronounced for the nucleation scheme T, and less pronounced for the scheme K. In addition, Fig. 2 indicates that the important nucleation rates occur for low temperatures by an increase of the supersaturation. This is especially the case for scheme T, where ice nucleation for the small particles at -65°C does not start until the relative humidity exceeds 167 %, while for the warm case at -45°C this occurs already at 147 %. Considering also the maximum supersaturation values given in Tab.1 that occur during the ascent of the air parcel it becomes obvious that for the cold case scheme T will not be able to nucleate small aerosol particles. Consequently the crystal numbers of scheme T in the cold cases are smaller than those of scheme K and D (Fig. 1).

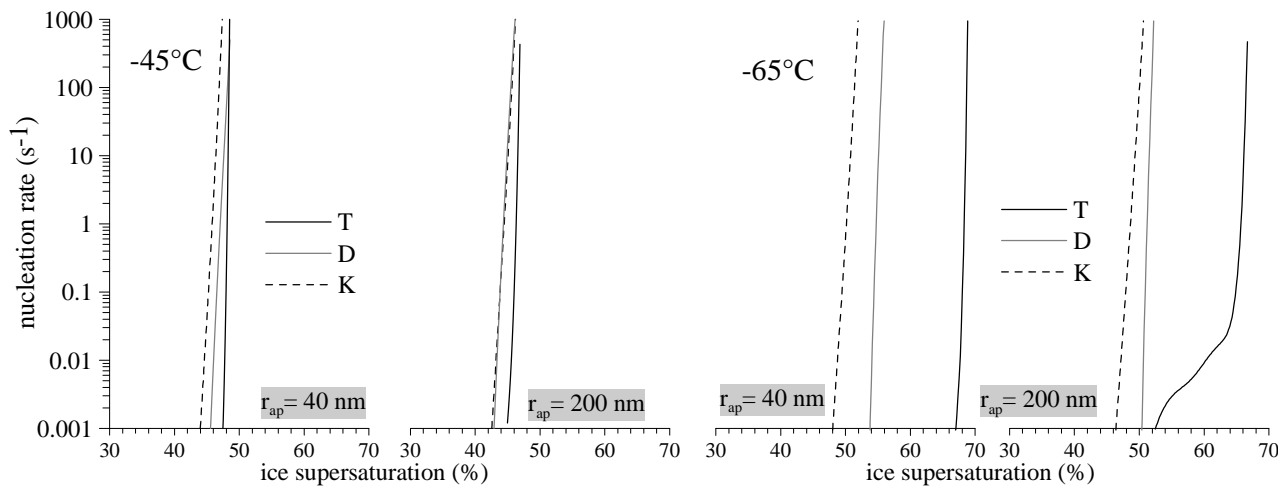


Figure 2. Homogeneous nucleation rate J (number/s) as a function of ice supersaturation for two different aerosol particle sizes and the three nucleation schemes T, K, and D.

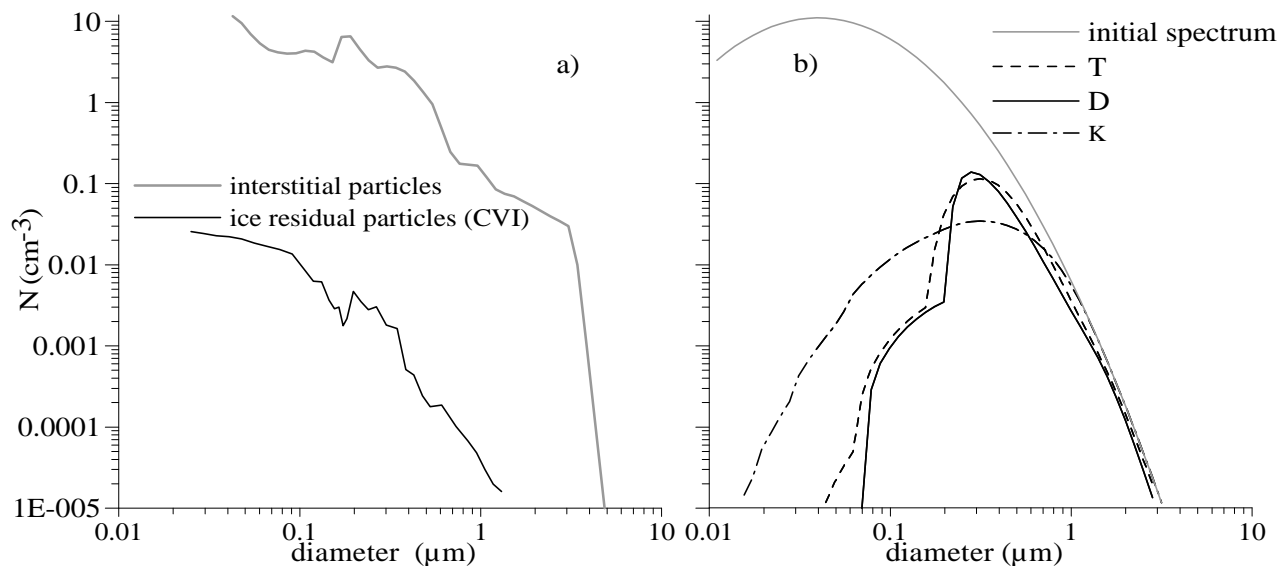


Figure 3. Comparison between interstitial and residual spectra. a) Measurements performed during INCA, on 30 March 2000 east of Punta Arenas, b) modelling results for the homogeneous nucleation rates T, K, and D.

This behaviour of scheme T disappears for the warm cases with 20 and 100 cm/s. The differences between nucleation rates T and K or D displayed in Figure 2 at -45°C are significantly smaller than for the cold case and thus the number concentrations of scheme T are in the same range as for K and D. Only for the warm case with 4 cm/s the values of T in Figure 1 remain again weaker than those of K and D. The lower maximum supersaturation of 41.6 % (Tab.1) in this case allows only the nucleation of a few large aerosol particles for scheme T while schemes K and D can activate significantly more particles around 41 % supersaturation (see warm case in Fig.2).

4.2 Comparison with the cloud residual particle spectra

Another helpful method for the assessment of the different parameterisations for homogeneous nucleation is the analysis of the particle residuals stemming from cirrus ice crystal spectra. This kind of measurements was performed by Ström et al. (2002) during the European cirrus campaign INCA (www.pa.op.dlr.de/inca/). Figure 3a shows observational results of 30 March 2000 of residual and interstitial particle spectra. Similar results were found for the northern hemisphere, indicating that only around 0.1 to 1% of the present aerosol particles nucleate and form ice crystals.

The modelling concept for ice crystals presented by eq. 2 treats explicitly the nucleus mass $m_{AP,N}$ and therefore allows the calculation of the residual particle spectra. Results for the three different schemes for homogeneous nucleation T, K, and D are displayed for the warm case with $w = 20$ cm/s in Figure 3b.

The graph of the three residual spectra reflects the nucleation behaviour discussed already in Figure 2: large particles will nucleate at lower supersaturation than small particles, thus, most large particles serve as ice nuclei while the small ones nucleate only slightly or not at all. The comparison with the measurements (Fig. 3a) suggests that all three nucleation schemes strongly overestimate the nucleation of large aerosol particles while the nucleation of the small ones is almost completely absent. A possible explanation for the discrepancy with the observation could be that not homogeneous but heterogeneous nucleation dominates in the atmosphere of INCA.

4.3 Heterogeneous nucleation

In order to see how heterogeneous nucleation influences the modelled residual aerosol spectra we perform the same calculation as in section 4.2 (warm case, $w = 20$ cm/s), however using the heterogeneous nucleation rates given in section 3.2. The results are displayed in Figure 4. The preference to nucleate large particle remains only visible for the approach of DeMott et al. (1997), named D'97. The parameterisation of Meyers et al (1992), named MEY, nucleates all particle size with the same efficiency as the nucleation rate (eq. 5) only depends on the ice supersaturation. A size dependency for the heterogeneous nucleation rate of DeMott et al. (1998), named D'98, also exists in eq. 4 (hidden in T_{eff}), but this cannot be well detected in Figure 4a due the low nucleation efficiency. The strength of nucleation rate D'98 is determined by two coefficients which were determined by only one flight in cirrus clouds.

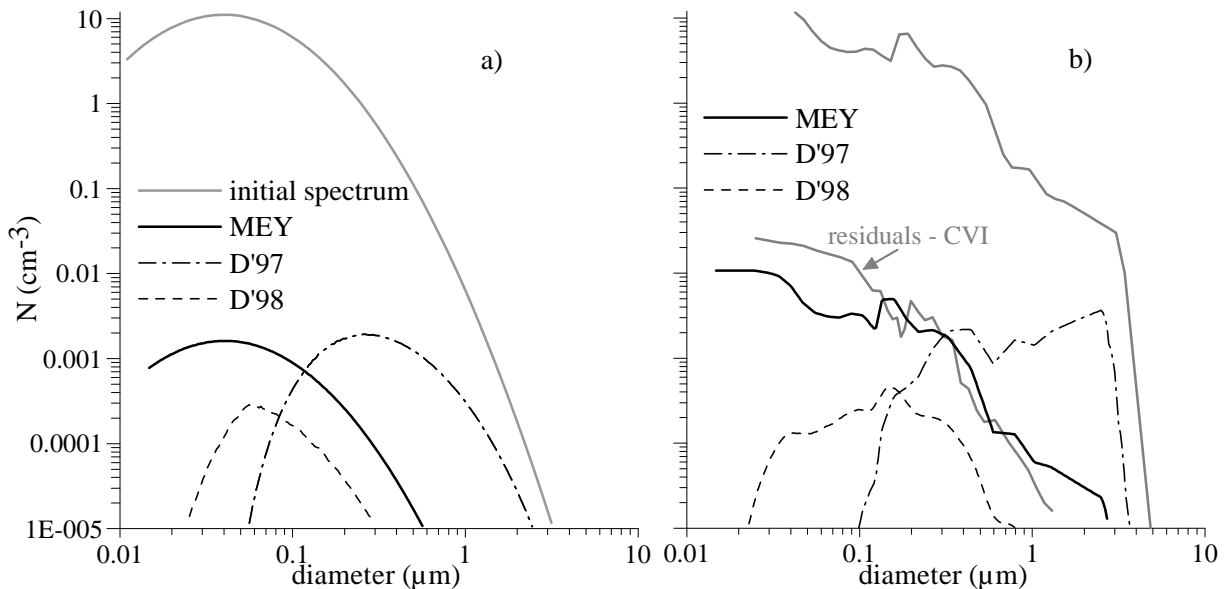


Figure 4. Modelling results for number distribution of residual particles using the heterogeneous nucleation rates MEY, D'97, and D'98. In a) a log normal distribution is used for the ambient aerosol particle spectra, in part b) the interstitial spectrum measured on 30 March 2000 during INCA (cp. Fig. 3).

The maximum supersaturation values obtained during the ascent of the air parcel using these heterogeneous nucleation rates differ clearly from those for homogeneous nucleation given in Table 1. While D'98 still reaches 44.6 % supersaturation, the maximum values of D'97 only gives 27.8 % and MEY just 15.3 %. Running homogeneous and heterogeneous nucleation both together in the air parcel Figure 4a will not change for the schemes MEY and D'97 as the high values of supersaturation needed for the homogeneous nucleation cannot be reached. In a combination of D'98 with one of the homogeneous schemes T, D, or K, however, both rates for nucleation become visible through two maxima in the residual spectra of Figure 4a (not displayed).

Similar to the above performed air parcel simulation for $w = 20$ cm/s and $T = -40$ °C we run the same three schemes for heterogeneous nucleation but with the observed aerosol spectrum given in Fig. 3a. The results are presented in Figure 4b. The behaviour of the different heterogeneous nucleation rates stay the same as already discussed in Figure 4a. It is surprising that the approach of Meyers et al. (1992) agrees best the observed crystal residual aerosol spectra. For the crystal number controlling factor F in equation 5 we have taken the value 1.

5 CONCLUSION

From the modelling results we can conclude that the ice crystal number depends in the first place on the strength of the vertical velocity, as this one determines the value of maximum supersaturation which can be reached. A clear importance of the temperature on the crystal number nucleation becomes less visible from the different case studies.

For mean and high updraft velocities the employed parameterisations for homogeneous nucleation typically differ by a factor of 2. For low velocities however the discrepancy between the results can increase to a factor of 5 and more. These differences result from the size dependency of the nucleation rates which vary significantly between the schemes T, K and D.

A comparison of the homogeneous nucleation model results for the ice crystal residual particles with those measured during the INCA experiment in cirrus clouds points out a dramatic discrepancy in the shape of the size dependency. Observations in cirrus clouds for the northern and southern hemisphere do not confirm a stronger nucleation efficiency for the larger aerosol particles but show rather a size independent nucleation efficiency.

Similar to the homogeneous nucleation the parameterisations for heterogeneous nucleation D'97 and D'98 deviate also from the observational results. This is due to the fact that these two approaches also consider a size dependency. Surprisingly the parameterisation of Meyers et al. (1992) which simply depends on the ambient ice supersaturation but does not consider the physico-chemical properties of the aerosol particles reproduces the observation reasonably well.

REFERENCES

- DeMott, P., D. C. Rogers, and S. M. Kreidenweiss, 1997: The susceptibility of ice formation in upper tropospheric clouds to insoluble aerosol components, *J. Geo. Res.*, 102, 19575-19584.
- DeMott P.J., Y. Chen, C.H. Twohy, D. Baumgardner, A.J. Heymsfield, and K.R. Chan, 1998: The role of heterogeneous freezing nucleation in upper tropospheric clouds: inferences from SUCCESS. *Geophys. Res. Lett.* 25, 1387-1390.
- Koop, T. H. P. Ng., B. Luo, A. Tsias, and T. Peter, 2000: Water activity as the determinant for homogeneous ice nucleation in aqueous solutions, *Nature*, 406, 611-614.
- Lin, R.-F., D. O'C Starr, P. J. DeMott, R. Cotton, K. Sassen, E. Jensen, B. Kärcher, X. Liu: Cirrus parcel model comparison project, 2002 : Phase 1: The critical components to simulate cirrus initiation explicitly, *J. Atm. Sci.*, 59, 15, 2305-2329.
- Martin J. J., P.K. Wang, H. R. Pruppacher: A theoretical determination with which Aerosols Particles are collected by simple Ice crystal Plates, 1980: *J. Atm. Sci.*, 37, 1628-1638
- Meyers M. P., P. J. DeMott, and W. R. Cotton: New primary Ice Nucleation Parametrizations in an Explicit Cloud Model, 1992: *J. Appl. Met.*, 31, 708-721.
- Pruppacher and Klett, : Microphysics of clouds and precipitation, 1997. Kluwer Academic Publisher. 2nd revised and enlarged edition. 954pp.
- Ström, J., et al., 2002: Aerosol and cirrus measurements at midlatitudes on the Southern hemisphere: An overview based on the first INCA experiment, *Air Pollut. Rep. 74, Rep. EUR 19,428 EN*, European Commission, Brussels.
- Tabazadeh, A., S. T. Martin, J. S. Lin, 2000: The effect of particle size and nitric acid uptake on the homogeneous freezing of aqueous sulfuric acid particles, *Geophys. Res. Lett.*, 27, No.8, 1111-1114
- Wang, P., J. Wusheng,: Collision efficiencies of Ice Crystals at Low Intermediate Reynolds Number Colliding with Supercooled Cloud Droplets, 2000: A Numerical Study, *J. Atmo. Sci.*, 57, 1001-1009.

Simulation of Contrail Coverage over the USA Missed During the Air Traffic Shutdown

Patrick Minnis³, Louis Nguyen, Donald P. Garber,
Atmospheric Sciences, NASA Langley Research Center, Hampton, Virginia, USA

David P. Duda
Hampton University, Hampton, Virginia, USA

Rabindra Palikonda, David R. Doelling
AS&M, Inc., Hampton, Virginia, USA

Keywords: contrails, remote sensing, September 11, contrail simulation, air traffic

ABSTRACT: Contrails were simulated for the northeastern USA during the first part of the air traffic shutdown following the 9-11 terrorist attacks. Analysis of military contrails observed during the shutdown provided a baseline set of contrail properties that were employed to tune a contrail prediction scheme using high-resolution numerical weather analyses and normal air traffic flight data. The simulation produced a large area of contrails that started developing around 1000 UTC, 12 September 2001 and peaked in areal coverage of more than 200,000 km² around 1800 UTC. The simulation results were used to alter existing infrared satellite images to visualize the area for air traffic conditions. Initial estimates of the contrail radiative forcing are biased low because of improper treatment of different contrails overlapping on the same satellite imager pixels. Improvements were suggested for a more accurate and complete simulation of the contrail properties.

1 INTRODUCTION

Following the tragic events of 11 September 2001, commercial and personal air traffic over the United States of America (USA) was halted for at least 36 hours with resumption of more normal flight activity by 15 September 2001. During the air traffic shutdown, the contrail coverage decreased dramatically. This lack of contrails over the USA was even noticed by astronauts. Analyses of weather data during the shutdown period indicate an anomaly in the diurnal range of surface air temperature that was attributed to the lack of contrails (Travis et al. 2003). Such an anomaly would result from the lack of radiative forcing by contrails and would indicate not only that contrails affect climate but they can also affect the daily weather. To determine if such an anomaly can be realistically attributed to the absence of normal air traffic, it is necessary to accurately estimate the radiative forcing that would have occurred if normal air traffic had occurred.

Normally, it is difficult to determine the radiative forcing by contrails because air traffic is relatively continuous throughout much of the day (Garber et al. 2003). New and old contrails overlap with each other and with natural cirrus clouds making it difficult to determine the evolution and dissipation of individual contrails and their radiative impacts. The air traffic shutdown was essentially complete by 1600 UTC, 11 September 2001. Thus, the air over the USA should have been free almost all cirrus clouds produced by commercial air traffic by ~ 0000 UTC 12 September. A few isolated contrails from military flights developed over the northeastern USA, an area normally criss-crossed by thousands of flights. By analyzing the evolution and decay of those contrails, Minnis et al. (2002) were able to relate the contrail formation to a specific relative humidity range and estimate the properties of the individual contrails during each hour of their lifetimes. Those initial analyses provide the basis for realistically simulating the effects of the missing air traffic. This paper continues that effort by simulating the contrails that would have

³ *Corresponding author:* Patrick Minnis, MS 420, NASA Langley Research Center, Hampton, VA, USA 23681.
Email: p.minnis@nasa.gov

developed during that fateful day and by providing preliminary estimates of their potential radiative impact.

2 DATA AND METHODOLOGY

The basic approach taken here is to use the satellite analyses of Minnis et al. (2002) to determine a relative humidity with respect to ice (RHI) for a given meteorological analysis that can serve as threshold for persistent contrail formation. Flight tracks from a normal air traffic day are then used to simulate the flights through the atmosphere as defined by the meteorological analysis. If the RHI at the location of the plane at a given instant exceeds the threshold RHI value (RHI_t) and the temperature is low enough according to the Appleman criteria, then a persistent contrail is defined for that location. Contrail processes such as spreading, advecting, and dissipating are simulated in a relatively crude fashion and their optical properties are estimated as functions of time. Each contrail is geo-located according to its width, length, and height. This information is then used to alter the satellite image for the given time and location. The original and altered infrared (IR, 10.8 μm) satellite images for each hour are then used to compute the contrail longwave radiative forcing (CLRF).

2.1 Data

Hourly data from the eighth Geostationary Operational Environmental Satellite (GOES-8) are used in the simulation. These were also used by Minnis et al. (2002) to analyze the isolated contrails. The GOES-8 4-km IR images from 12 September 2001 serve as the primary dataset, while 1-km IR and split window (12 μm) data from the NOAA Advanced Very High Resolution Radiometer (AVHRR) and Terra Moderate Resolution Spectroradiometer (MODIS) provide supplementary information.

The temperature (T) and humidity fields are specified using an early version of the NOAA Rapid Update Cycle (RUC) analysis that is based on a hybrid-isentropic model (Benjamin et al. 2003). The RUC reanalyses used here have a 25-hPa vertical resolution in the upper troposphere and a 4-km horizontal resolution, and are available at each hour. RHI is computed from the relative humidity with respect to liquid water derived by the model. The RUC RHI output is similar to the radiosonde profiles in the northeastern USA, but differ by as much as $\pm 20\%$ between 8 and 13 km. (Minnis et al. 2002). The RUC tends to smooth the vertical profiles, reducing the humidity at some locations and increasing it at others. The hourly temperatures, winds (V), and relative humidities were assigned to the satellite data taken closest in time.

It was assumed that the 12 September air traffic would have been identical to the traffic from the previous Thursday. Thus, the simulation uses linear flight tracks (Garber et al. 2003) from 5 September 2001 that were located within the domain bounded by 33°N, 52°N, 66°W, and 93°W. The position of the flight at a given time was associated with the values of T , RHI, and V of the nearest vertical level and the relevant 40-km RUC box.

2.2 Simulation process

To persist, contrails and cirrus require $RHI \geq 100\%$. Because of negative biases in the relative humidity measured at cold temperatures (Miloshevich et al. 1999), RHI infrequently exceeds 100% in the USA radiosonde record. Furthermore, the RUC model adjusts and smoothes the RHI field so that it differs from the radiosonde measurements. While the older version of the RUC used here (discontinued 18 April 2002) yields $RHI > 100\%$ more often than the radiosondes, it is still biased low. Thus, it is necessary to increase the RHI from radiosonde measurements for $T < 0^\circ\text{C}$ or set an artificially low value of RHI_t .

The threshold was determined by comparing the RUC RHI fields to satellite images of contrail and cirrus distributions using the RUC level having the greatest RHI values in the 150-350 hPa range. Figure 1 shows an example of contrails forming in heavy air traffic over the northeastern USA during 18 November 2001. The leading line of contrails in the Terra MODIS 11-12 μm brightness temperature difference image is located in east central Pennsylvania and New York (Fig. 1a). Contrails and cirrus cover most of the image west of that line. Comparison of the 225-hPa RHI contours (Fig. 1b) with the contrails indicate that few contrails formed over areas with $RHI < 80\%$. This value is slightly less than the 85% found by Duda et al. (2003) for a different day. Comparison

of the isolated contrails from 12 September yield a different threshold as expected since the RUC alters the humidity field from the measured values as noted earlier. Figure 2a shows a single, but broken linear contrail over Ohio and Pennsylvania at 1108 UTC, 12 September 2001. Cirrus clouds are evident in northern and southern Ohio as well as northeastern Pennsylvania. The contrail pressure was found to be closest to 225 hPa (Minnis et al. 2002). The corresponding RUC analysis (Fig. 2b) shows that the cirrus occurred for $RHI > 80\%$ while the contrail was persisting in air with RHI as low as 58%. Correction of the 1200-UTC local radiosonde data using the Miloshevich et al. (2001) formula indicate that the actual RHI in the domain is probably 30-40% greater than indicated by the RUC (Minnis et al. 2002). Thus, the actual RHI values could exceed 140% in portions (e.g., central Indiana) of domain and should be close to 110% in southeastern Pennsylvania. Comparisons of images and RUC analyses like those in Figure 2 for the remainder of the day led to the conclusion that $RHI_t = 70\%$ for 12 September.

Once formed, the contrails were allowed to spread based on wind shear. It was assumed that the contrails precipitated with a fall speed of 3 cm s^{-1} . This fall speed produced a spreading rate of 6 km h^{-1} , the same as that determined for the isolated military contrails. Although the isolated contrails spread to widths as large as 40 km, it was assumed that the maximum width would be 12 km because it corresponds to the length-weighted average width of the military contrails. No new nucleation was allowed so that the optical mass (OM) remained constant as the product of the optical depth (OD) and the width once the OD reached its peak according to the log-normal function,

$$OM = a \exp\{-0.5 [\ln(x / x_o) / b]^2\}, \quad (1)$$

where x is the mean contrail age, x_o is the time of peak OM (2.5 hours), a is peak contrail $OM = 0.6$, b is the width of the peak (0.5). This function mimics the average behavior of the isolated contrails in the same domain. The contrails are then advected each hour using the winds at the contrail altitude. In the new time step, the contrail is compared to the RHI at its new location. If $RHI < 70\%$ in the RUC box, the portion of the contrail within the box is deleted. It is also deleted if it is over 6 hours old to ensure that the average contrail lifetime is the same as that for the isolated contrails. The endpoints, width, and OD of each contrail are saved each hour.

The calculation of CLRF was accomplished in the following manner. The parameters for each contrail at a given hour were used to compute changes to the 4-km GOES-8 IR image by altering the brightness temperature T_{IR} of each pixel affected by the simulated contrail. Figure 3 shows a schematic drawing of four 4-km pixels divided into sixteen 1-km sub-pixels. The fractional contrail coverage in each 4-km pixel is simply the number of 1-km sub-pixels with centers between the lines defining the boundaries of the contrails based on the contrail endpoints and width. In Figure 3, pixel A has a fractional coverage $f_c = 9/16$ compared to $6/16$ for pixel D. The contrail optical depth for overlapped sub-pixels is simply the sum of the optical depths for the overlapping contrails. In Figure 3, $OD(B) = [13*OD(2) + 8*OD(1)] / 15$, while $OD(C) = 14*OD(1) / 14$. This formulation yields a value that can exceed the pixel contrail optical depth because it includes only portions of the pixel that contain contrails. But it maintains the true OD of the contrails in the pixels. As seen in the schematic drawing, a contrail may be less than 4-km wide, but it can affect two 4-km pixels. To obtain the effective optical depth of the contrails in the pixels, the pixel OD is multiplied by f_c . In the current simulation, however, the OD for each overlap pixel was computed using only the value of OD corresponding to the last contrail that affected the pixel resulting in an underestimate of OD for the pixel. The new brightness temperature of a given contrail pixel is

$$TC_{IR} = B^{-1}\{[1 - \epsilon(OD f_c)] B(T_{IR}) + \epsilon(OD f_c) B(TC)\} \quad (2)$$

where the emissivity ϵ is computed using the formula of Minnis et al. (1993) for an axi-symmetrical hexagonal ice column with a length of $20 \mu\text{m}$, B is the $10.8\text{-}\mu\text{m}$ Planck function, and TC is the contrail temperature. For this simulation TC is the temperature at 225 hPa. The longwave (5 - 100 μm) fluxes with (M_{LW}) and without (MC_{LW}) contrails is computed as in Minnis and Smith (1998) using a new set of coefficients based on broadband data from the Clouds and Earth's Radiant Energy System scanners. The narrowband IR fluxes (M_{IR}) were computed from the GOES-8 IR brightness temperatures as in Minnis and Smith (1998). The new formula,

$$M_{LW} = 69.56 + 5.516 M_{IR} - 0.0186 M_{IR}^2 + -0.123 M_{IR} \ln(h) \quad (3)$$

where h is the average column-weighted relative humidity (in percent) above the altitude corresponding to T_{IR} in the RUC profile up to 300 hPa. MC_{LW} is also computed from (3) using the contrail flux, MC_{IR} . The contrail radiative forcing is $CLRF = M_{LW} - MC_{LW}$, where the fluxes represent a single pixel or an average of many pixels over a given area.

The simulation process was performed using all GOES-8 pixels in the domain for each hour between 0945 and 2045 UTC.

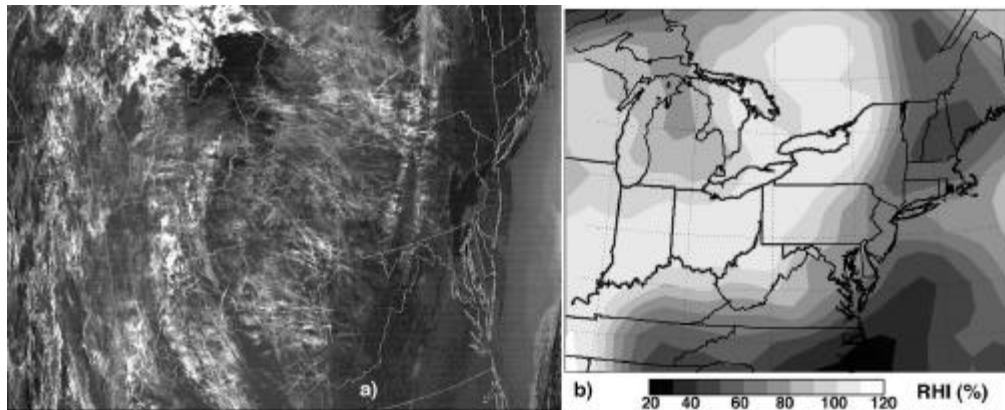


Figure 1. Contrails and humidity over northeastern USA, 18 November 2001. (a) Terra MODIS T11-T12 image, 1624 UTC. (b) 225-hPa RHI (%) from RUC reanalysis, 1600 UTC.

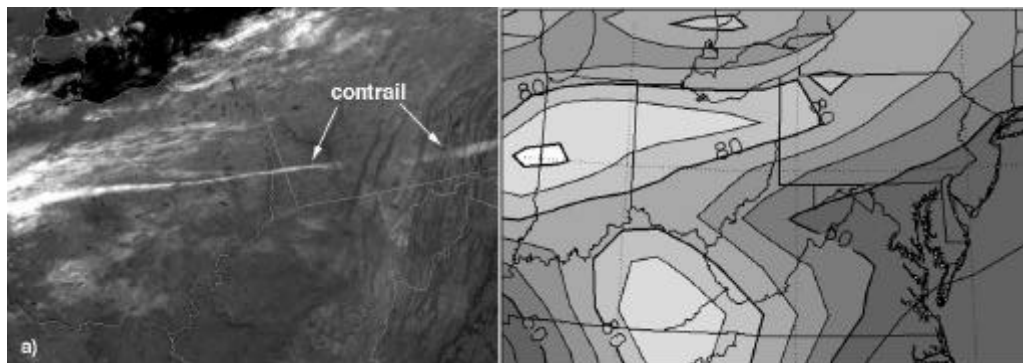


Figure 2. Extended contrail and humidity over northeastern USA, 12 September 2001. (a) NOAA-14 IR image, 1108 UTC. (b) RUC RHI (%) at 225 hPa, 1100 UTC; RHI < 50% in darkest areas.

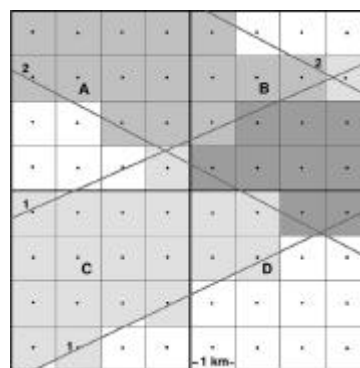


Figure 3. Schematic of method for altering 4-km GOES IR pixels (A - D). Boundaries of contrails 1 and 2 are denoted by the numbered gray lines. 1-km sub-pixels filled by light gray (contrail 1), medium gray (contrail 2), dark gray (overlap).

3 RESULTS & DISCUSSION

Figure 4 shows examples of the original GOES-8 IR images, the contrail masks, and the GOES-IR images containing the simulated contrails for 1045, 1345, 1645, and 1945 UTC. The southern extent of the domain is best represented by the simulated image, but the northern portion is cut off. At 1045 UTC (Fig. 4a), the air traffic for the normal day has just begun over the eastern North America resulting in the generation of a few contrails over South Carolina, western Pennsylvania, and southern Canada. The Canadian contrails are primarily imbedded in extant cirrus and would not be detectable and are cut off in the image. The simulated contrails in northwestern Pennsylvania are similar in appearance to the existing military contrail in southwestern Pennsylvania (Fig. 2 and Fig. 4a3). By 1345 UTC (Fig. 4b), the air traffic is well underway and the contrail coverage is rapidly increasing. The new simulated contrails continue to appear realistic compared to their real counterparts. For example, three military contrails cross West Virginia in an east-west direction while the simulated contrails are oriented north-south. Another east-west contrail in northern Virginia appears to be a continuation of the military contrail in West Virginia. A pronounced mass of overlapping contrails is evident over New Jersey. By 1645 UTC (Fig. 4c), that same mass has moved off the coast and thinned out somewhat (Fig. 4c3). Many new contrails formed while others dissipated. At 1945 UTC (Fig. 4d), many of the contrails have dissipated although the cirrus deck in western Pennsylvania and eastern Ohio has been enhanced considerably by the relatively old contrails that formed in that area. The few spreading contrails over New England appear less realistic than the younger ones, probably as a result of the uniform spreading process used in the simulation. Nevertheless, the resulting imagery, is relatively realistic overall in terms of appearance and compared to the actual contrails that were present.

The total contrail coverage and CLRF for the domain are plotted in Figure 5. The contrail coverage is based on the sum of f_c for the domain divided by total number of pixels, 307,200. The CLRF, however, is based on TC_{IR} , which was computed using the OD for only one of the contrails in the overlapped cases and not the sum of the two. The resulting value is, therefore, an underestimate of the CLRF. Contrail coverage (Fig. 5a) peaked at 1745 UTC with a value of 3.66% or slightly more than 200,000 km². This result is comparable to the average global linear contrail coverage estimated to be between 200,000 and 400,000 km². The total area covered by individual contrails (counting overlapped sub-pixels more than once) peaked at 1745 UTC with 8.85%, 2.4 times more than the actual number of pixels that would be identified as contrail pixels. Thus, overlapped pixels play a critical role in the climatic impact of contrails and need to be treated carefully. Because the mean OD was computed only for the individual contrails, it is underestimated. It peaked at a value of 0.257 at 1245 UTC and slowly dropped to 0.138 by 1945 UTC. The OD s should be roughly 2.5 times the values found here because of the impact of contrail overlap.

The unit CLRF (Fig. 5b) rises from a negligible value at 0945 UTC to a relatively broad maximum of ~ 6 Wm⁻² between 1245 and 1545 UTC. This maximum and the gradual decrease is mostly governed by the variation in OD . The total CLRF (contrail forcing relative to the entire domain) is dominated by the contrail coverage and rises to a maximum of 0.25 Wm⁻² between 1745 and 1845 UTC. The unit CLRF values are 2 - 4 times less than those found by Palikonda et al. (2003) from satellite observations of actual contrails. Some of the difference is due to the co-occurrence of the contrails with cirrus clouds, but the great portion of the difference is most likely due to the underestimate of contrail OD for the overlapped pixels. If the OD s were increased by 250%, then the unit CLRF would peak at 15.2 Wm⁻², a value closer to the daytime September 2001 mean for the linear contrails as derived from AVHRR data (Palikonda et al. 2003). Similarly, the maximum CLRF would be around 0.63 Wm⁻². Thus, more realistic values for the simulation can be obtained by multiplying those in Figure 5b by 2.5.

The simulation presented here represents the first step in theoretically evaluating the possible impact of contrails on the daily surface temperature and for explicitly representing contrails in mesoscale weather predictions. A number of improvements and additions are needed to complete the simulation. These include the proper assignment of optical depth for overlapped pixels, more realistic spreading and dissipation schemes, and computation of the shortwave radiative forcing.

This latter factor has a more direct and immediate impact on the surface temperature and should act to reduce the maximum daytime temperature more than the CLRF increases it. More detailed radiative transfer modelling will be needed for accurately estimating the shortwave component of the radiation effect. The radiative forcing will then need to be translated into changes in the surface air temperatures over the region to determine of the magnitude of the anomalies reported by Travis et al. (2003) can be realistically attributed to the absence of contrails during the shutdown. Additional improvements to the simulation should account for variations in contrail optical depths and dissipation rates in order to make the contrails more realistic.

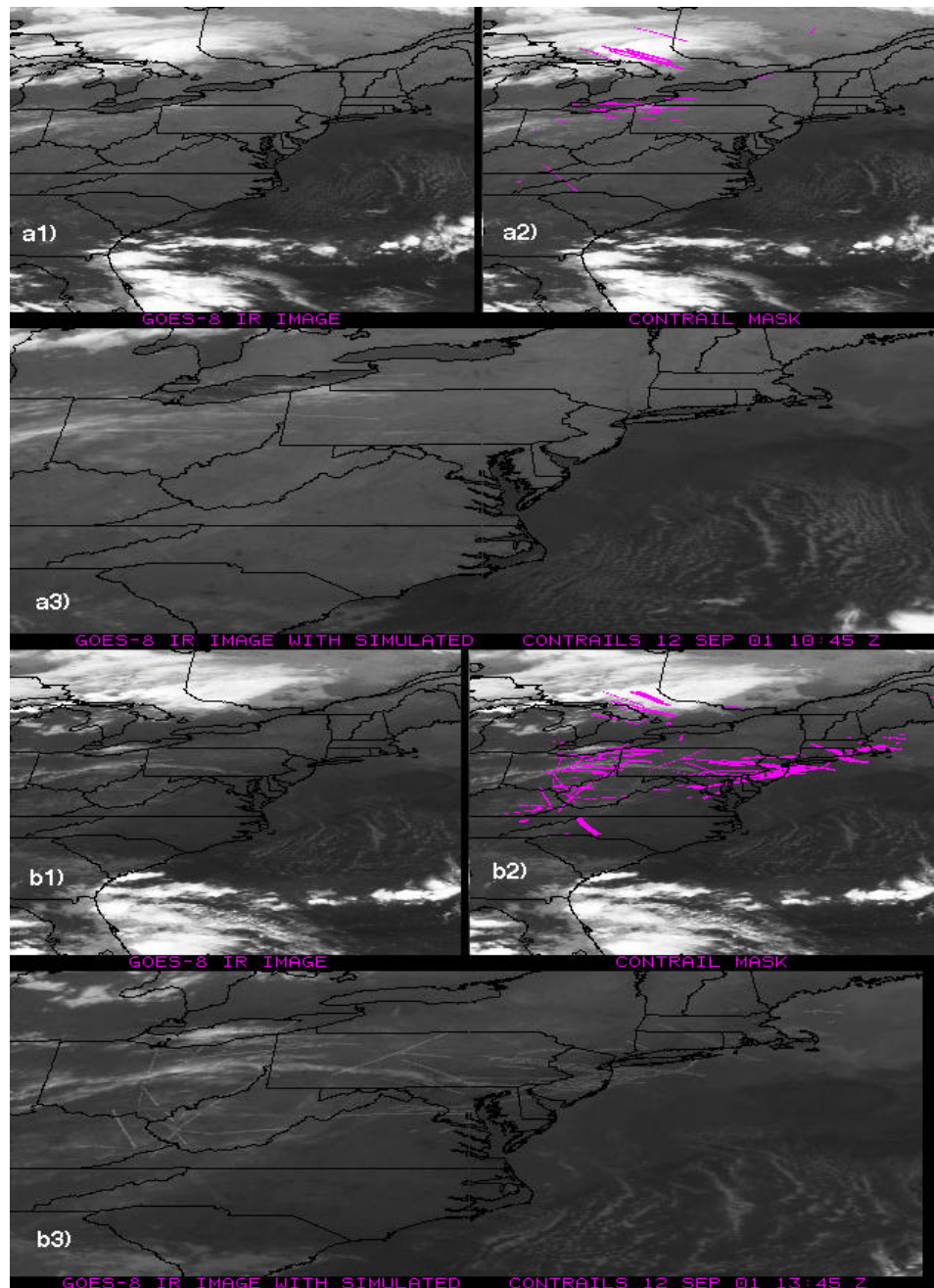


Figure 4. Simulated contrails for 12 September 2001 over northeastern USA. (a) 1045 UTC, (b) 1345 UTC. (1) GOES-8 IR image, (2) IR image with locations of simulated contrails, (3) IR image with simulated contrail IR brightness temperature.

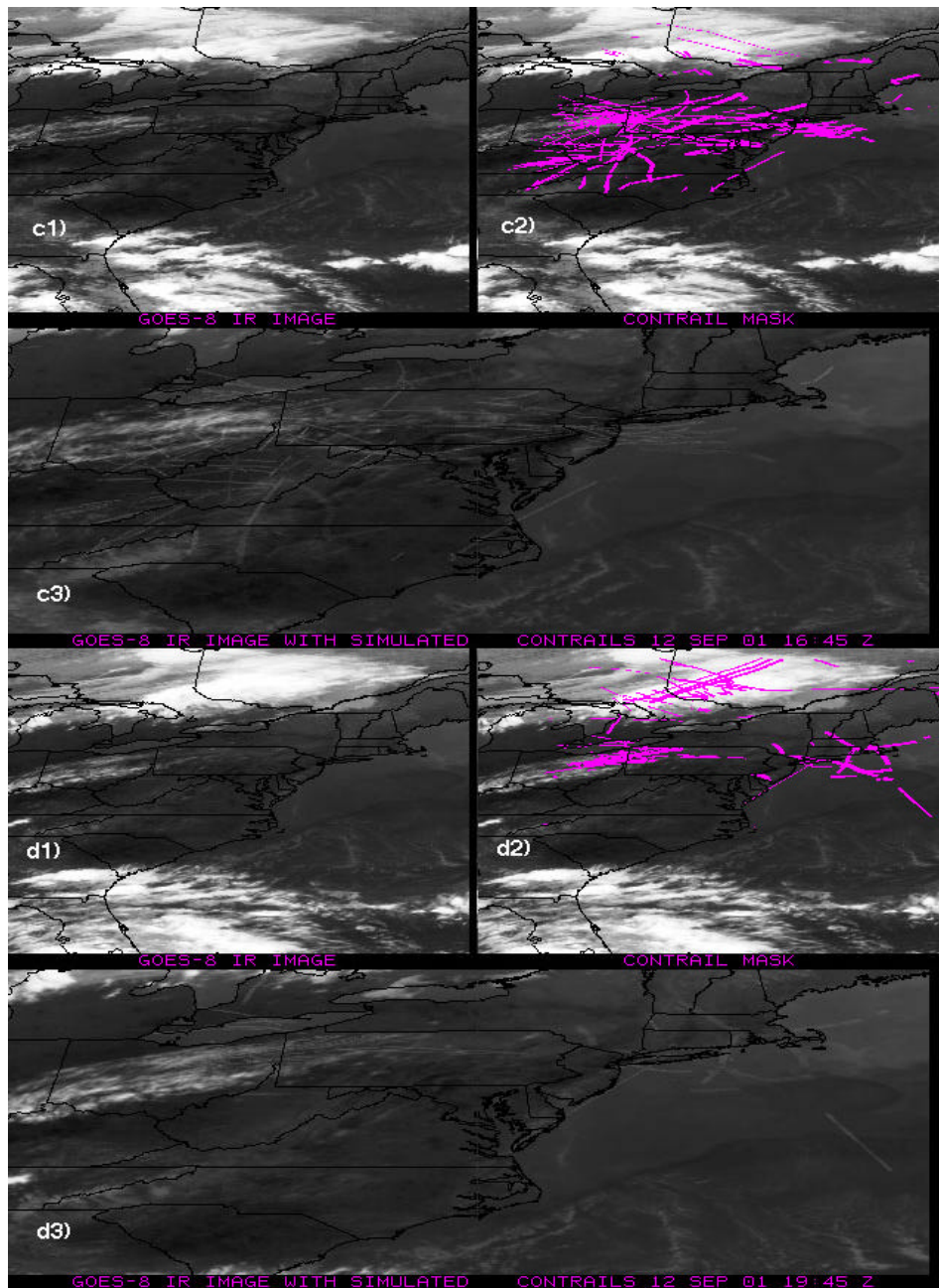


Figure 4 continued. (c) 1645 UTC and (d) 1945 UTC.

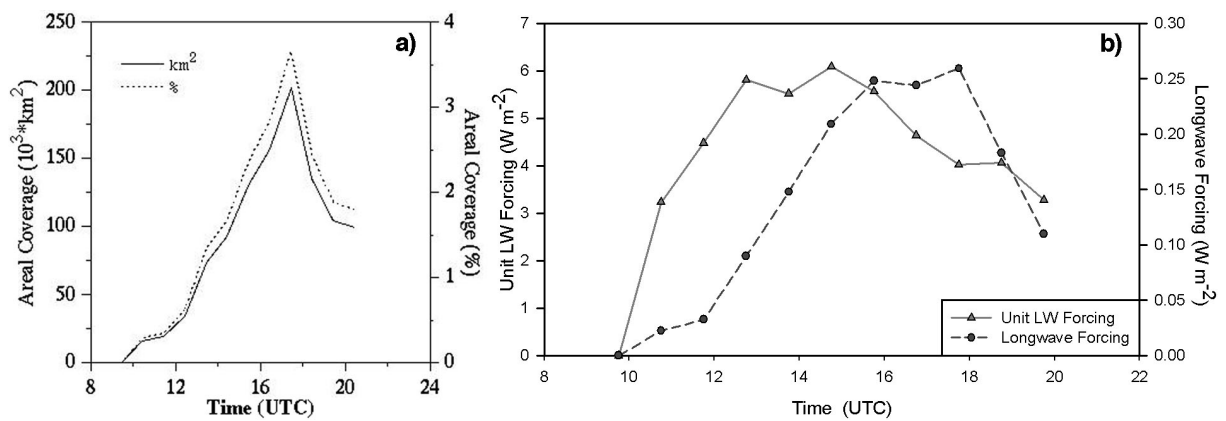


Figure 5. Simulated contrail effects over northeastern USA, 12 September 2001. (a) contrail coverage. (b) contrail longwave radiative forcing.

4 CONCLUDING REMARKS

This initial simulation during the air traffic shutdown, in general, appears to produce realistic contrails. They form in areas where the military contrails persist and are similar in appearance. They also dissipate in areas free of natural cirrus clouds. The analysis confirms the existence of large areas of clear, ice-supersaturated air that are available for additional cirrus formation. The simulations demonstrate that a huge area of contrails would have formed over the northeastern USA if air traffic was normal. This result may help explain of the temperature anomaly found over the same area. With the projected improvements, this simulation should help improve the prediction of contrail formation conditions and contrail lifetimes, and eventually aid the development of reliable predictions of future air traffic effects.

REFERENCES

- Benjamin, S. A., G. A. Grell, J. M. Brown, T. G. Smirnova, and R. Bleck, 2003: Mesoscale weather prediction with the RUC hybrid isentropic / terrain-following coordinate model. *Mon Wea. Rev.*, accepted.
- Duda, D. P., P. Minnis, P. K. Costulis, and R. Palikonda, 2003: CONUS contrail frequency estimated from RUC and flight track data. *Proc. European Conf. Aviation, Atmosphere, and Climate*, Friedrichshafen at Lake Constance, Germany, June 30 - July 3.
- Duda, D. P., P. Minnis, L. Nguyen, and R. Palikonda, 2003: A case study of contrail evolution over the Great Lakes. *J. Atmos. Sci.*, In press.
- Garber, D. P., P. Minnis, and P. K. Costulis, 2003: A USA commercial flight track database for upper tropospheric aircraft emission studies. *Proc. European Conf. Aviation, Atmosphere, and Climate*, Friedrichshafen at Lake Constance, Germany, June 30 - July 3.
- Miloshevich, L. M., H. Vömel, A. Paukkunen, A. J. Heymsfield, and S. J. Oltmans, 2001: Characterization and correction of relative humidity measurements from Vaisala RS80-A radiosondes at cold temperatures. *J. Atmos. Oceanic Technol.* **18**, 135-156.
- Minnis, P. and W. L. Smith, Jr., 1998: Cloud and radiative fields derived from GOES-8 during SUCCESS and the ARM-UAV Spring 1996 Flight Series. *Geophys. Res. Lett.*, **25**, 1113-1116.
- Minnis, P., Y. Takano, and K.-N. Liou, 1993: Inference of cirrus cloud properties using satellite-observed visible and infrared radiances, Part I: Parameterization of radiance fields. *J. Atmos. Sci.*, **50**, 1279-1304.
- Minnis, P., L. Nguyen, D. P. Duda, and R. Palikonda, 2002: Spreading of isolated contrails during the 2001 air traffic shutdown. *10th AMS Conf. Aviation, range, and Aerospace Meteorol.*, Portland, OR, May 13-16, 33-36.
- Palikonda, R., D. N. Phan, V. Chakrapani, and P. Minnis, 2003: Contrail coverage over the USA from MODIS and AVHRR data. *Proc. European Conf. Aviation, Atmosphere, and Climate*, Friedrichshafen at Lake Constance, Germany, June 30 - July 3.
- Travis, D., A. Carleton, and R. Lauritsen, 2002: Contrails reduce daily temperature range. *Nature*, **418**, 601.

CONUS Contrail Frequency Estimated from RUC and Flight Track Data

D. P. Duda*

Hampton University, Hampton, VA USA

P. Minnis, P. K. Costulis

Atmospheric Sciences, NASA Langley Research Center, Hampton, VA USA

R. Palikonda

Analytical Services and Materials, Inc., Hampton, VA USA

Keywords: air traffic, contrail coverage

ABSTRACT: Estimates of contrail frequency and coverage over the continental United States (CONUS) are developed using hourly meteorological analyses from the Rapid Update Cycle (RUC) numerical weather prediction model and commercial air traffic data from FlyteTrax. The potential contrail frequency over the CONUS is computed directly from RUC analyses using a modified form of the classical Appleman criteria for persistent contrail formation. The potential contrail frequency is adjusted to account for the occurrence of thick cloudiness in possible regions of persistent contrail formation. The air traffic density data is then combined with the potential contrail frequency to estimate the expected contrail coverage. This estimate is compared with a direct satellite estimate of contrail coverage based on an empirical contrail detection algorithm.

1 INTRODUCTION

Contrails can affect the global atmospheric radiation budget by increasing planetary albedo and reducing infrared emission. Our current knowledge of the magnitude of these effects is extremely uncertain; two recent estimates of global linear contrail radiative forcing (Minnis et al., 1999; Ponater et al., 2002) differ by nearly two orders of magnitude. Global radiative forcing is difficult to estimate since it depends on several poorly known factors including the global mean contrail coverage. Current theoretical estimates of global contrail coverage (Sausen et al., 1998; Ponater et al., 2002) are tuned to early estimates of linear contrail coverage determined visually from infrared satellite imagery over the North Atlantic and central Europe (Bakan et al., 1994). The estimates differ based on the parameterization used to diagnose contrails and the numerical weather analyses employed to determine the ambient conditions. Recent estimates of contrail coverage over these areas from an objective detection algorithm (Mannstein et al., 1999; Meyer et al., 2002) are significantly smaller than those given by Bakan et al. (1994). Additionally, a comparison of the empirical contrail coverage of Sausen et al. (1998) with contrail coverage analyses of Advanced Very High Resolution Radiometer (AVHRR) data taken over the continental United States (CONUS) (Palikonda et al., 1999) show they compare well in overall magnitude of coverage, but differ in spatial distribution. These results illustrate the current uncertainty in contrail coverage estimation, a key component in the determination of contrail climate effects.

Development of reliable methods for diagnosing persistent contrails and their physical and radiative properties from numerical weather analyses is essential for predicting future contrail climate impacts. Because air traffic is expected to grow by 2 to 5% annually (Minnis et al., 1999), it is becoming more important to estimate contrail coverage accurately.

To address this concern, we use actual flight data and coincident meteorological data to compute an estimate of contrail coverage over the CONUS. This estimate is compared with a satellite retrieval of contrail coverage based on an objective contrail detection algorithm.

*Corresponding author: David P. Duda, NASA Langley Research Center, Mail Stop 420, Hampton, VA 23681-2199 USA. Email: d.p.duda@larc.nasa.gov

2 DATA

2.1 Air traffic data

Commercial air traffic data from the FlyteTrax product (FT; FlyteComm, Inc., San Jose, CA) as compiled by Garber et al. (2003) were used to determine air traffic density over the continental United States during September 2001 and November 2001. The database consists of 2 or 5-minute readings of aircraft (flight number, aircraft type), position (latitude, longitude, altitude), and heading for every non-military flight over the USA and a portion of Canada, including related transoceanic flights. Although the FT database does not include military flights, it contains most of the air traffic over the CONUS. Air traffic densities were tabulated on a $1^\circ \times 1^\circ$ grid that extends from 20°N to 50°N in latitude, and from 135°W to 60°W in longitude.

2.2 Meteorological data

Atmospheric profiles of temperature and humidity were derived from the 40-km resolution, 1-hourly Rapid Update Cycle (RUC) analyses (Benjamin et al., 1998) in 25-hPa intervals from 400 hPa to 150 hPa. The RUC data were linearly interpolated at each pressure level to a $1^\circ \times 1^\circ$ grid that extends from 25°N to 56°N in latitude, and from 129°W to 67°W in longitude.

The RUC analyses at 00 UTC and 12 UTC were not used in this study to insure that the humidity fields for each hour were consistent. Before February 2002, a “quick-look” version of the 00 UTC and 12 UTC analyses was used. This version of the analysis does not include all available radiosonde data, and is noticeably drier in the upper troposphere than the analyses from other hours.

A major revision to the operational RUC model was implemented on 17 April 2002. The RUC20 model with 20-km horizontal resolution replaced the RUC40 model with 40-km horizontal resolution. The primary motivation for changes in the RUC model was improved quantitative precipitation forecasts. As a result, several changes in the way the model handles upper tropospheric moisture were added, including a more sharply defined tropopause, and the removal of most ice supersaturations for pressure levels less than 300 hPa (Benjamin et al., 2002).

The effect of these changes was to make the upper troposphere drier than in the RUC40. Thus, the relative humidity thresholds used to make the contrail diagnoses had to be changed for the RUC20. A serendipitous discovery of nearly simultaneous RUC20 (19 UTC) and RUC40 (20 UTC) model analyses from 26 May 2002 was used to relate the RUC20 humidity data to the older RUC40 data. The relative humidities with respect to ice (RHI) from the RUC20 analyses were adjusted based a level-by-level comparison of the mean RHI computed from the RUC20 and RUC40 data.

2.3 Satellite data

The satellite datasets for deriving contrail and cloud coverage consist of infrared radiances from the Sun-synchronous *NOAA-16* AVHRR 1-km imager (10.8 and 12.0 μm) and multispectral 1-km data from the MODERate Resolution Imaging Spectroradiometer (MODIS) on the *Terra* satellite. Half-hourly infrared data from the Geostationary Operational Environmental Satellite (*GOES* 8) imager (4-km resolution, 10.8 and 12.0 μm) was also used for tracking contrails over the continental US.

3 METHOD

Persistent contrail formation was computed according to the classical criteria of Appleman (1953) using the RUC profiles of temperature and humidity. The contrail formation algorithm follows Schrader (1997), modified with the aircraft propulsion efficiency parameter (η) of Busen and Schumann (1995). The mean value of the propulsion efficiency assumed for the present commercial fleet was 0.30 (Sausen et al., 1998). The saturation vapor pressure coefficients of Alduchov and Eskridge [1996, AERW(50,-80) and AERWi(0,-80)] were used to compute saturation vapor pressure over water and ice.

According to classical contrail formation theory, contrails can persist when the ambient air is supersaturated with respect to ice (that is, the environmental RHI is greater than 100 percent), but not with respect to water. In Sausen et al. (1998), the use of ECMWF reanalysis data required a contrail parameterization to compute persistent contrail coverage since the RHI in the ECMWF

model rarely exceed 100 percent. The RUC model contains a sophisticated cloud and moisture scheme that allows for ice-supersaturation. Assuming that the RUC upper tropospheric moisture variables are accurate, we can follow a much simpler statistical evaluation of potential persistent contrail frequency. For each $1^\circ \times 1^\circ$ grid location where the criterion for persistent contrails occurs at any level from 400 hPa to 150 hPa, a persistence indicator is given a value of 1 for each hourly analysis. The indicator equals zero when none of the levels satisfies the persistence criterion. The potential contrail frequency (PCF) over a time period becomes simply the frequency of occurrence of the persistence indicator at a particular location.

To compute the actual contrail coverage, the PCF must be multiplied by the air traffic density. For an initial estimate, we will assume that the air traffic density is sparse enough to relate contrail fractional coverage to traffic density linearly. An unknown quantity is the mean fractional persistent contrail coverage within an area resulting from a single flight track (c_{ft}). In this study c_{ft} was tuned so that the US mean contrail coverage would match monthly satellite-based contrail coverage estimates (Palikonda et al., 2003). The value of c_{ft} varied by only 5 percent between September 2001 (5.86×10^{-5}) and November 2001 (5.57×10^{-5}). Since the mean area of a $1^\circ \times 1^\circ$ grid cell in the midlatitudes is approximately $10,000 \text{ km}^2$, the mean coverage from a single flight track within a grid cell would be about 0.6 km^2 . No overlap of the contrails is assumed because the coverage is tuned to a satellite estimate and contrail altitude is not considered in this study. The total persistent contrail coverage (c_{sum}) in a grid cell is simply

$$c_{sum} = P \times c_{ft} \times n \quad (1)$$

where P is the potential contrail frequency, c_{ft} is the mean fractional persistent contrail coverage within a grid cell from a single flight track, and n is the total number of flight tracks within a grid cell. To account for the effects of natural cloudiness obscuring the detection of contrails, the persistence indicator used in the computation of PCF was set to zero whenever a grid box was more than 50 percent covered by high cloud.

4 RESULTS AND DISCUSSION

4.1 Potential contrail frequency

Figures 1 and 2 present the potential contrail frequency computed for September 2001 and November 2001 respectively. RUC analyses were available for only 26 of 30 possible days during each month. In both figures, the region with the highest PCF was the Pacific Northwest, where values reach 0.33 in September and 0.50 in November. Another region of high frequency in November is the eastern Midwest portion of the US. The overall distribution and the magnitude of potential contrail frequency changed dramatically as a result of changes in the synoptic-scale weather patterns between September and November. The mean PCF for grid points over the continental US was 0.118 in September and increased to 0.272 in November.

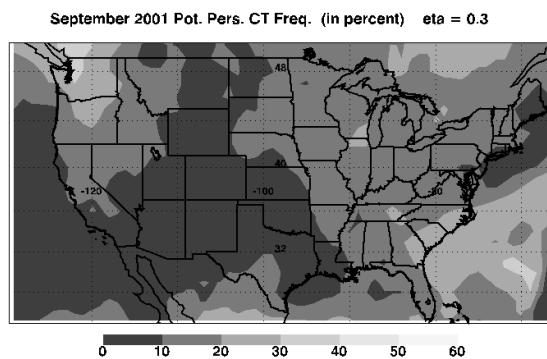


Figure 1: Potential persistent contrail frequency computed from RUC analyses for September 2001.

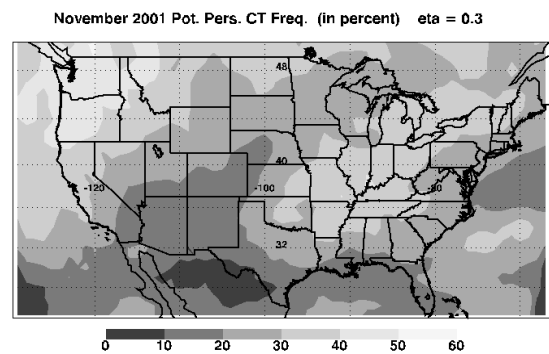


Figure 2: Potential persistent contrail frequency computed from RUC analyses for November 2001.

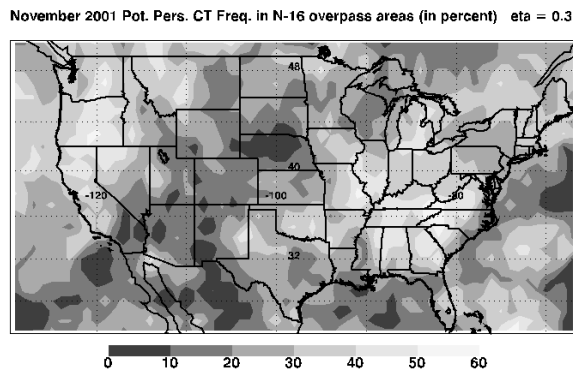


Figure 3. Potential persistent contrail frequency computed from RUC analyses during available RUC afternoon overpass times for November 2001.

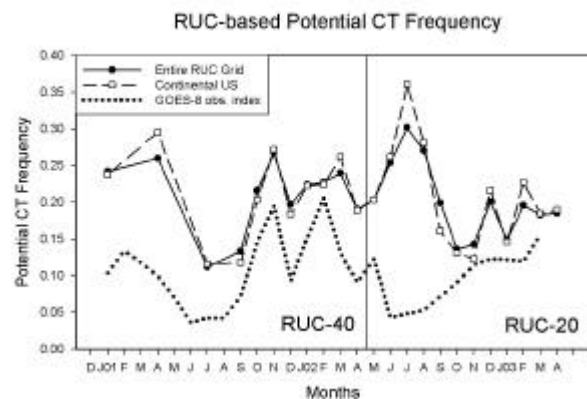


Figure 4. Time series of potential contrail frequency computed from RUC analyses between December 2000 and April 2003. The solid line is the frequency computed for all RUC grid points, while the dashed line only includes grid points over the CONUS. The dotted line indicates the *GOES-8* observation index.

Figure 3 presents the PCF computed for November 2001 during 54 afternoon overpasses of the *NOAA-16* satellite. To approximate the satellite coverage in the calculation of the contrail frequencies, only grid points within ± 12 degrees of longitude of the sub-satellite point at 37°N were counted during each overpass. Although the mean potential contrail frequency computed for the CONUS region was almost identical to the monthly average (0.269), the distribution of PCF shows much more variability due to the limited sample size.

To check the quality of the RUC-based potential contrail frequencies, they were compared to a daily, manual analysis of CONUS contrail coverage based on 4-km *GOES-8* imagery. The $10.8\ \mu\text{m}$ minus $12.0\ \mu\text{m}$ brightness temperature difference images between 1045 UTC and 0045 UTC were examined for the occurrence of contrails within each state of the US. For each day of the analysis, a persistence indicator value of 1 was given for each state in which at least one contrail appeared. The contrail frequency for each state is simply the percentage of the total analysed days with contrail occurrence. The mean of the contrail frequency for all states in the CONUS region was defined as the observation index. The comparison is shown in Figure 4.

As expected, the contrail frequencies computed from the RUC model are higher than the observation index since the index is based on observations of 4-km resolution data that miss narrow contrails. In addition, any satellite-based estimate is affected by obscuration by natural clouds. Both the potential contrail frequencies and the observation index show a similar seasonal cycle except for the summer months of 2002 when the RUC20 model data was used. The overestimate in potential contrail frequency during this period is likely the result of differences in the convective parameterization between the RUC40 and the RUC20.

4.2 Contrail coverage

Figure 5 shows a plot of persistent contrail coverage c_{sum} (assuming contrail coverage is proportional to air traffic density) computed for November 2001. The contrail coverage is heavily influenced by the air traffic density pattern, and is similar in appearance to Sausen et al. (1998), with a maximum of more than 0.03 in the eastern half of the CONUS, and relatively little coverage in the northern Great Plains. The mean theoretical contrail coverage for the CONUS is 0.0092. In high air traffic regions, however, contrail coverage may not be linearly related to air traffic density due to “saturation” effects (i.e. competition for moisture or overlapping of contrails in air traffic corridors may limit the number of linear contrails that are visible by satellite). If a square-root relation between coverage and air traffic is assumed, the contrail coverage is less dependent on air traffic density (Figure 6). High cloud coverage (cloud tops $> 5\ \text{km}$) for November 2001 (see Figure 7) was derived from *Terra* MODIS multispectral observations (Minnis et al., 2002), and was used in the estimate of c_{sum} to account for the effects of natural cloudiness obscuring the detection of contrails.

The satellite-based CONUS contrail coverage estimates for September and November 2001 (Palikonda et al., 2003) used NOAA AVHRR data and an objective contrail detection algorithm (Mannstein et al., 1999) to compute contrail coverage. The results from both September (not shown) and November (Figure 8) suggest that the contrail coverage may be more dependent on the potential contrail coverage (in other words, the environmental conditions) than the estimates in Figures 5 and 6 suggest. Several unresolved factors may account for this difference. These factors include the likelihood that contrail coverage is non-linearly related to air traffic density, and the contrail coverage saturates in high traffic areas. Also, the current analysis neglects the advection of contrails and assumes that the RUC40 analyses provide an accurate characterization of the upper tropospheric temperature and moisture fields over the entire domain.

November 2001 SIMULATED Pers. CT Coverage from N-16 (in percent) $\eta = 0.3$
(LINEAR relation between coverage and air traffic)

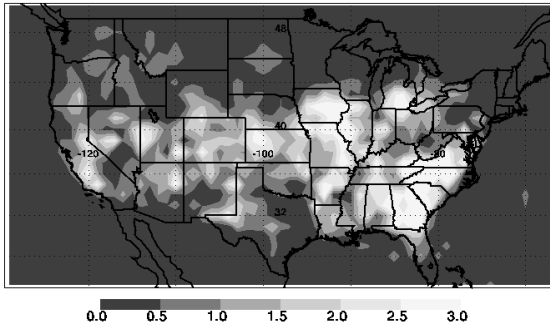


Figure 5: Persistent contrail coverage computed for November 2001 assuming linear relationship between contrail coverage and air traffic density.

November 2001 SIMULATED Pers. CT Coverage from N-16 (in percent) $\eta = 0.3$
(SQUARE ROOT relation between coverage and air traffic)

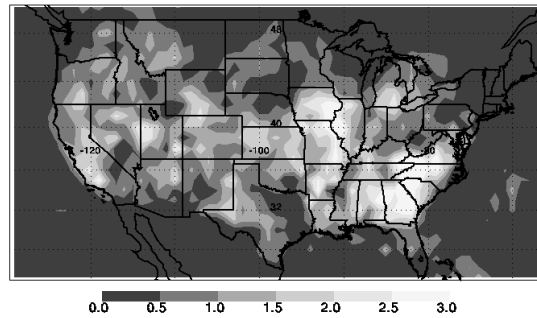


Figure 6: Persistent contrail coverage computed for November 2001 assuming square root relationship between contrail coverage and air traffic density.

November 2001 High Cloud Coverage from Terra (in percent)

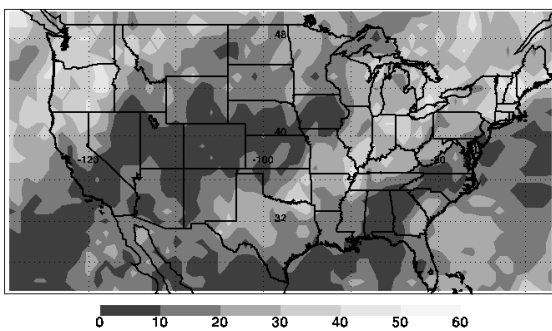


Figure 7. Cloud coverage above 5 km computed from *Terra* morning overpass measurements.

NOAA-16 derived CT coverage for November 2001 (in percent)

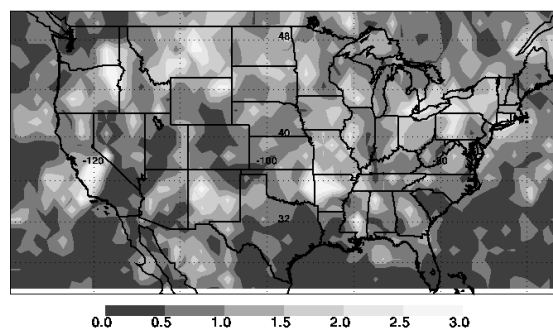


Figure 8. Contrail coverage computed from *NOAA-16* afternoon overpasses for November 2001 using an objective analysis.

5 CONCLUSIONS AND FUTURE WORK

The simulated persistent contrail coverage presented here is heavily influenced by the air traffic pattern, similar to earlier studies. The contrail coverage computed from *NOAA-16* imagery, however, is more closely related to the potential contrail frequency (and high cloud coverage) than air traffic density. Thus, the coverage of *line-shaped* contrails is non-linearly related to air traffic, and “saturation” effects are important in high traffic areas. Additional tuning and testing of the contrail coverage estimates is in progress. More work is necessary to compare satellite-based estimates of contrail coverage with potential coverage diagnosed from RUC analyses. The effects of flight altitude, synoptic-scale vertical motions, contrail advection, and RUC uncertainties have not been included in this study. More *NOAA-16* data must be analysed since a sample size of one or two months is still too small. The results from other satellite platforms such as *NOAA-17* (with a

crossover time approximately 4 hours before NOAA-I6) would help determine whether the relation between contrail coverage and air traffic changes throughout the day.

REFERENCES

- Alduchov, O. A., and R. E. Eskridge, 1996: Improved Magnus form approximation of saturation vapor pressure. *J. Appl. Meteor.* 35, 601–609.
- Appleman, H., 1953: The formation of exhaust condensation trails by jet aircraft. *Bull. Amer. Meteor. Soc.* 34, 14–20.
- Bakan, S., M. Betancor, V. Gayler, and H. Grassl, 1994: Contrail frequency over Europe from NOAA-satellite images. *Ann. Geophys.* 12, 962–968.
- Benjamin, S. G., J. M. Brown, K. J. Brundage, B. E. Schwartz, T. G. Smirnova, and T. L. Smith, 1998: The operational RUC-2. In: *Preprints, 16th AMS Conference on Weather Analysis and Forecasting*, Phoenix, AZ. American Meteorological Society, Boston, USA, pp. 249–252.
- Benjamin, S. G., J. M. Brown, K. J. Brundage, D. Dévényi, G. A. Grell, D. Kim, B. E. Schwartz, T. G. Smirnova, T. L. Smith, S. S. Weygandt, and G. S. Manikin, 2002: RUC20 – The 20-km version of the Rapid Update Cycle. *NWS Technical Procedures Bulletin No. 490*.
- Busen, R., and U. Schumann, 1995: Visible contrail formation from fuels with different sulfur contents. *Geophys. Res. Lett.* 22, 1357–1360.
- Garber, D. P., P. Minnis, and K. P. Costulis, 2003: A USA commercial flight track database for upper tropospheric aircraft emission studies. In: *Proceedings of the European Conference on Aviation, Atmosphere, and Climate*, June 30 - July 3, 2003, Friederichshafen at Lake Constance, Germany.
- Mannstein, H., R. Meyer, and P. Wendling, 1999: Operational detection of contrails from NOAA-AVHRR-data. *Int. J. Remote Sensing* 20, 1641–1660.
- Meyer, R., H. Mannstein, R. Meerkötter, U. Schumann, and P. Wendling, 2002: Regional radiative forcing by line-shaped contrails derived from satellite data. *J. Geophys. Res.* 107 (D10), doi: 10.1029/2001JD000426, 31 May 2002.
- Minnis, P., U. Schumann, D. R. Doelling, K. M. Gierens, and D. W. Fahey, 1999: Global distribution of contrail radiative forcing. *Geophys. Res. Lett.* 26, 1853–1856.
- Minnis, P., D. F. Young, B. A. Wielicki, D. P. Kratz, P. W. Heck, S. Sun-Mack, Q. Z. Trepte, Y. Chen, S. L. Gibson, R. R. Brown, 2002: Seasonal and diurnal variations of cloud properties derived for CERES from VIRS and MODIS data. In: *Proceedings of the 11th AMS Conference on Atmospheric Radiation*, June 3 - 7, 2002, Ogden, Utah, USA, pp.20–23.
- Palikonda, R., P. Minnis, D. R. Doelling, P. W. Heck, D. P. Duda, H. Mannstein and U. Schumann, 1999: Potential radiative impact of contrail coverage over continental USA estimated from AVHRR data. In: *Preprints, 10th AMS Conference on Atmospheric Radiation*, June 28–July 2, 1999, Madison, Wisconsin. American Meteorological Society, Boston, USA, pp. 181–184.
- Palikonda, R., D. N. Phan, and P. Minnis, 2003: Contrail coverage over the USA derived from MODIS and AVHRR data. In: *Proceedings of the European Conference on Aviation, Atmosphere, and Climate*, June 30 - July 3, 2003, Friederichshafen at Lake Constance, Germany.
- Ponater, M., S. Marquart, and R. Sausen, 2002: Contrails in a comprehensive global climate model: Parameterization and radiative forcing results. *J. Geophys. Res.* 107, 10.1029/2001JD000429, 3 July 2002.
- Sausen, R., K. Gierens, M. Ponater, and U. Schumann, 1998: A diagnostic study of the global distribution of contrails. Part I: Present day climate. *Theor. Appl. Climatol.* 61, 127–141.
- Schrader, M. L., 1997: Calculations of aircraft contrail formation critical temperatures. *J. Appl. Meteor.* 36, 1725–1729.

Contrail Coverage Derived from UARS MLS Measurements

M.Y. Danilin*, S.L. Baughcum
The Boeing Company, Seattle, Washington, USA

W.G. Read
NASA JPL, Pasadena, California, USA

Keywords: contrails, satellite measurements

ABSTRACT: We use Upper Atmosphere Research Satellite (UARS) Microwave Limb Sounder (MLS) measurements of relative humidity above ice (RHI) during 1991-1997 and the NASA 1992 air traffic scenario for deriving global contrail coverage. Additionally, we perform sensitivity studies of our results to subgrid processes and higher propulsion efficiency of future aircraft. We found that while our results are reasonably consistent with previously published model calculations and measurements, there are several poorly justified tuning parameters in contrail calculations and limitations of the MLS measurements used. Better RHI data sets near the tropopause and additional work is required in order to improve estimates of contrail coverage and optical properties.

1 INTRODUCTION

Condensation trails (contrails) are formed when hot and humid aircraft exhaust is mixed with cold and dry ambient air (Appleman, 1953). Contrails are the most uncertain aspect of the aviation impact on the atmosphere contributing to the climate change (IPCC, 1999). Indeed, uncertainties of direct radiative forcing (RF) by contrails are at least several times larger than those caused by aircraft CO₂ emissions, while indirect effects of contrails (i.e. via change of cloudiness) are even more uncertain (IPCC, 1999). Contrail RF on the global scale depends on their coverage and optical properties. Since only long-lived contrails, which persist at ice-supersaturated conditions, are important for climate change, high fidelity RHI measurements with good vertical and horizontal resolution over the globe are required for these calculations. Unfortunately, such an RHI data set does not exist yet. Usually, assimilated RHI values from the European Centre for Medium Weather Forecast (ECMFW) (Sausen et al., 1998) or ECHAM4 GCM calculations (Ponater et al., 2002) are used for contrail analysis. However, water vapor (H₂O) and temperature (T) (which are used to derive RHI) in the ECHAM4 GCM deviate from those observed in the real atmosphere (Marquart et al., 2003), thus introducing poorly quantified errors in contrail calculations. In order to avoid the use of potentially incorrect H₂O and T, we decided to use MLS measurements of RHI for our contrail calculations. We focus our paper on calculations of global contrail coverage only and perform several sensitivity studies of our results to parameters and assumptions used in our calculations.

2 DATA USED

The UARS MLS instrument retrieves humidity near the tropopause by using the 203 GHz radiometer (Read et al., 2001). MLS provides 1318 profiles daily with a vertical resolution of approximately 3 km and horizontal resolution of 100 km x 200 km covering the latitude band from 80°S to 80°N. We utilize MLS version 4.9 level 2 RHI data spanning the time period from October 1991 to October 1997 at the 316, 215, and 147 hPa pressure levels. We ignored MLS individual profiles with negative uncertainty and values larger than 230% following the recommendations of Read et al. (2001). In our analysis we used MLS measurements grouped in a 2°x2° resolution in January, March, July, and October, which provides 112,000-141,000 individual profiles for each

* *Corresponding author:* Dr. Mikhail Y. Danilin, The Boeing Company, MS 02-XL, P.O. Box 3707, Seattle, WA 98124-3707, USA. Email: Mikhail.Y.Danilin@boeing.com.

month. Since contrail evolution is a non-linear function of RHI, we calculated the RHI probability distribution (instead of RHI mean value) for each grid box for our contrail coverage calculations described below.

We used scheduled civil aircraft inventory for 1992 (Baughcum et al., 1996) using the distance flown as a measure of air traffic. The scheduled aviation flew about 9.5×10^9 nautical miles in 1992 with most intensive traffic in the Northern hemisphere (93% of all traffic).

3 ESTIMATING CONTRAIL COVERAGE

Our analysis is focused on long-lived contrails, which persist at ambient conditions with $\text{RHI} \geq 100\%$ and may affect climate. The following steps were made for estimating contrail coverage:

- 1) We checked that a contrail is formed at each grid box using the RHI probability distribution and assuming an overall propulsion efficiency of 0.3 (Schumann, 2000).
- 2) We calculated the contrail probability distribution at each level and each grid following the methodology of Ponater et al. (2002), using the threshold values for contrail and cirrus cloud formation of 50% and 70% for our baseline case. These reduced (i.e., $<100\%$) values are used in order to account for subgrid processes, since it is quite likely that there are small scale ice-supersaturated regions in a $100 \text{ km} \times 200 \text{ km} \times 3 \text{ km}$ MLS retrieval volume even at $\text{RHI} < 100\%$. The values of 50% and 70% used in our baseline case are somewhat arbitrary and we performed a sensitivity run with 95% and 90%.
- 3) Since the number of contrails is proportional to air traffic, at the next step we calculate contrail coverage in each grid box as a product of the contrail probability and number of flight miles.
- 4) We determine vertically integrated contrail coverage assuming a random overlap of contrails at individual levels (Sausen et al., 1998).
- 5) In order to make our calculations consistent with contrail coverage measurements over Europe (Bakan et al., 1994), we normalize the calculated visible contrail coverage field to the value of 0.375% over the region between 35°N - 75°N and 30°W and 30°E .

We considered contrails visible if their optical thickness $t > 0.02$. Calculating t , we assumed that:

- a) the vertical depth of contrails was 100 m (Ponater et al., 2002),
- b) their effective radius depends on ambient temperature and H_2O and is determined according to Lohmann and Kärcher (2002), and
- c) optical thickness was derived according to Ebert and Curry (1992).

Our calculations predict that visible contrails account for 80-85% of all contrails.

4 RESULTS AND DISCUSSION

Figure 1 shows the fractional coverage by contrails in a model grid as a function of RHI for the threshold values of contrail RHI_{co} and cirrus cloud formation RHI_{cl} of 50% and 70% (panel a) and 90% and 95% (panel b), respectively. The choice of these threshold values is somewhat arbitrary and our intention is to compare our results with those in Ponater et al. (2002). We applied equations (3) and (10) from Ponater et al. (2002) in deriving results shown in Figure 1. Panel (a) is used as our baseline case, while panel (b) is applied for our sensitivity analysis of the subgrid processes on contrail coverage. The areas under the contrail curves are quite different in these cases and we expect that this fact will affect our contrail coverage results as well.

Figure 2 depicts the geographical distribution of total contrail coverage in July for the RHI_{co} and RHI_{cl} values used in Figure 1. For the baseline case shown in the left panel, maximum contrail coverage is obtained over the regions with the most intensive air traffic, such as the United States, Europe and Japan. When we increased the RHI_{co} and RHI_{cl} values to 95% and 90%, respectively, and kept the contrail coverage equal to 0.375% over Europe (shown by a black rectangle) according to Bakan et al. (1994), the pattern of contrail coverage became more spotty. This behaviour may be understood as follows: for the small values of RHI_{co} and RHI_{cl} , the fractional coverage by contrails is a relatively broad function of RHI (see Figure 1), hence the pattern of contrails formed under broader atmospheric conditions and their coverage is similar to the air traffic pattern; while for high values of RHI_{co} and RHI_{cl} , the contrail coverage is determined by the geographical patterns of high

RHI in the ambient atmosphere. In order to better quantify the difference between these two runs, we show the results for visible contrail coverage in Table 1. To summarize, lack of knowledge about subgrid processes makes contrail calculations quite uncertain for some regions, such as Japan, where difference can easily be as large as a factor of 1.5.

Figure 1. Fractional coverage of contrail and cloud in a grid box as a function of RHI for the threshold values shown.

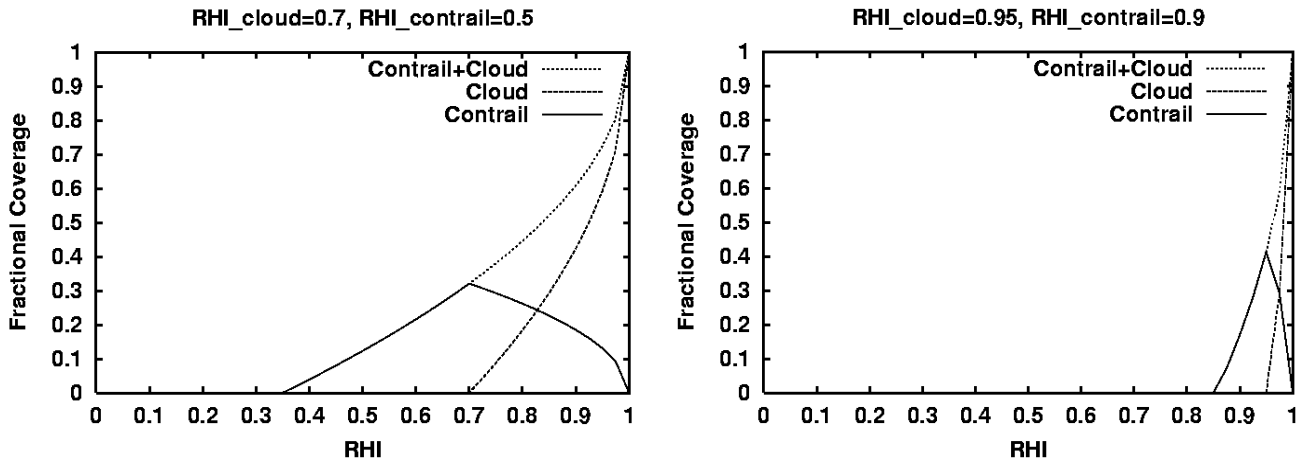


Table 1 compares our results for different sensitivity studies with available measurements. Overall, our baseline case calculations (third column) agree within 20%-40% with the observations at mid-latitudes. The largest discrepancies are obtained for the Thailand and Japan regions. It is possible that normalization of our results to the Bakan et al. (1994) data over Europe does not work in these regions. Indeed, this conventional way to normalize contrail coverage (Sausen et al., 1998; Ponater et al., 2002) implies that the probability distributions and uncertainties of RHI over Europe are the same for all other parts of the world regardless of local meteorology. This assumption is not very good, thus stimulating scientists to find a better way to account for available measurements in future contrail coverage calculations.

The fourth column of Table 1 depicts relatively high sensitivity of the contrail coverage to our representation of subgrid processes (i.e., $RHI_{cl}=95\%$ and $RHI_{co}=90\%$), particularly over USA and Japan. Obviously, results for Western Europe were little changed, since normalization over Europe remained intact.

The right column of Table 1 shows that the derived contrail coverage is not very sensitive to the vertical interpolation of MLS data from its 3 km vertical resolution to a 1 km vertical resolution of the air traffic scenario. In all of our previous cases, we linearly interpolated MLS RHI data, while in this last case we first linearly interpolated MLS H_2O and T values and then calculated RHI for the interpolated values of H_2O and T. The RHI_{co} and RHI_{cl} values of 50% and 70% were used in this case.

Future aircraft engines will have a higher propulsion efficiency (i.e., larger fraction of the fuel energy will be used to propel an airplane) (Schumann, 2000). Since the increased propulsion efficiency facilitates contrail formation, it is important to estimate its effect on contrail coverage. Figure 3 shows the increase of contrail coverage at two individual levels of the most intensive traffic at 10.5 and 11.5 km when propulsion efficiency is increased from 0.3 to 0.4. We found a tiny effect of the order of 0.01-0.02% over USA and Europe with even smaller effect in a vertically integrated contrail coverage. Thus, our results show that current atmospheric conditions are far from the threshold conditions for contrail formation and confirm a similar conclusion by Sausen et al. (1998).

Table 1. Annual visible contrail coverage (in %) according to the observations and our calculations with different threshold values and when vertical interpolation of MLS RHI measurements is used. The regions shown are defined as follows: USA (25°N-55°N, 130°W-65°W), Western Europe (40°N-55°N, 10°W-20°E), Japan (30°N-48°N, 126°E-148°E), and Thailand (0°N-25°N, 90°E-120°E). Observations for USA, Western Europe, Japan, and Thailand are based on (Minnis et al., 2003), (Meyer et al., 2002), (Meyer et al., 2003), and (Meyer et al., 2003), respectively.

Regions	Observations	70%, 50%	95%, 90%	MLS Interpolation
USA	1.24	0.95	1.26	1.00
Western Europe	0.82	1.11	1.20	1.13
Japan	0.25	0.40	0.63	0.49
Thailand	0.13	0.28	0.24	0.33
World	-	0.09	0.11	0.09

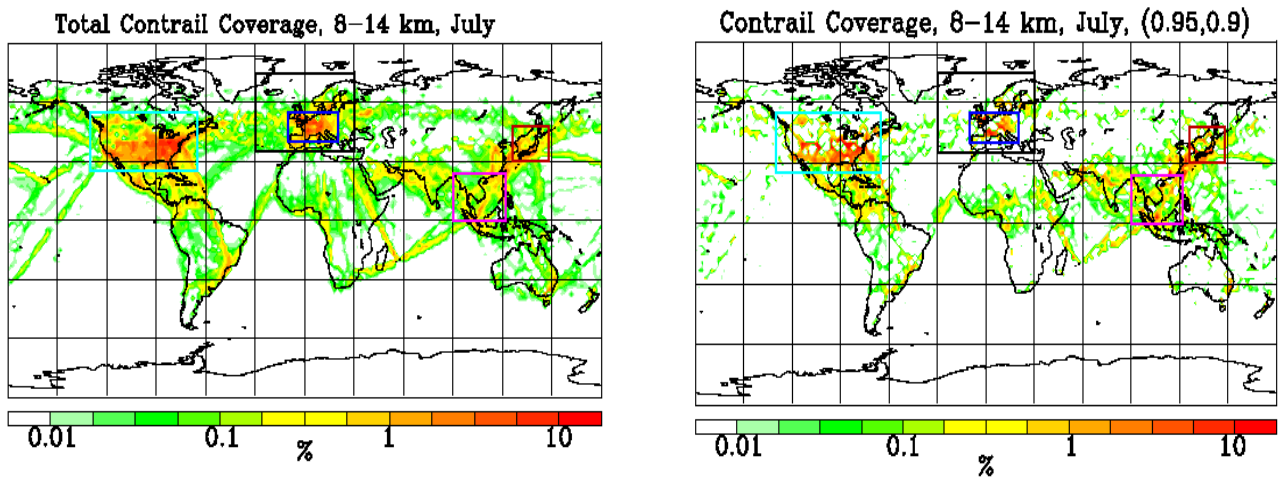


Figure 2. Contrail coverage in July for the RHI_{co} and RHI_{cl} values of 50% and 70% (left panel) and 90% and 95% (right panel), respectively.

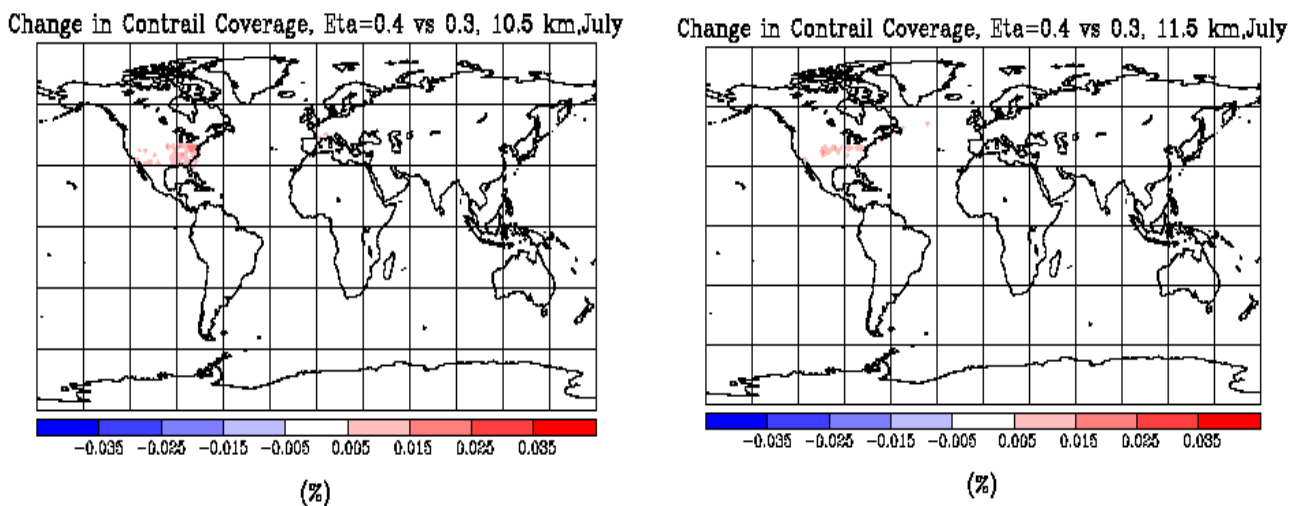


Figure 3. Change in contrail coverage (in %) at flight altitudes of 10-11 km and 11-12 km when the aircraft engine propulsion efficiency increased from 0.3 to 0.4.

5 SUMMARY

We estimated contrail coverage using for the first time UARS MLS measurements of RHI and the 1992 NASA air traffic scenario. Our major findings are:

- 1) Global and annually averaged visible contrail coverage is calculated to be 0.09% in our baseline case with the contrail and cirrus cloud threshold values of 50% and 70%, respectively; maximum contrail coverage (more than 1%) was predicted in the regions of the most intensive traffic, such as USA, Western Europe, and Japan.
- 2) Calculated contrail coverage is sensitive to the way that subgrid processes are addressed. For example, we calculated 0.11% of global and annually averaged visible contrail coverage using 95% and 90% as the threshold values for contrail and cirrus cloud formation. It is clear that the using a single set of values to account for subgrid scale variations in RHI at all locations and seasons is not the best approach but there is limited data to use for a more comprehensive analysis.
- 3) Potential improvements of the propulsion efficiency of future aircraft engines from 0.3 to 0.4 were calculated to not increase contrail coverage significantly.
- 4) Comparison of calculated contrail coverage with available data shows agreement within 20-40%; we speculate that one of the reasons for this disagreement is that normalization of our results over Europe according to Bakan et al (1994) does not work for other regions, such as the United States or Japan.

In order to improve future analysis of contrail coverage and optical properties, RHI global measurements with a better vertical and spatial resolution are required. For example, the relatively poor vertical resolution of MLS data limits our ability to evaluate the sensitivity of contrail coverage to changes in aircraft cruise altitudes. Future data sets also should span at least several years in order to get better statistics. Likely, merging satellite and in situ measurements (such as MOZAIC campaign data (Gierens et al., 1999)) may help if small-scale processes from in situ data can be properly accounted for in global satellite data. Also, better experimental constraints on the vertical extent of contrails and their optical properties as the contrail age are needed. Similarly, we expect that the optical properties of contrails will depend on temperature and RHI, producing contrails with different size particles. Little data is available on how contrail properties differ in different geographical regions (e.g., tropics versus mid-latitudes) or different seasons.

REFERENCES:

- Appleman, H., 1953: The formation of exhaust condensation trails by jet aircraft, *Bull. Amer. Meteor. Soc.*, *34*, 14-20.
- Bakan, S., M. Betancor, V. Gayler, and H. Graßl, 1994: Contrail frequency over Europe from NOAA satellite images, *Ann. Geophys.*, *12*, 962-968.
- Baughcum, S.L., T.G. Tritz, S.C. Henderson, and D.C. Pickett, 1996: Scheduled civil aircraft emission inventories for 1992: Database development and analysis, *NASA Contr. Rep. 4700*.
- Ebert, E.E., and J.A. Curry, 1992: A parameterization of ice cloud optical properties for climate model, *J. Geophys. Res.*, *97*, 3831-3836.
- Gierens, K., U. Schumann, M. Helten, H. Smit, and A. Marengo, 1999: A distribution law for relative humidity in the upper troposphere and lower stratosphere derived from three years of MOZAIC measurements, *Ann. Geophys.*, *17*, 1218-1226.
- IPCC, 1999: *Aviation and the global atmosphere*, (eds. J.E. Penner, D.H. Lister, D.J. Griggs, D.J. Dokken, and M. McFarland), Cambridge Univ. Press., 373 pp.
- Lohmann, U., and B. Kärcher, 2002: First interactive simulations of cirrus clouds formed by homogeneous freezing in the ECHAM general circulation model, *J. Geophys. Res.*, *107*, D10, 10.1029/2001JD000767.
- Marquart, S., M. Ponater, F. Mager, and R. Sausen, 2003: Future development of contrail cover, optical depth, and radiative forcing: Impacts of increasing air traffic and climate change, *J. Climate*, *16*, 2890-2904.
- Meyer, R., H. Mannstein, R. Meerkötter, U. Schumann, and P. Wendling, 2002: Regional radiative forcing by line-shaped contrails derived from satellite data, *J. Geophys. Res.*, *107*, D10, 10.1029/2001JD000426.

- Meyer, R., R. Buell, C. Leiter, H. Mannstein, S. Marquart, T. Oki, and P. Wendling, 2003: Contrail observations over Southern and Eastern Asia in NOAA/AVHRR data and comparisons to contrail simulations in a GCM, *Int. J. Rem. Sens.*, *in press*.
- Minnis, P., J.K. Ayers, R. Palikonda, and D. Phan, 2003: Contrails, cirrus trends, and climate, *J. Climate*, *submitted*.
- Ponater, M., S. Marquart, and R. Sausen, 2002: Contrails in a comprehensive climate model: Parameterization and radiative forcing, *J. Geophys. Res.*, *107*, D13, 10.1029/2001JD000429.
- Read, W.G., et al., 2001: UARS MLS upper tropospheric humidity measurements: Method and validation, *J. Geophys. Res.*, *106*, 32,207-32,258.
- Sausen, R., K. Gierens, M. Ponater, and U. Schumann, 1998: A diagnostic study of the global distribution of contrails, Part I: Present day climate, *Theor. Appl. Climatol.*, *61*, 127-141.
- Schumann, U., 2000: Influence of propulsion efficiency on contrail formation, *Aerosp. Sci. Techn.*, *4*, 391-401.

Observations of Contrails and Cirrus Over Europe

H. Mannstein*, U. Schumann

DLR-Institut für Physik der Atmosphäre Oberpfaffenhofen, Germany

Keywords: Contrail cirrus, air traffic, clouds

ABSTRACT: Condensation trails (contrails) and aircraft induced cirrus are nowadays a common feature at the mid latitude skies. The impact of aircraft induced cirrus changes has been roughly estimated before from observed decadal trends in cirrus cover but the direct attribution of observed cirrus changes to changes in aviation activity remains uncertain. In this paper the amount of additional cirrus induced from spreading contrails in humid air is estimated from the direct correlation between observed cirrus cover derived with suitable methods from METEOSAT and aviation flight density reported by EUROCONTROL at high spatial and temporal resolution. The results indicate that the radiative forcing from the additional cirrus is at least 10 times higher than that of linear contrails and aviation induced CO₂ increases.

1 INTRODUCTION

A contrail forms in the wake of an aircraft if the ambient air is cold and moist enough. The Schmidt-Appleman criterion quantifies the atmospheric conditions (Schumann, 1996). If the ambient air is not supersaturated with respect to ice, the contrail disappears within the next seconds. Otherwise the ice crystals grow by uptake of ambient moisture while the contrail is spreading due to dissipation and vertical wind shear (Minnis, 1998; Schumann, 2002) In this case the further development of the contrail is governed by the moisture and vertical motion of the ambient air and the sedimentation of the ice particles. Young contrails can be easily identified by their linear appearance (Bakan, 1994; Mannstein 1999), but during their ageing both, their macroscopic structure and their microscopic composition approach that of natural cirrus clouds. Optically thin cirrus has a positive climate impact (Liou, 1986; Boucher, 1999) i.e. it warms the Earth – atmosphere system. In the International Panel on Climate Change (IPCC) special report on ‘Aviation and the Global Atmosphere’ from 1999 the impact of linear (young) contrails is estimated to be in the same order of magnitude as the impact caused by emitted CO₂, the impact of aircraft induced cirrus (i. e. aged contrails and indirect influence on cirrus formation) is not quantified due to the ‘very poor’ knowledge.

2 AN ESTIMATE OF CONTRAIL CIRRUS COVERAGE

Independent from any measurements of cloud coverage the following considerations give a simplified estimate on the influence of air traffic on cirrus coverage: Over Europe in up to 25% of all cases super-saturation of water vapour with respect to ice is found in measurements performed by instruments operated on regular airliners (Gierens, 1999; Gierens, 2000). In most cases the Schmidt-Appleman criterion for contrail formation is fulfilled within these super-saturated areas. Part of them might be already filled by cirrus clouds or hidden by cirrus layers above, but in the remaining fraction air traffic leads to additional cloud coverage. Here this part of the super saturated regions is called c_{pot} , the fraction in time and space of the total area with potential contrail coverage.

Horizontal spreading rates of contrails between 1 and 8 km/h with a mean of about 4 km/h are found by Freudenthaler (1995) from tracking and scanning contrails with a LIDAR system. Considering a super saturated air parcel void of any contrails at the beginning, an air traffic density

* *Corresponding author:* Hermann Mannstein, DLR-Institut für Physik der Atmosphäre, Oberpfaffenhofen, D-82205 Wessling, Germany. Email: Hermann.Mannstein@dlr.de

given in km flight-path per km² and per hour during a time interval Δt leads to total length of contrails of $d\Delta t$ per unit area. The mean width of the contrails is $s_h \bar{t}$, where \bar{t} is the mean age of the contrails. Therefore the fractional coverage of spreading contrails is:

$$c_f = d\Delta t s_h \bar{t} \tag{1}$$

Already after 1 h of air traffic, - the mean contrail age is then 1/2 h-, the full coverage would be reached with an air traffic density of $d=0.5$ [km/km²/h]. Therefore an overlap of the evolving cirrus clouds has to be considered. Assuming N equal contrails, the remaining cloud free part is $1 - c_f = (1 - d\Delta t s_h \bar{t} / N)^N$. In the extreme case of infinitesimal random overlap ($N \rightarrow \infty$) the cirrus coverage reads as:

$$c_f = 1 - e^{-d\Delta t s_h \bar{t}} \tag{2}$$

Looking for the dependency of c_f on d Eq.(2) becomes clearer if $\Delta t s_h \bar{t}$ is replaced by $1/d^*$, where d^* represents the air traffic density leading to a full coverage at a given contrail age, spreading rate and time interval Δt without considering any overlap.

Now the total coverage with cirrus clouds written as a function of air traffic density can be written as:

$$c_{tot}(d) = c_0 + c_{pot} \left(1 - e^{-\frac{d}{d^*}}\right) \tag{3}$$

where c_0 gives the background cirrus coverage without any air traffic.

For longer time-scales also the decay of contrail cirrus has to be considered. From tracking cirrus clusters in METEOSAT data from June and July 1998 we found a half-life time in the order of 2.5 hours, but these data include strong mesoscale convective events and might therefore not represent the lifetime of contrail cirrus. Nevertheless the order of magnitude supports the assumption, that cirrus decay can be neglected at least for the first hour.

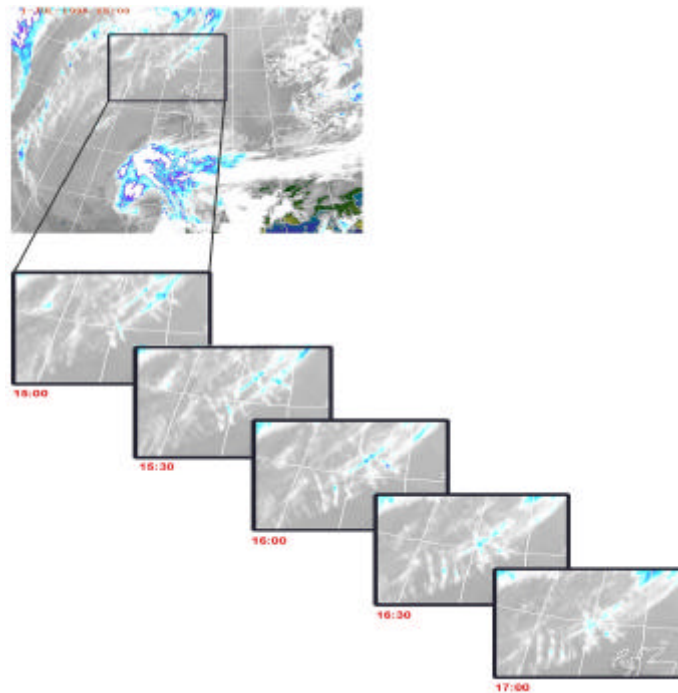


Figure 1: Contrail cirrus in METEOSAT images. Crossing a band of moist air with some cirrus clouds NW of Scotland the westbound air traffic on July 1st 1998 left bundles of contrails which remain visible in the METEOSAT infrared channel data for several hours.

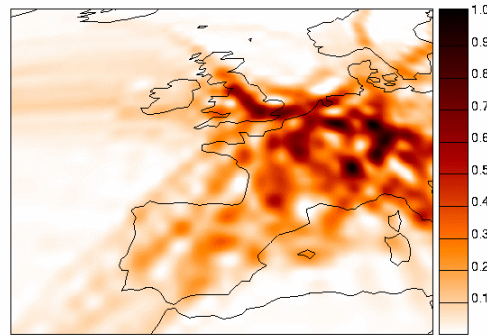


Figure 2: Mean air traffic density in June and July 1998. Flight paths above 8 km altitude according to EUROCONTROL data have been summarised into a $1^{\circ} \times 1^{\circ}$ grid. The air traffic density is given in km flight path per km^2 and per hour. The data is mapped into the METEOSAT projection by interpolation. All results refer to the region displayed here.

3 METHODS TO DETECT CIRRUS IN METEOSAT DATA

The main problem in cirrus detection by remote sensing methods is that no natural boundary exists which discriminates cirrus from clear sky. Therefore the amount of detected cirrus depends on the sensitivity of the sensor and the applied algorithm. Different methods will give different absolute values for cirrus coverage. High clouds, which are usually cirrus clouds, can be detected within the METEOSAT data making use of the water vapour (WV) channel, which has its main sensitivity in the upper troposphere. For this study we developed two different methods. The first one is based on the local spatial correlation between the equivalent blackbody temperatures in the infrared (IR) and the WV channel. A high positive correlation indicates an horizontally structured emitter in the upper troposphere - i.e. a high level cloud. Cirrus clouds down to an effective transmissivity in the visible of 0.3 should be detected by this method. The correlation coefficient is calculated for each pixel in a 7×7 pixel surrounding weighted with a rotationally symmetric Gaussian filter. A threshold of 0.5 is used to discriminate between background noise and clouds. Additionally all pixels with temperatures colder than -50°C are considered to be covered by cirrus clouds. This method will overestimate the cirrus coverage, as gaps are filled, some pixels adjacent to clouds are included, and the sub-pixel structure is not taken into account. On the other hand single young and narrow contrails cannot be detected, as their effect on the thermal emission is far below the sensitivity of the IR and WV sensors of METEOSAT. The second method has the aim to detect thin cirrus clouds and uses only the information in the WV channel: If the standard deviation of the equivalent blackbody temperature in a 5×5 pixel surrounding exceeds the normal noise level of 0.5 K, a cirrus cloud is assumed. This method detects more cirrus clouds, but has also a higher false alarm rate. To concentrate on thin cirrus clouds, the optically thick and therefore cold high clouds are excluded by a threshold of -50°C . This criterion was chosen to eliminate the possible correlation between strong convective clouds that in summer often occur in the afternoon over land and the air traffic, which also shows its maximum during daytime over land.

4 OBSERVATION OF CIRRUS

The direct observation of cirrus clouds resulting from air traffic is currently not possible because we do not know how to separate these clouds from natural cirrus clouds. Nevertheless the dependency of cirrus coverage on air traffic density as given in Eq.(3) can be verified. Due to the high spatial and temporal variation of air traffic, such a study is only possible with observations from geostationary satellites like METEOSAT. Concerning air traffic data, two data sets of the so called

'corrected scheduled flights' were available from EUROCONTROL, showing the flight path for every commercial flight over Europe defined by the time and altitude of passing way points. The data sets for the two time periods, from June 22 to July 27 1998 and from September 27 to October 21 2000 were processed by summarising all flight paths above 8 km to derive the air traffic density for each hour on an $1^{\circ} \times 1^{\circ}$ grid.

Cirrus coverage was derived with two different methods from half hourly METEOSAT data, which was obtained from the 'METEOSAT archive and retrieval facility' (MARF) of EUMETSAT. As shown in Fig. 3 the cirrus coverage determined by both methods increases with the air traffic density as expected by Eq. 3. In this figures the air traffic data within each hour is compared to the satellite data at the end of this hour. Therefore a Δt of 1 h and mean contrail age \bar{t} of $\frac{1}{2}$ h together with a estimated potential contrail coverage c_{pot} of 0.2 is used to calculate the expected values. The data was sampled into 7 classes of air traffic density with logarithmic class boundaries to account for the data distribution. c_0 in Eq. (3) is matched to result in the same mean cirrus coverage as in the data except for the class with the lowest air traffic density. This class comprises nearly 40% of all pixels. The cirrus coverage of this class therefore dominates the mean value, while the classes with low air traffic density ($d < 0.1$ [km²/km²/h]) show lower values. Due to the spatial and temporal coherence of the air traffic data these values seem to represent the cirrus coverage without essential influence of air traffic better then the values at $d=0$. With both methods of cirrus detection the mean cirrus coverage is 0.03 higher then c_0 , which results in a 14% higher cirrus coverage due to air traffic with the first cirrus detection method and in a 11% increase with the second method (thin cirrus).

Independent from any cirrus classification the equivalent blackbody temperature measured by the satellite shows also the expected variation with air traffic density. In both channels significantly lower temperatures are found at times and in areas with high air traffic density than in low traffic regions (Fig. 3, right). Again the class with air traffic close to zero deviates from the overall picture. Its mean temperature is close to the overall mean temperature and lower than the temperature of the low air traffic classes. Air traffic is positively correlated with land surface and daytime, both being warmer in summer and autumn, which would result in the opposite behaviour in the infrared data if this would not be masked by additional cirrus clouds.

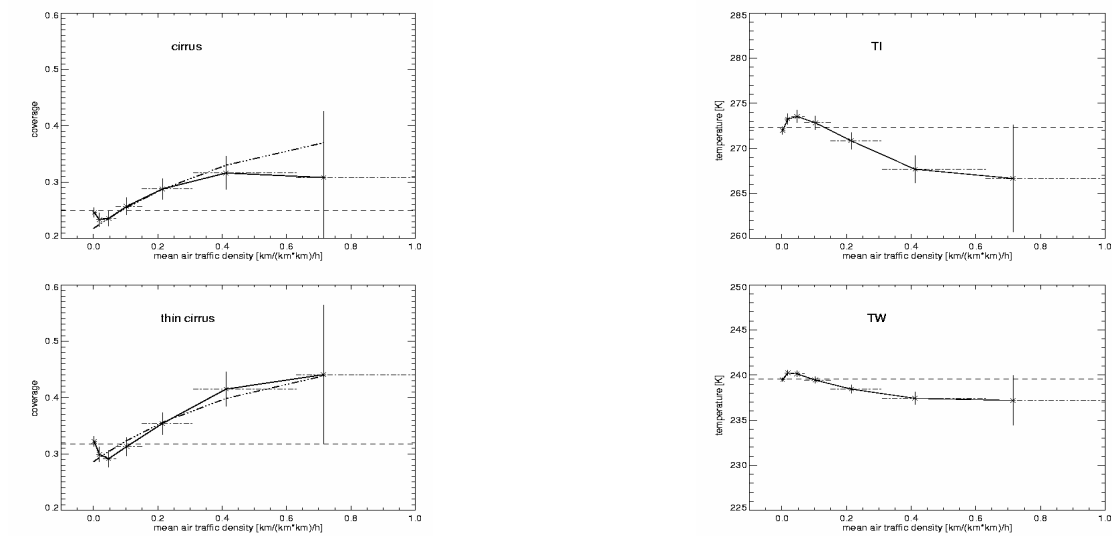


Figure 3: Cirrus coverage as a function of air traffic density. Two different versions of cirrus detection from METEOSAT data show a strong increase of cirrus cloudiness with increasing air traffic density. (Left side). Plotted is in each figure the mean cirrus coverage within seven air traffic density classes indicated by the dash-dotted horizontal bars. The vertical bars indicate the range of confidence for the single air traffic density classes, the horizontal dashed line the mean value of cloud coverage as defined by the algorithm. The theoretical cirrus coverage is indicated by the thick dash-dot-dotted curve. Equivalent mean blackbody temperature in the infrared (IR, left) and water vapour (WV, right) channel of METEOSAT data as a function of air traffic density are plotted on the right hand side.

5 CONCLUSIONS AND OUTLOOK

The statistical method to derive the cirrus coverage depending on air traffic density does not allow to infer the optical properties of these additional clouds. Thus it is not possible to calculate their radiative impact without further information. The analysis of linear contrails from NOAA14 AVHRR data for Central Europe (Meyer, R. & HM, in preparation) using an automated contrail detection algorithm described in Mannstein (1999) results in a mean contrail coverage for the same period and nearly the same area of 0.3%. Therefore it can be stated, that the coverage by additional cirrus clouds is in Europe about 10 times higher than by linear contrails. The optical depth of these additional cirrus cannot be less than 0.2, the optical depth usually attributed to linear contrails, otherwise they would not be detected by METEOSAT. Therefore we have to conclude, that the impact of the additional cirrus clouds is at least 10 times the effect of the linear contrails.

The high amount of contrail cirrus compared to linear contrails indicates, that the lifetime of contrail cirrus has to be measured in hours rather than in minutes. This leads to an additional temporal effect, which has not been considered in previous studies. During daylight conditions the cooling effect of cirrus clouds due to enhanced reflection nearly balances the warming effect in the infrared part of the spectrum, while after sunset only the warming effect is remaining. The cloud coverage by cirrus clouds resulting from contrails has a considerable time lag behind the air traffic. Therefore part of the impact of air traffic over Europe is shifted to the night hours, where only the warming effect of cirrus clouds is remaining.

In future studies it will be necessary to consider a further, secondary contrail effect. The additional ice particles formed in contrails can either lead to an enhanced net sedimentation rate resulting in a dryer upper troposphere, or to a reduced one, as the particles formed in contrails are smaller and therefore slower. The details of these processes depend strongly on the vertical motion and the small scale structure of the moisture field in this altitudes, which are both not known sufficiently.

REFERENCES

- Bakan, S., Betancor-Gothe, M., Gayler, V. & Grassl, H., 1994, Contrail frequency over Europe from NOAA-satellite images. *Ann. Geophys.*, 12, 962-968.
- Boucher, O., 1999. Air traffic may increase cirrus cloudiness. *Nature*, 397,30-31.
- Freudenthaler, V., Homburg, F. and Jäger, H., 1995. Contrail observations by ground-based scanning lidar: cross-sectional growth. *Geophys. Res. Lett.*, 22,3501-3504
- Gierens, K., Schumann, U., Helten, M., Smit, H. and Marenco, A., 1999. A distribution law for relative humidity in the upper troposphere and lower stratosphere derived from three years of MOZAIC measurements. *Ann. Geophys.*, 17,1218-1226
- Gierens, K., Schumann, U., Helten, M., Smit, H. and Wang, P., 2000. Ice-supersaturated regions and subvisible cirrus in the northern midlatitude upper troposphere. *J. Geophys. Res.*, 105(D18), 22,743-22,753
- Intergovernmental Panel on Climate Change (IPCC), 1999. *Aviation and the Global Atmosphere*. edited by J. E. Penner et al., Cambridge Univ. Press.
- Liou, K.N. Influence of cirrus clouds on weather and climate processes: a global perspective. *Mon. Wea. Rev.*, 114, 1167-1198 (1986).
- Mannstein, H., Meyer, R. & Wendling, P., 1999 Operational detection of contrails from NOAA-AVHRR-data, *Int. J. Remote Sensing*, 20(8), 1641-1660.
- Minnis, P., Young, D. F., Garber, D. P., Nguyen, L. N., Smith, W. L. Jr., and Palikonda, R.. 1998 Transformation of contrails into cirrus during SUCCESS, *Geophys. Res. Lett.*, 25(8), 1157-1160
- Sausen, R. and U. Schumann, 2000 *Estimates of the Climate Response to Aircraft CO₂ and NO_x Emissions Scenarios*, Climatic Change 44, 27-58.
- Schumann, U., 1994: On the effect of emissions from aircraft on the state of the atmosphere. *Ann. Geophys.* 12, 365-384.
- Schumann, U., 1996. On conditions for contrail formation from aircraft exhausts. *Met. Zeitschr.,N.F.*, 5, 4-23
- Schumann, U., 2002. Contrail cirrus. In Lynch et al.(Ed.):*Cirrus*, Oxford University Press, 231-255.

Potential Impact of Aviation-Induced Black Carbon on Cirrus Clouds: Global Model Studies with the ECHAM GCM

J. Hendricks*, B. Kärcher

DLR-Institut für Physik der Atmosphäre, Oberpfaffenhofen, Germany

A. Döpelheuer

DLR-Institut für Antriebstechnik, Köln-Porz, Germany

J. Feichter

Max-Planck-Institut für Meteorologie, Hamburg, Germany

U. Lohmann

Dalhousie University, Halifax, Canada

Keywords: Aviation, Black carbon, Cirrus

ABSTRACT: In this study, global simulations on the potential impact of aircraft-generated black carbon (BC) particles on cirrus clouds via heterogeneous nucleation were performed. The general circulation model ECHAM4 has been applied including predictions of major aerosol species and cloud condensate. In a first step, the global impact of aircraft BC emissions on the availability of potential heterogeneous ice nuclei (IN), such as BC or mineral dust particles, in the upper troposphere and lowermost stratosphere (UTLS) was quantified. The results suggest a significant large-scale contribution of aviation to the number concentration of potential heterogeneous IN. This indicates the possibility that aviation-induced BC can impact cirrus cloud formation. Hence, in a second step, potential impacts of aircraft BC particles on cirrus clouds were simulated. Sensitivity experiments were performed considering various scenarios of ice nucleating efficiencies of different types of potential heterogeneous IN. The model experiments indicate a potential of aviation-induced BC to induce significant perturbations in cirrus microphysical properties.

1 INTRODUCTION

Potential impacts of aviation-induced aerosols on cirrus occurrence frequency and cirrus optical properties have been discussed (e.g., IPCC, 1999). Aircraft exhaust particles, especially BC and sulphate aerosols, may perturb the aerosol population of the UTLS and may act as ice nuclei via heterogeneous or homogeneous ice nucleation. Recent studies suggest that the impact of aircraft sulphur emissions on cirrus properties via homogeneous freezing of sulphate aerosols is probably small (e.g., Lohmann and Kärcher, 2002). Hence, the question has been addressed whether aircraft-generated BC particles serving as heterogeneous IN may have a significant impact on cirrus cloudiness and cirrus microphysical properties.

No consistent physically-based quantification of the relative aviation impact on the availability of potential heterogeneous IN, such as BC and mineral dust particles, in the UTLS has been performed yet. Therefore, simulations on the contribution of surface sources as well as aircraft BC emissions to the total amount of BC and dust particles in the UTLS were performed here using a global model. Since the simulations indicate a potential of aviation to induce significant perturbations of the UTLS heterogeneous IN budget, the sensitivity of cirrus microphysical properties to aviation BC emissions was investigated in additional model experiments.

* *Corresponding author:* Johannes Hendricks, DLR-Institut für Physik der Atmosphäre, Oberpfaffenhofen, D-82234 Weßling, Germany. Email: Johannes.Hendricks@dlr.de

2 MODEL AND METHODOLOGY

The general circulation model ECHAM4 was applied including predictions of major aerosol species and cloud condensate (Feichter et al., 1996; Lohmann et al., 1999; Lohmann and Kärcher, 2002). The model treats the atmospheric cycles of sulphate aerosols, carbonaceous particles (organic carbon as well as BC), sea-salt, and mineral dust aerosols. Prognostic fields of particle mass concentrations of the respective aerosol types are calculated considering emissions of particles and particle precursors, gas-to-particle conversion, transport, and removal by wet and dry deposition. The BC emission sources considered include fossil fuel combustion as well as biomass burning. In order to calculate particle number concentrations from the simulated aerosol mass concentrations, prescribed lognormal particle size distributions typical for the respective aerosol type (Hess et al., 1998) are employed.

For the present study, the model was extended by aircraft BC emissions calculated from global aviation fuel consumption data for 1992 (DLR2 inventory) including the global distribution of aircraft fuel use and its annual cycle. BC mass and particle number emission rates are derived from these data employing altitude dependent aircraft BC mass and particle number emission indices (Döpelheuer, 2002). In order to assess the relative contribution of aviation to the total UTLS aerosol budget, aircraft-induced BC is treated separately from BC resulting from surface sources. The aviation-induced BC number concentration is calculated by considering the number-to-mass ratios typical for the fresh exhaust as well as by taking into account potential reductions in the number-to-mass ratio owing to interactions with background aerosols and cloud particles. A comparison of the results obtained with this model set-up to observational data of UTLS BC mass concentrations suggests a fair representation of the UTLS BC budget in the model. In regions where a relevant aviation impact on UTLS BC is simulated, the BC concentrations observed by Blake and Kato (1995) mostly agree within a factor of 2 with the corresponding modelled values.

Homogeneous ice nucleation is considered as described by Lohmann and Kärcher (2002). Heterogeneous instead of homogeneous nucleation can be considered by transforming the available heterogeneous IN into ice crystals at prescribed supersaturations. The mechanisms of cirrus cloud formation are still not well understood. Especially the details of the competition between homogeneous and heterogeneous ice nucleation as well as the ice nucleating efficiency of the different types of potential heterogeneous IN are still uncertain. In order to cope with these deficiencies in the present study, maximum potential aviation impacts on cirrus microphysical properties were estimated rather than quantifying the effect in detail. The following assumptions on ice cloud formation were made promoting the aviation impact: i) The maximum number concentration of aviation BC particles was assumed (number-to-mass ratios of fresh exhaust); ii) Heterogeneous instead of homogeneous nucleation is assumed at ice supersaturations larger than 130%, provided that the number of heterogeneous IN exceeds $0.5/\text{cm}^3$ (Gierens, 2003); iii) BC particles from aviation generally serve as efficient heterogeneous IN; iv) The number of ice crystals formed during nucleation events can be limited by the vertical velocity. However, the sub-grid vertical velocity is a very uncertain parameter in a global model. This can lead to underestimations of the potential aviation impact on ice clouds. Therefore we limit the number of heterogeneously formed ice crystals by the number heterogeneous IN available and not by the number predicted from the vertical velocity.

Two different scenarios were considered. In scenario 1, all BC and mineral dust particles available are assumed to serve as heterogeneous IN. This leads to heterogeneous nucleation dominating homogeneous nucleation in the northern hemisphere (NH). Simulations including/excluding aviation BC emissions were compared. In scenario 2, a model experiment where heterogeneous nucleation can exclusively occur on BC from aviation is compared to a simulation considering homogeneous nucleation only. All model runs were performed for a 10 year time period. A horizontal resolution of approximately 3.75×3.75 degrees is considered. The vertical range from the surface up to 10 hPa is covered by 19 layers. Note that aerosol impacts on the sub-grid-scale ice cloud coverage were not taken into account here.

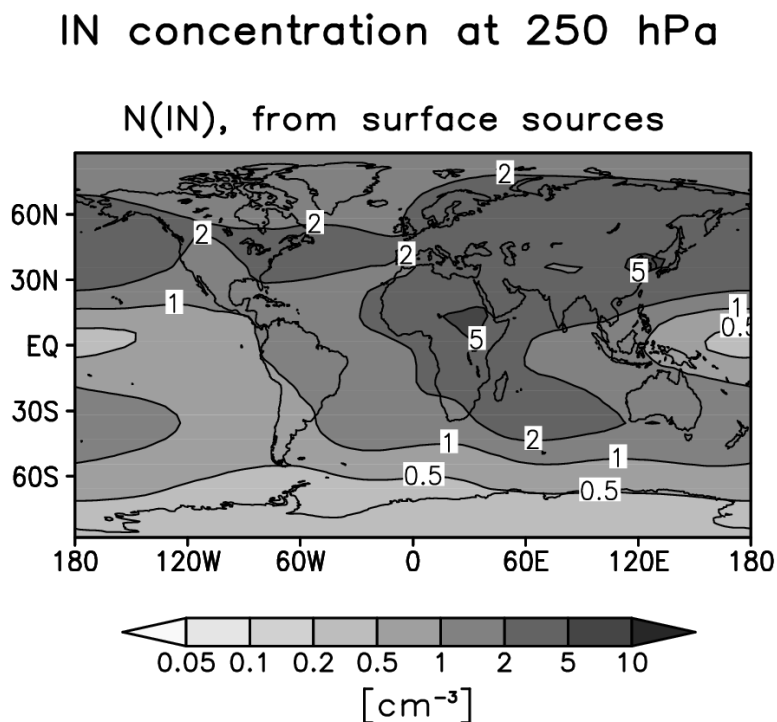


Figure 1: Annual mean number concentrations [$1/\text{cm}^3$] of potential heterogeneous IN (BC and mineral dust particles) at 250 hPa (main aircraft flight level). Only particles originating from surface sources are considered.

3 RESULTS AND DISCUSSION

The annual mean global distribution of the number concentration of potential heterogeneous IN particles (BC and mineral dust) simulated for the 250 hPa pressure level is shown in Figure 1. The 250 hPa level is chosen since it is located within the main flight levels. Only particles originating from the surface are considered. The annual mean concentrations of these particles at 250 hPa range between about 0.5 and 5 particles/ cm^3 . BC particles generally contribute to more than 50% (more than 70% at mid- and high latitudes) to these particle numbers. The major emission regions of BC from fossil fuel combustion are North America, Europe, and Southeast Asia. Due to upward transport of BC from the boundary layer, the plumes of these emission regions can clearly be identified at 250 hPa showing a significant spatial shift induced by westerly flows. The potential UTLS IN populations in the northern hemispheric equatorial regions as well as the southern hemisphere (SH) are to a larger extent influenced by BC emissions from biomass burning. The contribution of mineral dust particles is largest at low latitudes.

Large-scale number concentrations of aircraft-induced BC particles simulated for 250 hPa are highlighted in Figure 2. When reductions in the BC number-to-mass ratio due to ageing of aircraft exhaust (Section 2) are not considered, a maximum potential impact of aviation on the number concentration of UTLS BC particles or heterogeneous IN can be estimated. As displayed in Figure 2a, the maximum-estimate number concentrations of aircraft-generated BC particles at 250 hPa range between about 0.2 and $1/\text{cm}^3$ at northern midlatitudes where most of the aircraft activity takes place. Taking into account the number concentrations obtained for surface-related potential IN (Figure 1), this maximum estimate results in a relative increase in the potential IN number concentration at 250 hPa of more than 20% in large parts of the NH. The largest increase at 250 hPa ranges up to 40%. Even when an efficient exhaust ageing is considered (Figure 2b), the aviation-induced increase in the potential IN number concentration at 250 hPa exceeds 10% in large parts of the NH and amounts up to 20% in the most frequented flight areas. Hence, the simulations indicate a large potential of BC from aircraft to contribute significantly to the UTLS IN particle number concentration. Note that despite the large potential perturbations in IN number concentration, the aviation impact on the BC or potential IN mass concentration is small due to the comparably small sizes of BC particles from aviation.

IN concentration at 250 hPa

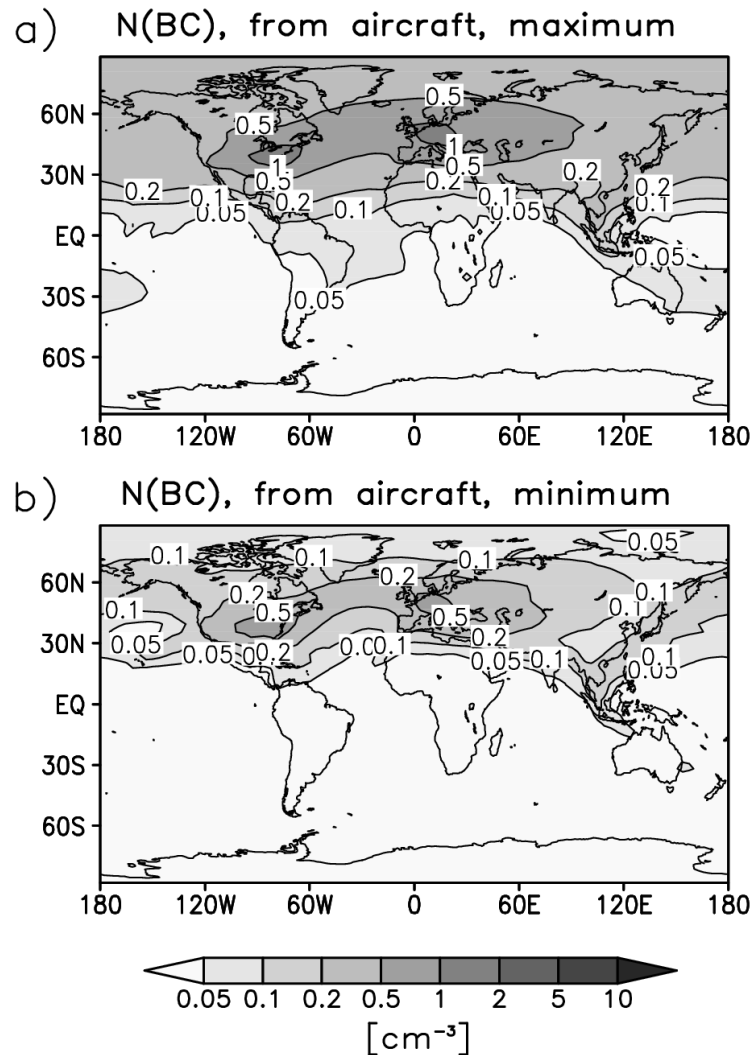


Figure 2: As Figure 1, but for BC particles from aircraft. a) BC number-to-mass ratios of fresh aircraft exhaust were considered. b) An efficient reduction of the aviation BC particle number-to-mass ratio during exhaust ageing was assumed.

Regarding the large potential aviation-induced increases in the heterogeneous IN number concentration, it should be evaluated whether these perturbations can result in significant changes in cirrus microphysical properties. As mentioned in Section 2, two different scenarios were considered to simulate maximum potential impacts of BC from aviation on ice cloud properties. Figure 3 highlights maximum estimates of the relative aviation impact on the annual mean ice crystal number concentration simulated for 250 hPa where the aircraft impact is largest. Note that typical annual mean (including cloud-free periods) ice crystal number concentrations simulated in the two scenarios range between 0.1 and 0.5/cm³ at the NH midlatitude 250 hPa level. The corresponding annual mean ice cloud frequencies range between 20 and 40%. In scenario 1 (Figure 3a), mineral dust particles and BC particles in general serve as heterogeneous IN. In this case, cirrus formation is dominated by heterogeneous nucleation in the NH since the NH UTLS number concentrations of heterogeneous IN mostly exceed 0.5/cm³ (Section 2). In agreement with the aircraft-induced increase in the heterogeneous IN concentration aviation BC emissions lead to an increase in ice crystal number concentration. Large increases are simulated which locally exceed 40%. The relative annual mean perturbation of ice crystal number density can be larger compared to the annual mean perturbation of heterogeneous IN since the ice cloud frequency is largest during winter when the IN perturbation exceeds its annual mean.

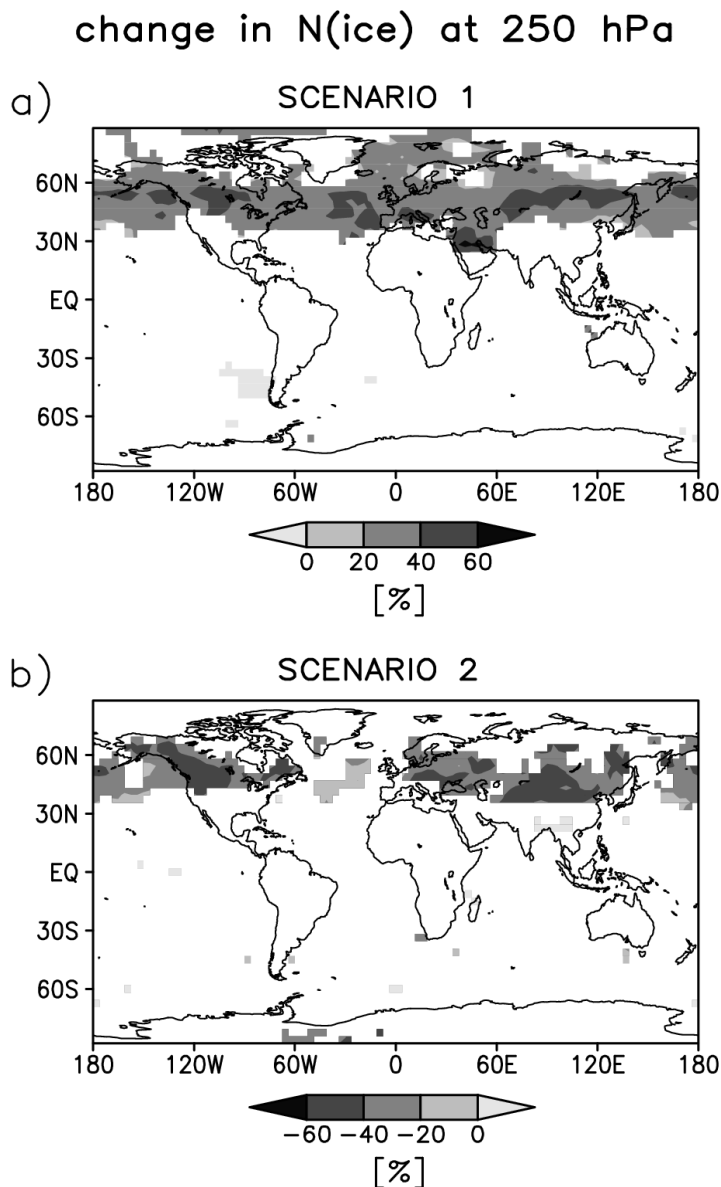


Figure 3: Relative change of the annual mean ice crystal number concentration induced by heterogeneous ice nucleation on BC particles from aviation, simulated in scenario 1 (a) and scenario 2 (b). Only those changes are shown which are significant on a 95% level of the student t-test. The results represent maximum estimates of potential aviation impacts.

In scenario 2, heterogeneous nucleation can occur on aviation-induced BC only (Section 2). The impact of heterogeneous nucleation in the corresponding model experiment is to compete with homogeneous nucleation, provided that sufficient amounts of BC from aviation are available. Figure 2b reveals that aviation causes a reduction of the ice crystal number concentration under these assumptions. The reduction is largest (>40%) in areas of strong orographic forcing where large updrafts lead to high ice crystal number concentrations resulting from homogeneous nucleation when ice formation on aviation BC is neglected. In both scenarios, the aviation impact is significant in large areas of the northern hemisphere. The aircraft-induced increases/decreases in the ice crystal number concentration are accompanied by decreased/increased crystal sizes. No significant aviation-induced changes in the ice water content were simulated.

4 CONCLUSIONS

The simulations performed here reveal that the large-scale impact of aviation BC emissions on the UTLS BC mass concentration is small. Nevertheless, the simulations suggest a significant aviation

impact on the number concentrations of UTLS BC particles and potential heterogeneous IN (BC and mineral dust particles). Large-scale increases of the potential heterogeneous IN number concentration of up to 50% were simulated. Maximum estimates of the potential impacts of aviation BC on cirrus microphysical properties were performed. Provided that BC particles from aviation serve as efficient heterogeneous IN, maximum increases or decreases in ice crystal number concentrations of more than 40% were simulated assuming that ‘background’ (no aviation impact) cirrus cloud formation is dominated by heterogeneous or homogeneous nucleation, respectively.

The uncertainties on the details of cirrus cloud formation are currently too large for a more detailed quantification of the aviation impacts on ice cloud properties. Further in-situ observations of aerosols and cirrus as well as laboratory measurements on ice particle formation and the nucleation ability of different aerosol types are urgently required to constrain future global model scenarios. The representation of aerosols in global models should be improved by including prognostic aerosol size distributions and composition. The representation of ice clouds should be further improved by i) considering more detailed parametrizations of ice nucleation mechanisms and subscale vertical fluxes; ii) including aerosol impacts on subscale ice cloud coverage; and iii) considering the dispersion of contrails to cirrus clouds.

REFERENCES

- Blake, D.F., and K. Kato, 1995: Latitudinal distribution of black carbon soot in the upper troposphere and lower stratosphere, *J. Geophys. Res.*, *100*, 7195-7202.
- Döpelheuer, A., 2002: *Anwendungsorientierte Verfahren zur Bestimmung von CO, HC und Ruß aus Luftfahrttriebwerken*, thesis, Deutsches Zentrum für Luft- und Raumfahrt, Report 2002-10, ISSN 1434-8454, Cologne, Germany.
- Feichter, J., E. Kjellström, H. Rodhe, F. Dentener, J. Lelieveld, and G.-J. Roelofs, 1996: Simulation of the tropospheric sulfur cycle in a global climate model, *Atmos. Environ.*, *30*, 1693-1707.
- Gierens, K., 2003: On the transition between heterogeneous and homogeneous freezing, *Atmos. Chem. Phys.*, *3*, 437-446.
- Hess, M., P. Köpke, and I. Schult, 1998: Optical properties of aerosols and clouds: The software package OPAC, *Bull. Americ. Met. Soc.*, *79*, 831-844.
- Intergovernmental Panel on Climate Change (IPCC), 1999: *Aviation and the Global Atmosphere*, edited by J. Penner *et al.*, Cambridge Univ. Press, New York.
- Lohmann, U., and B. Kärcher, 2002: First interactive simulations of cirrus clouds formed by homogeneous freezing in the ECHAM GCM, *J. Geophys. Res.*, *107*, 4105, doi:10.1029/2001JD000767.
- Lohmann, U., J. Feichter, C.C. Chuang, and J.E. Penner, 1999: Prediction of the number of cloud droplets in the ECHAM GCM, *J. Geophys. Res.*, *104*, 9169-9198.

Future Development of Contrails: Impacts of Increasing Air Traffic and Climate Change

S. Marquart*, M. Ponater, F. Mager, R. Sausen
DLR-Institut für Physik der Atmosphäre, Oberpfaffenhofen, Germany

Keywords: contrails, radiative forcing, aircraft, general circulation model, ECHAM

ABSTRACT: The future development of contrails is investigated by means of a contrail parameterization developed for the ECHAM general circulation model, considering changes in air traffic, aircraft technology, and climate change. Time slice simulations show an increase in both contrail cover and radiative forcing (RF) by roughly a factor of 4 between 1992 and 2050. The simulated contrail cover for 1992 agrees well with respective observations. Some sensitivities, such as the impact of different air traffic inventories, the effect of systematic errors in the model climate, the uncertainty due to short observation periods, and the impact of the daily cycle of air traffic are discussed.

1 INTRODUCTION

The expected increase in air traffic will certainly contribute to an increase in contrail cover. More efficient engines will lead to a colder exhaust gas and will, therefore, also facilitate contrail formation. These effects have already been studied by means of a diagnostic method based on the thermodynamic theory of contrail formation (Sausen et al., 1998; Gierens et al., 1999). Here, we investigate the future development of contrails in a changing background climate by means of a contrail parameterization developed for a general circulation model (GCM). We consider changes in air traffic and propulsion efficiency as well as increasing greenhouse gas concentrations in the atmosphere for the three time slices 1992, 2015, and 2050.

2 METHOD

The GCM contrail parameterization, which is based on the thermodynamic theory of contrail formation, was developed for the ECHAM4.L39(DLR) model (Ponater et al., 2002). Here, we use this parameterization together with an upgraded version of the ECHAM4 longwave radiation scheme (Räisänen, 1998; Marquart and Mayer, 2002), as was also done by Marquart et al. (2003). In contrast to the diagnostic approach of Sausen et al. (1998) the parameterization allows to estimate online, within a self-consistent framework, coverage and optical properties of the contrails as well as the resulting RF. For the future time slice simulations (2015, 2050), changes in background climate (increasing greenhouse gas concentrations, changing sea surface temperatures) are taken into account. In our reference simulation, we use 3D inventories of fuel consumption as a measure of air traffic for all time slices, neglecting the daily cycle of air traffic density (DLR, NASA inventories). The simulated contrail cover is calibrated to satellite observations of Bakan et al. (1994) in a way suggested by Marquart et al. (2003).

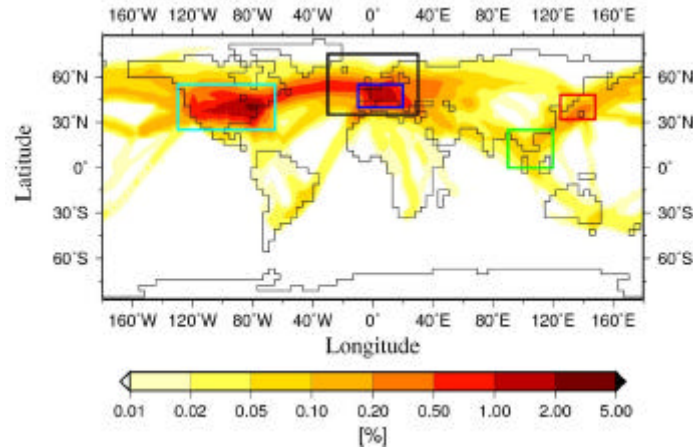
3 RECENT CONDITIONS

Contrail cover is determined in the GCM as fractional coverage within each model grid box. Summing up vertically, the total contrail cover is gained as 2D distribution. As an example, Figure 1

* *Corresponding author:* Susanne Marquart, Deutsches Zentrum für Luft- und Raumfahrt, Institut für Physik der Atmosphäre, Oberpfaffenhofen, D-82234 Wessling, Germany. Email: susanne.marquart@dlr.de

shows the annually averaged total contrail cover for 1992. The global distribution of the simulated stratosphere adjusted RF is shown in Figure 2 for January and July, while globally averaged values are given for different seasons in Table 1. Please note that the RF values presented here differ from those given by Ponater et al. (2002; their Fig. 7 and Table 2), because their values were calculated with the original ECHAM4 longwave radiation scheme (i.e., without the upgrade mentioned above).

Figure 1. Annually averaged total contrail cover for the 1992 time slice. Regions for which satellite based



contrail observations exist are marked. Black: Western Europe / East Atlantic (30°W-30°E/35-75°N; Bakan et al., 1994); Dark blue: Western Europe (10°W-20°E/40-55°N; Meyer et al., 2002a); Light blue: USA (130-65°W/25-55°N; Minnis et al., 2000); Red: Japan region (126-148°E/30-48°N; Meyer et al., submitted); Green: Thailand region (90-122°E/0-25°N; Meyer et al., submitted).

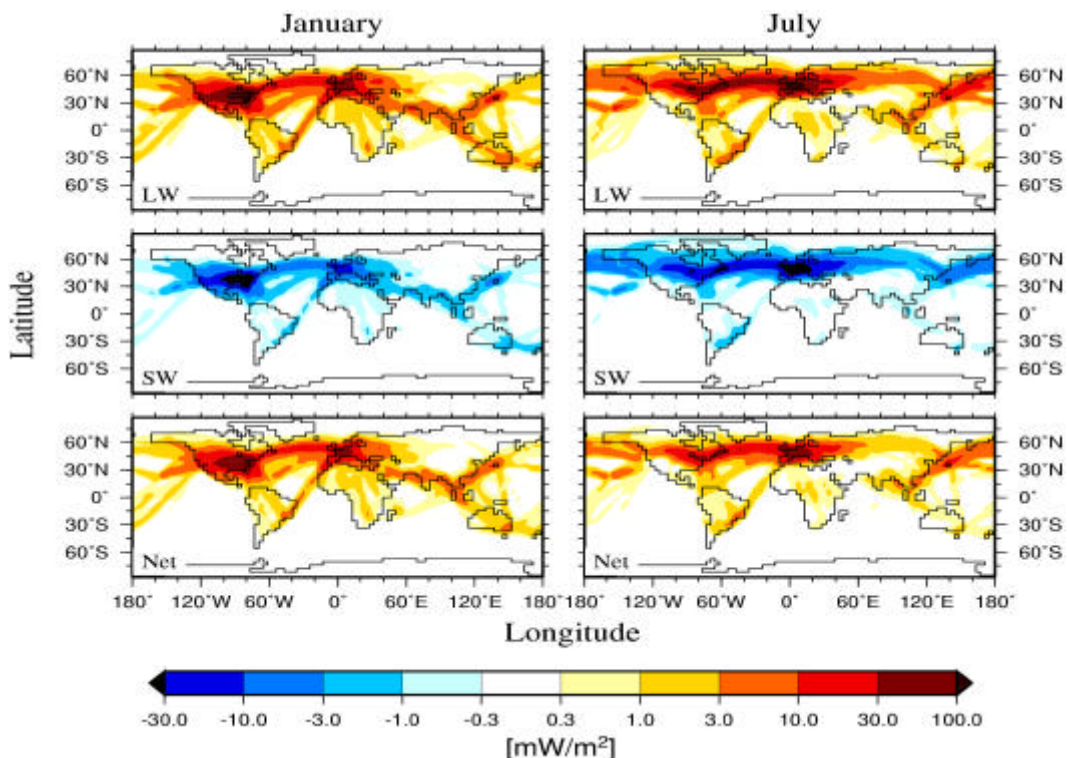


Figure 2. Stratosphere adjusted RF due to contrails for the 1992 time slice.

Table 1. Long term and globally averaged stratosphere adjusted RF due to contrails for 1992. Values in brackets are adjusted by a 25% offset to the longwave contrail RF (see Marquart and Mayer, 2002; Marquart et al., 2003).

RF [mW/m^2]	longwave	shortwave	net
January	3.3 (4.4)	-1.1	2.2 (3.3)
April	4.4 (5.8)	-1.6	2.8 (4.2)
July	2.9 (3.9)	-1.3	1.6 (2.6)
October	4.3 (5.7)	-1.5	2.8 (4.2)
Annual mean	3.7 (4.9)	-1.4	2.3 (3.5)

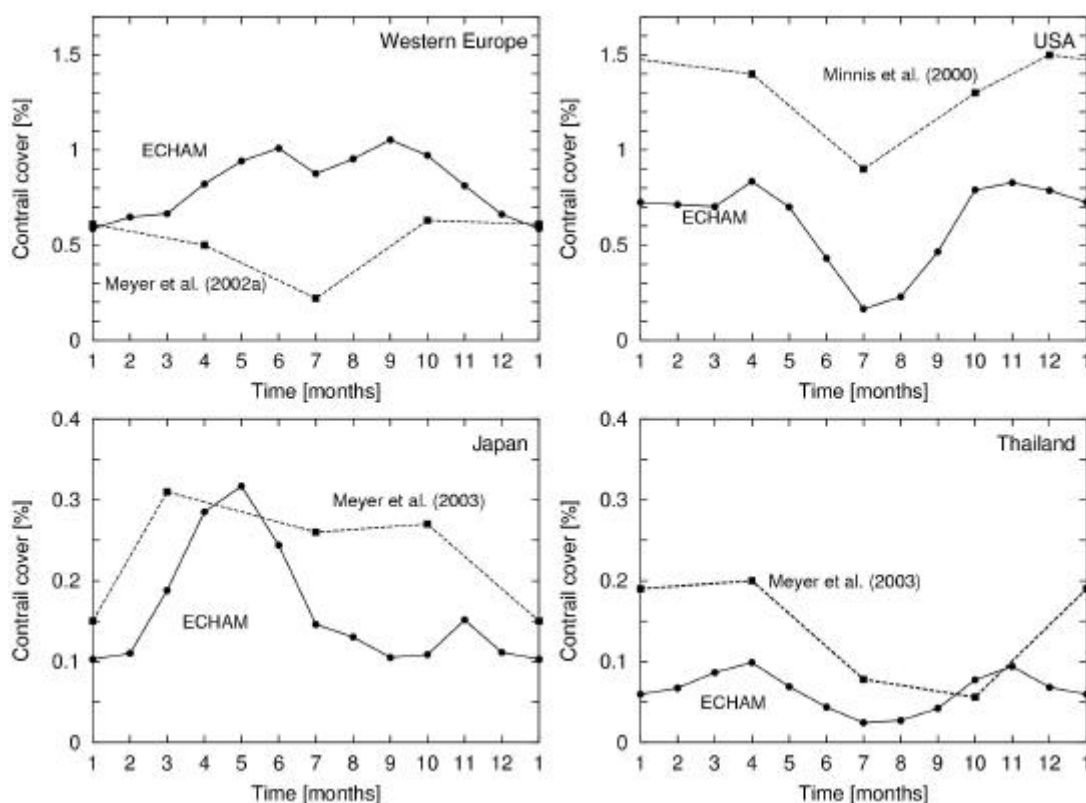


Figure 3. Annual cycle of total contrail cover over different geographical regions according to ECHAM simulations for the time slice 1992 and respective observations.

Figure 3 compares the annual cycle of the simulated total contrail cover to available observations for the geographical regions indicated in Figure 1. For Western Europe, the simulated contrail cover is higher than the observed one, while in the three other areas, the modelled contrail cover is mostly below the observational results. The qualitative annual cycle is quite similar in model and observation over USA and Japan (taking into account that observational data do not exist for all months), whereas in Europe and Thailand, some qualitative discrepancies appear. An obvious reason for the quantitative disagreement is a difference of up to 6 years between simulation and observations (Meyer et al., submitted). Further reasons for the discrepancies, both depending on model uncertainties and on observational deficiencies, are discussed in the next section.

4 SENSITIVITIES

4.1 Contrail cover

The regional distribution of contrail cover depends, among others, on the air traffic inventory used. In our 1992 reference case, we use fuel consumption (DLR inventory) as a measure of air traffic, because such inventories are also available for future time slices. The difference (as a ratio) to a simulation using flown distances instead, is shown in Figure 4a: While the contrail cover tends to be

slightly underestimated when using fuel consumption in Europe and USA (where many short-distance flights with small aircraft are performed), it is overestimated in most other regions of the world. The relative overestimation is most pronounced in Southeast Asia. Note, however, that with the recently created TRADEOFF data base, air traffic inventories including flown distances are becoming available also for future time slices (see the contribution of Fichter et al., this issue).

In order to quantify how the contrail cover simulated within the framework of the ECHAM4 GCM is affected by systematic errors in the model climate (e.g., the cold bias in the extra tropical lowermost stratosphere), offline diagnostic calculations using ERA instead of ECHAM4 temperature and humidity data were performed (Marquart et al., 2003). As shown in Figure 4b, the GCM simulated contrail cover tends to be overestimated in high northern latitudes, where the cold bias is most pronounced, whereas it is underestimated in the tropical warm bias regions.

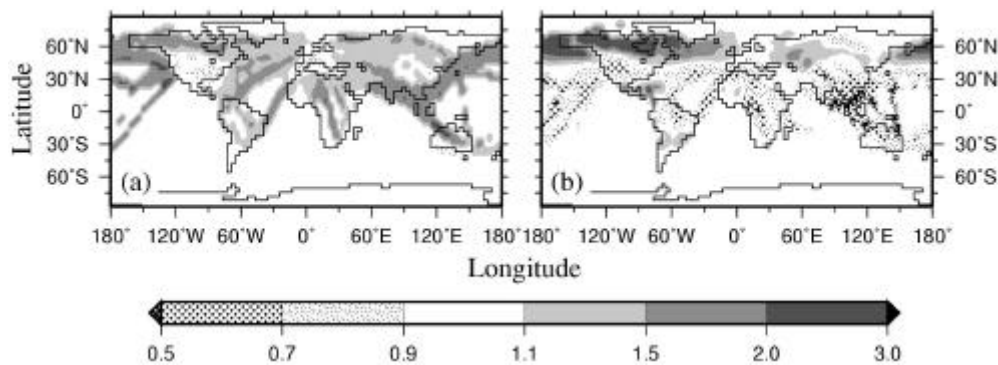


Figure 4. Ratios of total contrail cover between different scenarios for the time slice 1992. (a) Ratio between the reference case and a simulation where flown distances instead of fuel consumption were used; (b) Ratio between the reference case and a calculation where ERA temperature and humidity data instead of ECHAM4 data were used.

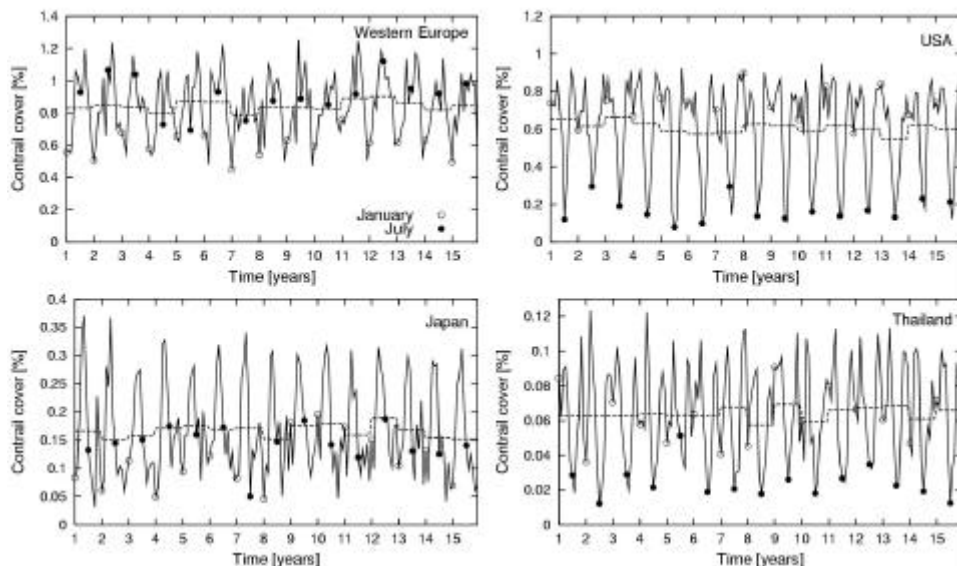


Figure 5. 15-year time series of total contrail cover over different regions according to ECHAM simulations for the time slice 1992. Solid lines: monthly means; dashed lines: annual means; hollow circles: January-means; filled circles: July-means.

The above mentioned contrail observations include maximal 2 years of data (although it has to be mentioned that the observational database for Western Europe was extended to 6 years recently; Meyer et al., 2002b). The mostly insufficient length of a 1 or 2 year time span for gaining representative qualitative and quantitative values is indicated in Figure 5, which shows a 15-year

time series of modelled contrail cover. Especially in the Japan and Thailand regions, the simulated year-to-year variability is remarkably large.

4.2 Radiative forcing

Although RF shows a number of sensitivities of different kinds, we focus here on the effect of the daily cycle of air traffic density (which is neglected in our reference case) on RF. While the diurnal cycle of longwave RF closely follows the daily cycle of air traffic, the diurnal cycle of shortwave RF additionally depends on the solar zenith angle. If the diurnal cycle is included in a GCM simulation for the 1992 air traffic, the global annual mean net RF decreases by less than 10% compared to our reference simulation. This comparatively small change arises mainly from a qualitatively different behaviour in different regions of the globe (Fig. 6): When the daily cycle is included, the shortwave impact is stronger (and the net RF is, therefore, smaller) in regions with high air traffic density during day, while it is weaker in long-distance flight corridors with the largest part of flights occurring during night. Further sensitivities of the RF results are presented in Marquart et al. (2003).

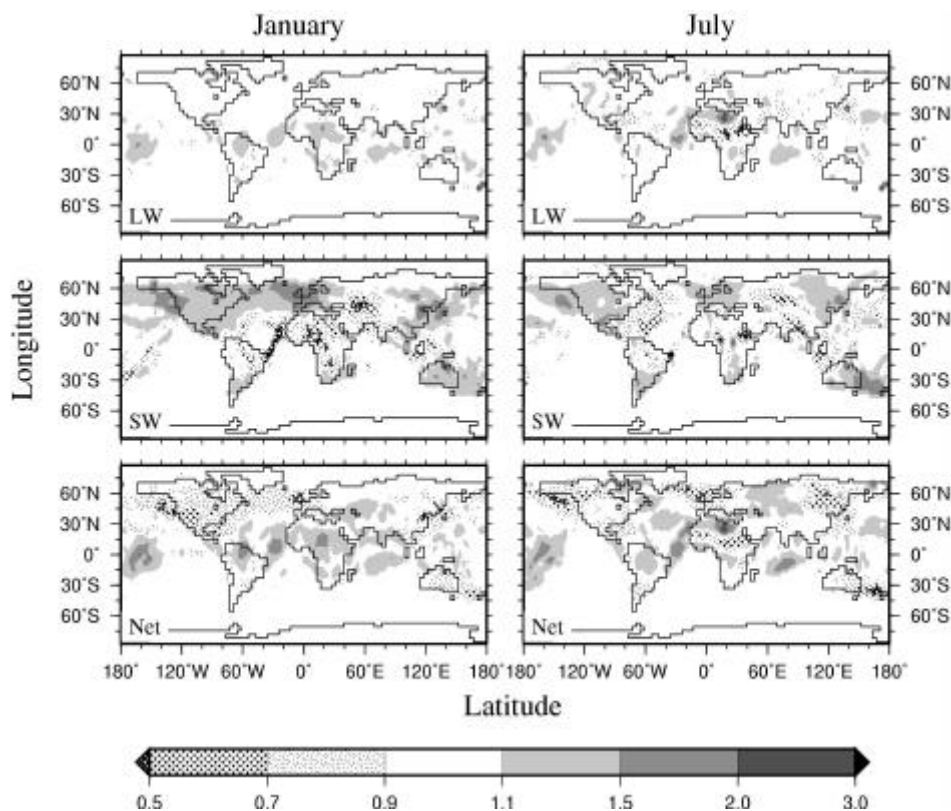


Figure 6. Ratio of longwave, shortwave, and net RF with/without including the daily cycle of air traffic density for the time slice 1992 for January and July.

5 FUTURE PROJECTIONS

The simulated future development of contrails up to the year 2050 is summarized in Table 2 (see also Marquart et al., 2003). Considering changes in air traffic, propulsion efficiency, and climate, contrail net RF increases from 3.5 mW/m^2 in 1992 to 9.4 mW/m^2 in 2015 and 14.8 mW/m^2 in 2050. If only changes in air traffic density are considered, the net RF depends quite linearly on the aviation fuel consumption. Growing propulsion efficiency leads to increases in contrail cover and RF, while climate change tends to reduce them. Optical depth increases slightly in a warmer climate.

Table 2. Annually and globally averaged contrail cover and RF components, as well as global annual fuel consumption in 1992, 2015, and 2050. Values in brackets are adjusted by a 25% offset to the longwave contrail RF (see Marquart and Mayer, 2002; Marquart et al., 2003). Changes in air traffic density, propulsion efficiency (η), and climate change are taken into account.

Year	Fuel [Tg/y]	η	Climate change	Cover [%]	LW RF [mW/m ²]	SW RF [mW/m ²]	Net RF [mW/m ²]
1992	112	0.3	-	0.06	3.7 (4.9)	-1.4	2.3 (3.5)
2015	271	0.3	no	0.13	8.6 (11.5)	-3.1	5.5 (8.4)
		0.4	no	0.15	10.1 (13.5)	-3.7	6.4 (9.8)
		0.4	yes	0.14	9.8 (13.1)	-3.7	6.1 (9.4)
2050	471	0.3	no	0.23	14.7 (19.6)	-5.3	9.4 (14.3)
		0.5	no	0.28	20.2 (26.9)	-7.4	12.8 (19.5)
		0.5	yes	0.22	15.5 (20.7)	-5.9	9.6 (14.8)

6 CONCLUSIONS

The future development of line-shaped contrails was investigated (as part of the EU project TRADEOFF) considering changes in air traffic, aircraft technology, as well as climate change by means of a contrail parameterization developed for the ECHAM4 GCM. Time slice simulations show an increase in contrail cover and RF by roughly a factor of 4 between 1992 and 2050. The simulated global mean RF is about a factor of 5 lower than the best estimate by IPCC (1999), rendering line-shaped contrails, from a climate change point of view, less important than thought some years ago. Please note, however, that contrail-to-cirrus transition was not included in our investigations. The total effect of air traffic on cirrus coverage will be an important topic in future research.

REFERENCES

- Bakan, S., M. Betancor, V. Gayler and H. Graßl, 1994: Contrail frequency over Europe from NOAA-satellite images. *Ann. Geophysicae* 12, 962-968.
- Gierens, K. R. Sausen and U. Schumann, 1999: A diagnostic study of the global distribution of contrails, Part II: future air traffic scenarios. *Theor. Appl. Climatol.* 63, 1-9.
- IPCC, 1999: *Aviation and the global atmosphere - A special report of IPCC working groups I and III*. Intergovernmental Panel on Climate Change, Cambridge University Press, Cambridge, UK and New York, NY, USA, 365 pp.
- Marquart, S. and B. Mayer, 2002: Towards a reliable GCM estimation of contrail radiative forcing. *Geophys. Res. Lett.* 29 (8), 1179, DOI 10.1029/2001GL014075.
- Marquart, S., M. Ponater, F. Mager and R. Sausen, 2003: Future development of contrail cover, optical depth and radiative forcing: Impacts of increasing air traffic and climate change. *J. Clim.* 16, 2890-2904.
- Meyer, R., H. Mannstein, R. Meerkötter, U. Schumann and P. Wendling, 2002a: Regional radiative forcing by line-shaped contrails derived from satellite data. *J. Geophys. Res.* 107 (D10), 4104, DOI 10.1029/2001JD000426.
- Meyer, R., H. Mannstein, R. Meerkötter and P. Wendling, 2002b: Contrail and cirrus observations over Europe from 6 years of NOAA-AVHRR data, *Proceedings of the Meteorological Satellite Data User's Conference*, EUMETSAT, Dublin, Ireland.
- Meyer, R., R. Büll, C. Leiter, H. Mannstein, S. Marquart, T. Oki and P. Wendling, 2003: Contrail observations over Southern and Eastern Asia in NOAA/AVHRR data and intercomparison to contrail simulations in a GCM, submitted to *Int. J. Remote Sensing*.
- Ponater, M., S. Marquart and R. Sausen, 2002: Contrails in a comprehensive global climate model: parameterisation and radiative forcing results. *J. Geophys. Res.* 107 (D13), 4164, DOI 10.1029/2001JD000429.
- Räisänen, P., 1998: Effective longwave cloud fraction and maximum-random overlap of clouds: a problem and a solution. *Mon. Wea. Rev.* 126, 3336-3340.
- Sausen, R., K. Gierens, M. Ponater and U. Schumann, 1998: A diagnostic study of the global distribution of contrails, Part I: Present day climate. *Theor. Appl. Climatol.* 61, 127-141.

A Study of Contrails in a General Circulation Model

A. Guldberg*

Danish Meteorological Institute, Copenhagen, Denmark

Keywords: Contrails, GCM, radiative forcing

ABSTRACT: The IFSHAM model is used for a study of contrails in a general circulation model. The IFSHAM model is a model based on the dynamical core from the ARPEGE-IFS, version 3, model and the physical parameterization package from the ECHAM-5 model. The contrail parameterization scheme of Ponater et al., 2002 has been implemented in the IFSHAM model in order to be able to study contrail formation. The scheme is based on thermodynamic theory and the principles of the models cloud scheme. Results for global contrail cover and radiative forcing are shown and compared with results from the few other model studies that exist and with observed data.

1 INTRODUCTION

In the IPCC special report ‘Aviation and the Global Atmosphere’, (IPCC, 1999) the estimate of the radiative forcing due to line shaped contrails is 0.02 W m^{-2} for 1992 air traffic conditions. In Ponater et al., 2002 the first parameterization of contrails for use in a general circulation model (GCM) is presented making it possible to estimate the climate impact of contrails from GCM experiments. An advantage of parameterizing contrails in a GCM is that contrail coverage and optical properties are then related to the instantaneous state of the atmosphere. Using this parameterization of contrails in the ECHAM-4 model, (Ponater et al., 2002), together with a modification of the long wave part of the models radiation scheme as described in Marquart and Mayer, 2002, results in an estimate of the radiative forcing due to line shaped contrails being 0.003 W m^{-2} for 1992 air traffic conditions, (Marquart and Mayer, 2002). This estimate is an order of magnitude less than the IPCC, 1999 estimate.

In the present study the contrail parameterization of Ponater et al., 2002 has been implemented in a GCM different from the one used by Ponater et al., 2002 in order to study the model dependency of the scheme. Results for contrail coverage and radiative forcing are shown and compared to the results of Ponater et al., 2002 and Marquart and Mayer, 2002.

2 MODEL AND EXPERIMENTS

The model used in this study is the IFSHAM model developed at the Danish Meteorological Institute by Shuting Yang. The model consists of the dynamical core from the ARPEGE-IFS model, version 3 (a description of an older version of the model can be found in Déqué et al., 1994) – and the physical parameterization package from the ECHAM-5 model (an older version of the model is described in Roeckner et al., 1996)

The IFSHAM model uses semi-lagrangian advection and a two time-level discretization. The cloud scheme is the PCI scheme (Lohmann and Roeckner, 1996), where cloud water and cloud ice are treated as separate prognostic variables. The radiation scheme consists of the Morcrette short wave scheme (Morcrette, 1991) and the RRTM scheme (Mlawer et al., 1997) for the long wave part.

The contrail parameterization scheme of Ponater et al., 2002 has been implemented in the IFSHAM model. Using this parameterization the actual contrail coverage is dependent on the air

* *Corresponding author:* Annette Guldberg, Danish Meteorological Institute, Lyngbyvej 100, DK-2100 Copenhagen, Denmark. Email: ag@dmi.dk

traffic density. The version 2 Deutsches Zentrum für Luft- und Raumfahrt (DLR) aircraft emission data set (Schmitt and Brunner, 1997) represents the air traffic density in the beginning of the 1990s and has been used to calculate the actual contrail coverage from the potential contrail coverage.

The horizontal resolution of the model in the presented experiments is spectral T63 truncation with a linear grid. For the vertical discretization is used hybrid coordinates and 31 vertical levels are used – the same 31 levels as used in the ECMWF Re-analysis Data set ERA-15 (Gibson et al., 1997). The time step used is 30 minutes. The model is run with climatological SST's and the experiments extend 3 annual cycles.

3 RESULTS

Figure 1a shows the geographical distribution of the average total contrail coverage. The global mean is 0.06 % which is somewhat less than the IPCC, 1999 estimate of 0.1 %. The geographical distribution is to a large extent determined by the main flight routes and have large maxima over central Europe and the eastern United States.

Figure 1b shows the contrail coverage at model level 11 corresponding to approximately 250 hPa and figure 1c the contrail coverage at model level 10 corresponding to approximately 220 hPa. It is seen that the contrail coverage over Europe and eastern United States is larger at 250 hPa than at 220 hPa, partly due higher air traffic density.

Figure 2a shows the instantaneous short wave radiative forcing at the top of the atmosphere (TOA) due to contrails averaged over the 3 simulated years. As expected the short wave forcing due to contrails is negative and has the largest values (numerically) over Europe and eastern United States where also the contrail coverage is largest. The geographical distribution and the global mean value of the short wave forcing – -1.4 mW m^{-2} – fits well the results obtained in Ponater et al., 2002.

Figure 2b shows the instantaneous long wave radiative forcing at TOA due to contrails. The long wave forcing is positive everywhere except for areas in the tropics. The geographical distribution is similar (except for the areas with negative values) to the results obtained in Ponater et al., 2002, but the values (as eg. reflected in a global mean of 1.5 mW m^{-2}) are small.

The negative values of the long wave forcing in the tropics are unexpected and an explanation needs to be found. To investigate this an experiment was made where only contrails – no natural clouds – were present in the call to the radiation scheme, meaning that the radiative forcing of contrails with no natural clouds present was determined. In this experiment the negative areas disappeared and the long wave forcing due to contrails were positive everywhere. This suggests that the negative values in figure 2b are due to cloud overlap problems.

Figure 2c shows the instantaneous net radiative forcing at TOA due to contrails. Positive net forcing is seen over the Atlantic and Pacific Oceans, over eastern United States, eastern Asia and Australia, whereas negative net forcing is seen over most of Europe, western United States and in many areas in the tropics. The global mean of the net radiative forcing – 0.09 mW m^{-2} – is small compared to the 3.2 mW m^{-2} estimated by Marquart and Mayer, 2002 and indeed small compared to the IPCC, 1999 estimate of 20 mW m^{-2} .

In the experiment where the radiative forcing due to contrails without natural clouds present is determined is the pattern of the net radiative forcing somewhat different: the areas with negative values in the tropics have disappeared, but now the net radiative forcing is negative almost everywhere on the northern hemisphere and the global mean of the net radiative forcing is negative: -0.7 mW m^{-2} .

A third experiment was performed in which the contrail coverage was increased having a global mean of 0.15 % (as compared to the experiment shown in figure 1a where the global mean is 0.06 %). The values of the short wave forcing and the long wave forcing are increased and the global means are more than doubled. The global mean of the short wave forcing is now -3.7 mW m^{-2} (compared to -1.4 mW m^{-2} in the experiment shown in figure 2a). The global mean of the long wave forcing due to contrails is 3.9 mW m^{-2} in the third experiment (compared to 1.5 mW m^{-2} in the experiment shown in figure 2b). But the net radiative forcing does not change that much: the global mean of the net radiative forcing in the third experiment is 0.14 mW m^{-2} (compared to 0.09 mW m^{-2} in the experiment shown in figure 2c) and the geographical distribution of the net radiative forcing

in the third experiment is almost identical to the geographical distribution of the first experiment, shown in figure 2c.

4 DISCUSSION

The contrail coverage obtained in the first experiment described and shown in figure 1 is in reasonable agreement with the contrail coverage obtained by Ponater et al., 2002, but the net radiative forcing shown in figure 2c is small and the geographical distribution showing areas with relatively large negative values is not in agreement with results obtained in other studies and an explanation needs to be found.

The geographical distribution of the net radiative forcing obtained in Ponater et al., 2002 also contains areas with negative values especially at the northern-most latitudes. But as explained in Marquart and Mayer, 2002 this is due to a problem of the long wave radiation scheme in ECHAM-4. The combination of the effective emissivity approach and the maximum-random cloud overlap assumption leads to a considerable underestimation of the long wave radiative forcing of the optically thin contrails. When modifying the long wave scheme as described in Marquart and Mayer, 2002 the contrail long wave forcing is increased and the net radiative forcing does not contain areas with negative values.

The long wave scheme (the RRTM scheme) used in the IFSHAM model is different from the long wave scheme used in ECHAM-4. The RRTM scheme does not use the effective emissivity approach, but uses true cloud cover and emissivity separately. Therefore the problem described in Marquart and Mayer, 2002 is not present in the IFSHAM model, but there could still be a problem in the way optically thin clouds are treated in the long wave scheme. This remains to be investigated.

Compared to the Ponater et al., 2002 study the contrail effective radii and the ice water path of this study is a smaller and the impact of this has to be determined in future experiments.

ACKNOWLEDGMENT

Many helpful discussions with Michael Ponater and Susanne Marquart are gratefully acknowledged.

REFERENCES

- Déqué, M., C. Dreveton, A. Braun, and D. Cariolle, 1994: The ARPEGE-IFS atmosphere model: a contribution to the French community climate modelling. *Clim. Dyn.* 10, 249-266
- Gibson, J. K., P. Källberg, S. Uppala, A. Hernandez, A. Nomura, and E. Serrano, 1997: ERA-15 Description. *ECMWF Re-analysis Project Report Series, 1*
- IPCC, 1999: Aviation and the Global Atmosphere [Penner, J. E. et al. (eds)]. *Cambridge University Press*, Cambridge, New York, USA, 370 pp
- Lohmann, U. and E. Roeckner, 1996: Design and performance of a new cloud microphysics scheme developed for the ECHAM general circulation model. *Clim. Dyn.* 12, 557-572
- Marquart, S. and B. Mayer, 2002: Towards a reliable estimation of contrail radiative forcing. *Geophys. Res. Lett.* 29 (8), 1179, doi:10.1029/2001GL014075, 20-1-20-4
- Mlawer, E. J., S. J. Taubman, P. D. Brown, M. J. Iacono, and S. A. Clough, 1997: Radiative transfer for inhomogeneous atmospheres: RRTM, a validated correlated-k model for the longwave. *J. Geophys. Res.* 102 (D14), 16,663-16,682
- Morcrette, J.-J., 1991: Radiation and cloud radiative properties in the European Centre for Medium Range Weather Forecasts forecasting system. *J. Geophys. Res.* 96, 9121-9132
- Ponater, M., S. Marquart, and R. Sausen, 2002: Contrails in a comprehensive global climate model: Parameterization and radiative forcing results. *J. Geophys. Res.* 107 (D13), 4164, doi:10.1029/2001JD000429, ACL 2-1-2-15
- Roeckner, E., K. Arpe, L. Bengtsson, M. Christoph, M. Claussen, L. Dümenil, M. Esch, M. Giorgetta, U. Schlese, and U. Schulzweida, 1996: The atmospheric general circulation model ECHAM-4: Model description and simulation of present-day climate. *Max-Planck-Inst. Meteorol. Rep. 218*, Hamburg, Germany, 90 pp

Schmitt, A. and B. Brunner, 1997: Emissions from aviation and their development over time. In: *Pollutants From Air Traffic – Results of Atmospheric Research 1992-1997* [Schumann, U. et al. (eds)], DLR-Forschungsber. 97-04, Dtsch. Zentrum für Luft- und Raumfahrt, Cologne, Germany, 27-52

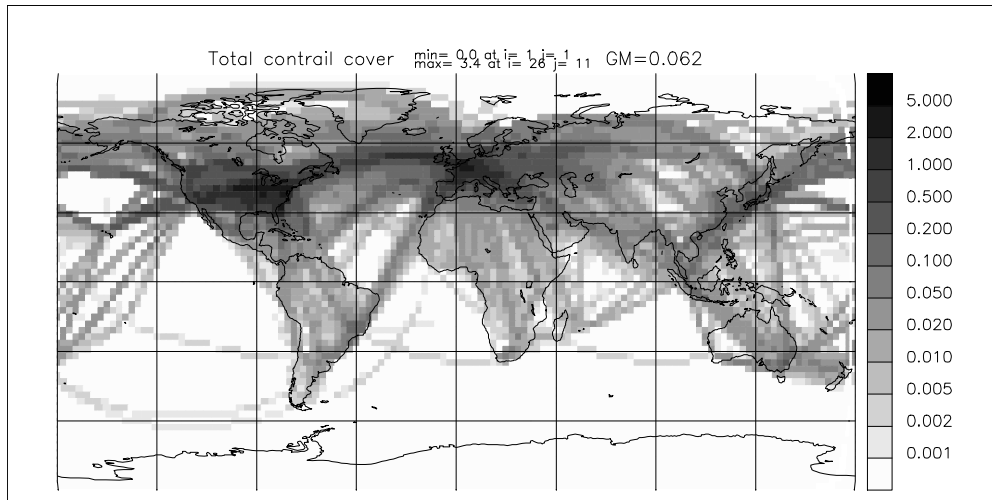


Figure 1a. Total contrail cover. Unit: %. Global mean 0.06 %

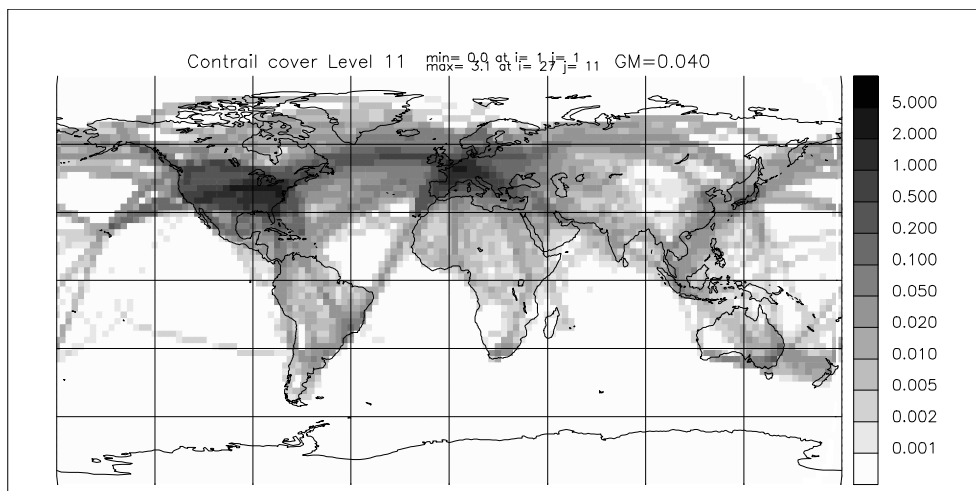


Figure 1b. Contrail cover at model level 11, corresponding to approximately 250 hPa. Unit: %

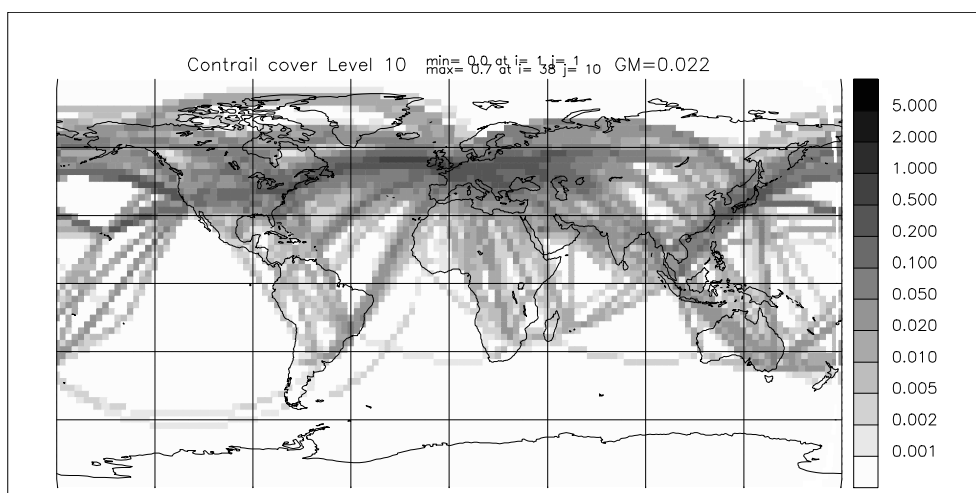


Figure 1c. Contrail cover at model level 10, corresponding to approximately 220 hPa. Unit: %

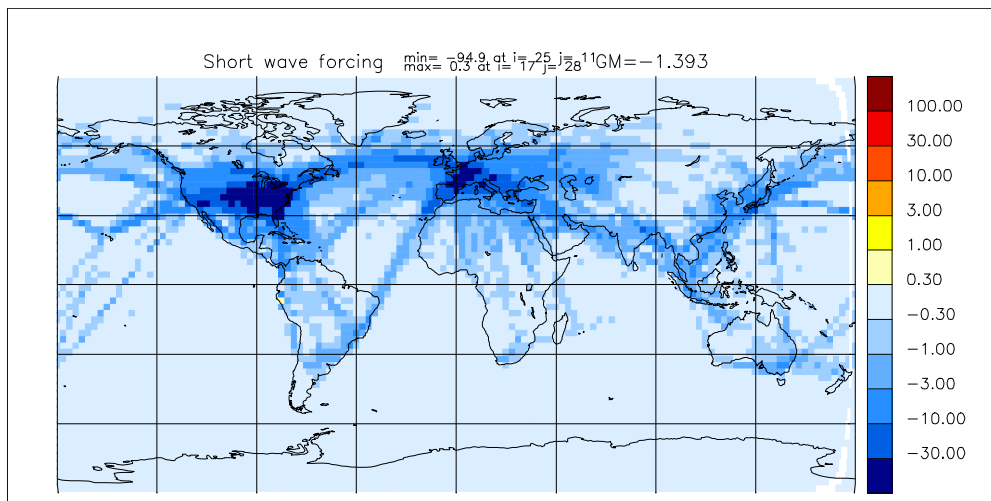


Figure 2a. Instantaneous short wave radiative forcing at TOA due to contrails. Unit: mW m^{-2}

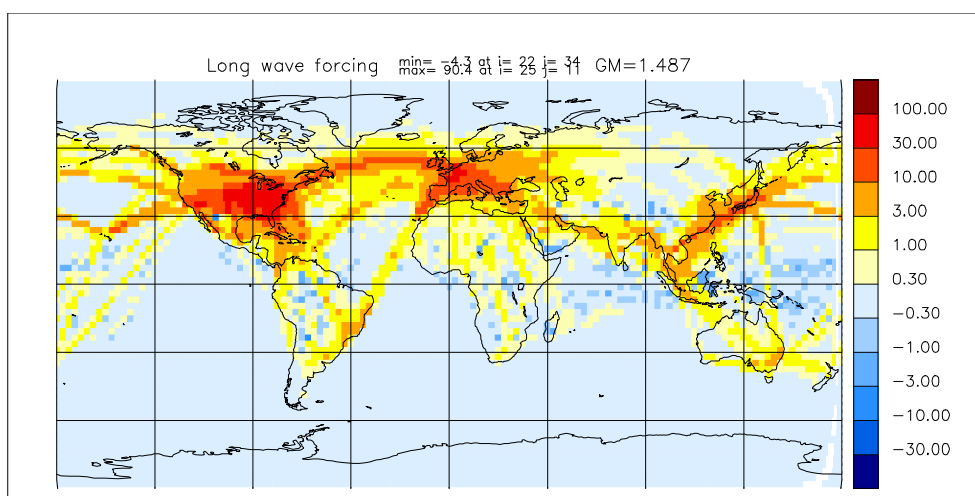


Figure 2b. Instantaneous long wave radiative forcing at TOA due to contrails. Unit: mW m^{-2}

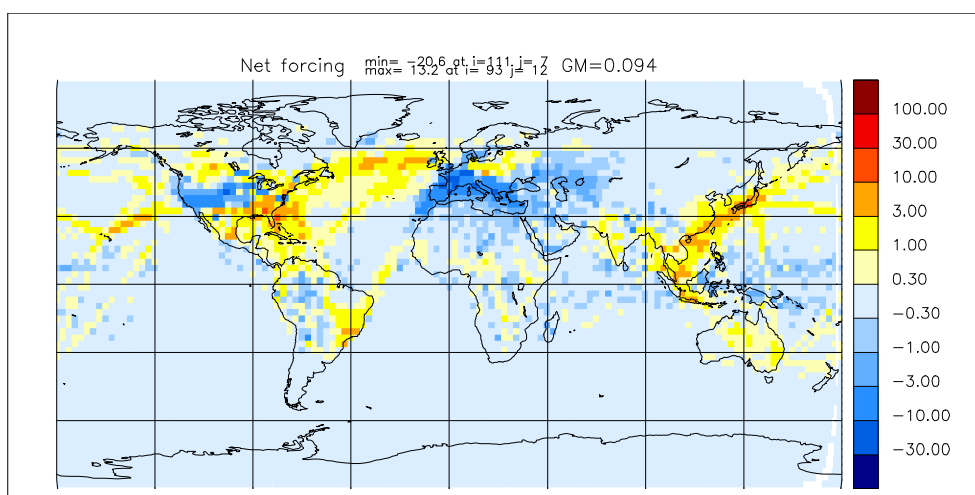


Figure 2c. Instantaneous net radiative forcing at TOA due to contrails. Unit: mW m^{-2} .

Hygroscopicity and wetting of aircraft engine soot and its surrogates: CCN/IN formation in UT

O.B.Popovicheva^{*}, N.M.Persiantseva, E.E. Lukhovitskaya
Institute of Nuclear Physics, Moscow State University, Moscow, Russia

N.K.Shonija, Zubareva N.A.
Chemical Department, Moscow State University, Moscow, Russia

J. Suzanne, D.Ferry, B.Demirdjian
CRMC2-CNRS, Campus de Luminy, Marseille, France

Keywords: engine soot, ice nucleation, contrails, cirrus clouds

ABSTRACT: Aircraft engine soot is characterized in respect to physico – chemical properties responsible for CCN formation. It demonstrates the surprisingly high hydrophilicity at the threshold contrail conditions that allows to estimate the water supersaturations needed for the ice nuclei formation in the plume. Sulfur-free aircraft combustor and kerosene flame soots are believed to represent the insoluble surrogates of BC in the UT. Soot agglomerated structure is suggested to amplify the heterogeneous cirrus cloud formation due to the inverse Kelvin effect in the ice-supersaturated regions of the UT.

1 INTRODUCTION

Formation of visible contrails in the UT is the most obvious effect of the aircraft emission into the atmosphere. Aircraft near-field observations confirm that non-volatile aerosols of the jet exhaust consist mainly of black carbon (BC) particles responsible for contrail formation (Petzold et al., 1998; Karcher et al., 1996). But the aircraft exhaust may also impact indirectly on the climate if exhaust particles act as ice nuclei (IN). In this context, antropogeneous ice nucleating aerosols in the UT have a special significance because they may allow ice nucleation at lower supersaturations that those required for homogeneous freezing, resulting in an increase of the area coverage of the cirrus clouds and changing its microphysics properties. Analysis of ice residuals taken in cirrus clouds showed that they are dominated by carbonaceous particles (Chen et al., 1998). However, there is considerable uncertainty regarding the quantitative estimate of the ice-nucleating ability of soot aerosols in the UT because 1) *in situ* measurements of ice nucleation are difficult, 2) laboratory studies of combustion soots show a surprising variation in their nucleation properties (Lamel and Novakov, 1995; Diehl and Mitra, 1998), and 3) the surface physical and chemical requirements for IN are complex and poorly understood.

Incorporation of soot aerosols into cloud particles depends on the wettability of their surface. Literature on wettability of BC yields a consistent picture of hydrophobicity. It means a nonzero water droplet contact angle which is traditionally associated with poor ability to adsorb water and high supersaturation needed for condensation growth. Lack of experimental data about the aircraft – generated soot properties led to assumption about its initial hydrophobicity and necessity for soot activation by sulphuric acid coating (Karcher et al., 1996). However, recent measurements of the water adsorption on soot produced by burning the sulfur – free fuel in the aircraft combustor showed (Popovicheva et al., 2000) that due to the microporous structure and chemical heterogeneity, such soot aerosols can acquire a substantial fraction of a water monolayer at the conditions of the young plume (Popovicheva et al., 2001). Laboratory-made soot surrogates produced by aviation fuel burning contain the reduced amount of soluble (Hallet et al., 1989) but may act as ice nuclei at low temperatures (Diehl and Mitra, 1998; Ferry et al., 2002). Moreover, the hygroscopic behaviour of jet

^{*} *Corresponding author:* Olga B. Popovicheva, Institute of Nuclear Physics, Moscow State University, 119 992, Moscow, Russia. Email: polga@mics.msu.su

engine soot (Hagen et al., 1992; Gysel et al., 2003) allow to assume their significant potential for CCN formation which is commonly attributed to sulphuric acid adsorbed on the soot surface.

This is why the comprehensive laboratory studies of hydration properties of original engine soot and its surrogates are extremely needed with purpose to clarify the mechanism of water adsorption and ice nucleation responsible for the soot – induced contrail and cirrus formation in the UT.

This paper is devoted to hydration and wetting properties of engine soot connected with its composition, solubility, and surface chemistry. Complementary studies of laboratory – made kerosene soots identify the specific features of soot surrogates for atmospheric researches. Knowledge about nature of water/soot interaction allow suggest the possible pathway of CCN/IN formation in the UT.



Figure 1. AFM image of engine soot

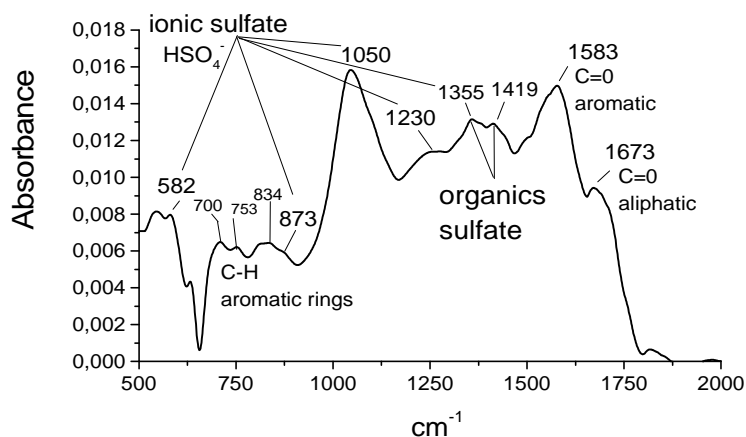


Figure 2. FTIR spectra of engine soot

2 AIRCRAFT ENGINE SOOT. PHYSICO-CHEMICAL PROPERTIES

The combustion chamber of a gas turbine engine D36KU has been used for engine soot production on the background facilities in CIAM, Moscow. The soot samples were collected at the combustor exit at the cruise combustion conditions using aviation kerosene TC1 containing 0.25 wt% of sulfur.

Atomic Force Microscopy (AFM) analysis of engine soot showed that it consists of the roughly spherical primary particles which are fused and well agglomerated (Fig.1). Transmission Electron Microscopy (TEM) analysis coupled by diffraction analysis demonstrated the amorphous microstructure of most part of soot and found well – crystallised particles associated either with graphite or chemical impurities. Particles with a mean diameters of 30 and 100 nm were found. Probably, the fused particles of the small micro and mesoporosity provide a low surface area which was obtained by a single point BET techniques in the range from 9 to 30 m²/g.

X-ray energy analysis (XREDS) coupled to TEM was used to examine the chemical composition of amorphous soot particles which was found to consist mainly of from carbon C~98 wt%, oxygen O~1.6 wt% and sulfur S~0.2 wt% (main fraction). Surprisingly high amount of chemical impurities was observed in the well- crystallized soot particles (fraction of impurities). They contain a large amount of Fe ~30 wt%, O~10 wt%, K~1.25 wt%, and Mn ~0.22 wt%, which are associated with the increased amount of S~2 wt%. Small amount (less than 0.05 wt%) of other elements like Si, Mg, B, Ca, and Cu was detected by emission spectroscopy. Variation of composition and large amount of impurities allow to suggest the high heterogeneity of the soot particle fractions in respect to its hygroscopicity. Finding of Fe and S in engine soot is correlated with composition measurements of ice residual particles in contrails (Petsold, et al. 1998).

Infrared spectroscopy allows to analysis the chemical nature of the soot surface and identify the functional groups which may be directly responsible for the interaction with water. FTIR spectra of engine soot is shown in Figure 2. The underlying absorption of the carbon skeleton, -C-C- and -C=C- groups, results in a broad combination of bands between 1000 and 1600 cm⁻¹. Peaks at 1673 and 1583 cm⁻¹ due to vibrations of the carbonyl C=O groups in aliphatic and aromatic structures are

known as the most active sites for the water adsorption. Weak bands around 3500 cm^{-1} , the region of hydroxyls O-H, does not allow to suggest the existence of carboxyl groups. Intensive peaks at $700, 753, 834,$ and 873 cm^{-1} joint with oscillation of C-H groups in substituted aromatics which may act as the most hydrophobic sites on the soot surface. But the most distinctive feature of engine soot is a set of peaks at $1355, 1230, 1050, 878$ and 582 cm^{-1} connected to vibrations of HSO_4^- ion. Moreover, the prominent region between 1350 and 1420 cm^{-1} is attributed by organics sulfates. It indicates that sulfur on the engine soot surface appears in derivatives of the sulphuric acid and may produce the strong active sites for the water adsorption. Therefore the assumption about the soot coverage by H_2SO_4 may be considered only as the simplest model of engine soot.

FTIR spectra of washed soot demonstrated the dramatic decrease of ionic and organics sulfur bands with small change of other functional groups. Ion chromatography analysis showed an ionic composition of the extracted water soluble compounds which is dominated by SO_4^{2-} $\sim 3.5\text{ wt}\%$ as well as Cl^- , CH_3COO^- , C_2H_4^- , and NO_3^- . Total amount of water soluble fraction (WSF) was estimated to be more $5\text{ wt}\%$. Volatile compound fraction (VCF) $\sim 17\text{ wt}\%$ was measured after heating at 300C for 30 min , that gives the estimation for the amount of volatile organics following the assumption of Ohta and Okita, 1984.

3 HYDRATION OF ENGINE SOOT AND CONTRAIL FORMATION

Gravimetric measurements of the water adsorption provide a direct demonstration of the engine soot hygroscopicity. Figure 3 shows the amount of water molecules adsorbed per unit surface, $N(\text{H}_2\text{O})$, versus the relative pressure, p/p_0 , at $T=295\text{K}$ and 240K . Engine soot features surprisingly high level of hydrophilicity because it is covered by a statistic water monolayer ($1\text{ML} \approx 10\text{ H}_2\text{O}$ per nm^2) already at $p/p_0 \approx 10^{-2}$. Such behaviour corresponds to adsorption on initial strong active sites which are connected to the high concentration of ionic and organics sulfates on the soot surface.

Water adsorption on engine soot is increased with decrease of temperature and at the plume saturation conditions $T \approx 240\text{K}$, soot adsorbs more than 20 ML . Such wettable surface may allow the spherical soot particles to grow water droplets large enough to overcome the Kelvin barrier. Water supersaturations S_w needed for the droplet growth may be obtained using the standard Koehler theory for partially soluble particles. It is found to be $\approx 4.6\%$ and 0.08% for the particles of radius 20 and 50 nm , correspondingly, if to assume the average WSF of $5\text{ wt}\%$ over all soot exhaust. It may be less for the most hydrophilic fraction of impurities containing much sulfur and higher for the more hydrophobic main fraction of soot particles. Since the maximum water supersaturations in the plume may reach 60% (Karcher et al, 1994) we may be concluded that the hygroscopic aircraft – generated aerosols may easily nucleate water and form ice particles in the cooled plume to fulfil the visibility criteria of the contrail formation.

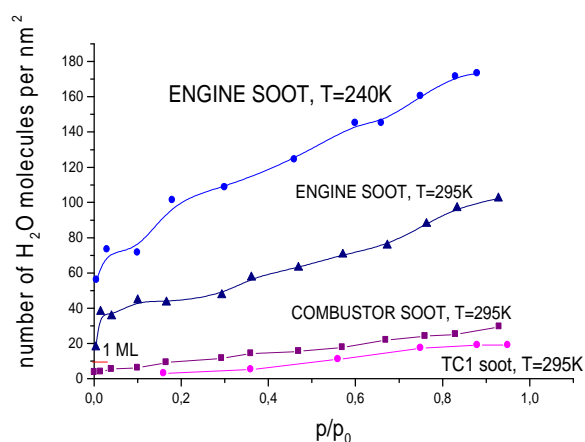


Figure 3. Water adsorption on soots



Figure 4. Water droplet on kerosene soot

4 SOOT SURROGATES FOR ATMOSPHERIC BC PARTICLES.

The analysis of the contrail threshold conditions at different fuel sulfur content suggested that soot may take up water even at zero sulfur amount (Karcher et al., 1996). It means that insoluble sulfur – free part of aircraft – generated soot may participate in the contrail formation. Moreover, BC particles coated with sulphuric acid were not found in large ice residual particles from contrails (Twohy and Gandrud, 1998) and sulfur was not observed in the ice residuals of cirrus clouds and interstitial aerosols (Petzold et al., 1998). It means that there is a sulfur-independent pathway of IN formation on the insoluble soot particles which is probably the most widely-distributed in the UT.

To determine the possible mechanism of ice formation on insoluble BC particles, sulfur-free combustor and kerosene flame soots were chosen as available surrogates. Kerosene flame soots were produced by burning the different aviation kerosenes in a lamp burner at the laboratory conditions. TEM analysis showed that there is a remarkable similarity in the roughly spherical shape of the primary particles between combustor, kerosene flame and engine soots. But the typical radius of primary surrogate soot particles was found to be near 20-50 nm (Ferry et al., 2002), no bigger particles were observed. Higher surface area in the range from 40 to 87 m²/g is appeared as the important characteristics of combustor and kerosene soots being in correlation with the significant microporosity of these soots.

The most prominent feature which differentiates laboratory-made surrogates from engine soot are the fractions of water-soluble and volatile compounds. In kerosene soots the WSF was found to be 0.3 wt% and only 0.0015 wt% is related with SO₄⁻ ion mass. The VCF was found near 1wt% including 0.6% of water. Such insoluble soot particles adsorb water at least one order of magnitude less than engine soot (see Fig.3). In the initial p/p₀ region the amount of water adsorbed is small that is related with reduced concentration the surface oxygen-containing groups that was confirmed by FTIR. Formation of water clusters and micropore filling is a possible mechanism of the increased adsorption at the p/p₀ > 0.6. At the highest relative pressures, adsorption may be connected with the capillary condensation in the meso- and macropores which take place in the interparticle cavities and may be filled by water due to the Kelvin effect.

Low hygroscopicity of surrogate soots is correlated with their low wettability. The contact angles for water/ice droplets on the soot surfaces were measured by classic technique of sessile drop measurements. The image of the water droplet on kerosene soot pillet is shown in Figure 4. Contact angles, θ , were found in a range from 70 up 80° for kerosene soots, and 63 degree for combustor soot. Absence of temperature dependence for contact angles under freezing was obtained.

5 ICE NUCLEATION ON INSOLUBLE BC PARTICLES AND CIRRUS FORMATION

Enhancement of the heterogeneous nucleation rate on the diesel soot in comparison with predicted by the Fletcher theory has been found in Chen et al., 1993. If to follow the Fletcher theory and assume the formation of critical embryos on isolated soot spherical particles, then the results of Chen et al., 1993 may be explained by the perfect wetting of the diesel soot surface (Kelvin activation), in despite of a fact that the water contact angle on this soot was being obtained $\cong 40^\circ$.

Our finding for kerosene soots as well as the studies of soot aerosols encountered in the UT show that they exist as the typical chain agglomerates of primary particles of radius 20-50 nm. Favorite condensation in the interparticle cavities of such soot agglomerates may arise a lower critical supersaturation in comparison with the Fletcher theory due to formation of water meniscus of the negative curvature as it is shown in Figure 5. QENS studies of water dynamics on kerosene soot (Ferry et al., 2002) showed that at T=220K and subsaturation conditions near 25 % of adsorbed water may exist as liquid – like water in supermicropores of 2 nm and 35 % transform into ice in soot mesopores and on the external surface. It means that ice nucleation will start in the interparticle cavities ~ 2 nm from a small amount of present liquid water. At the significant filling of mesopores the size of water meniscus is increased, the effect of confined water became to be negligible and water should freeze. With further increasing of the humidity the curvature become to be positive and finally reaches its maximum. This point corresponds the unstable state and means that any further increase in the relative humidity above the critical supersaturation results in the unconstrained condensation growth of particles (Orr et al., 1975).

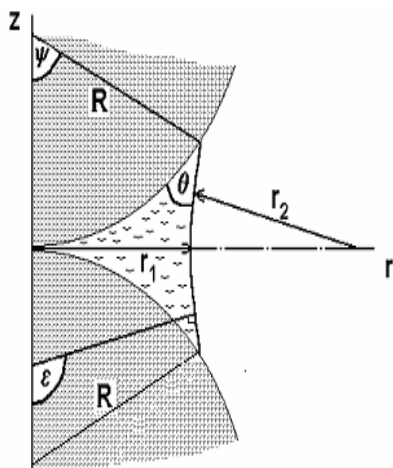


Figure 5. Water condensation between particles

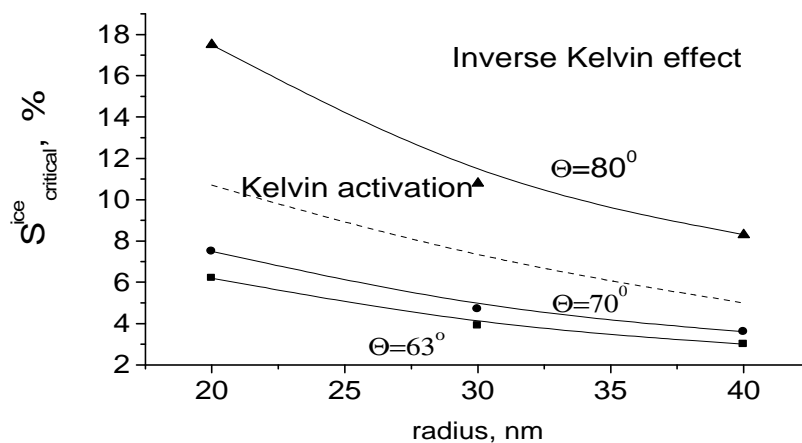


Figure 6. Ice supersaturation on soot particles

Figure 6 presents the critical supersaturation in respect to ice, S_i , at $T=220\text{K}$ assuming the inverse Kelvin effect for ice nucleation on soot agglomerates characterised by contact angles $\theta \cong 63^\circ$, 70° , and 80° . Kelvin activation describing the equilibrium supersaturation on totally wettable spherical particles is more efficient than the inverse Kelvin effect on soot of contact angle $\cong 73^\circ$.

The obtained data demonstrates that if the critical ice supersaturation in the UT may reach $\approx 5\%$, then the more hydrophilic insoluble soot particles characterized by $\theta \cong 63^\circ$ may act as cirrus cloud condensation nuclei. At the $S_i \approx 17.5\%$ the most hydrophobic BC particles with $\theta \cong 80^\circ$ will be activated. In situ observations show that in the UT there is a large supersaturation range in which heterogeneous nuclei may lead to the cirrus formation before atmospheric particles freeze homogeneously. Troposphere water vapor measurements demonstrate that the supersaturation with respect to ice is common in the UT (frequencies of about 30%), with maximum as high as 73% (Vay et al., 2000). So, insoluble BC particles represented by laboratory soot surrogates in this study may amplify the heterogeneous nucleation in the UT.

6 CONCLUSION

More than 10 experimental techniques were applied to characterize the physico-chemical properties of aircraft engine soot and its surrogates. High level of engine soot hygroscopicity is found to relate to sulfur content originated from the combustion, thus implying a significant role in the contrail formation. Sulfur-free combustor soot and laboratory made kerosene soots are more hydrophobic than engine soot. They are believed to represent the insoluble part of the aircraft-generated soot in the atmosphere. Following their hydration mechanism the inverse Kelvin effect may be assumed for the condensation process into interparticles cavities of the soot agglomerates. In ice supersaturated atmosphere such insoluble BC particles may amplify the heterogeneous ice nucleation process of cirrus clouds. This effect may dominate in the contrail formation process if the water-soluble fraction of the exhaust is relatively small, probably at low sulphur content.

7 ACKNOWLEDGEMENTS

Russian authors thanks to INTAS Program, project 00-0460 and CRDF, project RC1-2327-MO-02 for financial support.

REFERENCES

- Chen, C.-C., Hung, L.-C. and H.-K. Hsu, 1993: Heterogeneous nucleation of water vapor on particles of SiO₂, Al₂O₃, TiO₂, and carbon black. *J. Colloid Interface Sci.* 157,465-477.
- Chen, Y., Kreidenweis, S.M. 1998. Single particle analyses of ice nucleating aerosols in the upper troposphere and lower stratosphere. *Geophys. Res. Lett.* 25,1391.
- Diehl, K. and S.K. Mitra, 1998: A laboratory study of the effects of a kerosene-burner exhaust on ice nucleation and the evaporation rate of ice crystals. *Atmosph. Environ.* 32, 3145-3151
- Ferry, D., Suzanne, J., Popovicheva, O.B. and N.K. Shonija, 2002: Water adsorption and dynamics on kerosene soot under atmospheric conditions. *J. Geophys. Res.* 107, 4734-4744.
- Gysel M., Nyeki, S., Weingartner, E., Baltensperger, U., Giebl H., Hitzenberger, R., Petzold, A., and C. Wilson, 2003: Properties of jet engine combustion particles during the PartEmiss experiment; Hygroscopicity at subsaturated conditions. *Geophys. Res. Lett.*, 30, 1566-1570.
- Hagen, D.E., Trueblood, M.B. and P.D. Whitefield, 1992: A field sampling of jet exhaust aerosols. *Partic. Sci. Tech.* 10, 53-63
- Hallet, J., Hudson J.G. and Rogers C.F., 1989: Characterization of combustion aerosols for haze and cloud formation. *Aeros. Sci. Tech.* 10, 70-83.
- Karcher 1994: Transport of exhaust products in the near trail of a jet engine under atmospheric conditions. *J. Geophys. Res.*, 99, 14509-14512.
- Karcher, B., Peter, Th., Biermann U.M. and U. Schumann, 1996: The initial composition of jet condensation trails. *J. Atmos. Science* 53, 3066-3075
- Lamel, S. and P. Novakov, 1995: Water nucleation properties of carbon black and diesel soot particles. *Atmosph. Environ.* 29, 813-823.
- Ohta, S. and T. Okita, 1984: Measurements of particulate carbon in urban and marine air in Japanese areas. *Atmosph. Environ.* 18, 2423-2429.
- Orr, F.M., Scriven L.E., and A.P. Rivas, 1975: Pendular rings between solids: meniscus properties and capillary force. *J. Fluid Mech.* 67, 723-733.
- Petzold, A., Strom, J., Ohlsson, S. and F.P. Schroder, 1998: Elemental composition and morphology of ice-crystal residual particles in cirrus clouds and contrails. *Atmosph. Research.* 49, 21-34
- Popovicheva, O.B., Persiantseva N.M., Trukhin, M.E., Shonija, N.K., Starik, A.M., Suzanne J., Ferry D. and B. Demirdjian, 2000: Experimental characterization of aircraft combustion soot: microstructure, surface area, porosity, and adsorption. *Phys. Chem. Chem. Phys.* 2, 4421-4426.
- Popovicheva, O.B., Trukhin M.E., Persiantseva, N.M. and N.K. Shonija, 2001: Water adsorption on aircraft – combustor soot under young plume conditions. *Atmosph. Environ.* 35, 1643-1676.
- Twohy, C.H. and B.W. Gandrud, 1998: Electron microscope analysis of residual particles from aircraft contrails. *Geophys. Res. Lett.* 25, 1359-1362
- Vay, S.A., Anderson, B.E., Jensen E.J., Sachse, G.W., Ovarlez, J., Gregory, G.L., Nolf, S.R., and C.E. Sorenson, 2000: Tropospheric water vapor measurements over the North Atlantic during the subsonic assessment ozone and nitrogen oxide experiment (SONEX). *J. Geophys. Res.* 105, D3, 3745-3755.

Microphysics of Cirrus Clouds and its Dependency on Different Types of Aerosols

A. Mangold*, M. Krämer

FZ Jülich (FZJ), Institut für Chemie und Dynamik der Geosphäre (ICG-I): Stratosphäre, Jülich, Germany

O. Möhler, R. Wagner, H. Saathoff, S. Büttner, O. Stetzer, U. Schurath

FZ Karlsruhe (FZK), Institut für Meteorologie und Klimaforschung, IMK-AAF, Karlsruhe, Germany

C. Gieseemann, H. Teichert, V. Ebert

Universität Heidelberg, Physikalisch-Chemisches Institut, Heidelberg, Germany

Keywords: cirrus cloud, ice water content, aerosol, cirrus cloud microphysics

ABSTRACT: The ice water content (IWC), ice crystal number concentration and median diameter were investigated during ice cloud formation experiments in the big aerosol chamber AIDA of FZK. Sulphuric acid and ammonium sulphate solution droplets, as well as mineral dust particles and soot, coated with sulphuric acid, served as ice nuclei. The temperature range for the presented experiments was 200 K to 225 K. No clear influence of the aerosol type on the total IWC was found, except for a slight tendency of mineral dust towards a higher IWC compared to the other ice nuclei. Independent of the investigated aerosol types, the ice crystal number concentration increased with decreasing temperature, whereas the median diameter decreased. When using ammonium sulphate solution droplets instead of sulphuric acid solution droplets as ice nuclei (at the same critical cooling rate for ice nucleation), more and smaller ice crystals were formed.

1 INTRODUCTION

As upper tropospheric cirrus clouds play an important role for the earth's climate, it is essential to understand the formation of such clouds. A key issue remains a reliable parameterisation of the partitioning of the available water into the gas, liquid and solid phase during the process of ice nucleation and ice crystal growth. So far, there are only few experimental data providing direct access to the gas phase and the IWC (e.g. the recent CRYSTAL-FACE campaign of 2002, see <http://cloud1.arc.nasa.gov/crystallface/index.html>). For a proper parameterisation of the optical properties and the ice cloud microphysics, experimental data which examine the conditions under which different ice crystal number densities and size distributions form, are of major importance.

Measurements of water vapour and ice supersaturations inside cirrus clouds were carried out during the INCA campaign in 2000 (Ovarlez et al., 2002). Kärcher and Ström (2003) found that the dynamical variability during ice formation is a crucial factor for determining the ice crystal properties. Kärcher and Lohmann (2002) stated that in the case of sulphuric acid solution droplets the number of ice crystals formed via homogeneous freezing is rather insensitive to the aerosol size distribution compared to the influence of the updraft velocity. At higher updraft speeds and lower temperatures more ice crystals would nucleate this way. Kärcher (2002) underlined the essential role of updraft velocity and temperature for the microphysical and optical properties of subvisible cirrus clouds.

Here, we present results of laboratory measurements of the water partitioning during cirrus cloud formation, representing upper tropospheric conditions, for different temperatures and types of aerosol particles. The experiments were conducted at the AIDA aerosol chamber of FZK in 2002 at temperatures between 200 K and 225 K. Sulphuric acid and ammonium sulphate solution droplets, soot coated with sulphuric acid and mineral dust (Arizona Test Dust) served as nuclei for ice formation.

* Corresponding author: Alexander Mangold, Forschungszentrum Jülich GmbH, ICG-I, D-52425 Jülich, Germany. Email: a.mangold@fz-juelich.de

2 ICE NUCLEATION EXPERIMENTS

2.1 AIDA Aerosol and cloud chamber facility

The AIDA aerosol chamber is a large coolable and evacuable vessel of 84 m³ which can be cooled down to 183 K. The pressure range covers 0.1 hPa to 1000 hPa. For details on the instrumentation and on the ice nucleation experiments, see Möhler et al. (2003).

Under constant wall and gas temperatures, ice saturation was maintained by a thin ice layer on the chamber walls. The ice supersaturation necessary for the homogeneous or heterogeneous formation of ice crystals was achieved by ‘volume expansion’ due to controlled pumping, usually from 1000 hPa to 800 hPa. During pumping the ice supersaturation increased by up to 50 %/min.

The onset of ice formation was detected precisely by measuring the depolarisation of backscattered laser light with high sensitivity and time resolution of 1 Hz. The Lyman- α -fluorescence hygrometer (FISH) of FZJ was used to measure the total water content (gas phase + condensed phase). Simultaneously, the gas phase water concentration was directly measured in situ by absorption at 1370 nm with a tuneable diode laser (TDL). Number concentration and size distribution of the ice particles were obtained using in situ multi-path FTIR extinction spectroscopy.

2.2 Typical ice nucleation experiment

Figures 1-4 illustrate the water fluxes and partitioning during the ice formation process in the AIDA chamber. With the beginning of pumping (see Fig. 3 for the time series of the pressure, gas and wall temperature, respectively) the H₂O partial pressure (e) decreased (Fig. 1). When e dropped below the water vapour saturation pressure over ice with regard to the wall ($e_{\text{sat_ice_wall}}$), a water flux into the chamber started. Due to the expansion cooling, the gas phase water vapour saturation pressure over ice ($e_{\text{sat_ice_gas}}$) dropped below the actual water vapour pressure. As soon as the critical ice supersaturation (Fig. 4) was reached, ice particles began to form.

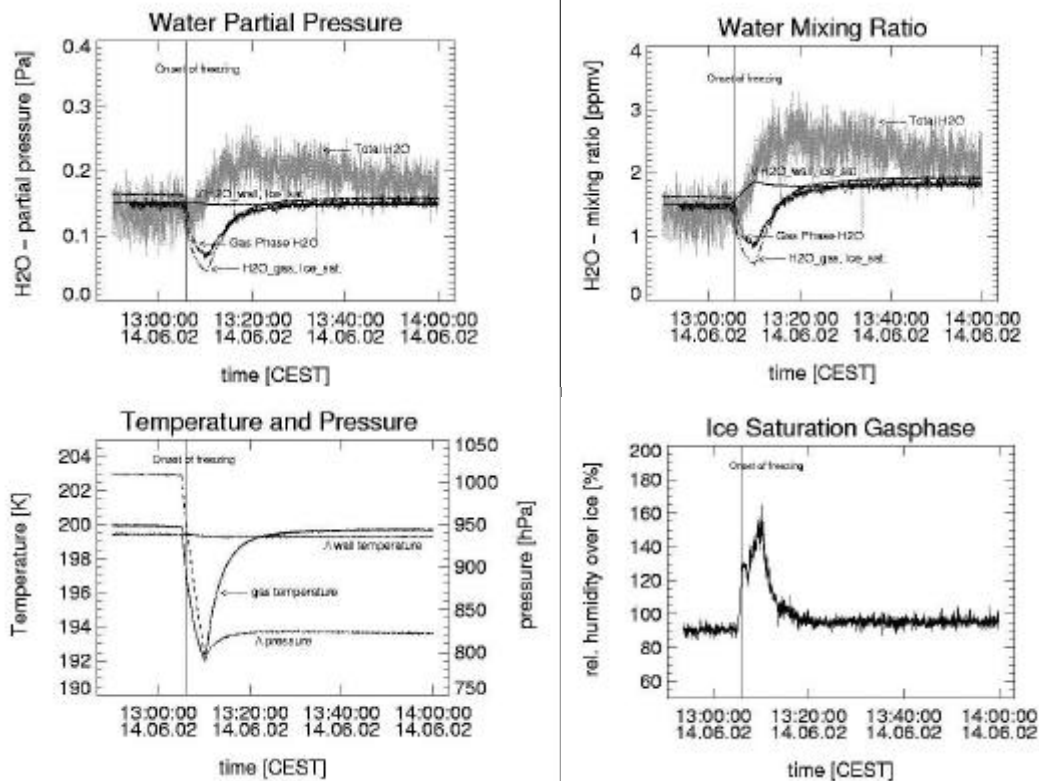
The lower water pressure over ice and the gradient between e and $e_{\text{sat_ice_wall}}$ triggered an ongoing water flux into the chamber and from the gas phase directly to the ice phase. This resulted in an increase in the total water signal. The decrease of the gas phase water (Fig. 2) was caused by the faster water transport from the gas volume to the ice nuclei compared to its transport from the chamber walls into the gas volume. The total water signal increased as long as $e_{\text{sat_ice_gas}}$ was below $e_{\text{sat_ice_wall}}$. At the same time the ice crystals grew as long as e was above or equal $e_{\text{sat_ice_gas}}$ ($rH_{\text{ice}} \geq 100\%$). With the increasing gas temperature after the end of pumping, $e_{\text{sat_ice_gas}}$ rose first above the actual value in the gas phase, rH_{ice} dropped below 100% and the ice crystals started to evaporate. As soon as $e_{\text{sat_ice_gas}}$ also exceeded the respective value for the ice covered walls of the chamber, a water flux back to these walls began. A source of uncertainty for the values of the water vapour saturation pressures remain the errors for the temperature measurements and the temperature inhomogeneities in the great chamber volume and of its walls, due to some hot spots caused e.g. by the heating of the inlet tube for the total water measurements. This uncertainty is ± 0.1 K at constant p and T conditions and rises up to less than ± 0.3 K during expansions, depending on pumping speed.

By subtracting the gas phase water vapour mixing ratio from the total water mixing ratio we are able to derive the ice water content directly from the measurements. The ice water content may be slightly underestimated due to ice particle sedimentation or impaction inside the chamber.

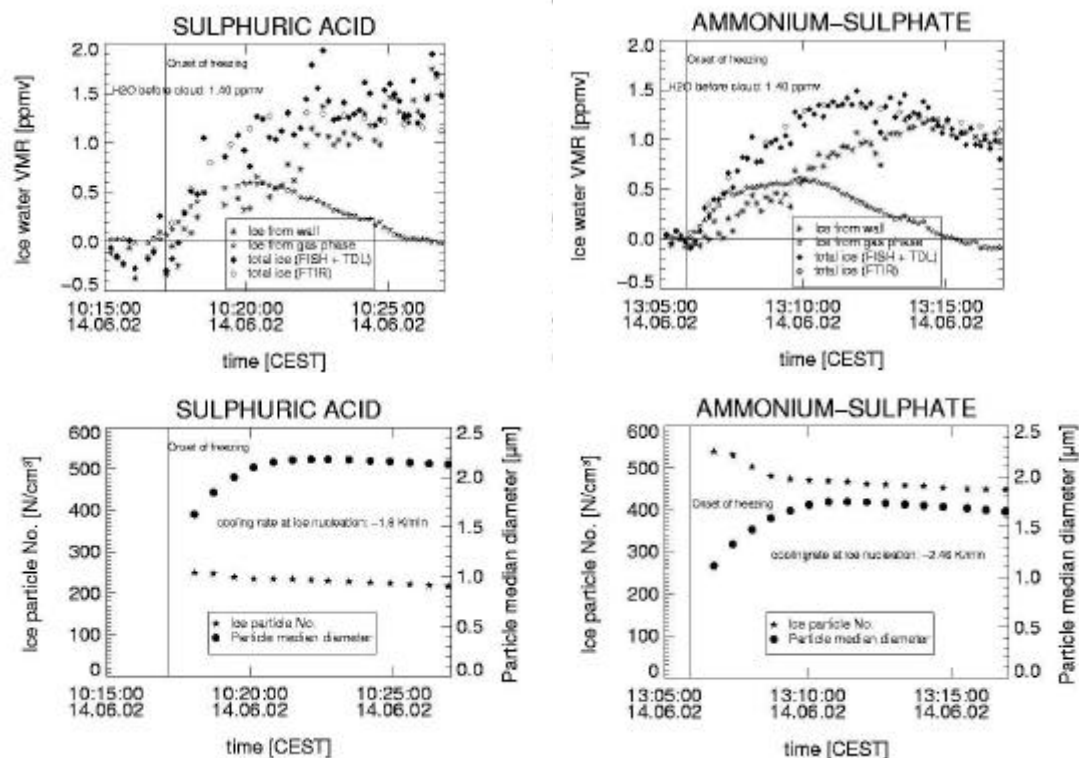
3 RESULTS

3.1 Ice cloud microphysics for two exemplary cases

Here we discuss the development of the ice phase for two experiments – one with sulphuric acid as ice nuclei and one with ammonium sulphate. Figures 5 (sulphuric acid) and 6 (ammonium sulphate) show the development of the IWC measured during the experiments – both the total IWC and the parts coming from the initial gas phase or the wall. Both experiments started at the same temperature (200 K), pressure (1000 hPa) and pumping rate. The beginning of the time axis is also the start of pumping.



Figures 1-4. Time series of the water partial pressure (Fig. 1, upper left), water mixing ratio (Fig. 2, upper right), gas temperature, wall temperature and pressure in the AIDA chamber (Fig. 3, lower left) and the relative humidity over ice (Fig. 4, lower right), measured by the TDL and calculated after Marti and Mauersberger (1993).



Figures 5-8. Exemplary cases for the development of the IWC. Figure 5 (upper left) shows the evolution of the IWC during an expansion experiment for sulphuric acid solution droplets as ice nuclei, whereas Figure 6 (upper right) displays the comparable experiment for ammonium sulphate solution droplets. The lower graphs show the development of the ice crystal number concentration and median diameter – both for sulphuric acid (lower left) and ammonium sulphate (lower right) solution droplets.

The initial aerosol number concentrations were $10,000 \text{ cm}^{-3}$ (sulphuric acid case) and 2850 cm^{-3} (ammonium sulphate case). The median diameter of the aerosol was $\sim 0.3 \mu\text{m}$ in both cases. We derived the amount of ice water coming from the gas phase from the TDL measurements by calculating the difference between the initial gas phase water content (average over 5 min before start of pumping) and the current value. The respective calculations with the total water measurements of the FISH yielded the part of ice water coming from the wall. The total IWC was given by subtracting the measured gas phase water from the measured total water. The total IWC was also obtained from the FTIR measurements by retrieving the ice crystal size distribution from the measured optical depth, adopting log-normally distributed particle sizes (for details see Wagner et al., 2003). The results presented here were derived by assuming Mie theory approximation to be valid. First test calculations applying the T-matrix method for nonspherical ice particles (finite cylinders, aspect ratio $D/L = 0.7$) indicate that the influence of particle asphericity on the IWC is well below 10 % for the range of ice crystal sizes covered by this work.

The agreement between both methods for determining the IWC was very good. The maximum value for the IWC was $\sim 1.3 \text{ ppmv}$. There was no clear difference between the two types of aerosols – both in the total ice water content and the ice water content coming either from the gas phase or the wall. In the sulphuric acid case, the FISH values showed greater scatter, caused by problems with the Lyman- α -lamp.

For the same experiments, Figures 7 (sulphuric acid) and 8 (ammonium sulphate) illustrate the evolution of the ice particle number concentration and their median diameter for the same time period as in Figures 5 and 6. Ammonium sulphate as ice nuclei yielded more but smaller ice crystals compared to sulphuric acid. This could be explained by the higher critical cooling rate for the experiment with ammonium sulphate. Note that in our experiments the pumping rates were always the same but that the onset of freezing was distinctly earlier for ammonium sulphate solution droplets. In our experimental set-up the temperature decrease was steepest at the beginning (see Fig. 3). This resulted in a higher critical cooling rate. Kärcher and Ström (2003) concluded that the amount of ice crystals produced depend strongly on the updraft velocity and therefore on the cooling rate. This could be one reason explaining our results of ice crystal number concentrations and median diameters. It also means that the critical ice supersaturation for ice formation was lower for ammonium sulphate solution droplets than for sulphuric acid. This seems to be in contrast to Koop et al. (2000), provided that the aerosol initially contained only aqueous particles but no crystalline ammonium sulphate. Preliminary data analysis revealed no indications that this would have been the case.

As explained in chapter 2.2, the slight decrease in ice crystal number concentration and median diameter could be ascribed to sedimentation or impaction inside the chamber and evaporation which started, when rH_{ice} dropped below 100 %. For the ice crystal parameters, derived from the FTIR measurements, the crystal asphericity causes a greater uncertainty in these parameters than for the IWC. Our preliminary error estimations are therefore $\pm 10 \%$ for the ice crystal median diameter and up to $\pm 20 \%$ for the number concentration.

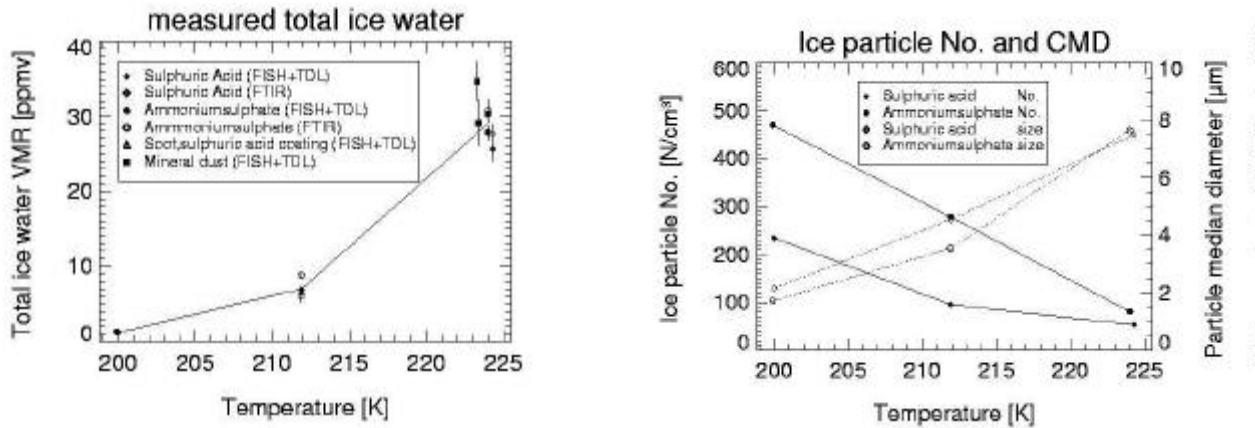
3.2 *Ice cloud microphysics – dependence on temperature and aerosol*

Figure 9 displays the maximum IWC as measured in the AIDA chamber for different types of aerosols and temperatures. All points correspond to experiments with the same pumping rate. It is obvious that with higher temperature the IWC increased. For temperatures of approximately 200 K and 210 K, there was hardly any difference for the investigated aerosols (also if we would zoom up the scale for the points at 200 K). However, at higher temperatures, there was a tendency towards higher IWC with mineral dust aerosol compared to sulphuric acid or ammonium sulphate solution droplets. The values for the IWC derived from the FTIR agreed very well with total water (FISH) and gas phase water (TDL) measurements.

Figure 10 shows the ice particle number concentration and size, obtained from the FTIR measurements, for both sulphuric acid and ammonium sulphate for a set of three different temperatures but identical pumping rates – for the point of time when the IWC reached its maximum. It clearly can be seen that in general, the number concentration increased with lower temperatures while the median diameter decreased. In the temperature range presented below, ammonium sulphate always produced more ice crystals than sulphuric acid, which were also

smaller, except for the case at ~ 224 K, when both aerosols yielded almost the same size of the ice crystals.

Table 1 summarises the most important values for our presented ice nucleation experiments – both for sulphuric acid and ammonium sulphate solution droplets. The accordance between the ice water measurements of the FISH – TDL and the FTIR, respectively, is striking.



Figures 9 and 10. The left graph (Fig. 9) shows the maximum IWC for different aerosols as ice nuclei for temperatures ranging from 200 K to 225 K. The right graph (Fig. 10) displays the ice particle number concentration and median diameter, derived from the FTIR, for both sulphuric acid and ammonium sulphate solution droplets for the same temperature range and the maximum IWC.

Table 1. Summarised results for sulphuric acid and ammonium sulphate solution droplets as ice nuclei

Temperature at ice nucleation [K]	Type of aerosol	Cooling rate at ice nucleation [K/min]	Ice particle number [N/cm ³]	Ice particle median diameter [µm]	Total IWC by FISH-TDL [ppmv]	Total IWC by FTIR [ppmv]
195.2	Sulph.acid	-1.60	234.4	2.153	1.14 ± 0.39	1.27
210.0	Sulph.acid	-2.66	95.3	4.537	6.84 ± 0.28	6.92
222.7	Sulph.acid	-3.31	52.7	7.496	25.62 ± 1.60	27.59
197.6	Amm.Sulph.	-2.46	469.8	1.719	1.25 ± 0.28	1.28
210.1	Amm.Sulph.	-2.72	278.5	3.550	6.80 ± 0.30	8.84
222.1	Amm.Sulph.	-3.12	80.5	7.547	27.81 ± 1.00	30.67

The values for the ice crystals and the ice water content correspond to the point of time when the measured ice water content has reached its maximum.

4 CONCLUSIONS

We measured the ice water content and the ice crystal number concentration and median diameter for different types of aerosols at temperatures ranging from 200 K to 225 K. As expected, the IWC generally decreased with decreasing temperature. We observed no clear influence of the aerosol type on the total IWC, except for the one experiment with mineral dust aerosol. That one showed a slight tendency towards a higher IWC compared to sulphuric acid and ammonium sulphate solution droplets. We found no clear difference between sulphuric acid and ammonium sulphate concerning the ice water coming either directly from the gas phase or from the wall.

The values for the total IWC, derived either from the FISH – TDL measurements or from the FTIR measurements, agreed very well. This affirms the possibility to gain information about ice clouds via these techniques.

Looking at the ice particle number concentration and median diameter, we found that with decreasing temperature, the ice crystal number increased and their size decreased – independent of the aerosol type investigated.

Our measurements revealed a difference for the resulting ice cloud microphysics between ammonium sulphate and sulphuric acid as ice nuclei. Ammonium sulphate produced, at the same critical cooling rate, more and smaller ice crystals.

REFERENCES

- Kärcher, B., 2002: Properties of subvisible clouds formed by homogeneous freezing. *Atmos. Chem. Phys.*, 2, 161-170.
- Kärcher, B. and U. Lohmann, 2002: A parameterization of cirrus cloud formation: Homogeneous freezing of supercooled aerosols. *J. Geophys. Res.*, 107(D2), 4010, doi:10.1029/2001JD000470.
- Kärcher, B. and J. Ström, 2003: The roles of dynamical variability and aerosols in cirrus cloud formation. *Atmos. Chem. Phys.*, 3, 823-838.
- Koop, T., B. Luo, A. Tsias, and T. Peter, 2000: Water activity as the determinant for homogeneous ice nucleation in aqueous solutions. *Nature*, 406, 611-614.
- Marti, J. and K. Mauersberger, 1993: A survey and new measurements of ice vapour pressure at temperatures between 170 K and 250 K. *Geophys. Res. Lett.*, 20, 363-366.
- Möhler, O., O. Stetzer, S. Schaefers, C. Linke, M. Schnaiter, R. Tiede, H. Saathoff, M. Krämer, A. Mangold, P. Budz, P. Zink, J. Schreiner, K. Mauersberger, W. Haag, B. Kärcher, and U. Schurath, 2003: Experimental investigation of homogeneous freezing of sulphuric acid particles in the aerosol chamber AIDA. *Atmos. Chem. Phys.*, 3, 211-223.
- Ovarlez, J., J.-F. Gayet, K. Gierens, J. Ström, H. Ovarlez, F. Auriol, R. Busen, and U. Schumann, 2002: Water vapour measurements inside cirrus clouds in Northern and Southern hemispheres during INCA. *Geophys. Res. Lett.*, 29(16), 1813, doi:10.1029/2001GL014440.
- Wagner, R., A. Mangold, O. Möhler, H. Saathoff, M. Schnaiter, and U. Schurath, 2003: A quantitative test of infrared optical constants for supercooled sulphuric acid and nitric acid droplet aerosols. *Atmos. Chem. Phys.*, 3, 1147-1164.

3-D Simulation of Contrail to Cirrus Transition - the Onset of Sedimentation

Johannes K. Nielsen*

Danish Meteorological Institute, Lyngbyvej 100, DK-2100 Kbh. Ø, Denmark.

Keywords: Wind shear, size distribution, sedimentation, contrail life time.

ABSTRACT: The processes controlling development of contrails into cirrus are deposition, sublimation, size dependent sedimentation and stretching due to wind shear. The interplay between these processes may be studied in detail with the Microphysical Cirrus (MPC) model. As an example, a specific scenario where contrails were observed over several hours is simulated. The results shows that within 30 minutes a contrail can spread out up to several kilometers horizontally.

1 INTRODUCTION

The increasing concerns about the radiational effects of aged contrails which have turned into cirrus clouds calls for detailed model studies of such processes. The quantities which are needed are specifically lifetime, horizontal and vertical extension and extinction coefficients. In other words, ultimately a contrail parameterization scheme which includes the aging of contrails based on known parameters like humidity, aviation intensity, wind shear etc. is needed. The initial processes in very young contrails has been simulated by Gierens and Jensen (1998), and a 2-D study by Ström and Gierens (2002) followed sedimentation of a cryoplane contrail up to 1.5 h. While the detailed flow dynamics of this study allowed to model the vortices of young contrails, the microphysical particle representation in this model was quite simplified.

This extended abstract focuses on the aging of contrails into cirrus, by employing a detailed microphysical box model embedded in a 3-D fluid simulation which takes into account wind transport and size dependent sedimentation.

2 THE MPC MODEL

The MicroPhysical Cirrus (MPC) model is an integrated model developed at DMI which combines a well tested microphysical box-model with a quite accurate 3-D advection scheme. The microphysical kernel was originally developed for simulations of PSC clouds (Larsen 2000), and as a consequence the MPC-model may be applied on PSC-clouds as well as cirrus clouds. The dynamical variables of the model are gas-phase mixing ratios of water and HNO₃, size-distributions (in these simulations 51 bins) of 4 different particle types, (supercooled ternary solutions, sulphuric acid tetrahydrate, nitric acid trihydrate and ice) and in-particle weight fractions of condensed phase constituents. The model includes nucleation processes and detailed sedimentation calculation on each size bin. Wind transport, sedimentation and parts of the particle growth processes are calculated by the Walcek-algorithm (Walcek 2000). At the present, the model is being combined with optical routines so that extinction coefficients and backscattering ratios can be calculated.

3 SIMULATION DETAILS

The wind pressure and temperature fields are interpolated ECMWF data. The initial humidity was initialized from a local radio sounding launched close to simulation start time (see Figure 1). The sounding shows a region with supersaturation around 11 km altitude. No corrections were applied to this sounding, and it is likely that it underestimates humidity near the tropopause. The simulation box follows the wind field (for 0.5 hour) in order to keep the cloud inside the box. The simulation

* Corresponding author: Johannes Nielsen, DMI, Lyngbyvej 100, DK 2100 KBHØ. Denmark, Email: jkn@dmi.dk

was initiated with a 150 seconds old contrail, which has been characterized by Gierens and Jensen (1998). The ice particle density of the contrails were initialized to 500 particles/ccm, with mean radius 1 micrometer. The initial contrail cross section was 250 m (horizontal) and 150 m (vertical). The simulation presented here was carried out on a laptop, during 10 hours. The grid is 36x36 x36, the maximum time step is 15 sec., and the number of logarithmically spaced size bins are 51 ([0.001:200] micrometer).

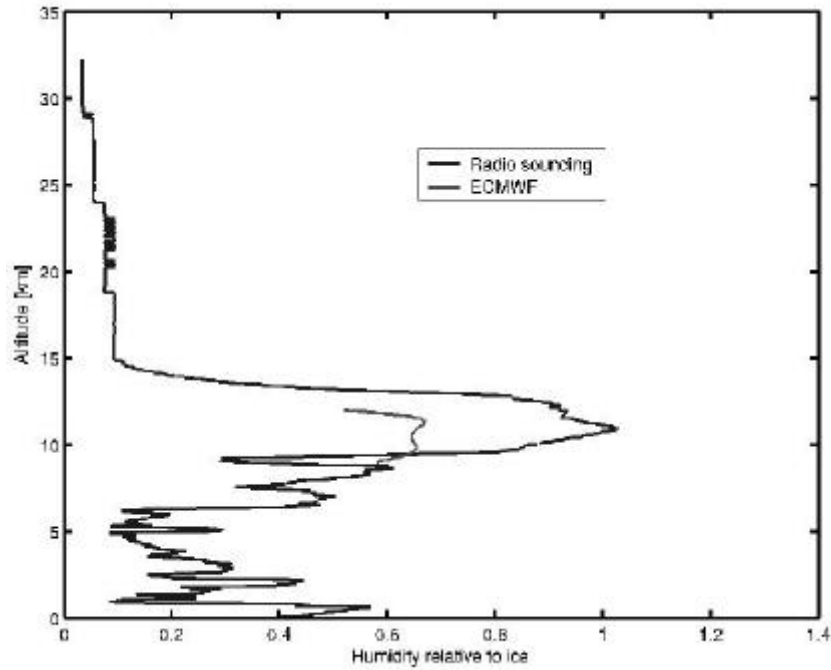


Figure 1. Humidity profile recorded from radiosounding Jægersborg March 16 03 12:00 UTC (DMI).

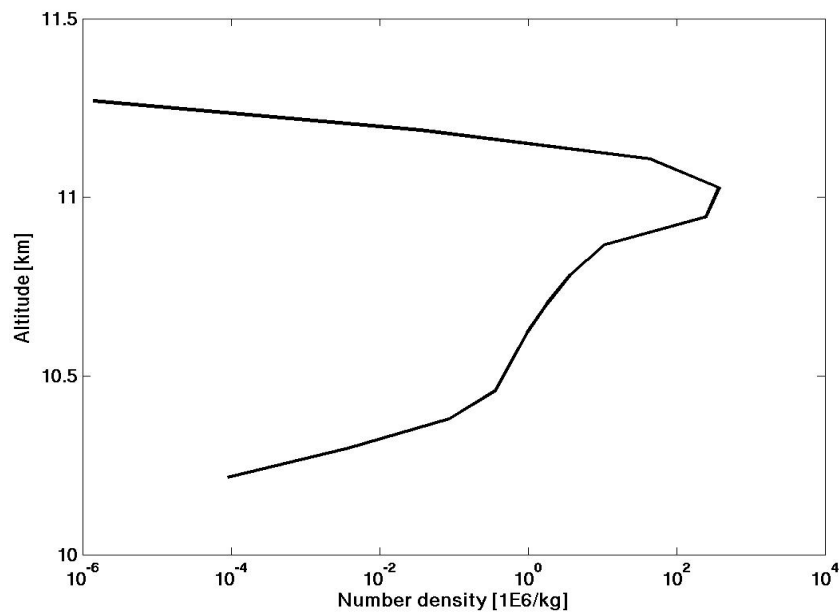


Figure 2. In cloud particle density 0.5 h into simulation.

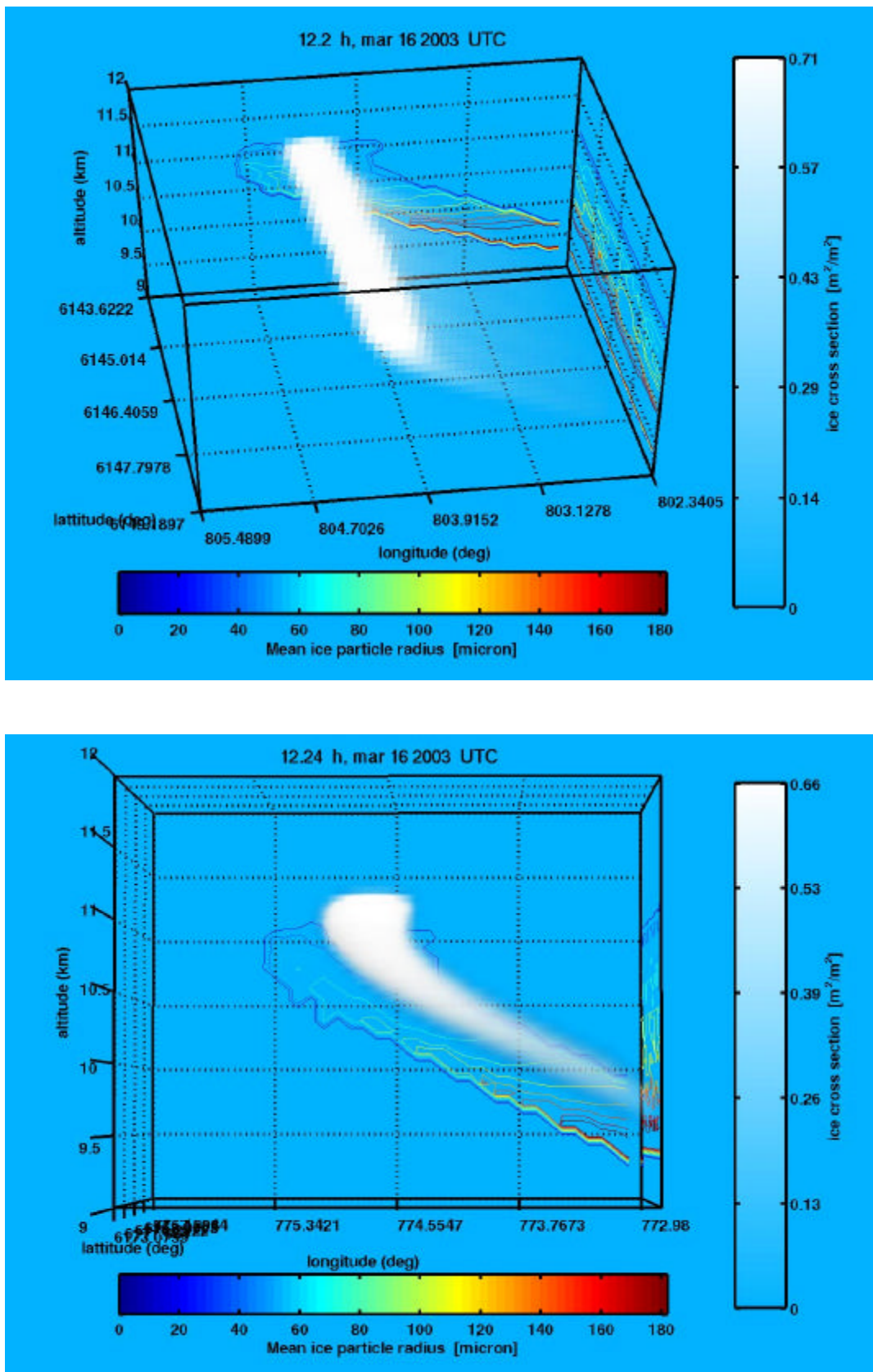


Figure 3: Two simulation snapshots Cloudplots are produced by superimposing layers of opacity proportional to the local cross-section density. Looking through the cloud one sees the integrated cross section area, which gives a quite good impression of the physical distribution of the cloud.

4 RESULTS

Sedimentation starts after a few minutes, and is speeded up as particles enter the humid region below the cloud. The largest particles occur in the first fall streak front which enters into a supersaturated region with a thickness of 1 km. Their radius grow up to a 180 micrometer (shown by contours at walls). As this front vanishes into the subsaturated region below 10 km altitude, the mean radius falls to below 50 micrometers in the bulk of the cloud. Even though the lower parts of the cloud appears quite dense, the number density is only about 5-10 particles per ccm. The cloud remains visible because of the larger particle size. Due to shear motion under the tropopause the contrail is spread out significantly. After 0.2 hour it ranges over about 2 km horizontally, and 1 km vertically. It then stays at this size because the lower parts begin to sublimate. The particle density in the upper part decreases of course during the 0.5 h simulation, but only to 65 % of the initial value, thus there is nothing to hinder the cloud from existing much longer (unfortunately it escaped out of the box in this simulation).

5 CONCLUSION

This extended abstract demonstrates that detailed simulations of contrail aging may indeed be performed. The contrail in this simulation persists for at least 0.5 h, - which is the duration of this relatively short simulation. It ranges over approximately 2 kilometers horizontally. In near future statistical analysis of several simulations of this kind spanning over a range of atmospheric conditions may help to parameterize the impact of cirrus clouds originating from airplane traffic in global models.

REFERENCES

- Gierens, K. and Jensen, E., 1998: A numerical study of the contrail-to-cirrus transition. *Geophys. Res. Lett.*, 25, 4341-4344.
- Larsen, N., 2000: Polar Stratospheric Clouds - Microphysical and optical models. *Technical Report, 00-06, Danish Meteorological Institute, Copenhagen.*
- Ström, L. and Gierens, 2002 : First simulation of cryoplane contrails. *J. Geophys. Res.* 107, (D18), 4346, doi:10.1029/2001JD000838, 2002.
- Walcek, C. J., 2000: Minor flux adjustment near mixing ratio extremes for simplified yet highly accurate monotonic calculation of tracer advection, *J. Geophys. Res.* 105, 9335-9348.

Heterogeneous nucleation effects on cirrus cloud coverage

K. Gierens*, S. Brinkop

DLR-Institut für Physik der Atmosphäre, Oberpfaffenhofen, Germany

Keywords: cirrus, indirect effect of 1st kind, heterogeneous nucleation

ABSTRACT: The indirect effect of 1st kind of aerosols is the effect of additional ice nuclei capable of heterogeneous nucleation on cirrus formation. It is usually thought to lead to enhanced cloud coverage. In this paper we discuss that this view may be too simple. Experiments conducted with a general circulation model and including both homogeneous and heterogeneous cirrus formation paths and a novel cirrus cover parametrisation showed reduced cloud coverage compared to a control run. Unfortunately, the results depend sensitively on a number of uncertain parameters. Thus an assessment of the climatic role of the indirect effect of aircraft aerosol does not seem to be in reach currently.

1 NOVEL PARAMETERISATIONS FOR CIRRUS CLOUD COVERAGE

The current investigation requires that both homogeneous and heterogeneous cirrus formation pathways are represented in the model and that the coverage resulting from both formation paths can be determined separately. In order to achieve this we implemented a switch in ECHAM's cloud physics routines that decides at every time step and in each grid box whether homogeneous or heterogeneous nucleation takes place (if at all). This is decided by means of a critical concentration of heterogeneous freezing nuclei that depends in particular on updraft speed, temperature, and the assumed ice supersaturation at which heterogeneous freezing would commence (for details see Gierens, 2003). Figure 1 gives some examples of the critical concentration.

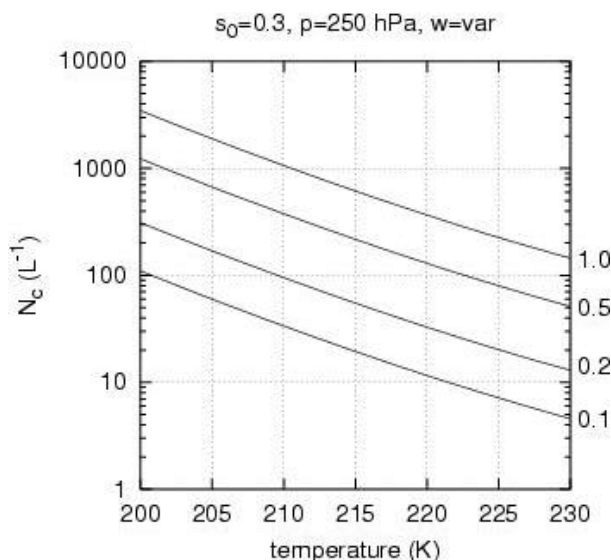


Figure 1. Critical concentration of heterogeneous freezing nuclei as function of temperature and updraft speed (curve parameter on the rhs of the figure). A threshold ice-supersaturation necessary for heterogeneous freezing of 0.3 (i.e. $Rhi=130\%$) was assumed for the calculation of the curves.

* Corresponding author: Klaus Gierens, DLR-Institut für Physik der Atmosphäre, Oberpfaffenhofen, D-82234 Wessling, Germany. Email: klaus.gierens@dlr.de

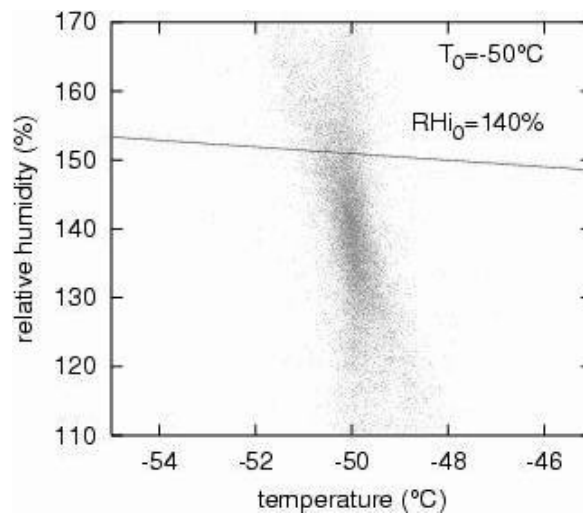


Figure 2. Statistical distribution of instantaneous fluctuations of temperature and relative humidity about grid scale values of $T_0 = -50^\circ\text{C}$ and $Rhi_0 = 140\%$ for a grid box in T42 resolution. The horizontal line marks the threshold for homogeneous freezing of aqueous solution droplets. All fluctuations (dots) that reach above the threshold imply cirrus formation.

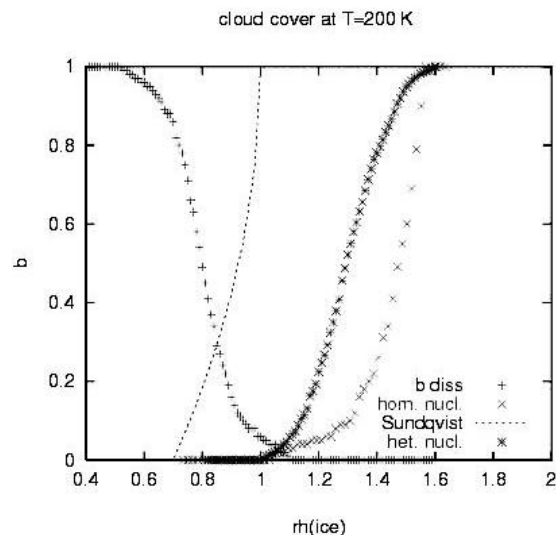


Figure 3. Relation between relative humidity with respect to ice and cirrus cloud cover as it results in ECHAM4 after implementation of the overlap integral method. The dashed line represents the traditional Sundqvist parameterisation, where an overcast sky is assumed already for ice saturation. In contrast the new parameterisations (\times and stars for homogeneous and heterogeneous nucleation, resp.) lead to an overcast sky only at high degrees of supersaturation. The curve “b diss” (+) shows the coverage that vanishes in a dissipation situation (i.e. decreasing relative humidity).

If in a certain situation the concentration of heterogeneous freezing nuclei exceeds the critical value, then heterogeneous nucleation occurs, otherwise homogeneous nucleation. A simultaneous action of both freezing processes in the same grid box is not considered. The number of ice crystals forming from a heterogeneous nucleation event equals the critical concentration or a certain fraction thereof (tuning parameter). In an homogeneous nucleation event it is given by the formulations of Kärcher and Lohmann (2002). The updraft speed in a large scale model should be augmented by a measure of the subgrid scale turbulent motions (e.g. TKE). Another currently uncertain parameter is the threshold supersaturation for heterogeneous freezing, for which we chose constant values of 0.3 for soot (if $T < -53^\circ\text{C}$) and 0.1 for mineral dust (if $T < -35^\circ\text{C}$). These values are obtained from recent laboratory measurements (DeMott et al., 1999; Möhler et al., 2003); however, the scatter in the measurement results is large, and thus the chosen thresholds are uncertain.

Cirrus cloud coverage, b , is parameterised using the method of overlap integrals. This novel method starts from a division of the state phase space $\{T, RH\}$ into two domains, one in which cirrus can form, and one where this is not the case. The demarcation line between these two domains is the critical supersaturation for (homogeneous or heterogeneous) nucleation. For homogeneous nucleation the critical supersaturation has been obtained from the laboratory results of Koop et al. (2000). For heterogeneous nucleation we use the aforementioned temperature-independent values. Second we use measured distributions of instantaneous random fluctuations of the state phase variables around their grid box mean values. The measured distributions (Gierens et al., 1997) can be fitted with an analytical function formed from two Lorentzian distributions. This 2D-function, centred in the phase space at the respective grid scale value for each box, can overlap partially with the domain where cirrus can be formed. An example of this for is shown in Figure 2 for cirrus coverage due to homogeneous nucleation.

The amount of overlap is the so-called overlap integral. Its value determines the fractional coverage of cirrus clouds. A corresponding formulation can be used for the dissipation of clouds. For this the critical "supersaturation" is -0.2 , i.e. when fluctuations of RH_i (relative humidity with respect to ice) reach below 80%, the cirrus fractional coverage is decreased. As a result, the parameterisation allows for supersaturation, and there is a hysteresis curve in a RH vs. b diagram (Figure 3).

2 FIRST SIMULATIONS WITH ECHAM

We have used the general circulation model ECHAM4 in T30, L19 resolution, and updated with the parameterisations for homogeneous cirrus formation by Kärcher and Lohmann (2002) to study the effect of a novel consistent cirrus cover parameterisation and heterogeneous freezing on cirrus coverage. Two five year runs have been performed: (1) a control run with homogeneous cirrus formation after Kärcher and Lohmann (2002) and with the traditional coverage parameterisation by Sundqvist (1978), and (2) a test case where the Sundqvist parameterisation has been replaced by our new parameterisation for cirrus coverage and a simple parameterisation for the heterogeneous freezing process.

The results presented here are preliminary since there are a couple of uncertain parameters involved and the model reacts quite sensitively to some of them: background aerosol concentration, freezing thresholds and critical humidities of aerosols. Nevertheless, they made us aware of some potential effects of heterogeneous nucleation on cirrus cloud coverage that we did not see so clearly before.

Figure 4 shows the effect of the new parameterisation on total cloud cover. There is not much of an effect in the lower and middle troposphere, as expected. Generally cirrus cover is reduced compared to the control run due to the higher thresholds to cirrus cover formation (Figure 3). In the control run cirrus cover is already possible if the humidity gets larger than 70% in a grid box. If supersaturation occurs then total overcast conditions are present.

A short sensitivity run with the new cirrus cover parameterisation for homogeneous nucleation only shows a stronger decrease in cirrus coverage compared to the control run and compared to the run with heterogeneous nucleation. For homogeneous cirrus cover development the critical thresholds for humidity and temperature are the most extreme (Figure 3). Thus, heterogeneous nucleation mainly increased cirrus cover in our simulation.

However, as heterogeneous freezing occurs before homogeneous freezing can act, the homogeneous pathway is suppressed to a large degree. Figure 5 shows that in the right panel the homogeneously formed clouds (broken contour) are only present in a shallow region in upper troposphere of the southern hemisphere, otherwise the tropopause region is dominated by heterogeneously formed cirrus (solid contours). In the simulation this is certainly a consequence of the low freezing threshold of $s_0=0.1$ at $T<238\text{K}$ assumed for mineral dust. Sensitivity studies with higher threshold values led to larger cirrus cover in the tropics because then the probability for homogeneous freezing increased which resulted in enhanced cirrus coverage. On the other hand, heterogeneously formed cirrus will usually have lower ice crystal number concentrations than homogeneously formed cirrus. This could lead to larger ice crystals (less competition for the

available water vapour; however, less supersaturation at freezing could balance this), stronger sedimentation, and eventually shorter average life times and hence lower cirrus amount.

In an assessment of the role of the indirect effect of 1st kind of aviation aerosols it is also necessary to compare the average optical thicknesses of both kinds of cirrus clouds, which could also be tested with the current set of simulations. It must be expected that heterogeneously formed cirrus is optically thinner than its counterpart formed homogeneously. This investigation has not yet been done so far.

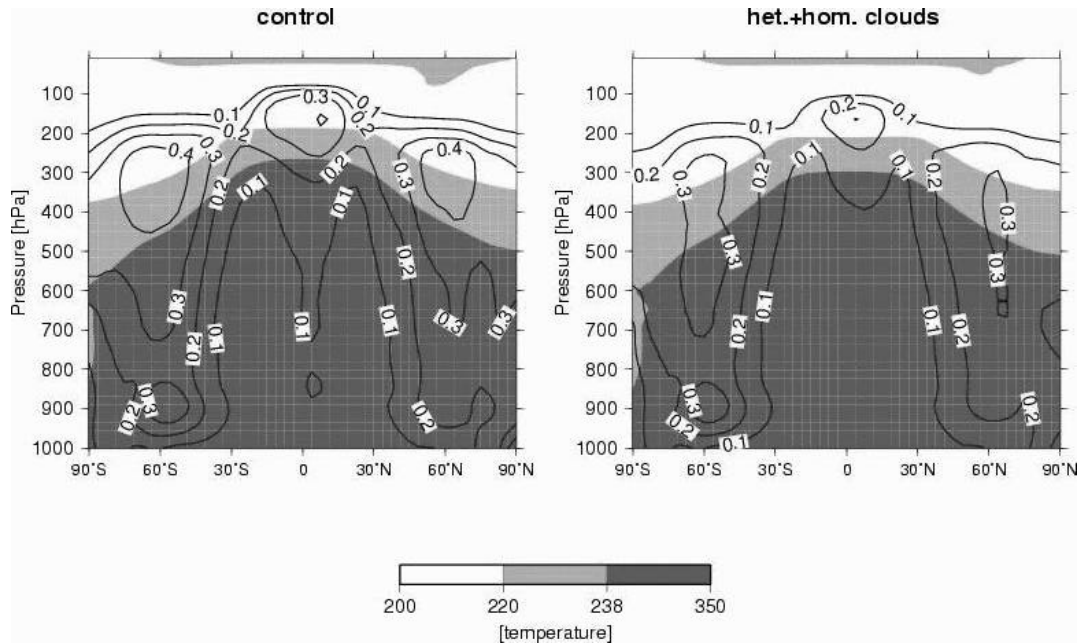


Figure 4. Zonally and annually averaged total cloud cover in a 5-years ECHAM4 simulation with Kärcher and Lohmann (2002) microphysics of homogeneous nucleation. Left panel: control run with Sundqvist (1978) parameterisation of cirrus coverage (without heterogeneous cirrus formation). Right panel: simulation with both homogeneous and heterogeneous freezing and with new parameterisation of cirrus coverage.

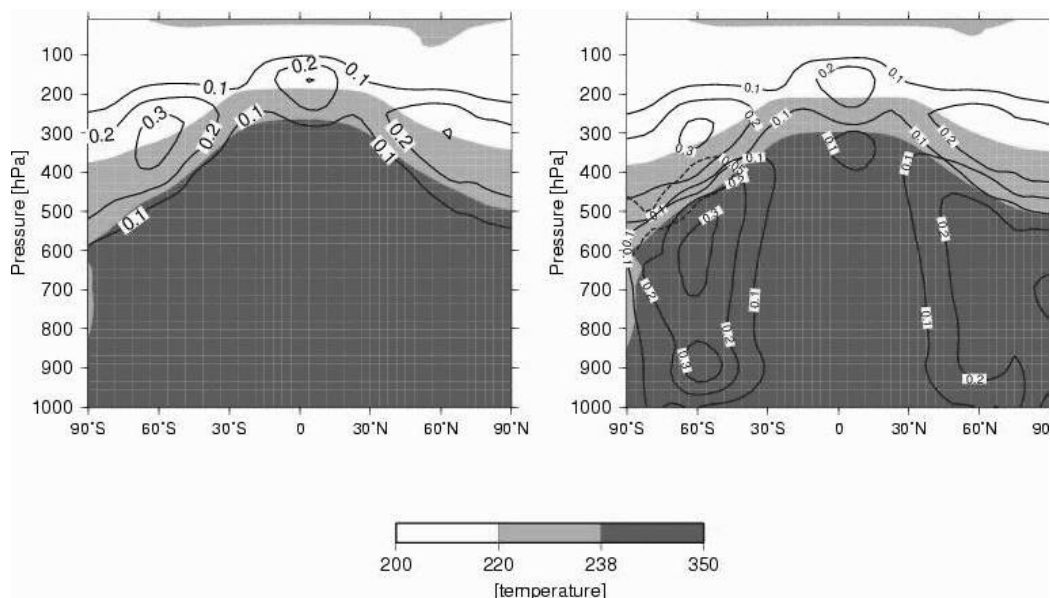


Figure 5. Run with new parameterisation of cirrus coverage. Left panel: Zonally and annually averaged cirrus coverage due to both homogeneous and heterogeneous nucleation. Right panel: Cloud coverage due to different formation pathways, heterogeneously formed cirrus (solid contours in the cold regime, $T < 238\text{K}$), homogeneously formed cirrus (dashed contour), and other clouds (solid contours in the warmer regime). It can be noted that due to the assumed low freezing threshold of mineral dust ($s_0 = 0.1$ at $T < 238\text{K}$) the homogeneous ice formation pathway is almost completely suppressed.

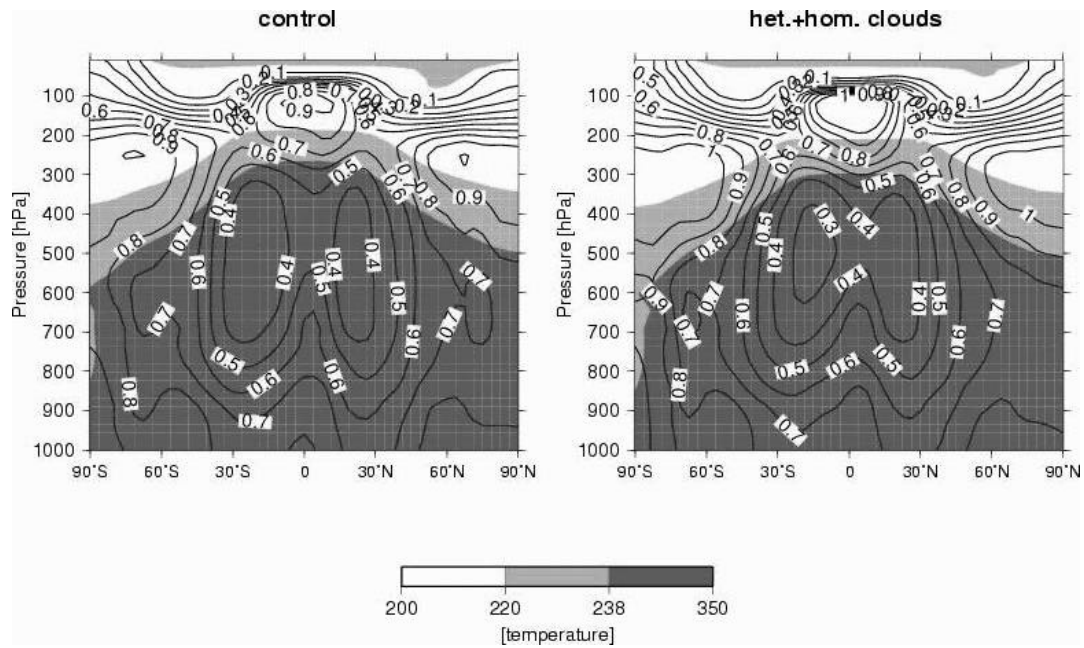


Figure 6. Zonally and annually averaged relative humidity with respect to ice in the control run (left) and the run with new parameterisations (right). It can be seen that the new parameterisations lead to higher average relative humidity values in the upper troposphere of both hemispheres and the tropics. Only in the subtropical subsidence zones there is no effect evident.

Figure 6 shows the effect of the new parameterisation on the average relative humidity field. It can be seen by comparing the left and right panels that the average relative humidity increases almost everywhere in the upper troposphere when the new parameterisation is used. The only exception are the subtropical subsidence zones in both hemispheres where a difference between the control and the sensitivity run is not obvious.

3 SUMMARY AND CONCLUSIONS

The atmosphere is loaded with different kinds of aerosol acting as possible nucleation sites for ice-crystals (black carbon, dust). These aerosol particles may become involved in heterogeneous cirrus formation processes at ice-supersaturations lower than those needed for homogeneous nucleation. Therefore it is generally believed that this so-called indirect effect of aerosol would lead to larger cirrus cloud coverage on average, compared to a hypothetical case with no aerosol emissions. However, this view is too simple. There are competing effects that must be considered in a complete assessment of the indirect effect. First, cirrus formed heterogeneously is probably optically thinner than homogeneously formed cirrus, because crystal numbers are less, and maximum supersaturation during the nucleation event is less. Second, after a heterogeneous cloud has formed the supersaturation is used up for a while, and a homogeneous cloud will not form whereas it would have been formed without the indirect effect. Third, lifetimes of heterogeneously formed clouds may differ systematically from those formed homogeneously. Preliminary results obtained with the ECHAM4 model (involving new parameterisations for cirrus coverage from heterogeneous and homogeneous processes) show indications for these possible effects. The evaluation of the two simulations is not yet complete, hence the causal chain of all these mechanisms is not yet known with sufficient degree of confidence. Unfortunately, there is considerable uncertainty in many of the parameters involved. Thus an assessment of the climatic role of the indirect effect of aircraft aerosols does not seem to be in reach currently.

REFERENCES

- DeMott, P.J., Y. Chen, S.M. Kreidenweis, D.C. Rogers and D.E. Sherman, 1999: Ice formation by black carbon particles. *Geophys. Res. Lett.* 26, 2429-2432.
- Gierens, K., U. Schumann, H.G.J. Smit, M. Helten and G. Zängl, 1997: Determination of humidity and temperature fluctuations based on MOZAIC data and parameterization of persistent contrail coverage for general circulation models. *Ann. Geophys.* 15, 1057-1066.
- Gierens, K., 2003: On the transition between heterogeneous and homogeneous freezing. *Atmos. Chem. Phys.* 3, 437-446.
- Kärcher, B. and U. Lohmann, 2002: A parameterization of cirrus cloud formation: Homogeneous freezing including effects of aerosol size. *J. Geophys. Res.* 107, doi: 10.1029/2001JD001429.
- Sundqvist, H., 1978: A parameterization scheme for non-convective condensation including prediction of cloud water content. *Quart. J. Roy. Meteor. Soc.* 104, 677-690.

Contrail Coverage over the USA Derived from MODIS and AVHRR Data

R. Palikonda⁴, D. N. Phan, V. Chakrapani
Analytical Sciences and Materials, Inc., Hampton, Virginia, USA

Patrick Minnis
Atmospheric Sciences, NASA Langley Research Center, Hampton, Virginia, USA

Keywords: air traffic, contrails, aircraft emission, remote sensing

1 INTRODUCTION

Contrails often lead to the development of additional cirrus clouds that can affect climate via the radiation budget. Evaluation of contrail coverage and optical properties is crucial for assessing the impact of current and future climatic effects of air traffic. Current estimates of contrail coverage over the United States of America (USA) have been based on a single NOAA-16 (N16) afternoon overpass time for recent studies and at four times of day for 1993-94 data from two satellites with different sensitivities and detection errors (Palikonda et al. 1999). Approximately 25,000 flights cross portions of the USA each day at different times of day. The commercial flight activity begins in earnest around 0600 LT and continues with high intensity before fading shortly before local midnight. Because spreading contrail lifetimes are generally less than 4-6 hours, the atmosphere should be cleansed of most contrail coverage by the beginning of the next day (Garber et al. 2003). Assuming that the state of the upper troposphere is, on average, the same during the day, this daily cycle should be reflected in the contrail properties and coverage. However, preliminary studies using NOAA-15 (N15)_morning overpasses suggest that the afternoon analyses may underestimate the contrail coverage because the spreading and saturation of contrails formed during the morning in areas of heavy air traffic might mask or diminish the contrails formed during the afternoon. To obtain a better assessment of the diurnal variation in contrail coverage, this study analyzes data taken during 2001 over the USA from N15 in the early morning period followed by N16 during the afternoon.

2 DATA AND METHODOLOGY

The satellite data used for this study include 1-km radiances from the morning (~0730 LT) N15 and mid-afternoon (~1430 LT) N16 Advanced Very High Resolution Radiometer (AVHRR) overpasses over the continental USA covering the domain between 25°N and 55°N and 65°W and 130°W. The domain is divided into a 30 x 65 1°-region grid. Images from all available overpasses are analyzed to calculate the contrail statistics. Only those regions having more than 90% of the expected number of pixels and having at least ten images each month are used in the monthly statistics. The Monterrey, California receiving station consistently had bad data from the N15 AVHRR resulting in the loss of many western regions in the statistics. In addition, many of the N15 overpasses for January and October yielded corrupted data and were not included in the results. The contrail mask, areal coverage, visible optical depth *OD*, and contrail longwave radiative forcing CLRF are computed as in Palikonda et al. (2002).

⁴ *Corresponding author:* Rabindra Palikonda, 1 Enterprise Parkway, Hampton, VA, USA 23666. Email: r.palikonda@larc.nasa.gov

3 RESULTS

Figures 1–4 show the monthly distribution of contrail cover over the domain. During April, for the morning overpass (N15, Fig 1a), maximum contrail coverage occurs over the southeastern states, off the coasts of Texas and Louisiana, and in northern Ohio. In the afternoon (N16, Fig 1b), maximum coverage occurs over North Dakota, Nevada, Washington, northern Mexico, and adjacent Pacific Ocean, areas not available from N15. The N15 maximum over the western Gulf of Mexico is still evident as a relative maximum in the N16 results. The domain averages are 1.29% and 0.71%

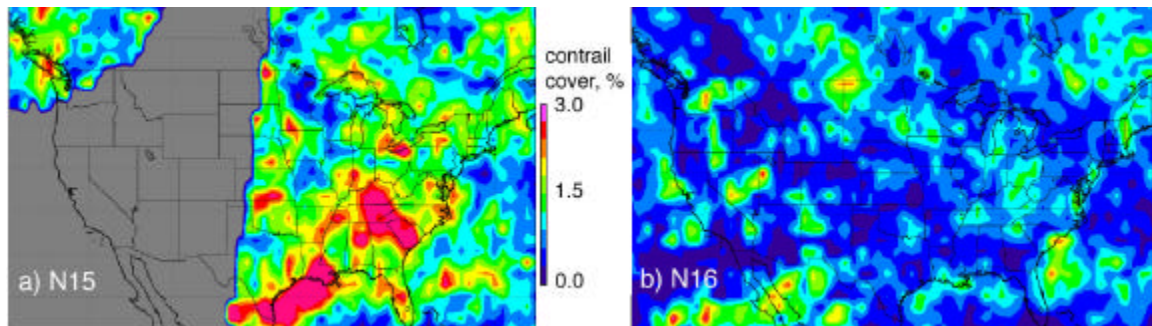


Figure 1. April 2001 daytime contrail coverage

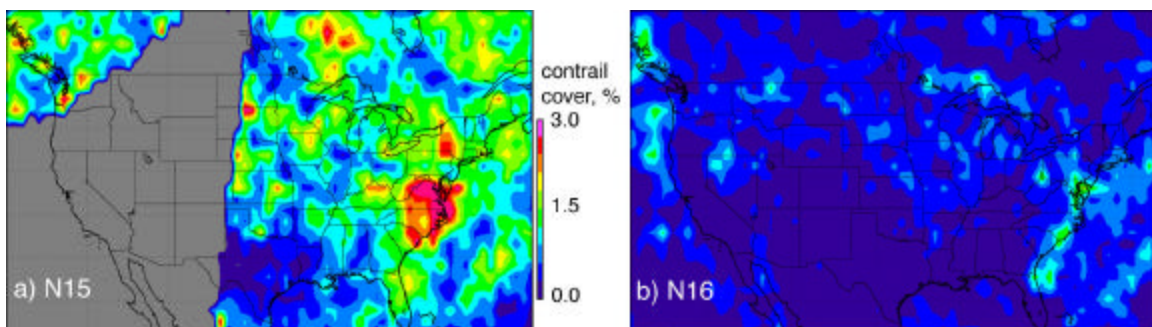


Figure 2. July 2001 daytime contrail coverage

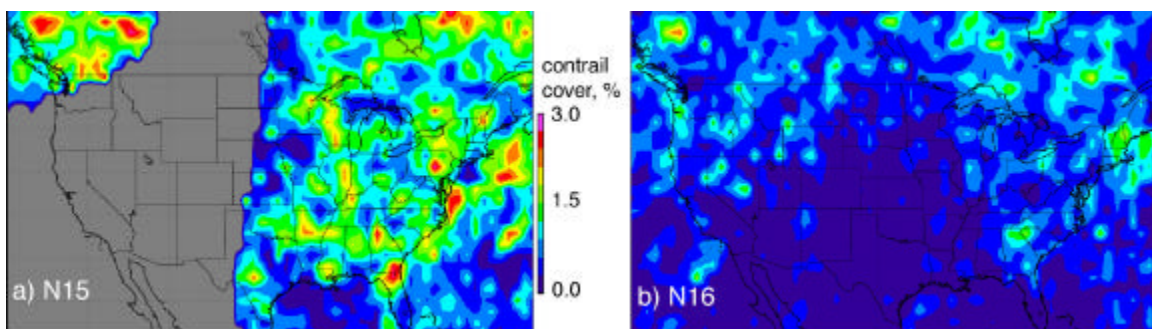


Figure 3. September 2001 daytime contrail coverage.

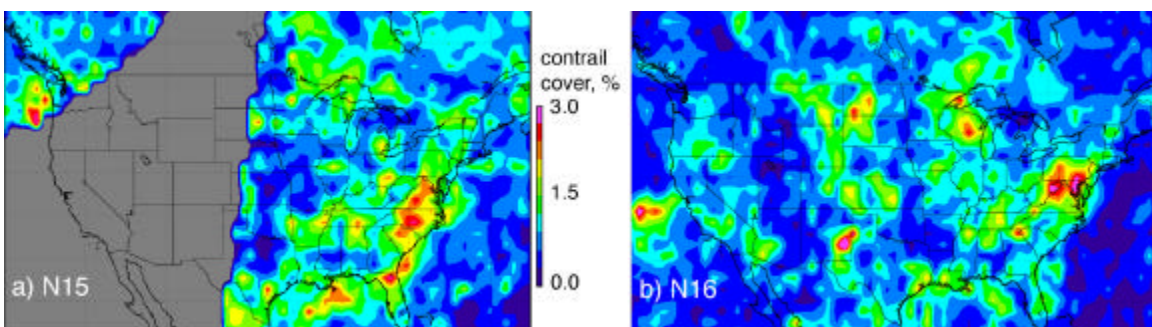


Figure 4. December 2001 daytime contrail coverage.

In the morning and afternoon, respectively. These means include differing numbers of regions. The morning July contrail cover (Fig. 2a) peaks over Virginia, North Carolina, South Carolina, and New York. Minimum coverage occurs over Texas, Louisiana, Alabama, and Minnesota. The areal coverage is almost 70% less during the afternoon (Fig. 2b). A local maximum occurred along the Atlantic coast from Maryland to Florida, and off the coasts of Oregon, Washington, and British Columbia. These areas of maximum coverage are similar to those in the N15 retrievals. The substantial morning-afternoon difference in areal coverage persists in September (Fig. 3). During the morning (Fig. 3a), maximum contrail coverage exceeds 2% over southwestern Canada, Georgia, Pennsylvania, and east of Virginia. The extensive contrail minimum in the afternoon (Fig. 3b) is defined by a triangle extending from southern California to South Dakota and to the tip of Florida. Maximum coverage occurred over British Columbia, Oregon, New England, Quebec, and Lake Winnipeg. During the winter, in the morning (Fig. 4a), contrail cover exceeds 1.5% over the southeastern states and Gulf of Mexico, off the coast of Oregon and Washington. The afternoon coverage during December (Fig. 4b) peaks over northern Virginia, West Virginia, Maryland, and Pennsylvania. Local maxima are seen over New Mexico, Wisconsin, and west of California.

The results, including the mean values for CLRF and OD , are summarized in Table 1 for the areas within the domain that are common to both N15 and N16 retrievals. The contrail coverage is greater during the morning than in the afternoon. Perhaps, this variation is a result of the atmosphere being cleaner (fewer flights) during early morning, so contrails are more easily observed and grow more. Also, the upper tropospheric humidity (UTH) is probably greater in the morning from previous day's convection and less in the mid-afternoon prior to convection. The coverage during the afternoon peaks during the winter and is at a minimum during July, differing by a factor of 3. The coverage in the morning is at a maximum during April and minimum during August and September. The most variation between morning and afternoon is seen during summer months, differing by a factor of 2 to 3. The least variation in coverage is during December, when the difference in UTH between morning and afternoon is probably smaller than during the warmer months. Other reasons for the difference include different sensitivities of the N15 and N16 brightness temperature differences (BTD) to the thresholds used for contrail detection and differences in the background temperatures.

The mean contrail optical depths in Table 1 vary with season to some degree. The summer maximum is around 20% greater than the February minimum. Optical depths retrieved from N16 averaged 0.29 compared to 0.26 from N15. This 12% difference is relatively consistent from month to month. The N15 and N16 monthly frequency distributions of contrail optical depth in Figure 5 are remarkably consistent. During all months, $0.2 < OD \leq 0.4$ for more than 30% of the contrails. Thicker contrails were observed more frequently in summer than during the winter and spring.

The contrail radiative forcing (Table 1) in the morning was greatest during the summer months and at a minimum during February. In the afternoon, the maximum and minimum CLRF occurred during April and July, respectively. CLRF depends on both the contrail coverage and its background. Unit CLRF, the ratio of CLRF to the fractional contrail coverage, varies from 8 Wm^{-2} in February to 18 Wm^{-2} during July in the morning. In the afternoon, CLRF varies from 6 Wm^{-2} in February to 27 Wm^{-2} during July indicating that the thermal contrast changed by a factor of 4 between winter and summer compared to a change of less than 50% between morning and afternoon.

On average, the contrail coverage ranges from a minimum of 0.68 during August to a maximum of 1.06 in February. Between February and May, the mean varies by less than 0.08. Similarly, between July and September, it varies by only 0.03. Thus, the periods of minima and maxima are broad and the actual extrema at a given time of day or in a given year could occur in different months than February and August. The mean minimum contrail OD (0.235) occurred during February while the maximum average (0.295) was found during July. Mean CLRF ranged from 0.075 Wm^{-2} in March to 0.145 Wm^{-2} during September.

Table 1. NOAA-15 & NOAA16 contrail properties, 2001.

Month	contrail cover (%)		OD		CLRF Wm^{-2}	
	N15	N16	N15	N16	N15	N16
January	N/A	0.92	N/A	0.25	N/A	0.11
February	1.19	0.93	0.23	0.24	0.10	0.06
March	1.11	0.86	0.24	0.26	0.10	0.05
April	1.29	0.71	0.25	0.28	0.11	0.14
May	1.40	0.55	0.27	0.31	0.12	0.06
June	1.17	0.44	0.26	0.30	0.15	0.04
July	1.08	0.33	0.28	0.31	0.18	0.09
August	0.97	0.38	0.27	0.30	0.18	0.03
September	0.96	0.45	0.28	0.30	0.18	0.11
October	N/A	0.71	N/A	0.31	N/A	0.09
November	1.04	0.84	0.26	0.28	0.13	0.07
December	0.91	0.80	0.26	0.28	0.14	0.07

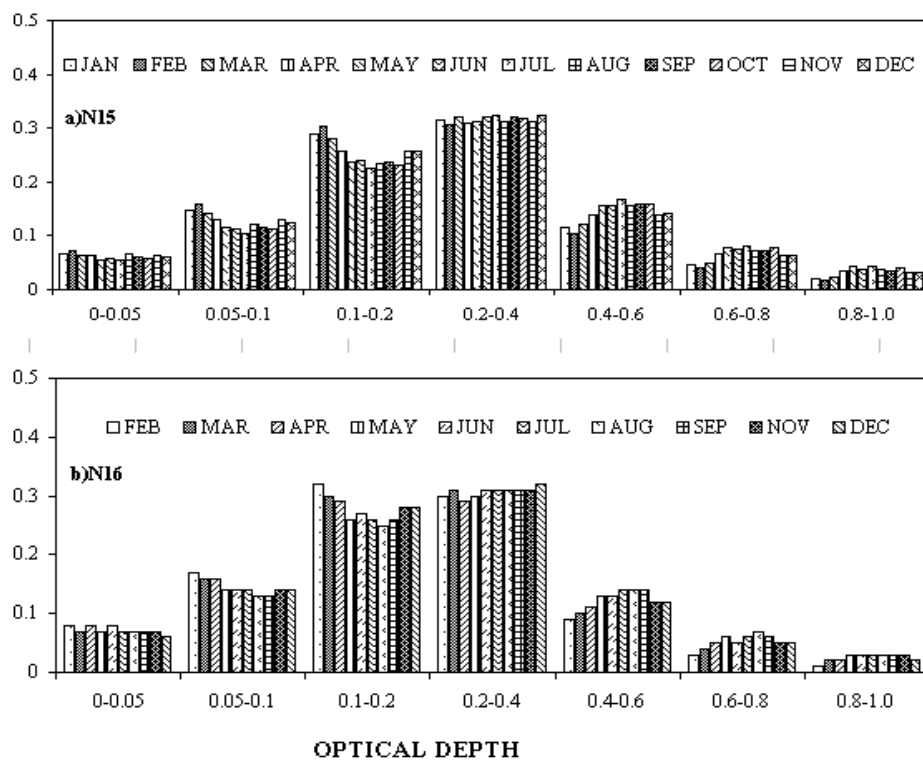


Figure 5. Histogram of daytime contrail optical depths from NOAA-15 and NOAA-16 over USA, 2001.

4 DISCUSSION

As noted earlier, the differences in contrail coverage between the two satellites may be due, in part, to different sensitivities of the 11 and 12- μm channels on the two AVHRRs. Each channel has a slightly different spectral response function and slightly different calibration. Small differences in each channel can translate to large differences in the BTDR relative to the pixel-use threshold value. Visually, the BTDR images from the two satellites are quite different when constructed using the same temperature range and contrast suggesting that the contrail retrievals would be different using the same methodology. The retrieval error rates have not been established yet. Palikonda et al. (1999) roughly estimated that the error rate for applying the same methodology to AVHRR data from NOAA-11 and 12 resulted in a 25% overestimate of the USA contrail coverage. Meyer et al. (2002) have developed more rigorous correction methods (e.g., false alarm rate, stationary artifacts, detection efficiency) for the NOAA-14 AVHRR contrail analysis that will be constructed for the data used here. Such techniques should account for the cirrus streaks and land forms that can be misinterpreted as contrails.

Table 2. Comparison of estimated USA contrail coverage (%).

Month	Current study 2001	Palikonda et al. (1999) 1993-94	Sausen et al. (1998) Theoretical
April	1.00	2.0	2.0
July	0.70	1.3	0.5
October	~0.85	1.9	1.9
December	0.88	2.1	1.6 (Jan)

Two conditions are necessary for contrail formation: air traffic and suitable atmospheric conditions. The air traffic over the USA is relatively heavy with more than 4000 km of potential contrails (flights above 7 km) every day in a given 1° box (Garber et al. 2003). Thus, the USA contrail coverage can be dominated by formation conditions. Duda et al. (2003) estimated the frequency of potential contrail conditions over the USA using Rapid Update Cycle (RUC) model data. Their Figure 1 showing potential coverage results for September 2001 are very similar to the afternoon contrail coverage in Figure 3. Similar correspondence was also found for November (not shown). Overall, the RUC-based potential USA contrail frequency during 2001 peaked during April at 30% and dropped to a minimum of ~12% during the summer months, nearly reaching a secondary peak in November followed by a decrease during December. The sequence is very similar to the observed contrail variation in Table 1. The contrail coverage is considerably less than the potential because the contrails can only be detected when they are not obscured by existing clouds and air-traffic coincides with the moisture. This consistency with contrail potential and the morning-afternoon optical depth consistencies in Figure 5 lend support to the relative validity of the retrievals.

Table 2 reveals that the contrail coverage is only half of that detected by Palikonda et al. (1999) from 1993-94 NOAA-11 and 12 AVHRR data and calculated by Sausen et al. (1998) using 1992 air traffic densities and multiple years of meteorological data. The relative seasonal variations between 1993-94 and 2001 are nearly identical. Because the air traffic should have increased by more than 30% or more between 1992 and 2001 (e.g., Minnis et al. 2003a), the contrail coverage should have increased. Part of the reduction may be due to missed contrails in the N16 images and to overestimates in the N11 and N12 analyses. Additionally, it should be repeated that the averages in Table 1 and for 2001 in Table 2 do not include a large portion of the western USA (Fig. 1), an area that is likely to account for less contrail coverage than the eastern USA. Minnis et al. (2003a) found a decrease in the frequency of persistent contrails over the USA during 1999 relative to 1993-94 that corresponded to a drop in upper tropospheric humidity (UTH) as indicated by the mean relative humidity (RH) at 300 hPa from the National Center for Environmental Prediction (NCEP) reanalyses data. As seen in Figure 6, the UTH was 45.5% during 1993-94 and dropped to 39.4% during 2001, one of the lowest values during the 30-year period. Since RH is a crucial factor in the formation of contrails, a reduction in RH should result in reduction of contrail cover. From correlations of mean cirrus cloudiness and UTH in areas without heavy air traffic, Minnis et al. 2003b found that cirrus coverage decreases by an average of 0.4%/U_{TH}. Thus, the cirrus amount would have diminished by ~2.5% over the USA between 1993-94 and 2001 and would likely include a decrease in contrails.

The phasing of the observed seasonal cycles in contrail coverage differs from the theoretical results of Sausen et al. (1998) in Table 2 and Ponater et al. (2002), but is consistent with the contrail frequency observations from surface observations (Minnis et al. 2003a). The observed seasonal range (200%) is only half of that (400%) observed from the surface and computed theoretically. This range difference decreases if only the N16 values are used. This discrepancy and the large N15-N16 contrail coverage difference during summer suggest that the N15 coverage could be overestimated during the summer. Additional analysis is needed to confirm this indication.

The seasonal variation in *OD* is similar to that computed by Ponater et al. (2002) with a maximum during the summer. Similarly, the greater occurrence of optically thick contrails is consistent with the greater maximum contrail optical depth computed by Ponater et al. (2002). However, the theoretical winter minimum relative to the summer maximum is significantly less than the observations. On average, the observed *OD*s are twice the value of those computed theoretically. The CLRF values also are considerably larger than those derived by Ponater et al. (2002). Part of the

difference is due to OD discrepancies. The remaining differences are likely a result of differences in the background temperatures and the diurnal cycle in contrail coverage that is not included here.

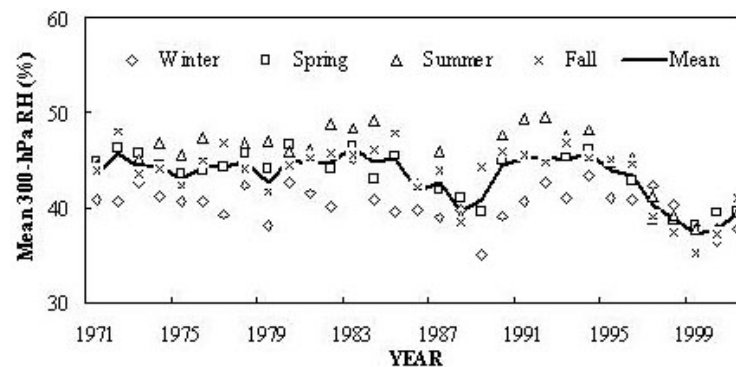


Figure 6. Seasonal and annual mean NCEP RH at 300 hPa over USA.

5 CONCLUSIONS

The preliminary results shown here confirm, for the most part, the relative seasonal variations in contrail coverage and optical depths. Over the USA, contrail coverage peaks during the large winter and early spring and bottoms out during the late summer. Contrail optical depth is greatest during summer. Uncertainties in the magnitudes of contrail coverage, optical depth, and radiative forcing are still large. Refinement of the automated contrail detection methods and detailed error assessments are needed to help resolve some of the remaining large differences between the theoretical calculations and the observations. Until these improvements are implemented, it will not be possible to determine conclusively if the current model estimates are sufficiently accurate for estimating contrail climate effects or whether additional improvements are needed. It is clear that interannual variations in UTH can have a large impact on contrail frequency and coverage. Such variability should be manifest in multi-year modelling results.

REFERENCES

- Duda, D. P., P. Minnis, P. K. Costulis, and R. Palikonda, 2003: CONUS contrail frequency from RUC and flight track data. *Proc. European Conf. On Aviation, Atmosphere and Climate*, Friedrichshafen at Lake Constance, Germany, June 30 – July 3.
- Garber, D. P., P. Minnis, and P. K. Costulis, 2003: A USA commercial flight track database for upper tropospheric aircraft emission studies. *Proc. European Conf. Aviation, Atmosphere, and Climate*, Friedrichshafen at Lake Constance, Germany, June 30 - July 3.
- Meyer, R., H. Mannstein, R. Meerkötter, U. Schumann, and P. Wendling, 2002: Regional radiative forcing by line-shaped contrails derived from satellite data. *J. Geophys. Res.* *107*, 10.1029/2001JD000426
- Minnis, P. J. K. Ayers, M. L. Nordeen, and S. Weaver, 2003a: Contrail frequency over the United States from surface observations. *J. Climate*, in press.
- Minnis, P., J. K. Ayers, R. Palikonda, and D. Phan, 2003b: Contrails, cirrus trends, and climate. *J. Climate*, submitted.
- Palikonda, R., P. Minnis, P. K. Costulis, D. P. Duda, 2002: Contrail climatology over the USA from MODIS and AVHRR data. *Proc. 10th Conf. on Aviation, Range, and Aerospace Meteorology*, Portland, OR, May 13-16, J9-J12.
- Ponater, M., S. Marquart, and R. Sausen, 2002: Contrails in a comprehensive global climate model: Parameterization and radiative forcing results. *J. Geophys. Res.*, *107*, 10.1029/2001JD000429.
- Sausen, R., K. Gierens, M. Ponater, and U. Schumann, 1998: A diagnostic study of the global distribution of contrails. Part 1: Present day climate. *Theor. Appl. Climatol.*, *61*, 127-141.

Contrail Coverage Over the North Pacific from AVHRR and MODIS Data

Patrick Minnis⁵

Atmospheric Sciences, NASA Langley Research Center, Hampton, Virginia, USA

Rabindra Palikonda, J. Kirk Ayers

AS&M, Inc., Hampton, Virginia, USA

Keywords: trans-Pacific air traffic, remote sensing, contrails, satellites

ABSTRACT: An increase of air traffic over the North Pacific during the last 30 years has been accompanied by an increase in cirrus coverage. To help alleviate the uncertainty in the contribution of air traffic to the cirrus increase, an analysis of linear contrail coverage over the region has been initiated using afternoon NOAA-16 AVHRR data. Contrail coverage over the domain between 25° and 55°N and between 120° and 150°W was 0.51% and 0.67% in August 2002 and February 2003, respectively. These preliminary values are twice the average expected from theoretical considerations. Contrail optical depths for the 2 months average 0.26 resulting in a mean unit contrail longwave radiative forcing of 15.5 Wm^{-2} , a value that is comparable to that estimated over the USA from daytime analyses. The seasonal variation is smaller than that over land. The contrail optical depths are twice the mean value expected from theoretical estimates. Efforts are underway to estimate the uncertainties in the results and to analyze additional satellite datasets.

1 INTRODUCTION

Cirrus cloud cover has been increasing over the North Pacific since the 1970's. Although part of the increase may be due to a rise in relative humidity, some of the change is likely caused by contrails forming and spreading as a result of transoceanic air traffic. Analysis of high-resolution satellite data is required to determine the contribution by linear contrails to that increase. The air traffic passes through a region where mean cirrus cloud coverage is generally about half that observed over land, while the upper tropospheric humidity, as indicated by the NCEP reanalysis at 300 hPa, is roughly 10% greater than that over land (Minnis et al. 2003). Thus, the atmosphere over pristine oceanic regions should be more susceptible to contrail-cirrus cloud initiation than that over land areas. Additionally, transoceanic flights travel greater lengths at high altitudes than their continental counterparts and, therefore, should tend to produce longer contrails. The expected linear contrail coverage from theoretical considerations (Sausen et al. 1998) varies between 0% in the mid-Pacific and 1% near San Francisco Bay (Fig. 1a). The flight corridors are well defined in Figure 1. Cirrus coverage rose between 0 and 0.6%/year between 1971 and 1996 (Minnis et al. 2003) over the same area with a maximum increase over northern California (Fig. 1b). Over the ocean, a broad area with the greatest trends in cirrus coverage is centered near 45°N at the western edge of the domain in Figure 1. There is no apparent correlation between the cirrus trends and the theoretically derived contrail coverage. Understanding how the contrails relate to the changes in cirrus coverage necessitates the development of some empirical data on the linear contrail coverage. To begin that effort, this paper presents preliminary analyses of contrails as derived from satellite data over the North Pacific. The retrieved properties are compared to similar quantities derived from data over the continental United States of America (USA) to examine the differences between contrails formed over marine and continental areas. They are also compared to the theoretical results. Preliminary statistics are presented.

⁵ *Corresponding author:* Patrick Minnis, MS 420, NASA Langley Research Center, Hampton, VA, USA 23681. Email: p.minnis@nasa.gov

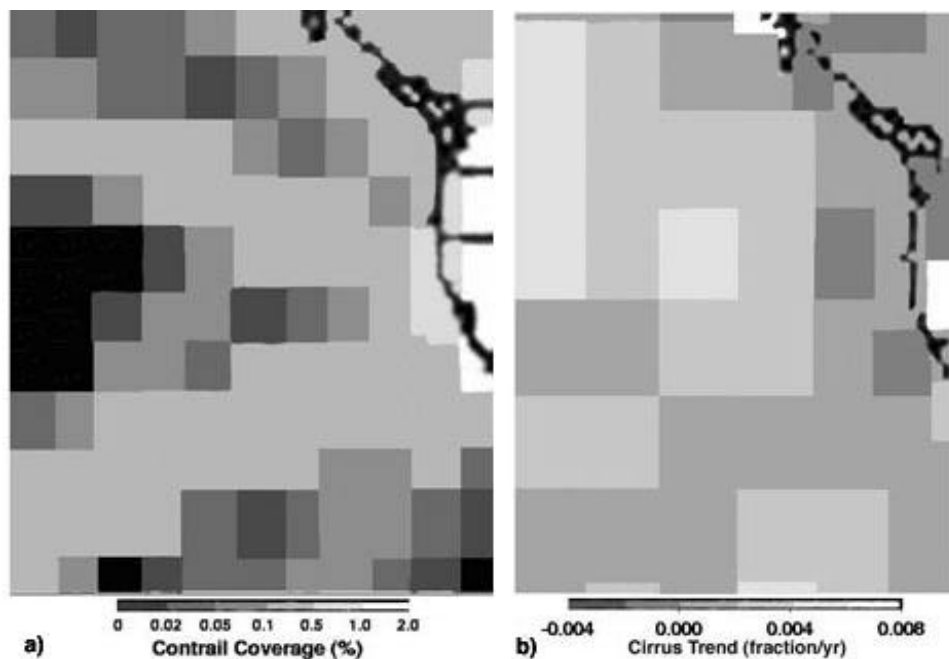


Figure 1: Theoretical linear contrail coverage in 1992 (a) and trend in surface-observed 1971-1996 cirrus coverage (a), and

2 DATA AND ANALYSIS

Advanced Very High Resolution Radiometers (AVHRR) have been taking 1-km multispectral data from the NOAA satellites since the 1980's, but most of the archived and real-time data over the broad ocean areas are for the 4-km Global Area Coverage (GAC) dataset. The NASA Earth Observing System satellites, *Terra* and *Aqua*, have been operating since March 2000 and August 2002, respectively. Each carries the Moderate Resolution Imaging Spectroradiometer (MODIS) that takes and archives multispectral data globally at resolutions from 0.25 to 1 km. Figure 2 shows examples of large contrails evident in the NOAA-16 AVHRR GAC imagery off the coast of California. Some of the trails exceed 1000 km in length and 20 km in width and they are evident in both the channel-4 infrared (IR, 11 μm) image (Fig. 2a) and, in Figure 2a, the 11-12 μm brightness temperature difference (T4-T5), a parameter commonly used to differentiate contrails from cirrus clouds. Such lengthy, fat contrails are not uncommon as seen in Fig. 3. The contrails in the NOAA-15 T4-T5 image (Fig. 3a) are from jets approaching California from the northwest while those in the 1-km MODIS image (Fig. 3b) are from planes approaching southern California from the southwest.

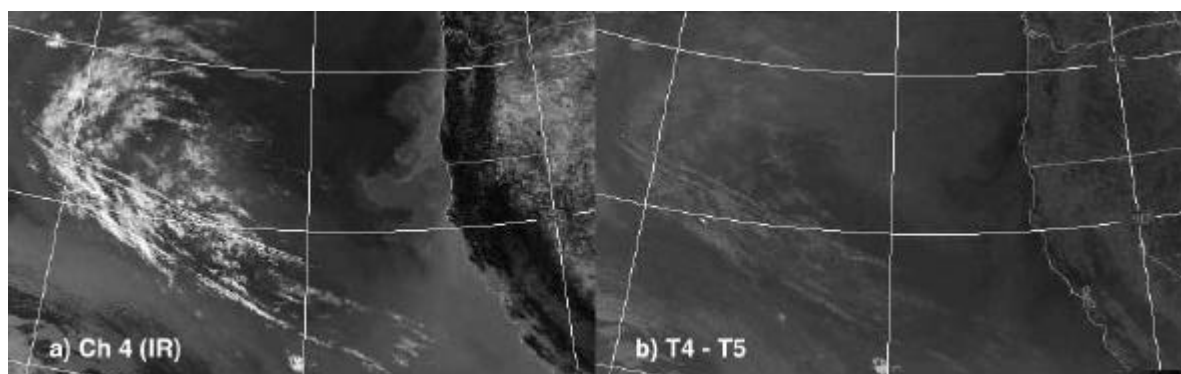


Figure 2: NOAA-16 AVHRR imagery at 1056 UTC, 13 August 2002: Infrared brightness temperature (a) and channel 4-5 brightness temperature difference.

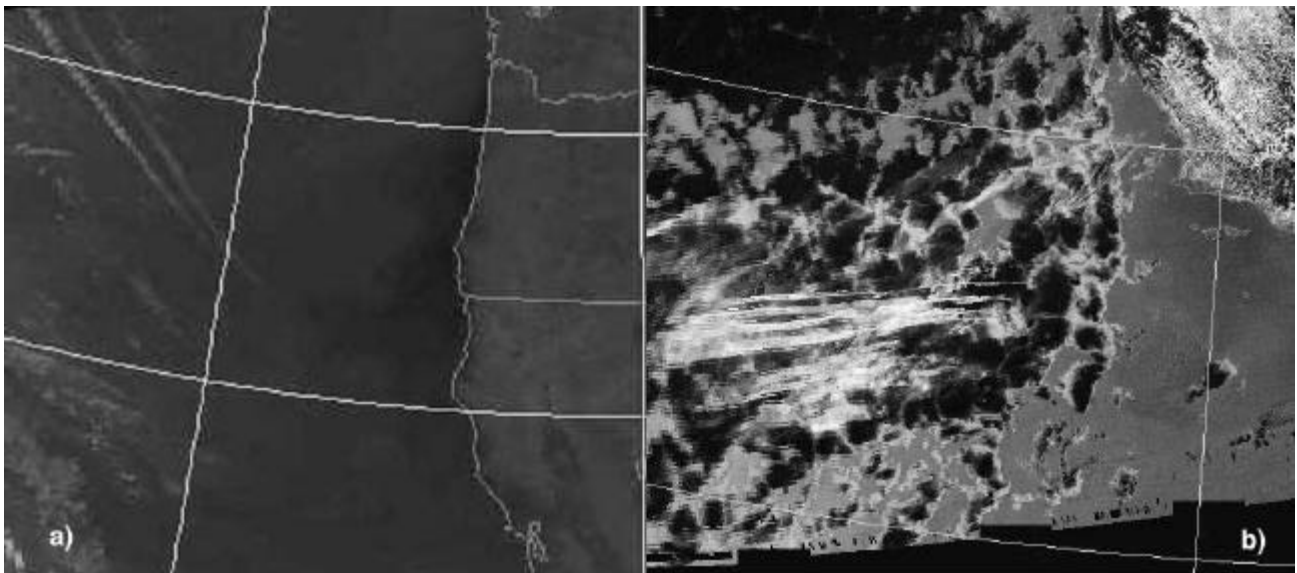


Figure 3: Contrails in the northeastern Pacific. (a) NOAA-15 AVHRR GAC T4-T5, 0230 UTC, 14 August 2002. (b) Aqua MODIS 1-km, 2054 UTC, 3 May 2003, T31-T32.

To quantify the contrail properties over the North Pacific, an automated algorithm (Mannstein et al. 1999) can be applied to 1-km AVHRR data from *NOAA-16* and to MODIS data from *Terra* and *Aqua* to derive contrail areal coverage. Contrail optical depth is computed with the method of Meyer et al. (2002) assuming that the contrail temperature is 224 K and that the contrail emissivity varies with optical depth (OD) according to the model of Minnis et al. (1993) for small ice crystals. Contrail longwave radiative forcing (CLRF) and the background temperature were computed using the methods of Palikonda et al. (2002, 2003). The initial analyses are performed on 1-km NOAA-16 AVHRR data taken from afternoon orbits during August 2002 and February 2003. The domain extends from 25°N to 55°N and from 120°W to 150°W corresponding to the plots in Figure 1.

3 RESULTS AND DISCUSSION

Figure 4 shows the distribution of contrail coverage over the domain for the two months. It is obvious that the derived contrail coverage in February (Fig. 4b) exceeds that found in August (Fig. 4a). During August, the greatest contrail coverage occurred around 47°N, 142°W with a secondary maximum near the west-southwest approach to San Francisco. Minimum coverage is seen in the southwestern corner of the domain, off the Oregon coast and inland. A general increase in contrail coverage during February is accompanied by a shift in the areal maximum to 42°N, 147°W. The southwestern corner remained relatively free of contrails. However, the contrail coverage is greatly increased over all of the approaches to the west coast cities. Overall, the mean contrail amounts during August 2002 and February 2003 are 0.51 and 0.67%, respectively.

The corresponding mean contrail optical depths for the domain are 0.27 and 0.26. The mean CLRF for both months is 0.09 Wm^{-2} . However, during February the unit or normalized CLRF (NCLRF) is 13.5 Wm^{-2} compared to 17.4 Wm^{-2} during August. The frequency distributions of OD and NCLRF are plotted in Figure 5. Optical depths vary according to a slightly skewed Gaussian distribution with a mode value around 0.20. The NCLRF distribution is highly skewed with a mode near 8 Wm^{-2} . This domain includes inland desert areas in Oregon and Washington that can become very warm during the afternoon even during winter. The large variability in NCLRF arises from the large range in background radiating temperatures. Contrails mixed with other cirrus clouds will tend to have small values of NCLRF while over clear areas NCLRF will be much larger, especially over land during the afternoon.

The contrail coverage values for both months are roughly twice the annual mean (0.30) from the results of Sausen et al. (1998). This difference could be due to a number of factors including the restricted sampling of the NOAA-16 afternoon orbit, a potential bias in the satellite retrievals (e.g.,

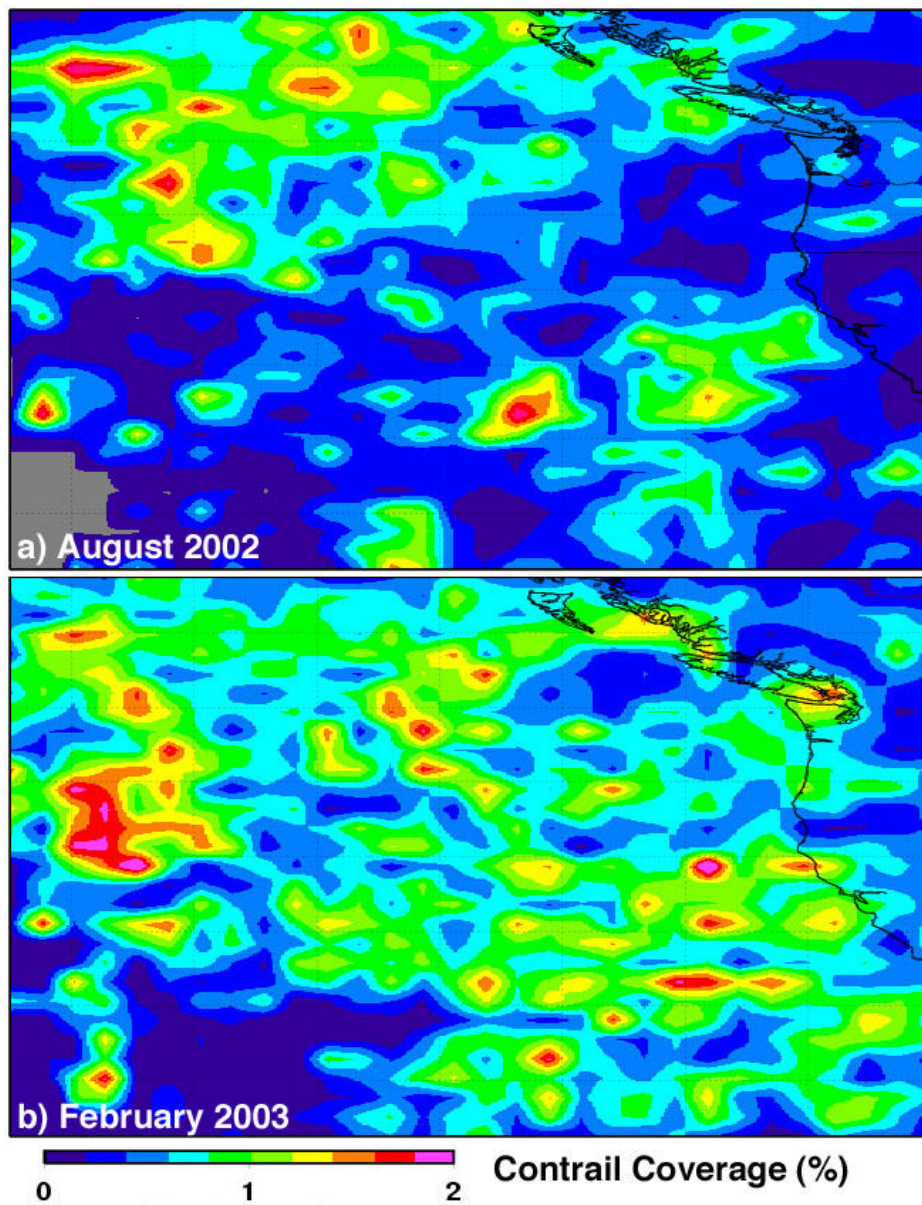


Figure 4. Mean contrail coverage derived from afternoon (1430 LT) NOAA-16 AVHRR data.

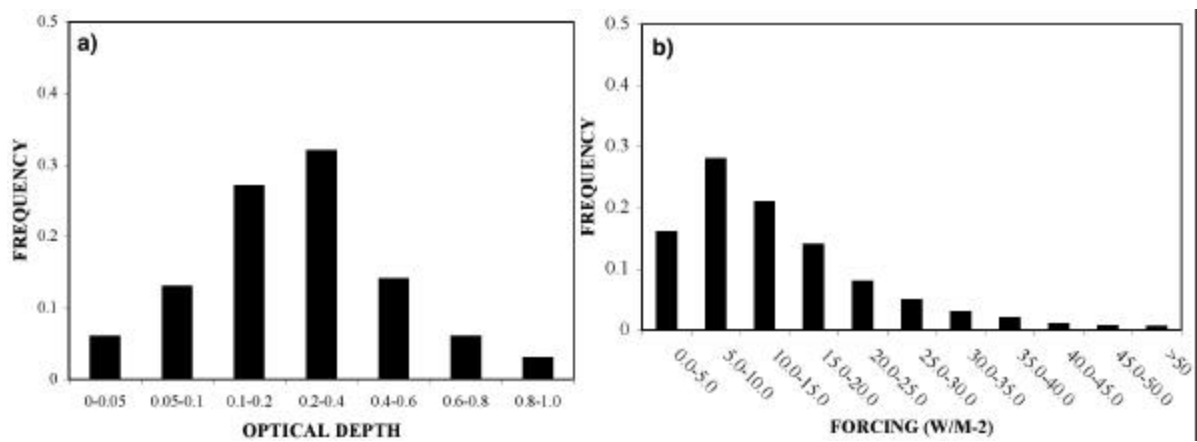


Figure 5. Frequency distributions of (a) contrail optical depth and (b) unit CLRF during February 2003.

Palikonda et al. 2003), an increase in trans-Pacific air traffic since 1992, differences in the upper tropospheric humidity between the model and the actual atmosphere, and a variety of other reasons. From the theoretical calculations of Ponater et al. (2002), it appears that summertime contrail coverage over the area should be larger than that during winter. This discrepancy with the current observations may arise from the same sources causing the differences in absolute contrail coverage. For instance, during winter, cirrus clouds are more abundant over the domain due to the more frequent passage of baroclinic disturbances. The opportunity for mistaking cirrus clouds during winter is enhanced at the same time as the potential for forming contrails. The overall effect may be that the overestimate of contrail coverage from the satellite analysis is greater during winter than during summer.

The afternoon NOAA-16 sampling may not be representative of the air traffic over the Pacific. While the air traffic over the USA is nearly constant for half of the day (Garber et al. 2003), scheduling of transoceanic flights differs from transcontinental traffic. Thus, the number of flights may be greater or less at other hours than at 1430 LT. Additional satellite overpass times should be analyzed.

The western maxima in contrail coverage (Fig. 4) are generally consistent with the maximum in cirrus trend (Fig. 1b) although the theoretical contrail coverage minimum extends into the same area. The flight tracks used in the Sausen et al. (1998) study are highly idealized and may not accurately represent the actual distribution of flight locations during the 2002-2003 period. Given the greater number of contrails in the northwestern part of the domain, it is likely that the conditions for contrail and cirrus formation are most favourable in that area. Thus, the errors in contrail detection may be greater in the same region. This issue requires further study.

The contrail optical depth distributions and mean values are nearly identical to those derived over the USA by Palikonda et al. (2003). The means are almost twice the magnitude found over Europe by Meyer et al. (2002) and estimated by Ponater et al. (2002) from theoretical calculations. The differences again may be related to mistaken cirrus clouds that are deeper than the average contrail or to an underestimate of contrail depth by the theoretical models. The February NCLRF mean is 5 Wm^{-2} greater than the wintertime mean for NOAA-16 results over the USA while the August NCLRF is 2 Wm^{-2} less than the corresponding USA summertime mean (Palikonda et al. 2003). This seasonal difference in the CLRF is likely due to the relatively stable background temperatures over the ocean. Over land, the contrast between the contrail and surface temperatures is much greater in summer than in winter.

4 CONCLUDING REMARKS

The results presented here constitute the first objective analysis of linear contrails over the western North Pacific. Both contrail coverage and optical depth are twice the annual average derived from theoretical considerations. Contrail longwave radiative forcing is much greater than computed theoretically. However, the results should be considered preliminary because no error analyses have been performed. Furthermore, the data were taken at only one time of day and may not represent the entire daily cycle.

This study has just begun. In the future, detailed error analyses will be performed to optimize the accuracy of the methodology for each satellite separately. A larger dataset including MODIS data and other NOAA satellites will be analyzed to determine the annual cycle and provide results that include all times of day. Shortwave radiative forcing will also be estimated for each retrieval to determine the net radiative forcing for these contrails. The results will be compared with the model-predicted temperature and humidity conditions to help improve the parameterization of contrails in climate models so that a more accurate assessment of contrail effects can be computed for the northwestern Pacific Ocean.

REFERENCES

- Garber, D. P., P. Minnis, and P. K. Costulis, 2003: A USA commercial flight track database for upper tropospheric aircraft emission studies. *Proc. European Conf. Aviation, Atmosphere, and Climate*, Friedrichshafen at Lake Constance, Germany, June 30 - July 3.
- Mannstein, H., R. Meyer, and P. Wendling, 1999: Operational detection of contrails from NOAA AVHRR data. *Int. J. Remote Sens.*, 20, 1641-1660.
- Meyer, R., H. Mannstein, R. Meerkötter, U. Schumann, and P. Wendling, 2002: Regional radiative forcing by line-shaped contrails derived from satellite data. *J. Geophys. Res.* 107, D10 10.1029/2001JD000426.
- Minnis, P., J. K. Ayers, R. Palikonda, and D. Phan, 2003: Contrails, cirrus trends, and climate. *J. Climate*, submitted.
- Minnis, P., Y. Takano, and K.-N. Liou, 1993.: Inference of cirrus cloud properties using satellite-observed visible and infrared radiances, Part I: Parameterization of radiance fields. *J. Atmos. Sci.*, 50, 1279-1304.
- Palikonda, R., P. Minnis, P. K. Costulis, and D. P. Duda, 2002: Contrail climatology over the USA from MODIS and AVHRR data. *Proc. 10th Conf. on Aviation, Range, and Aerospace Meteorology*, Portland, OR, May 13-16, J9-J12.
- Palikonda, R., D. N. Phan, and P. Minnis, 2002: Contrail coverage over the USA from MODIS and AVHRR data. *Proc. European Conf. Aviation, Atmosphere, and Climate*, Friedrichshafen at Lake Constance, Germany, June 30 - July 3.
- Ponater, M., S. Marquart, and R. Sausen, 2002: Contrails in a comprehensive global climate model: parameterisation and radiative forcing results. *J. Geophys. Res.*, 107, 10.1029/2001JD000429.
- Sausen, R., K. Gierens, M. Ponater, M. and U. Schumann, 1998: A diagnostic study of the global coverage by contrails, part I, present day climate. *Theor. Appl. Climatol.* 61, 127-141.

Survey of Cirrus Properties from Satellite Retrievals Using TOVS and AVHRR Observations

C. J. Stubenrauch*

C.N.R.S. – IPSL Laboratoire de Météorologie Dynamique (LMD), Ecole Polytechnique, Palaiseau, France

R. Meerkötter

DLR-Institut für Physik der Atmosphäre Oberpfaffenhofen, Germany

Keywords: satellite observations, cirrus, high clouds, time series, AVHRR, TOVS, ISCCP, INCA

ABSTRACT: The TOVS Path-B dataset provides atmospheric temperature and water vapor profiles as well as cloud and surface properties over the globe, at a spatial resolution of 1° latitude x 1° longitude. Their relatively high spectral resolution yields reliable cirrus properties, day and night. Over Europe, observations of the AVHRR instrument have been analysed by the APOLLO Processing scheme to identify cloud types, at a spatial resolution of 1 km. ISCCP offers a global cloud climatology with a good diurnal sampling. We present times series of thin and thick high cloud amount over this area with increasing air traffic. A more detailed study, using TOVS Path-B data, compares cirrus and atmospheric properties in the northern and southern hemisphere midlatitudes to investigate further the impact of anthropogenic influence on cirrus clouds.

1 INTRODUCTION

The increase in anthropogenic aerosols and in air traffic have led to theoretical and observational investigations of the impact on the formation of cirrus clouds. Contrails form when the hot and humid exhaust gases from the combustion of fuels by an aircraft mix with the ambient, cold atmosphere (Schumann, 1996). Their persistence depends on upper tropospheric humidity and temperature (Sausen et al., 1998, Kästner et al., 1999), since the aircraft emissions trigger the formation of additional clouds from natural water vapour present in the atmosphere. Over Europe and the USA, conditions for formation of contrails are less favourable in summer.

Only satellite observations are capable to give a continuous survey of the state of the atmosphere over the whole globe. Long time-series (twenty years) of reflected, scattered and emitted radiation from the earth's surface, atmosphere and clouds are available from imagers, using atmospheric window channels, and from vertical sounders, using CO_2 and H_2O sensitive channels. These measured radiances are transformed into cloud properties by inversion algorithms, relying on radiative transfer models. We use these satellite data to investigate the impact of air traffic and anthropogenic aerosols on the evolution of cirrus clouds, in two example studies: first we compare time series of high cloud amount over Europe, obtained by different satellite instruments and inversion algorithms, and second we analyse correlations between cirrus bulk microphysical properties and relative humidity, contrasting two midlatitude regions, one in the northern hemisphere (polluted) and the other in the southern hemisphere (pristine).

2 DATASETS

2.1 Atmospheric properties from TOVS Path-B

The TIROS-N Operational Vertical Sounder (TOVS) instruments aboard the NOAA Polar Orbiting Environmental Satellites consist, in particular, of the High resolution Infrared Radiation Sounder (HIRS/2) with 19 infrared (IR) spectral channels between 3.7 and 15 μm and one visible channel

* Corresponding author: Claudia J. Stubenrauch, C.N.R.S. Laboratoire de Météorologie Dynamique, Ecole Polytechnique, 91128 Palaiseau cedex, France. Email: stubenrauch@lmd.polytechnique.fr

and the Microwave Sounding Unit (MSU) with four microwave channels around 5 mm. At present, the TOVS Path-B dataset (Scott et al., 1999) provides eight years (1987-1995) of atmospheric temperature profiles (in 9 layers) and water vapour profiles (in 4 layers) as well as cloud and surface properties at a spatial resolution of 1°. So far, NOAA-10, NOAA-11 and NOAA-12 data have been processed at LMD, and results are being extended from 1979 until now.

Clouds are detected at HIRS spatial resolution (17 km at nadir) by a succession of threshold tests, which depend on the simultaneous MSU radiance measurements that probe through the clouds. To insure more coherence with the MSU spatial resolution, the HIRS radiances are averaged separately over clear pixels and over cloudy pixels over 100 km x 100 km regions. Average cloud-top pressure, p_{cld} , and effective cloud emissivity, $N_{\epsilon_{\text{cld}}}$, over cloudy pixels are obtained from four radiances in the 15 μm CO₂ absorption band (with peak responses from 400 to 900 hPa levels in the atmosphere) and one in the 11 μm IR atmospheric window by minimizing a weighted χ^2 (Stubenrauch et al., 1999).

Table 1 gives an overview of total and high cloud amount over the globe and selected regions, averaged from 1987 to 1995, as obtained from TOVS Path-B and ISCCP (Rossow and Schiffer, 1999). ISCCP D2 data provide monthly averages and cloud type statistics over 2.5° latitude x 2.5° longitude, from 3-hourly observations of imagers aboard geostationary and polar satellite imagers. The TOVS Path-B averages shown in Table 1 are from NOAA-10/12 data, with local observation time at 7h30 am and 7h30 pm. High clouds are defined by $p_{\text{cld}} < 440$ hPa, and are divided into three types, according to $N_{\epsilon_{\text{cld}}}$ (> 0.95 , $0.95-0.5$ and < 0.5) by TOVS and visible optical thickness, τ_{cld} , (> 23 , $3.6-23$ and < 3.6) by ISCCP, as deep convection, cirrus and thin cirrus. About 70% of the Earth's surface is covered by clouds, with about 10% more cloudiness over ocean than over land. The cover of high clouds is about 30%, with a maximum of about 47% in the tropics. Due to their relatively high spectral resolution, IR vertical sounders are more sensitive to cirrus than imagers; therefore TOVS Path-B indicates 8% more cirrus over the globe and up to 20% more cirrus in the tropics than ISCCP.

In the case of clear sky and thin clouds, the TOVS Path-B also provides profiles of atmospheric water vapour (Chaboureau et al., 1998). For the analysis in section 4, we estimate the upper tropospheric relative humidity (RH) from the TOVS Path-B water vapour columns between 500 and 300 hPa, and above 300 hPa, retrieved in the case of clear sky and thin cirrus ($N_{\epsilon} < 0.5$). Upper tropospheric relative humidity is the ratio of partial water vapour pressure and saturation vapour pressure, with respect to ice. Since the TOVS atmospheric profiles have a rather low vertical resolution and the saturation vapour pressure strongly depends on atmospheric temperature, we use the atmospheric temperature profile (with a vertical resolution of 30 levels in the troposphere) of the Thermodynamic Initial Guess Retrieval (TIGR) data set (Chevallier et al., 1998) closest to the observed atmospheric condition to compute the saturation vapour pressure and integrate it then over the columns. The average relative humidity around 300 hPa is then the mean of the relative humidity of these two columns. This is a rough but nevertheless gives estimate useful information on the state of the atmosphere. Within the frame of the EU project CIRAMOS, we retrieve mean effective ice crystal diameters, D_e , for large-scale semitransparent cirrus clouds (visible optical thickness between 0.7 and 3.8), using spectral cirrus emissivity differences between 11 and 8 μm (Rädel et al., 2003). This method is sensitive to diameters up to 80 μm . Ice water path (IWP) is then determined from the cirrus emissivity at 11 μm and the retrieved D_e .

Table 1. 8-year average cloud type amounts from TOVS Path-B and ISCCP (italic), over the globe, northern hemisphere and southern hemisphere midlatitudes (30°N-60°N, 30°S-60°S) and tropics (20°N-20°S).

Cloud type amounts (%)	global		ocean		land	
all	73	67	74	71	69	58
Deep convection	2.4	2.8	1.9	2.8	3.5	2.7
Cirrus + thin cirrus	27.3	19.1	26.9	18.0	27.8	21.7
Cloud type amounts (%)	NH midlatitudes		tropics		SH midlatitudes	
Deep convection	3.0	3.3	3.5	2.5	2.4	3.0
Cirrus + thin cirrus	27.7	20.3	44.8	24.9	21.8	16.5

2.2 Cloud identification over Europe from AVHRR/APOLLO

AVHRR data were analysed using the AVHRR Processing scheme Over cLOUDs, Land and Ocean (APOLLO), described by Kriebel et al. (2003). APOLLO makes use of all five spectral channels of the NOAA/AVHRR instrument during daytime and discretizes the data into four groups called cloud-free, fully cloudy, partially cloudy and snow/ice. In a next step, physical properties are derived. Within APOLLO, clouds are assigned to three layers according to their top temperatures. The layer boundaries are set to 700 hPa and 400 hPa and associated temperatures are derived from standard atmospheres. Each fully cloudy pixel is identified as thick or thin cloud, according to its brightness temperatures at 11 and 12 μm and, during daytime, its reflectances at 0.6 and 0.9 μm . Reflectances below a certain threshold identify thin clouds, with τ_{cld} typically less than 5. Thin clouds are taken as ice clouds, i.e. cirrus. Cloud cover of the partially cloudy pixels is derived from reflectances and temperatures of their cloud free and cloudy parts. Assuming horizontal homogeneity, these quantities are taken from the nearest fully cloudy and cloud free pixels. During daytime, cloud optical depth, liquid/ice water path and emissivity are calculated for each fully cloudy pixel by means of parameterization schemes that are based on the reflectance at 0.6 μm .

APOLLO is currently used to generate a high resolution cloud climatology ($0.01^\circ \times 0.0125^\circ$ in latitude and longitude) for the entire region of Europe (34°N - 72°N , 11°W - 32°E). This European cloud climatology (ECC) presently covers a period of 13 years from 1990 to 2002. It should be noted that the cloud products are derived from data of the noon overpasses of the satellites NOAA-11 (1990-1994), NOAA-14 (1995-2001), and NOAA-16 (2002). The generation of ECC products is an ongoing process, but it is also planned to extend the ECC further into the past, i.e. to the years before 1990.

3 HIGH CLOUD AMOUNT AND ITS TEMPORAL VARIABILITY

To study the feasibility of a trend analysis, we compare in Figure 1 the time-series of high thin and thick cloud amount of these different satellite cloud data sets over Europe. ISCCP data cover three-hourly observations, TOVS Path-B data cover observations at 7h30 am and 7h30 pm local time, and AVHRR/APOLLO data are derived from observations around 2h pm local time. A study of six-hourly TOVS Path-B data (from NOAA-10/-12 and NOAA-11 satellites) has shown that high thin cloud amount over Europe increases from about 7% in early morning to 12% in the afternoon. Whereas ISCCP and TOVS Path-B high clouds are defined by $p_{\text{cld}} < 440$ hPa, the AVHRR/APOLLO criterion is stricter: $p_{\text{cld}} < 400$ hPa. Also, the distinction between thin and thick clouds of these three datasets is not the same: TOVS Path-B separates thin cirrus at $\tau_{\text{cld}} < 1.5$, ISCCP at $\tau_{\text{cld}} < 3.6$ and AVHRR/APOLLO at $\tau_{\text{cld}} < 5$. From Figure 1 we conclude the following:

- The overall high cloud amount over Europe is about 23% / 19% / 13% with about 10% / 10% / 4% thin cirrus, according to TOVS Path-B, ISCCP and AVHRR/APOLLO respectively. Differences between these values can be explained by different sensitivity to thin cirrus, slightly different definitions of cloud types and different observation times.
- Interannual variability is the lowest for TOVS Path-B high clouds. Thin cirrus amount has a minimum of about 7% in winter and a maximum of about 13% in summer, the difference of seasonal minima and maxima is larger for thicker cirrus, with a minimum of about 6% in summer and maxima in early and late winter of about 16%. Exceptions of this behaviour are the winter of 1988/89 with about 5% less thick cirrus and the period from autumn 1989 to autumn 1990 with no seasonal change in thin cirrus. This could be related to the North Atlantic Oscillation (NAO): Before this period the NAO index is for several months negative and then changes to strong positive values again for several months positive. By observing a similar period in behaviour of the NAO index in 1993/94, we discover also a similar pattern of thin cirrus variability in Figure 1.
- Considering the ISCCP times-series, seasonal variations of thick cirrus are also of about 5%, with maxima in winter and minima in summer. The winter peaks are however narrower than those of the TOVS Path-B data set. The time-series of thick cirrus seems to be quite stable, with slightly smaller maxima in winters of 1988/89, 1991/92 and 1998/99. Thin cirrus amount shows a quite different behaviour: It is difficult to observe a systematic seasonal cycle over the whole data period of 20 years. However, one observes three different cycles characterized by a drop and then

a continuous increase of thin cirrus amount and an increase of its seasonal variability. The beginnings of these cycles coincide with changes of the NOAA afternoon satellites in 1984/85, 1988/89 and 1994/95. It is well known that all afternoon satellites continuously drifted during their operation by at least two hours in their observation time (NOAA-11 even four hours) from early afternoon to late afternoon.

- Thick high cloud amount of AVHRR/APOLLO and ISCCP compares on average very well. Seasonal minima and maxima agree well with TOVS Path-B data from NOAA-11 afternoon observations (shown on the poster). Exceptions are the winter minima in 1990/91 and 1991/92. Due to the drifting overpass times of the NOAA afternoon satellites the solar zenith angles increase at the time of cloud probing within the periods of NOAA-11 (1990-1994) and NOAA-14 (1995-2001). The change in the anisotropic bidirectional reflection distribution function of thin clouds causes therefore an increase of the signals in the visible AVHRR channels. Although APOLLO accounts for an anisotropy correction of measured signals to a certain degree, there is still a continuous reduction in the observed coverage of thin clouds during each satellite period. Therefore, thin high cloud amount of AVHRR/APOLLO is only shown for June and July, the months causing minimum anisotropy effects due to smaller solar zenith angles. The abrupt increases in thin cloud amount result during satellites changes.

Another possibility to study the anthropogenic impact on cirrus clouds is to contrast northern and southern hemisphere (NH / SH). Figure 2 presents a time-series of amount of cumulonimbus, cirrus and thin cirrus as obtained from TOVS Path-B, for NH midlatitudes and SH midlatitudes. Both hemispheres, are covered by about 15% cirrus, but the amount of thin cirrus is higher in the NH (10% compared to 7.5% in the SH). It is also interesting to note that in the NH midlatitudes thin cirrus have a pronounced seasonal cycle, whereas in the SH midlatitudes cirrus have a pronounced seasonal cycle. However, during the period of eight years, these high cloud amounts are quite stable. If there is a trend to see, it would be a slight decrease of cirrus, in both hemispheres.

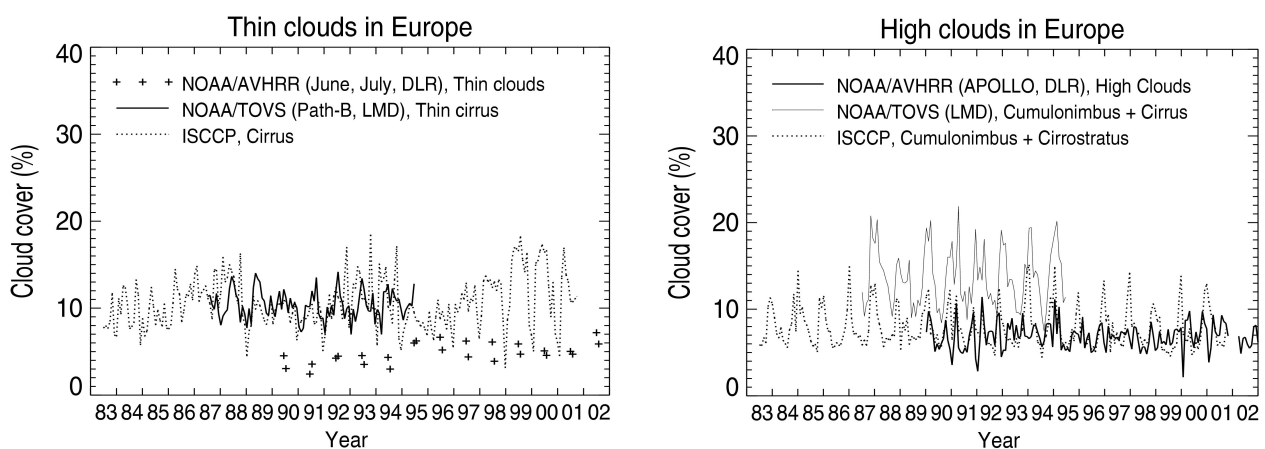


Figure 1. Time series of cloud amount of thin high clouds (left) and thick high clouds (right) over Europe, retrieved from observations of different satellite instruments and by different inversion algorithms.

4 CIRRUS PROPERTIES IN NORTHERN AND SOUTHERN HEMISPHERE (INCA REGIONS)

A second example of using satellite data to study the impact of anthropogenic influence on cirrus clouds is given by an analysis of correlations between cirrus properties and surrounding atmospheric conditions. We have selected the regions which have been thoroughly studied in the frame of the European project INCA (INterhemispheric differences in Cirrus properties from Anthropogenic emission), with measurement campaigns in Apr/May 2000 in the southern hemisphere (53°S) and in Sep/Oct 2000 in the northern hemisphere (55°N).

Figure 3 presents upper tropospheric relative humidity distributions in the case of clear sky, sky with very thin cirrus ($N_e < 0.3$) and sky with thin cirrus ($0.3 < N_e < 0.5$), separately for the NH and SH INCA regions, during autumn. In the case of clear sky, all these distributions follow an exponential law as observed in (Gierens et al., 1999). However, one observes a systematic difference in the distributions for very thin cirrus between the NH and SH INCA regions: In the SH INCA region, with few upper tropospheric aerosols, there are more situations with high relative humidity linked to cirrus than in the NH INCA region, chosen for high air traffic. These observations also agree with in-situ measurements of Overlaz et al. (2002).

In Figure 4 we compare correlations between bulk microphysical properties of thin cirrus ($0.3 < N_e < 0.4$) and upper tropospheric humidity in the NH and SH INCA regions, again separately during autumn. In general, D_e and IWP are slightly larger in the NH INCA region and their increase with relative humidity is slightly stronger than in the SH INCA region. However, D_e increases with IWP in the same manner in both regions, for situations with $RH < 70\%$ and $RH > 70\%$. To understand the differences in cirrus bulk microphysical properties between these two regions, one has to compare further the dynamical situation of the atmosphere in both hemispheres.

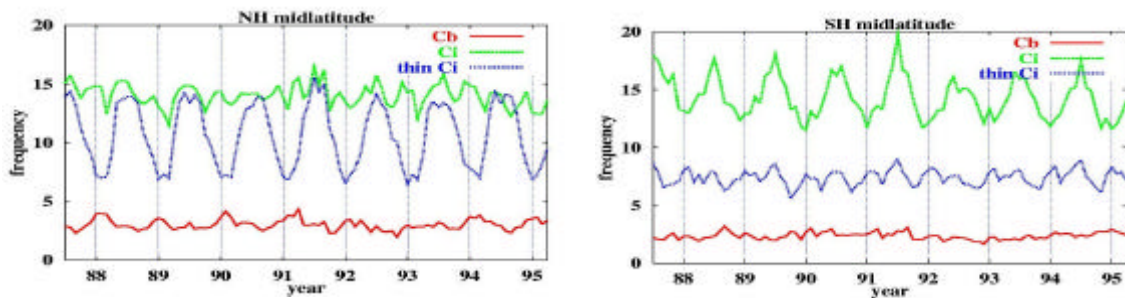


Figure 2. Time series of high cloud amount, separately for opaque, cirrus and thin cirrus, over NH midlatitudes (left) and over SH midlatitudes (right), derived from TOVS Path-B data, with observation time at 7h30 am and 7h30 pm.

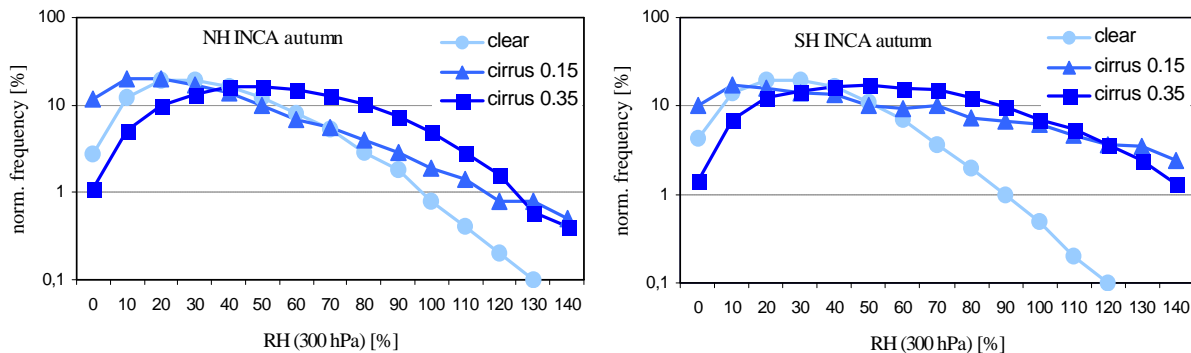


Figure 3: Upper troposphere relative humidity distributions of clear sky, sky with very thin cirrus and sky with thin cirrus, during autumn, in the INCA regions of the northern hemisphere (left) and of the southern hemisphere (right). Data are 8- year averages from TOVS-Path-B.

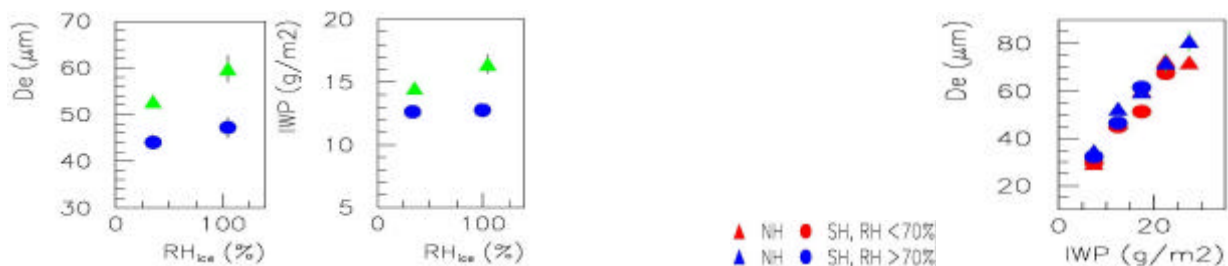


Figure 4: Right: D_e and IWP of thin cirrus for regions with low and high relative humidity, during autumn, in the INCA regions of NH (Δ) and of SH (\circ). Left: D_e as function of IWP for all situations. Data are 4-year averages from TOVS-Path-B.

5 CONCLUSIONS

We have investigated the feasibility of a trend analysis of cirrus amount by comparing three different satellite data sets over Europe: TOVS Path-B, ISCCP and AVHRR/APOLLO. These time series of thick and thin cirrus amount do not show any significant trend over Europe. Thin and thick cirrus amounts from TOVS Path-B, which should be the most reliable, are quite stable over an 8-year period, also by comparing NH and SH midlatitudes. Interannual variability of seasonal behaviour is possibly related to differences in NAO. Cyclic temporal variations in amount and seasonal variability of thin cirrus amount from ISCCP and AVHRR/APOLLO can be possibly explained by satellite drifts over their observation periods (up to four hours). We want to conclude that trend analyses have to be undertaken with great care, especially when seasonal variations are quite large. Only by removing effects related to technical problems such as satellite drifts, missing data, calibration etc. one can investigate very small trends.

By comparing correlations between atmospheric humidity and cirrus properties in NH and SH INCA regions, we observe that very thin cirrus in the SH are related to significantly broader upper tropospheric relative humidity distributions than those in the NH. Whereas D_e and IWP of semi-transparent cirrus are slightly larger on average in the NH than in the SH, correlations between them are the same in both hemispheres. In a next step, atmospheric winds have to be analyzed in these regions.

6 ACKNOWLEDGEMENTS

The authors want to thank K. Gierens and A. Chédin for interesting discussions on relative humidity and C. König, H. Mannstein, and G. Gesell for their support in processing the NOAA/AVHRR data.

REFERENCES

- Chaboureaud, J. P., A. Chédin, and N. A. Scott, 1998: Remote sensing of the vertical distribution of atmospheric water vapor from the TOVS observations: Method and validation. *J. Geophys. Res.* **103**, 8743-8752.
- Chevallier, F., F. Chéruiy, N. A. Scott, and A. Chédin, 1998: A neural network approach for a fast and accurate computation of a longwave radiative budget. *J. Appl. Meteor.* **37**, 1385-1397.
- Gierens, K., U. Schumann, M. Helten, H. Smit, and A. Marengo, 1999: A distribution law for relative humidity in the upper troposphere and lower stratosphere derived from three years of MOZAIC measurements. *Ann. Geophysicae* **17**, 1218-1226.
- Kästner, M. R. Meyer, and P. Wendling, 1999: Influence of weather conditions on the distribution of persistent contrails. *Meteorol. Appl.* **6**, 261-271.
- Kriebel, K.T., G. Gesell, M. Kästner, and H. Mannstein, 2003: The cloud analysis tool APOLLO: improvements and validations. *Int. J. Remote Sensing* **24**, 2389-2408.
- Ovarlez, J., J.-F. Gayet, K. Gierens, J. Strom, H. Ovarlez, F. Auriol, R. Busen, and U. Schumann, 2002: Water vapour measurements inside cirrus clouds in Northern and Southern hemispheres during INCA. *Geophys. Res. Lett.* **29**, 10.1029/2001GL014440.
- Rädel, G., C. J. Stubenrauch, R. Holz, and D. L. Mitchell, 2003: Retrieval of Effective Ice Crystal Size in the Infrared: Sensitivity Study and Global Measurements from the TIROS-N Operational Vertical Sounder. *J. Geophys. Res.* **108**, 10.1029/2002JD002801.
- Rossow, W. B., and R. A. Schiffer, 1999. Advances in understanding clouds from ISCCP. *Bull. Amer. Meteor. Soc.* **80**, 2261-2288.
- Sausen, R., K. Gierens, M. Ponater, and U. Schumann, 1998: A Diagnostic Study of the Global Distribution of Contrails. Part I: Present Day Climate. *Theor. Appl. Climatol.* **61**, 127-141.
- Schumann, U., 1996: On conditions for contrail formation from aircraft exhausts. *Meteorol. Z.* **5**, 2-23.
- Scott, N. A., A. Chédin, R. Armante, J. Francis, C. J. Stubenrauch, J.-P. Chaboureaud, F. Chevallier, C. Claud, and F. Chéruiy, 1999: Characteristics of the TOVS Pathfinder Path-B Dataset. *Bull. Amer. Meteor. Soc.* **80**, 2679-2701.
- Stubenrauch, C. J., A. Chédin, R. Armante, and N. A. Scott, 1999: Clouds as seen by Infrared Sounders (3I) and Imagers (ISCCP): Part II) A New Approach for Cloud Parameter Determination in the 3I Algorithms. *J. Climate* **12**, 2214-2223.

Comparison of Cirrus Cloud Properties in the Northern and Southern Hemisphere on the Basis of Lidar Measurements.

F. Immler, O. Schrems

Alfred-Wegener-Institut für Polar und Meeresforschung, Bremerhaven, Germany, fimmler@awi-bremerhaven.de

Keywords: Cirrus, Lidar

ABSTRACT: Cirrus cloud measurements have been performed during the INCA field campaigns in Punta Arenas/Chile (53.12°S, 70.88°W) and in Prestwick/Scotland (55.51°N, 4.60°W) in each hemisphere's fall in the year 2000. From lidar backscatter profiles at 532 nm and 355 nm the optical depth (OD) of the clouds is retrieved as well as base and top altitude of the clouds, the color index and the depolarization. Cloud layers with optical depths covering more than 3 orders of magnitude have been detected by the lidar, with a high share (35%) of subvisual cirrus at both sites. Differences in the results from the southern and the northern hemisphere are found in the lidar ratio and the depolarization behavior. While there is a large natural variability in cirrus properties, our results indicate a tendency towards bigger particles and columns in the southern hemisphere compared to smaller particles and small crystal plates in the northern hemisphere.

1 INTRODUCTION

The Mobile Aerosol Raman Lidar (MARL) of the Alfred Wegener Institute is a mobile backscatter lidar which was already operated during several field campaigns at various locations as well as aboard the German research vessel Polarstern to measure aerosol and clouds in the upper troposphere and lower stratosphere. In 2000, two field-experiments have been conducted within the European INCA 2000-project (Interhemispheric differences in cirrus cloud properties by anthropogenic emissions). The first one took place in the midlatitudes of the southern hemisphere (Punta Arenas/Chile, 53.12°S, 70.88°W) and the second campaign followed in September 2000 in Prestwick/Scotland (55.51°N, 4.60°W). The main objective of these investigations was to collect Lidar data of cirrus clouds from clean (Punta Arenas) and polluted (Prestwick) areas and to analyze this data in respect to differences that might be caused by air traffic or other anthropogenic emissions. During the four weeks of the campaigns, about 80 hours of Lidar measurements were gathered at each location, covering different types of cirrus clouds as well as background aerosols. A comparison of the two datasets reveals similarities as well as differences in the measured cirrus cloud properties.

2 CLOUD DETECTION BY LIDAR

MARL (Mobile Aerosol Raman Lidar) is a backscatter Lidar based on a linear polarized Nd:YAG Laser with 30 Hz repetition rate and 200 mJ pulse energy (@532 nm). The detection unit uses a 1.1 m cassegrain telescope and a multichannel polychromator which detects backscattered light at 532 nm and 355 nm, both separated in parallel and perpendicular polarization (with respect to the lasers linear polarisation). Furthermore, the system detects light backscattered from N₂ molecules with a Raman shift (607 and 387nm). The Raman signals allow the direct measurement of cloud and aerosol extinction. The system is capable for day- and nighttime operation, except for the Raman channels.

To detect clouds in the upper troposphere, the backscattered light is analyzed with respect to peaks that result from enhanced backscattering from cloud particles. Every atmospheric feature is included in the analysis, which creates a significant enhancement in the backscatter signal according to the following definition:

$$S(h) = \frac{d}{dh} \frac{P(h)}{P_{Ray}(h)} > 3\sigma \quad (1)$$

where $P(h)$ is the measured lidar backscatter signal and $P_{Ray}(h)$ is a simulated lidar signal from a purely molecular atmosphere. σ is the standard deviation of $S(h)$ calculated from Poisson-statistics of the signal count rates. The cloud base is the first altitude starting from 4 km that satisfies criterion (1). The cloud top height is defined as the altitude where $S(h)$ is back to zero and the integral of $S(h)$ is greater than zero. Whether every feature that creates such a signal is a cloud in the traditional meaning of this word needs to be discussed, however, here we call these atmospheric features clouds. Since our definition is based on the increasing slope of the backscatter signal instead of the total cloud backscatter, there is no lower detection limit in terms of the optical depth. In fact, this method is very sensitive and thin cloud with an optical depth of 10^{-3} can easily be detected in simulations. When using the perpendicular channel as $P(h)$ in eq. (1), the sensitivity of this method is even increased by about a factor of 10 in the case of depolarizing clouds like cirrus.

Besides cloud base and top height the optical depth, the depolarization and wavelengths dependence of the backscatter coefficient (color index) of the cloud can be inferred from the lidar data. Our analysis is based on the mean value of these quantities taken over one cloud layer as defined by the definition given above.

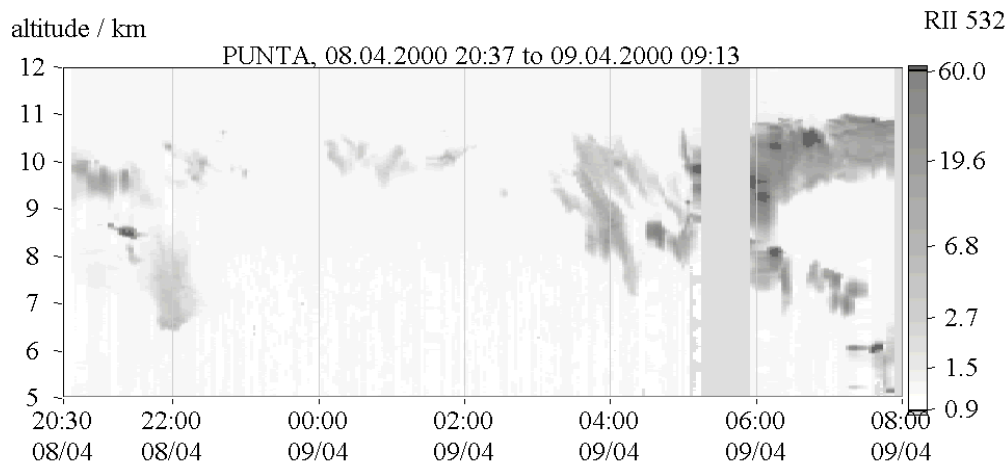


Figure 1. Lidar measurements of cirrus clouds in Punta Arenas on April 4th 2000. Plotted is the backscatter ratio as a function of time (UT) and altitude. Between 00:00 and 02:00 thin, subvisual cirrus were detected, at an altitude of around 10 km.

3 RESULTS

The ability of our lidar system to detect very thin clouds allow to study the properties of these so-called subvisual cirrus (Sassen et al., 1989) in comparison with visible cirrus clouds. It has been reported earlier (Immler and Schrems, 2002), that during both campaigns a considerable part of subvisual cirrus have been detected. In both, northern (NH) and the southern hemispheric (SH) campaigns, about 35% of the total detected clouds were subvisual.

The 'color' in terms of the color index

$$CI = \frac{\ln(b_{532})}{\ln(b_{355})} \cdot \frac{\ln(355)}{\ln(532)} \quad (2)$$

of this thin clouds is predominantly close to zero independent of the optical depth and the location of the campaign (Fig.2). This indicates that the particles of the detected cloud layers are rather large ($r_{eff} > 3 \mu\text{m}$) and give the cloud a white color. This could be understood as a good definition for cirrus clouds from the lidar perspective, since most aerosol types have a color index greater than 0.5

with the exception of Saharan dust, which exhibits a color index clearly below zero (Sasano and Browell, 1989). Together with the depolarization data (Fig. 2b) our data suggest that the great majority of the particle layers detected by the lidar in the upper troposphere are ice clouds, including those with an optical depth in the subvisual range.

The tendency towards higher values of the color index in the SH data (Punta Arenas) of Fig. 2a might be caused by the orography of the site where a mountain range to the west regularly induced lee waves in which cirrus were formed. The larger vertical wind speed within the lee-waves generates smaller cirrus particles (Gayet et al., 2002).

The depolarization that was measured in Punta Arenas tended to be larger than the one measured in Prestwick. This discrepancy between the NH and the SH data of the depolarization behavior is higher in the subvisual range. Since the color index and the depolarization are in general anti-correlated the highly depolarizing clouds refer to another fraction of the observed clouds than the ones with the large color index discussed above. These clouds have zero or slightly negative color indices.

For clouds in the visible range, the optical depth can be calculated directly from the lidar signals. Provided that the lidar ratio, i.e. the ratio between the extinction and the backscatter coefficient is constant throughout the cloud, this measurement allows the determination of the lidar ratio. The results are shown in Figure 3. In the NH the measured lidar ratios at 532 nm form a rather narrow distribution around 21 sr with a standard deviation of 7 sr. Values above 30 sr are rarely measured. This is different in the southern hemispheric where about 50% of the data are values above 30 sr.

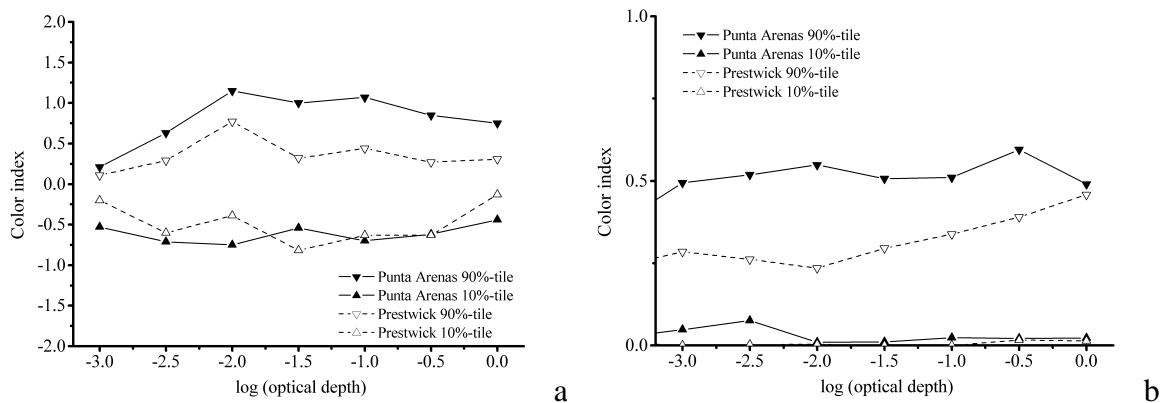


Figure 2. 10% and 90% quantiles of the color index and the depolarization (right) as a function of the optical depth

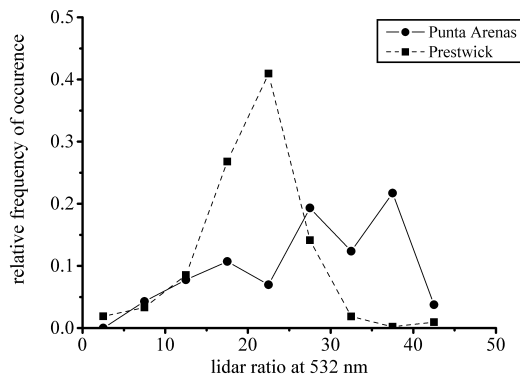


Figure 3. Relative frequency of occurrence of the lidar ratio of cirrus clouds determined with the lidar at the NH and SH locations.

4 CONCLUSIONS

The interpretation of lidar data of cirrus clouds in terms of properties of the cloud particles is not a straight forward task. Not only is the theoretical treatment of the scattering process difficult and time consuming, it is furthermore complicated by the fact that cirrus can contain particles of various sizes and shapes. However, an interesting approach has recently been developed by Reichardt et al. (2002) who uses the ray tracing technique to interpret the correlations of the depolarization and lidar ratio that were found in their measurements. It is shown that hexagonal columns depolarize more than plates while the lidar ratio is primarily a function of the aspect ratio (= length divided by width of the particle), particles with a stronger asphericity show a higher lidar ratio. While small particles tend to have an aspect ratio close to one, the aspect ratio will commonly differ significantly from unity for large particles. Thus, the lidar ratio is associated with particle size.

Based on this considerations, one may conclude from the lidar ratios measured in our study (Fig.3) that the particles of the clouds in the SH, visible and subvisible, tend to be larger and therefore have a higher lidar ratio, than the ones measured in the NH. Furthermore, the depolarization indicates a higher share of column-like particles in the southern hemisphere, while the northern hemispheric cirrus seem to be dominated by plates. This is most clearly the case for subvisual cirrus since in the SH, where a significantly larger fraction of subvisual clouds show high depolarization than in the NH (Fig. 2b).

However, it has to be noted that the extraction of microphysical information from lidar data is an underdetermined problem and that other explanations based on different types of particles are conceivable and could lead to different conclusions. Also, the limited size of our data base restricts our ability to draw general conclusions for cirrus properties in the northern and the southern hemisphere. One thing however that is save to conclude is, that there is a large natural variability in cirrus properties in both, northern and southern hemisphere, which is expressed by the wide range of optical depth and depolarization ratios of cirrus clouds determined by the lidar.

A detailed study of contrails and cirrus in the midlatitudes is currently being conducted with our lidar in Lindenberg (near Berlin/Germany), where radiosondes and sky cameras allow for a detailed characterization of the clouds and the meteorological condition under which they appear.

ACKNOWLEDGEMENT

Financial support by the Helmholtz Association through the "HGF Strategiefondsprojekt PAZI" is gratefully acknowledged.

REFERENCES

- Gayet J.-F., F. Auriol, F. Immler, O. Schrems, A. Minikin, A. Petzold, J. Ovarlez, J. Ström, 2002, Microphysical and optical properties of wave cirrus cloud sampled during the INCA experiment., AMS Proceedings of the 11th conference on cloud physics
- Immler F. and O. Schrems, 2002: Lidar measurements of cirrus clouds in the northern and southern hemisphere during INCA (55°N, 53°S): A comparative study *Geophys. Res. Lett.*, 29, 16, 10.1029/2002GL015077, pp. 56-1 to 56-4
- Reichardt J., Reichardt S., Hess M., McGee T.J., 2002: Correlations among the optical properties fo cirrus-cloud particels: Microphysical interpretation *J. Geophys. Res.*, 107, D21, 10.1029/2002JD002589, pp. 4562-4574
- Sasano Y., Browell E.V., 1989, Light scattering chracteristics of varoius aerosol types derived from multiple wavelength lidar observations., *Appl. Opt.*, 28(9), pp. 1670-1674
- Sassen K., M.K. Griffin, G.C. Dodd, 1989: Optical scattering and microphysical properties of subvisual cirrus clouds, and climatic implications *J. Appl. Meteor.*, pp. 91-98

A Fast Stratospheric Aerosol Microphysical Model

S. Tripathi*, X. Vancassel, R. Grainger

Atmospheric, Oceanic and Planetary Physics, Department of Physics, University of Oxford, United Kingdom

H. Rogers

Department of Chemistry, Cambridge University, United Kingdom

Keywords: stratospheric aerosol, modelling, particles

ABSTRACT: A fast Stratospheric Aerosol Microphysical Model (SAMM) has been developed to study aerosol behaviour in the lower stratosphere. This model simulates homogeneous binary nucleation, condensational growth, coagulation and sedimentation of sulphuric acid-water particles, in order to predict the composition and the size-distribution of stratospheric aerosols. The principal advantage of SAMM is that it is non-iterative. This feature allows high computational efficiency, which is essential as SAMM will be included in the global chemical transport model SLIMCAT. SAMM has been used to simulate background stratospheric aerosols and volcanically disturbed aerosol (not presented here), and has been shown to be in good agreement with observations and other modelling studies.

1 INTRODUCTION

Stratospheric aerosols can affect the global climate system in a variety of ways. These aerosols play a significant role in the Earth's radiative balance (Lacis et al., 1992) and in the attenuation of UV radiation (Michaelangeli et al., 1992). They also provide a surface for heterogeneous chemical reactions, which are important for ozone loss in the middle atmosphere (Hoffman and Solomon, 1989; Rodriguez et al., 1991). The magnitude of these effects is significantly enhanced when the background aerosol layer is perturbed by strong volcanic eruptions, or possibly by high-speed civil transport aircraft (Tie et al., 1994; Weisentein et al., 1997; Bekki and Pyle, 1992; Pitari et al., 1993). Stratospheric aerosols are mainly composed of supercooled sulphuric acid droplets (Steele and Hamill, 1981). The sulphuric acid fraction of the droplets, which is in the range of 50-80 %, is a strong function of the relative humidity and the ambient temperature (Steele and Hamill, 1981), and therefore varies with latitude and season. Several models have been developed to understand the role of stratospheric aerosols in the atmospheric system (e.g. Turco et al., 1979; Toon et al., 1988). In recent years, studies have been performed where aerosol microphysics has been added to the existing 2-D and 3-D models. One of the rare studies of 3-D simulations of the formation and development of stratospheric aerosols is for instance reported by Timmreck (2001) who emphasized the evolution and seasonal variation of stratospheric aerosols using the Hamburg climate model ECHAM4. There is a need for 3-D simulations of the effects of aircraft emissions on background stratospheric aerosols, including radiative and chemistry effects. Global studies are important because of the complex interactions between radiation, transport, chemistry and aerosol microphysics. This paper briefly describes SAMM, a box model of sulphuric acid-water aerosols.

Many microphysical models are based on iterative solutions. Computer processing time and memory use is an important issue in global simulations of atmospheric processes. Keeping this in mind, non-iterative solutions to growth and coagulation equations have been used in SAMM. These techniques have been developed by Jacobson et al. (1994, 1995, 1999, 2002).

* *Corresponding author:* Sachchida Tripathi, Department of Civil Engineering, Indian Institute of Technology, Kanpur 208016, India. Email: snt@iitk.ac.in

2 MODEL DESCRIPTION

2.1 Model overview

A size bin structure has been used to distribute particles as a function of their acid content (e.g. Sorokin et al., 2001). In a given bin the evolution of particle concentration, N , is described by the following equation

$$\frac{dN}{dt} = \left[\frac{dN}{dt} \right]_{\text{nuc}} + \left[\frac{dN}{dt} \right]_{\text{coag}} + \left[\frac{dN}{dt} \right]_{\text{cond}} + \left[\frac{dN}{dt} \right]_{\text{sed}} \quad (1)$$

where the subscripts nuc, coag, and cond mean respectively nucleation, coagulation, condensation and evaporation of H_2O and H_2SO_4 , and sed refers to sedimentation removal.

Particle formation has been achieved by a classical nucleation parameterization (Vehkamaki et al., 2002), which provides the rate of nucleation as well as the particle size and composition for a large range of temperature, sulphuric acid and water vapour concentrations.

Following Jacobson (2002), sulphuric acid condensation and nucleation have been treated as two competing mechanisms. This scheme provides, at each time step, the atmospheric concentration of the gas after condensation and the final H_2SO_4 concentration in the particles for any size bin, without using any iterative method. Particles have been assumed to achieve instantaneous equilibrium with water, as the rate of collision of water molecules is much higher than that of sulphuric acid (e.g. Steele and Hamill, 1981). Coagulation calculations have been carried out using the work of Jacobson et al. (1994), whose semi-implicit expression is computationally fast and numerically reliable, provided that the volume ratio between two adjacent bins remains rather small (e.g. Sorokin et al., 2001). Finally, particles have been removed from the system by sedimentation, using a very simple scheme. Particles fall velocities are calculated using expressions given by Pruppacher and Klett (1997). The main thermodynamic data (surface tension, density, activity) used to calculate fall velocities have been taken from Vehkamaki et al. (2002) in order to remain consistent with the nucleation scheme.

2.2 Selection of Model Parameters

We have performed several sensitivity studies to see the effects of the choice of number of size bins on predicted size distribution, and on the aerosol surface area. The aerosol surface area is an important parameter used to assess the impact of heterogeneous chemistry on the composition of the atmosphere. The lower and upper size particle radius limits adopted for SAMM are roughly 0.3 nm and 5 μm respectively. The upper size limit is based on the fact that in typical stratospheric conditions very few water-sulphuric acid particles become bigger than this size: those that do rapidly sediment from the atmosphere. The criterion for the lower size limit is set by the size of the newly formed particles due to nucleation. Figure 1 plots the background aerosol surface area as a function of the number of size bins used and the integration time-step for conditions typical of an altitude of 20 km. The calculated aerosol surface areas lie between 0.65 and 0.50 $\mu\text{m}^2/\text{cm}^3$. These values are comparable to those recommended for heterogeneous chemical reactions of atmospheric importance. Tie et al. (1994) reported a value of 0.6 $\mu\text{m}^2/\text{cm}^3$ for aerosol surface area at 20 km from their 2-D model calculations. It can be seen that little accuracy is gained by decreasing the model time step below about 2000 s. Therefore all the standard model runs used an 1800 s time-step (Figure 2) which generally corresponds to the integration time steps for dynamical processes used in global models. The influence of the size bins number on the aerosol surface area is not very high since using 20 or 70 bins leads only to a difference of approximately 10 %. However, the impact on the size distribution is larger, as already pointed out. A time step of 1800 s and a bin number of 44 was adopted for SAMM. Based on this evaluation, we expect computational errors < 0.005 %, 5 % and 40 % in the volume, surface area and number density respectively. These results should be kept in mind while examining results involving number densities or size ratios, as SAMM could overestimate the density of larger particles. However, using 44 bins provides reliable surface areas results.

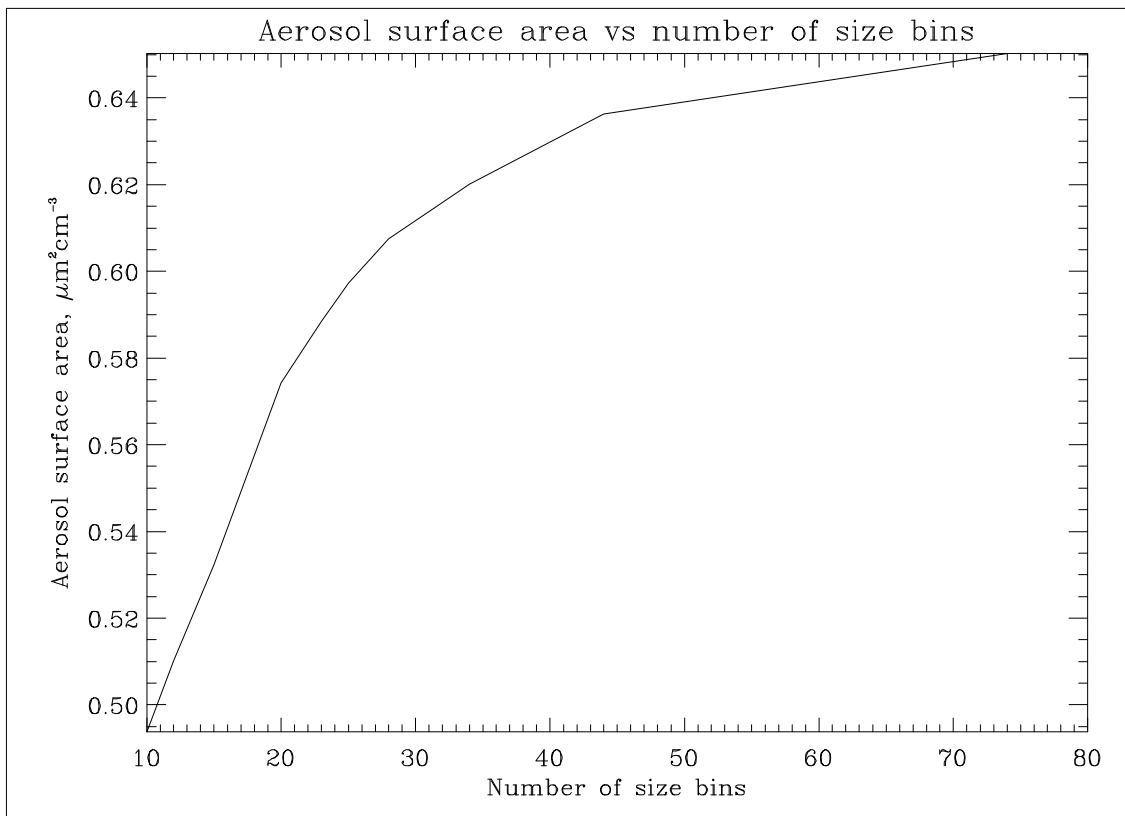


Figure 1. Aerosol surface area plotted as a function of the number of size bins used and the integration time step.

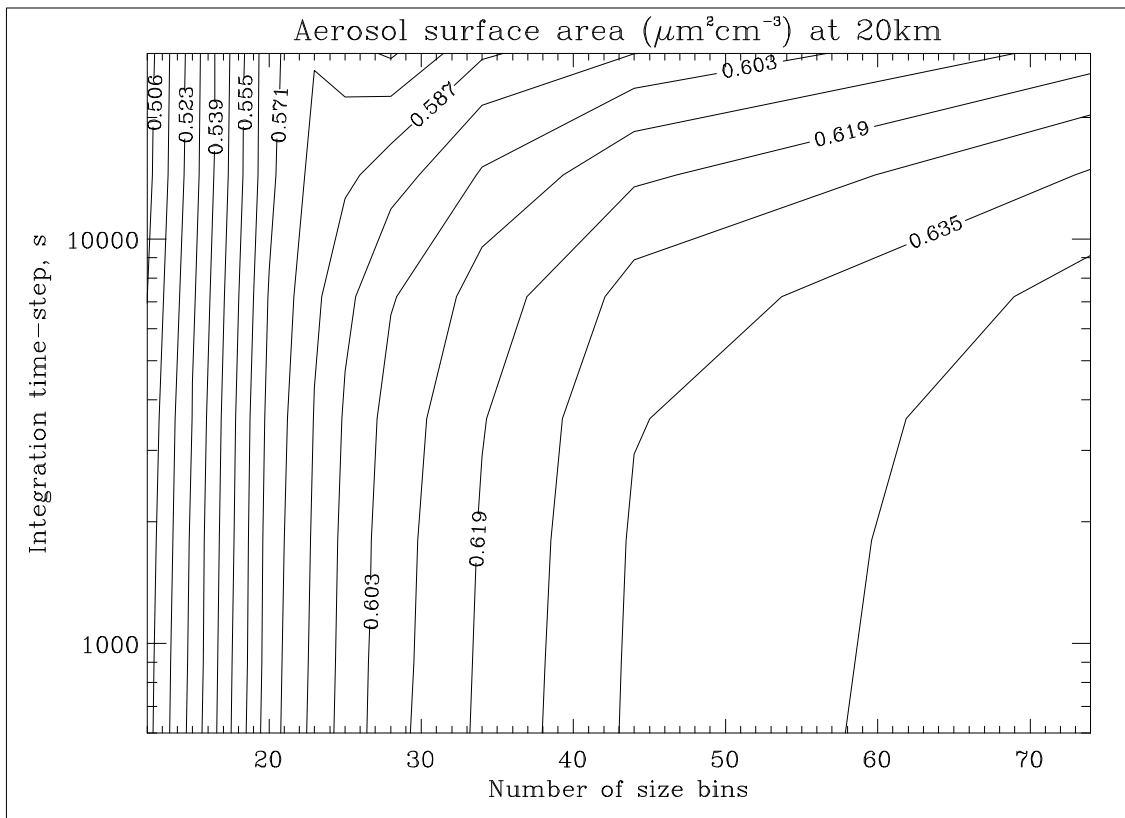


Figure 2. Aerosol surface area as a function of the number size bins used for an 1800 s time step.

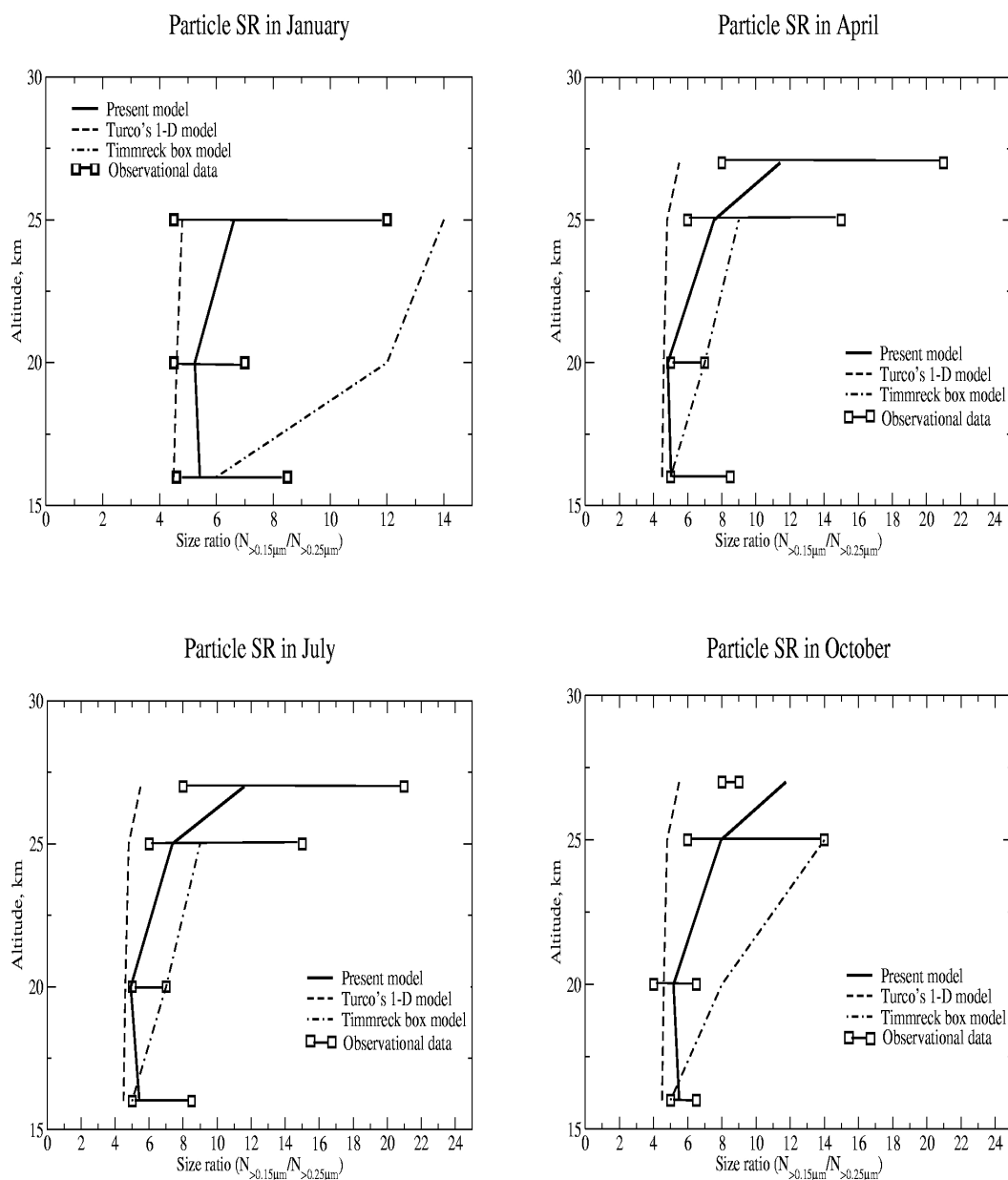


Figure 3. Numerical values of particle size ratio (SR) as a function of altitude for different seasonal conditions.

3 RESULTS

Figure 3 shows model-simulated aerosol mixing ratios together with observed values from Hofmann and Rosen (1981). SAMM compares well with observations and especially, it is able to reproduce the trends of particles size ratios as a function of altitude.

However, in January the altitude at which the maximum occurs is different from that predicted by Turco's model. Errors on number densities are high due to the effect of numerical diffusion and also to the absence of diffusion. This last process is, with sedimentation, responsible for the vertical transport of particles and was not included in these box model simulations. Comparing the plots in Figure 3, we do not see large seasonal variations in the aerosol mixing ratio; this is consistent with the earlier 1-D (Toon et al., 1979) and 0-D (Timmreck and Graph, 2000) model predictions. Furthermore, the total number concentration of particles is always between 4 and 8 cm^{-3} , which falls within the range reported by Weisenstein et al. (1997) who studied the stratospheric aerosols using a two-dimensional model.

4 CONCLUSION

A fast stratosphere aerosol microphysical model (SAMM) has been developed suitable for use in large 3-D global models. SAMM is able to provide accurate estimates of aerosol surface area using a small number of particle size bins. Besides the total surface area, the model is able to reproduce aerosol number concentration trends observed in the stratosphere. Future work will include extending SAMM to include processes involving ions and extend the treatment of aerosol composition to include multicomponent solutions. The inclusion of SAMM in a global model (SLIMCAT) will be the first step in assessing the impact of aircraft aerosol emissions in the lower stratosphere using the 3D model.

5 ACKNOWLEDGEMENTS

The authors acknowledge funding of this work by a NERC UTLS Ozone Grant. The authors would also like to thank H. Vehkamäki for providing them her nucleation scheme and for helpful discussions.

REFERENCES

- Bekki, S., and J. A. Pyle, 1992: Two-dimensional assessment of the impact of aircraft sulphur emissions on the stratospheric sulphate aerosol layer. *J. Geophys. Res.* 97, 15839-15847.
- Hofmann, D.J., and J.M. Rosen, 1981: On the background aerosol layer. *J. Atmos. Sci.* 32, 1446-1456.
- Hofmann, D. J., and S. Solomon, 1989: Ozone destruction through heterogeneous chemistry following the eruptions of El Chichón. *J. Geophys. Res.* 94, 5029-5041.
- Jacobson, M. Z., R. P. Turco, E. J. Jensen, and O. B. Toon, 1994: Modelling coagulation among particles of different composition and size. *Atmos. Environ.* 28, 1327-1328.
- Jacobson, M. Z., 1995: Numerical techniques to solve condensational and dissolutional growth equations when growth is coupled to reversible reactions, *Aerosol Sci. Technol.* 27, 491-498.
- Jacobson, M.Z., and R. C. Turco, 1995: Simulating condensational growth, evaporation, and coagulation of aerosols using moving and stationary size grid. *Aerosol Sci Technol.* 22, 73-92.
- Jacobson, M. Z., 1999: *Fundamentals of Atmospheric Modelling*, Cambridge University Press, Cambridge, UK.
- Jacobson, M. Z., 2002: Analysis of aerosol interactions with numerical techniques for solving coagulation, nucleation, condensation, dissolution, and reversible chemistry among multiple size distributions. *J. Geophys. Res.* vol. 107, 4366, doi: 10.1029/2001JD002044.
- Lacis, A., J. Hansen, and M. Sato, 1992: Climate forcing by stratospheric aerosols. *Geophys. Res. Lett.* 19, 1607-1610.
- Michaelangeli, D., M. Allen, Y. L. Yung, R. L. Shia, D. Crisp, and J. Eluszkiewicz, 1992: Enhancement of atmospheric radiation by an aerosol layer. *J. Geophys. Res.* 97, 865-974.
- Pitari, G., V. Rizi, L. Ricciardulli, and G. Visconti, 1993: High-speed civil transport impact: Role of sulphate, nitric acid trihydrate, and ice aerosols studied with a two-dimensional model including aerosol physics. *J. Geophys. Res.* 98, 23141-23164.
- Pruppacher, H. R., and J. D. Klett, 1997: *Microphysics of clouds and precipitation*, 2nd rev. and enl. ed. Kluwer Academic Publishers, Dordrecht.
- Rodriguez, J. M., M. K. W. Ko, and N. D. Sze, 1991: Role of heterogeneous conversion of N₂O₅ on sulphate aerosols in global ozone losses, *Nature*, 352, 134-137.
- Rosen, J. M., D. J. Hofmann, and J. Laby, 1975: Stratospheric aerosol measurements II. The worldwide distribution. *J. Atmos. Sci.* 32, 1457-1462.
- Russell, P. B., and P. Hamill, 1984: Spatial variation of stratospheric aerosol acidity and model refractive-index-implications of recent results. *J. Atmos. Sci.* 41, 1781-1984.
- Sorokin A., X. Vancassel, and P. Mirabel, 2001: On volatile particle formation in aircraft exhaust plumes. *Phys. Chem. Earth* 26, 557-561.
- Steele, H. M., and P Hamill, 1981: Effects of temperature and humidity on the growth and optical properties of sulphuric acid-water droplets in the stratosphere. *J. Aerosol Sci.* 12, 517-528.
- Tie, X., L. Lin, and G. Brasseur, 1994: Two-dimensional coupled dynamical/chemical/microphysical simulations of global distribution of El Chichón volcanic aerosols. *J. Geophys. Res.* 99, 16779-16792.

- Timmreck, C., and H. F. Graph, 2000: A microphysical model for simulation of stratospheric aerosol in a climate model. *Meteorologische Zeitschrift* 9, 263-282.
- Timmreck, C, 2001: Three-dimensional simulations of stratospheric background aerosol: First results of a multiannual GCM simulation. *J. Geophys. Res.* 106, 28313-28332.
- Toon, O. B., R. P. Turco, P. Hamill, C. S. Kiang, and R. C. Whitten, 1979: A one-dimensional model describing aerosol formation and evolution in the stratosphere: II, Sensitivity studies and comparison with observations. *J. Atmos. Sci.* 36,718-736.
- Toon, O. B., R. P. Turco, D. Westphal, R. Malone, and M. S. Liu, 1988: A multidimensional model for aerosols: Description of computational analogs. *J. Atmos. Sci.* 45, 2123-2143.
- Toon, O.B., R. P. Turco, J. Jordon, J. Goodman, and G. Ferry, 1989: Physical processes in Polar Stratospheric Clouds. *J. Geophys. Res.* 94, 11359-11380.
- Turco, R. P., P. Hamill, O. B. Toon, R. C. Whitten, and C. S. Kiang, 1979: A one-dimensional model describing aerosol formation and evolution in the stratosphere. Physical processes and mathematical analogs. *J. Atmos. Sci.* 36, 699-717.
- Vehkamaki, H., M. Kulmala, I. Napari, K.E.J Lehtinen, C. Timmreck, M.Noppel, and A. Laaksonen, 2002: An improved parameterisation for sulphuric acid/water nucleation rates for tropospheric and stratospheric conditions. *J. Geophys. Res.* 107, doi: 10.1029/2001GL013813.
- Weisenstein, D. K., P. K. Yue, G. K. W. Ko, N. D. Sze, J. M. Rodriguez, and C. J. Scott, 1997: Two-dimensional model of sulphur species and aerosol. *J. Geophys. Res.* 102, 13019-13053.

On the potential of the cryoplane technology to reduce aircraft climate impact

M. Ponater*, S. Marquart, L. Ström, K. Gierens, R. Sausen
DLR-Institut für Physik der Atmosphäre, Oberpfaffenhofen, Germany

G. Hüttig
Institut für Luft- und Raumfahrt, Technische Universität Berlin, Germany

Keywords: contrails, cryoplanes, aircraft, climate impact, technology transition

ABSTRACT: The quantitative potential of a switch to cryoplanes to reduce aircraft climate impact is investigated. Basic assumptions are the expected increase of air traffic between 1990 and 2050 and a smooth technology transition between 2015 and 2050. The study covers the effects of reduced CO₂ emissions, reduced NO_x emissions, and a change in contrail radiative impact to be expected from increased coverage and decreased optical depth in the cryoplane case. We find a typical value of about 20% reduction in aircraft induced radiative forcing on the 2050 horizon, if cryoplanes were introduced. Best estimates range between 16% and 29%, depending on the speed of the technology transition. Due to inherent scientific uncertainties this range widens to between 14% and 40%. Some further sources of uncertainty like cirrus cloud changes or possible CO₂ emissions from the liquid hydrogen production process could not be included in the current estimate.

1 INTRODUCTION

One technological option to reduce the climate impact of air traffic is a switch to alternative fuels like liquid hydrogen (LH₂). The main advantage of this so-called cryoplane technology over conventional kerosene engines is the elimination of, both, CO₂ and particle emissions, while a lower NO_x emission index is also expected due to the extended possibilities to employ lean burning (e.g., the “micromix combustion” described by Dahl and Suttrop, 1998). In contrast, the net effect of enhanced water vapour emissions of LH₂ engines on the stratospheric water vapour content has been estimated to be of little importance, as long as flight altitudes are not lifted upward (IPCC, 1999). A first attempt to assess net climate impact gain due to cryoplane operation (Marquart et al., 2001) suggested that the higher formation frequency of contrails (also resulting from more water vapour in the exhaust gas) may strongly counteract the various advantages at least on the shorter time range, as the effect of vanishing CO₂ emissions is mainly felt on longer time horizons. Here, we report on recent results yielded within the EU-project *CRYOPLANE*, which have extended the respective assessment basis in several respects: First, a number of more realistic transition scenarios has been developed. Second, the treatment of the contrail impact has been refined beyond the work of Marquart et al. (2001): Potentially different optical properties of contrails from cryoplanes due to the absence of particles in the exhaust have been included.

2 TOOLS AND METHODS

Several models were employed to quantify key parameters of aircraft climate impact on the microphysical up to the global scale. Contrail microphysics was simulated in the framework of the MESOSCOP model (e.g., Ström and Gierens, 2002). The global distribution of contrails including their radiative forcing was determined with the ECHAM4.L39(DLR) GCM using a parameterisation scheme of Ponater et al. (2002) and Marquart and Mayer (2002). The climate impact of atmospheric ozone changes caused by aircraft NO_x emissions was treated as in Grewe et al. (1999), some new

* *Corresponding author:* Michael Ponater, DLR-Institut für Physik der Atmosphäre, Oberpfaffenhofen, D-82234 Wessling, Germany. Email: michael.ponater@dlr.de

simulations for a crosscheck of the IPCC (1999) CTM results were run with the more recent coupled chemistry/climate model E39/C (Grewe et al., 2002). The evaluation of the transient transition scenarios to the cryoplane technology was done by applying of the global mean linear response model of Sausen and Schumann (2000).

3 CRYOPLANE CONTRAILS

3.1 Simulation of microphysical parameters

Two pairs of case studies for contrails behind either kerosene or hydrogen fuelled aircraft under the same ambient conditions have been described in detail by Ström and Gierens (2002). The number of these simulations was extended to scan the parameter space of possible ambient conditions (Fig. 1, left) in order to identify characteristic differences in ice water path, ice crystal concentration, optical depths etc. for a global assessment. The key parameter is the ice crystal size (effective radius r_{eff}). In MESOSCOPI, it is calculated as a spatial distribution from the respective distributions simulated for ice mass and ice crystal number concentration. This information must be translated to the bulk formulation in the global model, which only knows a mean effective radius for the grid box averaged contrails as a whole (Roeckner, 1995). As discussed in Ström and Gierens (2002), absolute values of r_{eff} and of the optical depth τ (taken as means over a 30 minute simulation) are sensitive to many uncertainties arising from background aerosols, ice crystal shape, presence of wind shear etc., but also to some ambiguity in determining the mean r_{eff} (mass weighted or crystal density weighted). We decided to characterise the different contrail optical properties by using the r_{eff} ratio (Fig. 1, right) between the conventional and the cryoplane case, which appears to be quite a robust quantity.

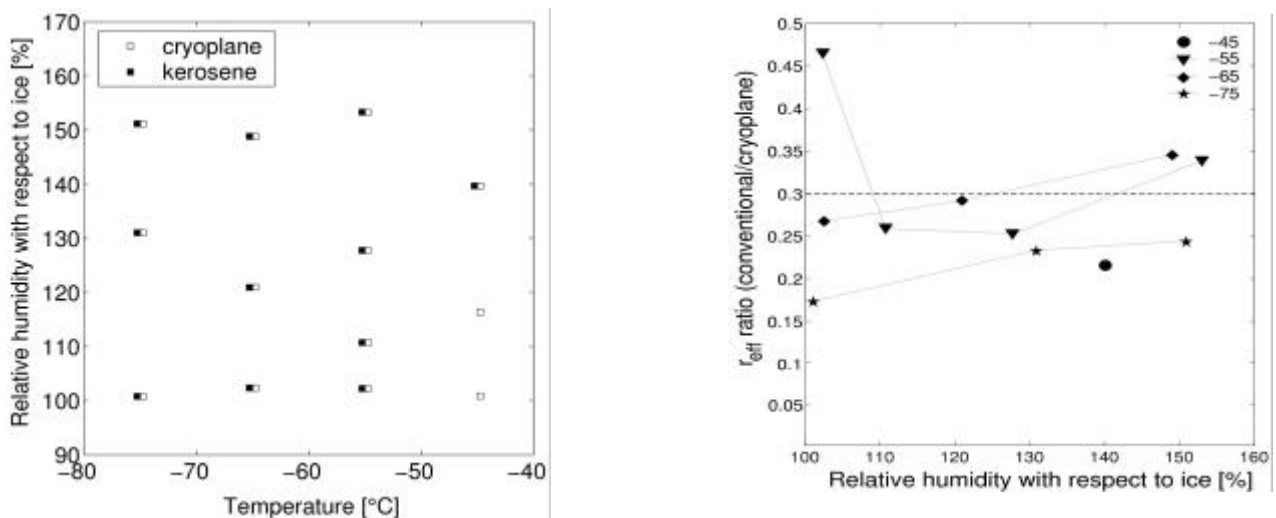


Figure 1. Left: Overview on the ensemble of contrail simulations performed with the MESOSCOPI microphysical model for various ambient temperature and supersaturation conditions (in two cases the thermodynamic theory does only allow contrails behind the cryoplane). Right: Ratio of the mean effective ice particle radii (conventional vs. cryoplane case) for the various pairs of MESOSCOPI simulations.

Rather than trying to define an analytical function of this ratio dependent on temperature and ice supersaturation we assumed r_{eff} in conventional contrails to be smaller by a factor of 0.3 than in cryoplane contrails. This implies that the optical depth of cryoplane contrails is smaller by a similar amount, as the contrail ice water content is mainly determined by the supersaturation in the ambient air and, thus, almost independent from the engine technology.

3.2 Simulation of global impact

In order to determine the global radiative forcing of contrails we have evaluated future scenarios for 2015 and 2050, assuming changes in, both, air traffic density and propulsion efficiency as described in Marquart et al. (2003). Potential changes in the background climate were not included. As the contrail parameterisation in the ECHAM4 global climate model is based on the thermodynamic theory, the changes of contrail coverage due to increasing propulsion efficiency (from 2015 to 2050), or a higher H₂O emission index (of LH₂ engines compared to kerosene engines) are implicitly accounted for (Marquart et al., 2001; Ponater et al., 2002). The difference in contrail optical properties was introduced by prescribing larger particles in the cryoplane case as explained in the previous subsection.⁶ The reference values of global mean contrail radiative forcing in a conventional aircraft scenario are 9.8 mW/m² and 19.5 mW/m² for 2015 and 2050, respectively. Note that these values are substantially smaller than those given by IPCC (1999) from methodical reasons discussed in detail by Ponater et al. (2002) and Marquart et al. (2003). The general reduction of estimated contrail climate impact compared to IPCC (1999) also implies an *a priori* reduction of the importance of respective changes due to a potential transition to the cryoplane technology.

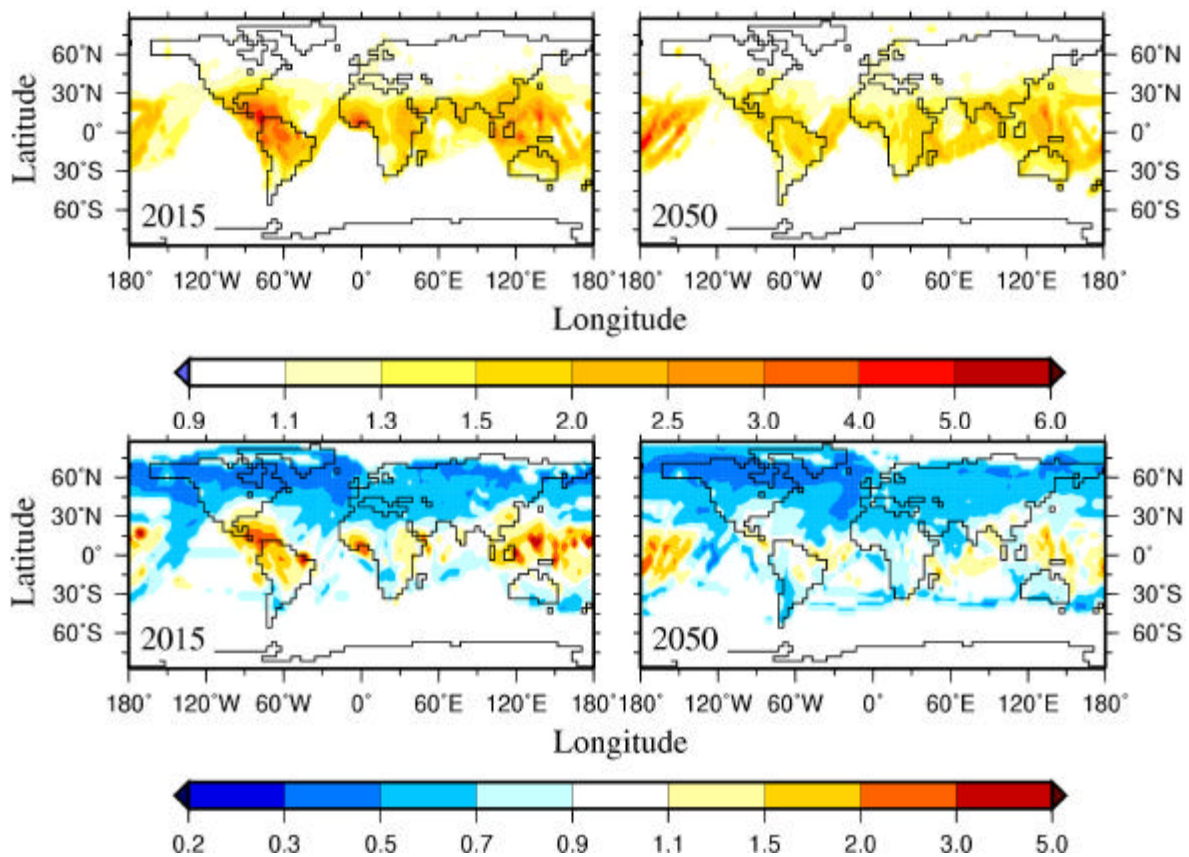


Figure 2. Ratio of the results yielded in a conventional aircraft scenario and a equivalent cryoplane scenario for the annually averaged coverage of all contrails (upper panels) and the associated net radiative forcing (lower panels), respectively. Two examples based on a 2015 (left) and a 2050 (right) aircraft scenario are displayed. Blue (yellow/red) colour indicates a smaller (larger) value for the cryoplane case.

Fig. 2 indicates the maximum impact of the technology transition for 2015 and 2050, relating pure cryoplane to pure conventional air traffic for each time slice. The upper panel shows the ratio of contrail coverage between the cryoplane and the conventional case, the lower panel the respective ratio of contrail radiative forcing. Contrail coverage is enhanced everywhere in the cryoplane

⁶ Actually, this means an increase from about 12 to 13 μm for normal contrails (Ponater et al., 2002) to 40 to 44 μm for cryoplane contrails.

scenarios as thermodynamic contrail formation is possible under less restrictive ambient conditions. However, in most regions of the world the effect of reduced optical depth outweighs the effect of increasing coverage. This holds, particularly, in the extratropics where air traffic density is highest. The net effect is a reduction of contrail global radiative forcing by about 18% in 2015 and by about 28% in 2050 (from 9.8 mW/m^2 to 8.0 mW/m^2 and from 19.5 mW/m^2 to 13.9 mW/m^2 , respectively). To illustrate the importance of changing optical properties we note that the radiative forcing in 2015 would increase from 9.8 mW/m^2 to 16.5 mW/m^2 , if the lower optical depth of cryoplane were not accounted for.

4 TRANSITION SCENARIOS

4.1 Technology transition

Several technological transition scenarios were developed within the *CRYOPLANE* project, three of which (designated as Cryo1, Cryo2, and Cryo3) have been evaluated for the present study and are described here. They assume introduction of the first cryoplanes between 2015 and 2020, followed by continuous transition during the period until 2050 (instead of the artificial instantaneous switch assumed in Marquart et al., 2001). Cryo1 represents a smoothed, stepwise approach with the EU taking the lead, followed 5 years later by a transition start in North America, and another five years later in Latin America, Asia, and the Middle East. In each case cryoplane introduction starts with the smallest aircraft, with long-range aircraft following about ten years after. Cryo2 assumes the fastest transition, starting a smooth world-wide transition of small and medium-sized aircraft in 2015, and of large aircraft in 2025. Transition of the whole fleet is complete in 2050. Cryo3 starts a world-wide transition later (2020) than Cryo2 but lets proceed it faster towards the end of the period.

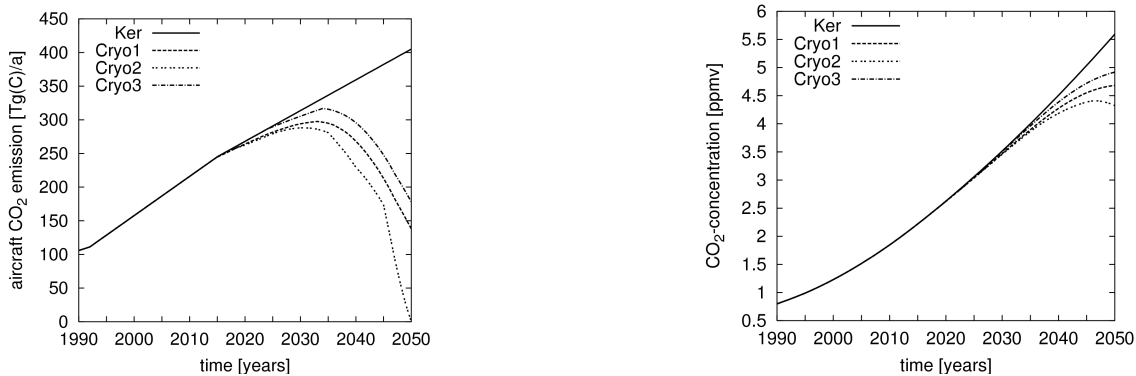


Figure 3. Temporal evolution of aircraft induced CO₂ emissions (left) and atmospheric CO₂ concentration increase (right) for a purely kerosene supported aircraft inventory (Ker) and for three transition scenarios to cryoplane technology (Cryo1/2/3, see text) from 1990 to 2015. The numbers indicate global mean values.

All emission scenarios are based on approved air traffic increase expectations (IPCC, 1999). The relative kerosene and LH₂ consumption has been calculated for every fifth year, thus CO₂, H₂O, and NO_x emissions can be derived, accordingly. As an example, Fig. 3 displays the time development of aircraft global mean CO₂ emissions for a purely kerosene supported scenario (Ker) and for the transition assumptions just described. There is no difference between the scenarios before 2015. The related CO₂ concentration change is derived from the linear response model of Sausen and Schumann (2000): Due to the long lifetime of CO₂, its concentration continues to rise for most scenarios until 2050 as long as CO₂ emission rates of the remaining conventional aircraft dominate the CO₂ removal rates from the atmosphere.

4.2 Climate impact change

The climate impact associated with the various scenarios is quantified in terms of the global mean radiative forcing in 2050 (Fig. 4). We also adopt the usual method of taking radiative forcing as a metric to compare individual components to the net effect (e.g., IPCC, 1999). The aircraft CO₂ forcing and its variability among the scenarios is directly related to the concentration changes shown in Fig. 3, right. The CO₂ contribution to the radiative impact gain drops from 73 mW/m² in Ker to 56 mW/m² in Cryo2, the fastest transition scenario. While this component can be regarded to be quantified with a good reliability, the other ones are more uncertain. The ozone contributions to the radiative forcing have been scaled linearly on the basis of global mean aircraft NO_x emissions, just as described in Marquart et al. (2001). Our best estimate with respect to the ozone effect is based on the availability of low-NO_x technology for conventional as well as for cryoplane engines. This results in a decrease of ozone radiative forcing in 2050 from 36 mW/m² (Ker) to 9 mW/m² (Cryo2). However, part of this effect is compensated by the impact of atmospheric NO_x increase on methane lifetime. Thus, in accordance with current estimates (IPCC, 1999; Isaksen et al., 2001), we reduce the ozone related values by 75%, which leaves a net impact of NO_x between about 9 mW/m² (Ker) and about 2 mW/m² (Cryo2). For the contribution of contrails we rely on the key numbers described in subsection 3.2. This implies a radiative forcing reduction at 2050 time horizon from 19.5 mW/m² (Ker) through 16 mW/m² (Cryo1) down to about 14 mW/m² (Cryo2).

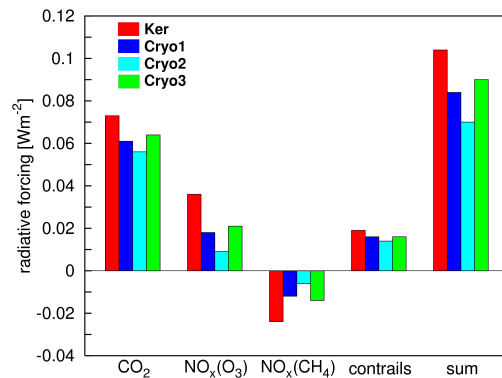


Figure 4. Radiative forcing best estimates (in W/m²) of CO₂, NO_x (through either O₃ or CH₄ concentration changes), and contrails at year 2050 for a conventional aircraft increase scenario (Ker) and three transition scenarios to cryoplanes (Cryo 1/2/3). The columns represent global mean values. The rightmost panel shows the sum of all displayed components, not including further contributions from soot and sulfur aerosols, stratospheric water vapour, and cloudiness beyond line-shaped contrails.

The sum of effects suggests a best estimate of the net climate impact reduction at 2050 from about 100 mW/m² for kerosene supported air traffic throughout the whole period to between 85 mW/m² and 72 mW/m² for the various cryoplane transition scenarios.

We recall that the radiative forcing of contrails and aircraft NO_x emissions is known only with considerable caveats. The respective general uncertainty discussions in IPCC (1999) continue to be valid. However, we have chosen key values for the radiative impact change due to cryoplanes that are rather conservative (i.e., on the low side), for example by including low-NO_x technology for conventional aircraft, and by employing the lower estimates for contrail climate impact by Marquart et al. (2003) instead of the respective values from Minnis et al. (1999) adopted by IPCC (1999) that yield a five times larger best estimate. This approach reduces the possibility that we overestimate the environmental gain by a cryoplane transition. However, if the LH₂ fuel could not be produced totally from renewable energy sources (but would cause extra CO₂ emissions in the production process), the climate impact gain would be diminished, of course. These, as other contributions, may easily be fed into the linear response model as soon as reliable key numbers become available.

5 DISCUSSION AND OUTLOOK

According to our best estimate a relative reduction of aircraft induced radiative forcing at 2050 by between 16% and 29% (depending on the speed of transition) could be achieved if cryoplanes were introduced. The uncertainty range widens to between 14% and 40%, if several inherent scientific uncertainties with respect to individual processes and effects are taken into account. Note also that these values depend on the year considered, due to the gradual increase of the CO₂ contribution (Fig. 3, right). Beyond the 2050 time horizon the environmental gain in the cryoplane scenarios would obviously grow, as the continuing CO₂ emissions of the kerosene supported fleet would further increase the effect of accumulated CO₂ concentration in the atmosphere.

We have not included in our best estimate most recent results (Morris et al., 2003; Gauss et al., 2003) suggesting that accumulation of aircraft water vapour emissions in the stratosphere may be more important than assumed by IPCC (1999) and by Marquart et al. (2001). However, we do not expect that it would make a qualitative change to our overall assessment. A potential uncertainty source of greater importance is contrail cirrus, which is now suspected to cause a larger climate impact than line-shaped contrails (e.g., Mannstein, this volume). There is no sufficient knowledge at this stage to include this effect in a quantitative assessment, but respective research is proceeding rapidly (see several contributions in this volume). More knowledge is also warranted with respect to the potential of producing large amounts of LH₂ from renewable energy sources. Finally, we note the necessity to have at least some measurements from observed cryoplane contrails in order to support the results of our contrail microphysics simulations.

REFERENCES

- Dahl, G., and F. Suttrop, 1998: Engine control and low-NO_x combustion for hydrogen fuelled aircraft gas turbines, *Int. J. Hydrogen Energy* 23 (8), 695-704.
- Gauss, M., I.S.A. Isaksen, S. Wong, and W.-C. Wang, 2003: Impact of H₂O emissions from cryoplanes and kerosene aircraft on the atmosphere, *J. Geophys. Res.* 107 (D13), 4304, doi: 10.1029/2002JD002623.
- Grewe, V., M. Dameris, R. Hein, I. Köhler, and R. Sausen, 1999: Impact of future subsonic aircraft NO_x emissions on the atmospheric composition, *Geophys. Res. Lett.* 26, 47-50.
- Grewe, V., M. Dameris, C. Fichter, and R. Sausen, 2002: Impact of aircraft NO_x emissions. Part I: Interactively coupled climate chemistry simulations, and sensitivities to climate chemistry feedback, lightning, and model resolution. *Meteorol. Z.* 11, 177-186.
- IPCC, 1999: Aviation and the global atmosphere. A special report of IPCC working groups I and III (Eds.: J.E. Penner, D.H. Lister, D.J. Griggs, D.J. Dokken, M. McFarland), Cambridge Univ. Press, 373pp.
- Isaksen, I., T.K. Berntsen, and W.-C. Wang, 2001: NO_x emissions from aircraft: Its impact on the global distribution of CH₄ and O₃ and on radiative forcing, *TAO*, 1, 63-78.
- Marquart, S., R. Sausen, M. Ponater, and V. Grewe, 2001: Estimate of the climate impact of cryoplanes. *Aerosp. Sci. Techn.* 5, 73-84.
- Marquart, S., and B. Mayer, 2002: Towards a reliable GCM estimation of contrail radiative forcing, *Geophys. Res. Lett.* 29, 1179, doi: 10.1029/2001GL014075.
- Marquart, S., M. Ponater, F. Mager, and R. Sausen, 2003: Future development of contrail cover, optical depth, and radiative forcing: Impacts of increasing air traffic and climate change. *J. Clim.* 16, 2890-2904.
- Minnis, P., U. Schumann, D.R. Doelling, K.M. Gierens, and D.W. Fahey, 1999: Global distribution of contrail radiative forcing, *Geophys. Res. Lett.* 26, 1853-1856.
- Morris, G.A., J.E. Rosenfield, M.R. Schoeberl, and C.H. Jackman, 2003: Potential impact of subsonic and supersonic aircraft exhaust on water vapor in the lower stratosphere assessed via a trajectory model. *J. Geophys. Res.* 108 (D3), 4103, doi: 10.1029/2002JD002614.
- Ponater, M., S. Marquart, and R. Sausen, 2002: Contrails in a comprehensive climate model: Parameterisation and radiative forcing results. *J. Geophys. Res.* 107 (D13), 4164, doi: 10.1029/2001JD000429.
- Roeckner, E., 1995: Parameterization of cloud radiative properties in the ECHAM4 model, *WCRP workshop proceedings, WMO/TD 713*, pp. 105-116, WMO, Geneva, 1995.
- Sausen, R., and U. Schumann, 2000: Estimates of the climate response to aircraft CO₂ and NO_x emission scenarios. *Clim. Change* 44, 27-58.
- Ström, L., and K. Gierens, 2002: First simulation of cryoplane contrails. *J. Geophys. Res.* 107 (D18), 4346, doi: 10.1029/2001JD000838.

Impact of Cruise Altitude on Contrails

C. Fichter*, S. Marquart, R. Sausen

DLR-Institut für Physik der Atmosphäre, Oberpfaffenhofen, Germany

D.S. Lee

Manchester Metropolitan University, United Kingdom

P.D. Norman

QinetiQ, Farnborough, United Kingdom

Keywords: contrails, radiative forcing, cruise altitude, aircraft

ABSTRACT: The ECHAM general circulation model and a recently developed contrail parameterisation were applied to a set of three-dimensional aircraft inventories with shifted cruise altitudes in a parametric study. Contrail coverage and radiative forcing, including regional and seasonal differences, for changed cruise altitudes of 610 m (2000 feet) increments were compared with a 'base case' scenario. The global annual mean contrail coverage decreased in an approximately linear manner to a maximum change of -45% for a decrease of 1830 m (6000 feet) in cruise altitudes. Our best estimate for radiative forcing by contrails is a decrease of 45% for the maximum shift in cruise altitudes. Fuel burn of the global fleet increased as a consequence of the downward shift in cruise altitudes.

1 INTRODUCTION

Actual cruise altitudes of aircraft are not optimised with respect to minimal overall environmental impact, but result mainly from fuel or flight time efficiency with the constraints imposed by aircraft aerodynamics and air traffic management. Climate impact is not considered in this process. However, this impact might be reduced by changing the flight altitude. Of particular interest is the impact of flight altitude on contrail formation.

According to the revised thermodynamic Schmidt-Appleman theory (Schumann, 1996), contrail formation depends on the overall propulsion efficiency of the aircraft, the emission index of water vapour and ambient atmospheric conditions of pressure, humidity, and temperature. Figure 1 shows the zonal mean potential contrail cover, which is a measure for the ability of the air to allow contrail formation (Sausen et al., 1998), for January and July mean conditions of the 1990s as calculated with the ECHAM4.L39(DLR) GCM (Land et al. 1999a; Land et al., 2002) extended by a parameterisation for persistent contrails (Ponater et al., 2002).

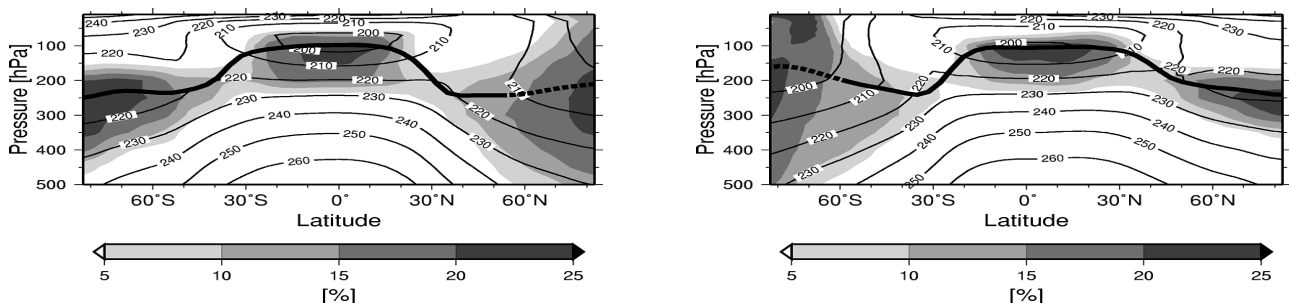


Figure 1: Five year zonal mean of potential contrail coverage (shading, in %) for January (left) and July (right) mean conditions as calculated by ECHAM4.L39(DLR). The bold line indicates the thermal tropopause, which is not well defined in the polar winter atmosphere (dotted). The isolines display the temperature [K].

* Corresponding author: Christine Fichter, Deutsches Zentrum für Luft- und Raumfahrt, Institut für Physik der Atmosphäre, Oberpfaffenhofen, 82234 Wessling, Germany. Email: christine.fichter@dlr.de

Table 1: Flown distance, fuel consumption, contrail cover, and net radiative forcing by contrails for the base case of the TRADEOFF aircraft emissions of the year 1991/1992, and relative changes arising from upward and downward shifting of the mean cruise altitude.

Case	Flown Distance	Fuel Consumption	Contrail Cover	net RF by Contrails ¹
+2kft	0%	- 0.45 %	+ 5.5 %	+ 5.3% (5,2%)
base case	1.71 10 ¹⁰ km	111.5 Tg	0.0472	1.9 mW/m ² (2.9 mW/m ²)
-2kft	0%	+ 2.69 %	- 12.7 %	- 15.8% (13,8 %)
-4kft	0%	+ 3.59 %	- 28.4 %	- 31.6 % (31,0 %)
-6kft	0%	+ 5.83 %	- 44.5 %	- 47.4 % (44,8 %)

¹ Values in brackets are adjusted by a 25% offset to the longwave contrail radiative forcing (Marquart and Mayer, 2002)

Areas that are cold and moist enough to allow the formation of persistent contrails mainly occur in the tropopause region. As aircraft usually cruise at altitudes between 200 and 250 hPa, they fly in regions where contrails are most likely to form especially in the extra-tropics. As a consequence, contrail coverage might be reduced by shifting cruise altitudes to higher or lower levels.

Sausen et al. (1998) studied the impact of cruise altitude on contrail coverage, by simply shifting the air traffic 1 km up and down relative to a base case. They did not consider aerodynamic constraints or the impact on fuel burn. In this study, the TRADEOFF aircraft emission inventory was used, which calculates 'real' shifts in mean cruise altitudes, including the impact on fuel consumption (Table 1). The TRADEOFF inventory comprises also the flown distance, i.e., the flown distances per grid box. The effects on contrail coverage were calculated by shifting the mean cruise altitude down by 2000 ft (610 m), 4000 ft (1220 m) and 6000 ft (1830 m) and up by 2000 ft (610 m). Regional and seasonal effects were studied, and the relationship between changes in flight altitude and contrail coverage was investigated.

2 AIRCRAFT EMISSION SCENARIOS

The three-dimensional aircraft emission inventories, representative for the year 1991/92, have been produced on the basis of the ANCAT/EC2 movements database using a similar methodology to that of Gardner et al. (1998). The data are provided in a horizontal resolution of 1° x 1° and a vertical resolution of 2000 feet (610 m). The four seasons are represented by the months January, April, July, and October. The vertical distribution of air traffic for the base case was taken from a statistical analysis of ~53,000 real flights. For the downward shifts, this distribution was applied by simply recalculating emissions by the incremental changes. In the case of the upward shift, not all aircraft could perform this, so only those that could do so were shifted upwards. A summary of the inventories is given in Table 1.

3 METHOD

A contrail parameterisation scheme (Ponater et al., 2002) for the ECHAM4.L39(DLR) general circulation model was utilised. In this scheme, an online determination of contrail coverage, optical properties of the contrails and the resulting radiative forcing is possible. The contrail coverage in a reference area was calibrated using satellite observations of Bakan et al. (1994). A detailed description of this calibration method is given by Marquart et al. (2003). In contrast to the diagnostic study of Sausen et al. (1998), we use flown distance instead of fuel consumption to compute contrail coverage. This approach is likely to provide more realistic results, especially if regions with predominantly short haul flights with narrow bodies, e.g., Europe, are compared with long haul traffic regions with wide bodies and high fuel consumption per km, e.g., the north Atlantic flight corridor (Gierens et al., 1999; Marquart et al., this issue). Furthermore, the TRADEOFF aircraft inventories provide a higher vertical and horizontal resolution than the DLR inventory used by Sausen et al. (1998).

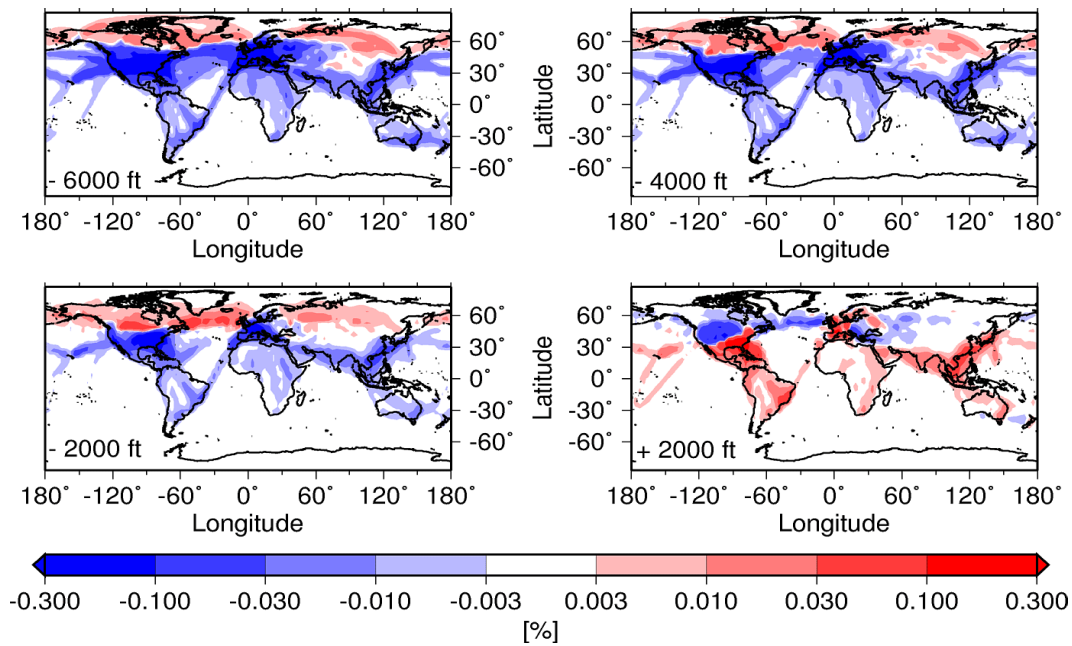


Figure 2: Absolute changes [% of the total area] of the annual mean contrail cover due to shifted flight altitudes by 6000 ft down (upper left), 4000 ft down (upper right), 2000 ft down (lower left), and 2000 ft up relative to the base case.

4 RESULTS AND DISCUSSION

4.1 The impact of flight altitude

Figure 2 shows the absolute changes of annual mean coverage by line-shaped contrails arising from changed cruise altitudes. The general pattern of changes in contrail coverage is similar for the three scenarios with lower cruise altitudes. In contrast to this, an almost inverted pattern appears for an up-shift of air traffic.

Downward shifting of cruise altitudes leads to a reduction of contrail coverage in the tropics and in parts of the mid-latitudes, but results in an increase of contrail coverage in the northern extratropics. In tropical regions the cruise altitudes of aircraft are usually located well below the tropopause (Fig. 1). If air traffic is shifted downwards it enters tropospheric regions with air that is too warm for contrail formation. Tropical contrail coverage is thus reduced with downward shifts in cruise altitudes. Figure 3 shows that nearly no contrails form in the tropics if cruise altitudes are lowered by 6000 feet.

Contrary to this, contrail coverage increases north of about 45°N , if aircraft cruise altitudes are shifted downwards. In the base case, air traffic occurs to some extent in the cold but dry stratosphere. Flying at a lower altitude in moister ambient air results in more contrails. The maximum increase in contrail coverage in the extra-tropics is associated with a downward shift of 2000 feet. In this case, cruise altitudes are shifted exactly into the region where conditions for contrail formation are optimal.

The distinct separation line between decrease and increase of contrail coverage due to downshift of air traffic mainly depends on ambient ice supersaturation and temperature. This line is shifted northwards, the more the cruise altitudes are shifted downwards. The short haul flights over the North American and European continents build an exception as they already occur in tropospheric regions and will be shifted into zones that are too warm for contrail formation when aircraft cruise at lower altitudes. However, shifting air traffic downwards results in an overall reduction of annual mean values of global contrail coverage. Almost half of all contrails disappear in the annual mean for the minus 6000 feet scenario (Table 1).

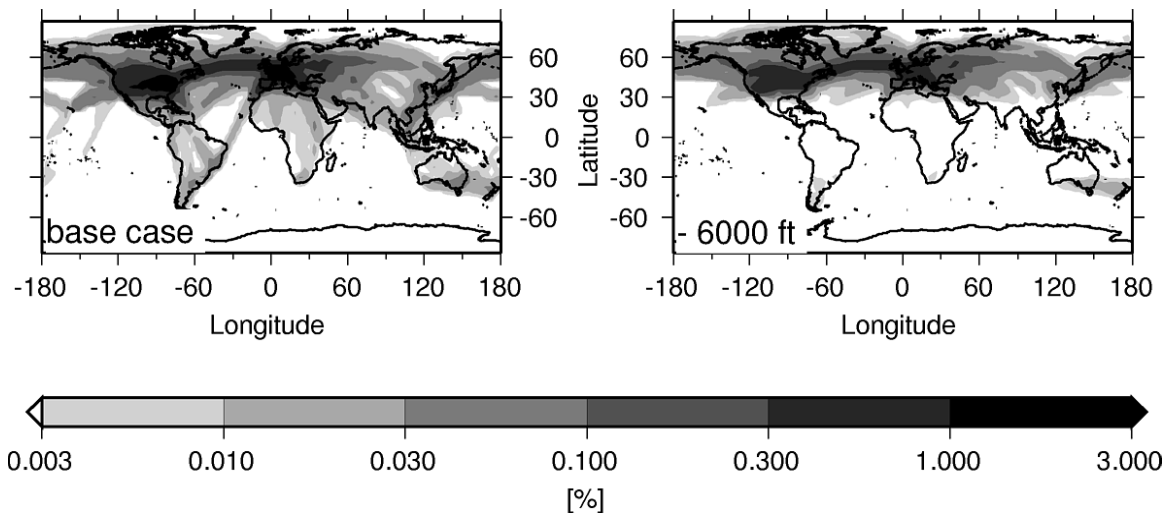


Figure 3: Geographical distribution of contrail cover for the base case aircraft emission scenario (left), and for an aircraft emission scenario with a 6000 ft lower cruise altitude.

Shifting the air traffic upward reveals an almost inverted pattern. Flying 2000 feet higher leads to an increase in contrail coverage over the tropics and parts of North America and Europe. In contrast to this, the remaining parts of the northern extra-tropics show a reduction of contrails. In the tropics air temperatures at usual cruise altitudes are mostly too warm for contrail formation. By shifting cruise altitudes upwards, air traffic enters colder regions where more contrails can be formed. Over the European and North American continents air traffic occurs to some extent in lower tropospheric regions, especially for short-range flights, so that an upwards shift of cruise altitudes does not imply shifting the air traffic into stratospheric regions where it would be too dry for contrail formation, but into colder tropospheric regions. Over Canada, the north-western parts of America, the north Atlantic flight corridor, Eastern Europe, the near Middle East and parts of Russia, cruise altitudes are high enough that shifting flight altitude up by 2000 feet has the consequence that a sufficiently large part of air traffic would enter the stratosphere, where ambient humidity is too low for contrail formation, and therefore an upwards shift of cruise altitudes results in a reduction of contrail cover.

4.2 Seasonal variation

As tropopause height, atmospheric temperature and humidity show large variability between summer and winter months, the impact of changes in cruise altitude on contrail coverage is highly sensitive to seasons. As an example, the geographical distribution of changes in contrail coverage due to downwards shifted air traffic by 6000 feet for January and July is shown in Figure 4.

The primary differences between January and July for a downwards shift of air traffic occur in the northern extra-tropics. In general, the separation line between increases and decreases in contrail coverage due to lower flight altitudes is shifted southwards in winter and northwards in summer. In January tropospheric regions in the extra-tropics are cold and moist enough that an increase in contrail coverage due to lower cruise altitudes results, whereas in July, the higher upper tropospheric temperatures in the extra-tropics prevent further contrail formation if air traffic is shifted down. This results in a relative decrease in contrail cover in July by about 50% over the North American and the European continents, and the north Atlantic flight corridor compared with the base case. A similar but less pronounced pattern is also found for a smaller downwards shift of air traffic by 2000 or 4000 feet (not shown).

Seasonal differences are found also for the plus 2000 feet scenario (not shown). In July an upwards shift of air traffic results in an overall increase in contrail cover except for very small regions over Canada and the Northeast Pacific and the Northeast of Europe. In several regions (e.g. Central Europe, North America, and South-East-Asia) this leads to a relative increase in contrail cover of more than 50% compared to the base case. In January however, increases in contrail cover are only found in the tropics, whereas in the extra-tropics contrail cover is reduced. The only exception is Central Europe, where flight altitude is so low that an up-shift still leads to an increase in contrail cover.

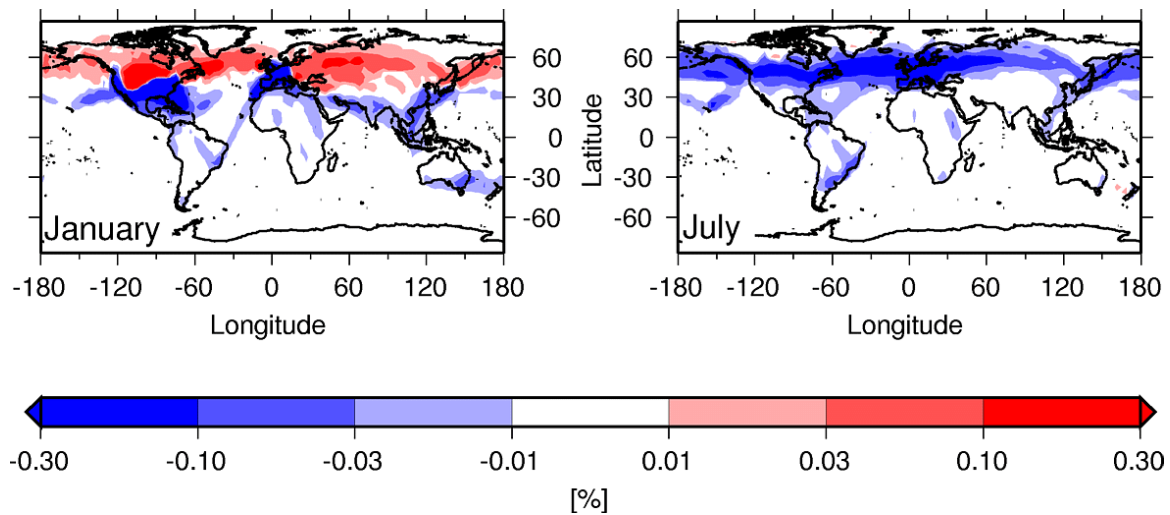


Figure 4: Geographical distribution of absolute changes in contrail cover due to 6000 feet lowered flight altitudes for January (left) and July (right).

Although the seasonal variation in global air traffic is almost negligible, global mean values of contrail coverage for January and July show very large seasonal differences for the investigated scenarios (Figure 5, left). They are even of opposite sign for an upwards shift of air traffic by 2000 feet. This seasonal differences in global contrail coverage mainly result from seasonal changes in meteorological conditions.

As the optical depth of contrails depends on ambient temperatures of contrail formation, values of optical depth are higher for lower flight altitudes and for warmer seasons (Ponater et al., 2002). However altitude dependence and seasonal variation in optical depth is very small compared to changes in total contrail coverage for different seasons and flight altitudes. Therefore seasonal differences in radiative forcing by contrails (Figure 5, right) are dominated by changes in total contrail coverage, as the curves for changes in contrail coverage and radiative forcing by contrails look qualitatively quite similar. Annual mean values for radiative forcing can be found in Table 1.

5 CONCLUSIONS

This parametric study allows a first estimation of the potential for mitigation of global environmental impacts of air traffic with respect to contrails and contrail radiative forcing by changing cruise altitudes. Strong seasonal sensitivity and considerable regional differences in contrail cover changes for the investigated emission scenarios were found. For global and annual mean values, the strongest reduction in contrail coverage were achieved by shifting air traffic down, whereas an upwards shift in air traffic resulted in a very small increase in contrail coverage. Our study shows a large potential for reducing the climate impact of aviation by including the constraint of minimal contrail formation in an air traffic management system. Evidently, this potential mitigation strategy could be optimised by considering changes in cruise altitude by latitude and season, as well as short-term changes in ambient parameters. Further work is necessary to investigate this. Moreover, quantitative estimates of aircraft impacts other than contrails need to be made before such mitigation strategies are suggested as practical options.

We note that the ECHAM4.L39(DLR) model suffers from a temperature error in the extratropical tropopause region ('cold bias'), which is expected to influence contrail formation (Marquart et al., 2003). Sensitivity experiments for varying flight altitudes were also run with a model version in which the cold bias is artificially reduced to half its value in the original model (Michael Ponater, pers. communication). Compared to the original model version contrail coverage and radiative forcing by contrails change only to a small extent in magnitude and not in sign. Therefore the main conclusions of this article appear to be largely insensitive to this temperature error.

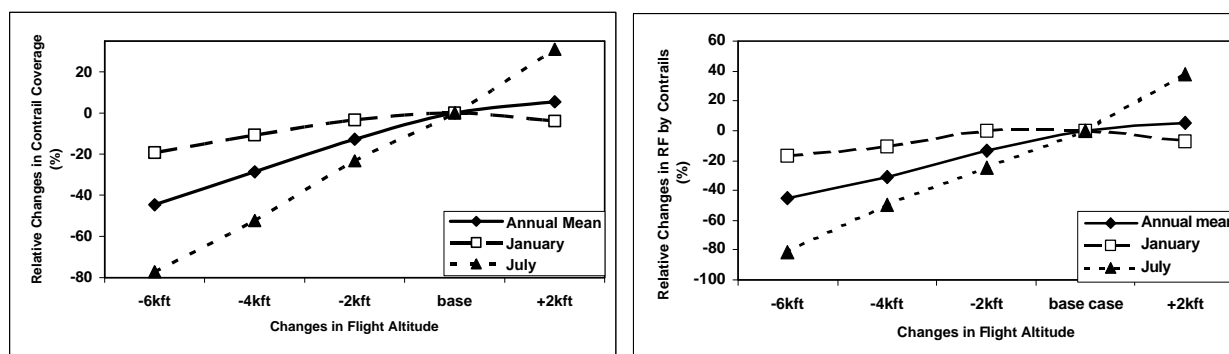


Figure 5: Relative changes in global mean contrail cover (left) and radiative forcing by contrails (right) as functions of changes in mean cruise altitude. The results for the annual mean and for the boreal winter and summer seasons are displayed.

Contrail radiative forcing is not the only aviation climate impact; also NO_x emissions impact upon ozone (Grewe et al., 2002; Gauss et al., this issue), fuel consumption and, therefore, CO_2 emissions, impacts on cirrus clouds, and furthermore influence on air traffic management and flight endurance must also be considered to provide a reliable estimate of the overall effects of changing flight altitudes.

6 ACKNOWLEDGEMENTS

This study forms a contribution to the European Fifth Framework Project, TRADEOFF (EVK2-CT-1999-0030) and funding from the European Commission is gratefully acknowledged. Further financial support was given by the AERO2K project in the Fifth Framework Programme. DSL and PDN were also supported by the UK Department for Transport and the Department for Trade and Industry, SM received support from the ‘Studienstiftung des Deutschen Volkes’.

REFERENCES

- Bakan, S., M. Betancor, V. Gayler and H. Graßl, 1994: Contrail frequency over Europe from NOAA-satellite images. *Ann. Geophysicae* 12, 962-968.
- Gardner, R.M., J.K. Adams, T. Cook, L.G. Lason, R.S. Falk, E. Fleuti, W. Förtsch, M. Lecht, D.S. Lee, M.V. Leech, D.H. Lister, B. Massé, K. Morris, P.J. Newton, A. Owen, E. Parker, A. Schmitt, H. ten Have, C. Vandenberg, 1998: ANCAT/EC2 global aircraft emission inventories for 1991/1992 and 2015. Report by the ECAC/ANCAT and EC working group. DERA, Farnborough, Hants.
- Gierens, K., R. Sausen and U. Schumann, 1999: A diagnostic study of the global distribution of contrails, Part II: Future air traffic scenarios. *Theor. Appl. Climatol.* 63, 1-9.
- Grewe, V., M. Dameris, C. Fichter and D.S. Lee, 2002: Impact of aircraft NO_x emissions. Part 2: Effects of lowering the flight altitude. *Meteorol. Z.*, 11(3), 197-205.
- Land, C., M. Ponater, R. Sausen and E. Roeckner, 1999a: The ECHAM4.L39(DLR) atmosphere GCM – Technical description and model climatology. *DLR-Forschungsbericht 1999-31*, ISSN 1434-8454.
- Land, C., J. Feichter and R. Sausen, 2002: Impact of the vertical resolution on the transport of passive tracers in the ECHAM4 model. *Tellus (B)*, 54, 344-360.
- Marquart, S. and B. Mayer, 2002: Towards a reliable GCM estimation of contrail radiative forcing. *Geophys. Res. Lett.* 29(8), 1179, DOI 10.1029/2001GL014075.
- Marquart, S. M. Ponater, F. Mager and R. Sausen, 2003: Future development of contrail cover, optical depth and radiative forcing: Impacts of increasing air traffic and climate change. *J. Climate* 16, 2890-2904.
- Ponater, M., S. Marquart and R. Sausen, 2002: Contrails in a comprehensive global climate model: parameterisation and radiative forcing results. *J. Geophys. Res.* 107 (D13), 4164, DOI 10.1029/2001JD000429.
- Sausen, R., K. Gierens, M. Ponater and U. Schumann, 1998: A diagnostic study of the global distribution of contrails. Part I: Present day climate. *Theor. Appl. Climatol.* 61, 127 -141.
- Schumann U. 1996: On conditions for contrail formation from aircraft exhausts. *Meteorol. Z., N.F.*, 5, 4-23.

Policies for Mitigating Contrail Formation from Aircraft

R.B Noland*, V. Williams
Centre for Transport Studies, Imperial College London

R. Toumi
Dept of Physics, Imperial College London

Keywords: Contrails, Climate Policy, Carbon emissions

ABSTRACT: One possible approach to mitigating the production of contrails from aircraft is to place restrictions on cruise altitudes based upon ambient atmospheric conditions. This research examined the ability to restrict cruise altitudes as a policy for reducing contrail formation. A simulation model of European airspace was used to examine seasonal altitude restrictions and the effect on carbon emissions (fuel burn), travel times and air traffic controller workload. Seasonal altitude restrictions were based upon monthly average atmospheric conditions. Results showed only a small increase in carbon emissions and travel times but more severe implications for controller workload. Further analyses examined longer haul North Atlantic flights that would need more severe altitude restrictions. Potential further research and policy implications are discussed.

1 INTRODUCTION

Recent research is suggesting that the radiative forcing impact of contrail induced cirrus cloud formation may be significantly larger than the effect of carbon emissions and the effects of contrails alone (Mannstein, 2003). In addition, forecast growth in international air traffic suggests that this will be a growing problem. Given this rather bleak outlook on the climate impacts of increased air travel, this paper evaluates a potential solution that could rapidly eliminate contrail formation and the formation of associated cirrus clouds.

Specifically, we evaluate a strategy of restricting aircraft cruise altitudes such that aircraft operate under atmospheric conditions that do not result in persistent contrail formation. Contrail formation is sensitive to both ambient temperature and humidity levels in the atmosphere. These will tend to vary with altitude. In general, contrails are less likely to form at lower altitudes where temperatures are warmer, but also may be less likely to form at very high altitudes where humidity levels are low. For the most part, aircraft cruise altitudes are within a temperature and humidity band that is conducive to contrail formation.

The analysis presented here focuses on the implications of reducing aircraft cruise altitudes to avoid the super-saturated air masses that are most conducive to contrail formation. Increasing cruise altitudes may also represent a potential solution, but many uncertainties remain about the radiative impacts of water vapour emissions in the lower stratosphere. In addition, the implementation of such a policy would be restricted, as most aircraft cannot fly at the higher altitudes required. Furthermore, those capable would still need to pass through air masses where contrails would form, so the radiative impacts of contrail and associated cirrus would not be eliminated. For these reasons, we focus on the impacts of reducing cruise altitudes.

In the sections that follow, we first discuss the criteria used for selecting altitude restrictions. This is followed by an analysis of effects in European air-space, calculated using an air-space simulation model, and also calculations for longer-haul flights using estimates for specific aircraft type. Policy issues are then elaborated upon with a specific discussion of the issues associated with policy implementation. More detailed analysis can be found in Williams et al. (2002, 2003).

* *Corresponding author:* Robert B. Noland, Centre for Transport Studies, Dept of Civil and Environmental Engineering, Imperial College London, London SW7 2AZ, UK. Email: r.noland@imperial.ac.uk

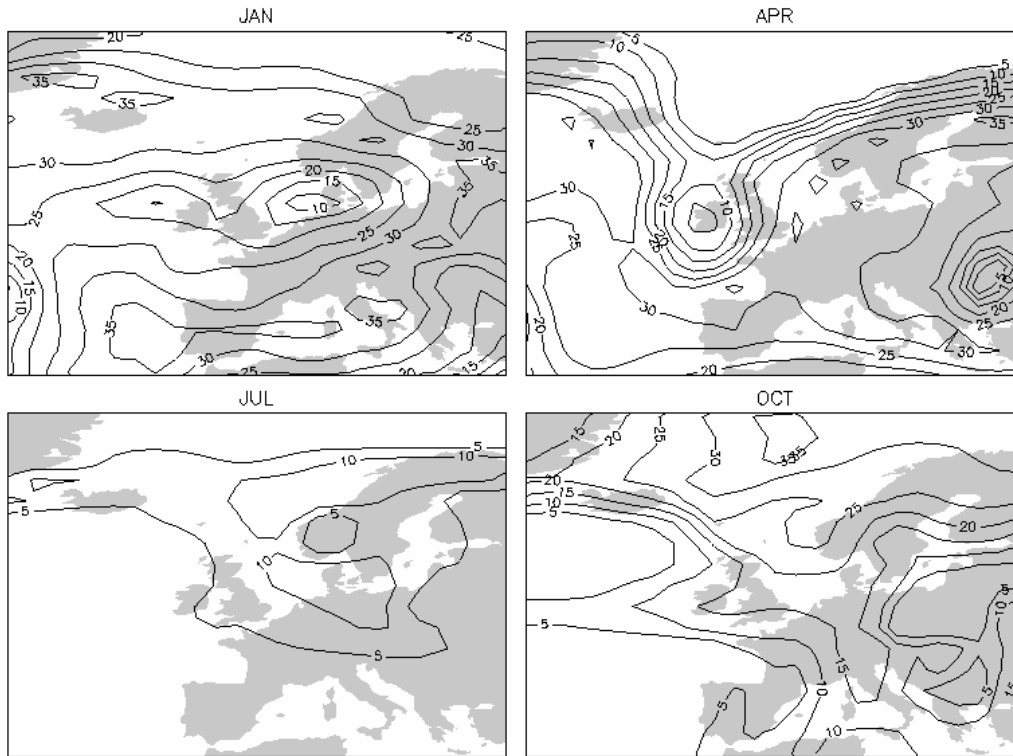


Figure 1: Potential contrail cover at an atmospheric pressure of 250mb

2 CALCULATION OF ALTITUDE RESTRICTIONS

In order to calculate the necessary altitude restrictions to minimize contrail formation it is first necessary to analyze atmospheric data to determine when and where contrails are likely to form. Calculations of the potential fractional contrail cover can be used to identify regions susceptible to contrail formation (Sausen et al. 1998). This is a measure of the maximum contrail coverage in a given area and is calculated from the mean atmospheric temperature and relative humidity over that area.

The NCEP/DOE AMIP-II Reanalysis (NCEP-II) dataset, which is a global analysis of atmospheric fields produced by assimilating land surface, ship, aircraft, satellite and other data, can be used to estimate potential contrail fraction. Using year 2000 monthly mean temperature and humidity data from NCEP-II data, on a range of atmospheric pressure levels spanning the range of flight cruise altitudes, we calculate potential contrail fraction using the method described by Sausen et al. (1998). Initially, maps of fractional cirrus cloud coverage were determined, using the parameterisation:

$$b_{Ci} = 1 - \left[\frac{1 - \max(U_i, U_{Ci})}{1 - U_{Ci}} \right]^{1/2} \quad (1)$$

where U_i is the relative humidity over ice and U_{Ci} is a threshold value (60%). Each point in the NCEP-II data represents an area of $2.5^\circ \times 2.5^\circ$. This calculation determines the fraction (b_{Ci}) of that area covered by cirrus when the mean relative humidity over ice for that area is U_i . A modification of the cirrus cloud parameterisation was then used to calculate the combined coverage of cirrus cloud and contrail, allowing the additional contribution from contrail (the potential contrail fraction) to be evaluated. The contrail effect was incorporated by replacing U_{Ci} in (2) with a critical relative humidity value derived from the Smidt Appleman relation (Sausen et al. 1998).

Figure 1 displays seasonal results for Europe for an atmospheric pressure of 250mb or around 10 km (33,000 ft) in altitude. As can be seen potential contrail coverage is significantly less prevalent during July and much greater in January. We then used this information to determine the flight level that matched only a 5% potential contrail fraction and derived a flight altitude ceiling on a monthly basis. This is shown in Figure 2 for Europe, the Northeastern US, and the North Atlantic. As can be seen, for the dataset analyzed, flight restrictions are much more severe for the latter two regions.

In all cases, one must keep in mind that the temperature and humidity data used to calculate contrail coverage is aggregated monthly mean data, on a $2.5^{\circ} \times 2.5^{\circ}$ spatial grid. Contrail coverage calculated from these monthly means may differ from the mean of contrail coverage calculated from daily or hourly data. It is likely that smaller levels of aggregation would lead to different results and that day-to-day variability may be substantial. This is important as it implies that altitude restrictions may in many cases be either more or less severe than those used in this analysis.

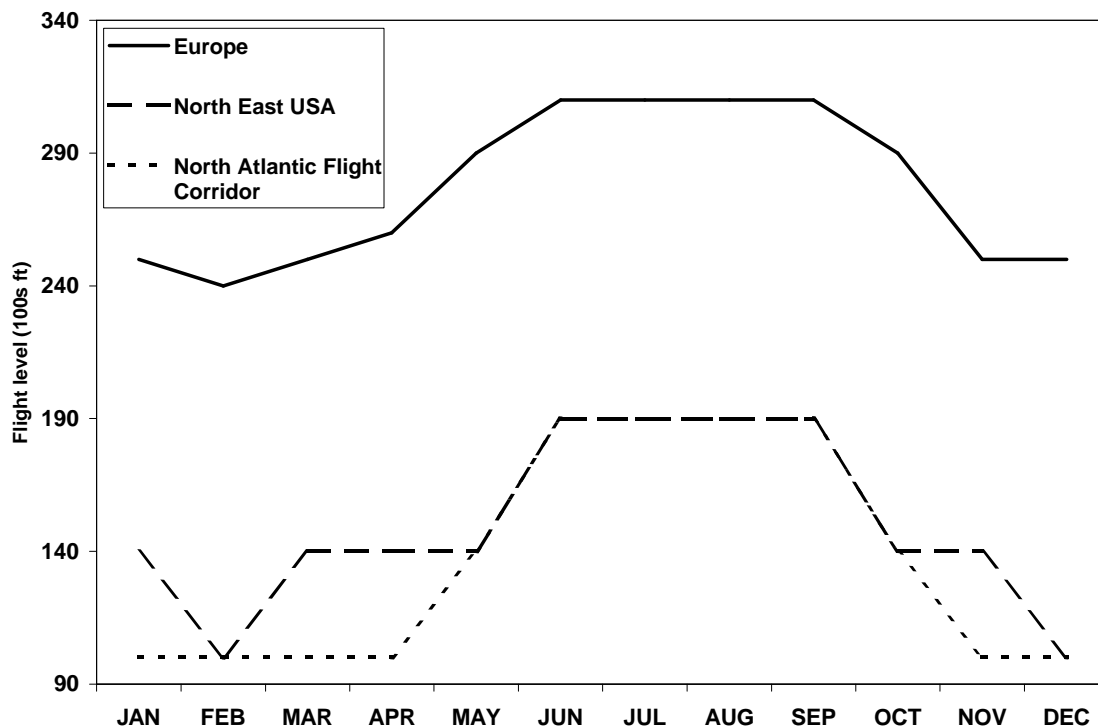


Figure 2. Seasonal variation in permitted flight levels for sectors of Europe, the Northeast USA, and the North Atlantic.

3 ANALYSIS OF IMPACTS

The impacts of restricting cruise altitudes were estimated using an airspace simulation model for European airspace and evaluation of aircraft performance data for longer haul flights. The simulation model used (the RAMS model) is widely used for management and planning of air traffic controller workloads. It provides a realistic simulation of the tasks initiated by air traffic controllers managing air traffic under congested conditions. An extended description of the model is provided in Williams et al. (2002).

This model was used to assess the impact of the altitude restrictions on fuel burn (i.e., carbon emissions), travel times, and controller workload. Fuel burn was calculated using Eurocontrol Experimental Centre base of aircraft data (BADA). Flight speed and rates of climb and descent were also specified using BADA performance tables. Over 71 aircraft types were included in the simulation which covered one day of air traffic on September 12, 1997. The region analyzed

covered the “5-states” region of Europe, shown in Figure 3, which also shows the boundaries of the air traffic control sectors within the simulation.

To assess impacts on long-haul flights, we used BADA data to examine changes in fuel burn and travel time for various aircraft types and distances ranging from 3000 to 6000 nautical miles. Given the more severe altitude restrictions calculated for trans-Atlantic and Northeastern US (see Figure 2), we opted to evaluate these trade-offs at altitudes of 18,000 and 31,000 feet. These calculations are intended to be indicative of the scale of impacts associated with a contrail restriction policy on long haul flights, in contrast to the more detailed analysis presented for European airspace.

For both the European airspace and the long haul analysis, altitude restrictions are enforced for the duration of the flight. This may lead to an overestimation of impacts, particularly for the longest flights, which would be likely to pass through regions requiring less stringent restrictions.

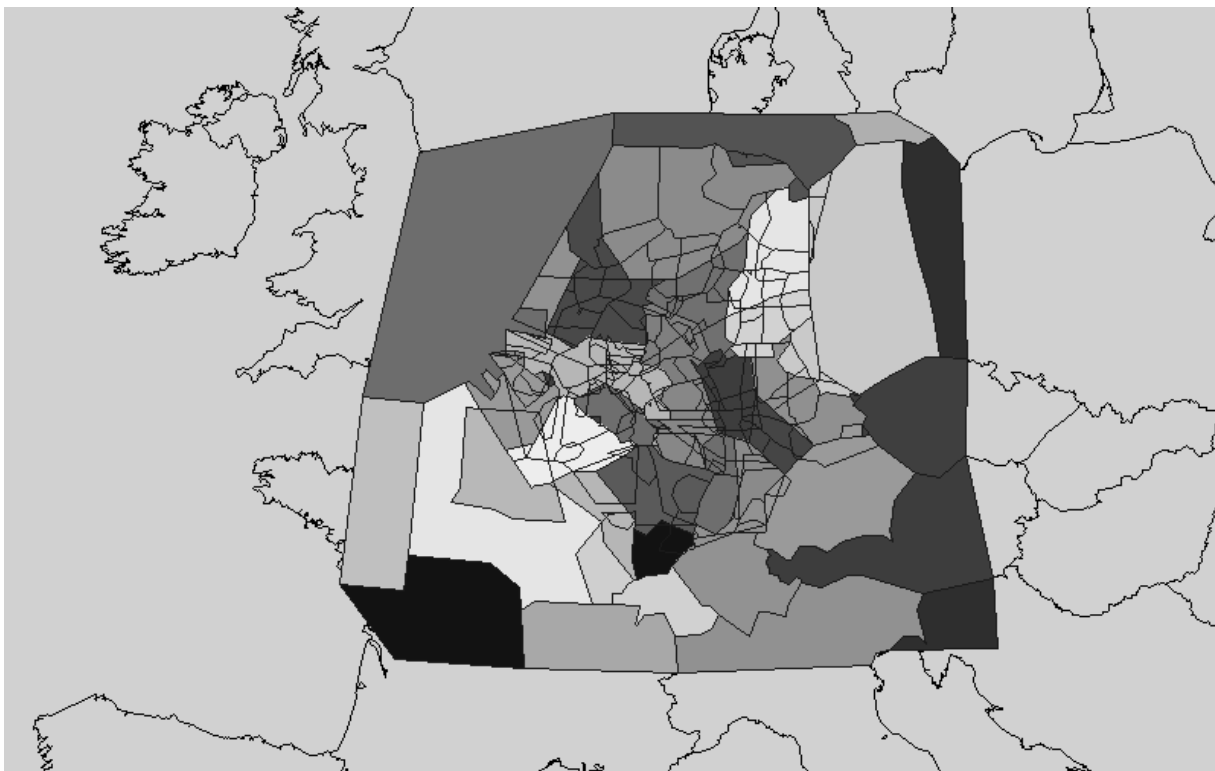


Figure 3. Coverage of the RAMS 5-states simulation. Air traffic control sector boundaries are marked.

3.1 Fuel burn (carbon emission) impacts

The impacts on fuel burn (i.e., carbon emissions) for the European simulations are detailed in Table 1. The total increase is only 3.9% over the unrestricted simulation. Given that this type of policy would virtually eliminate contrail formation (and associated cirrus clouds), the reduction in radiative forcing would not be off-set by the increase in carbon emissions.

Table 1. Change in fuel burn for European simulation.

Maximum flight level (in 100s of feet)	Months	% Change in fuel burn (compared to control simulation)
240	February	7.2
250	January, March, November, December	5.8
260	April	5.3
290	May, October	2.7
310	June, July, August, September	1.6
AVERAGE OVER YEAR		3.9

For long haul flights, estimated fuel burn is larger. With an altitude restriction of 18,000 feet this ranged from an increase of 20% for an Airbus 310 aircraft to as high as 60% for a Boeing 747-400. With a 31,000 feet altitude restriction, the increase ranged from about an 8% to 30% more fuel burn. Clearly a 60% increase in fuel burn may be less desirable, but even that may give a net reduction in radiative forcing, although this depends upon better knowledge of how to compare contrail and cirrus effects, which may only last a few hours, versus the many decades that carbon may remain in the atmosphere. The selection of aircraft is also critical and if this sort of policy were implemented, it is unlikely that those aircraft that suffer a large increase in fuel burn would still be flown under these conditions.

3.2 Travel time impacts

Travel time effects for the European simulation were found to be trivial. On average, travel times increase by less than one minute. The largest increase was about 17 minutes for one flight normally traversing the airspace at high altitude. The reason for this is that most of the flights within this sector are relatively short in duration and do not normally climb to high altitudes. Thus, the impacts of the altitude restrictions are relatively minor.

This is not the case for longer-haul flights. Again, travel time impacts were found to vary with the type of aircraft. For a distance of 6000 nm and an altitude of 18,000 ft, the Boeing 777-200 had an increased flight time of about 210 minutes. This is compared to the Boeing 747-200 with an increased flight time of only about 45 minutes. At an altitude restriction of 31,000 ft, some aircraft actually had about a 30 minute reduction in their flight time (due to less time spent in climb and descent modes).

These travel time increases may create some operational difficulties related to crew scheduling and even the feasible range of some flights. However, these differences are aircraft dependent and future design of aircraft could focus on optimising flight times at lower cruise altitudes, if this type of policy is desirable. In many cases, travel time increases of 30-60 minutes would probably be feasible.

3.3 Controller workload effects in European airspace

Previous studies have defined 'severe' controller workload in order to assess restrictions on airspace capacity. The definitions most commonly adopted are a total controller task time at or above 42 minutes (70%) in any one-hour period, or above 90 minutes (50%) in any three-hour period. These definitions of controller capacity are used to allow for controller actions such as the prioritisation of tasks, which are not directly specified in the controller task times.

Adopting the three-hour definition, the European simulations indicate that the imposition of cruise altitude restrictions would result in a dramatic increase in the number of sectors exceeding the threshold for capacity. In the control simulation, 7 sectors have a workload exceeding 50%. For the most restricted case, with maximum cruise altitudes constrained to 24,000ft, the total number of sectors in which the threshold is exceeded is 31.

Table 2: Number of conflicts for each air traffic control center, by altitude restriction

Air Traffic Control Center	Maximum permitted cruise altitude (100s feet)					Control simulation
	240	250	260	290	310	
AMSTERDAM	974	222	222	226	216	207
BREMEN	1353	133	137	138	144	137
CANAC	2108	305	307	304	299	310
DUSSELDORF	623	256	256	256	260	252
FRANKFURT	6071	606	626	586	583	587
KARLSRUHE	770	5407	5179	3883	3011	856
LUXEMBOURG	9	10	8	7	8	9
MAASTRICHT	0	4048	3828	2662	2176	902
PARIS	911	60	60	59	62	61
REIMS	510	1456	1390	1090	954	443
Total	13329	12503	12013	9211	7713	3764

An indication of the likely implications of the flight altitude restrictions on workload in each air traffic control centre can be obtained by considering the number of conflict events. At each triggered event in the model, such as a controller window entry, flight path trajectories within the controller window are compared to ensure that the required separation minima between aircraft are maintained. A violation of separation conditions is identified as a conflict and triggers the controller tasks necessary to determine a suitable resolution manoeuvre, such as a change in altitude for one of the aircraft in conflict. Each proposed resolution is checked against existing flight trajectories to avoid further separation violations. The total number of conflicts is found to increase with the severity of the altitude restriction applied, with the most restricted simulation having 3.5 times the conflicts as the unrestricted control simulation. The detail for each air traffic control center is shown in Table 2.

These effects on air traffic controller workload could be an impediment to implementation of an altitude restriction policy. However, this is primarily a function of the current design of air traffic control sectors, which are not optimised for the cruise altitudes which were simulated. For example, some high altitude sectors had no aircraft movements, while lower altitude sectors had a major increase in their traffic. Redesign of the existing air traffic control sectors could alleviate this problem.

4 CONCLUSIONS

This paper summarizes analysis previously presented in Williams et al. (2002, 2003). Results suggest that a policy of restricting aircraft cruise altitudes to levels where contrail formation does not occur, could be beneficial in reducing net radiative forcing. This is based upon average atmospheric conditions and disregards potential day-to-day variability in atmospheric conditions.

This suggests that a more attractive policy would be to require aircraft to avoid atmospheric air masses that are amenable to contrail formation by real-time flight planning. This would have the added benefit of minimizing the relatively small increases in carbon emissions in that selection of flight altitudes would not always require severe altitude restrictions, such as we examined for longer-haul flights.

Implementation issues are more problematic. Changes in flight journey times, while introducing various operational changes, are probably feasible. The key factor would be to select aircraft that both minimize journey time and fuel burn at the altitude that minimizes contrail production. Of more concern is the effect on existing air traffic control sectors. However, redesigning existing sectors to minimize climate impacts can probably alleviate this.

Further research in this area needs to explicitly examine the day-to-day variability in flight planning that would be necessary. The operational and cost impacts of this should also be evaluated (however, we imagine the cost to the airline industry would be significantly less than equalization of fuel taxes between transport modes). Finally, research needs to examine the best ways to redesign air traffic control sectors with the goal of minimizing environmental and climate impacts.

REFERENCES

- Mannstein, H., 2003, Observations of contrails and cirrus over Europe, Proceedings of the European Conference on Aviation, Atmosphere, and Climate.
- Sausen, R., K. Gierens, M. Ponater and U. Schumann, 1998: A Diagnostic Study of the Global Distribution of Contrails Part I: Present Day Climate, *Theoretical and Applied Climatology*, 61, 127-141.
- Williams, Victoria, Robert B. Noland, and Ralf Toumi, "Reducing the Climate Change Impacts of Aviation by Restricting Cruise Altitudes", *Transportation Research D*, 7(6), (2002): 451-464.
- Williams, Victoria, Robert B. Noland, and Ralf Toumi, 2003, "Air Transport Cruise Altitude Restrictions to Minimize Contrail Formation", *Climate Policy*, 3(3).

Greener by Design

J.E.Green*

Aircraft Research Association Ltd., Bedford, United Kingdom

Keywords: climate change, environmental impact of aviation, aircraft design, aircraft operations, aircraft emissions

ABSTRACT: Air Travel – Greener by Design is an initiative of the UK civil aviation community, embracing the aircraft and engine manufacturing industry, the airline and airport operators, the research community and government departments. Its primary objective is to identify and promote options for reducing the environmental impact of air travel. This paper considers what might be achieved within the next 50 years by advances in aircraft and engine technology and by a shift in design priority from minimising costs to minimising environmental impact. The emphasis of the paper is on climate change and it is suggested that, in the medium term, a substantial reduction in climate impact per passenger kilometre is potentially achievable. Present understanding of the effects of aviation on the atmosphere is, however, not yet sufficiently robust for this to be asserted with confidence. Atmospheric research, focussing on those effects of aviation which it may be possible to mitigate by design and operational changes, therefore remains a high environmental priority.

1 INTRODUCTION

In the coming century, the impact of air travel on the environment will become an increasingly powerful influence on aircraft design. Unless the impact per passenger kilometre can be reduced substantially relative to today's levels, environmental factors will increasingly limit the expansion of air travel and the social benefit that it brings. In the UK, the Air Travel - Greener by Design initiative is the response of the civil aviation community to this environmental challenge. Its participants are the main stakeholders in air travel - the aircraft and engine manufacturers, airline and airport operators, the research community and the appropriate government departments - and its primary objective is to assess and promote options for mitigating the environmental impact of aviation. More widely within Europe, the aeronautical research community has established the Advisory Council for Aeronautical Research in Europe (ACARE) and has set out a Strategic Research Agenda (ACARE, 2002) which gives high priority to, and sets ambitious goals for, reducing environmental impact.

Air Travel - Greener by Design established three sub-groups to study operations, technology and market-based options. This paper arises from the work of the Technology Sub-Group, of which the author is Chairman. The Sub-Group addressed the potential of technology and design to mitigate noise and air pollution around airports and to reduce the impact of air travel on climate change. It took 2050 as its time horizon, by when a fourfold increase in air traffic has been projected. The Sub-Group presented its first report in July 2001 and this was subsequently published in the open literature (Green, 2002). A later paper (Green, 2003) takes the discussion a stage further. The present paper draws on both these sources, focussing mainly on impact on climate change.

The paper considers briefly the potential role of regulation and economic instruments to mitigate environmental impact and the conflicts and trade-offs that arise, not only between commercial and environmental goals but also between different environmental goals. It then considers the main contributors to climate change, the challenges to technology that these present and the scope for reducing their impact by design and operational changes with today's technology standards. Finally, some conclusions are drawn and recommendations made for future research.

* *Corresponding author:* J.E.Green, Aircraft Research Association Ltd, Manton Lane, Bedford, MK41 7PF, United Kingdom. Email: greens@woburnhc.freeserve.co.uk

2 REGULATION AND TRADE-OFFS

Aircraft noise and emissions in the vicinity of airports are subject to international regulation under ICAO. The regulations are established by international consensus and historically have followed rather than led the reductions in noise and emissions achieved over the past 30 years. For both noise and emissions, ICAO has adopted more stringent standards only when they have been shown to be economically achievable. Nevertheless, the technical measures needed to achieve the standards have entailed weight and performance penalties and the work to develop and validate them has added to aircraft first costs. Since the 1970s, therefore, noise and emission reductions have imposed some economic penalty on all new civil aircraft.

In parallel with international regulation, local variants have emerged which override the ICAO rules. An example is the system of noise quota counts imposed by the UK Government for night-time operations from the three London airports. In response to this, the customers for the Airbus A380 have required the aircraft to meet approximately the same noise certification standards as the A340, an aircraft half the size. This demanding target has resulted in an engine of larger than optimum diameter and a consequent fuel burn penalty of the order of 1% to 2%, depending on range.

Concern about the impact of aviation on climate change is a relatively new phenomenon, lagging more than a decade behind concern about emissions in the vicinity of airports and two decades behind concern about noise. The Kyoto Protocol of 1997, which committed signatories to cutting greenhouse gas emissions by 12.5% of 1990 levels by 2012, explicitly excluded international aviation but, even so, the contribution of aviation to climate change has become increasingly prominent in the public eye. While there is as yet no ICAO regulation in this field, the subject is being considered by the ICAO Committee on Aviation Environmental Protection (CAEP). Other bodies, notably the European Union and the UK Government, are also considering possible financial incentives in the form, for example, of a tax or levy on aviation fuel

In a recent consultation paper, issued jointly by the UK Department of Transport and the Treasury (Department for Transport, 2003), estimates were given of the annual external costs of the environmental impact of UK civil aviation, as follows:

Noise	£25m
Local air quality	£119m - £236m
Climate change	£1,400m

The origins of these figures are set out in the reference. It is interesting to note that, although the external cost of air pollution around airports is estimated to be some five to ten times the cost of noise, complaints from the public about aircraft noise vastly exceed complaints about the effect of aircraft on air quality. The key point about these figures is that they lead to the conclusion in the paper that, "Aviation's principal externality, which can be translated into monetary terms, arises from the effects of greenhouse gases and the impact they have on climate change." This was also the view of the Technology Sub-Group and is the underlying theme of this paper.

There are, however, conflicts and trade-offs between commercial and environmental goals which complicate the picture. For example, the requirement cited above that the Airbus A380 should meet particular night time noise quota count levels entailed an increase in fuel burn which will increase not only operating costs but also CO₂ emissions. A more powerful conflict arises in engine design, where measures to increase engine thermal efficiency in order to reduce fuel burn and CO₂ emission result in increased NO_x emissions. Because NO_x emissions impact not only on air quality around airports but also on climate change, the trade off between NO_x and CO₂ emissions raises questions which have not yet been considered by the engine designer, whose focus is on commercial optimisation of the engine. A further example of conflict is raised by the possibility of reducing aircraft cruise altitude in order to reduce the risk of generating contrails, which have a powerful greenhouse effect, but thereby increasing fuel burn, operating costs and CO₂ emissions. These various conflicts have an important bearing on the technological and design compromises needed to achieve an appropriate balance between environmental and commercial goals. They also have a bearing on the form of regulation and economic instruments best suited to minimising environmental impact. In particular, they lead to the conclusion that measures such as levies on fuel, designed solely to reduce CO₂ emissions, are unlikely to achieve the best environmental outcome.

3 CONTRIBUTION OF AVIATION TO CLIMATE CHANGE

The various emissions from aircraft flying at altitude contribute to climate change through a range of different chemical and physical processes. Until the new evidence now emerging (some of which has been presented at the AAC Conference) has been fully assessed, the best available quantification of the effects of these processes is generally accepted to be that presented in "Aviation and the Global Atmosphere" (IPCC, 1999). For 1992, the IPCC estimate of the percentage contributions to the total radiative forcing due to aviation, rounded to the nearest 0.5%, and the assessed quality of the estimates of the individual components, are:

Contributor	percentage	quality of estimate
Carbon dioxide	+ 37.0	good
Ozone	+ 47.5	fair
Methane	- 29.0	poor
Water	+ 3.0	poor
Contrails	+ 41.5	fair
Cirrus cloud	not estimated	very poor
Sulphate aerosols	- 6.0	fair
Black carbon aerosols	+ 6.0	fair

The increase in ozone and decrease in methane are both the result of NO_x emission, the net effect of which is to contribute positively to radiative forcing. It is argued, however, that the two effects cannot be simply added to give a net contribution to radiative forcing. Because methane is a long-lived gas whilst ozone, and the NO_x which generates ozone and destroys methane, are short lived, the negative greenhouse effect of the methane destruction tends to be distributed globally whilst the effect of the ozone creation is localised around the main flight corridors and may thus have a greater effect on climate than represented by the overall impact on radiative forcing given in the table.

In 1999, the uncertainty about cirrus cloud generated by aircraft was considered too great to justify the inclusion of an estimate of the effect of aviation-induced cirrus cloud in the total estimate of radiative forcing. The uncertainty range in 1999 did, however, put the effect between 0% and 80% of the total forcing from all other sources, suggesting that it might well be a significant contributor, coupled to contrails. In this conference, Mannstein has presented evidence that the combined effect of persistent contrails and the cirrus cloud which develops from them may well constitute the greatest single contribution of aviation to climate change.

On the basis of the above table, three main contributors of aviation to climate change can be identified.

They are CO₂, NO_x and persistent contrails with their consequent cirrus. In the following sections we consider what might be done, by technological advance and changes in design and operation, to reduce the impact of these three. It will be argued that, in the medium term, reducing the impact of contrails and NO_x offers the greatest potential. Before doing so, however, it is appropriate to consider the lives in the atmosphere of the main greenhouse gases as shown in the following table (Rogers et al., 2002).

Carbon dioxide	50 - 100 years
Methane	8 - 10 years
Water	days (sea level) weeks (tropopause)
Ozone	week (sea level) months (tropopause)
NO _x	days (sea level) weeks (tropopause)

The conclusion to draw from this table is that, even if in the short and medium term contrails and NO_x are potentially the more rewarding targets, in the long term action to reduce CO₂ emissions is also essential. Although this is the most challenging of the three targets, the work of the Greener by Design Technology Sub-Group identified technologies by which substantial reductions in CO₂ emissions could be achieved, provided radical changes to aircraft design concepts are adopted.

4 CHALLENGES TO DESIGN AND TECHNOLOGY

In this section the three main contributors are considered in turn. Measures to reduce each, by changes in operating procedures, design and technological advance are discussed and the implications, if any, for the other contributors is noted.

4.1 *Reducing persistent contrails and cirrus cloud*

The atmospheric conditions under which contrails form are reasonably well understood (Lee et al., 2000), as are the conditions under which they quickly evaporate again. In order for contrails to persist and, with time, be distorted and dispersed by wind shear to form cirrus cloud, the air within the contrail, when the engine exhaust is extensively mixed with the ambient air, must be saturated or supersaturated with respect to ice. However, because an engine adds heat as well as water vapour to the air mass, the critical conditions of temperature and humidity for a contrail to persist depend on the propulsive efficiency of the engine. As engines have become more efficient, mean exhaust temperatures have fallen and the temperature-humidity boundary for the creation of a long lived contrail has moved upwards, so that contrails are found in warmer air today than in the 1970s.

Lee et al. observe that there is no current or envisaged technology that will inhibit the formation and persistence of contrails. If a kerosene-fuelled aircraft flies through an ice-saturated air mass, contrails will form and persist. That said, ice saturation tends to occur in defined volumes of cold, relatively humid air which have been characterised as “moist lenses” (Gierens et al., 1997). These have a maximum vertical extent of a few kilometres and a maximum horizontal extent of about 1,000km, the precise extent for a particular air mass depending on engine propulsive efficiency. As Lee et al. note, an individual lens could be avoided by flying under it, over it or around it.

Since aircraft generally fly at their most economical altitude, taking evasive action by flying higher or lower than optimum, or by making a detour to avoid saturated air, will increase fuel burn, cost and CO₂ emission. On the other hand, in addition to reducing contrail formation, flying lower might also reduce the impact on climate of NO_x emissions (Klug et al., 1996). Overall, the environmental benefit of avoiding contrails, particularly if coupled with a reduction in the impact of NO_x, seems likely to outweigh by a considerable margin the effect of increased CO₂ emission.

It would be premature to recommend evasive action as an operational procedure at this stage. The basic scientific understanding is not sufficiently robust. Neither air traffic management nor meteorological forecasting are currently well placed to support such a procedure. The possible impact of changes in flight altitude on the impact of NO_x emissions is not well understood. Evasive action would increase fuel burn, CO₂ emission and airline costs. Nevertheless, the recent evidence on cirrus presented at the AAC Conference by Mannstein suggests that a strategy of contrail avoidance could be a powerful way of reducing the impact of air travel on climate change, even though it would entail a small increase in CO₂ emissions. The possibilities of such a strategy merit more detailed investigation.

4.2 *Reducing the impact of NO_x*

NO_x emissions in the vicinity of the airport are already the subject of regulations drawn up by the ICAO Committee on Aviation Environmental Protection (CAEP). These regulations make allowance for the fact that, as engine overall pressure ratio is increased in order to achieve higher thermal efficiency and hence reduced fuel burn and CO₂ emission, the increased temperatures and pressures in the combustor lead to increased NO_x production. For example, the regulation currently in effect, CAEP-2, allows NO_x emission to increase by about one third for an increase in engine pressure ratio from 25 to 40. The best in-service combustor technology gives NO_x emissions appreciably below the CAEP-2 line but show a rather steeper variation with pressure ratio. Between these two pressure ratios, actual NO_x emissions for this class of combustor increase by a factor of 2.25. The corresponding increase in thermal efficiency gives a reduction in fuel burn of slightly less than 9%.

There are substantial research programmes in Europe and the United States aimed at low NO_x combustor technology. Although these are currently aimed at emissions in the vicinity of airports, any advances which reduce emissions here should also produce some reductions in emissions at cruise. Ambitious targets have been set for this research but the evidence to date suggests that

success is more likely at the medium pressure ratios of small engines than at the high pressure ratios of the large engines typical of long-range aircraft.

Besides the pursuit of more advanced combustor technology, the avenue of reducing NO_x emission by reducing engine pressure ratio is worth exploring. In the report of the Greener by Design Technology Sub-Group (Green, 2002), one recommendation was that a study should be made of the methodology of designing engines to minimise impact on climate rather than minimising fuel burn. This recommendation was taken up as part of a study of propulsion system optimisation (Whellens and Singh, 2002). The starting point was a baseline engine typical of a large, long-range aircraft, optimised for minimum fuel burn at cruise. An engine with the same thrust at cruise but optimised for minimum impact on climate had a substantially lower overall pressure ratio (11.5 as against 44 for the baseline engine) and lower turbine inlet temperature (1.300K as against 1,555K). The resulting impact on climate was estimated to be 46% lower than that of the baseline engine, but at an unacceptable fuel burn penalty of 21%. However, for a fuel burn penalty of only 5%, the estimated reduction in impact on climate was still between 30% and 40%.

This work employed a model of the effect of NO_x emissions on climate (Klug et al., 1996) which employed Global Warming Potential (GWP) as a metric for impact on climate. This metric is not now favoured by the atmospheric science community. The modelling by Klug et al. of the variation with altitude of the effect of NO_x also makes use of GWP and is therefore subject to the same reservations. Nevertheless, the trends found by Whellens and Singh are clearly qualitatively correct and the variation with altitude of the effects of NO_x, at altitudes around the tropopause, are also likely to be qualitatively similar to those derived by Klug et al. Clearly, advances in atmospheric science are needed to provide a more solid basis for assessing the environmental effects of NO_x and particularly their variation with altitude. Future aircraft and engine design could be significantly influenced by this knowledge.

4.3 Reducing CO₂ emissions

Reducing CO₂ emission equates exactly to reducing fuel burn. The appropriate cost/benefit metric is fuel burn per passenger kilometre. From a derivative of the well known Breguet range equation (Green, 2002), an expression for this metric can be written

$$W_{MF}/RW_P = (1 + W_E/W_P)(1.022\exp(R/X) - 1)/R \quad (1)$$

where W_{MF} is the mission fuel burned between engine start up and shut down, W_P is the payload, W_E the empty weight, R the range and X a range performance parameter defined by

$$X = H\eta L/D \quad (2)$$

where H is the calorific value of the fuel, η is the overall propulsion efficiency of the engine and L/D is the lift-to-drag ratio of the aircraft at cruise. It is usual to express H in Joules/kg but, since this has the dimension length, H can also be expressed in km. Then, since η and L/D are dimensionless, X can be expressed in km. For a kerosene-fuelled medium or long-range aircraft swept-winged aircraft with currently achievable values of η and L/D , X is approximately 30,000 km.

If aircraft range and payload are specified, Equation 1 shows that the only ways of reducing fuel burn per passenger kilometre are to reduce the ratio of empty weight to payload and to increase the value of the range parameter X . For kerosene-fuelled aircraft H is effectively fixed, leaving propulsion efficiency η and lift to drag ratio L/D as the only two variables which can be increased to increase X . The potential for reducing fuel burn by reducing empty weight and increasing propulsion and aerodynamic efficiency are now discussed in turn.

4.3.1 Reducing CO₂ by reducing empty weight

There is scope for reducing aircraft empty weight through the greater use of lightweight materials. In general this entails a cost penalty and the uptake of materials such as carbon fibre reinforced plastic (CFRP) has consequently turned out to be rather less than was forecast in the 1980s. For example, on the Airbus A330 and the Boeing 777, CFRP accounts for some 15% of the structure weight, as compared with "conservative" and "optimistic" forecasts of 25% and 65% respectively made in the mid 1980s (Peel, 1996). Cost will continue to be an inhibiting factor but the proportion

of civil aircraft structure made from specialised lightweight materials can be expected to increase over the coming years.

The potential for reducing weight by more efficient structural design must be limited for aircraft of the classical swept wing configuration, which has been evolving for more than 50 years. New manufacturing technology may lead to some weight saving, however, and a new configuration, such as a blended wing-body, would also have lower structural weight. Other potential developments, such as the More Electric Aircraft, should also yield weight reductions. Taking all potential advances together, the Greener by Design Technology Sub-Group (Green, 2002) projected a reduction of 15% in the empty weight of a classical swept-winged aircraft design by 2050. This would reduce the first term on the right-hand side of Equation 1, and hence fuel burn per passenger kilometre, by approximately 10%.

This term in Equation 1 can also be influenced by design parameters such as cruise Mach number and design range. Reducing cruise Mach number enables wing sweep to be reduced and/or wing thickness to be increased, thereby enabling wing weight to be reduced. Although today's aircraft are designed to be close to minimum fuel burn, it is probable that some reduction in fuel burn could be achieved by designing for a lower cruise Mach number. Whilst cruise Mach number has a relatively weak effect, this is not the case for design range. A comparison between two paper swept-winged aircraft designed to carry the same payload over ranges of 5,000km and 15,000km (Green, 2002) suggests that the empty weight of the long range aircraft is more than 40% greater than that of a medium range aircraft designed to carry the same payload. As a result, the first term on the right-hand side of Equation 1 is 22% smaller for the medium-range aircraft than for its long-range equivalent. The fuel benefit of the weight reduction associated with the change from a long-range to a medium-range design is approximately twice the benefit from the weight reduction that might be achieved by 50 years of technological advance.

4.3.2 Reducing CO₂ by increasing overall propulsion efficiency

Overall propulsion efficiency can be written

$$\eta = \eta_E \eta_P \quad (3)$$

where η_E is the thermal efficiency of the gas turbine and η_P is the propulsive efficiency of the jet. For the classical Joule or Brayton cycle for gas turbines, thermal efficiency η_E can be increased by further improvements in the aerodynamic efficiency of the compressor and turbine and by increasing the thermal efficiency of the basic cycle. The latter requires increasing both the engine overall pressure ratio and turbine entry temperature and hence, for a given standard of combustor technology, increasing NO_x emission. Although this route of increasing pressure and temperature is the one which engine design has been following for the past 50 years, for reasons set out more fully elsewhere (Green, 2002 and 2003) it is thought environmentally not to be an appropriate way forward.

The second component η_P in Equation 3 is the propulsive efficiency of the jet, sometimes known as the Froude efficiency. For the engine in isolation, η_P reduces monotonically as the specific thrust (net thrust divided by total air mass flow through the engine) is reduced or bypass ratio increased. However, it is found (Birch, 2000) that, because engine weight and nacelle drag increase as engine diameter is increased to reduce specific thrust, today's large engines are close to the economic optimum in terms of fuel burn, weight and operating costs. Further reduction in specific thrust increases Froude efficiency but, because of its side effects, also increases fuel burn. Consequently, if further increases in engine pressure ratio and turbine entry temperature are resisted for environmental reasons, there seems to be little prospect of a significant increase in the overall propulsion efficiency of conventional turbofan engines above the best of today's levels.

In the Greener by Design studies, two alternatives to the conventional turbofan were considered (Green, 2002). The first was the inter-cooled recuperative (ICR) turbofan engine cycle, in which the compressor flow is cooled part-way through compression by heat exchange with the fan stream and then heated at the end of compression by heat exchange with the turbine exhaust (Plohr et al., 1999). At the expense of considerably increased weight and complexity, the cycle is predicted to yield a

higher thermal efficiency and potentially lower NO_x emission than a conventional turbofan of the same thrust. The components of the ICR engine are the subject of an EU technology programme. The second alternative to the turbofan was the advanced contra-rotating propeller or unducted fan system. This has an appreciably lower specific thrust than today's turbofans but avoids the fan-cowl weight and drag penalties of the turbofan. It was extensively studied in the late 1980s and shown to be a practicable system for aircraft with cruise Mach numbers up to approximately 0.8. Concerns about first cost, maintenance, noise and safety, combined with the relatively low cost of fuel and hence low savings in direct operating costs, led to it being shelved. As a candidate for future aircraft, it is not suitable for installation on low wings and would be limited to rear-engined, high winged or possibly flying wing configurations. It remains nevertheless one of the few identifiable technologies which could achieve a significant reduction in fuel burn for all classes of aircraft where a limitation of cruise Mach number to around 0.8 is acceptable.

4.3.3 Reducing CO₂ by reducing drag

In Equation 2, with H effectively constant, the second variable which influences fuel burn per passenger kilometre is L/D, the lift-to-drag ratio. Since in 1g flight lift is equal to aircraft weight, the technological challenge is to reduce aircraft drag for a given weight of aircraft. For the classical swept-winged aircraft with underslung turbofan engines, this is a stern challenge. The first aircraft of this configuration was the Boeing B-47 Stratojet, which first flew in 1947. After more than 50 years of development, this configuration is now highly refined aerodynamically and the scope for further improvement is small. To achieve a significant reduction in drag and fuel burn, some more or less radical departure from the classical aircraft is needed.

The Greener by Design technology report (Green, 2002) presented the results of a study of a set of 13 different aircraft, ranging from a long-range kerosene-fuelled swept-winged aircraft typical of today's large aircraft to a hydrogen-fuelled flying wing with all-over laminar flow control and unducted fan propulsion. To illustrate the effects of introducing new technology, the projected reduction in fuel burn per passenger kilometre is shown below for a more limited set of aircraft. The baseline is a classical swept-winged aircraft with a design range of 5,000km. The first variant is a similar aircraft with hybrid laminar flow control (HLFC) applied to the wing, empennage and nacelles by suction through fine holes in the surface over the forward parts of the treated components. Next is the widely discussed blended wing-body, without laminar flow control. Third is a flying wing, based on a design study by Handley-Page in the 1960s (Lachmann, 1961), which achieves all-over laminar flow by the all-over application of surface suction. All four of the above aircraft have turbofan engines. The fifth variant is the laminar flying wing with unducted fan propulsion.

configuration	design range km	%fuel burn reduction
swept wing, medium range	5,000	-
swept wing, medium range with HLFC	5,000	16.5
blended wing-body	6,000	19.6
laminar flying wing	9,000	51.5
laminar flying wing with unducted fan	9,000	57.2

The reductions in this table for the two medium term technologies, hybrid laminar flow control and the blended wing-body, are greater than any advances that might be expected in the medium term from either weight reduction through wider use of lightweight materials or improvements in propulsion efficiency, including the introduction of unducted fan propulsion. Beyond that, the all laminar flow flying wing offers a really substantial reduction in fuel burn. Drag reduction appears to be by far the most potent technology available for reducing CO₂ emission by civil aircraft.

4.3.4 The significance of range

In the preceding discussion of Equation 1, the effect has been considered of varying empty weight and the range performance parameter X with payload and range R held fixed. As is evident from the equation, however, range has a strong influence on fuel burn per passenger kilometre. For swept-winged aircraft of today's technology standard, it is found (Green, 2002) that the most fuel efficient

design range is about 4,000km: aircraft with a design range of 15,000km are appreciably less fuel efficient. This observation led to the thought that it might be more fuel efficient to undertake long-range journeys in a series of stages of around 4,000km rather than in a single stage. To illustrate the point, the table below compares the aircraft and fuel burn needed to carry a given payload over a distance of 15,000km in a single stage in a long range aircraft and in three stages of 5,000km in a medium range aircraft.

design range [km]	payload [tonne]	stage fuel [tonne]	take-off weight [tonne]	empty weight [tonne]	total fuel [tonne]
15,000	44.8	120.4	300.0	134.8	120.4
5,000	44.8	28.6	169.0	95.6	85.8

The aircraft needed to make the journey in a single stage has an empty weight some 40% greater than the medium-range aircraft and requires 40% more fuel to complete its task. Its take off weight is nearly 80% greater and its noise levels will be correspondingly higher. Its capital and running costs will also be higher. The Greener by Design technology report recommended that a full system study should be made of undertaking long distance travel in a series of shorter stages. A maximum stage length of 7,500km was suggested.

Although the Greener by Design study focussed primarily on medium and long range aircraft, it is important not to lose sight of the fact that more than half the aviation fuel burned is on flights over less than 3,000km, much of it in smaller aircraft for which the more radical flying wing configurations are not credible candidates. The future potential for reducing fuel burn over the shorter ranges is not very great. The introduction of hybrid laminar flow control, unducted fan propulsion and structural weight reduction are the three most promising technologies for this class of aircraft. In addition, reducing NO_x and contrails are important objectives for short and medium range travel, just they are for the longer ranges.

4.4 Design and operational questions

Although the preceding sections have focussed on the potential for reducing impact on climate through technological advance, it appears that the potential for reducing this impact by changes in design philosophy and in operational procedures is no less important. Some key questions are:

- Can contrail formation be reduced by adjusting flight paths to avoid regions of ice-saturated air, what is needed by way of meteorological information and air traffic management systems to achieve this, what would be the net effect on climate change, allowing for the consequent increase in CO₂ emission, and what would be the economic cost to the airlines?
- Within reasonable commercial limits, what is the potential for reducing overall impact on climate by designing engines which have lower overall pressure ratio and consequently lower NO_x emissions but higher specific fuel consumption and CO₂ emissions?
- Would reducing cruise altitude significantly reduce the impact of NO_x?
- What would be the environmental, commercial and operational consequences of progressively replacing long-range aircraft by medium range ones and undertaking long-distance journeys in two or three stages?
- What would be the effect of reducing cruise Mach number (a) for turbofan powered aircraft and (b) to enable a transition from turbofan to unducted fan propulsion?

Underlying these questions is the broader one of how to develop a methodology for designing for minimum environmental impact rather than for minimum operating costs and, beyond that, how to strike the best balance between environmental and commercial objectives.

5 CONCLUSIONS AND RECOMMENDATIONS

- 1) In the long term, impact on climate is the most important environmental effect of aviation.

- 2) Reducing persistent contrails and NO_x are probably the two most potent means of reducing this impact: in each case, the best environmental result is likely to entail some increase in CO₂ emissions.
- 3) Because CO₂ is such a long-lived greenhouse gas, reducing its emission is a key long term goal: drag reduction is the most potent technology but weight reduction and adoption of the unducted fan to increase propulsion efficiency can also contribute. Aircraft design parameters – design range, cruise altitude and cruise Mach number are also significant factors.
- 4) To achieve large reductions in CO₂ emission will require radical aircraft design changes – the adoption of laminar flow control technology and, for large aircraft, a change to the flying wing or blended wing-body configuration.
- 5) Regulatory and economic measures should be framed so as to promote the greatest possible reduction in impact on climate: measures aimed solely at reducing CO₂ emission will probably do more harm than good.
- 6) In research, the most immediate priority is to continue to strengthen understanding of the effects of aviation on the atmosphere.
- 7) In technology, demonstration of the practicability of hybrid laminar flow control in airline service is a priority. Demonstration of practicable ultra low NO_x combustion technology at realistic engine pressure ratios is also urgently needed. Among more radical concepts, demonstration of the practicability of the ICR engine cycle and the blended wing-body layout are also needed and, looking further ahead, the all laminar flying wing merits re-examination.
- 8) In design, methodologies for designing to minimise environmental impact and for balancing environmental and commercial objectives need to be developed. Multi-segment long-distance travel also merits a full system study.
- 9) The challenge to technology and design is severe. The timescales for introducing new technology and new design concepts are long. The need for research and demonstration is urgent.

REFERENCES

- ACARE, 2002: *Strategic Research Agenda* www.acare4europe.org
- Birch, N.T., 2000: 2020 vision: the prospects for large civil aircraft propulsion. *Aeronaut. J.* 104 (1038), 347-352.
- Department for Transport, 2003: *Aviation and the environment: using economic instruments*. Department for Transport, London, United Kingdom.
- Gierens, K., Schumann, U., Smit, H.G.J., Helten, M. and Zangl, G., 1997: Determination of humidity and temperature fluctuations based on MOZAIC data and parameterisation of persistent contrail coverage for general circulation models. *Ann. Geophys.* 15, 1057-1066.
- Green, J.E., 2002: Greener by Design – the technology challenge. *Aeronaut. J.* 106 (1056), 57-113.
- Green, J.E., 2003: Civil aviation and the environmental challenge. *Aeronaut. J.* 107 (1072), 281-299.
- IPCC, 1999: *Aviation and the Global Atmosphere*. Cambridge University Press, Cambridge, United Kingdom and New York, NY, USA, 373pp.
- Klug, H.G., Bakan, S. and Gayler, V., 1996: Cryoplane – quantitative comparison of contribution to anthropogenic greenhouse effect of liquid hydrogen aircraft versus conventional aircraft. European Geophysical Society, XXI General Assembly, The Hague, The Netherlands.
- Lachmann, G.V. (ed), 1961: *Boundary Layer and Flow Control*. Pergamon Press.
- Lee, D.S., Clare, P.E., Haywood, J., Kärcher, B., Lunnon, R.W., Pilling, I., Slingo, A. and Tilston, J.R., 2000: *Identifying the uncertainties in radiative forcing of climate from aviation contrails and aviation-induced cirrus*. DERA/AS/PTD/CR000103.
- Peel, C.J., 1996: Advances in materials for aerospace. *Aeronaut. J.* 100 (1000), 487-503.
- Rogers, H.L., Lee, D.S., Raper, D.W., Foster, P.M.deF., Wilson, C.W. and Newton, P.J., 2002: The impacts of aviation on the atmosphere. *Aeronaut. J.* 106 (1064), 521-546.
- Whellens, M.W. and Singh, R., 2002: Propulsion system optimisation for minimum Global Warming Potential. Proceedings of ICAS 2002 Congress, Toronto, Paper 7111.

Climate responses to aviation NO_x and CO₂ emissions scenarios

D. S. Lee*

Manchester Metropolitan University, International Centre for Aviation and the Environment, Department of Environmental and Geographical Sciences, Manchester, United Kingdom

R. Sausen

DLR-Institut für Physik der Atmosphäre Oberpfaffenhofen, Germany

Keywords: Aircraft emissions, climate response modelling, radiative forcing

ABSTRACT: The linear climate response model of Sausen and Schumann (2000) was used to further investigate the changes of global mean surface temperature and sea level in response to emissions of aviation CO₂ and NO_x. The parameters of the model were reviewed in the light of more recent data so that it represented mean climate model responses reported in the IPCC's Third Assessment Report, rather than the original parent climate model, ECHAM3. As in its original formulation, aviation emissions of NO_x and CO₂ resulted in a greater temperature increase from O₃ forcing than for CO₂. As a result, the CO₂ temperature response increased by 70% and the O₃ response by 58% because of the increased temperature response of a doubling of CO₂. The main sensitivity of the model remains as identified previously: the value of the equilibrium surface temperature response of O₃ from aviation NO_x emissions, further assessments of which are needed. A new global aviation emission scenario was investigated with the newly parameterized model, based upon recent industry information that suggests that the fleet global emission index for NO_x may be reduced some 10 years earlier than previously estimated. This resulted in a smaller O₃ response of 20% by 2050, when compared with the original (non NO_x-aggressive) scenario. It is recommended that the model should be further developed so that a more complete picture of climate responses can be obtained.

1 INTRODUCTION

Aircraft emissions may influence climate by a number of emissions and effects, as has been shown in detail in the report of the Intergovernmental Panel on Climate Change (IPCC) 'Aviation and the Global Atmosphere' (IPCC, 1999). Gas turbine engines burning kerosene emit a number of trace gases and particles and can trigger the formation of contrails and cirrus clouds. Amongst the emitted species, carbon dioxide (CO₂) is formed at a constant ratio to the fuel consumed; emissions of nitrogen oxides (NO_x=NO₂+NO) result in the formation of ozone (O₃) and destruction of a small amount of methane (CH₄) – a climate warming gas that comes from other sources. Particles may have direct warming or cooling effects, depending upon their composition, but in combination with emitted water vapour may also trigger the formation of contrails, which if persistent can have a warming effect as can any subsequent cirrus cloud formed.

The degree to which aircraft emissions affect climate is measured with the climate metric, radiative forcing. This metric has been adopted by the IPCC and the scientific community at large because of its usefulness in assessing different effects on climate. The radiative forcing concept has both strengths and weaknesses (Shine and Forster, 1999; Fuglestedt *et al.*, 2003), particularly in the context of some aviation effects. Radiative forcing of climate occurs when an agent disturbs the radiative balance of the Earth's atmosphere: when the atmosphere is perturbed it re-establishes radiative equilibrium with a consequential warming or cooling of climate, depending upon the nature of the climate forcing agent.

* *Corresponding author:* David S. Lee, Manchester Metropolitan University, International Centre for Aviation and the Environment, Department of Environmental and Geographical Sciences, John Dalton Building Chester Street, Manchester M1 5GD, United Kingdom. Email: D.S.Lee@mmu.ac.uk

For the past three decades or more, aircraft engine manufacturers and research agencies have put considerable effort into developing technologies that reduce the fuel consumption and NO_x emissions of aircraft. Engine technology has now advanced so far that in order to further reduce fuel consumption and, as a consequence, CO₂ emissions, overall engine pressure ratios may increase further. As a result of the higher temperatures and pressures, NO_x emissions become more difficult to reduce. The radiative forcings (RFs) for CO₂ and O₃ from aviation for 1992 were not greatly dissimilar; 0.018 and 0.023 W m⁻², respectively (IPCC, 1999). However, using a climate response model, Sausen and Schumann (2000) found a greater environmental response in terms of a globally-averaged increase in surface temperature from O₃ than from CO₂. Thus, there are two potential tradeoffs; the engine technology CO₂ vs NO_x trade-off and the CO₂ vs O₃ global temperature response trade-off. Simple climate response models such as that of Sausen and Schumann (2000) – hereafter S&S – may be used to perform climate simulations that allow efficient exploration of emissions scenarios, particularly where the climate response is small and the necessary integration time is long.

In this study, we use the S&S model to further explore aviation emission scenarios that help to target where emissions reductions may best ameliorate climate impacts. The model is updated based on recent estimates of climate parameters from the IPCC's Third Assessment Report – or TAR – (IPCC, 2001), so that a 'generalized response model' is formulated and the results compared with the original form of the model, which is based upon the performance of ECHAM3/LSG, its parent GCM. Further, updated technology information from the aviation industry is used to formulate a simple further global scenario of NO_x emissions. Finally, recommendations are made for further study and model development.

2 MODEL DESCRIPTION AND STUDY DESIGN

The S&S (2000) linear response model takes the form of a convolution integral that predicts CO₂ concentration, CO₂ radiative forcing (RF), normalized RF from O₃ (from aircraft NO_x) and the resultant changes in global mean surface temperature and sea-level. The model is 'tuned' to perform similarly to its parent GCM, ECHAM3/LSG. A full description of the model and its parameters may be found in S&S (2000). Here, a generalized version of the model was formulated that approximates to a mean response of GCMs used in the TAR, rather than being ECHAM-specific. The TAR mean temperature response to a CO₂ doubling was 3.8 K (cf 2.246 K from ECHAM3/LSG); and the RF from CO₂ in the TAR was estimated to be 1.46 W m⁻² (cf 1.56 W m⁻² from IPCC Second Assessment Report). The mean sea-level rise for a doubling of CO₂ was not changed, despite the higher value that was given by TAR.

The emissions scenarios utilized include 'Fa1' and 'Fa2' from the IPCC (1999) aviation scenarios formulated for the IPCC by FESG (1998) using ICCAIA (1997) technology trend scenario data. These emissions data spanned 1992 to 2050. Data prior to 1992 were taken from the estimations of S&S (2000).

The Fa1 and Fa2 scenarios have an underlying GDP growth rate taken from the IS92a scenario. The descriptors '1' and '2' refer to the two technology scenarios, TS1 and TS2, which considered different technology trends. In TS1, it is assumed that fuel efficiency of production aircraft in 2050 will be some 40 – 50% better than 1997, and that the fleet average LTO NO_x will be 10 – 30% below CAEP/2 limits by 2050. In TS2, it is assumed that the emphasis is on NO_x, rather than fuel efficiency, with fuel efficiency of production aircraft in 2050 will be some 30 – 40% better than 1997, and that the fleet average LTO NO_x will be 50 – 70% below CAEP/2 limits by 2050. In this study, an additional scenario has been formulated, denoted 'Fa3', based upon an ICCAIA report (ICCAIA, 2000) that suggested that NO_x levels might be reduced some 10 years earlier than suggested by the original ICCAIA (1997) work for the IPCC. As a simple first case assumption, the existing ICCAIA technology scenario 2 (for ambitious NO_x reductions) was modified such that the fleet EINO_x reduced by the same incremental amount, but at an earlier starting date by 10 years. This assumption also results in lower peak fleet EINO_x values.

3 RESULTS

3.1 Model sensitivity to generalized parameters

The model was run in two modes, 'TAR' and 'ECHAM3/LSG', which refer to the generalized model based upon TAR mean GCM parameters and the original formulation, respectively. Simulations were run in both modes and example output is given at the time horizon, 1990 in Table 1 below.

Table 1 Comparative results and percent change for ECHAM and TAR model modes

Simulation	Time horizon, 1990
Fa1 RF ($W m^{-2}$) ECHAM3/LSG	0.0215
Fa1 RF ($W m^{-2}$) IPCC TAR	0.0201
	-6.5%
Fa1 ΔT (K) CO_2 ECHAM3/LSG	0.0037
Fa1 ΔT (K) CO_2 IPCC TAR	0.0063
	+70%
Fa1 ΔT (K) O_3 ECHAM3/LSG	0.019
Fa1 ΔT (K) O_3 IPCC TAR	0.032
	+58%
Fa1 Δh (cm) CO_2 ECHAM3/LSG	0.037
Fa1 Δh (cm) CO_2 IPCC TAR	0.037
	No change

The evolution of changes in global mean surface temperatures according to the two model formulations are shown in Fig. 1.

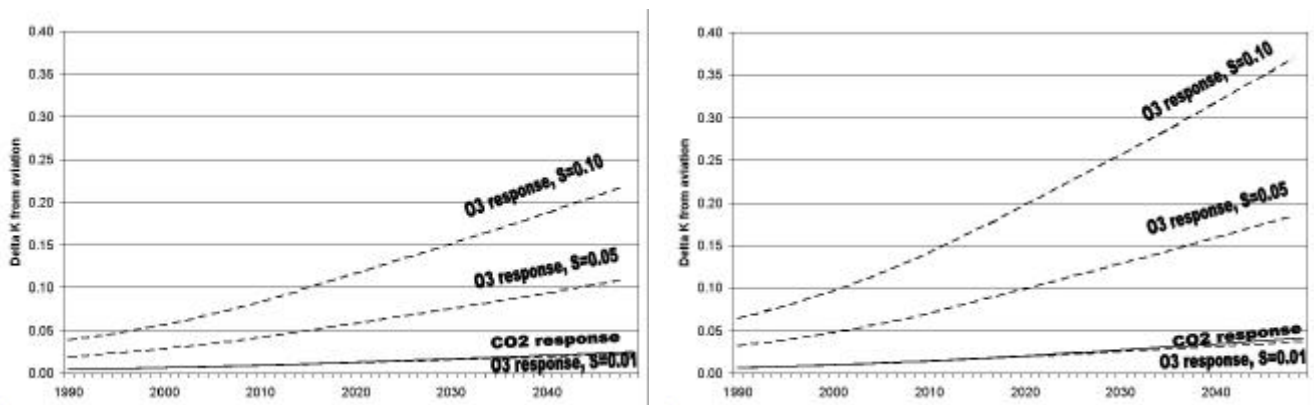


Figure 1. Temperature response from CO_2 and O_3 , 'ECHAM3/LSG' (S&S) model mode (left panel) and 'TAR' model mode with parameter updates (right panel). Scenario F1a and different values of the parameter S from S&S have been considered.

3.2 Climate responses to technology scenarios

The three emission scenarios in terms of $EINO_x$ are shown in Fig. 2. Only the effects of NO_x on O_3 were considered in terms of temperature response, which is shown in Fig. 3. This shows that if it is assumed that improved NO_x technology is introduced 10 years earlier than previously assumed in IPCC (1999), and fleet $EINO_x$ reduces at the same rate as assumed in Fa2, then by 2050, the increased warming effect from O_3 is reduced by 20% over the Fa1 'base case'.

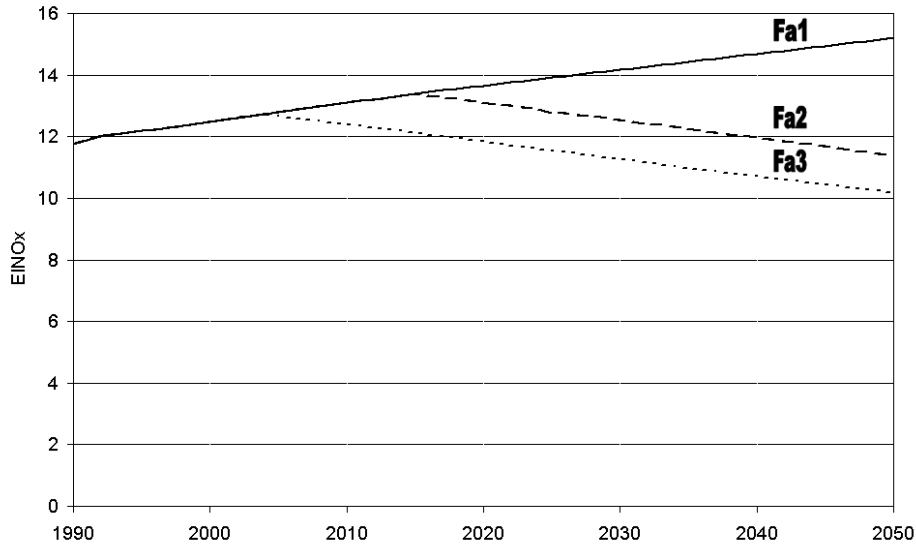


Figure 2. Assumed time evolution of global fleet EINO_x, 1990 to 2050.

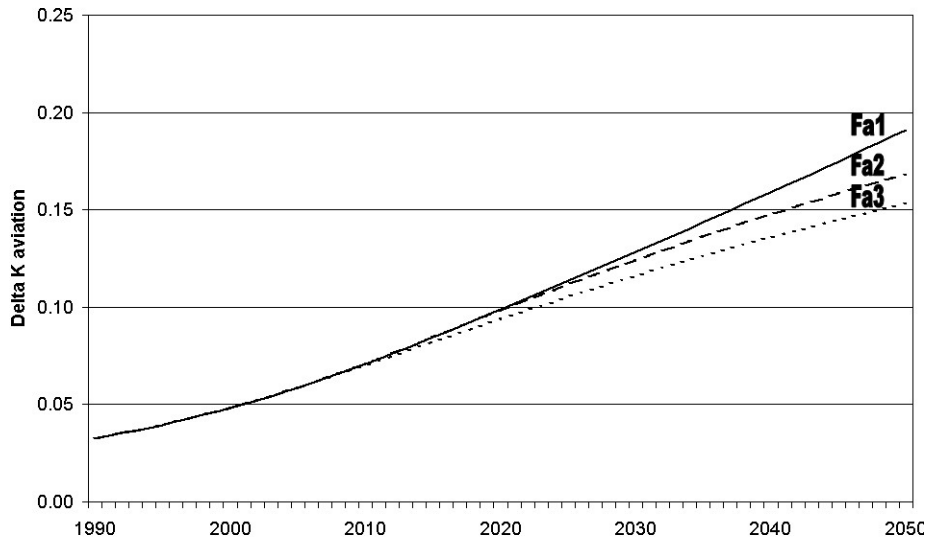


Figure 3. Temperature response from O₃; Fa1, Fa2 and 'Fa3' scenarios (TAR model mode)

3.3 Uncertainties in aviation growth scenarios

The 'central' scenario used by the IPCC (1999) was Fa1. Global traffic statistics from ICAO between 1995 and 2000 showed that aviation growth and emissions followed the Fe scenario more closely up. If long-term growth of aviation is unaffected by recent events and the Fe1 scenario prevails, the combined temperature response from CO₂ and O₃ will be approximately 29% greater than Fa1 by 2050, as shown in Fig. 4.

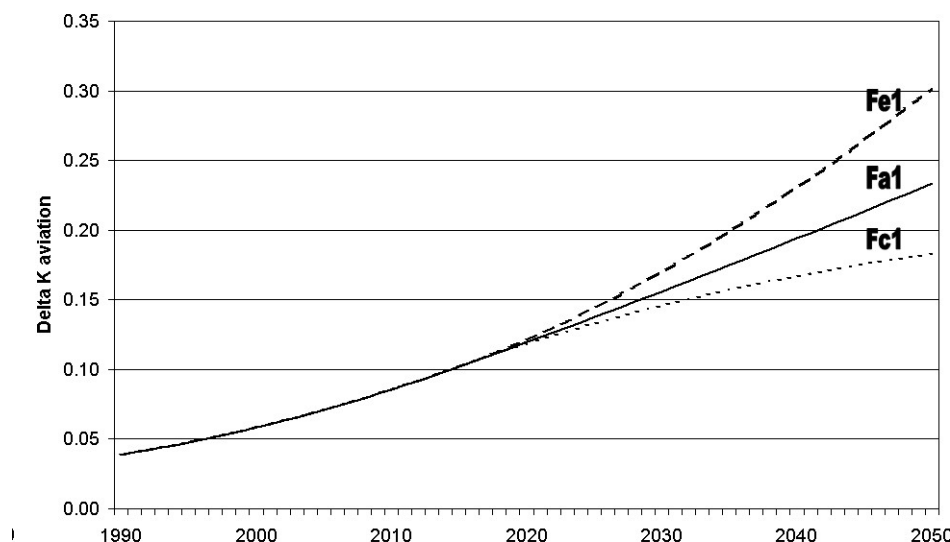


Figure 4. Total temperature response from CO_2 & O_3 ; Fa1, Fe1 and Fc1 scenarios (TAR model mode)

4 DISCUSSION

The work here provides some updates of the original work of Sausen and Schumann (2000). If a generalized ‘TAR’ linear response model is formulated, then the impact of CO_2 increases substantially (70%), as does the response from O_3 (58%). The underlying reason for this is the changed assumption in the temperature response to a doubling of CO_2 : according to the IPCC TAR (IPCC, 2001), the mean temperature response of 17 models to a doubling of CO_2 was 3.8 K. In the TAR model mode, the aviation CO_2 impact is a smaller fraction (18%) of the total temperature response from $CO_2 + O_3$ by 2050, assuming a best estimate of the equilibrium temperature response to a perturbation of O_3 .

If aviation growth follows the Fe scenario (based upon IS92e), rather than Fa (IS92a), then the total impacts will be larger than originally calculated by S&S (2000). Opposing this trend is the so-called ‘Fa3’ scenario formulated here: in this, NO_x impacts on O_3 follow a lower growth rate because of improvements in the NO_x technology.

The conclusions on the relative impacts of O_3 to CO_2 were shown in the previous work of S&S (2000) to be highly dependent on the equilibrium response temperature of aviation-induced O_3 (taken from Ponater *et al.*, 1999). This is a parameter that is not easily computed as it requires a coupled GCM-CTM simulation. Evidently, more estimates from coupled GCM-CTMs are needed to quantify this response more robustly.

5 CONCLUSIONS

Qualitatively, the results of the model show that more benefits may accrue from targeting NO_x reductions than CO_2 in terms of climate response – as did the original S&S model. Updated parameters in the model (‘TAR mode’) do not change this conclusion. This conclusion depends on the equilibrium temperature response for O_3 from aircraft – a poorly quantified parameter. Further calculations of this parameter are required.

The CO_2 response in the ‘TAR mode’ is increased by 70% and the O_3 response by 58%, compared to the ‘ECHAM3/LSG mode’; in the TAR mode, CO_2 was 18% of the total temperature response in 2050.

A new emissions scenario based upon industry data shows a reduced temperature increase of 20% from O_3 , over the base case Fa1 scenario.

The model could accommodate a parameterization of the CH₄ and other responses to aircraft NO_x emissions to give a fuller overall climate response.

REFERENCES

- FESG, 1998: Report 4. Report of the Forecasting and Economic Analysis Sub-Group (FESG): Long-range scenarios. International Civil Aviation Organization Committee on Aviation Environmental Protection Steering Group Meeting, Canberra, Australia, January 1998.
- Fuglestedt, J. S., T. K. Berntsen, O. Godal, R. Sausen, K. P. Shine, and T. Skodvin, 2003: Metrics of climate change: assessing radiative forcing and emission indices. *Climatic Change* 58, 267–331.
- ICCAIA, 1997: 2050 fuel efficiency and NO_x technology scenarios. ICAO/CAEP-4/Working Group 3 (emissions) fourth meeting, 12-14th November 1997, Bern, Switzerland.
- ICCAIA, 2000: Summary of aircraft and engine short-to-medium term technology status of CAEP/5. ICAO/CAEP/WG3 (emissions – technical) meeting, 15-16th June 2000, Cleveland, Ohio.
- IPCC, 1999: Aviation and the Global Atmosphere. Intergovernmental Panel on Climate Change, Cambridge University Press, UK.
- IPCC, 2001: Climate Change 2001, the Scientific Basis. Third Assessment Report of Working Group I Report. Cambridge University Press, UK.
- Ponater, M., R. Sausen, B. Feneberg, and E. Roeckner, 1999: Climate effect of ozone changes caused by present and future air traffic. *Climate Dynamics* 15, 631–642.
- Sausen, R. and U. Schumann, 2000: Estimates of the climate response to aircraft CO₂ and NO_x emissions scenarios. *Climatic Change* 44, 27–58.
- Shine, K. P. and P. M. de F. Forster, 1999: The effect of human activity on radiative forcing of climate change: a review of recent developments. *Global and Planetary Change* 20, 205–225.

Aviation, Atmosphere and Climate - What has been learned

U. Schumann

DLR-Institut für Physik der Atmosphäre Oberpfaffenhofen, Germany

Keywords: Aviation, Atmosphere, Subsonic, Supersonic, Assessments

ABSTRACT: High-lights of the Conference "Aviation, Atmosphere, and Climate" in Friedrichshafen, Germany, June 30 to July 3 2003 are summarized based on a personal view of the author. The aviation induced cirrus changes were in the center of this conference. Initiation of an amendment to the IPCC assessment including assessments of other traffic modes is recommended.

1 INTRODUCTION

In the long term, the impact on climate change is the most important environmental effect of aviation (Green, this conference). The impact of aircraft emissions on the global atmosphere has been assessed under guidance of the Intergovernmental Panel of Climate Change in 1999 (IPCC, 1999), see also Schumann et al. (2001). This conference saw many papers adding considerably to our understanding and revising some of the conclusions given in earlier assessments. The present paper summarizes the talk given at the end of the Conference based on material circulated before the meeting and the material presented at the conference.

2 REVISION OF THE IPCC ASSESSMENT

2.1 Subsonic aviation

According to IPCC (1999), the global mean radiative forcing by air traffic in 1992 was 0.05 W/m^2 . The contrail radiative forcing (RF) was estimated for an optical depth of the contrail cirrus of 0.3, contrail cloud cover of 0.087 % and fixed flight level (200 hPa). The cirrus cloud effect was not quantified but estimated from cirrus trends in correlation with air traffic. The given total did not include cirrus change. ICAO expected a 5 to 10-fold rise of air traffic until 2050, for which the RF was expected to increase by a factor of 4.

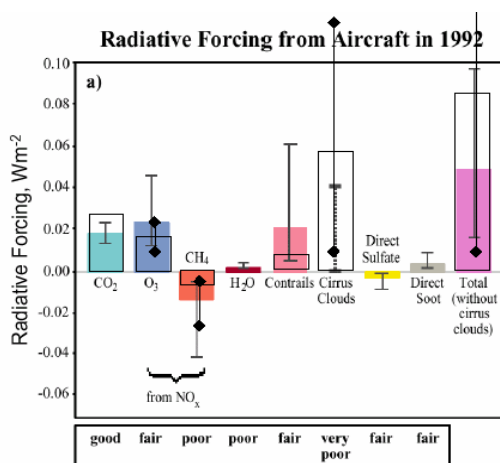


Figure 1. Radiative forcing (RF) from air traffic in 1992 from IPCC (1999; colored columns and bars with end-lines) and revised estimates (white columns and bars with diamonds) based on recent research results (EU-project TRADEOFF, papers by Marquart et al (2003), Mannstein, and others at this conference). The revised RF from CO₂ applies to the year 2000. Note that the revised total now includes the cirrus clouds.

Based on TRADEOFF and other studies (such as related papers), a revised RF figure can be suggested as shown in Fig. 1. The major changes come from a reduced optical thickness of line-shaped contrails, and first estimates of aviation induced cirrus cover changes. The revised RF value given for CO₂ in this figure, which is larger than the value given in the previous assessment for 1992, applies to the year 2000.

The level of scientific understanding has not changed significantly. For example, the scientific understanding of O₃/CH₄ changes, which was classified as "fair/poor" in IPCC (1999) can, to the authors opinion, not yet be classified as being "good/fair": The present models all use similar emission assumptions for CH₄ and hydrocarbons, hence they may not yet include all uncertainties from emissions from the biosphere on the CO/OH/CH₄ budgets. Also, the treatment of vertical mixing in and out of the boundary layer is not well treated in the models.

It was suggested to no longer distinguish between line-shaped contrails and cirrus changes in the future. Instead one should have one bar for contrail effects (the direct effect) and one bar for the aerosol induced cirrus change effect (the indirect effect) in the future.

2.2 *Supersonic aviation*

IPCC (1999) concluded that 1000 high speed civil transport (HSCT) aircraft, with an EI(NO_x) of 5 g/kg, flying at Mach 2.4, would cause 0.5 % O₃ column reduction, O₃ reduction occurring mainly above 19 km altitude, strong contribution from H₂O emissions to O₃ reduction, large importance of sulfate loading, and a RF up to 0.1 W m⁻², mainly from H₂O increases.

The impact of supersonic aircraft on radiative forcing is smaller than assessed by IPCC (1999). For the same HSCT fleet, recent studies suggest a 3 % O₃ column reduction, O₃ reduction mainly above 15 km altitude, strong contribution from NO_x to O₃ reduction, a reduced importance of sulfate loading, and a RF of up to 0.05 W m⁻², mainly from H₂O increases.

3 EMISSIONS

Many new results have been presented from projects such as PARTEMIS, EXCAVATE, and PAZI. Soot gets hydrated and may act as IN also without fuel sulfur. The hygroscopicity of soot increases with fuel sulfur content, so that soot may act more easily as cloud condensation nuclei (CCN) when burned from fuels with high sulfur content. Soot particles may contribute CCNs and also ice nucleation nuclei (IN) to the upper troposphere and lower stratosphere (UTLS). Fuel sulfur increases the number of ice particles formed in contrails but the increase in the number of ice particles formed is far less than linear in the fuel sulfur content (found in experiments SULFUR and AIDA). A lower reaction rate for SO₂ with OH has been computed (Zellner et al.). The finding implies that a considerable fraction of the SO₃ found experimentally to be emitted from engines must have been formed in the combustor; this needs to be further investigated. The conversion fraction of fuel sulfur to H₂SO₄ increases slightly with power setting and most results indicate values of 1 to 5%, i.e. far less than expected a few years ago. Engines emit electrically charged ions formed in the combustor (chemi-ions, Cis), which turn more easily than neutral particles into CCNs after growth by uptake of condensing sulfuric acid and of other condensable gases, but an increase in CCNs in the free atmosphere due to CIs emitted from aircraft has not yet been observed in the real atmosphere. Engines emit organic volatile material, the amount increases with power setting. Hydrocarbon measurements have been presented (e.g. Kurtenbach et al.; e.g. from PARTEMIS). It is recommended that the data get classified into condensable and non-condensables. Considerable progress has been made in modeling soot formation. The results have been compassed successful with laboratory measurements. A new test facility has been developed to study soot formation at pressure values representative for real engines. But real engines (with complex details of geometry and high pressure) are not yet been modeled and measured realistically. Hence, soot formation and the composition of emissions at combustor exit (such as OH, SO₃) need further investigations.

4 OZONE AND METHANE

Many new results have been presented from projects such as TRADEOFF. Data from previous UTLS experiments have been made available without grid averaging for model validation. New data are becoming available on CO, NO, NO_y and others from the projects EULINOX, INCA, CARIBIC, MOZAIC, CRYSTAL-FACE etc. Chemical transport models (CTMs) have been improved, with respect to dynamics and chemistry, and now include tropospheric and stratospheric chemistry consistently. However, the results from various state-of-the-art CTMs still show large variability, mainly because of insufficient resolution, unknown background concentrations, and different treatment of heterogeneous chemistry on aerosols and ice. The largest uncertainty in background NO_x stems from unknown contributions from lightning. Modeling transport near the tropopause may require very high resolution (see below).

With inclusion of heterogeneous processes on aerosols and ice, the NO_x impact on ozone is smaller than for pure gas phase chemistry. The impact of NO_x on CH₄ life time appears to be smaller than assessed in IPCC (1999). This size of this impact depends strongly on the representation of vertical transport in the troposphere in the CTMs.

The question of how far the RF due to increased O₃ and reduced CH₄ cancel each other with respect to climate impact (changes in surface temperatures etc.) has still not been determined in spite of the fact that the tools (global circulation models) required for such studies do exist now; it is suggested to study this effect now with the existing tools.

The climate impact (change in surface temperature etc.) is only approximately proportional linearly to the radiative forcing. Recent studies show that ozone increases in the UTLS have a stronger impact on climate than expected from the RF value.

Plume processes occur at scales of meters to kilometers and are, therefore, not directly resolved by large scale CTMs. The plume process details are not included in most of previous CTM/GCM studies. Instead most CTMs assume that the emitted species get mixed over the respective grid box (with horizontal scales of the order 10 to 300 km and vertical scales of the order 1 km) of the model immediately after emissions. Details of plume processes are important for conversion of NO_x to NO_y and for ozone formation and important for ice formation in plumes. Most of the plume processes that lead to contrail formation are sufficiently well understood. With respect to NO_y and O₃ chemistry, the various studies find very different importance of the impact of plume (Plumb, this conference, and Kraabøl et al. (2002) find either 3 or 18 % change in ozone formation due to plume processes). Although this uncertainty is only a small part of the total uncertainty of present CTMs, the impact of plume processes on air chemistry needs further clarification.

With respect to emissions from supersonic aircraft in the mid stratosphere, the change in the reaction rates found for reactions of NO_x with OH implies a larger importance of NO_x emissions and a reduced importance of H₂O emissions for stratospheric ozone destruction.

5 AEROSOLS, CONTRAILS AND CIRRUS

Aircraft emit gases and particles which influence cloud formation. Two kinds of effects of aircraft emissions on cloud formation can be distinguished: 1) by spreading contrails in supersaturated air masses (the direct effect), and 2) by aerosol from aviation accumulated in the UTLS over several days affecting cirrus properties (the indirect effect). The direct effect is clearly visible to ground observers and observations by satellites from space. The indirect effect has not been identified in observations in the real atmosphere but has been identified from numerical simulations. The indirect effect may induce positive or negative RF.

This topic was at the center of the present conference. Many new results have been presented from projects such as INCA, CRYSTAL-FACE, PAZI, PARTS, and others. The direct effect was discussed in several papers at this conference in terms of line-shaped contrail and cirrus changes in correlation to traffic in the last few hours. The indirect effect (from sulfuric acid droplets and soot) and their treatment in cirrus models was discussed with respect to aviation impact for the first time. The observed long-term cirrus changes, as discussed by Zerefos et al. (see also IPCC, 1999; and Minnis et al., 2003), are due to the combined direct and indirect effects.

Aerosol and cirrus differences in clean/dirty air masses (as found in the INCA experiment) support the assumption that differences in aerosols may cause changes in cirrus cloud properties, but cirrus formation depends also strongly on the vertical motions in the atmosphere.

Ice forms homogeneously from solution droplets or heterogeneously by interaction of liquid and solid particles at ice saturation above 100 % and below the critical humidity for homogeneous nucleation (near about 160%). Soot represents an important fraction of aerosol in the UTLS (see Baumgardner et al., this conference). Biomass burning in the tropics and aviation contribute considerably to the soot number density in the upper troposphere. Soot may induce heterogeneous ice nucleation and hence may represent the most important aviation aerosol impacting cirrus formation, but the quantitative effect is still to be determined. Modeling of heterogeneous nucleation of cirrus crystals is now becoming feasible but the models are still in their infancy. New data on the HNO_3 deposition on ice become available (important, e.g., for washout and denitrification of the polar stratosphere):

The cover by line-shaped contrails has been computed for given traffic and temperature/humidity fields. However the results are not yet in sufficient agreement with observations; instead contrail cover is found to be non-linearly related to traffic density. The largest contrail cover occurs even for weak traffic density in regions with high potential contrail cover.

Results presented at this conference confirm that aviation has caused an increase in cirrus cover by a few percent regionally. This was shown by long-term ISCCP data trends (Zerefos et al.; in particular over continental USA, and the North Atlantic flight corridor) and by direct correlation between METEOSAT cirrus and aviation data (Mannstein; over Europe). The trends are not fully correlated with traffic everywhere. Cirrus cover variations due to annual variability or trends in UT humidity partially mask the effect of aviation.

With respect to the quantitative RF resulting from contrail cirrus, several estimates are available: From ISCCP trend analysis, Minnis et al. (2001) conclude a „spreading factor“ of 3.9. Zerefos et al. do not quantify this spreading factor but the derived cirrus trends are very similar compared to Minnis et al. (2001).

Minnis et al. (2003) conclude, that the RF from both linear contrails and the resulting contrail-generated cirrus clouds would be 15.3 mW m^{-2} . Within the project TRADEOFF (Isaksen et al.), this contribution was estimated far larger: 60 to 100 mW m^{-2} . Mannstein finds that the change in cirrus cover over Europe is 10 times larger than the cover by line-shaped contrails and concludes that the RF would be 10 times larger for the same optical properties, or even larger if contrail cirrus is optically thicker than line-shaped contrails; He concludes an RF of 30 - 90 mW m^{-2} , using the 3 - 9 mW m^{-2} range for line-shaped contrails.

The conference saw the first model results presented for soot impact on cirrus formation (Hendricks, Penner). The results show that the effects are potentially of important magnitude but the magnitude is not yet sufficiently known for a reliable assessment. Even the sign is uncertain: It appears that additional soot may reduce the number of ice particles forming and hence reduce their optical depth and the induced RF.

A contrail analysis has been performed with meteorology computed for present and future climate from a global circulation model. The results indicate that for the same amount of traffic, the line-shaped contrail cover would be smaller in a future climate because of a warmer upper troposphere.

Travis et al. (2002b) claim observable changes in the daily temperature range (DTR) due to reduced contrails in the three days period of 11-14 Sept. 2001, when air traffic over parts of the USA was reduced. They report that the DTR was 1 K above the 30-year average for the three days grounding period, adding evidence that jet aircraft do have an impact on the radiation budget over the US. However the DTR in 1982 was also nearly 1 K above the average and certainly for other reasons (Travis et al., 2002a). Hence, the statistical significance of the data is too weak to justify a strong conclusion.

6 OPEN ISSUES

6.1 Nitrogen Oxides (NO_x)

Although the scientific understanding of the processes and the quality of chemical transport models (CTMs) has increased considerably since IPCC (1999), the quantification of the impact of NO_x from aviation on ozone and methane is still very uncertain. Errors of the order of a factor of two are still likely to occur in present assessment studies. The uncertainties are due to errors in representation of transport (convective transports in the troposphere, transport near and across the tropopause, washout by rain etc.), cloud physics (cirrus and others), horizontal and vertical distribution of lightning NO_x sources (which may be improved in future studies using data from the projects MOZAIC, CARIBIC, TROCCINOX, CRYSTAL-FACE etc.), emissions at the surface, treatment of boundary layer chemistry and transport, climate/chemistry interaction, coupling to ocean and biosphere, and (to the authors opinion mainly) insufficient numerical resolution.

A recent study by Birner et al. (2002) shows that a stably stratified inversion forms just above the tropopause at scales of a few hundred meters. Hence, CTMs need to have 100 m vertical resolution (and a comparable resolution horizontally) in order to resolve the transport near the tropopause correctly. Findings of CTMs with various resolution performed so far do show little impact of resolution. However such studies remain inconclusive since they do not resolve important small scale structures such as the inversion near the tropopause. It is suggested to put far more emphasis on developing numerical schemes with high resolution. This should include a combination of homogeneously refined grids and nesting near the tropopause. The emphasis on resolution does not mean that other transport processes are unimportant such as vertical mixing in deep convection. Models dealing with supersonic aviation should include the whole stratosphere in order to represent the age of air masses in the stratosphere correctly.

It is suggested to perform a special workshop (perhaps within the coming ACCENT network of excellence funded by the EC) to develop a long-term model development strategy. At the end one should have a few very good CTMs and GCMs.

A long-term strategy for experiments in this field is also needed. It is recommended to enhance cooperation between modelers and experimenters. It was pointed out that the future of MOZAIC is in danger. Once the instruments are demounted from the present MOZIAC aircraft, a continuation will be difficult because of required certification. The data available from many experiments (such as NOXAR and GOME) show differences which are in part due to inter-annual variability, which is hard to detect from short time measurements. Therefore, the use of the many years of MOZAIC data is important.

6.2 Aerosols and Contrails

Aviation impact on climate may be largest via cirrus changes. The quantification of this impact has been advanced but the state of scientific understanding is still poor. The direct and indirect effects of aviation on cirrus are still not understood sufficiently for reliable quantification. Observational evidence for the direct effect is good, for the indirect effect it is still poor. Soot appears to be the most important aviation aerosol impacting cirrus formation, however models are still in an early development stage and atmospheric observations on soot impact on cirrus are few. In particular the fate of (aging) soot after emission has not yet been determined experimentally.

A prerequisite for assessments of the impact of aerosols and contrails on cirrus is a better understanding of cirrus formation. Correct modeling of the relative humidity and cirrus formation requires better information on vertical motions in the upper troposphere, distribution and freezing properties of heterogeneous ice nuclei, and physical parameterizations of subgrid-scale processes. For correct modeling of the occurrence of CCNs one would also need better knowledge of the distribution of condensable gases such as H_2SO_4 .

As a new topic it was suggested to study the impact of aircraft emissions on the hydrological cycle. Changes in sedimentation and precipitation may be very important for climate and may be affected by cirrus changes due to aviation. Precipitation is one of the most difficult subject of meteorology. It needs long-term efforts to account for aircraft impact on precipitation. A further new topic of potential importance, the impact of cosmic rays was mentioned, see Eichkorn et al. (2002) and the editorial in Science, 298, of 20 Dec. 2002.

6.3 Mitigation

The potential impacts of different fuels, different engines, high speed transport, other flight levels or other flight routing on the aviation impact has still not be finally understood. Mitigation effects studied at this conference included cryoplanes (driven by liquid hydrogen, LH2, instead of kerosene) and changes in flight altitudes. LH2 fuel may be a viable alternative to kerosene in terms of climate impact if LH2 can be produced safely and with low climate impact. Reduced flight altitudes reduce the NO_x impact on ozone (and on methane) and may reduce the occurrence of line-shaped contrails. Whether this justifies a pledge for lower flight altitudes remains open. A reduction in flight levels would increase the emissions of CO₂ and has several negative impacts on flight endurance, air traffic management, and convenience of the passengers (e.g. due to increased turbulence and enlarged travel duration). The impact of changes in flight altitudes in cirrus formation is unknown. Also the impact on methane is not yet reliably determined.

The studies presented are necessary steps in developing environmentally sustainable aviation with growing air traffic. However, it may be that the mitigation effects are small compared to economic implications and the studies are not yet reliable enough for drastic changes in aviation procedures. It may turn out that the best strategy is to fly just above the tropopause in the dry lower stratosphere (where contrails remain short-lived, where NO_x impact on O₃ is small, where aircraft operate efficiently, and where turbulence levels are small). One may also consider to adjust the flight altitudes to the actual meteorology, e.g., to avoid contrails by avoiding flights in air masses with large relative humidity (above ice saturation).

7 CONCLUSIONS

In spite of considerable progress made, more research is needed to better understand both atmospheric and combustion science with respect to aviation impact on the global atmosphere. The topic of cirrus changes due to spreading contrails and soot emissions was at the center of the present conference, but the level of scientific understanding of this topic is still poor. It is recommended to initiate an amendment to the IPCC assessment which includes also the assessments of other traffic modes (such as by cars, trains, ships etc).

REFERENCES

- Birner, Th., A. Dörnbrack and U. Schumann, 2002: How sharp is the tropopause at midlatitudes? *Geophys. Res. Lett.*, 29 (14), 10.1029/2002GL015142.
- Eichkorn, S., Wilhelm, S., Aufmhoff, H., Wohlfrom, K. H., Arnold, F., 2002: Cosmic ray-induced aerosol-formation, first observational evidence from aircraft-based ion mass spectrometer measurements in the upper troposphere, *Geophys. Res. Lett.*, 29, No. 14, 10.1029/2002GL015044.
- Kraabol, A. G., T. K. Berntsen, J. K. Sundet, and F. Stordal, 2002: Impacts of NO_x emissions from subsonic aircraft in a global three-dimensional transport model including plume processes. *J. Geophys. Res.*, 107, No. D22, 4655, doi:10.1029/2001JD001019, 13 pp.
- IPCC, 1999: *Aviation and the Global Atmosphere*, A Special Report of Intergovernmental Panel on Climate Change, Cambridge Univ. Press, Cambridge, UK, pp. 373.
- Marquart, S., M. Ponater, F. Mager, and R. Sausen, Future development of contrail cover, optical depth, and radiative forcing: Impacts of increasing air traffic and climate change, *J. Climate*, 16, 2890-2904, 2003.
- Minnis, P., R. Palikondra, D.R. Doelling, U. Schumann, K. Gierens, 2001: *Changes in cirrus cloudiness and their relationship to contrails*, Proceedings American Meteorological Society, Boston, Mass, USA, paper no. 11.9, 4 pp.
- Minnis, P., J. K. Ayers, R. Palikonda, and D. Phan, 2003: Contrails, cirrus trends, and climate, Submitted to *J. Clim.*
- Schumann, U., J. Ström, F. Arnold, T. K. Berntsen, P. M. de F. Forster, J.-F. Gayet, and D. Hauglustaine, 2001: Aviation impact on atmospheric composition and climate, in: *European Research in the Stratosphere 1996-2000*, Chapter 7, EUR 19867, pp. 257-307, European Commission, Brussels.
- Travis, D. J., A. M. Carleton, R. G. Lauritsen, 2002a: Jet aircraft contrails: Surface temperature variations during the aircraft groundings of September 11-13, 2001. 10 th *Conference on Aviation, Range &*

Aerospace Meteorology, 13-16. May 2002, Portland, Oregon, American Meteorological Society, paper J1.1.

Travis, D. J., A. M. Carleton, R. G. Lauritsen, 2002b: Contrails reduce daily temperature range, brief communications, *Nature*, 418, 601.

List of Participants

Abu-Abbas, Othman

Telecommunication & Navigation Institute
P.O.Box 23778 Safat
13098 Kuwait
oboabas@hotmail.com

Aigner, Manfred

DLR, Institut für Verbrennungstechnik
Pfaffenwaldring 38-40
70569 Stuttgart
Germany
manfred.aigner@dlr.de

Al-Daithan, Zayed

Telecommunication & Navigation Institute
P.O.Box 23778 Safat
13098 Kuwait
zaldaithan@yahoo.com

Amanatidis, Georgios

European Commission
DG Research
LX46 2/85
1049 Brussels
Belgium
georgios.amanatidis@cec.eu.int

Anderson, Bruce

MS 483
NASA Langley Research Center
Hampton, Virginia
23681 USA
b.e.anderson@larc.nasa.gov
bruce.e.anderson@nasa.gov

Anderson, Donald

Office of Earth Sciences
Code YS, NASA Headquarters
300 E St SW
Washington DC 20546
USA
danders1@hq.nasa.gov
danderson@hq.nasa.gov

Arnold, Frank

Max-Planck-Institut für Kernphysik
P.O.Box 103980
69117 Heidelberg
Germany
frank.arnold@mpi-hd.mpg.de

Balis, Dimitris

Laboratory of Atmospheric Physics
Aristotle University of Thessaloniki
Box 149 54124 Thessaloniki
Greece
balis@auth.gr

Baughcum, Steven Boeing Company

P.O.Box 3707
MC 02-XL
Seattle WA 98 124
USA
Steven.L.Baughcum@boeing.com

Baumgardner, Darrel

2400 Central Avenue, Suite A
Boulder, CO 80301
USA
darrel@servidor.unam.mx

Belitz, Thomas

BDLI
Friedrichstrasse 152
10117 Berlin
Germany
belitz@bdli.de

Braun-Unkhoff, Marina

DLR
Institut für Verbrennungstechnik
Pfaffenwaldring 38-40
70565 Stuttgart
Germany
Marina.Braun-Unkhoff@dlr.de

Brunner, Dominik

Inst. for Atmospheric and Climate Science
ETH Zurich
Switzerland
dominik.brunner@iac.umnw.ethz.ch

Bukovnik, Monika

Lastenstr. 26-38
1230 Wien
Austria
bukovnik@psia.at

Celikel, Ayce

SEE Business Area
EUROCONTROL Experimental Centre
BP15 Centre du Bois des Bordes 91222
Bretigny-sur-Orge Cedex
France
ayce.celikel@eurocontrol.int

Chesneau, Sylvie

Eurocontrol Experimental Centre
B.P.15, F-91222 Bretigny sur Orge Cedex
France
sylvie.chesneau@eurocontrol.int

Crowther, Richard

Centre for Atmospheric Science
Department of Chemistry
University of Cambridge
Lensfield Road
Cambridge, CB2 1EW
UK
richard.crowther@atm.ch.cam.ac.uk

Danilin, Michael

The Boeing Company
MS 0R-RC
P.O. Box 3707
Seattle, WA 98124
USA
danilin@h2o.ca.boeing.com,
myd1490@h2o.ca.boeing.com

Dessens Olivier

Centre for Atmospheric Science
Department of Chemistry
University of Cambridge
Lensfield Road
Cambridge, CB2 1EW
UK
olivier.dessens@atm.ch.cam.ac.uk

Deuber Odette

Öko-Institut
Novalisstr. 10
D-10115 Berlin
Germany
o.deuber@oeko.de

Dewes Winfried

DLR Büro Brüssel
98, rue du Trône
5010 Bruxelles
Belgium
Winfried.Dewes@dlr.de

Doerr Thomas

Rolls-Royce Deutschland ltd&Co KG
Eschenweg 11
15827 Dahlewitz / Berlin
Germany
thomas.doerr@rolls-royce.com

Duda David

NASA Langley Research Center
Mail Stop 420, 21 Langley Boulevard
Hampton, VA 23681-2199
USA
d.p.duda@larc.nasa.gov

Eleftheratos Kostas

Laboratory of Climatology
and Atmospheric Environment,
Department of Geology
University of Athens
15784 Athens
Greece
kele@auth.gr

Elliff Ted

Eurocontrol Experimental Centre
B.P.15
91222 Bretigny sur Orge Cedex
France
ted.elliff@eurocontrol.int

Fabian Peter

Waldvögeleinstr.3
80995 München
Germany
fabian@met.forst.tu-muenchen.de

Falk Robert

Dept of Trade and Industry
Room 476
151 Buckingham Palace Road
London, SW1W 9SS
UK
robert.falk@dti.gsi.gov.uk

Farmery Mike

Shell Centre
London
SE1 7NA
UK
mike.farmery@shell.com

Fichter Christine

DLR Oberpfaffenhofen
Institut fuer Physik der Atmosphaere
82234 Wessling
Germany
christine.fichter@dlr.de

Fiebig Markus

DLR Oberpfaffenhofen
Institut fuer Physik der Atmosphaere
82234 Wessling
Germany
Markus.Fiebig@dlr.de

Frank Peter

DLR, Institut für Verbrennungstechnik
Pfaffenwaldring 38-40
70569 Stuttgart
Germany
peter.frank@dlr.de

Friedl Randall

Jet Propulsion Lab
4800 Oak Grove Drive
Mail Stop 180-404
Pasadena, CA 91109
USA
rfriedl@jpl.nasa.gov

François Garnier

ONERA, Département Physique
Unité Environnement Atmosphérique
29 Ave de la Division Leclerc
92 320 Châtillon
France
Francois.Garnier@onera.fr

Gauss Michael

Department of Geophysics
PO 1022 Blindern
0315 Oslo
Norway
michael.gauss@geofysikk.uio.no

Geigle Klaus Peter

DLR, Institut fuer Verbrennungstechnik
Pfaffenwaldring 38-40
70569 Stuttgart
Germany
klauspeter.geigle@dlr.de

Gerlinger Peter

DLR, Institut für Verbrennungstechnik
Pfaffenwaldring 38-40
70569 Stuttgart
Germany
peter.gerlinger@dlr.de

Ghazi Anver

European Comission
DG Research
LX46 2/114
1049 Brussels
Belgium
anver.ghazi@cec.eu.int

Gierens Klaus

DLR Oberpfaffenhofen
Institut fuer Physik der Atmosphaere
82234 Wessling
Germany
klaus.gierens@dlr.de

Goos Elke

DLR, Institut für Verbrennungstechnik
Pfaffenwaldring 38-40
70569 Stuttgart
Germany
Elke.Goos@dlr.de

Gössling Stefan

Service Management Lund University
Campus Helsingborg
Box 882, 25108 Helsingborg
Sweden
stefan.gossling@humecol.lu.se

Grainger Roy

Clarendon Lab
Parks Road
Oxford OX1 3PU
UK
r.grainger@physics.ox.ac.uk

Green John

1 Leighton Street, Woburn
Milton Keynes, MK17 9PJ
UK
greens@woburnhc.freeserve.co.uk

Grewe Volker

DLR Oberpfaffenhofen
Institut fuer Physik der Atmosphaere
82234 Wessling
Germany
volker.grewe@dlr.de

Guldborg Annette

Danish Meteorological Institute
Lyngbyvej 100
2100 Copenhagen O
Denmark
ag@dmi.dk

Gysel Martin

Paul Scherrer Institut
Laboratory of Atmospheric
Chemistry
5232 Villigen PSI
Switzerland
martin.gysel@psi.ch

Haag Karlheinz

Leiter Umweltkonzepte Konzern
FRA KU
Lufthansa Basis
60546 Frankfurt am Main
Germany
karlheinz.haag@dlh.de

Harris Neil Richard Peter

European Ozone Research Coordinating Unit
14 Union Rd
Cambridge
CB2 1HE
UK
Neil.Harris@ozone-sec.ch.cam.ac.uk

Hauglustaine Didier

LSCE, CEN Saclay
Orme des Merisiers
Bat. 709
91191 Gif-sur-Yvette Cedex
France
hauglustaine@cea.fr

Hayashi Shigeru

National Aerospace Laboratory
7-44-1 Jindaiji Higashi
Chofu Tokyo 182-8522
Japan
hayashi@nal.go.jp

Hendricks Johannes

DLR Oberpfaffenhofen
Institut fuer Physik der Atmosphaere
82234 Wessling
Germany
Johannes.Hendricks@dlr.de

Herms Erika

DGAC, Service Technique de la Navigation
Aérienne
1 av. du Dr. M. Grynfogel
BP1084, 31035 Toulouse Cedex
France
erika.herms@aviation-civile.gouv.fr

Hitzenberger Regina

Institute for Experimental Physics
Boltzmannng. 5
1090 Wien
Austria
hitz@ap.univie.ac.at

Hofmann David

Climate Monitoring and Diagnostics
Laboratory
325 Broadway St.
Boulder, Colorado
USA
David.J.Hofmann@noaa.gov

Hume Chris

Airbus UK, New Filton House
Future Projects Office
(Building 09B-10, No. 7 D.O.)
Bristol BS99 7AR
UK
chris.hume@airbus.com

Immler Franz

Telegrafenberg A43
14473 Potsdam
Germany
fimmler@awi-potsdam.de

Isaksen Ivar

Institut for Geofysikk
Universitetet i Oslo
PB 1022, Blindern 0315
Oslo
Norway
ivar.isaksen@geofysikk.uio.no

Jacobs Ole

Deutsche Lufthansa AG
FAC, B6.48
60549 Frankfurt
Germany
ole.jacobs@dlh.de

Jelinek Frank

EUROCONTROL
Experimental Centre
Centre de Bois des Bordes
B.P.15
91222 Bretigny sur Orge Cedex
France
frank.jelinek@eurocontrol.int

Kärcher Bernd

DLR Oberpfaffenhofen
Institut fuer Physik der Atmosphaere
82234 Wessling
Germany
bernd.kaercher@dlr.de

Katragkou Eleni

Max Planck Institute for Nuclear Physics
Saupfercheckweg 1
69117 Heidelberg
Germany
eleni.katragkou@mpi-hd.mpg.de

Klein Angelika

Flughafen Düsseldorf GmbH
Nachbarschaftsdialog und Immissionsschutz
Postfach 300363
40403 Düsseldorf
Germany
a.klein@dus-int.de

Köhler Marcus

Centre for Atmospheric Science
University of Cambridge, Chemistry
Department
Lensfield Road
Cambridge CB2 1EW
UK
marcus.koehler@atm.ch.cam.ac.uk

Krämer Martina

Forschungszentrum Jülich
ICG-I: Stratosphäre
52425 Jülich
Germany
m.kraemer@fz-juelich.de

Krebs Waldemar

DLR Oberpfaffenhofen
Institut fuer Physik der Atmosphaere
82234 Wessling
Germany
waldemar.krebs@dlr.de

Kurtenbach Ralf

Bergische Universität Wuppertal (BUW)
Fachbereich 9/ Physikalische Chemie
Gaußstraße 20
42119 Wuppertal
Germany
kurtenba@uni-wuppertal.de

Lee David

Dept of Environmental and Geographical
Sciences
Manchester Metropolitan University
John Dalton Extension, Chester Street
Manchester M1 5GD
UK
D.S.Lee@mmu.ac.uk

Leigh Phil

Biosphere-Atmosphere Interactions and
Environmental Chemistry Group
Dept of Environmental Science
Institute of Environmental and Natural
Sciences
Lancaster University, Lancaster, LA1 4YQ
UK
p.leigh@lancaster.ac.uk

Madden Paul

ML92, Rolls-Royce plc
P.O. Box 31
Derby DE24 8BJ
UK
paul.madden@rolls-royce.com

Mäder Claudia

Umweltbundesamt, Fachgebiet II 6.1
Bismarckplatz 1
14193 Berlin
Germany
claudia.maeder@uba.de

Mangold Alexander

Forschungszentrum Jülich GmbH, ICG-I
52425 Jülich
Germany
a.mangold@fz-juelich.de

Mannstein Hermann

DLR Oberpfaffenhofen
Institut fuer Physik der Atmosphaere
82234 Wessling
Germany
Hermann.Mannstein@dlr.de

Marizy Corinne

Airbus France, Acoustics & Environment Dept
P.O. Box M0112/4
316 route de Bayonne
31060 Toulouse Cedex 03
France
corinne.marizy@airbus.com

Marquart Susanne

DLR Oberpfaffenhofen
Institut fuer Physik der Atmosphaere
82234 Wessling
Germany
susanne.marquart@dlr.de

Meilinger Stefanie

Max-Planck Institut für Chemie
Postfach 3060
55020 Mainz
Germany
smeili@mpch-mainz.mpg.de

Miake-Lye Richard C.

Aerodyne Research, Inc.
45 Manning Road
Billerica, MA 01821-3976
USA
rick@aerodyne.com

Minikin Andreas

DLR Oberpfaffenhofen
Institut fuer Physik der Atmosphaere
82234 Wessling
Germany
andreas.minikin@dlr.de

Mirabel Philippe

Université Louis Pasteur
1, rue Blaise Pascal
67084 Strasbourg
France
mirabel@illite.u-strasbg.fr

Möhler Ottmar

Forschungszentrum Karlsruhe, IMK-AAF
Postfach 3640
76021 Karlsruhe
Germany
Ottmar.Moehler@imk.fzk.de

Moldanova Jana

Box 470 86
40258 Göteborg
Sweden
janam@ivl.se

Monier Marie

Laboratoire de Météorologie Physique
24, Avenue des Landais
63177 Aubière
France
monier@opgc.univ-bpclermont.fr

Natarajan Sukina

Department of Physics and Astronomy
University College London
Gower Street
WC1E 6BT
UK
sukina.natarajan@ucl.ac.uk

Nielsen Johannes K.

Danish Meteorological Institute
Lyngbyvej 100
2100 KbhØ
Denmark
jkn@dmi.dk

Noland Robert

Centre for Transport Studies
Dept. of Civil & Environmental Engineering
Imperial College London
London SW7 2AZ
UK
r.noland@imperial.ac.uk

Palikonda Rabindra

suite 300
1 Enterprise Parkway
Hampton, VA 23666
USA
r.palikonda@larc.nasa.gov

Penner Joyce

Dept. of Atmospheric
Oceanic, and Space Sciences
University of Michigan
2455 Hayward St.
Ann Arbor, MI 48109-2143
USA

Petzold Andreas

DLR Oberpfaffenhofen
Institut fuer Physik der Atmosphaere
82234 Wessling
Germany
andreas.petzold@dlr.de

Pitari Giovanni

Dipartimento di Fisica
 Universita' L'Aquila
 67010 Coppito
 L'Aquila
 Italy
gianni.pitari@aquila.infn.it

Plumb Ian

CSIRO Telecommunications and Industrial
 Physics
 PO Box 218
 Lindfield, NSW 2070
 Australia
Ian.Plumb@csiro.au

Ponater Michael

DLR Oberpfaffenhofen
 Institut fuer Physik der Atmosphaere
 82234 Wessling
 Germany
michael.ponater@dlr.de

Popovicheva Olga

Deaprtment of Microelectronics
 Institute of Nuclear Physics
 Moscow State University
 Vorobiev Gory
 119 992, Moscow
 Russia
olga@mics.msu.su
olga@mics.msu.su
OPopovitcheva@mics.msu.su

Prather Michael

Earth System Science Dept
 UC Irvine
 Irvine, CA 92697-3100
 USA
mprather@uci.edu

Quesne Agnes

Eurocontrol Experimental Centre
 B.P.15
 91222 Bretigny sur Orge Cedex
 France
agnes.quesne@eurocontrol.int

Rodriguez Jose M.

RSMAS/MAC
 University of Miami
 4600 Rickenbacker Causeway
 Miami, FL 33149
 USA
jrodriguez@rsmas.miami.edu

Saueressig Gerd

Deutsche Lufthansa AG, FRA KU
 Lufthansa Basis Tor 21
 60546 Frankfurt
 Germany
gerd.saueressig@dlh.de

Sausen Robert

DLR Oberpfaffenhofen
 Institut fuer Physik der Atmosphaere
 82234 Wessling
 Germany
robert.sausen@dlr.de

Schaffrath Stefan

Public Relations, FRA CI/B
 Lufthansa Basis
 60546 Frankfurt am Main
 Germany
stefan.schaffrath@dlh.de

Schumann Ulrich

DLR Oberpfaffenhofen
 Institut fuer Physik der Atmosphaere
 82234 Wessling
 Germany
ulrich.schumann@dlr.de

Slavinskaya Nadja

Institut für Verbrennungstechnik
 DLR Stuttgart
 Germany

Smith James

Eurocontrol Experimental Centre
 B.P.15
 91222 Bretigny sur Orge Cedex
 France
james.smith@eurocontrol.int

Sorokin Andrey

CIAM
 Aviamotornaya 2
 111116, Moscow
 Russia
sorokin@ciam.ru

Ström Johan

Institute of Applied Environmental Research
 (Air Pollution Laboratory),
 Stockholm University
 Frescativägen 54
 10691 Stockholm
 Sweden
johan@itm.su.se

Stubenrauch Claudia

Laboratoire de Météorologie Dynamique
Ecole Polytechnique
91128 Palaiseau cedex
France
stubenrauch@lmd.polytechnique.fr

Suzanne Jean

Département de Physique
Faculté des Sciences de Luminy
Case 901
13288 Marseille cedex 9
France
suzanne@crmc2.univ-mrs.fr

Vancassel Xavier

Université Louis Pasteur Strasbourg
1 rue Blessig
67084 Strasbourg
France
vancassel@illite.u-strasbg.fr

Velthoven Peter van

KNMI
P.O.box 201
3730 AE De Bilt
The Netherlands
velthove@knmi.nl

Volz-Thomas Andreas

PO Box 1913
52425 Jülich
Germany
a.volz-thomas@fz-juelich.de

Waibel Andreas

Frankfurt Airport Center
Hugo-Eckner-Ring B.6.49
60549 Frankfurt/Main
Germany
andreas.waibel@dlh.de

Wey Chowen

NASA GRC, MS 60-6
21000 Brookpark Road
Cleveland OH44135
USA
Chowen.C.Wey@grc.nasa.gov

Wiesen Peter

Bergische Universitaet Wuppertal
Fachbereich 9 / Physikalische Chemie
Gaußstr. 20
42097 Wuppertal
Germany
wiesen@uni-wuppertal.de

Wilson Chris

Mappin St.
Sheffield
S1 3JD
UK
c.w.wilson@sheffield.ac.uk

Wobrock Wolfram

24, Ave. des Landais
Laboratoire de Meteorologie-Physique
Univ. Blaise Pascal
Clermont-Ferrand
63177 Aubiere Cedex
France
wobrock@opgc.univ-bpclermont.fr

Wuebbles Donald

Univeristy of Illinois
Department of Atmospheric Sciences
105 S. Gregory St.
Urbana, IL 61801
USA
wuebbles@atmos.uiuc.edu

Yamada Hideshi

National Aerospace Laboratory
Aeropropulsion research Center
7-44-1 jindaijihigashi
Chofu Tokyo 182-8522
Japan
yamasyu@nal.go.jp

Zahn Andreas

Forschungszentrum Karlsruhe
Institute for Meteorology and Climate
Research
P.O. Box 3640
76021 Karlsruhe
Germany
andreas.zahn@imk.fzk.de

Zellner Reinhard

Institut für Physikalische Chemie
Universität Essen
Universitätsstrasse 5-7
45117 Essen
Germany
reinhard.zellner@uni-essen.de

Index of Authors

Aigner M.	25, 102, 197	Ebert V.	272
Anderson B.E.	27, 85	Feichter J.	197, 249
Anderson D.E.	134	Ferreira Gago C.	73
Arnold F.	41	Ferry D.	207, 266
Aufmhoff H.	197	Fichter C.	322
Ayers J.K.	295	Fiebig M.	41, 91, 197
Ballenthin J.	27	Flentje H.	197
Baltensperger U.	41	Flossmann A.	217
Baughcum S.L.	79, 134, 140, 145, 184, 238	Frank P.	59, 102, 197
Bergmann D.J.	134	Friedl R.R.	134
Berntsen T.K.	190	Fritzsche L.	41, 91
Beuermann J.	178	Garber D.P.	96, 224
Beyerle G.	197	Garnier F.	73
Blake D.	27	Gauss M.	122, 190
Bläsner M.	197	Geigle K.-P.	102, 197
Borrmann S.	197	Gerlinger P.	197
Boudries H.	27, 85	Ghazi A.	3
Branhan H.-S.	27	Giebel H.	41
Brasseur A.-L.	73	Gierens K.	197, 282, 316
Braun-Unkhoff M.	59, 102	Giesemann C.	272
Bregman B.	128	Gleitsmann G.	19
Brenninkmeijer C.	151	Gollinger K.	197
Brinkop S.	197, 282	Goos E.	59
Brunner D.	128	Gössling S.	156
Bukovnik M.	110	Graf J.	197
Busen R.	197	Grainger R.	310
Büttner S.	272	Green J.E.	334
Canagaratna M.	27, 85	Grewe V.	116, 122, 190
Chakrapani V.	288	Grimm F.	178
Costulis K.P.	96, 232	Guldberg A.	261
Cuenot B.	73	Gysel M.	41
Curtius J.	197	Haag W.	197
Danilin M.Y.	238	Han H.-S.	27
Demirdjian B.	266	Hauglustaine D.	122, 190
Dessens O.	162, 166	Hendricks J.	178, 197, 249
Doelling D.R.	224	Henseler S.	197
Döpelheuer A.	197, 249	Hitzenberger R.	41
Duda D.P.	224, 232	Hock N.	197
Dutta M.	140, 184	Hudgins C.	27
		Hughes K.J.	41

Hunton D.	27	Noland R.B.	328
Hurley C.D.	41	Noll B.	197
Hüttig G.	316	Norman P.D.	322
Immler F.	197, 306	Nyeki S.	41, 91
Isaksen I.	122, 166, 190	Onasch T.	85
Jain A.K.	184	Palikonda R.	224, 232, 288, 294
Kalivoda M.T.	110	Paoli R.	73
Kapernaum M.	25, 52	Patten K.O.	140
Kärcher B.	197, 249	Persiantseva N.M.	266
Katragkou E.	41	Peter T.	178
Kiendler A.	197	Petrea M.	52
Köhler M.	122, 173	Petzold A.	41, 91, 178, 197
Krämer M.	178, 197, 213, 272	Phan D.N.	288
Krüger V.	25, 102	Pitari G.	166, 190
Kruse H.	197	Plant J.	27
Kurtenbach R.	41, 52	Plohr M.	197
Lee D.S.	122, 322, 343	Plumb I.C.	79, 145
Linke C.	213	Ponater M.	197, 255, 316
Logan J.A.	134	Popovicheva O.B.	207, 266
Lohmann U.	197, 249	Pui D.	27
Lörzer J.C.	52	Puxbaum H.	41
Lückerath R.	102	Pyle J.A.	162, 173
Lukhovitskaya E.E.	266	Rainer P.	25
Madden P.	41	Randeniya L.K.	79
Mager F.	255	Read W.G.	238
Mancini E.	190, 166	Rodriguez J.M.	134
Mangold A.	197, 213, 272	Rogers H.L.	162, 166, 173, 310
Mannstein H.	197, 244	Rognerud B.	166
Marquart S.	197, 255, 316, 322	Rother T.	197
McEchern M.	27	Rotman D.A.	134
Meerkötter R.	300	Saathoff H.	213, 272
Meier A.	178	Sausen R.	190, 197, 255, 316, 322, 344
Meijer E.W.	128, 190	Schaefers S.	197
Meilinger S.	178	Schiller C.	178, 197
Meyer R.	197	Schlager H.	178
Miake-Lye R.	27, 37, 85	Schmid H.	197
Miller T.	27	Schnaiter M.	213
Minikin A.	197	Schneider J.	197
Minnis P.	96, 224, 232, 288, 294	Schneider-Kühnle Y.	102
Mirabel P.	67	Schrems O.	197, 306
Möhler O.	197, 213, 272	Schumann U.	41, 197, 244, 349
Monier M.	217	Schurath U.	197, 213, 272
Nguyen L.	224	Segers A.	128
Niedojadlo A.	52	Shonija N.K.	207, 266
Nielsen J.K.	278		

Slavinskaya N.	59, 102
Somnitz H.	19
Sorokin A.	67
Stein C.	41, 91
Stetzer O.	197, 272
Stilp T.	197
Stricker W.	102, 197
Ström J.	197
Ström L.	316
Stubenrauch C.J.	300
Suzanne J.	207, 266
Teichert H.	272
Thornhill L.	27
Timmreck C.	197
Toumi R.	328
Tripathi S.	310
Tsurikov M.	102
Vancassel X.	67, 310
Velthoven P.F.J. van	128
Viggiano A.	27
Vohralik P.F.	79, 145
Vrchoticky S.	41
Wagner R.	213, 172
Wahl C.	25, 41, 52, 197
Weimer S.	197
Wendling P.	197
Wiesen P.	41, 52
Wilhelm S.	197
Williams V.	328
Wilson C.W.	41
Winstead E.	27
Wobrock W.	217
Wohlfrom K.-H.	197
Wollny A.	197
Wormhoudt J.	27, 85
Worsnop D.	27, 85
Wuebbles D.J.	140, 184
Zaccardi V.	37
Zahn A.	151
Zellner R.	19
Zubareva N.A.	266